

Asymmetric Catalysis with Octahedral Chiral- at-Metal Iridium and Rhodium Complexes

A DISSERTATION

In

Chemistry

Presented to the Faculties of Philipps-Universität Marburg in Partial Fulfillment
of the Requirements for the Degree of Doctor of Science
(Dr. rer. nat.)

Chuanyong Wang

Jiangsu, P. R. China

Marburg/Lahn 2016

Die vorliegende Dissertation entstand in der Zeit von August 2013 bis November 2016 am Fachbereich Chemie der Philipps-Universität Marburg unter der Betreuung von Herrn Prof. Dr. Eric Meggers.

Vom Fachbereich Chemie der Philipps-Universität Marburg (Hochschulkenziffer: 1180) als Dissertation am 04.11.2016 angenommen.

Erstgutachter:	Prof. Dr. Eric Meggers
Zweitgutachter:	Prof. Dr. Armin Geyer
weitere Mitglieder Prüfungskommission:	Prof. Dr. Jörg Sundermeyer

Tag der mündlichen Prüfung: 13.12.2016

Acknowledgements

There are so many people to thank over the last three years. It would be impossible to finish my research projects and write this thesis without the generous help and constant encouragement of people around me.

First and foremost, I would like to express my sincere gratitude to Prof. Meggers for letting me enter his group and for outstanding supervision during my studies. To be honest, I had doubts when I first started my project, because it was a challenge for me to switch from organometallic chemistry to asymmetric catalysis. Prof. Meggers is a creative chemist and a great teacher, and he taught me how to do a research project from reaction design to manuscript preparation. His extensive knowledge and dedication towards the work inspired me a lot. I would also like to thank my master supervisor Prof. Qi Shen for introducing me to do my Ph.D. study in the Meggers group.

Next, I am very much thankful to Prof. Geyer and Prof. Sundermeyer for being the doctoral committee members and referring my thesis.

Furthermore, I am very grateful to thank all the members in the Meggers group. Dr. Lili Zhang, thank you for your kind help of synthesizing the substrates for my Chem. Eur. J. paper. Secretaries Ina Pinnschmidt and Andrea Tschirch, thank you for your patience with explaining so many important documents. Dr. Liang-A. Chen, Dr. Haohua Huo, Dr. Xiaodong Shen, Jia Ma, Yu Zheng, Jie Qin and Xiaoqiang Huang, thank you for your great support for publications. Thomas Mietke, thank you for translating the abstract of the thesis into German version. Dr. Chen Fu, Wei Zuo, Dr. Xiao Zhang, Yuqi Tan, Dr. Shipeng Luo, Dr. Qi Zhang, Dr. Cornelia Ritter, Elisabeth Martin, Markus Dörr, Rajathees Rajaratnam, Melanie Helms, Jens Henker, Thomas Cruchter, Timo Völker, Dr. Vladimir Larionov, thank you for your kind cooperation and you guys made my life easier.

In addition, I wish to thank the facilities directors in chemistry department: Dr. Klaus Harms in the X-ray crystallography; Dr. Xiulan Xie in the NMR department; and Dr. Uwe Linne of MS facility. Besides, I want to thank Philipp Röse for conducting the cyclic voltammetry studies.

Last but not the least, I would like to thank my lovely family and best friends for all their continued support and endless encouragement over the years. I wish all of you the life of happiness and prosperity.

Publications

1. C. Wang, K. Harms, E. Meggers, Catalytic Asymmetric C_{sp3}-H Functionalization under Photoredox Conditions by Radical Translocation and Stereocontrolled Alkene Addition, *Angew. Chem. Int. Ed.* **2016**, *55*, 13495–13498.
2. C. Wang, J. Qin, X. Shen, R. Riedel, K. Harms, E. Meggers, Asymmetric Radical-Radical Cross-Coupling through Visible-Light Activated Iridium Catalysis, *Angew. Chem. Int. Ed.* **2016**, *55*, 685–688.
3. C. Wang, Y. Zheng, H. Huo, P. Röse, L. Zhang, K. Harms, G. Hilt, E. Meggers, Merger of Visible Light Induced Oxidation and Enantioselective Alkylation with a Chiral Iridium Catalyst, *Chem. Eur. J.* **2015**, *21*, 7355–7359.
4. C. Wang, L.-A. Chen, H. Huo, X. Shen, K. Harms, L. Gong, E. Meggers, Asymmetric Lewis Acid Catalysis Directed by Octahedral Rhodium Centrochirality, *Chem. Sci.* **2015**, *6*, 1094–1100.
5. M. Helms, C. Wang, B. Orth, K. Harms, E. Meggers, Proline and α -Methylproline as Chiral Auxiliaries for the Synthesis of Enantiopure Bis-Cyclometalated Iridium(III) Complexes, *Eur. J. Inorg. Chem.* **2016**, 2896–2901.
6. H. Huo, C. Wang, K. Harms, E. Meggers, Enantioselective, Catalytic Trichloromethylation through Visible-Light-Activated Photoredox Catalysis with a Chiral Iridium Complex, *J. Am. Chem. Soc.* **2015**, *137*, 9551–9554.
7. X. Shen, H. Huo, C. Wang, B. Zhang, K. Harms, E. Meggers, Octahedral Chiral-at-Metal Iridium Catalysts: Versatile Chiral Lewis Acids for Asymmetric Conjugate Additions, *Chem. Eur. J.* **2015**, *21*, 9720–9726.
8. H. Huo, X. Shen, C. Wang, L. Zhang, P. Röse, L.-A. Chen, K. Harms, M. Marsch, G. Hilt, E. Meggers, Asymmetric Photoredox Transition-Metal Catalysis Activated by Visible Light, *Nature* **2014**, *515*, 100–103.
9. H. Huo, C. Fu, C. Wang, K. Harms, E. Meggers, Metal-Templated Enantioselective Enamine/H-bonding Dual Activation Catalysis, *Chem. Commun.* **2014**, *50*, 10409–10411.

Abstract

This thesis details the applications of a class of chiral-at-metal iridium(III) and rhodium(III) complexes for asymmetric catalysis.

A rhodium-based asymmetric catalyst Δ -**RhO** is introduced which derives its optical activity from octahedral centrochirality. Besides serving as the exclusive source of chirality, the rhodium center functions as a Lewis acid to activate α,β -unsaturated 2-acyl imidazoles by two point binding and thereby catalyzes the asymmetric Michael addition of CH-acidic β -dicarbonyl compounds, for which the rhodium catalyst is found to be superior to its iridium congener (chapter 3.1). Due to its straightforward proline-mediated synthesis, high catalytic activity, and tolerance towards moisture and air, this chiral-at-rhodium complex has been used as chiral Lewis acid catalyst for many other asymmetric transformations in the Meggers group.

The chiral-at-metal complexes Δ -**IrO** and Δ -**IrS** are investigated as highly efficient dual function photoredox/chiral Lewis acid catalysts in asymmetric photoactivated reactions. A simple chiral iridium complex Δ -**IrO** is capable of catalyzing the visible light activated α -aminoalkylation of 2-acyl-1-phenyl imidazoles, thereby serving as a “2-in-1” catalyst by combining photoinduced oxidation with asymmetric alkylation (chapter 3.2). Moreover, its derivative Δ -**IrS** is successfully utilized to the catalytic enantio- and diastereoselective redox coupling of trifluoromethyl ketones with tertiary amines to form 1,2-diamino alcohols (chapter 3.3). This single catalyst strategy provides new avenues for the synthesis of non-racemic molecules.

An alternative strategy of merging the chiral Lewis acid Δ -**RhS** with photoredox catalyst *fac*-[Ir(ppy)₃] is well applied to the asymmetric photoredox-mediated C(sp³)-H functionalization. This synthetic strategy exploits a radical translocation (1,5-hydrogen transfer) from an oxygen-centered to a carbon-centered radical with a subsequent stereocontrolled radical addition, affording C-C bond formation products with high enantioselectivities (up to 97% *ee*). Notably, the previously developed dual function catalyst Δ -**IrS** is not applicable for this asymmetric transformation (chapter 3.4).

Zusammenfassung

In der vorliegenden Dissertation wird die Anwendung neuer Iridium(III)- und Rhodium(III)-Komplexe mit metallzentrierter Chiralität in der asymmetrischen Katalyse erläutert.

Es wird eine neue Klasse chiraler Rhodium(III)-Komplexe vorgestellt, die ihre optische Aktivität ausschließlich durch ihre oktaedrische metallzentrierte Chiralität erhält. Darüber hinaus wirkt das Metallzentrum nicht nur exklusiv als Quelle der Chiralität, sondern als reaktives, LEWIS-saures Zentrum. Zum Einsatz kommt Δ -**RhO** bei der Aktivierung von α,β -ungesättigten 2-Acylimidazolen in der asymmetrischen Michael-Addition mit CH-aciden β -Dicarbonylen. In dieser Reaktion zeigt Δ -**RhO** im Vergleich zu seinem Δ -**IrO**-Analogon überlegene Aktivität (Kapitel 3.1). Bedingt durch seine einfache Prolin-vermittelte Synthese, seine hohe katalytische Aktivität, die hohe Stabilität an Luft und einer Toleranz gegenüber Feuchtigkeit, wird der „chiral-at-metal“ Komplex Δ -**RhO** in der Arbeitsgruppe MEGGERS mittlerweile in einer Vielzahl asymmetrischer Katalysen als chiraler LEWIS-Säure-Katalysator eingesetzt.

Weitere Untersuchungen hinsichtlich der Eignung von Δ -**IrO** und Δ -**IrS** als bifunktionelle Photoredox/LEWIS-Säure Katalysatoren in asymmetrischen, durch Licht aktivierte Reaktionen, wurden in den folgenden Projekten durchgeführt. Der einfach gehaltene chirale Iridium(III)-Komplex Δ -**IrO** ist in der Lage, die durch sichtbares Licht aktivierte α -Aminoalkylierung von 2-Acyl-1-phenylimidazol zu katalysieren. Dabei fungiert Δ -**IrO** als "2-in-1"-Katalysator durch die Kombination von photoinduzierter Oxidation und asymmetrischer Alkylierung (Kapitel 3.2). Des Weiteren wurde das Derivat Δ -**IrS** erfolgreich für die enantio- und diastereoselektive Redox-Kupplung von Trifluormethylketonen mit tertiären Aminen zur Synthese von 1,2-Diaminoalkoholen eingesetzt (Kapitel 3.3). Die gezeigte Strategie, einen einzelnen multifunktionellen Katalysator zu verwenden, ebnet neue Wege zur Synthese nicht-racemischer Verbindungen.

Als alternative konnte der chirale LEWIS-Säure-Katalysator Δ -**RhS** mit dem Photoredox-Katalysator *fac*-[Ir(ppy)₃] in der asymmetrischen, photoredox-vermittelten C(sp³)-H Funktionalisierung eingesetzt werden. In dieser Strategie wird eine 1,5-Wasserstoff-Verschiebung genutzt, um ein Sauerstoffradikal in ein Kohlenstoffradikal zu überführen, welches unter katalysatorkontrollierter C-C-Bindungsknüpfung

Produkte mit hohem Enantiomerenüberschuss erzeugt (bis zu 97% *ee*). Beachtenswert ist, dass der analoge bifunktionelle Iridiumkomplex Δ -**IrS** nicht für diese Reaktion geeignet ist (Kapitel 3.4).

Table of Contents

Acknowledgements	I
Publications	III
Abstract	V
Zusammenfassung	VII
Table of Contents	IX
Chapter 1: Theoretical Part	1
1.1 Introduction	1
1.2 Asymmetric Catalysis with Octahedral Chiral only-at-Metal Complexes	2
1.2.1 Octahedral Chiral only-at-Metal Ruthenium(II) and Cobalt(III) Complexes for Asymmetric Catalysis	2
1.2.2 Octahedral Chiral only-at-Metal Iridium(III) Complexes for Asymmetric Catalysis	3
1.3 Asymmetric Photocatalysis Activated by Visible Light	8
1.3.1 Dual Catalyst Systems in Asymmetric Photoredox Catalysis	8
1.3.2 Single Catalyst Systems in Asymmetric Photoredox Catalysis.....	16
1.4 Conclusions	20
Chapter 2: Aim of the Work	23
Chapter 3: Results and Discussion	25
3.1 Asymmetric Lewis Acid Catalysis Directed by Octahedral Rhodium Centrochirality	25
3.1.1 Catalyst Design.....	25
3.1.2 Catalyst Synthesis.....	25
3.1.3 Catalytic Reactions.....	29
3.1.4 Mechanistic Investigations	34
3.1.5 Conclusions	37
3.2 Merger of Visible Light Induced Oxidation and Enantioselective Alkylation with Chiral Iridium Catalyst	39
3.2.1 Reaction design	39
3.2.2 Initial Experiments and Reaction Optimization	40
3.2.3 Substrate Scope	42
3.2.4 Plausible Mechanism.....	45
3.2.5 Mechanistic Investigations	46
3.2.6 Conclusions	51
3.3 Asymmetric Radical-Radical Cross-Coupling through Visible Light Activated Iridium Catalysis	53
3.3.1 Reaction Design	53

3.3.2 Initial Experiments and Reaction Optimization	54
3.3.3 Substrate Scope	56
3.3.4 Plausible Mechanism.....	59
3.3.5 Mechanistic Investigations	60
3.3.6 Conclusions	64
3.4 Catalytic Asymmetric C(sp³)-H Functionalization under Photoredox Conditions by Radical Translocation and Stereocontrolled Alkene Addition.....	66
3.4.1 Reaction Design	66
3.4.2 Initial Experiments and Reaction Optimization	67
3.4.3 Substrate Scope	69
3.4.4 Plausible Mechanism.....	73
3.4.5 Mechanistic Investigations	74
3.4.6 Conclusions	79
Chapter 4: Summary and Outlook.....	81
Chapter 5: Experimental Part	88
5.1 Materials and Methods	88
5.2 Asymmetric Lewis Acid Catalysis Directed by Octahedral Rhodium Centrochirality	91
5.2.1 Synthesis of the Rhodium Catalysts Λ - RhO and Δ - RhO	91
5.2.2 Catalytic Reactions with Δ - IrO and Δ - RhO	94
5.2.3 Investigation of the Stability of Rhodium Catalyst Λ -/ Δ - RhO	100
5.2.4 Investigation of the Proposed Catalyst-Coordinated Substrate Intermediate	102
5.2.5 The Acetonitrile Exchange Rates: Δ - RhO vs. Δ - IrO	103
5.2.6 Single Crystal X-Ray Diffraction.....	105
5.3 Merger of Visible Light Induced Oxidation and Enantioselective Alkylation with Chiral Iridium Catalyst	106
5.3.1 Synthesis of Substrates	106
5.3.2 Iridium-Catalyzed Photoredox Reactions.....	113
5.3.3 Substrate-Coordinated Iridium Complex (Proposed Intermediate A).....	122
5.3.4 Synthesis of the Proposed Intermediate Iridium Enolate Complex B	124
5.3.5 Control Reactions	124
5.3.6 Single-Crystal X-Ray Diffraction Studies.....	125
5.4 Asymmetric Radical-Radical Cross-Coupling through Visible Light Activated Iridium Catalysis	126
5.4.1 Synthesis of Substrates	126
5.4.2 Iridium-Catalyzed Photoredox Reactions.....	132
5.4.3 Mechanistic Investigations	148
5.4.4 Single-Crystal X-Ray Diffraction Studies.....	153
5.5 Catalytic Asymmetric C(sp³)-H Functionalization under Photoredox Conditions by Radical Translocation and Stereocontrolled Alkene Addition.....	154
5.5.1 Synthesis of Substrates	154
5.5.2 Rhodium-Catalyzed Photoredox Reactions.....	159

5.5.3 Synthetic Transformations	175
5.5.4 Mechanistic Investigations	177
5.5.5 Single-Crystal X-Ray Diffraction Studies.....	185
Chapter 6: Appendices	188
6.1 List of Abbreviations.....	188
6.2 List of Figures	190
6.3 List of Schemes	196
6.4 List of Tables.....	197
6.5 List of Synthesized Comounds	198
6.5.1 List of Iridium/Rhodium Complexes	198
6.5.2 List of Organic Compounds	199
6.6 List of Spectra of Compounds.....	204
6.6.1 NMR spectra of Iridium/Rhodium Complexes	204
6.6.2 CD Spectra of Enantiopure Rhodium Complexes.....	211
6.6.3 HPLC Spectra of Compounds	213
6.7 List of Crystal Structure Data.....	277
Statement.....	301
Curriculum Vitae.....	302

Chapter 1: Theoretical Part

1.1 Introduction

Asymmetric catalysis is a fundamental methodology in modern chemistry and is particularly important in the field of pharmaceuticals, as the different enantiomers or diastereomers of a molecule often have different biological activity.¹ Thalidomide is a striking example that illustrates the difference in which the (*R*)-enantiomer acts as a sedative in contrast to deformities caused by the (*S*)-enantiomer (Figure 1).² Therefore, the asymmetric synthesis of enantiomerically pure compounds is under intense scrutiny.

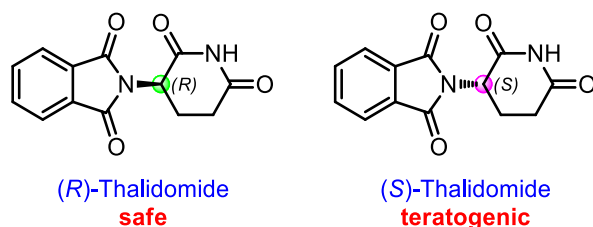
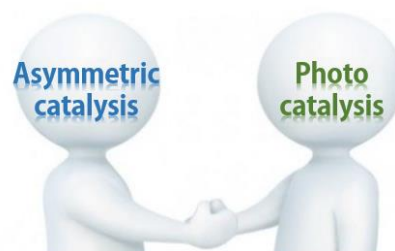


Figure 1 Structures of (*R*)-thalidomide and (*S*)-thalidomide.

Photocatalysis has seen growing interest not only in the reactions of small molecules such as H₂O (water splitting)³ and CO₂ (forming solar fuels)⁴, but also in organic synthesis.⁵ Particularly, the recent progress in this area has been promoted by using visible light as a driving force, providing a number of otherwise unachievable modes of molecular transformations.⁶

Combining these two aspects, visible light induced asymmetric photocatalysis is appreciated as a powerful tool to achieve high efficiency and selectivity in asymmetric synthesis.⁷ Whereas asymmetric catalysis is considered as an economic strategy to obtain enantiopure compounds, visible



light can assist in generating highly reactive intermediates under mild conditions and at the same time providing an environmentally friendly and sustainable source of energy for activating chemical reactions.

This chapter will be divided into two parts: 1) summarize some typical examples of asymmetric catalysis with octahedral chiral only-at-metal complexes; 2) discuss two systems of visible light

activated asymmetric catalysis, namely dual catalyst systems based on the combined use of photoredox with chiral catalyst or single chiral catalyst systems.

1.2 Asymmetric Catalysis with Octahedral Chiral only-at-Metal Complexes

A crucial role in asymmetric catalysis is the development of efficient chiral catalysts. Octahedral chiral only-at-metal complexes are an emerging class of catalysts for catalytic asymmetric synthesis of non-racemic compounds.⁸ For the developed octahedral chiral only-at-metal complexes, the central transition metal always serves as a structural anchorpoint and provides metal centrochirality, catalysis is mediated through the ligand sphere, thereby merging organocatalysis with transition metal catalysis.

1.2.1 Octahedral Chiral only-at-Metal Ruthenium(II) and Cobalt(III) Complexes for Asymmetric Catalysis

In 2003, the Fontecave group reported asymmetric oxidation of sulfide with an octahedral ruthenium(II) complex Λ -**Ru1** in which the ruthenium ion is coordinated by two 2,9-dimethyl-1,10-phenanthroline ligands and two labile acetonitrile molecules (Figure 2). Despite the low enantioselectivity obtained (18% *ee*), this study reveals the first experimental validation of the concept that an octahedral chiral only-at-metal complex has the potential to catalyze enantioselective oxidations.⁹ Later, they reported asymmetric transfer hydrogenation with a dinuclear ruthenium catalyst Λ -**Ru2**, in which the Λ -[Ru(2,2'-bipyridine)₂(2,2'-bipyrimidine)]²⁺ moiety serves as a chiral bidentate ligand for a second, catalytically active ruthenium complex. The low enantioselective (26% *ee*) can be rationalized by the large distance between the chiral and catalytic centers.¹⁰

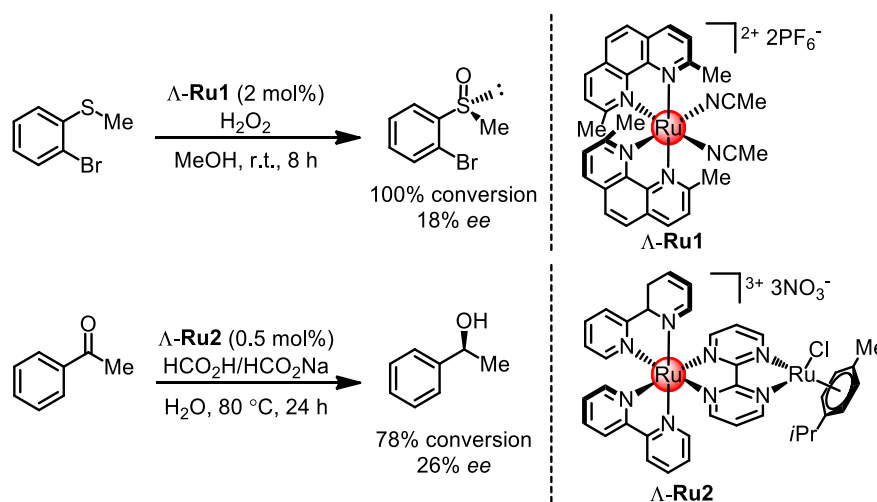


Figure 2 Asymmetric catalysis by octahedral chiral-at-metal ruthenium(II) complexes.

In 2008, Gladysz and co-workers demonstrated asymmetric conjugate addition with a simple octahedral chiral-at-metal Werner complex.¹¹ As shown in Figure 3, the enantiopure chiral-at-metal cobalt(III) complex Δ -Co is capable of catalyzing the Michael addition of dimethyl malonate to cyclopentenone in CH_2Cl_2 to afford the adduct in 78% yield, albeit with a low enantioselectivity of just 33% *ee*. The chirality induction in this reaction relies on the stereogenic octahedral cobalt center and N-H bonds (H-bonding donors).

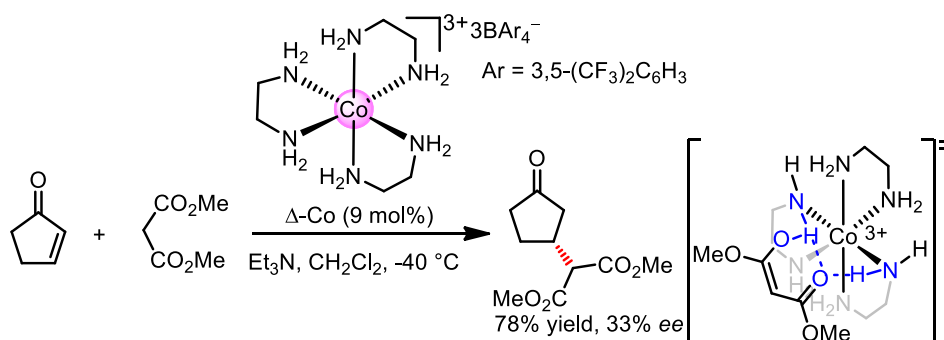


Figure 3 Asymmetric Michael addition by a chiral-at-metal Werner complex.

1.2.2 Octahedral Chiral only-at-Metal Iridium(III) Complexes for Asymmetric Catalysis

For the past several years, the Meggers group has successfully designed and synthesized a series of octahedral chiral-at-metal iridium(III) complexes for asymmetric catalysis.

In 2013, the Meggers group reported a chiral-at-metal iridium(III) complex Λ -Ir1 for the highly efficient catalytic asymmetric transfer hydrogenation of β,β -disubstituted nitroalkenes (Figure 4).¹² The design of the substitutionally inert biscyclometalated iridium complex Λ -Ir1 was inspired by the non-covalent organocatalyst thiourea.¹³ While the pyrazole moiety acts as a double H-bonding donor for the nitroalkene, a hydroxy group serves as a H-bonding acceptor for the Hantzsch ester (Figure 5). Notably, although the iridium complex relies only on the formation of three hydrogen bonds, it exceeds the performance of most organocatalysts with respect to enantioselectivities (up to 99% *ee*) and catalyst loadings (down to 0.1 mol%). This work is of great significance as it reveals the potential of octahedral metal complexes as chiral scaffolds for the design of high-performance asymmetric catalysts.

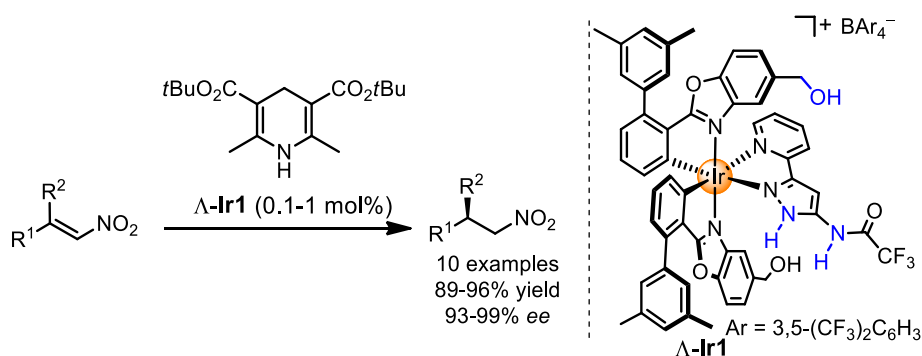


Figure 4 Asymmetric transfer hydrogenation catalyzed by a chiral-at-metal iridium(III) complex.

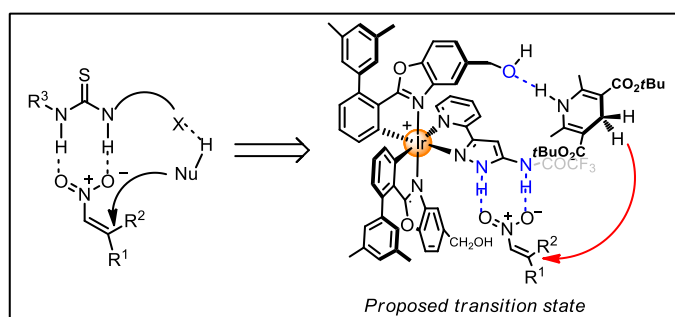


Figure 5 Proposed transition state of Δ -Ir1 in asymmetric transfer hydrogenation.

This non-covalent metal-templated complex was further applied to a more challenging transformation, namely enantioselective Friedel-Crafts alkylation of indoles to β,β -disubstituted nitroolefins. By using 1 mol% of Δ -Ir2, all-carbon quaternary centers can be created in high enantioselectivities of up to 98% ee (Figure 6). Since the iridium catalyst functions completely as a H-bonding catalyst, the high reactivity and enantioselectivity of Δ -Ir2 are superior to the performance of Δ -Ir1 (70% ee with 5 mol% catalyst loading) which can be rationalized by the H-bonding affinity of the carboxamide ($-\text{CONEt}_2$, Δ -Ir2) over the hydroxyl group ($-\text{OH}$, Δ -Ir1) in combination with the preferred conformation of the amide group, thereby placing the amide oxygen in an ideal position for H-bonding with the indole nucleophile. Notably, tested thiourea organocatalysts only provided very low enantioselectivities for this challenging formation.¹⁴

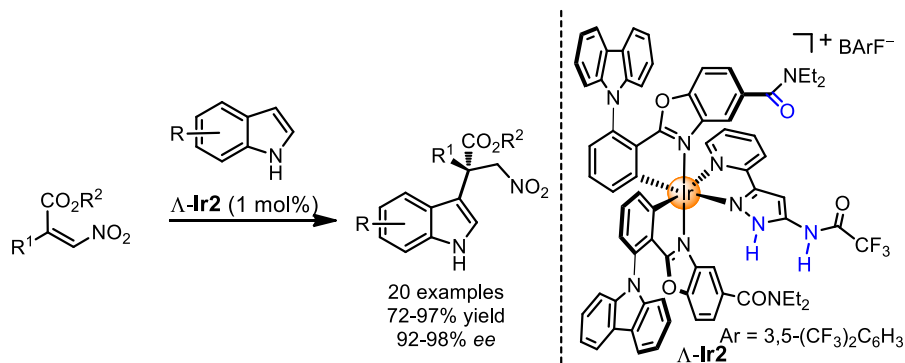


Figure 6 Asymmetric Friedel-Crafts alkylation catalyzed by a chiral-at-metal iridium(III) complex.

Inert octahedral metal complexes are general, powerful templates for the efficient design of bifunctional catalysts. The developed octahedral 3-aminopyrazolato iridium(III) complexes Λ -**Ir3** and Λ -**Ir4** as chiral Brønsted base catalysts are suitable for highly effective asymmetric sulfa-Michael addition and aza-Henry reactions, permitting catalyst loadings down to 0.02 and 0.25 mol%, respectively (Figure 7). The observed high reactivity and stereoselectivity can be rationalized by the bifunctional mode of action in which the iridium catalyst, after the initial proton transfer, controls a ternary complex through defined H-bonding interactions (Figure 8).¹⁵

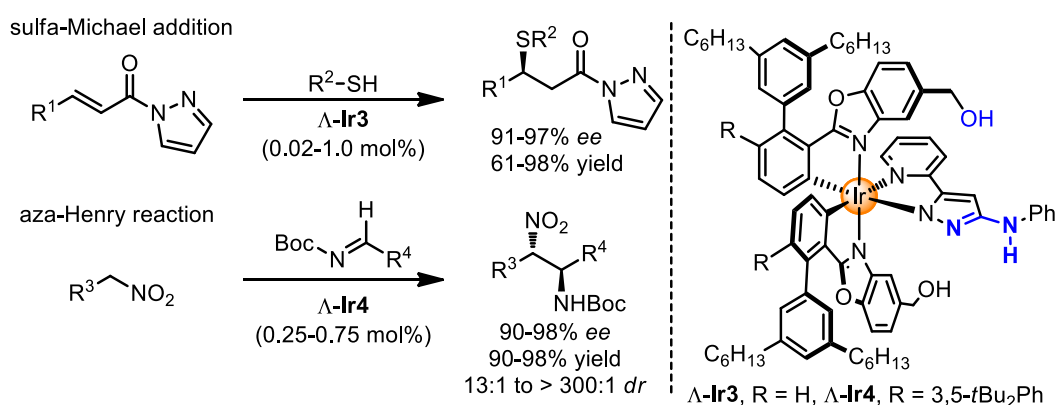


Figure 7 Asymmetric sulfa-Michael and aza-Henry reactions catalyzed by chiral Brønsted base catalysts.

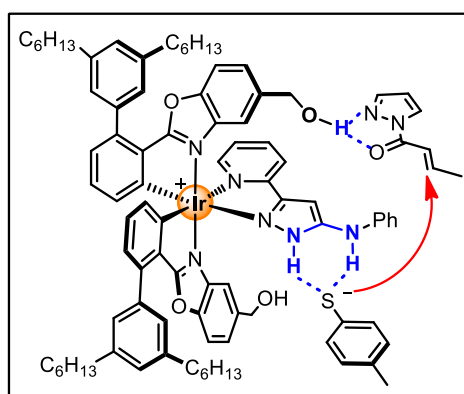


Figure 8 Proposed ternary complex for the asymmetric sulfa-Michael addition catalyzed by Λ -**Ir3**.

Asymmetric enamine/H-bonding dual activation catalyst is presented as another successful example for the power for a metal-templated design of “organocatalyst” (Figure 9). An octahedral chiral-at-metal complex Λ -**Ir5** catalyzes the enantioselective α -amination of aldehydes with high enantioselectivities of up to 97% *ee* and catalyst loadings down to 0.1 mol%. Mechanistically, this highly efficient chiral iridium complex can be rationalized by a dual activation catalysis which converts the aldehyde into a nucleophilic enamine, while at the same time activating the azodicarboxylate electrophile through H-bonding with one OH-group (Figure 10).¹⁶ Notably, Λ -**Ir5** constitutes one of the most efficient catalysts for the enantioselective α -amination of aldehydes to date.

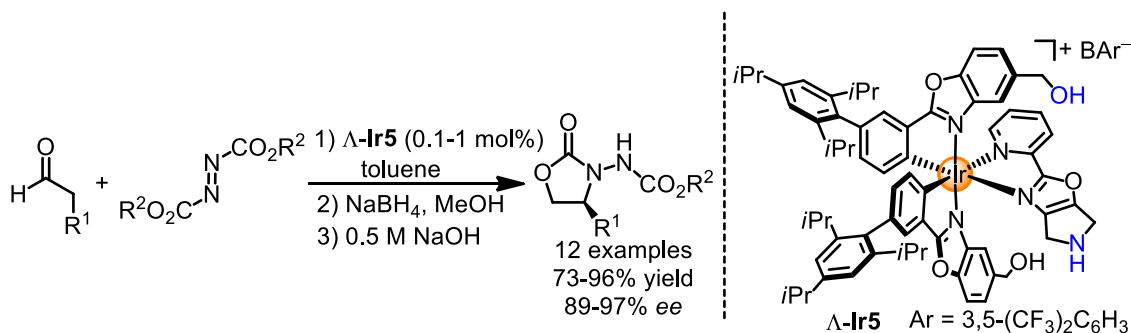


Figure 9 Asymmetric catalysis by enamine/H-bonding dual activation chiral-at-metal Iridium(III) catalyst.

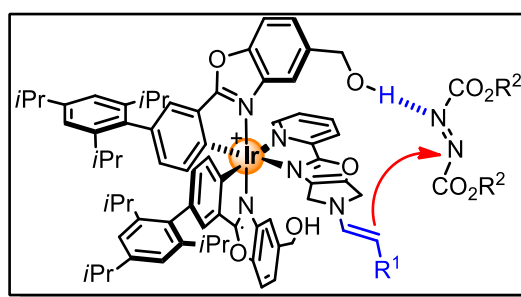


Figure 10 Proposed enamine/H-bonding mechanism model of the asymmetric α -amination catalyzed by iridium complex Δ -Ir5.

Having demonstrated several remarkable asymmetric transformations directed by the ligand sphere of the stereogenic iridium center, the Meggers group further modified the metal-templated system to Lewis acid catalysts. In 2014, the Meggers group introduced a substitutionally labile chiral-at-metal iridium(III) complex Δ -IrO. As shown in Figure 11, the catalytic activity investigation demonstrated that the chiral complex Δ -IrO can effectively catalyze the enantioselective Friedel-Crafts addition of indoles to α,β -unsaturated 2-acyl imidazoles with high yields (75-99%) and excellent enantioselectivities (90-98% ee) at low catalyst loadings (0.25-2 mol%).¹⁷

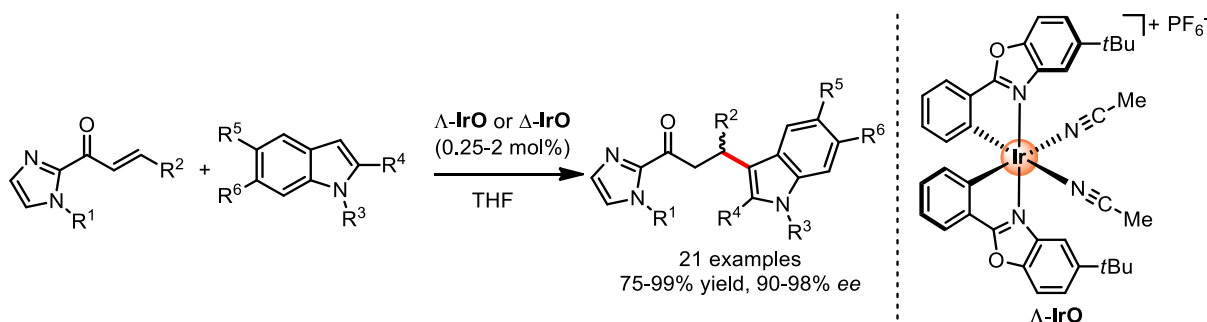


Figure 11 Asymmetric Friedel-Crafts reaction by a simple chiral-at-metal Lewis acid catalyst.

The iridium complex Δ -IrO serves as a chiral Lewis acid by activating α,β -unsaturated 2-acyl imidazoles through bidentate N,O-coordination. Despite its substitutional lability, the metal-centered chirality is maintained throughout the catalysis. A proposed model for the asymmetric induction in the

course of the indole addition by using Λ -IrO as catalyst is shown in Figure 12 and demonstrates that *Re* face of the alkene is sterically shielded effectively by one *tert*-butyl group, and the *Si* face is leaving open for the approach of nucleophile. This novel class of reactive chiral-at-metal complexes has been proven to be of high value for a variety of asymmetric transformations in the Meggers group.¹⁸

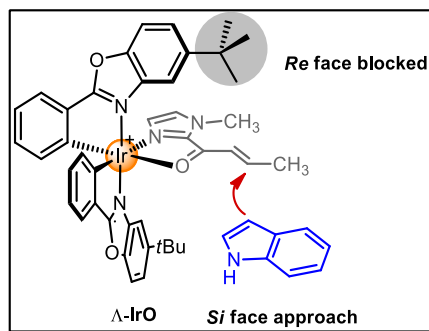


Figure 12 Proposed reaction model of enantioselective Friedel-Crafts addition with Λ -IrO.

1.3 Asymmetric Photocatalysis Activated by Visible Light

In homogeneous photocatalysis, photoredox catalysis employs small quantities of a light-sensitive compound (photocatalyst) that, when excited by light, can mediate the transfer of electron or energy between chemical compounds.¹⁸ Desired features of common photocatalysts are as follows: 1) photostability; 2) long excited-state lifetime; 3) strong absorption in the visible region; 4) high reduction or oxidation potential to achieve electron transfer to substrates. Alongside organic dyes and inorganic semiconductors, the most widely-applied and effective photocatalysts are coordinatively saturated transition-metal-pyridyl complexes which are outlined in Figure 13.¹⁹

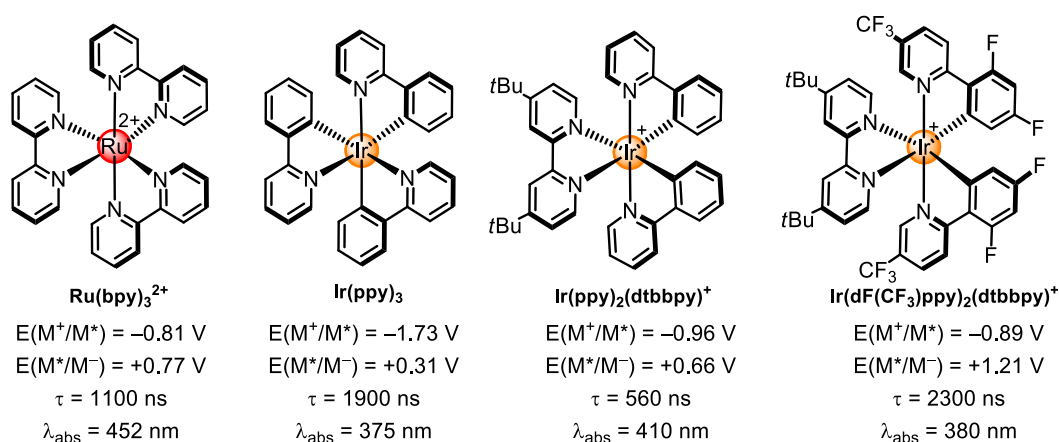


Figure 13 The common classic transition metal photocatalysts (vs. SCE).

1.3.1 Dual Catalyst Systems in Asymmetric Photoredox Catalysis

The combination of visible light redox catalysts with chiral catalysts has enabled a number of highly enantioselective photoinduced reactions. The following section summarized some representative catalytic asymmetric transformations utilizing dual photoredox organocatalysis or transition-metal catalysis.

1) Dual photoredox organocatalysis: covalent interactions

In 2008, MacMillan's group reported the first example of the combination of visible light induced photoredox catalysis and asymmetric organocatalysis.²⁰ Accordingly, the reaction of aldehydes with bromo diethylmalonates or phenacyl bromides in the presence of [Ru(bpy)₃]Cl₂, chiral imidazolidinone and 15 W compact fluorescent lamp (CFL) afforded α -alkylation products with highly enantioselectivities of up to 99% *ee* (Figure 14). The generality of this dual photoredox organocatalytic protocol was demonstrated by further investigating the enantioselective α -trifluoromethylation²¹ and α -benzylation of aldehydes.²²

A mechanism for this transformation combining an enamine catalytic cycle and a photoredox catalytic cycle is shown in Figure 14. It is generally accepted that a photoredox catalytic cycle results in the reductive, heterolytic cleavage of the benzyl bromide or phenacyl bromide to afford electron deficient carbon radical which rapidly added to the electron rich double bond of chiral intermediate enamine in a stereocontrolled fashion. The generated α -aminoalkyl radical is oxidized to iminium ion *via* single electron transfer (SET). The iminium ion intermediate is further hydrolyzed to form the α -alkylation product, and thereby regenerate the amine catalyst for a new catalytic cycle. It is most likely that product-forming step would be chain-propagating reduction of the alkyl electrophile substrates by the intermediate α -amino radical.²³

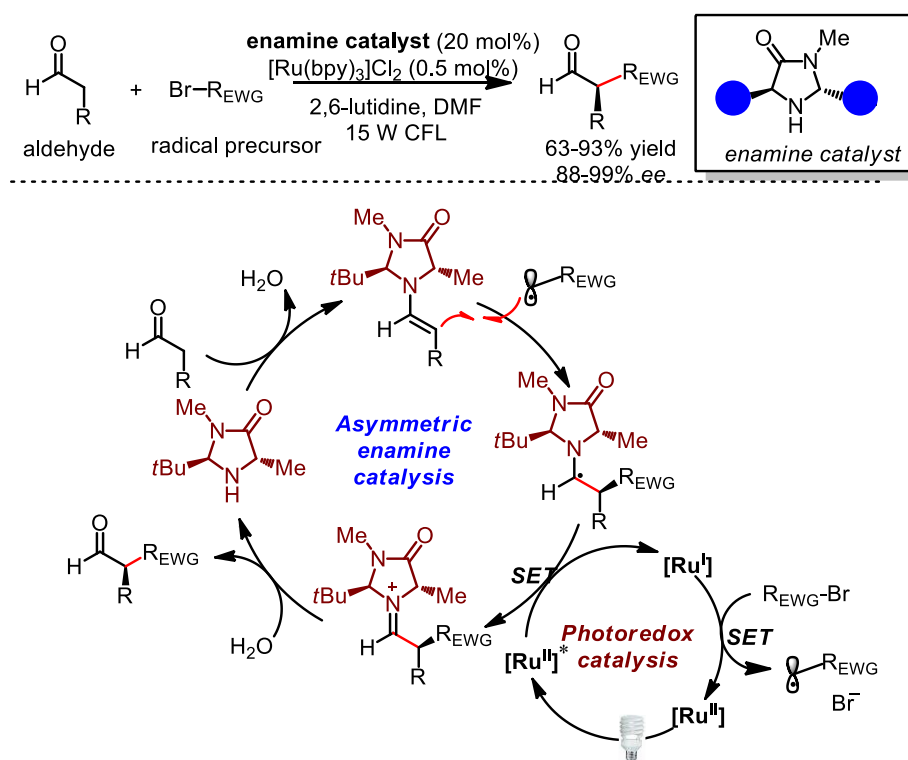


Figure 14 Enantioselective α -functionalization of aldehydes *via* dual photoredox enamine catalysis.

Following MacMillan's initial work, several other research groups have merged enamine catalysis with photocatalysis. For example, Zeiter, König, and Pericàs revealed that transition metal photocatalysts could be replaced by organic dyes and inorganic semiconductors in this asymmetric photoredox enamine catalysis system.²⁴ Luo and co-workers extended this strategy and applied to the enantioselective α -alkylation of β -ketocarboxyls by merging photoredox catalysis with chiral primary amine catalysis (Figure 15).²⁵ The reactions enable the creation of all-carbon stereocenters with excellent enantioselectivities (up to 99% *ee*) and a broad substrate scope (28 examples). The author proposed that

the high asymmetric induction can be rationalized by a hydrogen bond in the transition state between the protonated tertiary amine (N-H as hydrogen bond donor) of the intermediate enamine and the intermediate phenacyl radical (C=O as hydrogen bond acceptor).

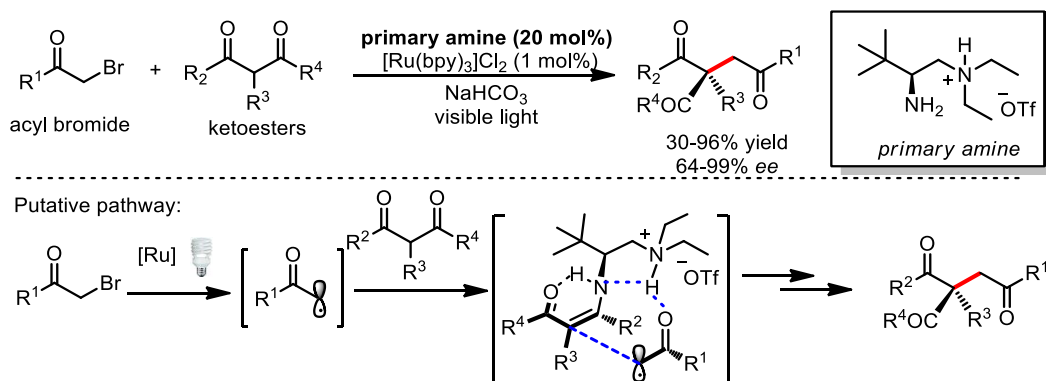


Figure 15 Asymmetric α -photoalkylation of β -ketocarboxylates with a combination of chiral primary amine and photoredox catalyst.

Recently, Melchiorre and co-workers reported an excellent work about the enantioselective radical conjugate addition to β,β -disubstituted cyclic enones driven by UV light (365 nm) or visible light.²⁶ The outlined visible light activated iminium dual catalysis platform enables challenging quaternary carbon stereocenters to be constructed in a highly enantioselective manner (Figure 16). The critical to their success is the design of a chiral organic catalyst, containing a redox-active carbazole moiety, which drives the formation of iminium ion intermediates and the stereoselective trapping of photogenerated carbon-centred radicals. The key step in the catalytic transformation is the rapid intramolecular electron transfer between the electron-rich carbazole and the α -iminyl radical cation, thereby forging the corresponding enamine and avoiding the undesired β -scission event.

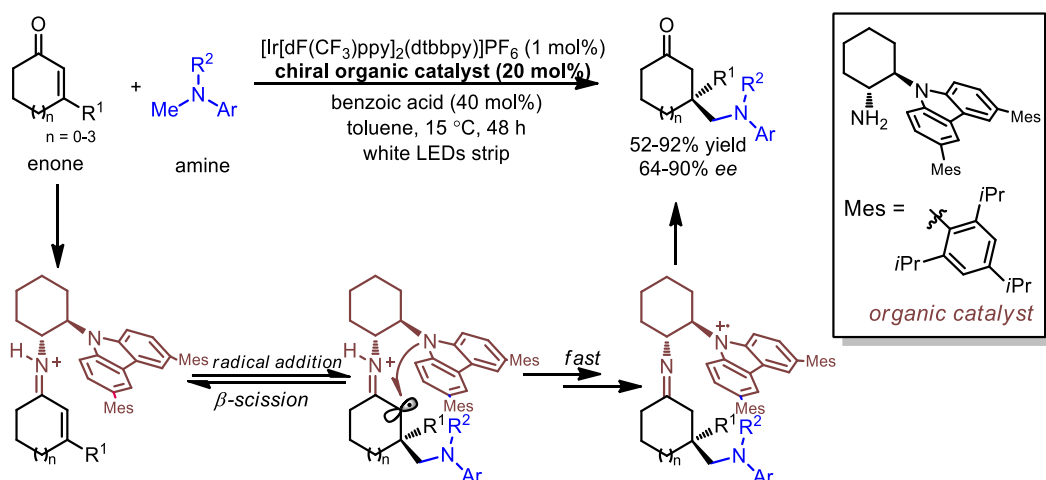


Figure 16 Asymmetric radical conjugate addition by photoredox iminium dual catalysis.

In 2012, the Rovis group identified a productive dual catalysis mode which enables the catalytic asymmetric α -acylation of tertiary amines.²⁷ Through the powerful combination of chiral *N*-heterocyclic carbene (NHC) catalyst and photoredox catalyst $[\text{Ru}(\text{bpy})_3]\text{Cl}_2$, the α -acylation products could be produced in high yields (up to 94% yield) with high enantioselectivities (up to 92% *ee*). Mechanistically, single-electron oxidation of a tertiary amine followed by hydrogen atom abstraction results in the formation of iminium ion. Meanwhile, interaction of a chiral NHC catalyst with an aldehyde generates the nucleophilic Breslow-type complex. The chiral Breslow intermediate intercepts the newly formed iminium ion, thereby forming the non-racemic α -amino ketone product. The stoichiometric amount of oxidant *m*-dinitrobenzene (*m*-DNB) are needed for this asymmetric transformation (Figure 17).

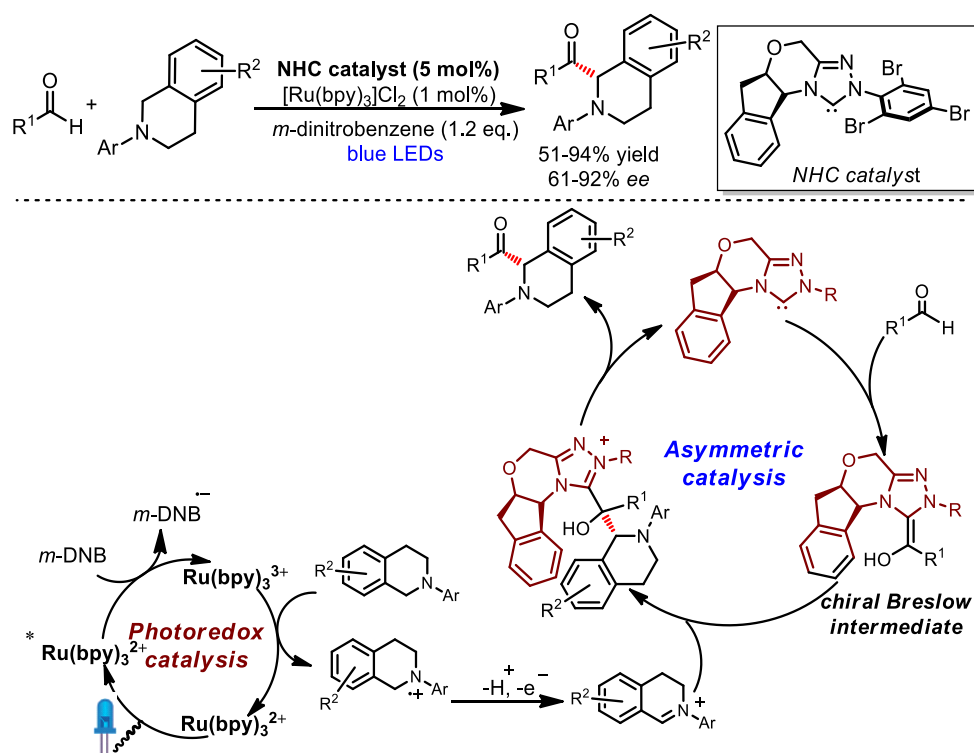


Figure 17 Asymmetric α -acylation of tertiary amines by photoredox carbene dual catalysis.

2) Dual photoredox organocatalysis: noncovalent interactions

In 2013, the Knowles group reported a photoinduced proton-coupled electron transfer (PCET) protocol for the asymmetric reductive coupling of ketones and hydrazones.²⁸ Accordingly, the exposure of ϵ -hydrazino arylketones to blue light in the presence of $[\text{Ir}(\text{ppy})_2(\text{dtbbpy})]\text{PF}_6$, the chiral phosphoric acid, and Hantzsch ester (HE) provided the *syn* 1,2-amino alcohols with 45-96% yield and 77-95% *ee* (Figure 18). Mechanistically, photoactivated $[\text{Ir}^{\text{III}}]^*$ accepts an electron from Hantzsch ester to generate $[\text{Ir}^{\text{III}}]^{-\bullet}$. The phosphoric acid forms a H-bonding with the aryl ketone, followed by an electron transfer

from the $[\text{Ir}^{\text{III}}]^{*}$ to the aryl ketone in concert with proton transfer from the Brønsted acid to the oxygen of the formed ketyl radical. The enantioselective radical cyclization is based on the H-bonding between the chiral phosphate anion and the OH-group of the ketyl. Hantzsch ester acts as a terminal reduction agent in the catalytic cycle.

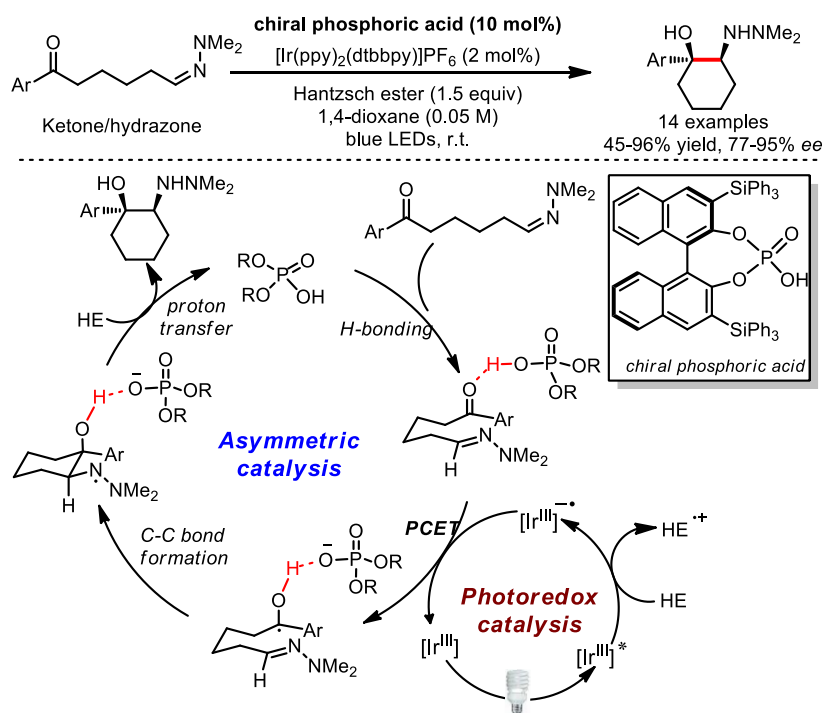


Figure 18 Enantioselective aza-pinacol cyclizations by a chiral phosphoric acid catalyst and a photoredox catalyst.

In 2014, Stephenson and Jacobsen reported a sequential two-step asymmetric Mukaiyama Mannich reaction.²⁹ With the employment of a chiral thiourea H-bonding catalyst combined with a photoredox catalyst $[\text{Ru}(\text{bpy})_3]\text{Cl}_2$ under the irradiation of blue LEDs, single-electron oxidation of *N*-aryl tetrahydroisoquinolines followed by nucleophilic addition with silyl enol ethers afforded α -alkylated products in 11-72% yields and 42-99% ee (Figure 19). In the first step, 1-chlorinated products are generated from 1,2,3,4-tetrahydroisoquinolines by photooxidation with stoichiometric oxidant carbon tetrachloride. In the second step, the addition of the chiral thiourea results in the formation of an intermediate contact ion pair (a H-bonded chloride anion and the iminium ion), which enantioselectively reacts with the silyl enol ether to provide the non-racemic compounds with moderate to high enantioselectivities.

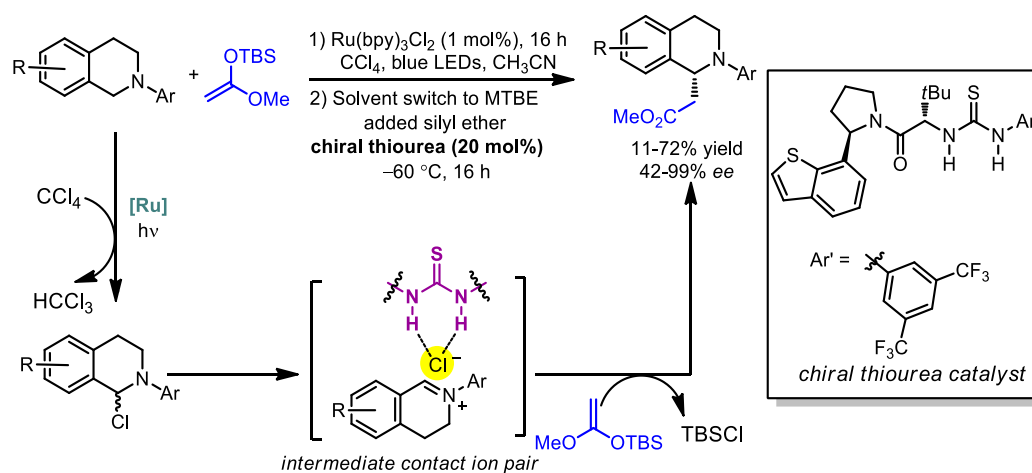


Figure 19 Asymmetric α -acylation of tertiary amines by photoredox hydrogen bonding dual catalysis.

Recently, the Ooi group developed a redox neutral, highly enantioselective α -coupling of *N*-arylaminoethanes with *N*-sulfonyl imines under visible light irradiation. By using chiral arylaminophosphonium ion and iridium complex $[\text{Ir}(\text{ppy})_2(\text{Me}_2\text{Phen})]\text{BAr}$ ($\text{Ar} = 3,5\text{-(CF}_3)_2\text{C}_6\text{H}_3$) as co-catalyst, the coupling products were achieved with 60-90% yields and 85-98% *ee*.³⁰ In their proposed mechanism (Figure 20), photoexcited iridium catalyst is reductively quenched by *N*-arylamine. The thereby generated $[\text{Ir}^{\text{II}}]$ serves as a strong reducing agent and transfers a single electron to imine under formation of a prochiral radical anion. The chiral aminophosphonium ion (H-bonding donor) undergoes counterion exchange with the prochiral radical anion to form a chiral ion pair, thereby reacting with deprotonated α -aminoalkyl radical to afford the coupling product. The critical success factor is that chiral ion controls the enantiofacial approach of the oxidatively generated α -aminoalkyl radical.

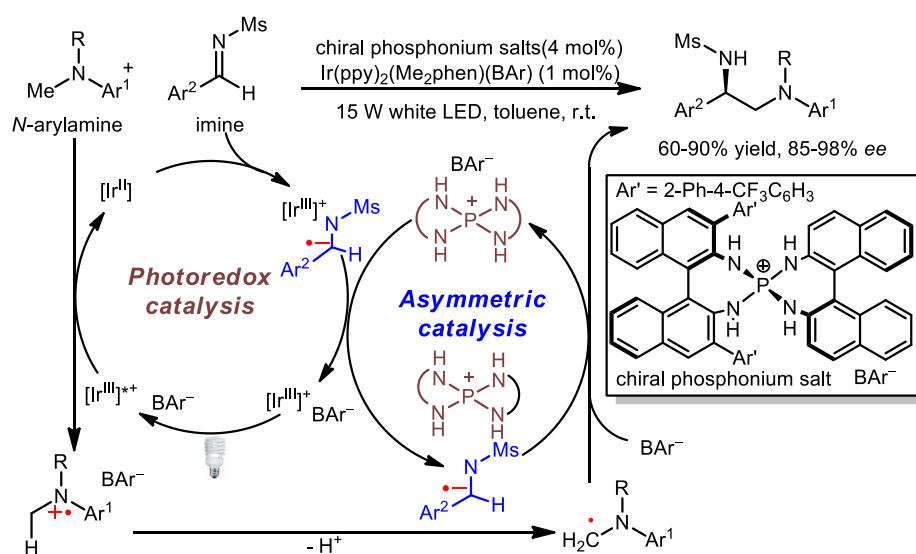


Figure 20 Enantioselective radical coupling reaction with chiral arylaminophosphonium ion catalyst and iridium photoredox catalyst.

3) Dual photoredox transition-metal catalysis: Lewis acid catalyst

In 2014, the Yoon group developed a dual catalysis strategy in asymmetric [2+2] photocycloadditions of α,β -unsaturated ketones to the corresponding cyclobutanes.³¹ Employing 1 mol% of $[\text{Ru}(\text{bpy})_3]\text{Cl}_2$ and 10 mol% $\text{Eu}(\text{OTf})_3$ with 20 mol% of dipeptide-derived chiral ligand led to form the 1,2-*trans*-cycloadducts with high enantioselectivities of up to 97% *ee*. Interestingly, by simply switching to saturated dipeptide ligand, the 1,2-*cis*-cycloadducts were generated as the major products (Figure 21). Mechanistically, the crucial step is the single-electron reduction of a chiral Lewis acid coordinated aryl enone to generated radical anion. The intermediate radical anion can react with another Michael acceptor to form a chiral Lewis acid mediated radical which subsequently undergoes intermolecular cyclization. In this protocol, the requirement of the Lewis acid catalyst for both reactivity and stereoselectivity prevents undesired background reaction. And recently, the author extended this strategy for the asymmetric [3+2] photocycloaddition of aryl cyclopropyl ketones, which enables the enantiocontrolled construction of densely substituted cyclopentane structures not synthetically accessible using other catalytic methods.³²

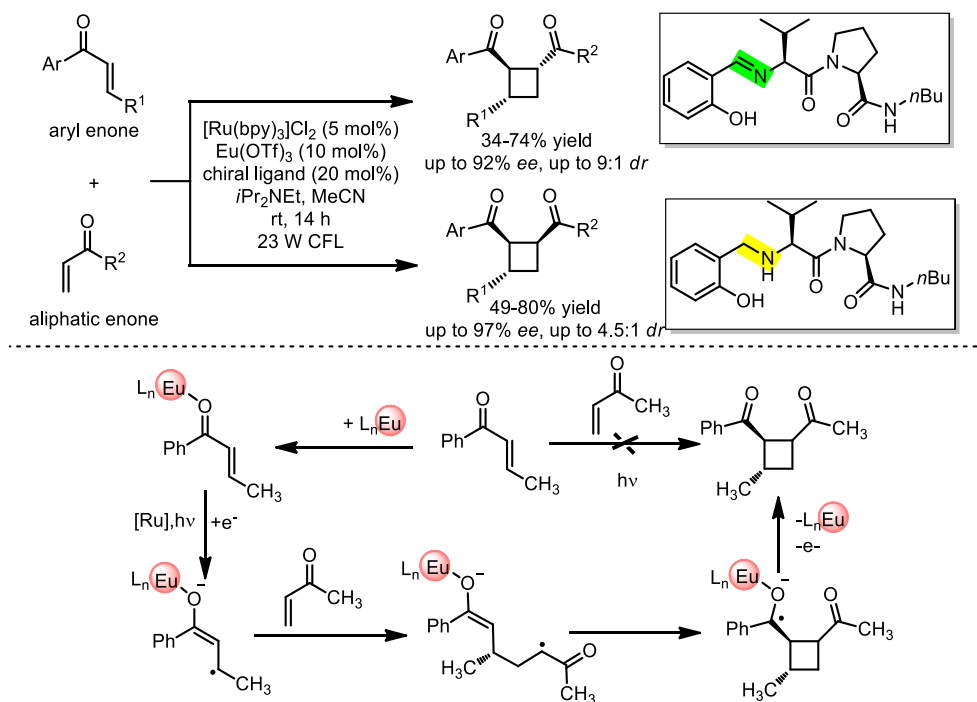


Figure 21 Enantioselective [2+2] photocycloadditions with a photoredox catalyst and a stereocontrolling Lewis acid.

The principle of cooperative Lewis acid-photoredox catalysis was further applied to the asymmetric Giese addition of photogenerated α -amino radicals to Michael acceptors by Yoon's group.³³ Chiral pybox ligand and relay auxiliary are two key points for achieving the radical addition products with high

levels of enantiocontrol (up to 96% *ee*). Notably, the Lewis acid here is not directly involved in the photoinduced electron transfer step. Rather, the chiral Lewis acids control the rate and selectivity of a step independent of the photoredox process itself (Figure 22).

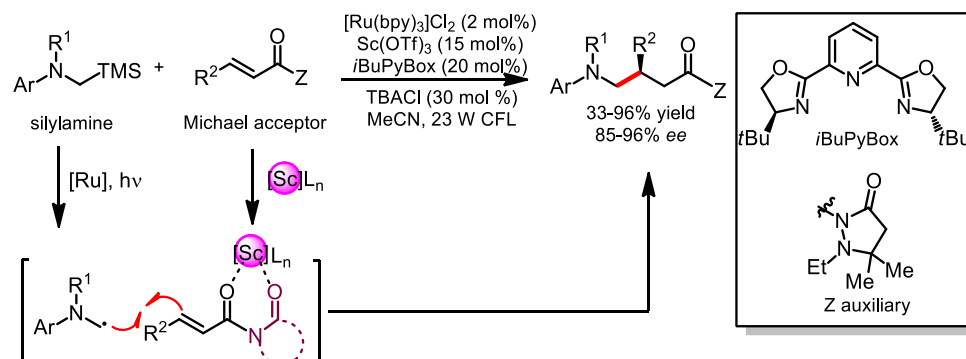


Figure 22 Enantioselective radical addition with cooperative Lewis acid-photoredox catalysis.

4) Dual photoredox transition-metal catalysis: Nickel catalyst

In 2016, MacMillan and Fu performed an elegant work of the enantioselective decarboxylative $C(sp^3)$ - $C(sp^2)$ cross-coupling reaction of α -amino acids with aryl halides by interfacing photoredox and nickel catalysis.³⁴ This method is very practical and useful because non-racemic benzylic amine products can be formed by using low-cost α -amino acids as radical precursors (Figure 23). Mechanistically, photocatalyst-mediated oxidation and decarboxylation of an α -amino acid produce a prochiral α -amino radical. Meanwhile, activation of an aryl halide *via* oxidative addition lead to a chiral Ni(II)-aryl complex, which intercept the newly generated α -amino radical. The resulting diorganonickel(III) adduct then undergoes reductive elimination to achieve the C-C bond formation. The presence of a chiral ligand induces enantioselectivity and the last reductive elimination of diorganonickel(III) intermediate is proposed as the stereocontrol step.

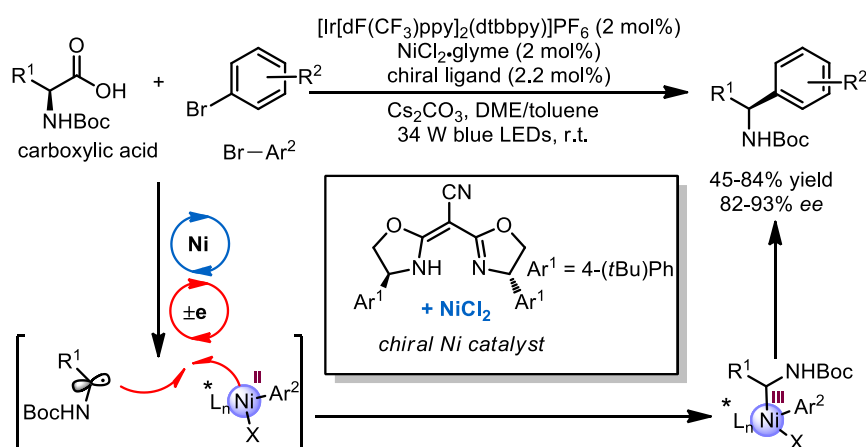


Figure 23 Enantioselective $C(sp^3)$ - $C(sp^2)$ cross-coupling reaction by interfacing photoredox and nickel catalysis.

1.3.2 Single Catalyst Systems in Asymmetric Photoredox Catalysis

1) Organocatalysis with electron donor-acceptor (EDA) complex

Melchiorre's group demonstrated that the synthetic potential of chiral enamines is not limited to the ground-state domain (enamines as nucleophiles or SOMO activation)³⁵, but can be further expanded by exploiting their photochemical activity. In 2013, Melchiorre and co-workers reported visible light induced asymmetric α -alkylation of aldehydes with electron deficient benzyl bromides and phenacyl bromides in the presence of the chiral secondary amine (Figure 24, pathway a).³⁶ Although the compounds used in the reaction system do not contain any photoactive unit, they guide the photoactivation of the substrate by inducing the in-situ formed chiral electron donor-acceptor (EDA) complex. The EDA complex is able to absorb visible light and triggers a single electron transfer (SET) from the enamine to the organobromide substrate. In addition, quantum yield measurements established that a radical chain propagation mechanism is operative.

Interestingly, the recent mechanistic studies from the Melchiorre group show another radical initiation pathway (Figure 24, pathway b) that the chiral enamine can directly reach an electronically excited state upon light absorption and then act as an effective photoinitiator to induce carbon-centered radical formation by reduction of the bromomalonate through SET process.³⁷

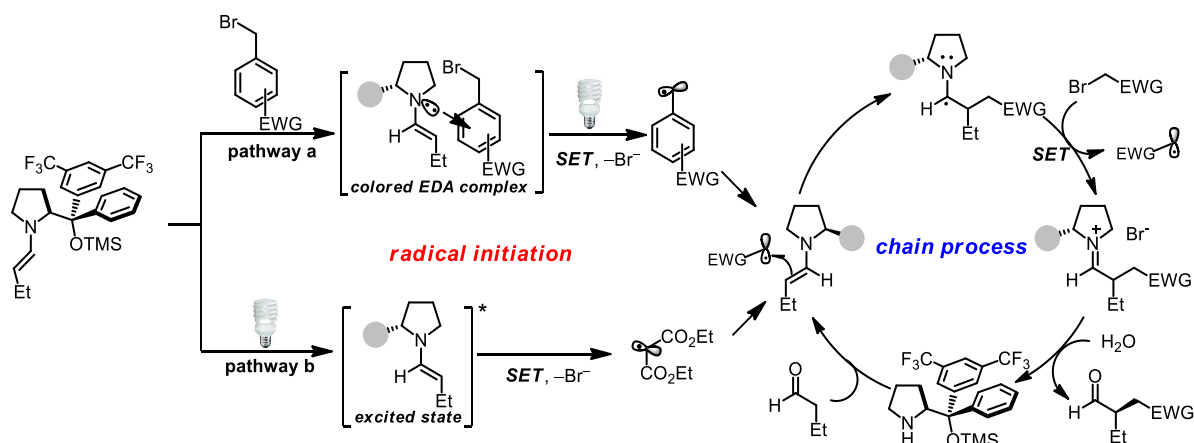


Figure 24 Visible light induced asymmetric α -alkylation of aldehydes *via* radical initiation step and chain process.

2) Organocatalysis with hydrogen bonding catalyst

The Bach group recently reported an organocatalyst for enantioselective intramolecular [2+2]-photocycloaddition reactions induced by visible light.³⁸ By using the enantiopure thioxanthone as single catalyst, the intramolecular cycloaddition products were achieved with good yields (79-95%) and high enantioselectivities (87-94% *ee*).

With respect to the organocatalyst, it is based on a 1,5,7-trimethyl-3-azabicyclo[3.3.1]nonan-2-one scaffold connected to a thioxanthone chromophore *via* an oxazole moiety. The mechanistic model assumes the binding of the 4-substituted chinolones to the catalyst through a double H-bonding as depicted in Figure 25. The thioxanthone not only serves as the light-absorbing molecule and transfers the energy to the chinolone, but also provides the asymmetric induction by allowing the attack of the double bond only from one prochiral face, thereby affording the cycloaddition product in an enantioselective fashion. The author mentioned that the enantiopure thioxanthone catalyst can be recovered in high yields after the reaction which demonstrate that visible light induced catalyst decomposition is not severe.

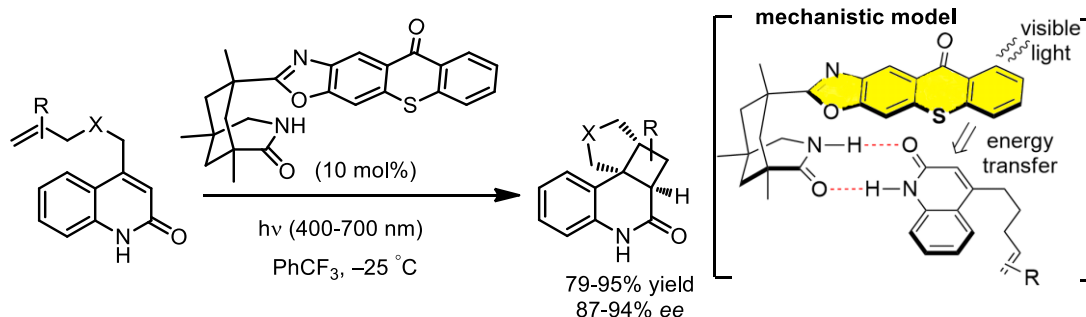


Figure 25 Photoinduced asymmetric [2+2] intramolecular cycloaddition *via* energy transfer process.

3) Metal catalysis: chiral-at-metal iridium(III) complex

In 2014, the Meggers group reported a highly efficient chiral-at-metal iridium Λ -IrS for the visible light induced enantioselective α -alkylation of 2-acyl imidazoles.³⁹ As shown in Figure 26, under visible light irradiation, 2 mol% of iridium catalyst Λ -IrS is able to catalyze the reaction between 2-aryl imidazoles and electron deficient benzyl bromides in high yields (up to 100% yield) and with high enantioselectivities (up to 99% *ee*).

Mechanistically, the catalysis is initiated by the coordination of 2-acyl imidazole to the iridium catalyst, followed by deprotonation to form the iridium enolate complex. The subsequent addition of the reductively generated electrophilic carbon radical to form the ketyl radical intermediate. Oxidation of the ketyl radical to the carbonyl group by single electron transfer (SET) provides the iridium-coordinated product, which is subsequently released. The SET process either regenerates the iridium photoredox catalyst or leads to the reduction of another organobromide substrate, thereby initiating a chain process. Proposed key intermediate is the iridium enolate complex, which not only provides the crucial asymmetric induction but also serves as the in-situ generated active photoredox catalyst.

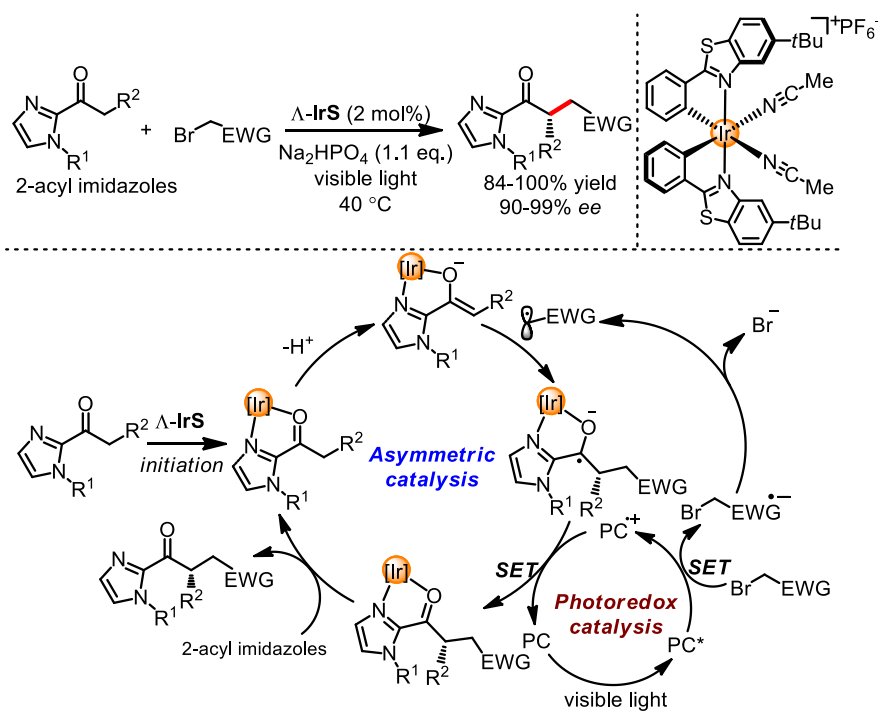


Figure 26 Enantioselective α -alkylation of 2-acyl imidazoles with a single chiral-at-metal iridium catalyst. PC = photoredox catalyst.

4) Metal catalysis: chiral copper(I) complex

Very recently, the Fu group described a copper-based chiral catalyst derived from commercially available components can achieve asymmetric C-N cross-coupling reactions of racemic tertiary alkyl chlorides with high enantioselectivities of up to 99% *ee* (Figure 27).⁴⁰ In this method, an in-situ formed chiral copper(I) complex in which copper cation is coordinated with two chiral phosphine ligands and one monoanionic carbazolide is responsible for the photocatalysis and the enantioselective C-N bond construction.

Mechanistically, the first step is the binding of the nucleophile to copper to form a copper-nucleophile complex. Irradiation of the copper-nucleophile complex leads to an excited-state copper adduct which then engages in electron transfer with the alkyl halide to generate an alkyl radical. Then, C-N bond formation between the nucleophile and the alkyl radical occurs through an inner sphere pathway involving a copper-nucleophile complex. This work is of great significance because it stands at a previously unexplored intersection of asymmetric synthesis, catalysis with earth-abundant metals, visible light induced processes, and cross-coupling reactions of alkyl electrophiles, each of them represents an important current theme in organic synthesis.

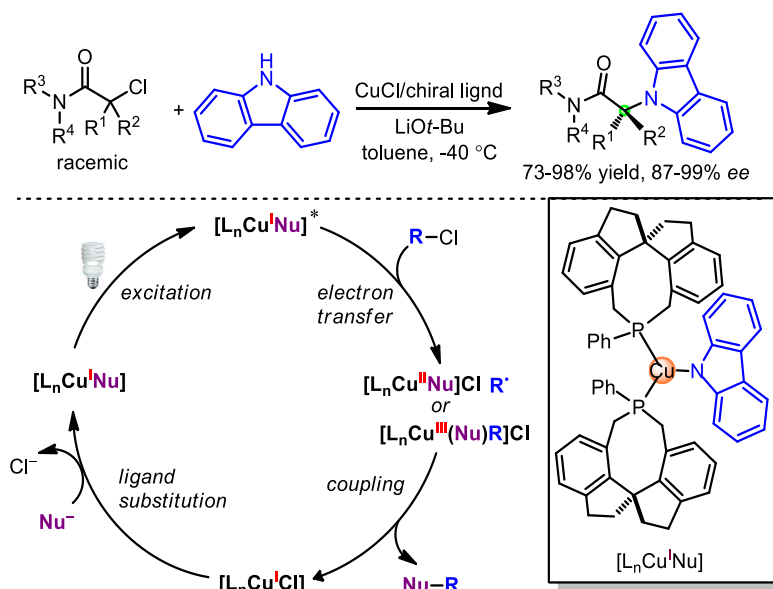


Figure 27 Enantioselective C-N cross-coupling with an in-situ chiral copper catalyst.

1.4 Conclusions

Octahedral chiral-at-metal complexes have developed not only because of their importance in fundamental stereochemistry but also because of their application as asymmetric catalysts in organic synthesis.

In above examples of asymmetric catalysis, several inert octahedral transition-metal complexes are presented as chiral templates, in which the transition metal serves as a structural center, whereas catalytic transformation is mediated through the organic ligand sphere. Among them, chiral-at-metal iridium complexes developed by the Meggers group exhibited impressive properties, achieving high enantioselectivities with low catalyst loadings. Remarkably, a chiral Lewis acid iridium catalyst should be of high practical value since it provides an excellent substrate scope for the highly enantioselective Friedel-Crafts addition of indoles to α,β -unsaturated 2-acyl imidazoles at low catalyst loadings. This high performance indicates the value of a direct chirality transfer from the chiral metal center to the coordinated substrate.

Under irradiation with visible light, highly enantioselective transformations could be achieved by merging photocatalyst with chiral catalyst or using a single catalyst. A variety of reaction types are developed *via* photoinduced electron transfer or energy transfer processes. The highly reactive intermediates, directed asymmetric induction and the tolerance of the reaction conditions to a wide range of functional groups enable the application of these reactions to the synthesis of various enantiopure compounds. The encouraging work from the Meggers group, a single chiral-at-metal iridium complex catalyzed the visible light activated asymmetric α -alkylation, provide new opportunities to realize different kinds of enantioselective photoredox catalysis with single chiral-at-metal complexes.

References

- 1 R. Hoffmann, *The Same and Not the Same*, Columbia University, Press: New York, **1995**.
- 2 G. Blaschke, H. P. Kraft, K. Fickentscher, F. Köhler, *Arzneim. Forsch.* **1979**, *29*, 1640–1642.
- 3 J. Xing, W. Q. Fang, H. J. Zhao, H. G. Yang, *Chem. Asian J.* **2012**, *7*, 642–657.
- 4 J. Low, J. Yu, W. Ho, *J. Phys. Chem. Lett.* **2015**, *6*, 4244–4251.
- 5 a) D. P. Hari, B. König, *Angew. Chem. Int. Ed.* **2013**, *52*, 4734–4743; b) F. Dénès, M. Pichowicz, G. Povie, P. Renaud, *Chem. Rev.* **2014**, *114*, 2587–2693; c) J. W. Beatty, C. R. J. Stephenson, *Acc.*

- Chem. Res.* **2015**, *48*, 1474–1484; d) J.-R. Chen, X.-Q. Hu, L.-Q. Lu, W.-J. Xiao, *Chem. Soc. Rev.* **2016**, *45*, 2044–2056.
- 6 a) C. R. Jamison, L. E. Overman, *Acc. Chem. Res.* **2016**, *49*, 1578–1586; b) M. Kozłowski, T. Yoon, *J. Org. Chem.* **2016**, *81*, 6895–6897.
- 7 a) E. Meggers, *Chem. Commun.* **2015**, *51*, 3290–3301; b) C. Wang, Z. Lu, *Org. Chem. Front.* **2015**, *2*, 179–190; c) R. Brimiouille, D. Lenhart, M. M. Maturi, T. Bach, *Angew. Chem. Int. Ed.* **2015**, *54*, 3872–3890; d) M. Peña-López, A. Rosas-Hernández, M. Beller, *Angew. Chem. Int. Ed.* **2015**, *54*, 5006–5008.
- 8 L. Gong, L.-A. Chen, E. Meggers, *Angew. Chem. Int. Ed.* **2014**, *53*, 10868–10874.
- 9 M. Chavarot, S. Ménage, O. Hamelin, F. Charnay, J. Pécaut, M. Fontecae, *Inorg. Chem.* **2003**, *42*, 4810–4816.
- 10 O. Hamelin, M. Rimboud, J. Pecaute, M. Fontecave, *Inorg. Chem.* **2007**, *46*, 5354–5360.
- 11 C. Ganzmann, J. A. Gladysz, *Chem. Eur. J.* **2008**, *14*, 5397–5400.
- 12 L.-A. Chen, W. Xu, B. Huang, J. Ma, L. Wang, J. Xi, K. Harms, L. Gong, E. Meggers, *J. Am. Chem. Soc.* **2013**, *135*, 10598–10601.
- 13 a) Y. Takemoto, *Org. Biomol. Chem.* **2005**, *3*, 4299–4306; b) W.-Y. Siau, J. Wang, *Catal. Sci. Technol.* **2011**, *1*, 1298–1310; c) P. M. Pihko, Ed. *Hydrogen Bonding in Organic Synthesis*; Wiley-VCH: Weinheim, Germany, **2009**, Chapter 6.
- 14 L.-A. Chen, X. Tang, J. Xi, W. Xu, L. Gong, E. Meggers, *Angew. Chem. Int. Ed.* **2013**, *52*, 14021–14025.
- 15 J. Ma, X. Ding, Y. Hu, Y. Huang, L. Gong, E. Meggers, *Nat. Commun.* **2014**, *5*, 5531.
- 16 H. Huo, C. Fu, C. Wang, K. Harms, E. Meggers, *Chem. Commun.* **2014**, *50*, 10409–10411.
- 17 H. Huo, C. Fu, K. Harms, E. Meggers, *J. Am. Chem. Soc.* **2014**, *136*, 2990–2993.
- 18 P. Cieśla, P. Kocot, P. Mytych, Z. Stasicka, *J. Mol. Catal. A-Chem.* **2004**, *224*, 17–33.
- 19 a) C. K. Prier, D. A. Rankic, D. W. C. MacMillan, *Chem. Rev.* **2013**, *113*, 5322–5363; b) N. A. Romero, D. A. Nicewicz, *Chem. Rev.* **2016**, *116*, 10075–10166.
- 20 D. A. Nicewicz, D. W. C. MacMillan, *Science* **2008**, *322*, 77–80.
- 21 D. A. Nagib, M. E. Scott, D. W. C. MacMillan, *J. Am. Chem. Soc.* **2009**, *131*, 10875–10877.
- 22 H.-W. Shih, M. N. Vander Wal, R. L. Grange, D. W. C. MacMillan, *J. Am. Chem. Soc.* **2010**, *132*, 13600–13603.

- 23 M. A. Cismesia, T. P. Yoon, *Chem. Sci.* **2015**, *6*, 5426–5434.
- 24 a) M. Neumann, S. Földner, B. König, K. Zeitler, *Angew. Chem. Int. Ed.* **2011**, *50*, 951–954; b) M. Cherevatskaya, M. Neumann, S. Földner, C. Harlander, S. Kümmel, S. Dankesreiter, A. Pfitzner, K. Zeitler, B. König, *Angew. Chem. Int. Ed.* **2012**, *51*, 4062–4066; c) P. Riente, A. Mata Adams, J. Albero, E. Palomares, M. A. Pericàs, *Angew. Chem. Int. Ed.* **2014**, *53*, 9613–9616.
- 25 Y. Zhu, L. Zhang, S. Luo, *J. Am. Chem. Soc.* **2014**, *136*, 14642–14645.
- 26 J. J. Murphy, D. Bastida, S. Paria, M. Fagnoni, P. Melchiorre, *Nature* **2016**, *532*, 218–222.
- 27 D. A. DiRocco, T. Rovis, *J. Am. Chem. Soc.* **2012**, *134*, 8094–8097.
- 28 L. J. Rono, H. G. Yayla, D. Y. Wang, M. F. Armstrong, R. R. Knowles, *J. Am. Chem. Soc.* **2013**, *135*, 17735–17738.
- 29 G. Bergonzini, C. S. Schindler, C.-J. Wallentin, E. N. Jacobsen, C. R. J. Stephenson, *Chem. Sci.* **2014**, *5*, 112–116.
- 30 D. Uraguchi, N. Kinoshita, T. Kizu, T. Ooi, *J. Am. Chem. Soc.* **2015**, *137*, 13768–13771.
- 31 J. Du, K. L. Skubi, D. M. Schultz, T. P. Yoon, *Science* **2014**, *344*, 392–396.
- 32 A. G. Amador, E. M. Sherbrook, T. P. Yoon, *J. Am. Chem. Soc.* **2016**, *138*, 4722–4725.
- 33 L. R. Espelt, I. S. McPherson, E. M. Wiensch, T. P. Yoon, *J. Am. Chem. Soc.* **2015**, *137*, 2452–2455.
- 34 Z. Zuo, H. Cong, W. Li, J. Choi, G. C. Fu, D. W. C. MacMillan, *J. Am. Chem. Soc.* **2016**, *138*, 1832–1835.
- 35 a) T. D. Beeson, A. Mastracchio, J.-B. Hong, K. Ashton, D. W. C. MacMillan, *Science* **2007**, *316*, 582–585; b) H.-Y. Jang, J.-B. Hong, D. W. C. MacMillan, *J. Am. Chem. Soc.* **2007**, *129*, 7004–7005.
- 36 E. Arceo, I. D. Jurberg, A. Álvarez-Fernández, P. Melchiorre, *Nat. Chem.* **2013**, *5*, 750–756.
- 37 A. Bahamonde, P. Melchiorre, *J. Am. Chem. Soc.* **2016**, *138*, 8019–8030.
- 38 R. Alonso, T. Bach, *Angew. Chem. Int. Ed.* **2014**, *53*, 4368–4371.
- 39 H. Huo, X. Shen, C. Wang, L. Zhang, P. Röse, L.-A. Chen, K. Harms, K. Marsch, G. Hilt, E. Meggers, *Nature* **2014**, *515*, 100–103.
- 40 Q. M. Kainz, C. D. Matier, A. Bartoszewicz, S. L. Zultanski, J. C. Peters, G. C. Fu, *Science* **2016**, *351*, 681–684.

Chapter 2: Aim of the Work

1) Synthesis and catalytic activity of chiral rhodium Lewis acid catalyst

The inert octahedral chiral-at-iridium complexes provide ideal environments to induce asymmetry. However, efforts to exploit highly desirable features of chiral-at-rhodium complexes have met with great challenges, mainly due to limited methods to synthesize enantiopure rhodium complexes.¹

The Meggers group has recently introduced a substitutionally labile yet configurational stable chiral-at-metal iridium Lewis acid catalyst. The iridium center serves as a dual function of activating a substrate through bidentate coordination and at the same time provides the asymmetric induction.² In this work, we wish to accomplish the first isostructural synthesis of chiral-at-metal rhodium(III) complex, and subsequently, we would like to search for different reactions for the comparison of the catalytic properties of the homologous chiral iridium and rhodium Lewis acid catalysts. Stability and the potential racemization of such rhodium complex should be considered.

2) Development of visible light induced asymmetric photoredox catalysis with chiral-at-metal complexes

General solutions for interfacing visible light induced photoredox chemistry and asymmetric catalysis with single catalysts are highly desirable. The Meggers group has recently reported a single chiral-at-metal iridium complex catalyzed the visible light induced asymmetric α -alkylation of 2-acyl imidazoles.³ Several useful information can be obtained: 1) the chiral-at-metal iridium complex can serve as “2-in-1” catalyst by combining photoinduced reduction with asymmetric alkylation; 2) the chiral catalyst can not be dissociated or racemized under visible light irradiation; 3) highly effective asymmetric induction can be mediated by the propeller-like C_2 -symmetrical ligand sphere. All these informations potentially provide opportunities for reaction design by having a closer control over the entire reaction path.

The aim of this research part is the development of new and efficient visible light mediated asymmetric reactions with newly developed chiral-at-metal iridium or rhodium complexes. For instance, the activation of α -C(sp³)-H bond of tertiary amines represents an important organic synthesis process. Although oxidation of amines into iminium ions or α -aminoalkyl radicals *via* photoinduced electron

transfer has been extensively studied,⁴ only a few asymmetric methodologies are available. Whether the oxidation potentials of such chiral-at-metal iridium complexes are positive for activating α -C(sp³)-H bonds need further investigation.

References

- 1 a) A. H. Krotz, L. Y. Kuo, T. P. Shields, J. K. Barton, *J. Am. Chem. Soc.* **1993**, *115*, 3877–3882; b) L. Ghizdavu, B. Kolp, A. von Zelewsky, H. Stoeckli-Evans, *Eur. J. Inorg. Chem.* **1999**, 1271–1279; c) L. Ghizdavu, A. von Zelewsky, H. Stoeckli-Evans, *Eur. J. Inorg. Chem.* **2001**, 993–1003; d) N. Yoshinari, T. Konno, *Inorg. Chem.* **2008**, *47*, 7450–7452; e) S. Mollin, S. Blanck, K. Harms, E. Meggers, *Inorg. Chim. Acta* **2012**, *393*, 261–268.
- 2 H. Huo, C. Fu, K. Harms, E. Meggers, *J. Am. Chem. Soc.* **2014**, *136*, 2990–2993.
- 3 H. Huo, X. Shen, C. Wang, L. Zhang, P. Röse, L.-A. Chen, K. Harms, K. Marsch, G. Hilt, E. Meggers, *Nature* **2014**, *515*, 100–103.
- 4 a) P. J. DeLaive, B. P. Sullivan, T. J. Meyer, D. G. Whitten, *J. Am. Chem. Soc.* **1979**, *101*, 4007–4008; b) J. Hu, J. Wang, T. H. Nguyen, N. Zheng, *Beilstein J. Org. Chem.* **2013**, *9*, 1977–2001; c) J. W. Beatty, C. R. J. Stephenson, *Acc. Chem. Res.* **2015**, *48*, 1474–1484; d) K. Nakajima, Y. Miyake, Y. Nishibayashi, *Acc. Chem. Res.* **2016**, *49*, 1946–1956.

Chapter 3: Results and Discussion

3.1 Asymmetric Lewis Acid Catalysis Directed by Octahedral Rhodium Centrochirality

3.1.1 Catalyst Design

Chiral Lewis acid catalysts play a significant role in asymmetric catalysis because many reactions are amenable to Lewis acid activation.¹ Recently, the Meggers group has developed a chiral-at-metal iridium(III) complex (Δ -**IrO**)² as a novel type of chiral Lewis acid catalyst in which the metal center is cyclometalated by two achiral bidentate ligands in a propeller type fashion and thereby provides the sole source of chirality. Herein, we wish to synthesize an octahedral chiral-at-metal rhodium(III) complex. The designed structure of Δ -**RhO**, like its congener Δ -**IrO**, consists of two cyclometalating benzoxazoles and two coordinated acetonitrile ligands. We hope the rhodium center can also serve as the source of centrochirality and Lewis acidity in the catalytic asymmetric reactions (Figure 28).

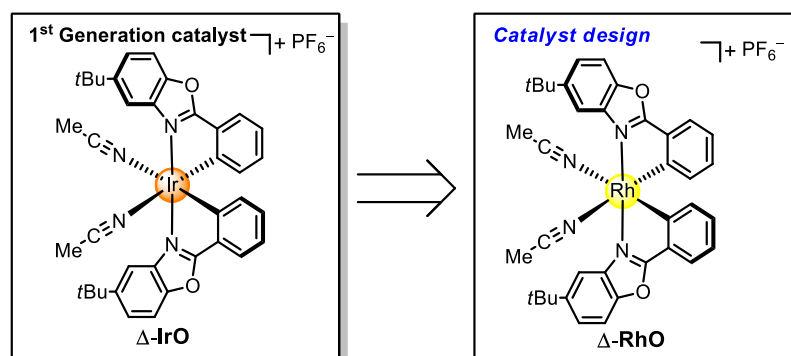
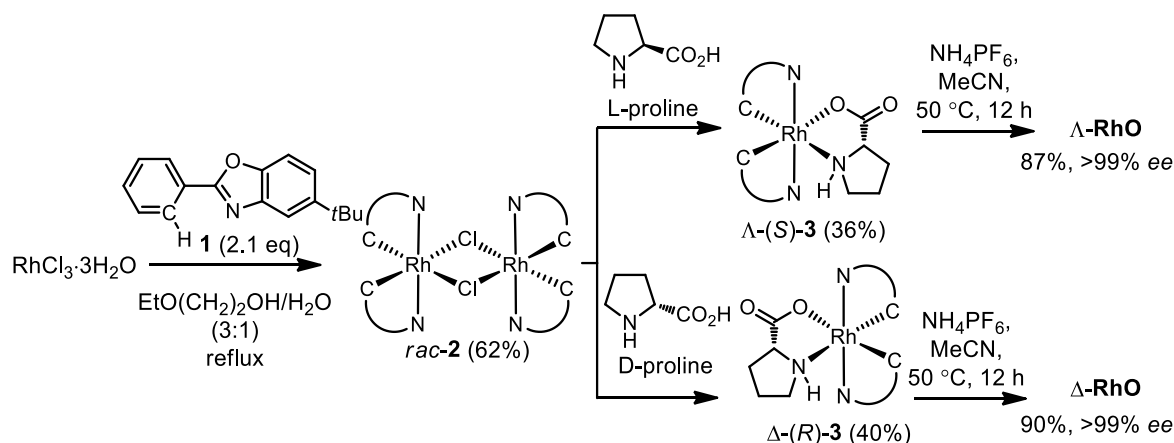


Figure 28 Catalyst design for the chiral-at metal rhodium complex.

3.1.2 Catalyst Synthesis

The study was started by developing a synthesis of the complex Δ -**RhO**. The methodology was developed by the Meggers group.³ Accordingly, RhCl_3 hydrate was reacted with *tert*-butyl-2-phenylbenzoxazole (**1**) in a mixture of 2-ethoxyethanol and water under reflux to provide the rhodium dimer complex *rac*-**2** (Scheme 1). The subsequent reaction with D-proline afforded the prolinato-rhodium complexes Δ -(*R*)-**3** and Λ -(*R*)-**3** as a mixture of diastereomers, and Δ -(*R*)-**3** is isolable in a straightforward fashion in a yield of 40% with high purity by just washing the mixture of diastereomers

with $\text{CH}_2\text{Cl}_2/\text{Et}_2\text{O}$. Exposure of $\Delta\text{-}(R)\text{-3}$ to NH_4PF_6 in acetonitrile at $50\text{ }^\circ\text{C}$ for 12 h resulted in a substitution of D-proline by two acetonitrile ligands under complete retention of configuration to afford $\Delta\text{-RhO}$ in a yield of 90%. Notably, $\Delta\text{-RhO}$ is air stable, moisture tolerant and can be purified by standard flash silica gel chromatography. The mirror-imaged complex $\Lambda\text{-RhO}$ is accessible in an analogous fashion by using the chiral auxiliary L-proline instead.



Scheme 1 Proline-mediated synthesis of the enantiomerically pure rhodium(III) complexes $\Lambda\text{-RhO}$ and $\Delta\text{-RhO}$.

It is worth noting that the prolinato-rhodium complexes $\Delta\text{-}(R)\text{-3}$ and $\Lambda\text{-}(R)\text{-3}$ can not be separated by chromatography due to a limited stability of the complexes. The isolation of $\Delta\text{-}(R)\text{-3}$ or its enantiomer $\Lambda\text{-}(S)\text{-3}$ is based on the different solubilities of the diastereomers in solutions. Whereas $\Lambda\text{-}(R)\text{-3}$ is very soluble in a mixture of $\text{CH}_2\text{Cl}_2/\text{Et}_2\text{O}$, its diastereomer $\Delta\text{-}(R)\text{-3}$ is insoluble. Thus, $\Delta\text{-}(R)\text{-3}$ could be obtained by washing with $\text{CH}_2\text{Cl}_2/\text{Et}_2\text{O}$ (for details, see experimental part). The structure of $\Delta\text{-}(R)\text{-3}$ is demonstrated by single crystal X-ray crystallography (Figure 29).⁴ Notably, other tested auxiliaries⁵ did not provide rhodium auxiliary complexes with distinct solubilities and were not stable enough for a resolution *via* silica gel chromatography. Chiral proline here serves as a cheap and readily available powerful chiral auxiliary for the synthesis of enantiopure rhodium complexes. This method provides opportunity for the large-scale synthesis of enantiomerically pure transition metal complexes.

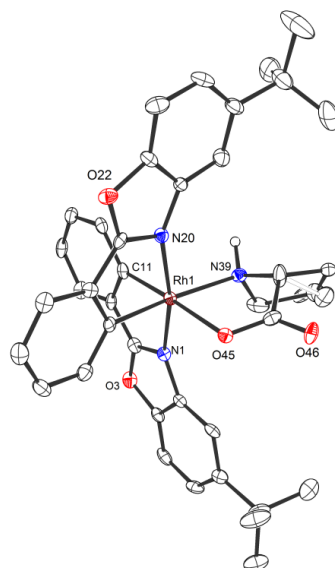


Figure 29 Crystal structure of Δ -(*R*)-**3**. Hydrogen atoms are omitted for clarity. ORTEP drawing with 50% probability thermal ellipsoids.

Thus, following this convenient proline-mediated synthesis, Λ - and Δ -**RhO** can be obtained in a non-racemic fashion as verified by CD-spectroscopy (Figure 30). HPLC on a chiral stationary phase demonstrates that the chiral-at-rhodium complexes are virtually enantiopure (Figure 31). Furthermore, time dependent stability tests by ^1H NMR and HPLC confirm that the relative and absolute metal-centered configuration is completely retained in solution over many days (for details, see experimental part).

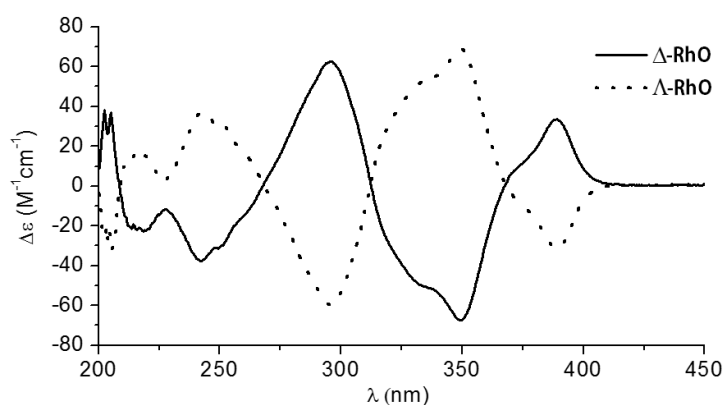


Figure 30 CD spectra (0.2 mM in CH_3OH) of Λ - and Δ -**RhO**.

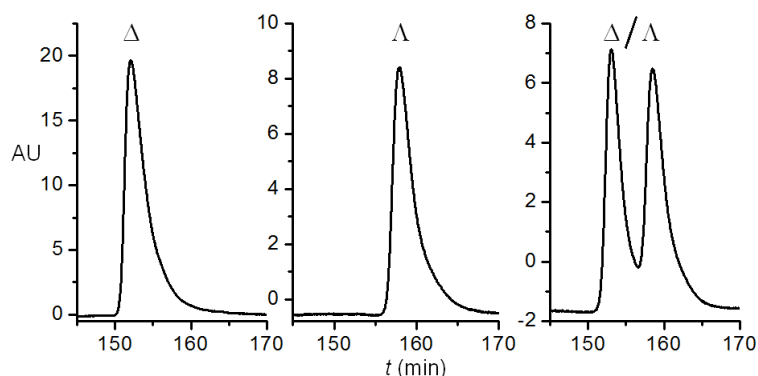


Figure 31 Chiral HPLC traces demonstrating the enantiopurity of synthesized Δ - and Λ -**RhO**. HPLC conditions: Daicel Chiralpak IB (250 \times 4.6 mm), flow rate = 0.6 mL/min, 0.1% aq. TFA with MeCN as eluent (30% to 41% in 60 min).

A structure of Δ -**RhO** was obtained by single crystal X-ray diffraction and verifies the Δ -configuration at the rhodium center (Figure 32, left). As expected, affected by the lanthanide contraction, the period 5 transition metal complex Δ -**RhO** and its period 6 congener Δ -**IrO** (Figure 32, right) possess almost identical structures. For example, the lengths of the bonds between the transition metals and the cyclometalating benzoxazoles differ just in the range of 0.009 and 0.022 Å. However, the bonds to the coordinated acetonitrile ligands are notably longer in Δ -**RhO** compared to Δ -**IrO** by 0.041–0.043 Å, thereby indicating more exchange labile acetonitrile ligands in Δ -**RhO**.

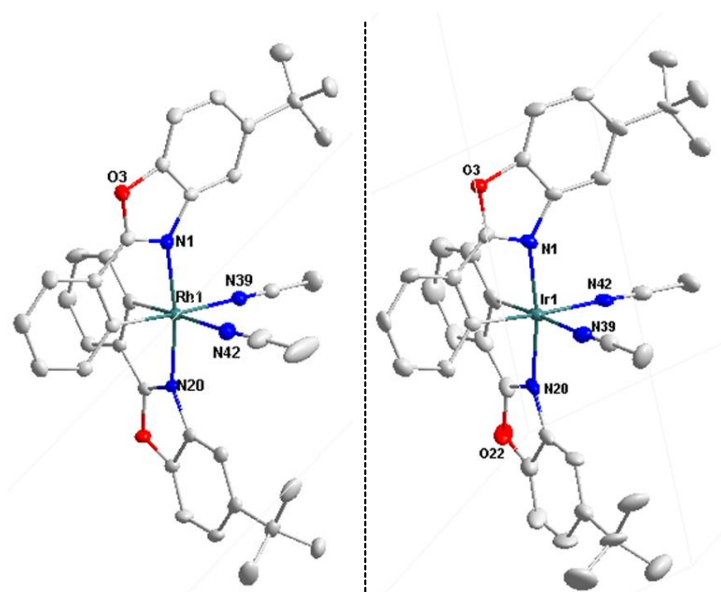


Figure 32 Crystal structures of Δ -**RhO** (left) and Δ -**IrO** (right). The hexafluorophosphate counteranion and hydrogen atoms are omitted for clarity. Selected bond lengths (Å): N1-Rh1 = 2.056(2), N20-Rh1 = 2.044(2), N39-Rh1 = 2.142(3), N42-Rh1 = 2.155(3); N1-Ir1 = 2.054(9), N20-Ir1 = 2.044(6), N39-Ir1 = 2.111(6), N42-Ir1 = 2.100(9).

3.1.3 Catalytic Reactions

With the novel Lewis acid catalyst Δ -**RhO** in hand, we next searched for different reactions for the comparison of the homologous catalysts Δ -**IrO** and Δ -**RhO**. Preliminary works of the following asymmetric conjugate additions by using Δ -**IrO** as catalyst were explored by Haohua Huo (a former Ph.D. student in the Meggers group).

1) Asymmetric Friedel-Crafts alkylation

First reaction is the enantioselective Friedel-Crafts addition of indoles to α,β -unsaturated 2-acyl imidazoles which is effectively catalyzed by Δ -**IrO**.² As shown in Figure 33, although 1 mol% Δ -**RhO** catalyzes the addition of indole to α,β -unsaturated 2-acyl imidazole **4a** affording the Friedel-Crafts product (*R*)-**5a** with 94% yield and respectable 95% *ee* after 40 h, reaction time, yield, and enantioselectivity can not quite match the performance of the homolog Δ -**IrO** (96% yield and 96% *ee* after 20 h).

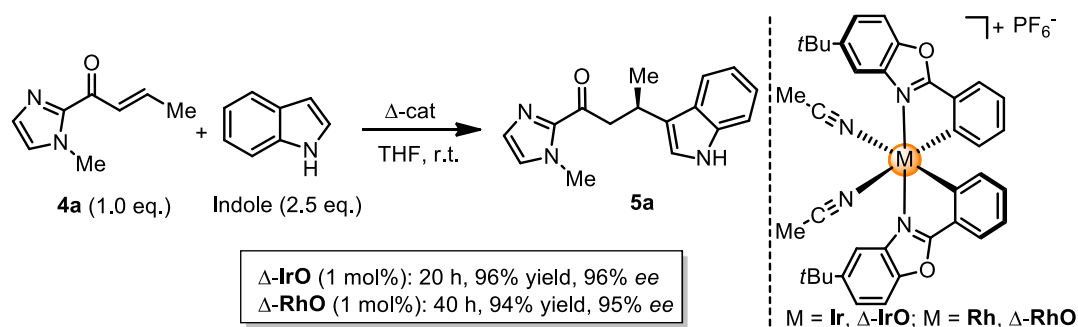
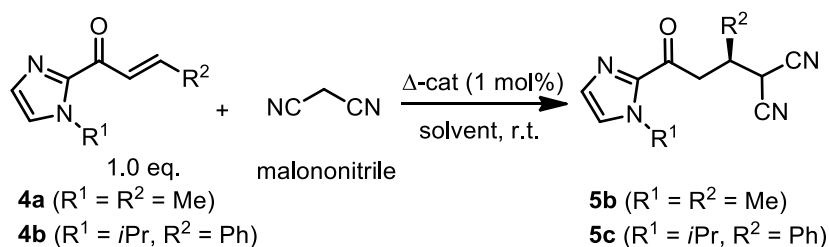


Figure 33 Asymmetric Friedel-Crafts alkylation catalyzed by Δ -**IrO** and Δ -**RhO**.

2) Asymmetric addition of malononitrile

Next, the Michael addition of 2-acyl imidazoles **4a** with malononitrile was investigated. As shown in Table 1, the addition of malononitrile to **4a** catalyzed by 1 mol% Δ -**RhO** in THF at room temperature afforded the adduct (*R*)-**5b** with a significantly higher *ee* value of 88% (entry 2) compared to 70% using Δ -**IrO** (entry 1). After a brief survey of reaction conditions (entries 3-8), THF (0.5 M) and malononitrile (1.2 eq.) are favorable to get a high enantioselectivity of 92% *ee* (entry 8). It is worth noting that the rhodium catalyst is tolerant towards moisture and air, and the presence of 1 mol% H₂O and air atmosphere did neither affect the yield nor the enantioselectivity (entries 9 and 10). Upon the best conditions (entry 8), the addition of malononitrile to substrate **4b** catalyzed by Δ -**RhO** afforded the product (*R*)-**5c** with 91% yield and 95% *ee* after 28 h, reaction time, yield, and enantioselectivity are superior to the performance of the homolog Δ -**IrO** (entries 11 and 12).

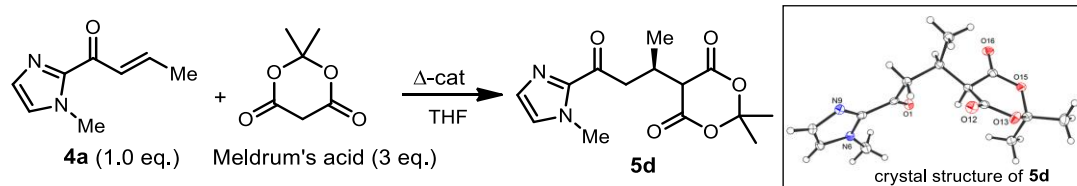
Table 1 Asymmetric addition of malononitrile.^a

entry	catalyst ^b	substrate	solvent ^c	malononitrile	<i>t</i> (h)	yield (%) ^d	<i>ee</i> (%) ^e
1	$\Delta\text{-IrO}$	4a	THF (1 M)	3.0 eq.	16	99	70
2	$\Delta\text{-RhO}$	4a	THF (1 M)	3.0 eq.	16	98	88
3	$\Delta\text{-RhO}$	4a	DCM (1 M)	3.0 eq.	16	96	87
4	$\Delta\text{-RhO}$	4a	MeOH (1 M)	3.0 eq.	16	97	83
5	$\Delta\text{-RhO}$	4a	THF (0.5 M)	3.0 eq.	16	97	91
6	$\Delta\text{-RhO}$	4a	THF (0.25 M)	3.0 eq.	16	97	91
7	$\Delta\text{-RhO}$	4a	THF (0.5 M)	2.0 eq.	16	96	91
8	$\Delta\text{-RhO}$	4a	THF (0.5 M)	1.2 eq.	16	96	92
9 ^f	$\Delta\text{-RhO}$	4a	THF (0.5 M)	1.2 eq.	16	96	92
10 ^g	$\Delta\text{-RhO}$	4a	THF (0.5 M)	1.2 eq.	16	96	92
11	$\Delta\text{-RhO}$	4b	THF (0.5 M)	1.2 eq.	28	91	95
12	$\Delta\text{-IrO}$	4b	THF (0.5 M)	1.2 eq.	96	40	88

^a Reaction conditions: 2-acyl imidazole **4a** or **4b** (0.20 mmol), malononitrile (0.24 mmol or 0.40 mmol or 0.60 mmol) in solvent with catalyst $\Delta\text{-IrO}$ or $\Delta\text{-RhO}$ (1 mol%) under nitrogen atmosphere at room temperature. ^b Catalyst loadings in brackets given in mol%. ^c Concentration of solvents are given in brackets. ^d Isolated yields. ^e Enantioselectivities were determined by HPLC analysis. ^f under air. ^g with 1% H₂O.

3) Asymmetric addition of Meldrum's acid

Meldrum's acid is widely used as a nucleophile in organic synthesis due to its adequate acidity ($pK_a = 4.83$).⁶ As shown in Table 2, by using $\Delta\text{-RhO}$ (1 mol%) as catalyst, the Michael addition of Meldrum's acid with 2-acyl imidazole **4a** provided the expected product (*R*)-**5d** with 85% *ee* compared to just 68% *ee* with $\Delta\text{-IrO}$ (entries 1 and 2). The enantioselectivity for the $\Delta\text{-RhO}$ catalyzed reaction can be further improved significantly by either reducing the temperature to 5 °C (entry 4, 94% *ee*) or increasing the catalyst loading to 2 mol% (entry 5, 95% *ee*), as both ways can inhibit the background reaction efficiently (entry 3).

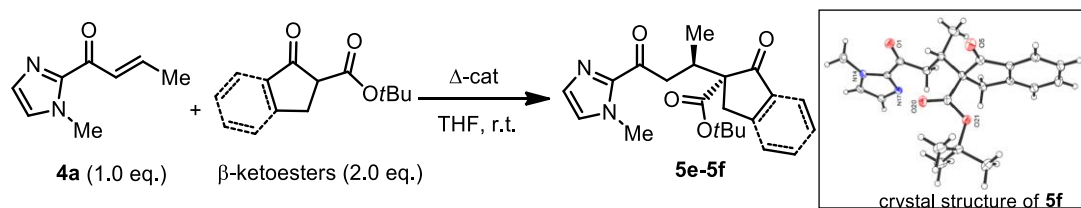
Table 2 Asymmetric addition of Meldrum's acid.^a

entry	catalyst ^b	T (°C)	t (h)	yield (%) ^c	ee (%) ^d
1	Δ -IrO (1 mol%)	25	16	99	68
2	Δ -RhO (1 mol%)	25	16	99	85
3	none	25	16	8.5	n.d.
4	Δ -RhO (1 mol%)	5	16	97	94
5	Δ -RhO (2 mol%)	25	6	96	95

^a Reaction conditions: 2-acyl imidazole **4a** (0.20 mmol), Meldrum's acid (0.60 mmol) in THF (0.2 mL) with catalyst Δ -IrO or Δ -RhO under nitrogen atmosphere at room temperature. ^b Catalyst loadings in brackets given in mol%. ^c Isolated yields. ^d Enantioselectivities were determined by HPLC analysis. n.d. = not determined.

4) Asymmetric addition of β -ketoesters

Interestingly, Δ -RhO (1 mol%) is even capable of catalyzing the formation of an all-carbon quaternary stereocenter (Table 3). The reaction of *tert*-butyl 2-oxocyclopentane-1-carboxylate with acyl imidazole **4a** yields **5e** with 99% *ee* and 4:1 *dr* (entry 1). Under the same conditions, Δ -IrO displays inferior performance with 97% *ee* and 3:1 *dr* and a low yield of just 41%. Δ -RhO (1 mol%) also catalyzes the addition of 2,3-dihydro-1-oxo-1*H*-indene-2-carboxylic acid *tert*-butyl ester to acyl imidazole **4a** providing the adduct **5f** in 92% yield with 96% *ee* and 14:1 *dr*. Δ -IrO performs similar for this transformation although the catalysis rate is somewhat sluggish and requires an elongated reaction time (72 h) for a complete conversion (entry 2).

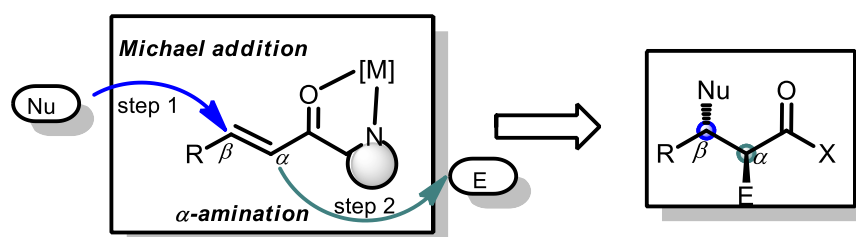
Table 3 Asymmetric addition of β -ketoesters.^a

entry	β -ketoester	product	catalyst ^b	<i>t</i> (h)	yield (%) ^c	<i>ee</i> (%) ^d
1			$\Delta\text{-IrO}$ (1 mol%)	96	41	97 (3:1 <i>dr</i>)
			$\Delta\text{-RhO}$ (1 mol%)	48	83	99 (4:1 <i>dr</i>)
2			$\Delta\text{-IrO}$ (1 mol%)	72	89	97 (10:1 <i>dr</i>)
			$\Delta\text{-RhO}$ (1 mol%)	20	92	96 (14:1 <i>dr</i>)

^a Reaction conditions: 2-acyl imidazole **4a** (0.20 mmol), β -ketoester (0.40 mmol) in THF (0.4 mL) with catalyst $\Delta\text{-IrO}$ or $\Delta\text{-RhO}$ under nitrogen atmosphere at room temperature. ^b Catalyst loadings in brackets given in mol%. ^c Isolated yields. ^d Enantioselectivities were determined by HPLC analysis; diastereoselectivities were determined by ¹H NMR analysis of the crude products.

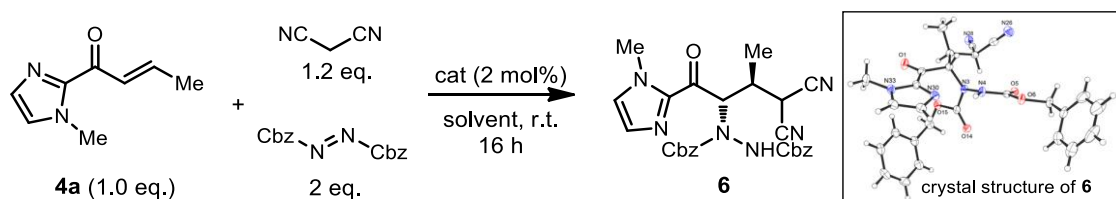
5) Asymmetric cascade reactions

Asymmetric cascade sequences provide an ecologically and economically desirable approach to organic synthesis.⁷ Taking into account that the asymmetric additions of α,β -unsaturated 2-acyl imidazoles are efficiently catalyzed by the iridium and rhodium complexes, and this class of catalysts exhibits impressive catalytic activity in the asymmetric α -amination of 2-acyl imidazoles through enolate activation mode (Liang-A. Chen's work, a former Ph.D. student in the Meggers group)⁸, we were wondering if the cascade reaction could be realized which combine two intermolecular and stereoselective steps involving a Michael addition/amination pathway (Figure 34).

**Figure 34** Reaction design of the asymmetric cascade reaction.

The asymmetric cascade strategy was first examined by the mixture of α,β -unsaturated 2-acyl imidazole **4a**, malononitrile and diethyl azodicarboxylate in isopropanol with *rac*-**IrO** as catalyst, to our disappointment, only Michael addition product **5b** was observed (Table 4, entry 1). Encouragingly, by using *rac*-**RhO** (2 mol%) as catalyst (entry 2), the desired product **6** was provided with 40% yield (mixture of two diastereoisomers). After a brief screen of solvents, a high yield of 82% and diastereoselectivity of 4:1 *dr* can be achieved (entry 4). The enantioselectivity of the major diastereoisomer was observed as 92% *ee* when Δ -**RhO** was used as chiral catalyst (entry 5).

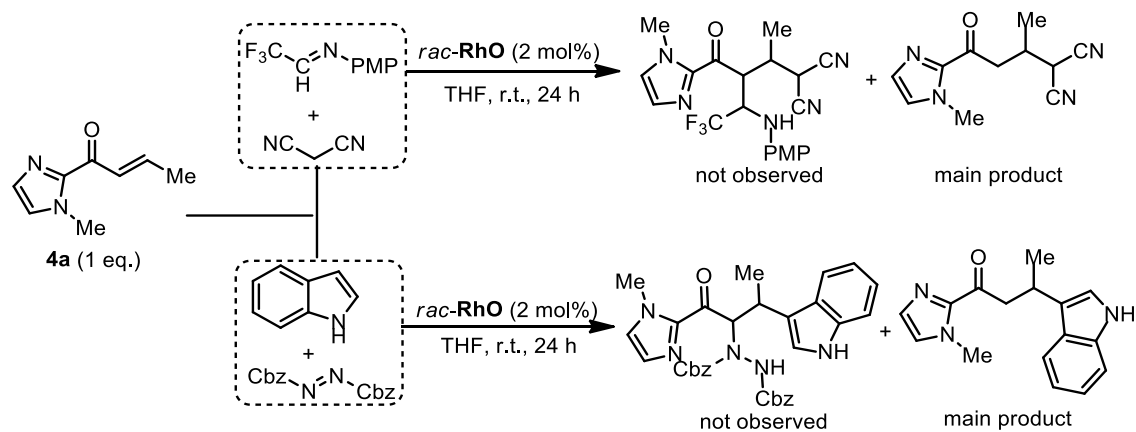
Table 4 Asymmetric cascade reaction.^a



entry	solvent ^b	catalyst (2 mol%)	yield (%) ^c	<i>ee</i> (%) ^d
1	<i>i</i> PrOH (2 M)	<i>rac</i> - IrO	0	n.d.
2	<i>i</i> PrOH (2 M)	<i>rac</i> - RhO	40	n.d.
3	CH ₂ Cl ₂ (1 M)	<i>rac</i> - RhO	48	n.d.
4	THF (1 M)	<i>rac</i> - RhO	83	n.d.
5	THF (1 M)	Δ - RhO	82	92 (<i>dr</i> 4:1) ^e

^a Reaction conditions: 2-acyl imidazole **4a** (0.2 mmol), malononitrile (0.24 mmol) and *(E)*-dibenzyl diazene-1,2-dicarboxylate (0.4 mmol) in solvent with catalyst Δ -**IrO** or Δ -**RhO** under nitrogen atmosphere at room temperature. ^b Concentration of solvents are given in brackets. ^c Isolated yields. ^d Enantioselectivities were determined by HPLC analysis. ^e Diastereoselectivity was determined by the isolated yield of each isomer. n.d. = not determined.

The above described alkene alkylation and amination processes afford straightforward access to the product **6** which have two adjacent stereogenic centers with high enantioselectivity. However, the substrate scope of this catalytic tandem reaction is narrow. For example, only the Michael addition product (step 1) was afforded when replacing malononitrile to indole or switching diethyl azodicarboxylate to imine electrophile (Scheme 2). It is probably because either the intermediate enolate complexes are difficult to generate or the in-situ formed enolate complexes could not efficiently attack to other electron deficient double bonds.



Scheme 2 Some limitations for asymmetric cascade reaction.

3.1.4 Mechanistic Investigations

1) Proposed mechanism and reaction model

A plausible mechanism of asymmetric conjugate additions is outlined in Figure 34. Δ -**RhO**, analogous to Δ -**IrO**, apparently serves as a chiral Lewis acid which coordinates in a bidentate fashion to the α,β -unsaturated 2-acyl imidazole, forming intermediate rhodium complex **I**. The activated double bond in complex **I** could be attacked by the nucleophile, thereby forging the intermediate enolate complex **II**. After protonation, the rhodium coordinated product **III** is subsequently released the product upon coordination to a new substrate molecule, thereby starting a new catalytic cycle.

In the stereocontrol model, Δ -**RhO** coordinates in two-point fashion to the α,β -unsaturated acyl imidazole, thereby shielding *Si* prochiral face of the alkene and raising its electrophilicity, so that an asymmetric induction is provided in the course of the addition of the deprotonated carbon nucleophiles to the prochiral β -carbon (Figure 35). ^1H NMR spectra recorded in CD_2Cl_2 at room temperature after the addition of substrate **4a** to catalyst Δ -**RhO** support the fast bidentate coordination of **4a** to the rhodium complex (see experimental part). The mode of reaction is also supported by a crystal structure of **RhO-I**, which was obtained upon mixing of the racemic rhodium catalyst with an α,β -unsaturated 2-acyl imidazole substrate **4b** at room temperature, confirming the anticipated two-point coordination of the acyl imidazole to the rhodium center upon replacement of the two labile acetonitrile ligands (Figure 36).

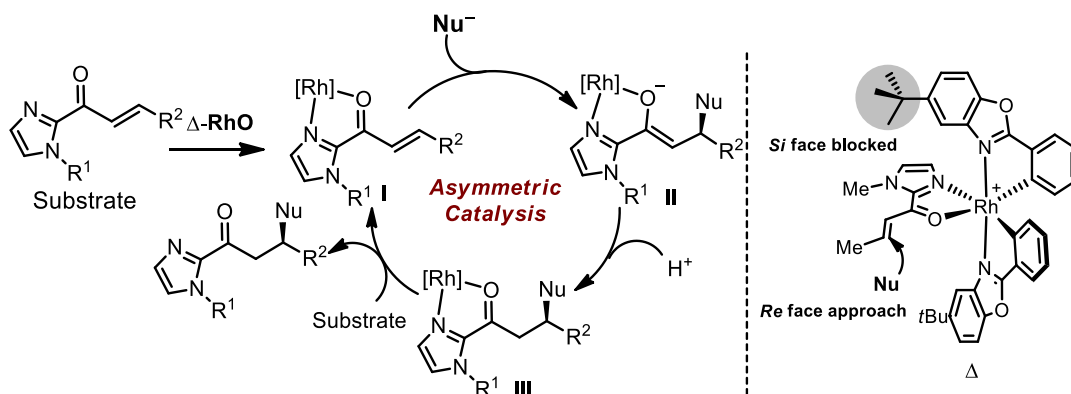


Figure 35 Proposed mechanism for Δ -RhO catalyzed asymmetric additions and reaction model for the asymmetric induction in the transition state in which one face of the alkene is shielded by the C_2 -symmetrical ligand sphere.

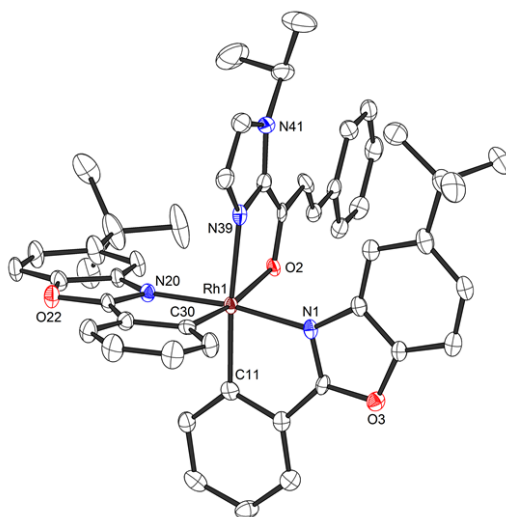


Figure 36 Crystal structure of substrate-coordinated rhodium intermediate complex **RhO-I**. Hydrogen atoms and the hexafluorophosphate counteranion are omitted for clarity. ORTEP drawing with 50% probability thermal ellipsoids.

2) The acetonitrile exchange experiments

It is quite intriguing that the congeners Δ -RhO and Δ -IrO differ in their catalytic performance despite their isostructural nature, with the iridium catalyst being superior for the asymmetric Friedel-Crafts reaction, whereas the rhodium congener providing higher turnover frequencies and, in most cases, higher enantioselectivities for the shown Michael additions of β -dicarbonyl compounds. ^1H NMR experiments of Δ -RhO/ Δ -IrO with bipyridine reveal that the acetonitrile exchange rates are much faster in Δ -RhO compared to Δ -IrO which is consistent with longer coordinative bonds of the metal-coordinated acetonitrile ligands in Δ -RhO compared to Δ -IrO (Figure 37).

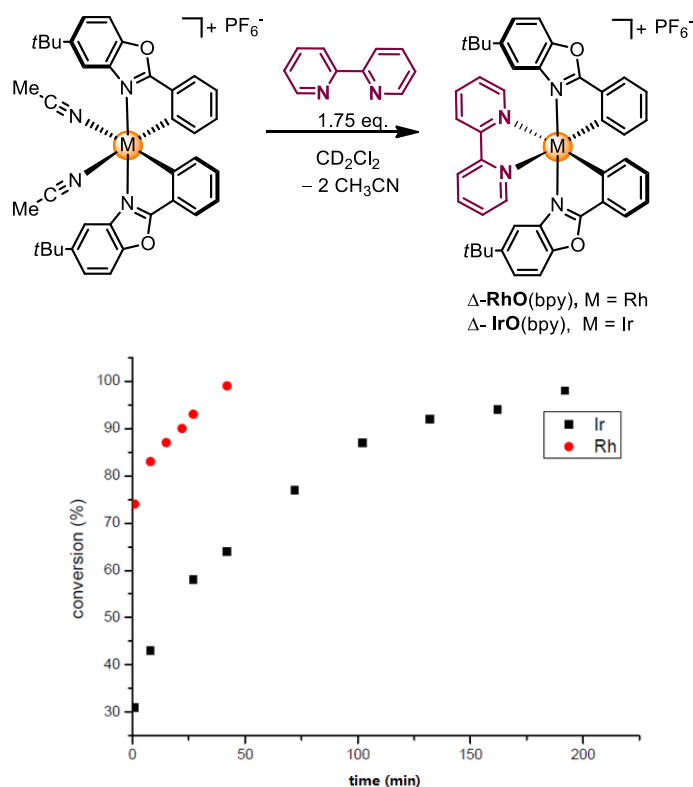


Figure 37 The acetonitrile exchange experiments of $\Delta\text{-RhO}$ and $\Delta\text{-IrO}$ in the presence of bipyridine.

It is therefore plausible that the superior catalytic activity of the more coordinatively labile $\Delta\text{-RhO}$ over the more inert $\Delta\text{-IrO}$ for the Michael additions with β -dicarbonyl compounds is due to substrate coordination and/or release being the rate limiting steps in the catalytic cycle, while it is the nucleophile addition step for the Friedel-Crafts reaction in which the aromaticity of the pyrrole ring is lost temporary in the course of the addition. The observed higher turnover frequencies for the rhodium-catalyzed Michael additions may also contribute to the observed higher enantioselectivities since a higher turnover frequency suppresses the undesired, uncatalyzed background reaction.¹⁰

3.1.5 Conclusions

In conclusion, the first example of an asymmetric catalyst which derives both its optical activity and Lewis acidity from an octahedral rhodium stereocenter was developed. This novel, configurationally surprisingly stable chiral Lewis acid is conceptually very simple, as it just contains achiral mono- and bidentate ligands, and it can be accessed conveniently in an enantiomerically pure fashion through a proline-mediated synthesis. Interestingly, although isostructural to its iridium congener, the two homologs differ significantly in their catalytic Lewis acid activity, with the rhodium complex demonstrating advantages as catalyst for the Michael addition of CH-acidic β -dicarbonyl compounds to α,β -unsaturated 2-acyl imidazoles and the cascade reaction of α,β -unsaturated 2-acyl imidazole with malononitrile and diethyl azodicarboxylate. The superiority of the rhodium catalyst over its iridium congener can in large parts be attributed to a significantly higher lability of the two accessible rhodium coordination sites which allow higher turnover frequencies and turnover numbers.

References

- 1 Selected reviews and accounts covering aspects of chiral Lewis acid catalysis: a) K. Narasaka, *Synthesis* **1991**, 1–11; b) S. Saito, H. Yamamoto, *Chem. Commun.* **1997**, 1585–1592; c) K. A. Jørgensen, M. Johannsen, S. Yao, H. Audrain, J. Thorhauge, *Acc. Chem. Res.* **1999**, *32*, 605–613; d) J. S. Johnson, D. A. Evans, *Acc. Chem. Res.* **2000**, *33*, 325–335; e) G. Desimoni, G. Faita, K. A. Jørgensen, *Chem. Rev.* **2006**, *106*, 3561–3651; f) S. Kobayashi, C. Ogawa, *Chem. Eur. J.* **2006**, *12*, 5954–5960; g) S. Kanemasa, M. Hasegawa, F. Ono, *Chem. Rec.* **2007**, *7*, 137–149; h) J. Christoffers, G. Koripelly, A. Rosiak, M. Rössle, *Synthesis* **2007**, 1279–1300; i) M. North, D. L. Usanov, C. Young, *Chem. Rev.* **2008**, *108*, 5146–5226; j) S. Liao, X.-L. Sun, Y. Tang, *Acc. Chem. Res.* **2014**, *47*, 2260–2272.
- 2 H. Huo, C. Fu, K. Harms, E. Meggers, *J. Am. Chem. Soc.* **2014**, *136*, 2990–2993.
- 3 a) M. Helms, Z. Lin, L. Gong, K. Harms, E. Meggers, *Eur. J. Inorg. Chem.* **2013**, 4164–4172; b) L. Gong, M. Wenzel, E. Meggers, *Acc. Chem. Res.* **2013**, *46*, 2635–2644; c) C. Fu, M. Wenzel, E. Treutlein, K. Harms, E. Meggers, *Inorg. Chem.* **2012**, *51*, 10004–10011.
- 4 For reports on non-racemic, chiral octahedral rhodium(III) complexes, see: a) A. H. Krotz, L. Y. Kuo, T. P. Shields, J. K. Barton, *J. Am. Chem. Soc.* **1993**, *115*, 3877–3882; b) A. Sitlani, C. M. Dupureur, J. K. Barton, *J. Am. Chem. Soc.* **1993**, *115*, 12589–12590; c) L. Ghizdavu, B. Kolp, A. von Zelewsky, H. Stoeckli-Evans, *Eur. J. Inorg. Chem.* **1999**, 1271–1279; d) L. Ghizdavu, A. von Zelewsky, H. Stoeckli-Evans, *Eur. J. Inorg. Chem.* **2001**, 993–1003; e) L. Ghizdavu, O. Lentzen, S. Schumm, A. Brodkorb, C. Moucheron, A. Kirsch-De Mesmaeker, *Inorg. Chem.* **2003**, *42*, 1935–1944; f) N. Yoshinari, T. Konno, *Inorg. Chem.* **2008**, *47*, 7450–7452; g) S. Mollin, S. Blanck, K. Harms, E. Meggers, *Inorg. Chim. Acta* **2012**, *393*, 261–268.
- 5 Enol oxazolines and thiazolines as chiral auxiliaries, see B. Huang, L. Wang, L. Gong, E. Meggers, *Chem Asian J.* **2013**, *9*, 2274–2280.
- 6 P. Müller, A. Ghanem, *Org. Lett.* **2004**, *6*, 4347–4350.
- 7 Y. Wang, H. Lu, P.-F. Xu, *Acc. Chem. Res.* **2015**, *48*, 1832–1844.
- 8 C. Wang, L.-A. Chen, H. Huo, X. Shen, K. Harms, L. Gong, E. Meggers, *Chem. Sci.* **2015**, *6*, 1094–1100.

3.2 Merger of Visible Light Induced Oxidation and Enantioselective Alkylation with Chiral Iridium Catalyst

3.2.1 Reaction design

The development of methods for fundamental functionalizations, as well as protocols for the construction of chiral molecules is an ongoing challenge. Recently, the Meggers group reported for the first time that a single chiral-at-metal complex Δ -IrS can serve as an effective catalyst for the visible light induced enantioselective α -alkylation of 2-acyl imidazoles with electron deficient benzyl bromides and phenacyl bromides under reductive activation.¹ We were wondering whether this class of chiral iridium catalysts could also be capable of catalyzing asymmetric photoredox processes which instead proceed through oxidative chemistry. As shown in Figure 38, the designed reaction of the electrophilic iminium ion with the nucleophilic iridium enolate complex might produce a non-racemic compound. We hypothesized the intermediate iridium enolate complex could provide the crucial asymmetric induction as well as serve as the active photocatalytic species.

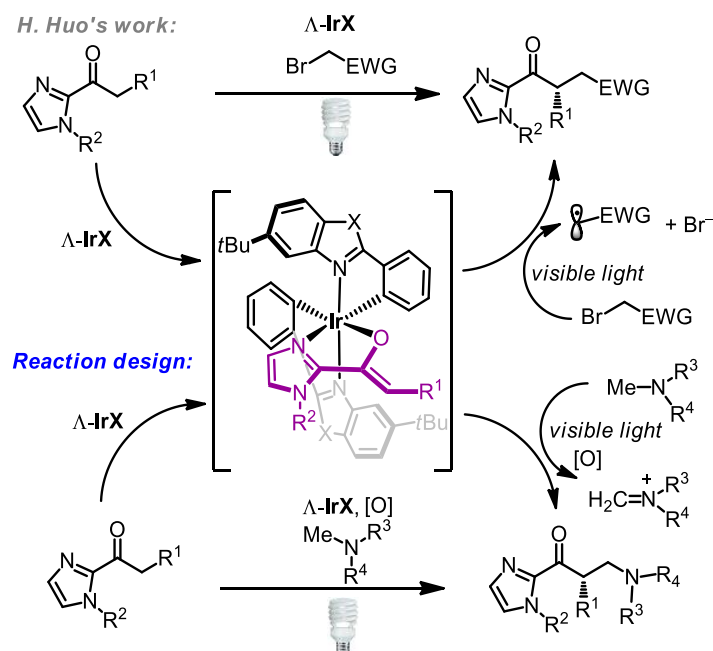


Figure 38 Reaction design for photoactivated asymmetric catalysis with chiral iridium(III) Lewis acids.

3.2.2 Initial Experiments and Reaction Optimization

The initial experiments were inspired by Stephenson and co-workers, who utilized the oxidation of *N*-phenyl tetrahydroisoquinolines with bromotrichloromethane (BrCCl_3) to generate the iminium ion under photoredox conditions.² This study was started by investigating the reaction of 2-acyl imidazole **7a''** with dimethylaniline ($E_{\text{ox}} \approx +0.78 \text{ V vs. SCE}$)³ and carbon tetrabromide (CBr_4) under visible light irradiation. In the presence of the previously developed dual function photoredox/chiral Lewis acid catalyst $\Delta\text{-IrO}$ (3 mol%), the expected C-C bond formation product **8** was obtained in 34% yield after irradiation of 16 h (Figure 39). However, racemization was observed in the course of the reaction. The enantioselectivity of product **8** was dropped dramatically from 96% to 0% *ee* during the reaction time from 1 h to 16 h. Control experiment in the absence of iridium catalyst showed that about 10% of *rac*-**8** was observed after 16 h of the reaction. As the product **8** is stable in the solution, the observed racemization phenomenon might be explained by the reversibility of this Mannich reaction.⁴

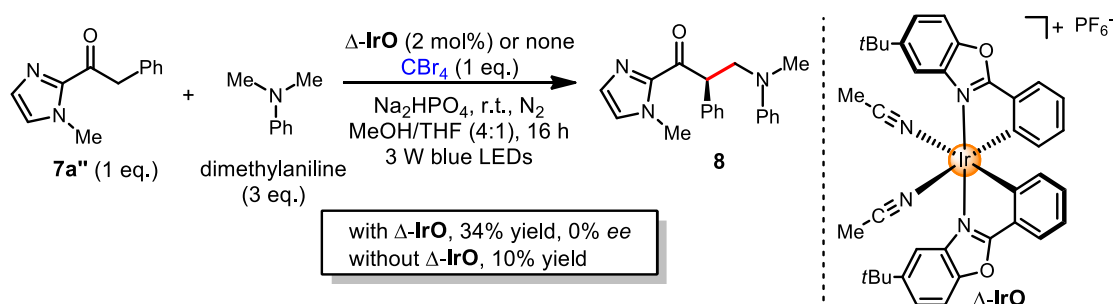
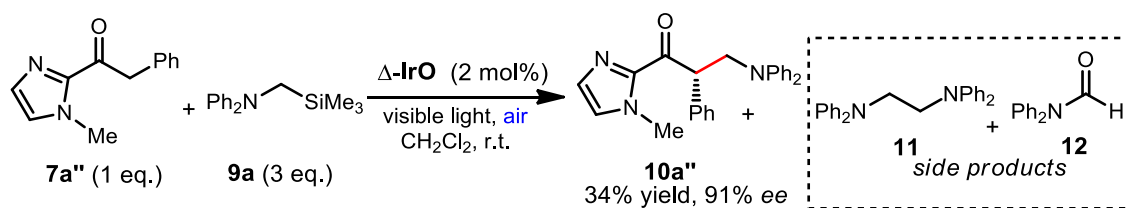


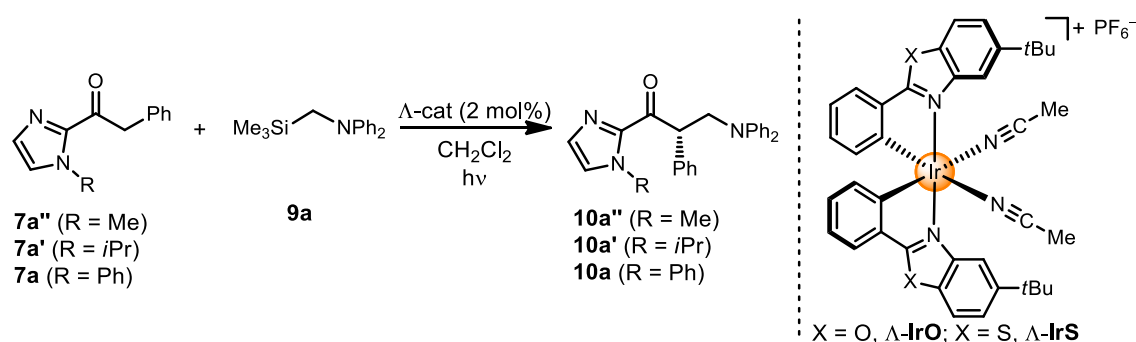
Figure 39 Asymmetric photoactivated α -aminoalkylation of 2-acyl imidazole **7a''** with dimethylaniline.

To get non-racemic product under mild conditions, we next used α -silylamines ($E_{\text{ox}} \approx +0.44 \text{ V vs. NHE}$) as precursors. The silyl group in α -silylamines not only serves as a redox handle to facilitate a single electron oxidation, but also results in a subsequent rapid cleavage of the C-Si bond under release of α -aminoalkyl radicals, which then be involved in iminium chemistry after further oxidation.⁴ Thus, the reaction of 2-acyl imidazole **7a''** and *N,N*-diphenyl-*N*-(trimethylsilyl)methylamine **9a** was carried out in the presence of the enantiomerically pure iridium complex $\Delta\text{-IrO}$ (2 mol%), while exposed to air (Scheme 3). Encouragingly, irradiation with visible light in form of a standard 12 W energy saving household lamp for 20 h afforded the expected product **10a''** in 34% yield and 91% *ee*. However, the reaction is not straightforward and the intermediate α -aminoalkyl radical can either form a dimer **11** via homocoupling or be oxidized to form amide **12** in the presence of oxygen.² The isolated side products, on the other hand, provide good evidence in support of a radical pathway of the reaction.



Scheme 3 Asymmetric photoactivated α -aminoalkylation of 2-acyl imidazole **7a''** with α -silylamine **9a**.

Improved results were obtained after the modification of the 2-acyl imidazole substrate (Table 5). Accordingly, replacing the *N*-methyl imidazole moiety (**7a''**) with *N*-isopropyl imidazole (**7a'**) provided the aminoalkylation product **10a'** with an increased yield of 48% and 90% *ee* after 20 h of irradiation (entries 1 and 2). However, the best results were obtained with the *N*-phenyl imidazole substrate **7a**, giving 92% yield and 97% *ee* after just 6.5 h of photolysis (entry 3). Notably, excess α -silylamine **9a** is crucial for high yield of the product (entries 4 and 5). Control experiments in the absence of catalyst (no reaction) or performed in the dark (very sluggish and incomplete reaction after an elongated reaction time of 48 h) reveal that it is the combination out of chiral iridium complex Δ -IrO and visible light that is required for an efficient reaction (entries 6 and 7). It is also worth noting that the catalyst Δ -IrS,¹ which was found superior for the reported asymmetric photo-reductive C-C bond formation, turned out to be inferior for the here investigated photo-oxidative activation (entry 8 compared to entry 3).

Table 5 Optimization of the enantioselective photoactivated α -aminoalkylation of 2-acyl imidazoles.^a

entry	substrate	catalyst	$h\nu^b$	ratio of 7 and 9a	t (h)	yield (%) ^c	ee (%) ^d
1 ^e	7a''	Δ - IrO	yes	1:3	20	34	91
2	7a'	Δ - IrO	yes	1:3	20	48	90
3	7a	Δ - IrO	yes	1:3	6.5	92	97
4	7a	Δ - IrO	yes	1:2	20	71	97
5	7a	Δ - IrO	yes	2:1	20	49	97
6	7a	none	yes	1:3	20	0	n.d.
7	7a	Δ - IrO	no	1:3	48	18	94
8	7a	Δ - IrS	yes	1:3	20	51	97

^a Reaction conditions: Reactions performed in CH_2Cl_2 (0.5 mL) with 2-acyl imidazole (0.2 or 0.4 mmol) and α -silylamine **9a** (0.2 or 0.4 or 0.6 mmol) in the presence of catalyst (2 mol% or none) at room temperature under an atmosphere of air. ^b 12 W white light energy saving lamp. ^c Isolated yield. ^d Determined by chiral HPLC analysis. ^e Shown for comparison. n.d. = not determined.

3.2.3 Substrate Scope

After the optimized conditions were identified, the scope of the asymmetric photoinduced α -aminoalkylation with catalyst Δ -**IrO** was then tested. Figure 40 shows that the reaction of a variety of 2-acyl imidazoles with N,N -diaryl- N -(trimethylsilyl)methylamines in the presence of Δ -**IrO** (2-4 mol%) and under air while illuminating with visible light provided the expected alkylation products in 61-93% yields and with excellent enantioselectivities of 90-98% ee . The 2-acyl- N -phenyl imidazole substrates tolerate steric (products **10b** and **10c**), electron donating (product **10d**) and electron accepting (product **10e**) substituents in the phenyl moiety, and it can be replaced by the heteroaromatic thiophene (product **10f**). Furthermore, a 2-propionic imidazole (product **10g**) as well as a 2-butyric imidazole (product **10h**) were aminoalkylated in the α -position of the carbonyl group with high enantioselectivities, although an increased catalyst loading of 4 mol% and more active silylmethylamine are required to achieve

satisfactory results. With respect to silyl methylamines, different substituents are tolerated in the phenyl groups (**10i-k**), and one phenyl can be replaced by a naphthyl group (**10l**).

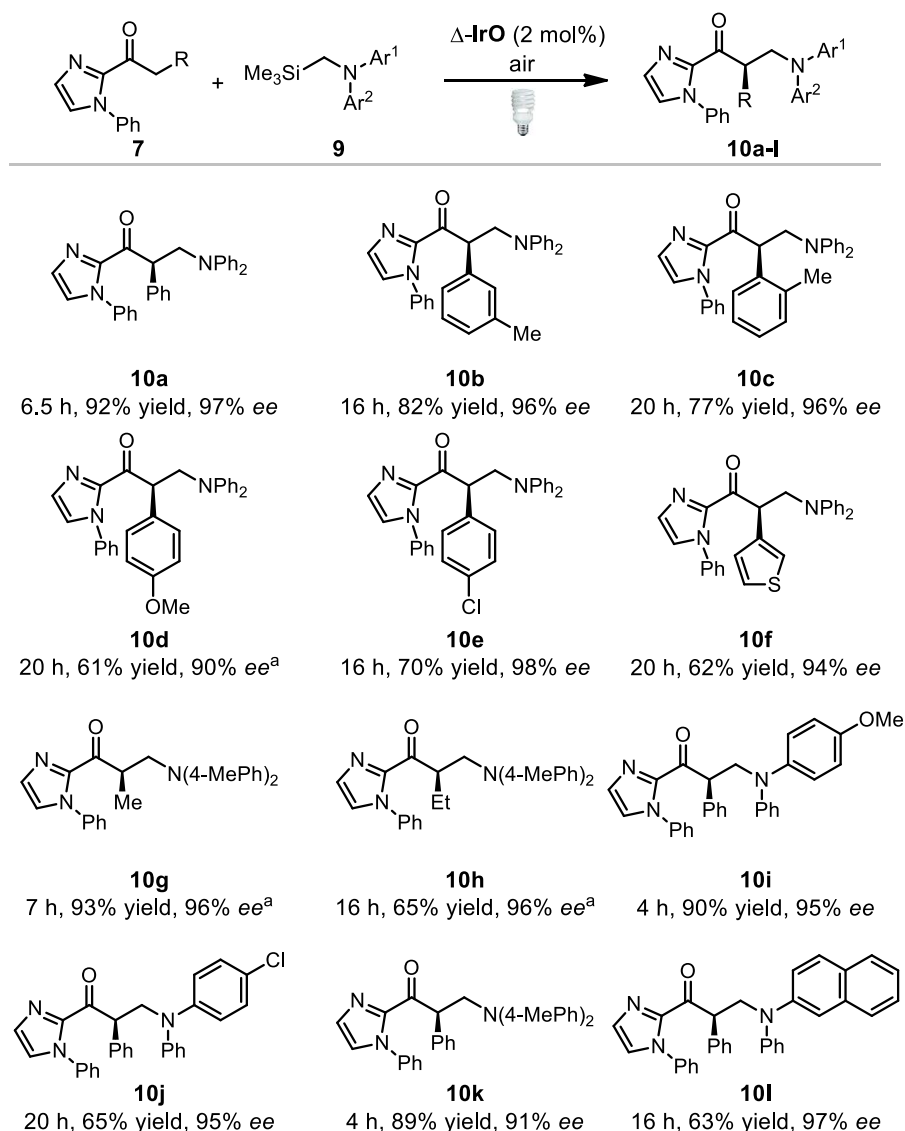


Figure 40 Substrate scope of the asymmetric photoinduced α -aminoalkylation. ^a Catalyst loading of 4 mol%.

Unfortunately, the application of this α -aminoalkylation technology to other substrates did not succeed (Figure 41). The α -silyl and the two aryl groups are required for this transformation. When one aryl group was replaced by aliphatic group (methyl, isopropyl or n-butyl group), both the yields and enantioselectivities dropped dramatically. Without α -silyl group or one aryl group was replaced by electron-withdrawing group (-COOMe), the expected product was not observed under the standard conditions. However, with additional 1.2 equivalent of oxidant CBr_4 , the C-C bond formation product was obtained, albeit in a low yield. These results support that the α -silyl and two aryl groups are crucial

for reducing the oxidation potential of amines.⁴

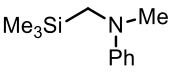
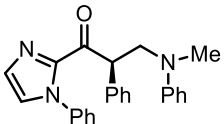
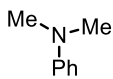
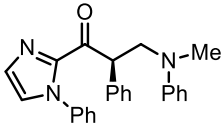
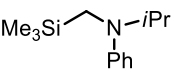
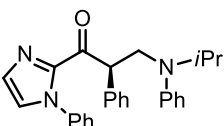
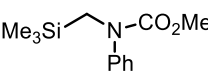
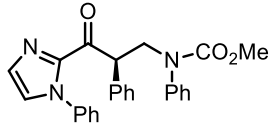
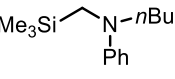
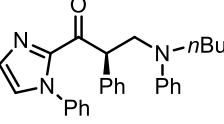
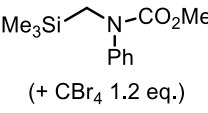
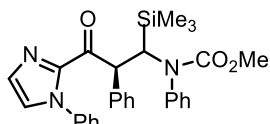
<i>Substrate</i>	<i>Product</i>	<i>Substrate</i>	<i>Product</i>
	 20 h, 54% yield, 45% ee		 not observed
	 20 h, 27% yield, 15% ee		 not observed
	 20 h, 17% yield, n.d. ee	 (+ CBr ₄ 1.2 eq.)	 16 h, 25% yield, n.d. ee

Figure 41 Some limitations of the substrate scope with respect to silyl methylamines. n.d. = not determined.

3.2.4 Plausible Mechanism

A plausible mechanism in which photoredox catalysis intertwines with asymmetric catalysis is outlined in Figure 42. Herein, the catalytic cycle is initiated upon coordination of the 2-acyl imidazole substrate **7** to the iridium complex $\Delta\text{-IrO}$ in a bidentate fashion under release of the two labile monodentate acetonitrile ligands to provide the substrate coordinated intermediate **A**. The subsequent reversible deprotonation in α -position of the carbonyl group affords the nucleophilic iridium enolate intermediate **B**. Meanwhile, an electrophilic iminium ion is generated by an iridium-photoinduced oxidation of the α -silylamine **9** with oxygen serving as the terminal oxidant according to the generally accepted photoredox catalysis cycle.⁵ The reaction of the iminium ion with the iridium enolate complex **B** occurs in a stereocontrolled fashion dictated by the metal-centered chirality and provides the iridium coordinated product **C**, which is subsequently released the product **10** upon coordination to a new substrate molecule **7**, thereby initiating a new catalytic cycle. A series of investigations have been executed to verify the proposed mechanism in the following section.

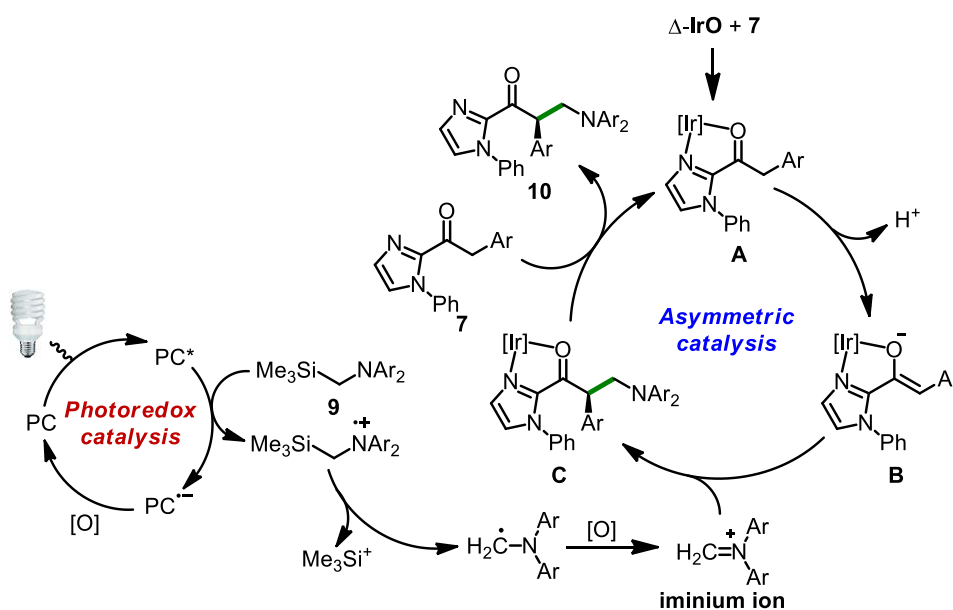


Figure 42 Plausible mechanism for the photoinduced asymmetric catalysis. PC = iridium photoredox catalyst, most likely intermediates **A** and **C**. [O] = oxidant in form of molecular oxygen and superoxide anion.

3.2.5 Mechanistic Investigations

1) Crystal structure analysis

The catalytic cycle was firstly investigated by verifying the involvement of the proposed iridium intermediate **A** and enolate intermediate **B**. Accordingly, upon reaction of an excess substrate **7a** with racemic Δ/Λ -IrO we could isolate the proposed intermediate **A** and subsequent deprotonation generated intermediate enolate **B** (Ar = Ph). A crystal structure of enolate intermediate **B** is shown in Figure 43 and reveals that a Λ -configuration at the iridium center shields the *Si*-face of the α -enolate carbon and directs the addition of the electrophile to the *Re*-face, thereby being consistent with the observed *S*-configuration of the alkylation product when using the catalyst with Λ -configuration at the metal.

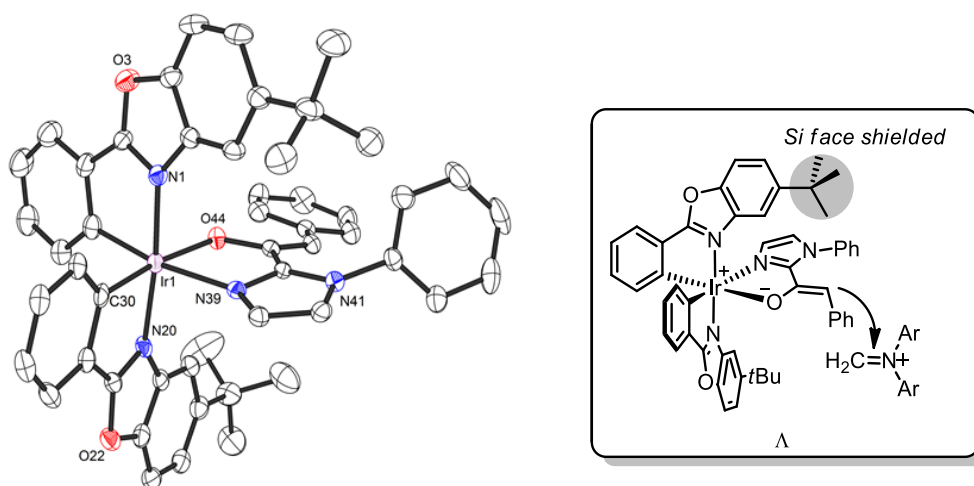


Figure 43 Crystal structure of the proposed complex **B** (left) and proposed model for the asymmetric photoinduced α -aminoalkylation (right).

2) Evaluating the Catalytic Activities of Complexes A and B

It is safe to assume that at the beginning of the reaction, due to the bidentate nature of the 2-acyl imidazole substrate and a high substrate/catalyst ratio of 50, all iridium catalyst will be captured by the imidazole substrate, while an equilibrium may exist between the cationic intermediate **A** and the deprotonated enolate intermediate **B**.⁶ The involvement of the enolate complex **B** as a photoredox catalyst in this reaction was excluded based on a simple experiment which is outlined in Figure 44. The replacement of Δ -IrO with the enolate complex **B** showed that it was not capable of catalyzing the photoinduced reaction at all, whereas on the other hand the cationic intermediate **A** displayed almost the same catalytic activity compared to Δ -IrO. Thus, the substrate-coordinated intermediate **A** must be the

active photoredox catalyst at the beginning of the reaction, probably complemented later by the related product-coordinated intermediate **C**.

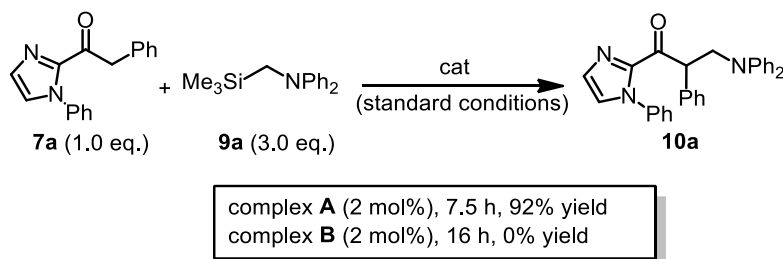
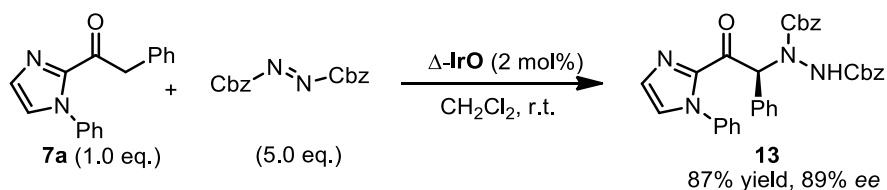


Figure 44 Evaluating the catalytic activities of complexes **A** and **B**.

3) Control experiments

Enolate chemistry

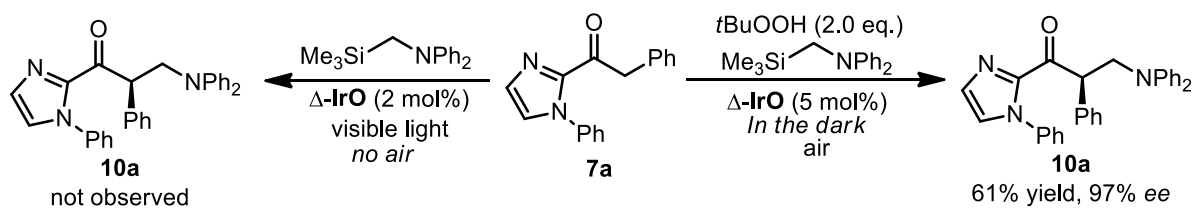
The involvement of an enolate complex **B** in the catalytic cycle is further supported by a reaction of **7a** with the electrophile dibenzyl diazodicarboxylate catalyzed by Δ -**IrO** which afforded the α -amination product **13** in 87% yield and 89% *ee*, apparently through the intermediate formation of a nucleophilic iridium enolate complex (Scheme 4). Thus, Δ -**IrO** is capable of catalyzing enolate chemistry as has been recently also demonstrated for a related iridium and rhodium complex⁷ and the observed enantioselective C-C bond formation can be explained with the stereoselective reaction between the chiral iridium enolate **B** and an intermediate iminium ion.



Scheme 4 The control experiment with dibenzyl diazodicarboxylate.

Iminium chemistry

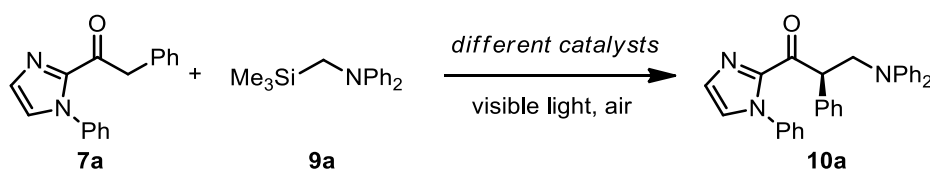
The formation of the electrophile through chemical oxidation –replacing the photoinduced oxidation– also provides the desired C-C bond formation product in an enantioselective fashion as shown for the oxidant *t*BuOOH (Scheme 5). The oxidative formation of the iminium ion intermediate starting from the oxidation of α -silylamine along the pathway of photoinduced single electron oxidation with a photoredox catalyst, followed by rapid desilylation, and further oxidation by air is well established⁸ and consistent with the observation that the absence of air completely suppresses the formation of the desired product.⁹



Scheme 5 The control experiments with *t*BuOOH in the dark or without air.

4) The replacement of iridium catalyst $\Delta\text{-IrO}$ with a dual catalyst system

Next, the requirement for a photoredox process was verified. We thereby exploited the circumstance that, in contrast to biscyclometalated iridium complexes which are well established photoredox catalyst, there are few cases for the analogous rhodium complex $\Delta\text{-RhO}$.¹⁰ The replacement of iridium in catalyst $\Delta\text{-IrO}$ with rhodium $\Delta\text{-RhO}$ therefore allows us to dissect the catalytic and photoredox activity of $\Delta\text{-IrO}$. Accordingly, the reaction of imidazole **7a** with amine **9a** in the presence of $\Delta\text{-RhO}$ (2 mol%) under irradiation with visible light provided the C-C bond formation product **10a** only in very low yield (6% after an elongated reaction time, compare entries 1 and 2 of Table 6). Revealingly, when combined $\Delta\text{-RhO}$ with the established photoredox catalyst $[\text{Ir}(\text{ppy})_2(\text{dtbbpy})]\text{PF}_6$ (1.0 mol%)¹¹ or $[\text{Ru}(\text{bpy})_3]\text{Cl}_2 \cdot 6\text{H}_2\text{O}$ (0.5 mol%),¹² the reaction provided the product **10a** with good conversions and high enantioselectivities. Consistent with our proposed mechanism, neither the Lewis acid catalyst $\Delta\text{-RhO}$ (entry 2) nor photocatalyst (entries 3 and 4) alone are capable of catalyzing the asymmetric photoreaction, apparently because asymmetric enolate catalysis and photoinduced amine oxidation have to proceed hand in hand, which can be achieved with a dual catalyst system (entries 5 and 6) or even more efficiently with the single catalyst $\Delta\text{-IrO}$. It is also worth noting that the weaker photooxidant but highly efficient singlet oxygen sensitizer *meso*-tetraphenylporphyrin (TPP)¹³ provides only a reduced yield of 30% after an elongated reaction time (entry 7), thereby supporting the notion that singlet oxygen does not have a major contribution to the observed oxidation of the α -silylamines in this reaction scheme.

Table 6 Single versus dual catalysis for the photoactivated α -aminoalkylation of 2-acyl imidazoles.^a

entry	catalyst	<i>t</i> (h)	conv.(%) ^b	<i>ee</i> (%) ^c
1 ^d	Δ - IrO (2.0 mol%)	6.5	quant.	97
2	Δ - RhO (2.0 mol%)	16	6	n.d.
3	[Ir(ppy) ₂ (dtbbpy)]PF ₆ (1.0 mol%)	16	0	n.d.
4	[Ru(bpy) ₃]Cl ₂ ·6H ₂ O (0.5 mol%)	16	0	n.d.
5	Δ - RhO (2.0 mol%) + [Ir(ppy) ₂ (dtbbpy)]PF ₆ (1.0 mol%)	24	84	94
6	Δ - RhO (2.0 mol%) + [Ru(bpy) ₃]Cl ₂ ·6H ₂ O (0.5 mol%)	24	72	94
7	Δ - RhO (2.0 mol%) + TPP ^e (0.5 mol%)	24	30	90

^a Reaction conditions: Reactions performed in CH₂Cl₂ (0.5 mL) with 2-acyl imidazole **7a** (0.2 mmol) and α -silylamine **9a** (0.6 mmol) at room temperature under an atmosphere of air while illuminating with a 12 W white light energy saving lamp. ^b Determined by ¹H NMR. ^c Determined by chiral HPLC analysis; ^d Shown for comparison. ^e *meso*-Tetraphenylporphyrin. n.d. = not determined.

5) UV/Vis-absorption spectra

The absorbance spectra of the substrate **7a** coordinated iridium complex **A** (Ar = Ph) and catalyst *rac*-**IrO** were measured in solution of CH₂Cl₂. As shown in Figure 45, the intermediate **A** absorbs visible light with a longer wavelength absorbance band in the visible region ($\lambda_{\text{max,abs}} = 398$ nm) compared to catalyst *rac*-**IrO** ($\lambda_{\text{max,abs}} = 375$ nm).

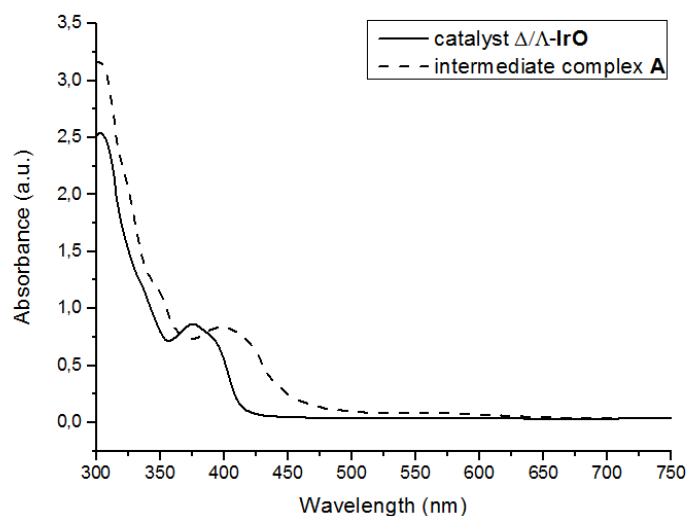


Figure 45 UV/Vis-absorbance spectra of intermediate complex **A** and racemic catalyst Δ/Δ -**IrO**. Measured as solution in CH₂Cl₂. a.u. = absorbance units.

6) Luminescence quenching experiments

In order to further verify the potential photoredox catalyst involving in the photoredox cycle, *rac*-**IrO** and intermediate **A** and $[\text{Ir}(\text{ppy})_2(\text{dtbbpy})]\text{PF}_6$ were selected to perform the luminescence quenching experiments with quencher **9a** (Figure 46). Notably, $[\text{Ir}(\text{ppy})_2(\text{dtbbpy})]\text{PF}_6$ is a photoredox catalyst that has been used for the photo-oxidative cleavage of C-Si bond.^{5e} The iridium complex **A** photoluminescence ($\lambda_{\text{max,em}} = 516$ and 552 nm) is efficiently quenched by the α -silylamine **9a** in a dose dependent fashion as shown with a Stern-Volmer plot compared to catalyst *rac*-**IrO** and $[\text{Ir}(\text{ppy})_2(\text{dtbbpy})]\text{PF}_6$, which can be explained by a quenching of the excited state of **A** through electron transfer from the electron donor **9a**.

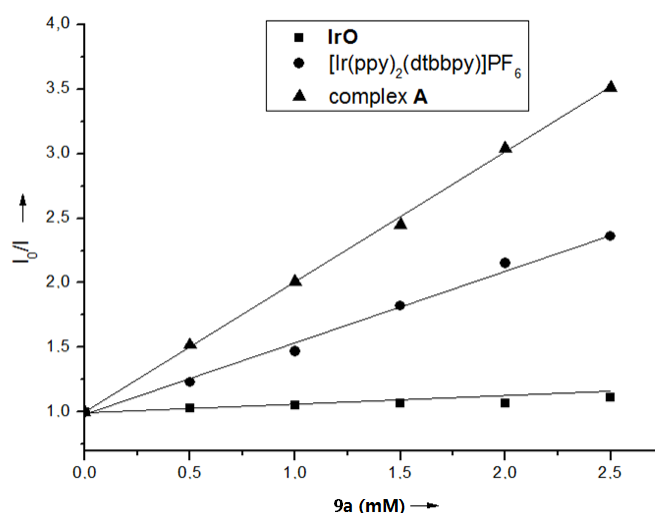


Figure 46 Stern-Volmer plots. I_0 and I = luminescence intensities in the absence and presence of the indicated concentrations of the α -silylamine **9a**, respectively. All experiments were performed in CH_2Cl_2 .

7) Cyclic voltammetry measurements

The cyclic voltammetry was tested by Philipp Röse, a graduate student in Prof. Hilt group (Department of Chemistry, University of Marburg). From the DPV in combination with the emission spectrum (Figure 47), the excited state reduction potential ($E_{\text{red}}^* = E_{\text{red}} + E^{00}$) of complex **A** (Ar = Ph) can be estimated according to the Rehm-Weller approximation, with the E^{00} transition energy calculated from the luminescence peak ($\lambda_{\text{max,em}} = 516$ nm, 2.403 eV) and E_{red} from DPV measurements (-0.98 V vs. Ag/AgCl): $E_{\text{red}}^* = \approx +1.4$ V vs. Ag/AgCl in THF.

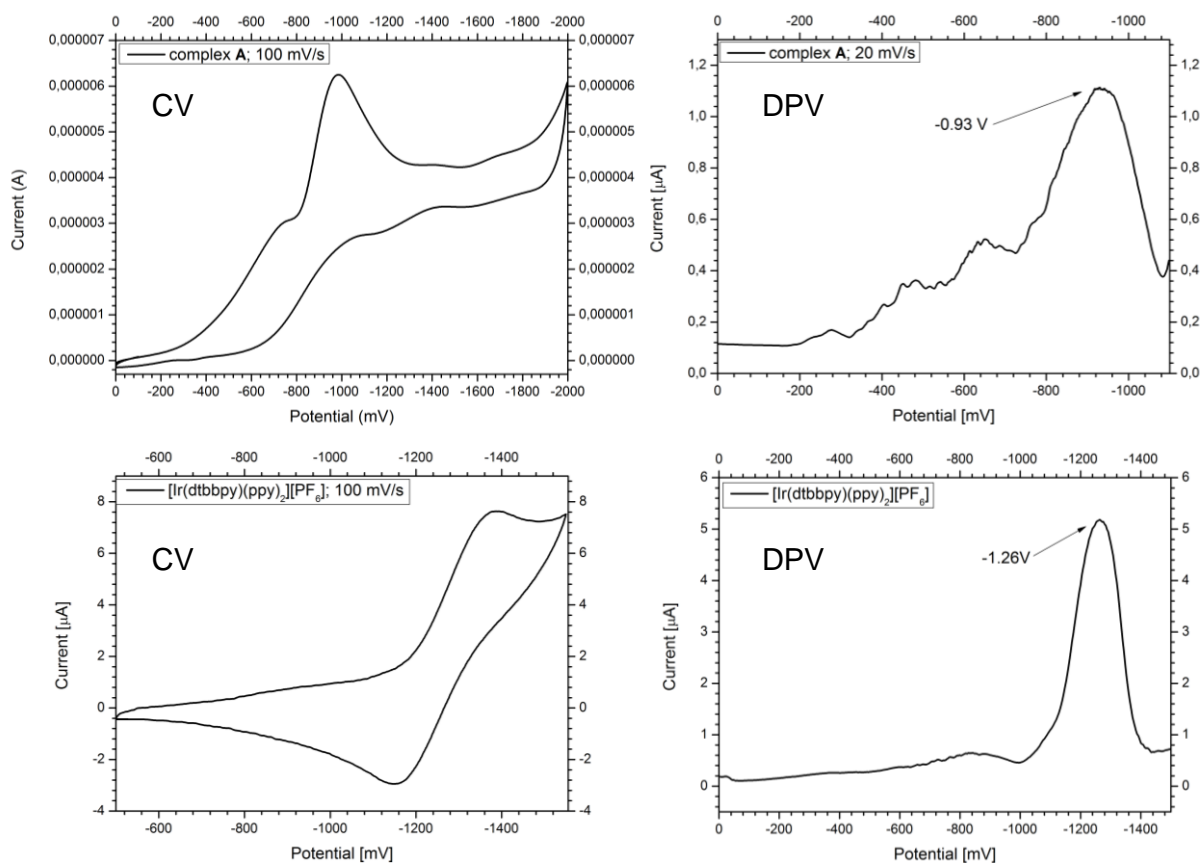


Figure 47 Cyclic voltammograms (CV) and differential pulse voltammograms (DPV) of the complex **A** and the reference iridium complex $[\text{Ir}(\text{ppy})_2(\text{dtbbpy})]\text{PF}_6$ in THF containing 0.1 M $n\text{Bu}_4\text{NBF}_4$.

3.2.6 Conclusions

In conclusion, a visible light activated asymmetric aerobic α -aminoalkylation of 2-acyl imidazoles has been developed. From the perspective of the catalyst, it is intriguing that the metal center is capable of serving multiple functions at the same time: it constitutes the exclusive center of chirality, the catalytically active Lewis acid center, and additionally functions as the key component of the photoredox catalyst that is formed in situ. From the perspective of the catalytic reaction, the photo-oxidative activation and net oxidation of the here featured asymmetric catalysis complements our previous work on a redox neutral reaction in which the photoactivation occurred in a reductive fashion. It is fascinating that the metal-centered configuration (the exclusive source of chirality in the catalyst) retains throughout the catalysis, considering the oxidative conditions and the exposure to light. This conceptionally simple reaction scheme may provide new avenues for the green synthesis of non-racemic molecules.

References

- 1 H. Huo, X. Shen, C. Wang, L. Zhang, P. Röse, L.-A. Chen, K. Harms, K. Marsch, G. Hilt, E. Meggers, *Nature* **2014**, *515*, 100–103.
- 2 a) P. J. DeLaive, B. P. Sullivan, T. J. Meyer, D. G. Whitten, *J. Am. Chem. Soc.* **1979**, *101*, 4007–4008; b) J. Hu, J. Wang, T. H. Nguyen, N. Zheng, *Beilstein J. Org. Chem.* **2013**, *9*, 1977–2001; c) J. W. Beatty, C. R. J. Stephenson, *Acc. Chem. Res.* **2015**, *48*, 1474–1484.
- 3 S. Zbaida, W. G. Levine, *Chem. Res. Toxicol.* **1991**, *4*, 82–88.
- 4 B. Cooper, W. Owen, *J. Organomet. Chem.* **1971**, *29*, 33–40.
- 5 a) U. C. Yoon, P. S. Mariano, *Acc. Chem. Res.* **1992**, *25*, 233–240; b) G. Pandey, *Synlett* **1992**, 546–552; c) P. Renaud, L. Giraud, *Synthesis* **1996**, 913–926; d) M. Schmittel, A. Burghart, *Angew. Chem. Int. Ed. Engl.* **1997**, *36*, 2550–2589; e) Y. Miyake, Y. Ashida, K. Nakajima, Y. Nishibayashi, *Chem. Commun.* **2012**, *48*, 6966–6968; f) Y. Miyake, Y. Ashida, K. Nakajima, Y. Nishibayashi, *Chem. Eur. J.* **2014**, *20*, 6120–6125.
- 6 H. Huo, C. Fu, K. Harms, E. Meggers, *J. Am. Chem. Soc.* **2014**, *136*, 2990–2993.
- 7 C. Wang, L.-A. Chen, H. Huo, X. Shen, K. Harms, L. Gong, E. Meggers, *Chem. Sci.* **2015**, *6*, 1094–1100.
- 8 a) J.-i. Yoshida, S. Isoe, *Tetrahedron Lett.* **1987**, *28*, 6621–6624; b) E. Meggers, E. Steckhan, S. Blechert, *Angew. Chem. Int. Ed. Engl.* **1995**, *34*, 2137–2139.
- 9 The involvement of H₂O₂ in this process can be excluded since a reaction in the presence of H₂O₂ as an oxidant afforded the desired product only in low yields and with low enantiomeric excess (13% conversion after 16 h with 47% *ee*).
- 10 a) Y. Tan, W. Yuan, L. Gong, E. Meggers, *Angew. Chem. Int. Ed.* **2015**, *54*, 13045–13048; b) X. Shen, K. Harms, M. Marsch, E. Meggers, *Chem. Eur. J.* **2016**, *22*, 9102–9105.
- 11 [Ir(ppy)₂(dtbbpy)]⁺: $E_{\text{red}}^* = +0.66$ vs. SCE. See: M. S. Lowry, J. I. Goldsmith, J. D. Slinker, R. Rohl, R. A. Pascal, G. G. Malliaras, S. Bernhard, *Chem. Mater.* **2005**, *17*, 5712–5719.
- 12 [Ru(bpy)₃]²⁺: $E_{\text{red}}^* = +0.77$ vs. SCE. See: K. Kalyanasundaram, *Coord. Chem. Rev.* **1982**, *46*, 159–244.
- 13 TPP: $E_{\text{red}}^* = +0.62$ V vs. NHE (corresponds to +0.38 V vs. SCE). See: J. R. Darwent, P. Douglas, A. Harriman, G. Porter, M.-C. Richoux, *Coord. Chem. Rev.* **1982**, *44*, 83–126.

3.3 Asymmetric Radical-Radical Cross-Coupling through Visible Light Activated Iridium Catalysis

3.3.1 Reaction Design

A single chiral-at-metal iridium complex Δ -IrO has been proven to be very efficient dual function catalyst in visible light induced enantioselective α -aminoalkylation of 2-acyl imidazoles with silylmethylamines (chapter 3.2).¹ Despite its novelty, one may criticize that it is not atom economical reaction as a trimethylsilyl (TMS) group is released during the formation of α -aminoalkylation product. In this case, commercially available or easily prepared tertiary amines are more favorable as reducing agents in photoredox chemistry. Compared with the well established iminium ion, the application of α -aminoalkyl radical to asymmetric coupling reaction or nucleophilic addition under photoredox conditions still remains challenging (Figure 48).²

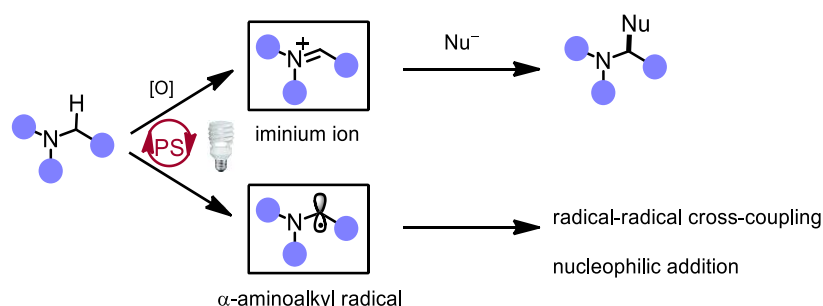


Figure 48 Two possible pathways for α -C(sp³)-H bond functionalization of tertiary amines by photoredox catalysis.

On the other hand, the enantioselective radical-radical cross-coupling reaction, which is used as a powerful tool for asymmetric transformations, still remains in its infancy when compared with other highly developed reactions.³ Normally, in order to control the selective bond formation, a persistent radical and a transient radical should be engaged in the radical-radical cross-coupling reaction according to the persistent radical effect.⁴ Therefore, we envisioned that it is possible to transfer the reactive ketyl radical to a persistent one by stabilizing it through coordination to the chiral iridium Lewis acid catalyst after protonation. Then, once a transient carbon-centered radical is added, a selective radical-radical cross-coupling reaction could be achieved. Herein, we designed a catalytic and asymmetric process that closely interlocks a visible light activated single electron transfer between two substrates with the stereocontrolled radical-radical cross-coupling of an intermediate radical pair, namely the

enantioselective redox coupling of ketones with tertiary amines to 1,2-diaminoalcohols (Figure 49). A big challenge is whether the α -amino radical and ketyl radical could be simultaneously generated in a single photoredox catalytic cycle.

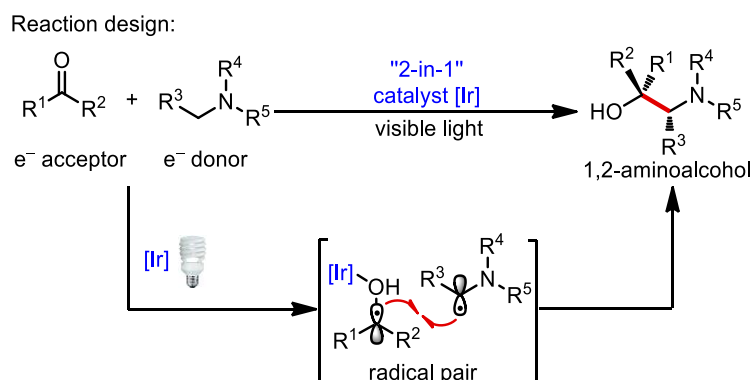


Figure 49 Linking (photoinduced) single electron transfer between a donor substrate and an acceptor substrate to asymmetric radical-radical recombination with a single iridium catalyst.

3.3.2 Initial Experiments and Reaction Optimization

The study was started by investigating the reaction of 2-acetyl imidazole **14a'** with tertiary amine **15a** under photoredox conditions (Table 7). In the presence of the previously developed dual function photoredox/chiral Lewis acid catalyst Δ -**IrO**¹ (3 mol%) under irradiation with a 23 W compact fluorescent lamp (CFL), the desired product **16a'** was not observed (entry 1). Encouragingly, using instead the more electron-deficient trifluoroacetyl imidazole **14a** provided the coupling product **16a** with 69% yield and 95% *ee* (entry 2). Replacing the solvent CH_2Cl_2 with CHCl_3 improved the yield to 75%, albeit under the cost of slightly reduced enantioselectivity (entry 3). The reaction is very sensitive to solvent effect and other tested solvents did not provide satisfactory results (entries 4-6). With the catalyst Δ -**IrS** instead of Δ -**IrO**, yields and enantioselectivities could be further enhanced (entries 7 and 8). In CHCl_3 , 82% yield and excellent 98.6% *ee* were observed. Effects of *N*-substitutions on the 2-acyl imidazoles were also investigated (entries 9-11) and the best results were still obtained with the *N*-phenyl imidazole substrate **14a**. Control experiments in the absence of the catalyst or in the dark demonstrate that this reaction crucially depends on the presence of the iridium catalyst and light, otherwise no traces of product were monitored (entries 12 and 13). It is also worth noting that no C-C coupling product is formed when using the common photoredox catalyst $[\text{Ru}(\text{bpy})_3]\text{Cl}_2 \cdot 6\text{H}_2\text{O}$ or $[\text{Ir}(\text{ppy})_2(\text{dtbbpy})]\text{PF}_6$ or a dual catalyst system combining $[\text{Ir}(\text{ppy})_2(\text{dtbbpy})]\text{PF}_6$ and Δ -**RhO** (entries 14-16).⁵

Table 7 Initial experiments and optimization of the visible light induced asymmetric C-C bond formation.^a

15a

16

R¹ = Ph, R² = CH₃ (**14a'**)
 R¹ = Ph, R² = CF₃ (**14a**)
 R¹ = Me, R² = CF₃ (**14b'**)
 R¹ = 4-FC₆H₄, R² = CF₃ (**14c'**)
 R¹ = 4-OMeC₆H₄, R² = CF₃ (**14d'**)

X=O: Δ-IrO, X=S: Δ-IrS

entry	sub.	catalyst	$h\nu^b$	solvent	yield (%) ^c	ee (%) ^d
1	14a'	Δ-IrO (3.0)	CFL	CHCl ₃	0	n.d.
2	14a	Δ-IrO (3.0)	CFL	CHCl ₃	75	95
3	14a	Δ-IrO (3.0)	CFL	CH ₂ Cl ₂	69	97
4	14a	Δ-IrO (3.0)	CFL	EtOAc	42	68
5	14a	Δ-IrO (3.0)	CFL	toluene	30	11
6	14a	Δ-IrO (3.0)	CFL	MeCN	0	n.d.
7	14a	Δ-IrS (3.0)	CFL	CH ₂ Cl ₂	72	98.9
8	14a	Δ-IrS (3.0)	CFL	CHCl ₃	82	98.6
9	14b'	Δ-IrS (3.0)	CFL	CHCl ₃	40	98
10	14c'	Δ-IrS (3.0)	CFL	CHCl ₃	66	90
11	14d'	Δ-IrS (3.0)	CFL	CHCl ₃	67	92
12	14a	Δ-IrS (3.0)	none	CHCl ₃	0	n.d.
13	14a	none	CFL	CHCl ₃	0	n.d.
14	14a	[Ru(bpy) ₃]Cl ₂ ·6H ₂ O (0.5)	CFL	CHCl ₃	0	n.d.
15	14a	[Ir(ppy) ₂ (dtbbpy)]PF ₆ (1.0)	CFL	CHCl ₃	0	n.d.
16	14a	[Ir(ppy) ₂ (dtbbpy)]PF ₆ (1.0) + Δ-RhO (3.0)	CFL	CHCl ₃	0	n.d.

^a Reaction conditions: 2-acyl imidazoles **14** (0.2 mmol), amine **15a** (0.6 mmol), and catalyst (entries 1-13, **16**: 3.0 mol%, entry 14: 0.5 mol%, entry 15: 1.0 mol%) in the indicated solvent (0.4 mL) irradiated for 22 h under an atmosphere of nitrogen at room temperature. ^b Light source: 23 W compact fluorescent lamp (CFL) at a distance of approximately 5 cm from the Schlenk tube. ^c Isolated yields. ^d Determined by HPLC on chiral stationary phase. n.d. = not determined.

3.3.3 Substrate Scope

Having identified the optimal conditions for this visible light activated asymmetric aminoalkylation of trifluoromethyl ketones, the scope of the amine partner was first examined (Figure 50). The reactions between 2-trifluoroacetyl imidazole **14a** and various *N*-methyl-diarylamines (**15a-h**) provided the respective 1,2-aminoalcohols (**16a-h**) in satisfactory yields (60-82%) and with high enantioselectivities (91-98% *ee*). Crystal structure of **16g** was obtained to determine the absolute configuration of the products. However, the two aryl groups, which reduce the oxidation potential of amines, are required for obtaining satisfactory results. When one aryl group was replaced by heterocyclic group (-Py) or aliphatic group (-Me), the C-C bond formation products were obtained with very low yields (Figure 51). It is noteworthy that we found empirically that certain reactions provide better results under white light irradiation (CFL), whereas others prefer blue light (blue LEDs).

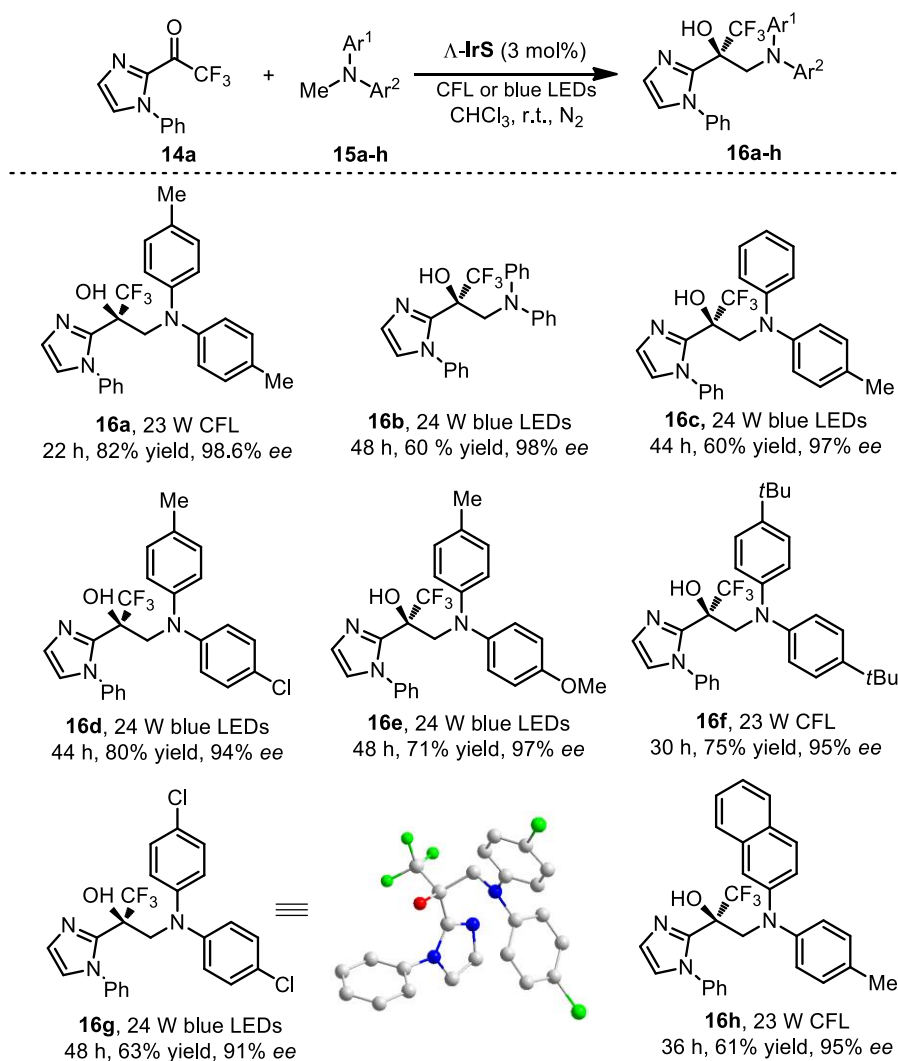


Figure 50 Substrate scope with respect to *N*-methyl-diarylamines.

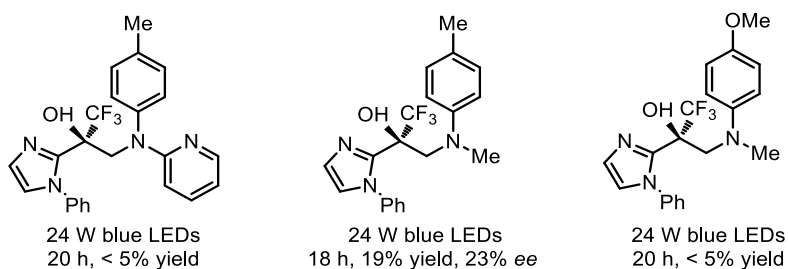


Figure 51 Some limitations of substrate scope with respect to amines.

Cyclic tertiary amines are relatively simple to synthesize and have been successfully utilized in the α -amino radical chemistry to generate α -heteroaryl amines by MacMillan and other research groups.⁶ Herein, the reaction of substrate **14a** with 2-phenylisoindoline was investigated. However, the expected α -aminoalkylation product was not observed. Encouragingly, by using a more reactive *N*-phenyl tetrahydroisoquinoline as radical precursor, the C-C bond formation product **18a** was obtained with diastereoselectivity of 3:1 *dr* and enantioselectivity of 72% *ee* (the major diastereoisomer), and at a catalyst loading of 5 mol%, even 8:1 *dr* and 94% *ee* were reached (Figure 52).

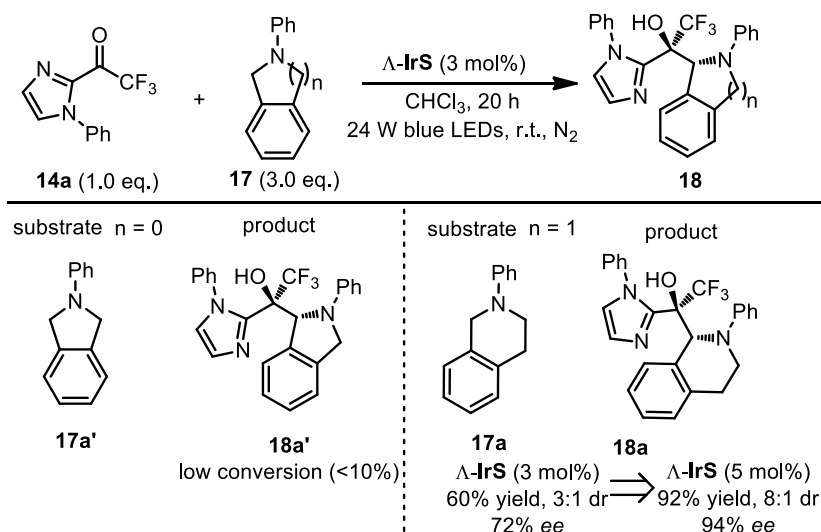


Figure 52 Reaction condition screening of cyclic tertiary amines.

Thus, the substrate scope with respect to *N*-aryl tetrahydroisoquinolines was tested by using 5 mol% Δ -IrS (Figure 53). As expected, a series of C-C bond formation products (**18a-f**) were obtained with good diastereoselectivities (4:1 to 10:1 *dr*) and high enantioselectivities (94-98% *ee*) (Figure 53). Notably, a bromine (Br) substituent promoted the product excellent yield and enantioselectivity. However, a *p*-methoxyphenyl (PMP) substituent, which serves as a well-established protecting group for the nitrogen atom,⁷ can not be used here because of the limited stability of the product.

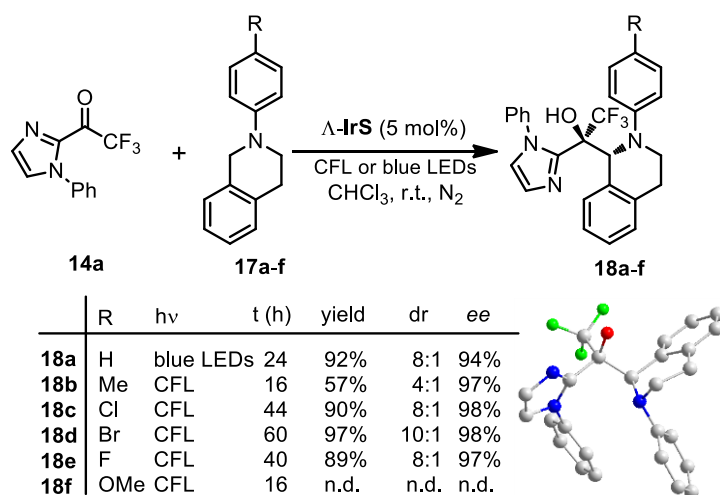


Figure 53 2-Aryl-1,2,3,4-tetrahydroisoquinolines as amine substrates for enantio- and diastereoselective reactions. Relative configurations are assigned based on a crystal structure of **18a**. n.d. = not determined.

Another interesting aspect to investigate with this aminoalkylation chemistry would be to extend the imidazole moiety to other coordination groups. Herein, 2-acyl pyridines were chosen due to the prevalence of pyridines and piperidines in bioactive compounds.⁸ The reaction of 2-trifluoroacetyl pyridine with amine **15a** in the presence of catalyst Δ -IrS (3 mol%) under irradiation with a 24 W blue LEDs afforded the coupling product **20a** with 74% yield and 93% *ee*. Steric effect of the pyridine substrates in this asymmetric aminoalkylation was then investigated. By using pyridine substrate with methyl substitute group at 4 and 5-position, the C-C bond coupling products **20b** and **20c** were afforded with moderate yields and good enantioselectivities, while 3-position substituted pyridine substrate was failed to convert to the desired product **20d** efficiently. Further investigation of other coordination groups, such as thiazole and ester, did not give any satisfactory results (Figure 54).

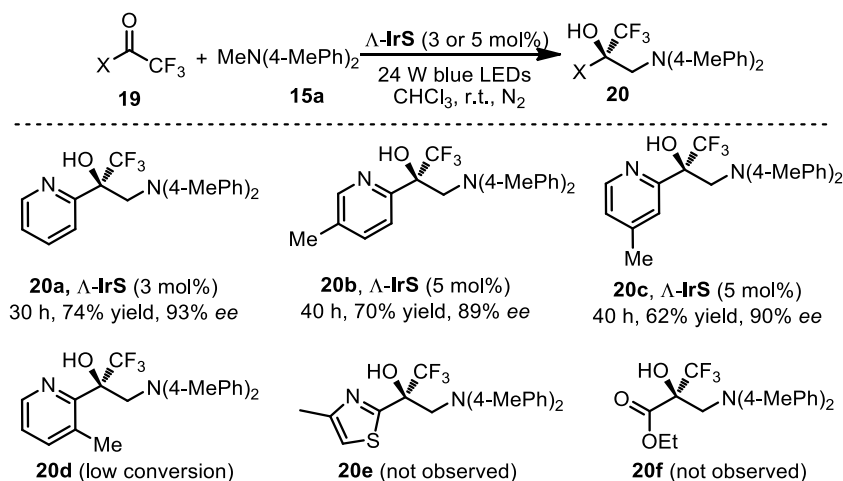


Figure 54 Asymmetric C-C bond cross coupling with other coordination groups.

3.3.4 Plausible Mechanism

A plausible mechanism is shown in Figure 55. The catalytic process starts with the photoactivation of the iridium-coordinated trifluoromethyl ketone **I** to its excited state **II** (step 1), which induces a single electron transfer from a tertiary amine, thereby generating an amino radical cation in addition to a reduced iridium complex which can be described as an iridium-coordinated ketyl radical **III** (step 2). This is followed by a proton transfer (step 3) and a radical-radical cross-coupling between the electron-rich α -amino radical and the electron-deficient ketyl **IV** (step 4) which is stereochemically controlled by the chiral iridium complex **V**. Finally, the product is replaced by a new substrate (step 5). Several investigations have been executed to verify the proposed mechanism in the following section.

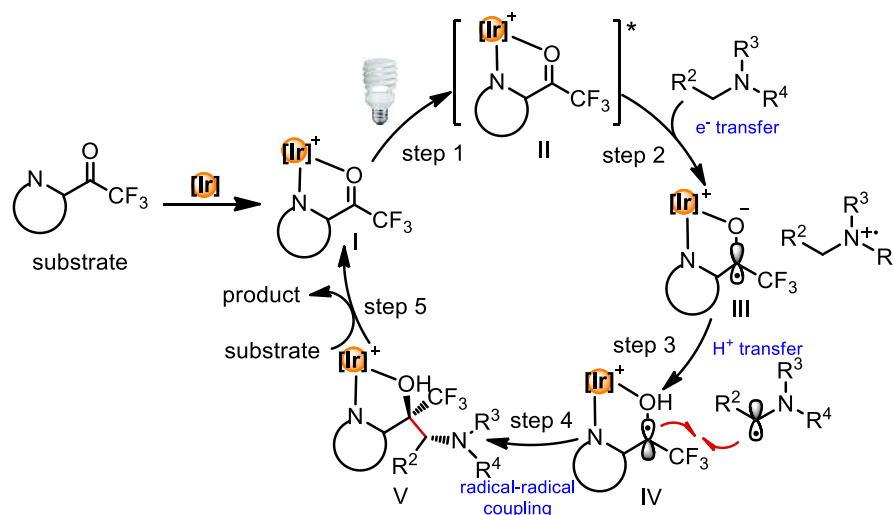


Figure 55 Putative mechanism for the visible light activated catalytic asymmetric process.

3.3.5 Mechanistic Investigations

1) Substrate-coordinated iridium complex **IrS-I**

To start with, the iridium intermediate complex **IrS-I** was synthesized by reacting of substrate **14a** with Δ/Λ -**IrS** in toluene/ CHCl_3 at 50 °C overnight. The freshly prepared complex **IrS-I** catalyzed the photoinduced C-C bond coupling reaction with an almost identical efficiency compared to Δ/Λ -**IrS** (Figure 56). In addition, the absorbance spectra of racemic Δ/Λ -**IrS** and intermediate complex **IrS-I** were measured in solution of CHCl_3 (0.2 mM). As shown in Figure 57, compared to Δ/Λ -**IrS**, the complex **IrS-I** displays a bathochromically shifted long wavelength absorbance maximum with an additional shoulder at around 600 nm. With the efficient catalytic reactivity and good absorption property, complex **IrS-I** is most likely the active photoredox catalyst in the catalytic cycle mentioned above.

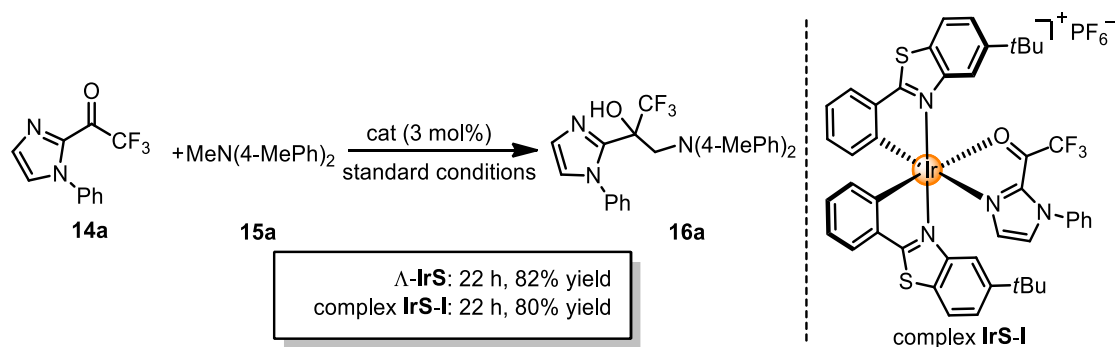


Figure 56 Evaluation of the catalytic activity of intermediate complex **IrS-I**.

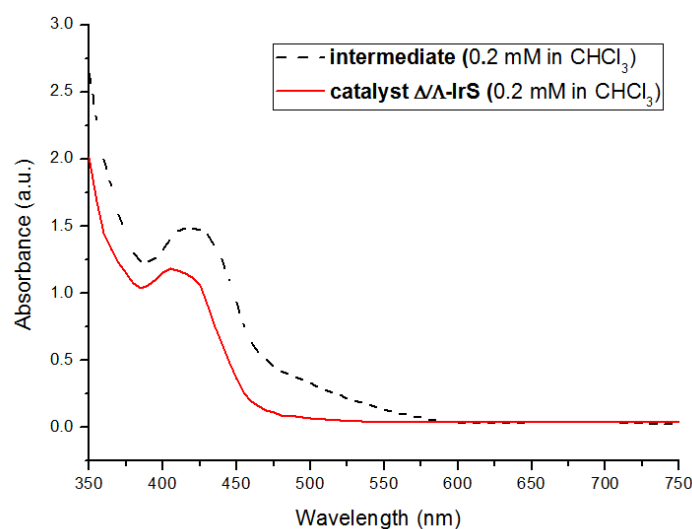
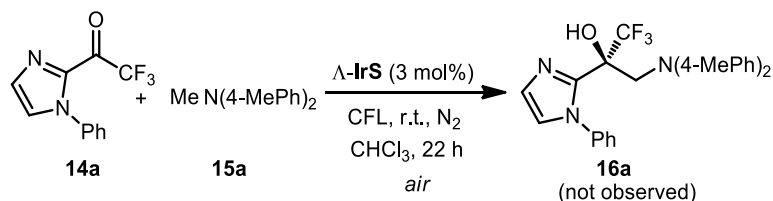


Figure 57 UV/Vis-absorbance spectra of Δ/Λ -**IrS** and intermediate complex **IrS-I**. Measured in solution of CHCl_3 (0.2 mM). a.u. = absorbance units.

2) Control experiments

Control experiment in the presence of air

The reaction was performed in a 10 mL test tube under an atmosphere of air (air balloon), no C-C coupling product was formed (detected by crude ^1H NMR of the mixture after 22 h of irradiation), being consistent with the presence of intermediate radicals which react with oxygen in a diffusion controlled fashion.



Scheme 6 Control experiment in the presence of air.

Control experiment in the dark with chemical initiator

Can the reaction be chemically initiated, potentially with a chemical one-electron oxidant? If so, a reaction conducted in the dark but in the presence of the iridium complex as a Lewis acid might be able to determine whether there is turnover (a chain) or not.⁹ Thus, the reaction was performed in the dark in the presence of catalyst $\Delta/\Delta\text{-IrS}$ and one-electron oxidant, like Cp_2FePF_6 , $(\text{BrC}_6\text{H}_4)_3\text{NSbCl}_6$ and $\text{Ce}(\text{NH}_4)_2(\text{NO}_3)_6$. However, no C-C bond coupling product **16a** was detected by ^1H NMR after stirring at room temperature for 22 h. It provides good evidence that no chain process exists in the catalytic cycle (Figure 58).

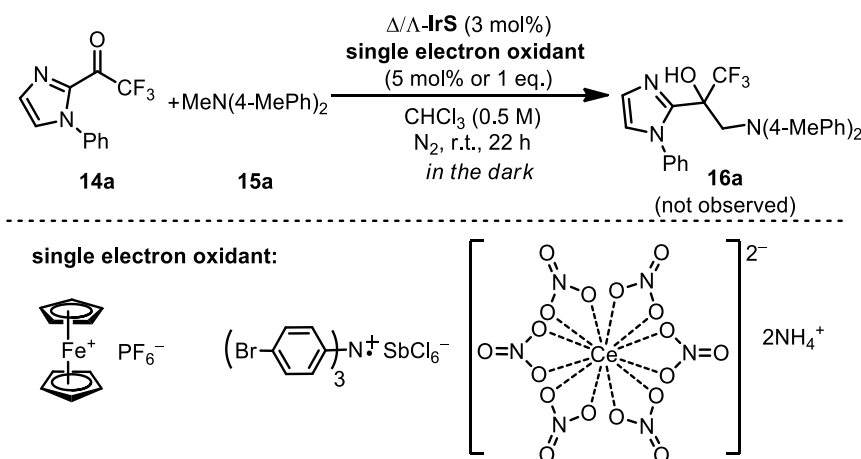


Figure 58 Control experiment in the dark with chemical initiators.

3) Trapping experiments

Trapping experiments of α -aminomethyl radical

Trapping experiments of electron-rich α -aminomethyl radicals have been well established.¹⁰ In the presence of dibenzyl azodicarboxylate, a hydrazone C-N coupling product is formed in high yield which can be traced back to a reaction of the proposed intermediate (nucleophilic) α -aminomethyl radical with the (electrophilic) N=N double bond, followed by reduction and protonation. Likewise, in the presence of EWG-alkene acrylonitrile or methyl acrylate, the addition/cyclization product **22a** or **22b** together with **16a** are afforded, which again provide good evidence to demonstrate the existence of α -aminomethyl radical (Figure 59).

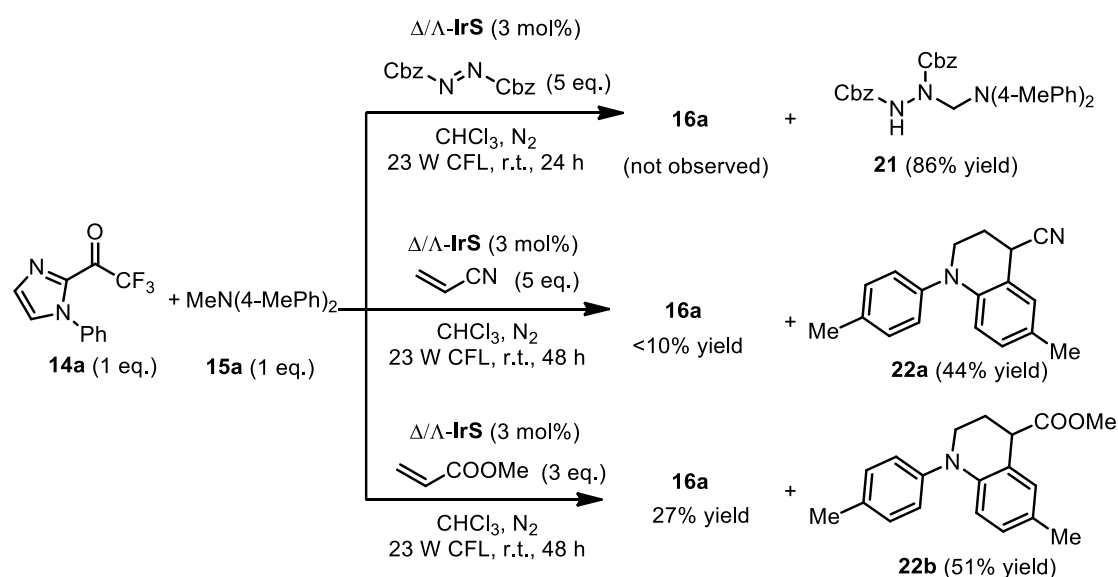
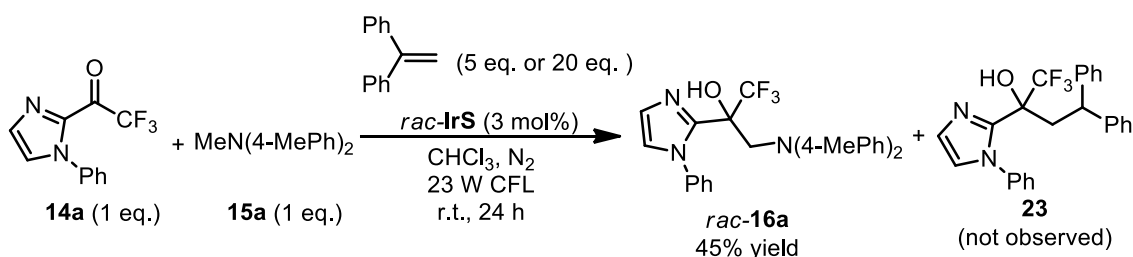


Figure 59 Trapping experiments of α -aminomethyl radical.

Trapping experiment of ketyl radical

Pinacol coupling product was not observed from the model reaction which probably because the resulting stabilized ketyl radical **III** is a persistent radical that possesses relatively little propensity towards homodimerization.⁴ To capture the ketyl radical, electron rich alkene, ethene-1,1-diylidibenzene, was used under the modified reaction conditions. Unfortunately, only the aminoalkylation product **16a** was observed (Scheme 7). Since the evidence of ketyl radical is limited, radical addition pathway which electron-rich α -aminomethyl radical adds to the iridium-coordinated electron-deficient C=O double bond could not be completely excluded.¹¹



Scheme 7 Trapping experiment of ketyl radical in the presence of ethene-1,1-diyldibenzene.

4) Quantum yield

The quantum yield was measured by standard ferrioxalate actinometry. The relevant data was collected and calculated by Xiaodong Shen (a former Ph.D. student in the Meggers group). The moles of products formed were determined by crude ^1H NMR. The quantum yield of the model reaction **14a** + **15a** \rightarrow **16a** with ferrioxalate actinometry was determined to be 0.09. A quantum yield of ≤ 1 in agreement with the expected closed catalytic cycle. According to the control experiments in the presence of chemical one-electron oxidants and quantum yield, it is safety to say that no chain process is possible with one photon being required for each C-C bond formation event.¹²

5) Stereochemistry model

The photogenerated α -amino radical interacts with the persistent ketyl radical within the chiral environment of the iridium complex, which provides impressively high enantioselectivity. The observed absolute configuration of the C-C bond coupling reaction, providing *S*-configuration at the carbon next to the OH group when using Λ -**IrS**, is consistent with this mechanistic picture in which the prochiral *Si*-face of the iridium-coordinated ketyl is effectively shielded by one *tert*-butyl group of the propeller-type ligand sphere, providing an excellent stereochemical control of the radical process (Figure 60).

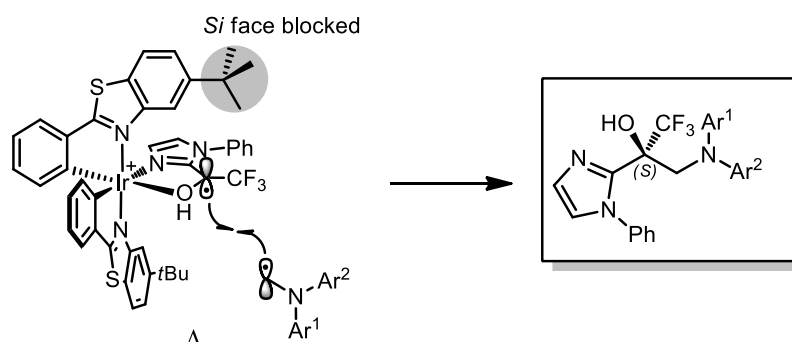


Figure 60 Model for the asymmetric induction in the course of the radical-radical recombination shown for selected substrates.

3.3.6 Conclusions

In conclusion, a unique catalytic asymmetric process in which a visible light driven single electron transfer reaction between a donor substrate and a catalyst-bound acceptor substrate is followed by a stereocontrolled radical-radical recombination was introduced. Using a chiral iridium complex as dual chiral Lewis acid/photoredox catalyst, 1,2-aminoalcohols are synthesized from trifluoromethylketones and tertiary amines with high enantioselectivities of up to 99% *ee*. Such non-racemic CF₃-containing compounds might be useful building blocks for the synthesis of bioactive compounds.¹⁷ It is also worth noting that this mild method follows the spirit of sustainable chemistry, not only because the activation energy is provided by visible light as an abundant light source, but also since in the course of the C-C bond formation with the implementation of one or two new stereocenters, no waste products are generated, thereby constituting a perfect atom economy.

References

- 1 H. Huo, X. Shen, C. Wang, L. Zhang, P. Röse, L.-A. Chen, K. Harms, K. Marsch, G. Hilt, E. Meggers, *Nature* **2014**, *515*, 100–103.
- 2 C. Wang, Y. Zheng, H. Huo, P. Röse, L. Zhang, K. Harms, G. Hilt, E. Meggers, *Chem. Eur. J.* **2015**, *21*, 7355–7359.
- 3 L. J. Rono, H. G. Yayla, D. Y. Wang, M. F. Armstrong, R. R. Knowles, *J. Am. Chem. Soc.* **2013**, *135*, 17735–17738.
- 4 H. Fischer, *Chem. Rev.* **2001**, *101*, 3581–3610.
- 5 C. Wang, L.-A. Chen, H. Huo, X. Shen, K. Harms, L. Gong, E. Meggers, *Chem. Sci.* **2015**, *6*, 1094–1100.
- 6 a) A. G. Condie, J. C. González-Gómez, C. R. J. Stephenson, *J. Am. Chem. Soc.* **2010**, *132*, 1464–1465; b) M. Rueping, C. Vila, R. M. Koenigs, K. Poschary, D. C. Fabry, *Chem. Commun.* **2011**, *47*, 2360–2362; c) P. Kohls, D. Jadhav, G. Pandey, O. Reiser, *Org. Lett.* **2012**, *14*, 672–675; d) D. P. Hari, B. König, *Org. Lett.* **2011**, *13*, 3852–3855; e) A. Noble, D. W. C. MacMillan, *J. Am. Chem. Soc.* **2014**, *136*, 11602–11605; f) C. K. Prier, D. W. C. MacMillan, *Chem. Sci.* **2014**, *5*, 4173–4178; g) M. H. Shaw, V. W. Shurtleff, J. A. Terrett, J. D. Cuthbertson, D. W. C. MacMillan, *Science* **2016**, *352*, 1304–1308.
- 7 J. M. M. Verkade, L. J. C. Hemert, P. J. L. M. Quaedflieg, P. L. Alsters, F. L. Delfta, F. P. J. T. Rutjesa, *Tetrahedron Lett.* **2006**, *47*, 8109–8113.
- 8 Pyridine and its derivatives in heterocycles in natural product synthesis: K. C. Majumdar, S. K. Chattopadhyay, Eds. Wiley-VCH: Weinheim, **2011**, Chapter 8, 267.
- 9 D. A. Khobragade, S. G. Mahamulkar, L. Pospíšil, I. Císařová, L. Rulíšek, U. Jahn, *Chem. Eur. J.* **2012**, *18*, 12267–12277.
- 10 Y. Miyake, K. Nakajima, Y. Nishibayashi, *Chem. Eur. J.* **2012**, *18*, 16473–16477.
- 11 L. Ruiz Espelt, I. S. McPherson, E. M. Wiensch, T. P. Yoon, *J. Am. Chem. Soc.* **2015**, *137*, 2452–2455.
- 12 For a recent discussion of closed catalytic cycles versus chain processes in photoredox reactions, see: a) M. D. Kärkäs, B. S. Matsuura, C. R. J. Stephenson, *Science* **2015**, *34*, 1285–1286; b) M. A. Cismesia, T. P. Yoon, *Chem. Sci.* **2015**, *6*, 5426–5434.

3.4 Catalytic Asymmetric C(sp³)-H Functionalization under Photoredox Conditions by Radical Translocation and Stereocontrolled Alkene Addition

3.4.1 Reaction Design

In chapter 3.3, we developed a catalytic asymmetric C(sp³)-H functionalization protocol that allows tertiary amines to undergo α -aminoalkylation of trifluoromethyl ketones to achieve 1,2-diamino alcohols (through radical-radical cross-coupling). Besides the functional group at its α -position, there are many other powerful strategies that have been emerged for the functionalization of C(sp³)-H bonds.¹

Recently, Chen and co-workers introduced a visible light induced release of alkoxy radicals from *N*-alkoxyphthalimides and applied it to the selective C(sp³)-H functionalization by exploiting an 1,5-hydrogen atom transfer (1,5-HAT).² Radical translocation³ has been used extensively for the functionalization of remote C(sp³)-H bonds, but to our knowledge the combination with a catalytic asymmetric C-C bond formation remains elusive. Therefore, we envisioned to merge this photoredox-mediated C-H functionalization with asymmetric catalysis as shown in Figure 61 by trapping the intermediate (electron rich) carbon-centered radical in a stereocontrolled fashion with an acceptor-substituted alkene catalyzed by a chiral Lewis acid. Challenges include the compatibility of the individual steps with respect to the reactivity of the radical intermediates and the kinetics of the individual steps, as well as the ability to control the relative and absolute stereochemistry of the radical reaction in a catalytic fashion.

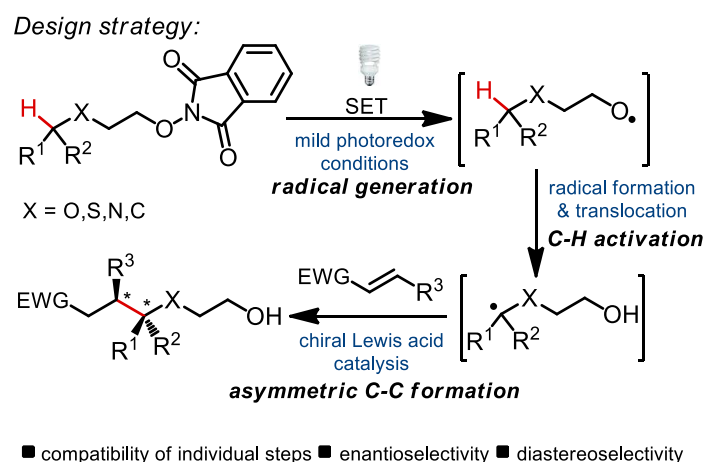


Figure 61 Reaction design of photoredox-mediated C-H functionalization with asymmetric catalysis.

3.4.2 Initial Experiments and Reaction Optimization

This study was started by investigating the reaction of α,β -unsaturated acyl imidazole **24a'** with *N*-alkoxyphthalimide **25a** and Hantzsch ester (HE) under photoredox conditions. In the presence of the previously developed dual function photoredox/chiral Lewis acid catalyst Δ -**IrS**⁴ (3 mol%), to our disappointment, the desired product **26a'** was not achieved. Encouragingly, when α,β -unsaturated acyl pyrazole **24a** was used as a Michael acceptor instead, the C-C bond formation product **26a** was obtained in 85% yield after irradiation of 20 h. However, no enantioselectivity was observed (Figure 62).

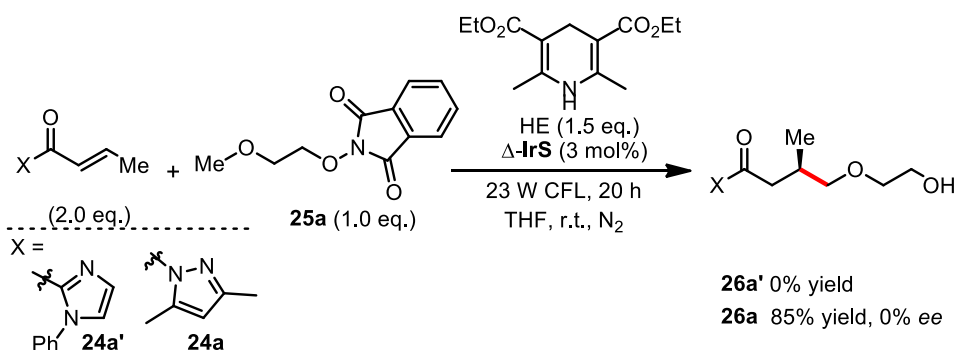
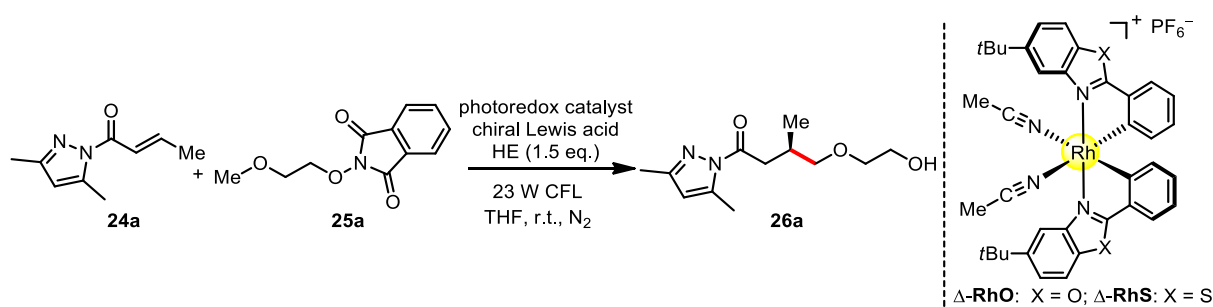


Figure 62 Initial experiments with two different Michael acceptors.

Thus, the optimization began with the reaction of α,β -unsaturated acyl pyrazole **24a** and *N*-alkoxyphthalimide **25a** under photoredox conditions (Table 8). When the dual catalyst system of a chiral Lewis acid Δ -**RhO**⁵ (3 mol%) in combination with a photoredox catalyst *fac*-[**Ir(ppy)**₃] (1 mol%) was applied to this system, the reaction proceeded in 60% yield and 18% *ee* (entry 1). The enantioselectivity was improved to 79% *ee* when Δ -**RhS**⁶ (3 mol%) was used as the chiral Lewis acid (entry 2). At a catalyst loading of 8 mol%, even 92% *ee* was reached (entry 5). Other photoredox catalysts, such as [Ir(ppy)₂(dtbbpy)]PF₆ and [Ru(bpy)₃](PF₆)₂, were inferior to *fac*-[Ir(ppy)₃] (entries 3 and 4). The reaction is sensitive to solvent effects (entries 6 and 7) and the light source, as blue LEDs provided a somewhat lower enantioselectivity (entry 8). Control experiments verified that both visible light and Hantzsch ester are essential for product formation (entries 9 and 10). In the absence of the chiral Lewis acid Δ -**RhS**, product **26a** was still formed (75% yield), albeit as a racemic mixture (entry 11). It is worth noting that in the absence of the additional photoredox catalyst *fac*-[Ir(ppy)₃] (entry 12) or both *fac*-[Ir(ppy)₃] and Δ -**RhS** (entry 13), the product **26a** was still generated but with significantly reduced efficiency. UV/Vis-absorbance spectra of the individual substrates and Hantzsch ester suggest that this should be due to the direct photoexcitation of the Hantzsch ester.⁷

Table 8 Reaction development.^a

entry	catalyst	photoredox catalyst	$h\nu^b$	solvent	t (h)	yield (%) ^c	ee (%) ^d
1	$\Delta\text{-RhO}$ (3.0)	<i>fac</i> -[Ir(ppy) ₃] (1.0)	CFL	THF	20	60	18
2	$\Delta\text{-RhS}$ (3.0)	<i>fac</i> -[Ir(ppy) ₃] (1.0)	CFL	THF	20	61	79
3	$\Delta\text{-RhS}$ (3.0)	[Ir(ppy) ₂ (dtbbpy)]PF ₆ (1.0)	CFL	THF	20	76	36
4	$\Delta\text{-RhS}$ (3.0)	[Ru(bpy) ₃](PF ₆) ₂ (1.0)	CFL	THF	20	< 5	n.d.
5	$\Delta\text{-RhS}$ (8.0)	<i>fac</i> -[Ir(ppy) ₃] (1.0)	CFL	THF	40	70	92
6	$\Delta\text{-RhS}$ (8.0)	<i>fac</i> -[Ir(ppy) ₃] (1.0)	CFL	CH ₂ Cl ₂	40	13	86
7	$\Delta\text{-RhS}$ (8.0)	<i>fac</i> -[Ir(ppy) ₃] (1.0)	CFL	DMF	40	21	60
8	$\Delta\text{-RhS}$ (8.0)	<i>fac</i> -[Ir(ppy) ₃] (1.0)	blue LEDs	THF	40	69	86
9	$\Delta\text{-RhS}$ (8.0)	<i>fac</i> -[Ir(ppy) ₃] (1.0)	none	THF	40	0	n.a.
10 ^e	$\Delta\text{-RhS}$ (8.0)	<i>fac</i> -[Ir(ppy) ₃] (1.0)	CFL	THF	40	0	n.a.
11	none	<i>fac</i> -[Ir(ppy) ₃] (1.0)	CFL	THF	20	75	n.a.
12	$\Delta\text{-RhS}$ (8.0)	none	CFL	THF	40	33	92
13	none	none	CFL	THF	20	56	n.a.

^a Reaction conditions: 2-Acyl pyrazole **24a** (0.4 mmol), *N*-alkoxyphthalimide **25a** (0.2 mmol), Hantzsch ester (none or 0.3 mmol) with chiral Lewis acid catalyst (none or 3 or 8 mol%) and photoredox catalyst (none or 1 mol%) in solvent (1.0 mL) at room temperature for 20–40 h under an atmosphere of nitrogen.

^b 23 W compact fluorescent lamp (CFL) or 6 W blue LEDs. ^c Isolated yield. ^d Enantiomeric excess determined by HPLC on chiral stationary phase. ^e Control experiment without Hantzsch ester. n.a. = not applicable, n.d. = not determined.

It is worth noting that compared to *N*-alkoxyphthalimide **25a** ($n = 1$), *N*-alkoxyphthalimide **25a'** ($n = 0$) and **25a''** ($n = 2$) were not suitable for the reaction (Figure 63). The results are in agreement with Curran's work⁸ and can be rationalized by the possible transition state involved in the HAT process. It is currently accepted that the ideal arrangement of the three atoms involved in the transition state of intramolecular HAT is linear (low energetic cost). The six-membered transition structure can readily accommodate a C–H–O angel close to 180°. Thus, 1,5-HAT is a more favorable process compare to 1,4-HAT or 1,6-HAT.

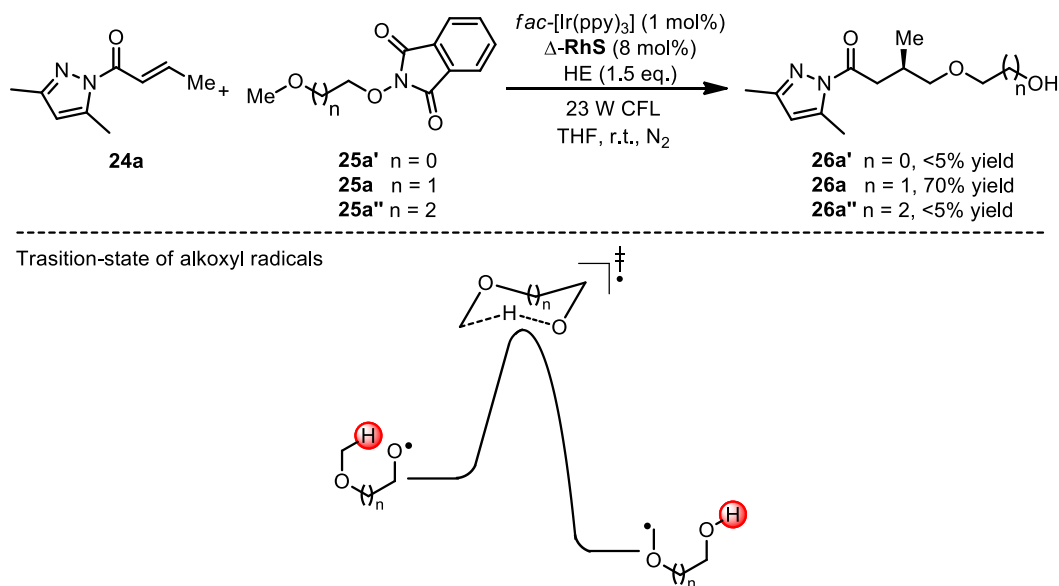


Figure 63 Transition-state of alkoxy radicals.

3.4.3 Substrate Scope

After the optimized conditions were established, we next tested the substrate scope of the asymmetric photoinduced C(sp³)-H functionalization. Figure 64 shows that the reaction of a variety of 2-acylpyrazoles **24a-j** with *N*-alkoxyphthalimide **25a** in the presence of Δ -RhS, *fac*-[Ir(ppy)₃] and Hantzsch ester while illuminating with visible light provided the expected C-C bond formation products **26a-j** in 51-80% yields and 82-97% *ee*. The reaction was tolerant of aliphatic substituents, regardless of acyclic and cyclic paraffins (**26a-f**). Notably, ethoxy- and benzyloxy-substituted **24g** and **24h** are favorable here, affording the corresponding products **26g** and **26h** in good yields and high stereoselectivities, respectively. The electronic effects have a significant influence upon substituents on the aromatic moieties, and with electron-donating substituents, the radical addition products (**26i** and **26j**) were obtained in moderate yields and good enantioselectivities. As for the aromatic moiety with no substituent or electron-withdrawing substituent, the undesired reductive homocoupling of alkene was the main process.⁹

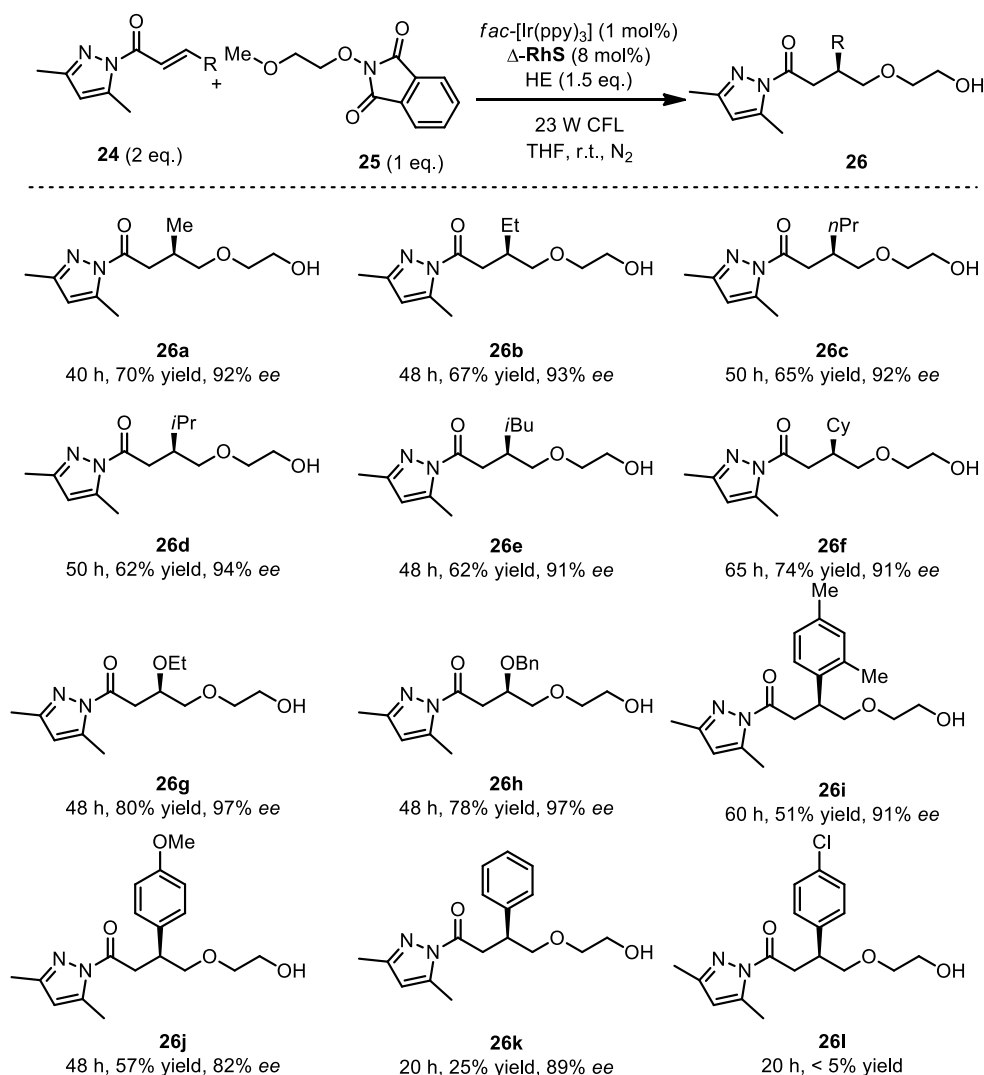


Figure 64 Substrate scope with respect to α,β -unsaturated 2-acyl pyrazoles.

To further expand the scope, a wide range of tertiary *N*-alkoxyphthalimides were applied to the reaction, affording the adducts in 54-85% yields and with 86-97% *ee* (**26m-26u**). Secondary *N*-alkoxyphthalimide with aromatic substitutes were also suitable for the reaction and afforded the corresponding products (**26v** and **26w**) with diastereoselectivities of up to 3:1 and enantioselectivities of up to 97% *ee* (Figure 65). The effort to improve the diastereoselectivity by changing reaction temperature or catalyst loadings of $\Delta\text{-RhS}$ was not succeeded. In addition, this α -heteroatom activation is not limited by oxygen, α -sulfur activated C-H bonds also work well under the standard condition (Figure 66), while α -nitrogen activated C-H bonds could not give satisfactory results. For unactivated C-H bonds, low yields may be rationalized by high reactivity of the intermediate alkoxy radical or carbon-centered radical and once generated, it was rapidly trapped by Hantzsch ester, thereby forming alcohol as a side product.

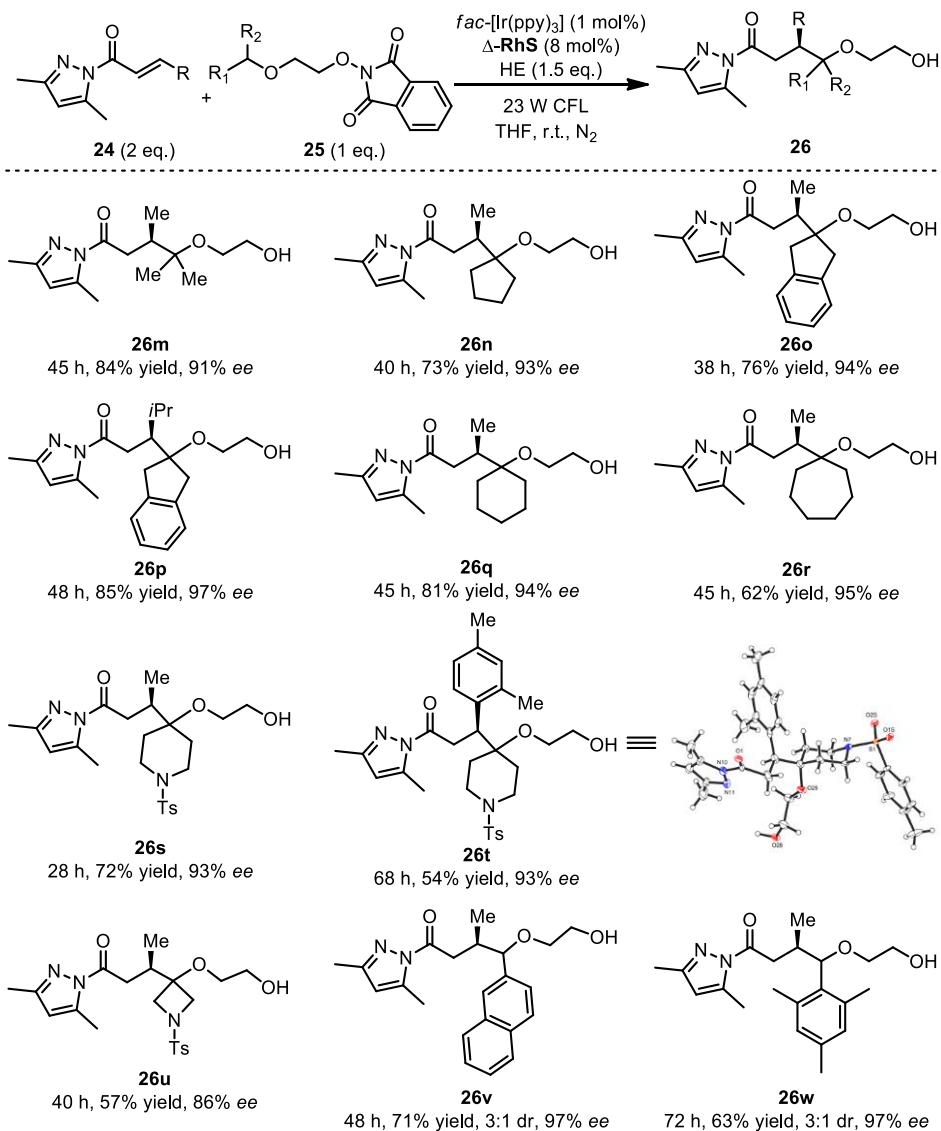


Figure 65 Substrate scope with respect to *N*-alkoxyphthalimides. Crystal structure of **26t** was obtained to determine the absolute configuration of the products.

Substrate	Product	Substrate	Product
	 26x 38 h, 49% yield, 86% ee		 26y 45 h, 72% yield, 92% ee
	not observed		not observed
	 < 5% yield		 20 h, 18% yield (24 W blue LEDs)

Figure 66 Limitation with respect to *N*-alkoxyphthalimides.

The formation of quaternary carbon stereocenters in a catalytic enantioselective fashion is promising and challenging. Unfortunately, the reactions of several 2-acyl pyrazoles with *N*-alkoxyphthalimide **25a** for the construction of quaternary carbon stereocenters were not succeeded under standard conditions (Figure 67). Comparing to Melchiorre's recent work¹⁰, we thought that the chiral Lewis acid catalyst Δ -**RhS** might not efficiently activate 2-acyl pyrazoles with two substituted groups in β -position due to its crowded coordination atmosphere.

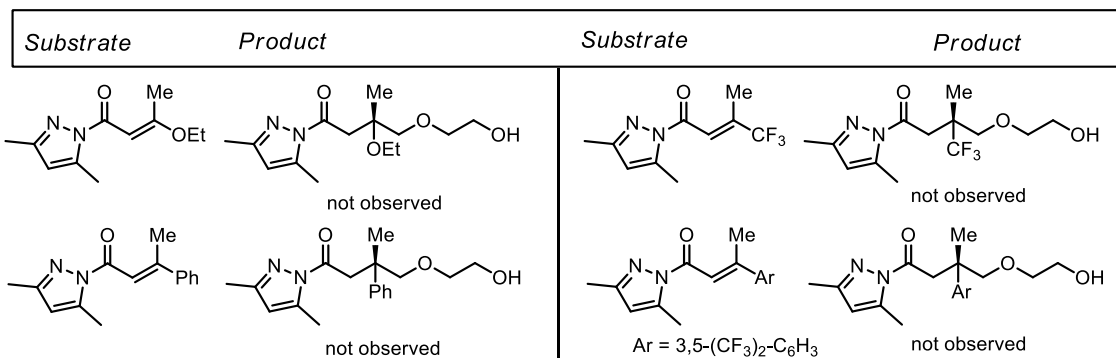


Figure 67 Some limitations for the construction of quaternary carbon stereocenters.

It is noteworthy to mention that *N*-acyl pyrazole is a very useful precursor for the conversion into other functionality. As shown in Figure 68, the aminolysis of product **26s** underwent smoothly to yield **27** without compromise any of enantiopurity, while the treatment of **26s** with NaBH₄ afforded diol **28** without detectable racemization.¹¹

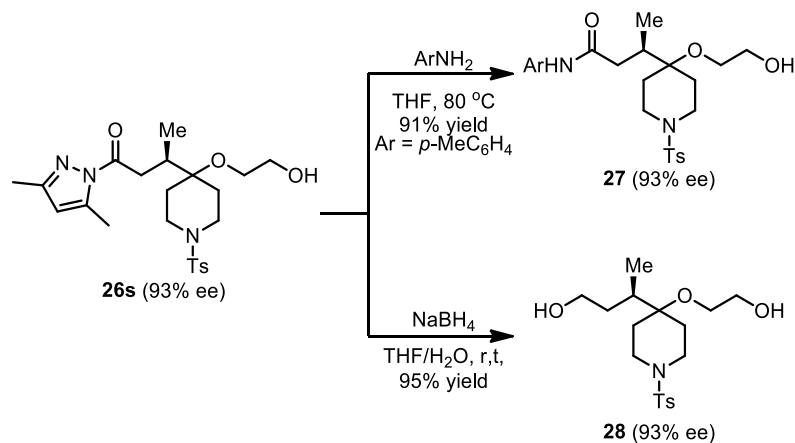


Figure 68 Exemplary transformations starting with one *N*-acyl pyrazole.

3.4.4 Plausible Mechanism

A plausible mechanism is shown in Figure 69 and starts with the photoactivation of $fac-[Ir(ppy)_3]$, whose excited state $[Ir(ppy)_3]^*$ is reductively quenched by the Hantzsch ester.⁷ Thereby generated $fac-[Ir(ppy)_3]^-$ serves as a strong reducing agent and transfers a single electron to *N*-alkoxyphthalimide (redox handle) under formation of an *N*-alkoxyphthalimide radical anion, which is subsequently protonated by the oxidized Hantzsch ester (radical cation), and then undergoes a homolytic N-O bond cleavage under formation of an alkoxy radical. The alkoxy radical engages in an intramolecular 1,5-hydrogen atom transfer (HAT) to yield a carbon-centered radical,¹² which adds to N,O-rhodium-coordinated 2-acyl pyrazole substrate (**RhS-I**), thereby generating the secondary radical intermediate (**RhS-II**). This radical intermediate is further trapped by the Hantzsch ester radical to provide rhodium-bound product (**RhS-III**). The observed high enantioselectivity in this new process demonstrates that the chiral Lewis acid Δ -**RhS** strongly accelerates the radical addition so that it is capable of outcompeting the prevailing racemic background reaction.¹³

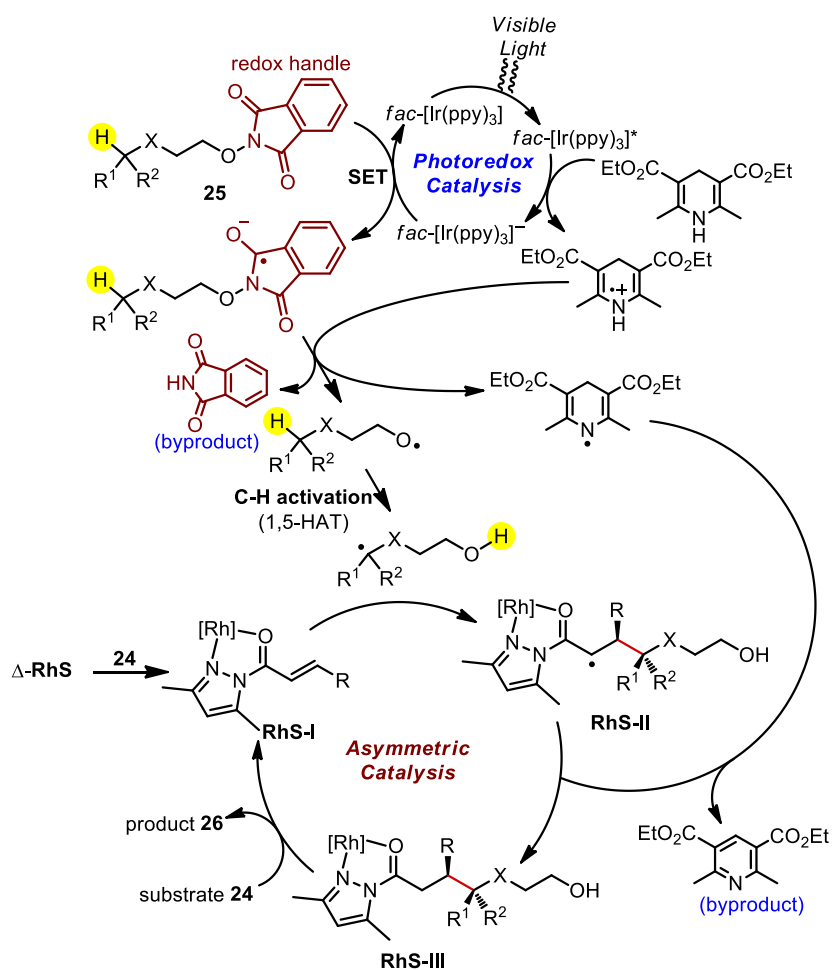


Figure 69 Proposed mechanism which is consistent with the observed product formation and the mechanistic experiments.

3.4.5 Mechanistic Investigations

1) Crystal structure analysis of the proposed rhodium intermediate **RhS-I**

The catalytic cycle was first investigated by verifying the involvement of the proposed rhodium intermediate **RhS-I**. Accordingly, upon reaction of an excess substrate **24a** with racemic Λ/Δ -**RhS** we could isolate the proposed intermediate **RhS-I**. A crystal structure of intermediate **RhS-I** is shown in Figure 70 (left). The stereocontrol model reveals that a Δ -configuration at the rhodium center shields the *Re*-face of the carbon in β -position and directs the addition of the electron-rich radical to the *Si*-face, thereby being consistent with the observed *R*-configuration of the alkylation product when using the catalyst with Δ -configuration at the metal (Figure 70, right).

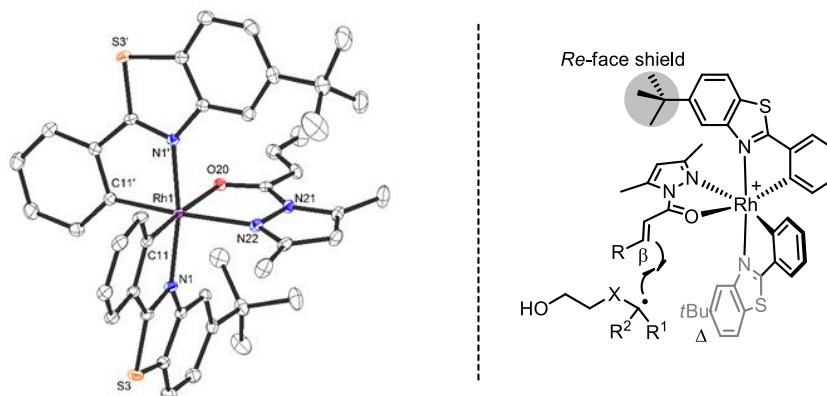
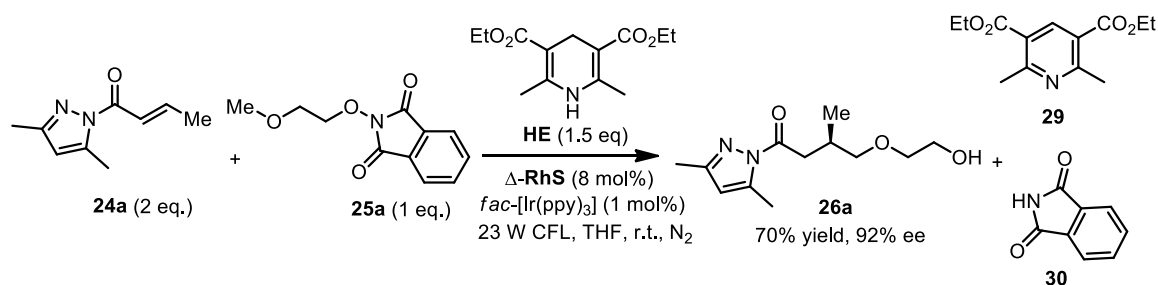


Figure 70 Crystal structure of proposed intermediate **RhS-I** (left, hydrogen atoms and the hexafluorophosphate counteranion are omitted for clarity) and stereochemical model (right).

2) Isolation of byproducts and a side product

Isolation of byproducts

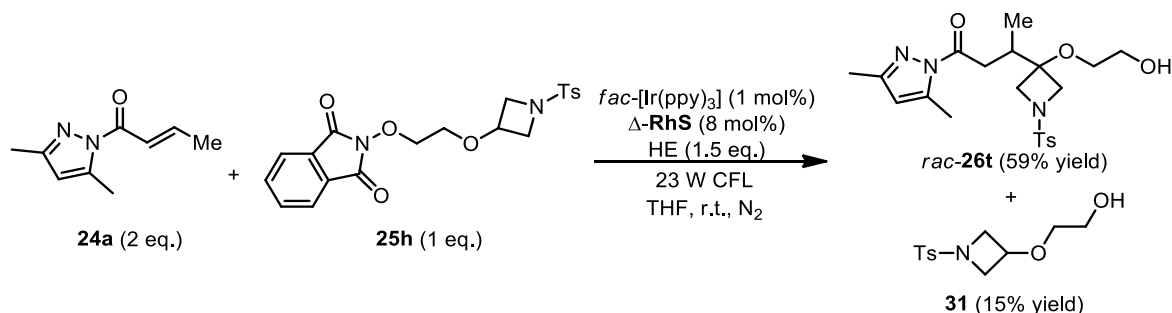
The expected byproducts diethyl 2,6-dimethylpyridine-3,5-dicarboxylate (**29**) and isoindoline-1,3-dione (**30**) could be isolated under the standard conditions. Accordingly, compound **29** was generated by oxidation of Hantzsch ester, while compound **30** was formed by reduction of *N*-alkoxyphthalimide **25a**.



Scheme 8 Isolation of byproducts **29** and **30**.

Isolation of a side product

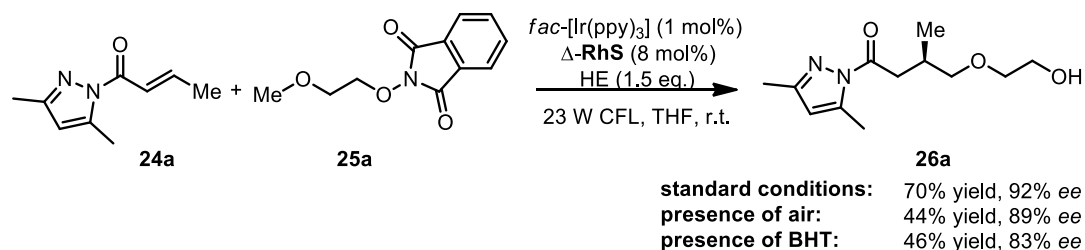
2-((1-Tosylazetididin-3-yl)oxy)ethanol **31** was isolated as a side product with 15% yield in the relatively sluggish conversion reaction Scheme 9. This further supports our proposed mechanism and can be explained by a competing undesired reduction of the initial oxygen- or carbon-centered radicals.



Scheme 9 Isolation of a side product **31**.

3) Control reactions

The presence of air or the radical inhibitor BHT (5 eq.) results in a reduced yield and enantioselectivity of the C-C bond formation product **26a**, which provides evidence for a radical pathway (Scheme 10). The intermediate carbon-centered radical serving as a relatively stabilized radical that could not be trapped efficiently by oxygen or BHT. These results are in agreement with Haohua Huo's work¹³ and may explain why the product **26a** was still formed with about 45% yield.

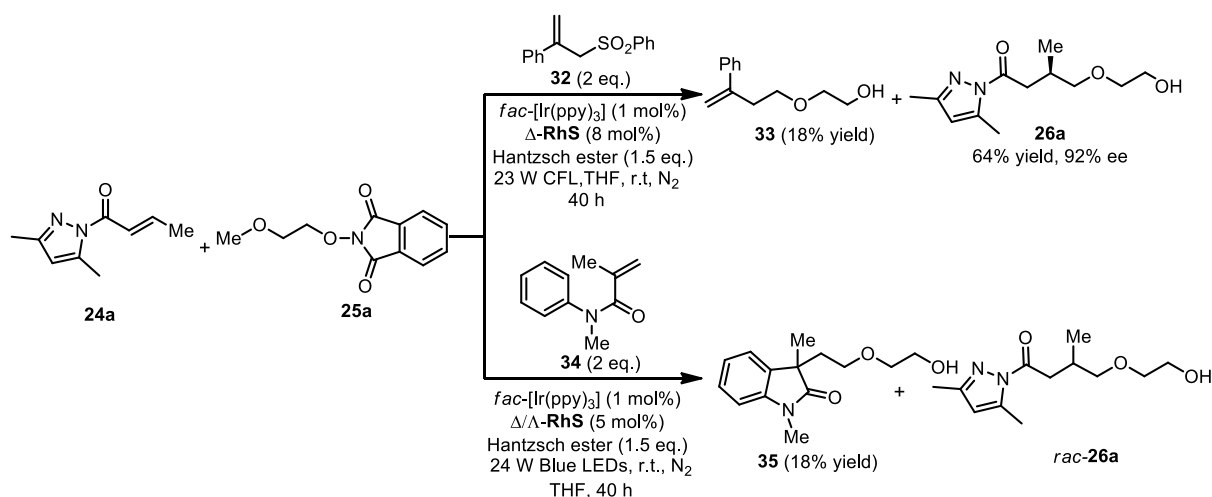


Scheme 10 Probing radical pathway in the presence of air or BHT.

4) Trapping experiments

The proposed intermediate carbon-centered radical was verified by trapping experiments with competing electron deficient alkenes (Scheme 11). For example, when 2 equivalents of ((2-phenylallyl)sulfonyl)benzene **32** were added to the reaction under standard conditions, the C(sp³)-H allylation adduct **33** was isolated with 18% yield. *N*-arylacrylamides are currently magic reagents for trapping carbon radicals by sequential intermolecular addition of radicals followed by intramolecular cyclization.¹⁴ When 2 equivalents of *N*-methyl-*N*-phenylmethacrylamide **34** were added to the reaction

under modified conditions, the addition/cyclization product **35** was isolated as a yield of 18%.



Scheme 11 Trapping experiments in the presence of alkene **32** or **34**.

5) UV/Vis-absorption spectra

The absorption spectra of the possible metal photoredox catalysts of the reaction were measured in THF. As shown in Figure 71, not only *fac*-[Ir(ppy)₃] ($\lambda_{\text{max}} = 370$ nm) but also the Lewis acid catalyst **RhS** ($\lambda_{\text{max}} = 395$ nm) and the intermediate **RhS-I** ($\lambda_{\text{max}} = 390$ nm) have absorption in the visible region.

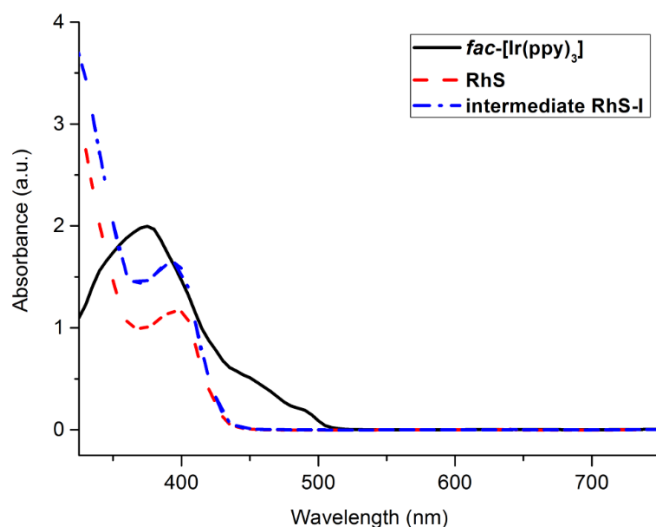


Figure 71 UV/Vis-absorption spectra of the used photoredox catalyst, the Lewis acid catalyst **RhS** and intermediate **RhS-I**. Measured as solutions in THF (0.2 mM). a.u. = absorbance units.

The absorption spectra of the substrate **25a** and Hantzsch ester were measured in THF as well. As shown in Figure 72, substrate **25a** does not absorb in the visible part of the spectrum, while the Hantzsch ester exhibits an absorption band in the near UV, with a maximum at about 350 nm. Notably, the absorbance of the mixture of **25a** and Hantzsch ester is the same as that of Hantzsch ester in the visible light region. The absorption spectrum of Hantzsch ester and control experiment (Table 8, entry 13)

support that the Hantzsch ester can also be photoexcited and reduce the *N*-alkoxyphthalimide in the absence of *fac*-[Ir(ppy)₃] and **RhS**, but it is not the major pathway of the *N*-alkoxyphthalimide reduction.

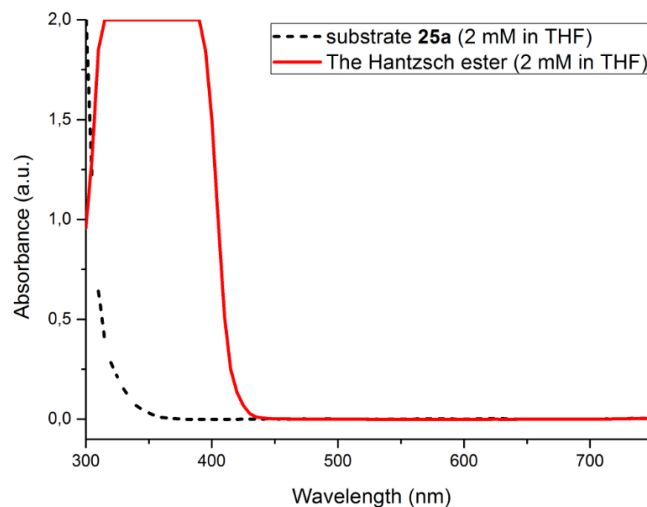


Figure 72 UV/Vis-absorption spectra of substrate **25a** and Hantzsch ester. Measured as solutions in THF (2 mM). a.u. = absorbance units.

6) Luminescence quenching experiments

Quenching experiments with fac-[Ir(ppy)₃] in the absence of intermediate RhS-I

Stern-Volmer plots (Figure 73) illustrate that the luminescence emission of *fac*-[Ir(ppy)₃] is quenched efficiently by the Hantzsch ester, in contrast to the substrates 2-acyl pyrazole **24a** or *N*-alkoxyphthalimide **25a**, which supports the proposed catalytic mechanism in which electron transfer from Hantzsch ester to the excited state *fac*-[Ir(ppy)₃]^{*} occurs and is at the center of the redox process.

This observation is also in agreement with recent studies by Chen.²

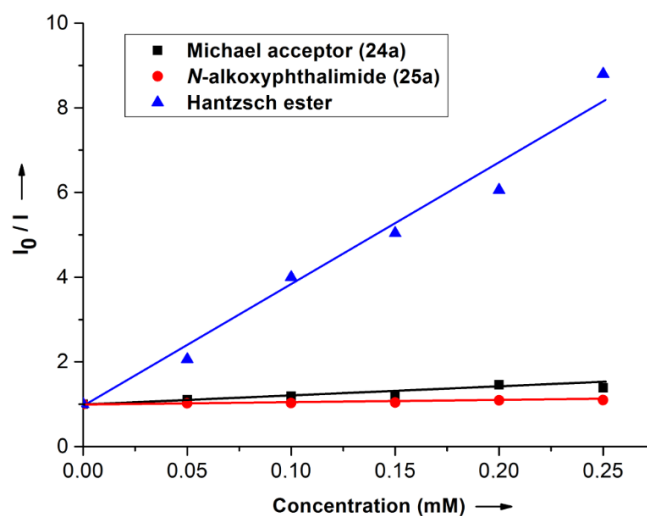


Figure 73 Stern-Volmer plots. I_0 and I are respective luminescence intensities in the absence and presence of the indicated concentrations of the corresponding quencher.

*Quenching experiments with fac -[Ir(ppy)₃] in the presence of intermediate **RhS-I***

When the quenching experiments were performed in the presence of intermediate **RhS-I**, a decreased luminescence of fac -[Ir(ppy)₃] was observed. Despite the lower luminescence intensity of the iridium sensitizer, the quenching of the photoexcited state of fac -[Ir(ppy)₃] by Hantzsch ester can be observed which is demonstrated by the emission intensity of the mixture solution of fac -[Ir(ppy)₃] and intermediate **RhS-I** and Hantzsch ester (Figure 74).

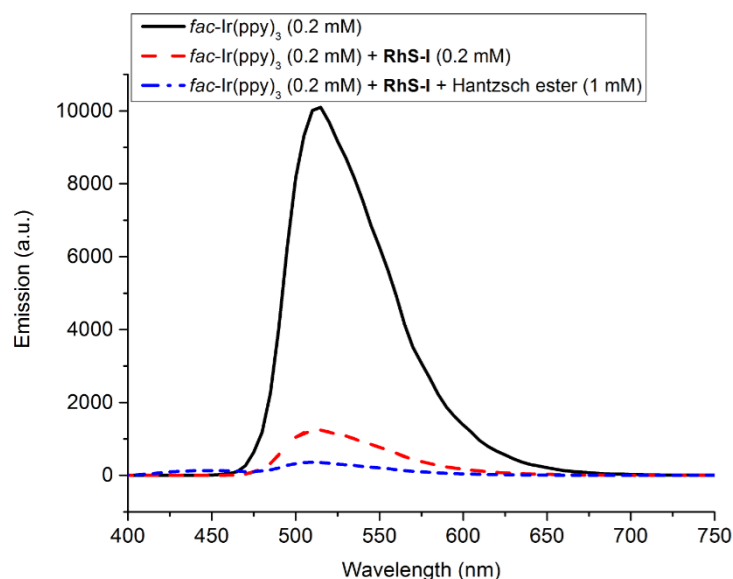


Figure 74 Emission spectra of the photoactive species. The photoactive species were measured as solutions in THF (0.2 mM). a.u. = arbitrary unit.

7) Quantum yield measurement

The quantum yield was measured by standard ferrioxalate actinometry. The moles of product formed was measured by GC analysis using dodecane as internal standard (for details, see experimental part). The quantum yield of the model reaction $24a + 25a \rightarrow 26a$ with ferrioxalate actinometry was determined to be 0.05 which is consistent with the proposed absence of a chain process.¹⁵

3.4.6 Conclusions

In summary, this work shows how C(sp³)-H bond functionalization through radical translocation can be merged with a catalytic asymmetric C-C bond formation by combining visible light activated photoredox catalysis with chiral Lewis acid catalysis. By using dual catalysis strategy, radical addition products were achieved with enantioselectivities of up to 97% *ee*, and with some diastereoselectivity (3:1 *dr*). We believe that this method is practically valuable since it makes use of the functionalization of unactivated C(sp³)-H bonds, at the same time introduces two stereocenters, and employs simple activating groups, namely *N*-alkoxyphthalimides as known redox-active radical precursors, as well as *N*-acyl pyrazoles as Lewis-acid-activatable functional groups.

References

- 1 For reviews on different strategies of catalytic asymmetric C-H functionalization, see: a) H. M. L. Davies, J. R. Manning, *Nature* **2008**, *451*, 417–424; b) R. Giri, B.-F. Shi, K. M. Engle, N. Maugel, J.-Q. Yu, *Chem. Soc. Rev.* **2009**, *38*, 3242–3272; c) M. P. Doyle, R. Duffy, M. Ratnikov, L. Zhou, *Chem. Rev.* **2010**, *110*, 704–724; d) S. A. Girard, T. Knauber, C.-J. Li, *Angew. Chem. Int. Ed.* **2014**, *53*, 74–100; e) C. Zheng, S.-L. You, *RSC Adv.* **2014**, *4*, 6173–6214.
- 2 J. Zhang, Y. Li, F. Zhang, C. Hu, Y. Chen, *Angew. Chem. Int. Ed.* **2016**, *55*, 1872–1875.
- 3 a) M. E. Wolff, *Chem. Rev.* **1963**, *63*, 55–64; b) G. Majetich, K. Wheless, *Tetrahedron* **1995**, *51*, 7095–7129; c) J. Robertson, J. Pillai, R. K. Lush, *Chem. Soc. Rev.* **2001**, *30*, 94–103; d) A. Gansäuer, T. Lauterbach, S. Narayan, *Angew. Chem. Int. Ed.* **2003**, *42*, 5556–5573; e) Ž. Čeković, *J. Serb. Chem. Soc.* **2005**, *70*, 287–318; f) F. Dénès, F. Beaufils, P. Renaud, *Synlett* **2008**, 2389–2399; g) J. Sperry, Y.-C. Liu, M. A. Brimble, *Org. Biomol. Chem.* **2010**, *8*, 29–38; h) M. C. Haibach, D. Seidel, *Angew. Chem. Int. Ed.* **2014**, *53*, 5010–5036; i) M. Nechab, S. Mondal, M. P. Bertrand, *Chem. Eur. J.* **2014**, *20*, 16034–16059.
- 4 a) H. Huo, X. Shen, C. Wang, L. Zhang, P. Röse, L.-A. Chen, K. Harms, M. Marsch, G. Hilt, E. Meggers, *Nature* **2014**, *515*, 100–103; b) H. Huo, C. Wang, K. Harms, E. Meggers, *J. Am. Chem. Soc.* **2015**, *137*, 9551–9554; c) C. Wang, J. Qin, X. Shen, R. Riedel, K. Harms, E. Meggers, *Angew. Chem. Int. Ed.* **2016**, *55*, 685–688.

- 5 C. Wang, L.-A. Chen, H. Huo, X. Shen, K. Harms, L. Gong, E. Meggers, *Chem. Sci.* **2015**, *6*, 1094–1100.
- 6 J. Ma, X. Shen, K. Harms, E. Meggers, *Dalton Trans.* **2016**, *45*, 8320–8323.
- 7 For photoinduced electron transfer by direct excitation of Hantzsch ester with visible light, see also:
a) X.-Q. Zhu, Y.-C. Liu, J.-P. Cheng, *J. Org. Chem.* **1999**, *64*, 8980–8981; b) J. Jung, J. Kim, G. Park, Y.-M. You, E. J. Cho, *Adv. Synth. Catal.* **2016**, *358*, 74–80; c) W. Chen, H. Tao, W. Huang, G. Qang, S. Li, X. Cheng, G. Li, *Chem. Eur. J.* **2016**, *22*, 9546–9550.
- 8 D. P. Curran, D. Kim, H. Liu, W. Shen, *J. Am. Chem. Soc.* **1988**, *110*, 5900–5902.
- 9 H. A. Reichard, M. McLaughlin, M. Z. Chen, G. C. Micalizio, *Eur. J. Org. Chem.* **2010**, 391–409.
- 10 J. J. Murphy, D. Bastida, S. Paria, M. Fagnoni, P. Melchiorre, *Nature* **2016**, *532*, 218–222.
- 11 Y. Zheng, Y. Yao, L. Ye, Z. Shi, X. Li, Z. Zhao, X. Li, *Tetrahedron* **2016**, *72*, 973–978.
- 12 For selected recent examples on 1,5-HAT initiated by alkoxyl radicals, see: a) C. G. Francisco, A. J. Herrera, E. Suárez, *J. Org. Chem.* **2002**, *67*, 7439–7445; b) H. Zhu, J. G. Wickenden, N. E. Campbell, J. C. T. Leung, K. M. Johnson, G. M. Sammis, *Org. Lett.* **2009**, *11*, 2019–2022; c) R. Kundu, Z. T. Ball, *Org. Lett.* **2010**, *12*, 2460–2463; d) H. Zhu, J. C. T. Leung, G. M. Sammis, *J. Org. Chem.* **2015**, *80*, 965–979.
- 13 H. Huo, K. Harms, E. Meggers, *J. Am. Chem. Soc.* **2016**, *138*, 6936–6939.
- 14 a) G. Bencivenni, T. Lanza, R. Leardini, M. Minozzi, D. Nanni, P. Spagnolo, G. Zanardi, *J. Org. Chem.* **2008**, *73*, 4721–4724; b) Z.-S. Li, W.-X. Wang, J.-D. Yang, Y.-W. Wu, W. Zhang, *Org. Lett.* **2013**, *15*, 3820–3823; c) D. Li, T. Yang, H. Su, W. Yu, *Adv. Synth. Catal.* **2015**, *357*, 2529–2539; d) D. Li, H. Ma, W. Yu, *Adv. Synth. Catal.* **2015**, *357*, 3696–3702.
- 15 a) M. D. Kärkäs, B. S. Matsuura, C. R. J. Stephenson, *Science* **2015**, *34*, 1285–1286; b) M. A. Cismesia, T. P. Yoon, *Chem. Sci.* **2015**, *6*, 5426–5434.

Chapter 4: Summary and Outlook

4.1 Summary

In this thesis, a class of octahedral chiral-at-metal complexes **IrO(S)** and **RhO(S)** have been successfully applied to asymmetric reactions (Figure 75). Accordingly, rhodium complexes Δ -**RhO** and Δ -**RhS** have been demonstrated as very efficient chiral Lewis acid catalysts in asymmetric Michael additions and visible light induced asymmetric Giese radical addition, respectively. Iridium complexes Δ -**IrO** and Δ -**IrS** have been proven to be capable of serving as dual chiral Lewis acid/photoredox catalysts in visible light activated asymmetric α -aminoalkylation and radical-radical cross-coupling reaction, respectively. These novel octahedral chiral-at-metal iridium and rhodium complexes provide new opportunities for the efficient and economical synthesis of highly enantioenriched molecules.

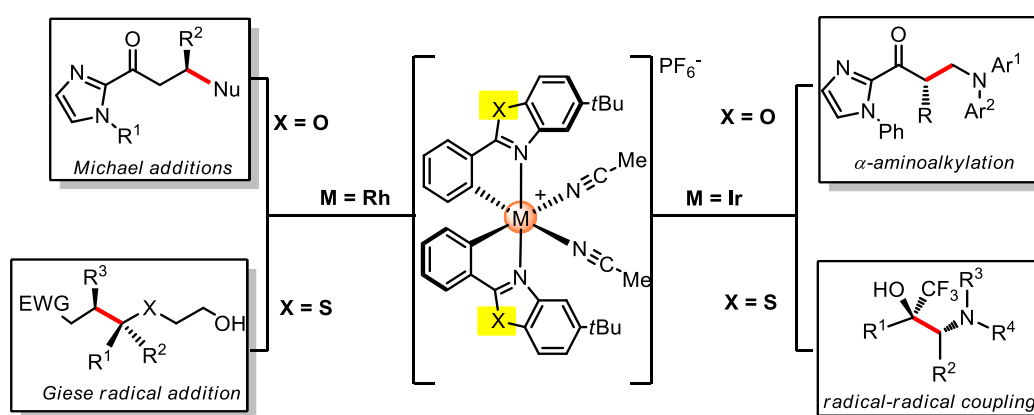


Figure 75 An overview for the thesis.

1) Asymmetric Lewis acid catalysis directed by octahedral rhodium centrochirality

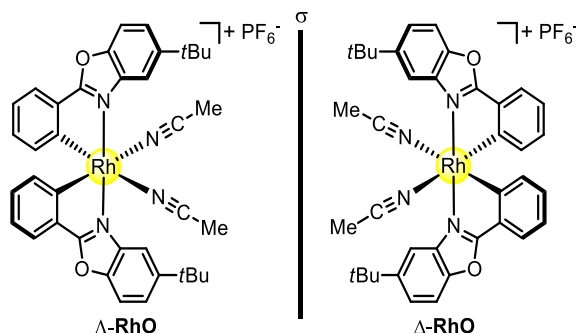


Figure 76 Enantiomers of a substitutionally labile yet configurationally stable chiral-at-metal rhodium(III) Lewis acids Δ -**RhO** and Δ -**RhO**.

A rhodium-based asymmetric catalyst which derives its optical activity from octahedral centrochirality was introduced (Figure 76). The chiral Lewis acid complexes Δ -**RhO** and Δ -**RhO** were synthesized according to chiral proline-mediated strategy developed by the Meggers group. Accordingly, the reaction of dimer *rac-2* with D-proline afforded the prolinato-rhodium complexes Δ -(*R*)-**3** and Δ -(*R*)-**3** as a mixture of diastereomers, and Δ -(*R*)-**3** is isolable in a straightforward fashion with high purity by just washing the mixture of diastereomers with $\text{CH}_2\text{Cl}_2/\text{Et}_2\text{O}$. The virtually enantiopure Δ -**RhO** was yielded after stereospecific substitution of D-proline by two acetonitrile ligands. The mirror-imaged complex Δ -**RhO** is accessible in an analogous fashion by using the chiral auxiliary L-proline instead (Figure 77).

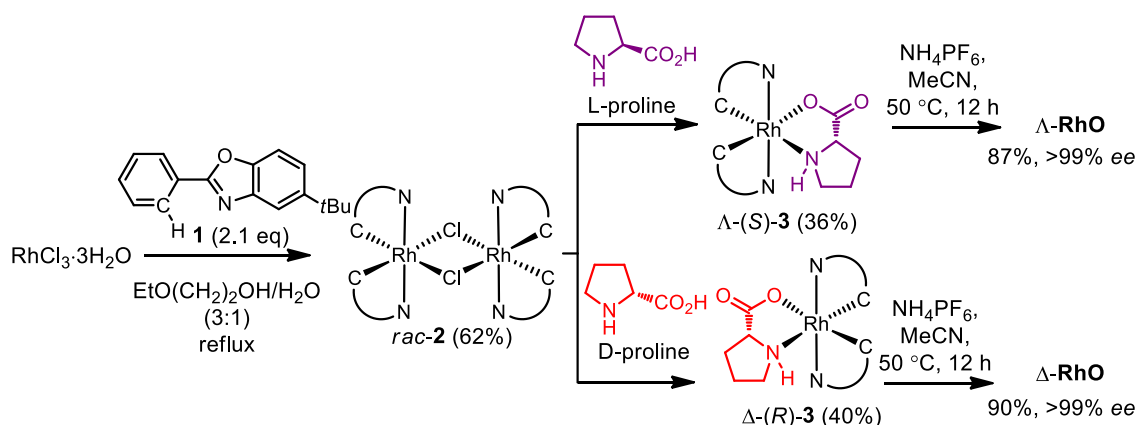


Figure 77 Synthesis of the enantiomerically pure Lewis acid complexes Δ -**RhO** and Δ -**RhO**.

Besides providing the exclusive source of chirality, the rhodium center serves as a Lewis acid by activating 2-acyl imidazoles through two-point-binding and enabling a very effective asymmetric induction mediated by the propeller-like C_2 -symmetrical ligand sphere. Applications of asymmetric

Chapter 4: Summary and Outlook

Michael additions as well as asymmetric cascade reaction are disclosed, for which the rhodium catalyst is found to be overall superior to its iridium congener (Figure 78). By virtue of its straightforward proline-mediated synthesis, high catalytic activity, and tolerance towards moisture and air, this novel class of chiral-at-rhodium catalysts has been proven to be of widespread use for a variety of asymmetric transformations in the Meggers group.

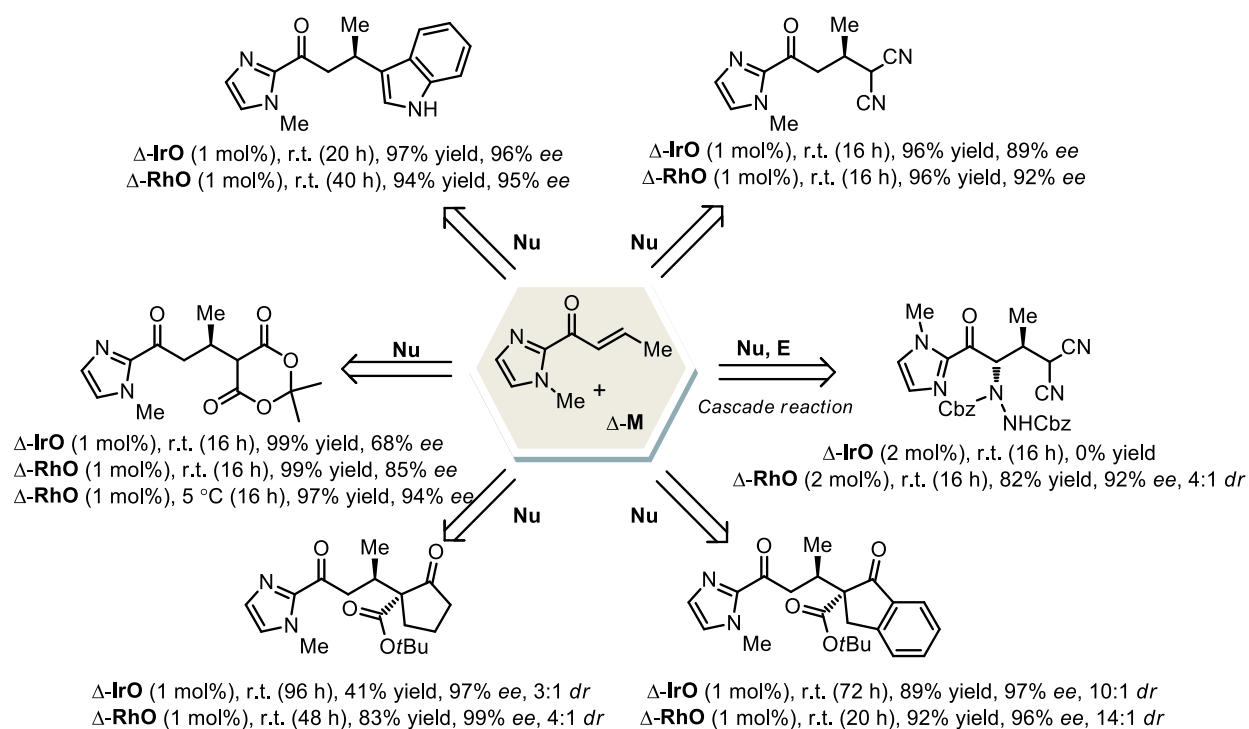


Figure 78 Catalytic asymmetric conjugate additions and cascade reaction catalyzed by Δ -IrO and Δ -RhO.

2) Merger of visible light induced oxidation and enantioselective alkylation with chiral iridium catalyst

A visible light activated asymmetric α -aminoalkylation of 2-acyl imidazoles catalyzed by a single chiral iridium complex was developed. In the presence of a conventional household lamp and under an atmosphere of air, the oxidative coupling of 2-acyl-*N*-phenyl imidazoles with α -silylamines provide aminoalkylated products in 61-93% yields with high enantioselectivities (90-98% *ee*). Mechanistically, the catalytic cycle is started by the formation of the substrate coordinated intermediate **A**. The subsequent deprotonation in α -position of the carbonyl group affords the nucleophilic iridium enolate intermediate **B**. The reaction of the enolate complex **B** with the newly formed iminium ion (generated by an iridium-photocatalyzed oxidation of the α -silylamine with oxygen serving as the terminal oxidant) occurs in a stereocontrolled fashion dictated by the metal-centered chirality and provides the iridium coordinated product **C**. The intermediate **C** subsequently released the product upon coordination to a new substrate, thereby initiating a new catalytic cycle (Figure 79). This conceptionally simple reaction scheme may provide new avenues for the green synthesis of chiral molecules.

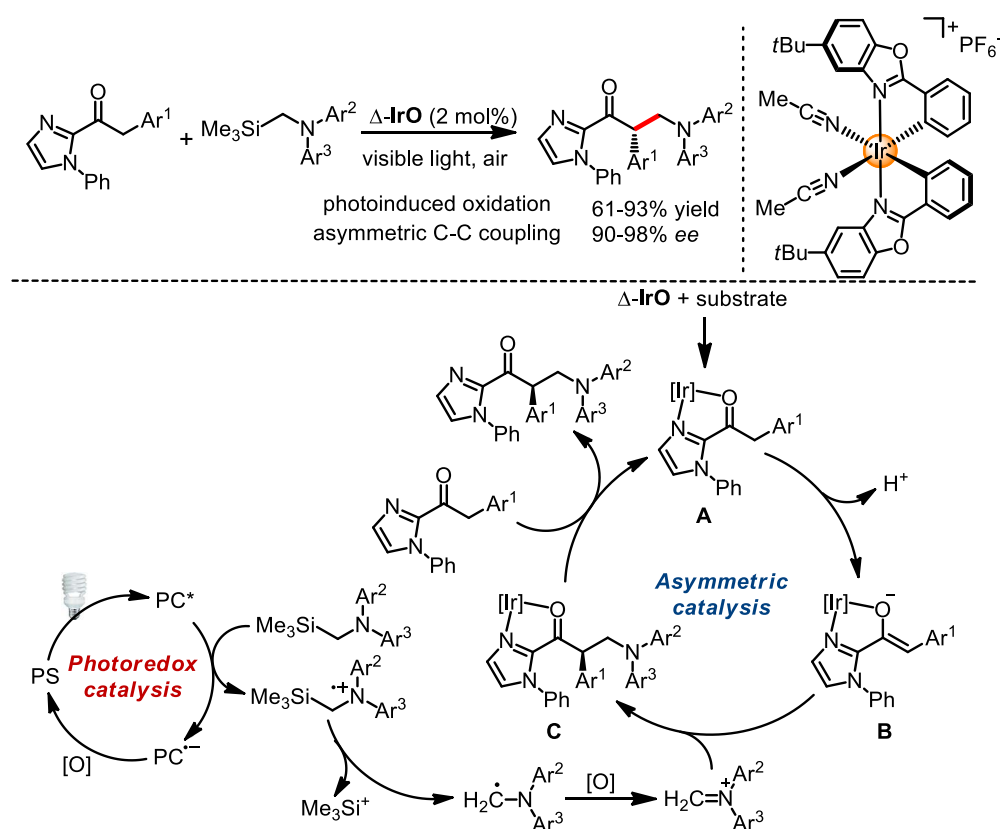


Figure 79 Visible light activated asymmetric α -aminoalkylation of 2-acyl imidazoles with a chiral iridium complex Δ -IrO. PC = photoredox catalyst.

3) Asymmetric radical-radical cross-coupling through visible light activated iridium catalysis

A catalytic process of asymmetric radical-radical cross-coupling through visible light activated iridium catalysis was introduced. Combining single electron transfer between a donor substrate and a catalyst-activated acceptor substrate with a stereocontrolled radical-radical recombination enables the catalytic enantio- and diastereoselective synthesis of 1,2-aminoalcohols from trifluoromethyl ketones and tertiary amines. With a dual function chiral iridium complex acting as both a Lewis acid and a photoredox catalyst, enantioselectivities of up to 99% *ee* and where applicable, with diastereoselectivities of up to 10:1 *dr* were achieved (Figure 80). A quantum yield of <1 supports the proposed catalytic cycle in which at least one photon is needed for each asymmetric C–C bond formation mediated by single electron transfer. It is also worth noting that this mild method follows the spirit of sustainable chemistry, not only because the activation energy is provided by visible light as an abundant light source, but also since in the course of the C–C bond formation with the implementation of one or two new stereocenters, no waste products are generated, thereby constituting a perfect atom economy.

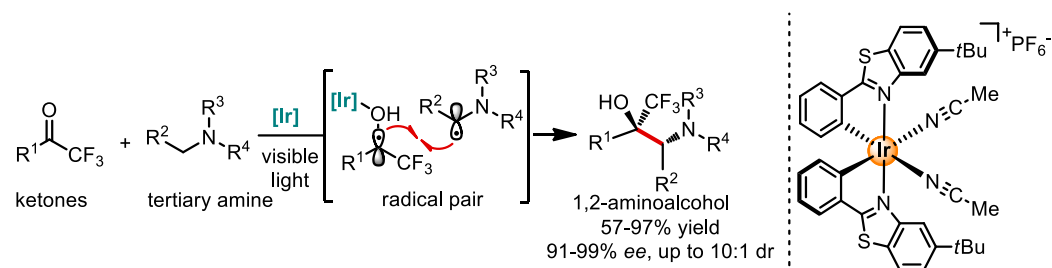
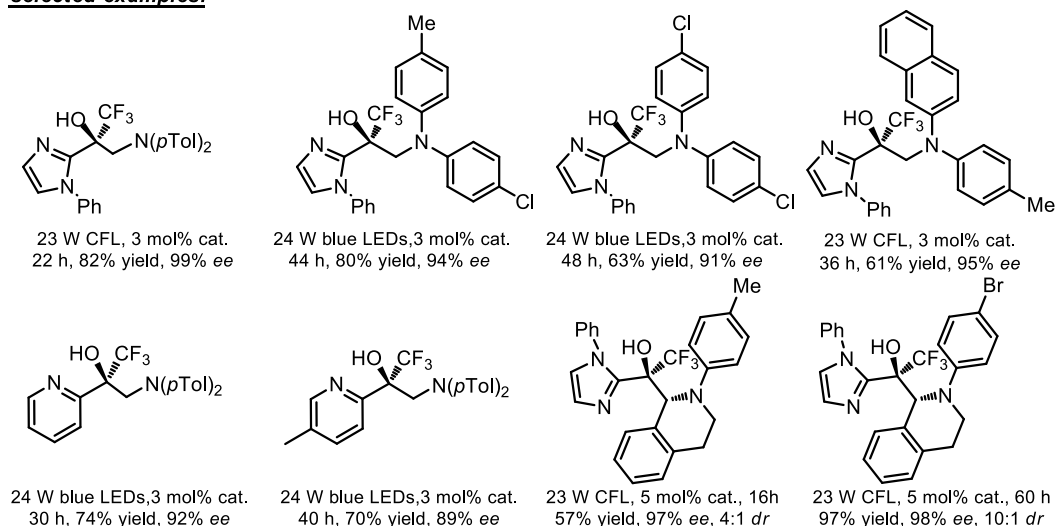
**selected examples:**

Figure 80 Visible light activated asymmetric radical-radical cross-coupling with a chiral iridium complex Δ -IrS.

4) Catalytic asymmetric C(sp³)-H functionalization under photoredox conditions by radical translocation and stereocontrolled alkene addition

How photoredox-mediated C(sp³)-H activation through radical translocation can be combined with asymmetric catalysis was demonstrated. Upon irradiation with visible light, α,β -unsaturated *N*-acyl pyrazoles react with *N*-alkoxyphthalimides in the presence of a rhodium-based chiral Lewis acid catalyst Δ -RhS and the photoredox catalyst *fac*-[Ir(ppy)₃] to provide C-C bond-formation products with high enantioselectivities (up to 97% *ee*) and, where applicable, with some diastereoselectivities (3:1 *dr*). Mechanistically, the synthetic strategy exploits a radical translocation (1,5-hydrogen transfer) from an oxygen-centered to a carbon-centered radical with a subsequent stereocontrolled radical alkene addition. It is worth noting that *N*-acyl pyrazole is a very useful precursor for the conversion into other carbonyl functionality as shown for the representative conversion into a diol and an amide (Figure 81).

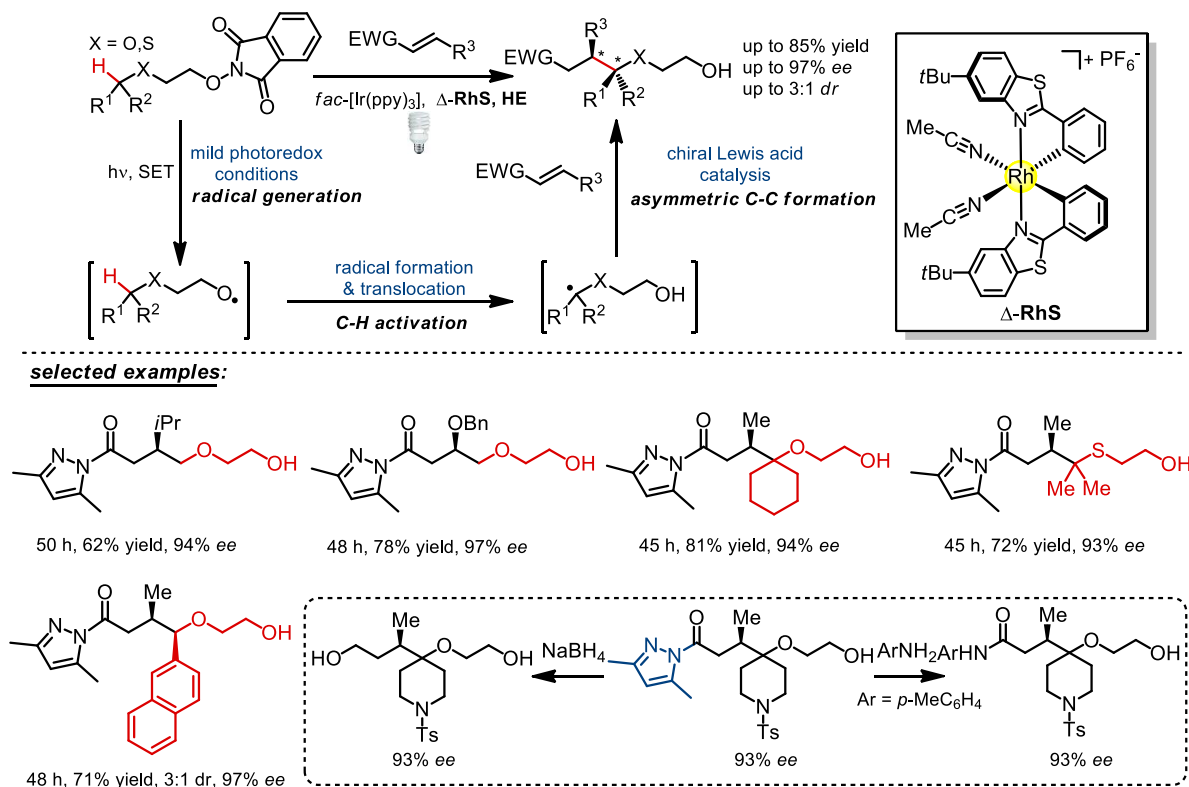


Figure 81 Visible light activated asymmetric C(sp³)-H functionalization with a chiral Lewis acid Δ -RhS and a photoredox catalyst *fac*-[Ir(ppy)₃].

4.2 Outlook

The work described in this thesis contributes to the development of new catalysts and synthetic strategies. Further investigations can be focus on the following aspects:

1) Nowadays, one of the most challenging projects in organic synthetic methodology is visible light induced asymmetric C(sp³)-H functionalization. Radical translocation is an old but very useful strategy which has been discussed in chapter 3.4. However, the complexity certainly limits the practical application. The simultaneous use of iridium and rhodium complexes and the stoichiometric amount of the Hantzsch ester required make the reaction less attractive for large scale synthesis. Very recently, the Knowles group and the Rovis group simultaneously reported symmetric photoredox catalyzed C-C bond formation by directed cleavage of traditionally non-reactive C(sp³)-H bonds (through intramolecular 1,5-HAT) and their subsequent addition to readily available alkenes, no waste products are generated. These results suggest that enantioselectivity photoredox catalyzed C-C bond formation products can be formed by combining our chiral rhodium Lewis acid catalysts with the newly developed C(sp³)-H functionalization approaches.

2) Although high enantioselectivities could be achieved by using chiral-at-metal complexes in chapter 3.2-3.4, the substrates limitation is obvious and such imidazole or pyrazole coordination group is always required which makes the products less usable. How to make the products more general and practical? Maybe iridium-templated Brønsted acid or co-catalysts of the combination of rhodium-templated Brønsted acid with photocatalysis would give opportunities to activate carbonyl substrates, thereby reacting with intermediates in a stereocontrolled fashion under photoredox conditions.

3) In recent years, ruthenium(II), iridium(III) and platinum(II) complexes with cyclometalated arylpyridines and related ligands have become the most studied systems because they display highly tunable emission energies and can reach very high quantum yields. The González-Herrero group recently developed a variety of platinum(IV) complexes with cyclometalated arylpyridines which exhibit impressively luminescence properties. However, the application of these platinum(IV) complexes in photoredox catalysis is rarely. Next work may focus on the synthesis of a platinum(IV) Lewis acid catalyst which contains two achiral bidentate ligands and two labile acetonitriles, and thereby investigates its catalytic properties in asymmetric photoredox catalysis.

Chapter 5: Experimental Part

5.1 Materials and Methods

All reactions were carried out under an atmosphere of nitrogen with magnetic stirring. The catalysis reactions were performed using standard Schlenk glassware techniques.

Solvents and Reagents

Solvents were distilled under nitrogen from calcium hydride (CHCl_3 , CH_2Cl_2 , CH_3CN and DMF), magnesium turnings/iodine (MeOH) or sodium/benzophenone (Et_2O , THF and toluene). HPLC grade solvents, such as 2-methoxyethanol, ethanol and 1,4-dioxane used directly without further drying. All reagents were purchased from Acros, Alfa Aesar, Sigma Aldrich, TCI, ChemPur and Fluorochem and used without further purification.

Chromatographic Methods

The course of the reactions and the column chromatographic elution were monitored by thin layer chromatography (TLC) [Macherey-Nagel (ALUGRAM®Xtra Sil G/UV254)]. Flash column chromatography was performed with silica gel from Merck (particle size 0.040-0.063 mm).

Nuclear Magnetic Resonance Spectroscopy (NMR)

^1H NMR, proton decoupled ^{13}C NMR, and proton coupled ^{19}F NMR spectra were recorded on Bruker Avance 300 system (^1H NMR: 300 MHz, ^{13}C NMR: 75 MHz, ^{19}F NMR: 282 MHz) spectrometers at ambient temperature. Chemical shifts are given in ppm on the δ scale, and were determined after calibration to the residual signals of the solvents, which were used as an internal standard. NMR standards were used are as follows: ^1H NMR spectroscopy: $\delta = 7.26$ ppm (CDCl_3), $\delta = 5.32$ ppm (CD_2Cl_2), $\delta = 2.50$ ppm (DMSO-*d*6), $\delta = 3.31$ ppm (CD_3OD); ^{13}C -NMR spectroscopy: $\delta = 77.0$ ppm (CDCl_3), $\delta = 53.8$ ppm (CD_2Cl_2), $\delta = 118.26$, 1.32 ppm (CD_3CN), $\delta = 206.26$, $\delta = 39.52$ ppm (DMSO-*d*6), $\delta = 49.0$ ppm (CD_3OD). ^{19}F NMR spectroscopy: $\delta = 0$ ppm (CFCl_3). The characteristic signals were specified from the low field to high field with the chemical shifts (δ in ppm). ^1H NMR spectra peak

multiplicities indicated as singlet (s), doublet (d), doublet of doublet (dd), doublet of doublet of doublet (ddd), triplet (t), doublet of triplet (dt), quartet (q), multiplet (m). The coupling constant J indicated in hertz (Hz).

High-Performance Liquid Chromatography (HPLC)

Chiral HPLC was performed with an Agilent 1200 Series or Agilent 1260 Series HPLC System. All the HPLC conditions were detailed in the individual procedures. The type of the columns, mobile phase and the flow rate were specified in the individual procedures.

Infrared Spectroscopy (IR)

IR measurements were recorded on a Bruker Alpha-P FT-IR spectrometer. The absorption bands were indicated a wave numbers ν (cm^{-1}). All substances were measured as films or solids.

Mass Spectrometry (MS)

High-resolution mass spectra were recorded on a Bruker En Apex Ultra 7.0 TFT-MS instrument using ESI or APCI or FD technique. Ionic masses are given in units of m/z for the isotopes with the highest natural abundance.

Circular Dichroism Spectroscopy (CD)

CD spectra were recorded on a JASCO J-810 CD spectropolarimeter. The parameters we used as follows: from 600 nm to 200 nm; data pitch (0.5 nm); band with (1 nm); response (1 second); sensitivity (standard); scanning speed (50 nm/min); accumulation (5 times). The concentration of the compounds for the measurements was 0.2 mM. The formula for converting θ to ϵ is shown as below.

$$\Delta\epsilon = \frac{\theta[m\text{ deg}]}{32980 \times c(\text{mol} / L) \times L(\text{cm})}$$

C = concentration of the sample; L = thickness of the measurement vessel

Crystal Structure Analysis

Crystal X-ray measurements and the crystal structure analysis were carried out by Dr. Klaus Harms (Chemistry Department, Philipps University of Marburg). X-ray data were collected with a Bruker 3

circuit D8 Quest diffractometer with MoK α radiation (microfocus tube with multilayer optics) and Photon 100 CMOS detector. Scaling and absorption correction was performed by using the SADABS¹ software package of Bruker. Structures were solved using direct methods in SHELXS² and refined using the full matrix least squares procedure in SHELXL-2013³ or SHELXL-2014⁴. The Flack parameter is a factor used to estimate the absolute configuration of the compounds.⁵ The hydrogen atoms were placed in calculated positions and refined as riding on their respective C atom, and Uiso(H) was set at 1.2 Ueq(Csp²) and 1.5 Ueq(Csp³). Disorder of PF₆ ions, solvent molecules or methylene groups was refined using restraints for both the geometry and the anisotropic displacement factors.

UV/Vis Analysis Spectroscopy

UV/Vis measurements were taken on a Spectra Max M5 microplate reader in a 10.0 mm quartz cuvette.

Optical Rotation Polarimeter

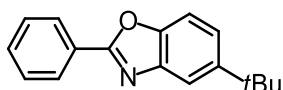
Optical rotations were measured on a Krüss P8000-T or Perkin-Elmer 241 polarimeter with $[\alpha]_D^{20}$ or $[\alpha]_D^{25}$ values reported in degrees with concentrations reported in g/100 mL.

5.2 Asymmetric Lewis Acid Catalysis Directed by Octahedral Rhodium Centrochirality

5.2.1 Synthesis of the Rhodium Catalysts Λ -RhO and Δ -RhO

1) Synthesis of benzoxazole ligands

5-*tert*-Butyl-2-phenylbenzo[*d*]oxazole (**1**)

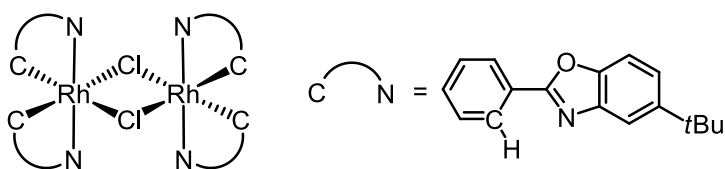


The compound **1** was synthesized following a published procedure with slight modifications.⁶ A solution of 2-amino-4-*tert*-butylphenol (0.825 g, 5.0 mmol) and benzaldehyde (0.5 mL, 5.0 mmol) in *m*-xylene (16.0 mL) was stirred at 120 °C for 30 min. 4-Methoxy-TEMPO (46.5 mg, 5 mol%) was added to the mixture and the reaction was stirred at this temperature for further 8 h under an oxygen atmosphere. The reaction mixture was cooled to room temperature and concentrated under reduced pressure. The residue was purified by flash chromatography on silica gel (EtOAc/hexane = 1:20) to obtain the product **1** (1.152 g, 4.6 mmol, yield: 92%) as a white solid.

¹H NMR (300 MHz, CDCl₃) δ 8.29–8.22 (m, 2H), 7.81 (d, J = 1.8 Hz, 1H), 7.56–7.48 (m, 4H), 7.42 (dd, J = 8.6, 1.9 Hz, 1H), 1.40 (s, 9H).

All spectroscopic data are in agreement with the literature.⁷

2) Precursor rhodium complex *rac-2*



The new complex *rac-2* was synthesized according to a route reported by Mesmaeker for rhodium(III) μ -chloro-bridged dimers with related cyclometalated ligands.⁸ Accordingly, 5-*tert*-butyl-2-phenylbenzo[*d*]oxazole **1** (1.030g, 4.1 mmol) was added to RhCl₃·3H₂O (526.6 mg, 2.0 mmol) in a mixture of 2-ethoxyethanol and water (3:1, 92.0 mL). The reaction mixture was heated at 120 °C for 24 h under an atmosphere of nitrogen. The resulting precipitate was collected by centrifugation, washed with methanol and dried to obtain the product *rac-2* (792.4 mg, 0.62 mmol, yield: 62%) as a pale yellow

solid.

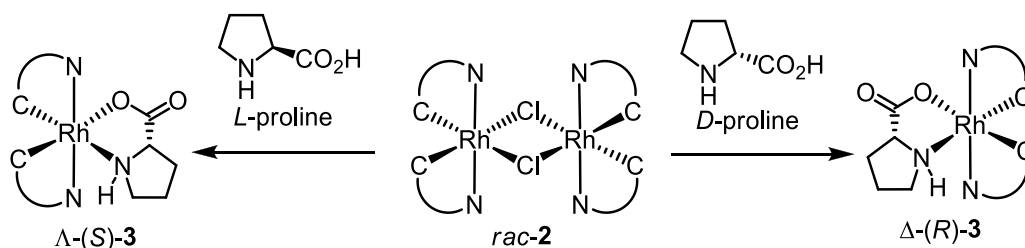
^1H NMR (300 MHz, CD_2Cl_2) δ 8.38 (t, $J = 1.2$ Hz, 4H), 7.58 (dd, $J = 7.6, 1.3$ Hz, 4H), 7.31–7.20 (m, 8H), 6.97 (td, $J = 7.4, 0.9$ Hz, 4H), 6.77 (td, $J = 7.6, 1.5$ Hz, 4H), 6.12 (d, $J = 7.9$ Hz, 4H), 1.22 (s, 36H).

^{13}C NMR (75 MHz, CD_2Cl_2) δ 170.4 (4C), 164.8 (4C), 164.4 (4C), 149.0 (4C), 148.0 (4C), 139.6 (4C), 133.6 (4C), 131.4 (4C), 125.5 (4C), 124.1 (4C), 123.1 (4C), 115.8 (4C), 110.5 (4C), 35.4 (4C), 31.8 (12C).

IR (film): ν (cm^{-1}) 3055, 2957, 2870, 1589, 1526, 1441, 1373, 1271, 1196, 1120, 1075, 1027, 929, 892, 808, 727, 702, 647, 448.

HRMS (ESI, m/z) calcd for $\text{C}_{68}\text{H}_{64}\text{RhN}_4\text{O}_4\text{Cl} [\text{M}-\text{Cl}]^+$: 1241.2721, found: 1241.2709.

3) Rhodium auxiliary complexes Λ -(S)-3 and Δ -(R)-3



The new rhodium auxiliary complexes Λ -(S)-3 and Δ -(R)-3 were synthesized according to a reported method⁹ with some modifications. To a solution of NaOMe (16.2 mg, 0.30 mmol) in methanol (16.0 mL), L-proline (34.5 mg, 0.30 mmol) or D-proline (34.5 mg, 0.30 mmol) was added in one portion. The mixture was stirred for 10 min, to which a suspension of rhodium dimer (201.3 mg, 0.15 mmol) was added. The mixture was stirred and heated at 50 °C for 12 h. After the mixture cooled to room temperature, CH_2Cl_2 (16.0 mL) was added. The reaction mixture was stirred for a further 12 h to give a clear, yellow solution. The solvent was removed in vacuo and the mixture of two diastereoisomers was washed by dichloromethane/diethyl ether (1:6, v/v) until the filtrate was almost colorless. The residual insoluble solid was dried and collected as Λ -(S)-3 (77.4 mg, 36%) or Δ -(R)-3 (86.1 mg, 40%). The absolute configurations of the obtained Λ -(S)/ Δ -(R) configured rhodium(III) complexes were assigned by an X-ray crystal structure of Δ -(R)-3. CD spectroscopy confirmed that they are enantiomers.

^1H NMR (300 MHz, CD_2Cl_2) δ 8.17 (d, $J = 1.8$ Hz, 1H), 7.84–7.79 (m, 2H), 7.73 (dd, $J = 15.2, 8.8$ Hz, 2H), 7.63 (td, $J = 9.0, 1.8$ Hz, 2H), 7.36 (d, $J = 1.6$ Hz, 1H), 7.10–7.07 (m, 2H), 6.95 (td, $J = 7.5, 1.5$ Hz, 2H), 6.76 (d, $J = 7.7$ Hz, 1H), 6.49 (d, $J = 7.7$ Hz, 1H), 4.34–4.17 (m, 2H), 2.80–2.67 (m, 1H), 2.30–2.13 (m, 2H), 2.07–1.94 (m, 1H), 1.68–1.53 (m, 2H), 1.45 (d, $J = 7.6$ Hz, 18H).

^{13}C NMR (75 MHz, CD_2Cl_2) δ 180.5, 172.7, 172.6, 171.5, 171.4, 167.4, 167.0, 166.1, 165.7, 151.4, 150.6, 149.09, 149.06, 138.9, 138.3, 135.4, 134.4, 131.7, 131.3, 131.2, 131.0, 126.3, 126.0, 124.3, 124.2, 123.5, 123.1, 115.7, 112.2, 111.5, 111.1, 64.3, 49.7, 35.8, 35.6, 32.0, 31.9, 30.4, 27.3.

IR (film): ν (cm^{-1}) 3146, 3056, 2958, 1591, 1524, 1445, 1373, 1270, 1191, 1122, 1077, 1033, 928, 814, 773, 648, 550, 449.

Δ -(*S*)-**3**:

HRMS (ESI, m/z) calcd for $\text{C}_{39}\text{H}_{41}\text{RhN}_3\text{O}_4$ $[\text{M}+\text{H}]^+$: 718.2147, found: 718.2133.

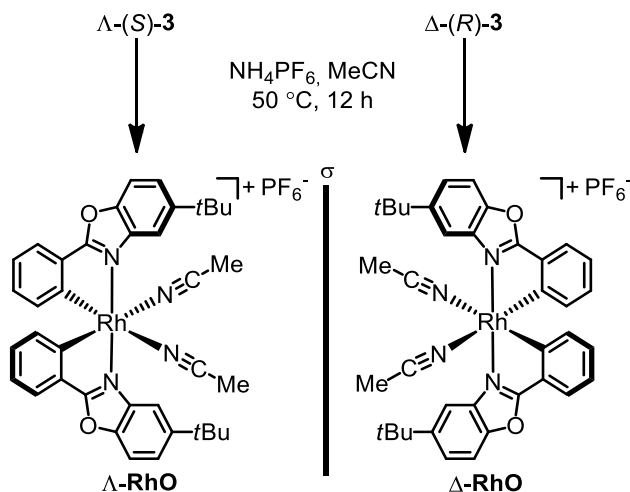
CD (MeOH): λ , nm ($\Delta\epsilon$, $\text{M}^{-1}\text{cm}^{-1}$) 394 (−18), 353 (+26), 295 (−23), 253 (+15), 233 (−4), 216 (+35), 203 (−53).

Δ -(*R*)-**3**:

HRMS (ESI, m/z) calcd for $\text{C}_{39}\text{H}_{40}\text{RhN}_3\text{O}_4\text{Na}$ $[\text{M}+\text{Na}]^+$: 740.1966, found: 740.1930.

CD (MeOH): λ , nm ($\Delta\epsilon$, $\text{M}^{-1}\text{cm}^{-1}$) 394 (+9), 353 (−12), 295 (+14), 253 (−6), 233 (+4), 216 (−15), 203 (+30).

4) Synthesis of non-racemic rhodium catalysts



A suspension of the rhodium auxiliary complex Δ -(*S*)-**3** (71.7 mg, 0.10 mmol) or Δ -(*R*)-**3** (71.7 mg, 0.10 mmol) and NH_4PF_6 (163.0 mg, 1.00 mmol) in acetonitrile (20.0 mL) was heated at $50\text{ }^\circ\text{C}$ for 12 h under nitrogen in the dark. The reaction mixture was concentrated to dryness and subjected to flash silica gel chromatography (100% CH_2Cl_2 to $\text{CH}_2\text{Cl}_2/\text{CH}_3\text{CN} = 15:1$) to give the enantiopure catalyst Δ -**RhO** (72.2 mg, 0.09 mmol, 87%) or Δ -**RhO** (74.7 mg, 0.09 mmol, 90%) as a pale yellow solid. The absolute configurations of the obtained Δ - and Δ -configured rhodium(III) complexes were verified by CD spectroscopy and confirmed by an X-ray crystal structure of Δ -**RhO**. The enantiomeric purity was

verified by HPLC analysis with a chiral stationary phase.

^1H NMR (300 MHz, CD_2Cl_2) δ 7.88 (d, $J = 1.6$ Hz, 2H), 7.80–7.74 (m, 6H), 7.09 (td, $J = 7.5$, 0.9 Hz, 2H), 6.94 (td, $J = 7.6$, 1.5 Hz, 2H), 6.40 (d, $J = 7.8$ Hz, 2H), 2.31 (s, 6H), 1.46 (s, 18H).

^{13}C NMR (75 MHz, CD_2Cl_2) δ 171.5, 160.2, 159.8, 151.2, 148.9, 138.2, 133.5, 132.4, 130.6, 126.3, 125.3, 124.6, 122.0, 113.4, 112.0, 35.7, 31.9, 3.7.

IR (film): ν (cm^{-1}) 2957, 1593, 1528, 1446, 1381, 1274, 1193, 1126, 1081, 1033, 931, 835, 730, 649, 555, 449.

Λ -RhO:

HRMS (ESI, m/z) calcd for $\text{C}_{38}\text{H}_{38}\text{RhN}_4\text{O}_2$ $[\text{M}-\text{PF}_6]^+$: 685.2044, found: 685.2036.

CD (MeOH): λ , nm ($\Delta\epsilon$, $\text{M}^{-1}\text{cm}^{-1}$) 390 (–33), 350 (+69), 295 (–61), 242 (+36), 228 (+3), 218 (+16), 204 (–30).

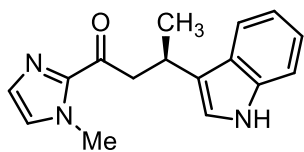
Δ -RhO:

HRMS (ESI, m/z) calcd for $\text{C}_{38}\text{H}_{38}\text{RhN}_4\text{O}_2$ $[\text{M}-\text{PF}_6]^+$: 685.2044, found: 685.2026.

CD (MeOH): λ , nm ($\Delta\epsilon$, $\text{M}^{-1}\text{cm}^{-1}$) 390 (+34), 350 (–70), 295 (+61), 242 (–36), 228 (–14), 218 (–24), 204 (+34).

5.2.2 Catalytic Reactions with Δ -IrO and Δ -RhO

1) General procedure for asymmetric Michael additions. To a solution of catalyst Δ -IrO¹⁰ (1 mol%) or Δ -RhO (1 or 2 mol%) in distilled, anhydrous THF was added the acylimidazole **4a** or **4b** (0.20 mmol) in a Schlenk tube. After being stirred at room temperature for 20 min, the corresponding nucleophile was added at room temperature or 5 °C. The reaction was stirred at the indicated temperature for the indicated time (monitored by TLC) under nitrogen atmosphere. Afterwards, the mixture was concentrated under reduced pressure. The residue was purified by flash chromatography on silica gel (EtOAc/hexane = 1:2 to 2:1) to afford the products **5a-f**. The dr values were determined by ^1H NMR analysis of the crude products, and the ee values were determined by chiral HPLC chromatography using a Chiralpak IC or AD-H column.

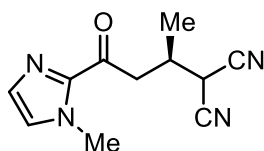
(R)-3-(1*H*-Indol-3-yl)-1-(1-methyl-1*H*-imidazol-2-yl)butan-1-one (5a)

Starting from **4a** (30.2 mg, 0.2 mmol) and 1*H*-indole (58.6 mg, 0.5 mmol) according to the general procedure to give **5a** as a white solid (catalyzed by Δ -**IrO**: 51.9 mg, yield: 97%, *ee*: 96%; catalyzed by Δ -**RhO**: 50.2 mg, yield: 94%, *ee*: 95%). Enantiomeric excess established by HPLC analysis using a Chiralpak IC column (HPLC: IC, 254 nm, hexane/isopropanol = 85:15, flow rate 0.5 mL/min, 40 °C, t_r (major) = 22.4 min, t_r (minor) = 25.9 min); $[\alpha]_D^{20} = +13.8^\circ$ (*c* 0.5, CH₂Cl₂) for 95% *ee* of **5a** ($[\alpha]_D^{20} = -14.5^\circ$ (*c* 2.7, CH₂Cl₂) for 96% *ee* of product with *S*-configuration)¹⁰.

¹H NMR (300 MHz, CDCl₃) δ 8.41 (br s, 1H), 7.67 (d, *J* = 7.8 Hz, 1H), 7.34–7.28 (m, 1H), 7.22–7.05 (m, 3H), 7.01–6.95 (m, 2H), 3.93 (s, 3H), 3.91–3.78 (m, 1H), 3.66–3.34 (m, 2H), 1.40 (d, *J* = 6.9 Hz, 3H).

¹³C NMR (75 MHz, CDCl₃) δ 192.4, 143.4, 136.5, 128.9, 127.0, 126.7, 121.9, 121.5, 120.3, 119.3, 119.1, 111.2, 46.8, 36.2, 27.2, 21.8.

All spectroscopic data were in agreement with the literature.¹⁰

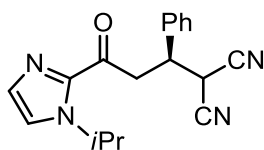
(R)-2-(4-(1-Methyl-1*H*-imidazol-2-yl)-4-oxobutan-2-yl)malononitrile (5b)

Starting from **4a** (30.2 mg, 0.2 mmol) and malononitrile (15.8 mg, 0.24 mmol) according to the general procedure to give **5b** as a colorless oil (catalyzed by Δ -**IrO**: 41.5 mg, yield: 96%, *ee*: 89%; catalyzed by Δ -**RhO**: 41.5 mg, yield: 96%, *ee*: 92%). Enantiomeric excess established by HPLC analysis using a Chiralpak AD-H column (HPLC: AD-H, 254 nm, hexane/isopropanol = 90:10, flow rate 1.0 mL/min, 25 °C, t_r (major) = 22.8 min, t_r (minor) = 24.1 min); $[\alpha]_D^{20} = -33.2^\circ$ (*c* 0.4, CH₂Cl₂) for 92% *ee* of **5b**.

¹H NMR (300 MHz, CDCl₃) δ 7.15 (s, 1H), 7.08 (s, 1H), 4.37 (d, *J* = 4.9 Hz, 1H), 3.99 (s, 3H), 3.47 (dd, *J* = 18.0, 5.3 Hz, 1H), 3.28 (dd, *J* = 18.0, 8.2 Hz, 1H), 2.89–2.71 (m, 1H), 1.36 (d, *J* = 6.9 Hz, 3H).

¹³C NMR (75 MHz, CDCl₃) δ 189.6, 142.4, 129.8, 127.9, 112.5, 111.5, 41.6, 36.2, 31.9, 28.2, 17.3.

All spectroscopic data were in agreement with the literature.¹¹

(R)-2-(3-(1-Isopropyl-1H-imidazol-2-yl)-3-oxo-1-phenylpropyl)malononitrile (5c)

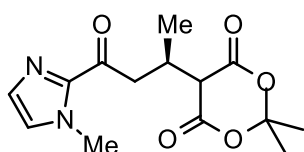
Starting from **4b** (45.8 mg, 0.2 mmol) and malononitrile (15.8 mg, 0.24 mmol) according to the general procedure to give **5c** as a colorless oil (catalyzed by Δ -**IrO**: 24.7 mg, yield: 40%, *ee*: 88%; catalyzed by Δ -**RhO**: 55.8 mg, yield: 91%, *ee*: 95%). Enantiomeric excess established by HPLC analysis using a Chiralpak AD-H column (HPLC: AD-H, 254 nm, hexane/isopropanol = 70:30, flow rate 0.8 mL/min, 25 °C, t_r (minor) = 13.0 min, t_r (major) = 23.6 min); $[\alpha]_D^{20} = -0.4^\circ$ (*c* 0.8, CH₂Cl₂) for 95% *ee* of **5c**.

¹H NMR (300 MHz, CDCl₃) δ 7.46–7.35 (m, 5H), 7.30 (d, *J* = 0.9 Hz, 1H), 7.19 (d, *J* = 0.8 Hz, 1H), 5.42 (dt, *J* = 13.4, 6.7 Hz, 1H), 4.53–4.45 (m, 1H), 4.03–3.88 (m, 2H), 3.87–3.72 (m, 1H), 1.41 (dd, *J* = 8.6, 6.7 Hz, 6H).

¹³C NMR (75 MHz, CDCl₃) δ 188.7, 141.5, 136.5, 130.2, 129.2, 129.0, 128.2, 122.1, 112.0, 111.7, 49.5, 41.7, 41.2, 29.3, 23.55, 23.52.

IR (film): ν (cm⁻¹) 3034, 2983, 2909, 2254, 1670, 1497, 1465, 1454, 1395, 1371, 1254, 1199, 1162, 1087, 971, 914, 772, 731, 700, 671, 646, 591, 548, 488, 407.

HRMS (ESI, *m/z*) calcd for C₁₈H₁₈N₄ONa [M+Na]⁺: 329.1373, found: 329.1369.

(R)-2,2-Dimethyl-5-(4-(1-methyl-1H-imidazol-2-yl)-4-oxobutan-2-yl)-1,3-dioxane-4,6-dione (5d)

Starting from **4a** (30.2 mg, 0.2 mmol) and 2,2-dimethyl-1,3-dioxane-4,6-dione (86.5 mg, 0.6 mmol) according to the general procedure to give **5d** as a white solid (catalyzed by Δ -**IrO**: 58.3 mg, yield: 99%, *ee*: 68%; catalyzed by Δ -**RhO**: 58.3 mg, yield: 99%, *ee*: 85%). Enantiomeric excess established by HPLC analysis using a Chiralpak AD-H column (HPLC: AD-H, 254 nm, hexane/isopropanol = 90:10, flow rate 0.8 mL/min, 40 °C, t_r (major) = 24.9 min, t_r (minor) = 26.6 min); $[\alpha]_D^{20} = -3.3^\circ$ (*c* 0.8, CH₂Cl₂) for 95% *ee* of **5d** (catalyzed by Δ -**RhO** (2 mol%) at room temperature).

¹H NMR (300 MHz, CDCl₃) δ 7.13 (d, *J* = 0.9 Hz, 1H), 7.03 (s, 1H), 4.22–4.16 (m, 1H), 3.98 (s, 3H), 3.56 (dd, *J* = 7.2, 5.0 Hz, 2H), 3.24–3.10 (m, 1H), 1.77 (d, *J* = 5.8 Hz, 6H), 1.21 (d, *J* = 7.0 Hz, 3H).

¹³C NMR (75 MHz, CDCl₃) δ 192.3, 165.2, 164.7, 142.9, 129.2, 127.2, 104.7, 49.3, 41.9, 36.2, 28.9,

28.4, 26.9, 17.3.

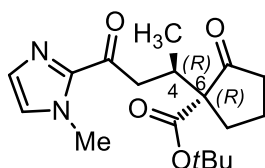
IR (film): ν (cm⁻¹) 3136, 2928, 2883, 1780, 1739, 1667, 1459, 1408, 1298, 1200, 1151, 1086, 1053, 991, 958, 914, 871, 787, 698, 670, 634, 596, 544, 496, 426.

HRMS (ESI, m/z) calcd for C₁₄H₁₉N₂O₅ [M+H]⁺: 295.1288, found: 295.1282.

(R)-tert-Butyl

1-((R)-4-(1-methyl-1H-imidazol-2-yl)-4-oxobutan-2-yl)-2-

oxocyclopentanecarboxylate (5e)



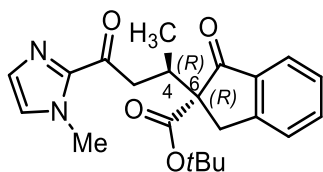
Starting from **4a** (30.2 mg, 0.2 mmol) and *tert*-butyl 2-oxocyclopentanecarboxylate (73.7 mg, 0.4 mmol) according to the general procedure to give **5e** (major product) as a colorless oil (catalyzed by Δ -**IrO**: 27.4 mg, yield: 41%, *ee*: 97%, *dr*: 3:1; catalyzed by Δ -**RhO**: 55.5 mg, yield: 83%, *ee*: 99%, *dr*: 4:1). The *dr* was determined by ¹H NMR and the enantiomeric excess established by HPLC analysis using a Chiralpak AD-H column (HPLC: AD-H, 254 nm, hexane/isopropanol = 95:5, flow rate 0.5 mL/min, 40 °C, t_r (minor) = 26.4 min, t_r (major) = 29.5 min); $[\alpha]_D^{20} = +13.1^\circ$ (c 1.4, CH₂Cl₂) for 99% *ee* of **5e**.

¹H NMR (300 MHz, CDCl₃) δ 7.08 (d, J = 0.8 Hz, 1H), 6.99 (s, 1H), 3.96 (s, 3H), 3.22 (dd, J = 16.6, 10.3 Hz, 1H), 3.08–2.97 (m, 1H), 2.74 (dd, J = 16.6, 2.6 Hz, 1H), 2.50–2.30 (m, 2H), 2.21–2.06 (m, 1H), 2.01–1.85 (m, 3H), 1.42 (s, 9H), 0.94 (d, J = 6.7 Hz, 3H).

¹³C NMR (75 MHz, CDCl₃) δ 214.5, 191.2, 169.2, 143.2, 128.9, 127.0, 82.0, 65.8, 41.7, 38.6, 36.2, 32.4, 29.4, 27.9, 19.4, 16.4.

IR (film): ν (cm⁻¹) 3112, 2970, 2868, 1743, 1715, 1673, 1462, 1405, 1368, 1283, 1246, 1151, 1125, 1005, 979, 914, 834, 775, 695, 589, 549, 434.

HRMS (ESI, m/z) calcd for C₁₈H₂₇N₂O₄ [M+H]⁺: 335.1965, found: 335.1964.

(*R*)-*tert*-Butyl 2-((*R*)-4-(1-methyl-1*H*-imidazol-2-yl)-4-oxobutan-2-yl)-1-oxo-2,3-dihydro-1*H*-indene-2-carboxylate (5f**)**

Starting from **4a** (30.2 mg, 0.2 mmol) and *tert*-butyl 1-oxo-2,3-dihydro-1*H*-indene-2-carboxylate (92.9 mg, 0.4 mmol) according to the general procedure to give **5f** (major product) as a colorless oil (catalyzed by Δ -**IrO**: 68.1 mg, yield: 89%, *ee*: 97%, *dr*: 10:1; catalyzed by Δ -**RhO**: 70.4 mg, yield: 92%, *ee*: 96%, *dr*: 14:1). Enantiomeric excess established by HPLC analysis using a Chiralpak AD-H column (HPLC: AD-H, 254 nm, hexane/isopropanol = 97:3, flow rate 0.5 mL/min, 25 °C, t_r (major) = 84.2 min, t_r (minor) = 168.0 min); $[\alpha]_D^{20} = -96.9^\circ$ (c 0.7, CH_2Cl_2) for 97% *ee* of **5f**. The *dr* value was determined by ^1H NMR as shown below (Figure 82).

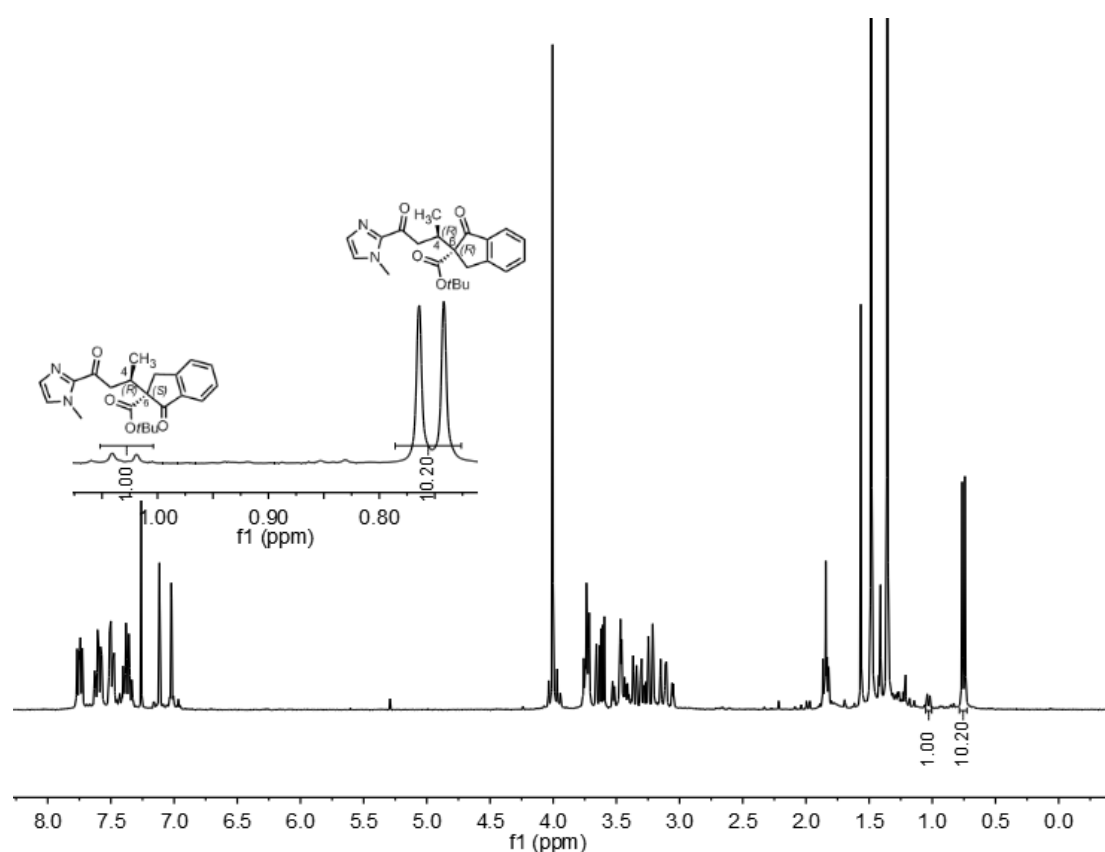


Figure 82 ^1H NMR of the crude product **5f** and its diastereomer **5f'**. Calculated *dr* = 1:10.

^1H NMR (300 MHz, CDCl_3) δ 7.74 (d, $J = 7.6$ Hz, 1H), 7.65–7.56 (m, 1H), 7.50 (d, $J = 7.7$ Hz, 1H), 7.45–7.31 (m, 1H), 7.13 (d, $J = 0.9$ Hz, 1H), 7.03 (s, 1H), 4.01 (s, 3H), 3.69 (d, $J = 17.5$ Hz, 1H), 3.51–

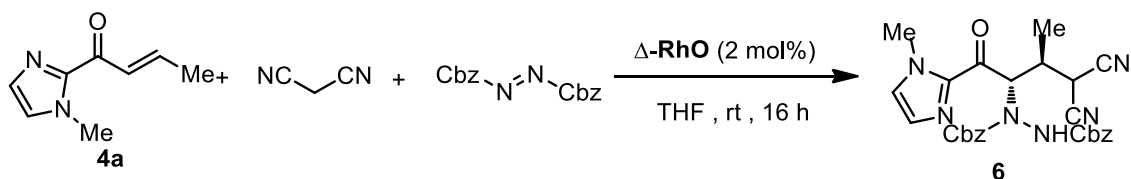
3.39 (m, 1H), 3.32–3.18 (m, 2H), 3.09 (dd, $J = 16.3, 2.8$ Hz, 1H), 1.36 (s, 9H), 0.76 (d, $J = 6.7$ Hz, 3H).

^{13}C NMR (75 MHz, CDCl_3) δ 202.4, 191.2, 169.3, 154.1, 143.3, 136.0, 135.2, 128.9, 127.6, 127.0, 126.3, 124.6, 82.1, 65.9, 42.4, 36.3, 33.1, 33.0, 27.8, 15.2.

IR (film): ν (cm^{-1}) 2969, 2930, 1705, 1673, 1604, 1464, 1406, 1369, 1332, 1252, 1213, 1146, 1092, 986, 913, 844, 769, 743, 694, 651, 590, 517, 466.

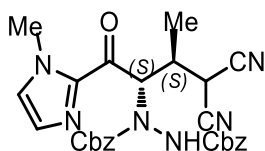
HRMS (ESI, m/z) calcd for $\text{C}_{22}\text{H}_{27}\text{N}_2\text{O}_4$ $[\text{M}+\text{H}]^+$: 383.1965, found: 383.1962.

2) Procedure for asymmetric cascade reaction.



To a solution of catalyst $\Delta\text{-RhO}$ (3.2 mg, 2 mol%) in distilled, anhydrous THF (0.2 mL) was added the acylimidazole **4a** (30.2 mg, 0.20 mmol) in a Schlenk tube. After being stirred at room temperature for 20 min, malononitrile (15.9 mg, 0.24 mmol) and (E) -dibenzyl diazene-1,2-dicarboxylate (119.3 mg, 0.40 mmol) were added. The reaction was stirred at room temperature for 16 h under nitrogen atmosphere. Afterwards, the mixture was concentrated under reduced pressure. The residue was purified by flash chromatography on silica gel (EtOAc/hexane = 1:4 to 1:2) to afford the diastereomeric mixture of **6** as a white solid (84.3 mg, yield: 82%, ee of the major diastereoisomer: 92%, dr : 4:1 (after purified by flash chromatography)). The ee values were determined by HPLC analysis using a Chiralpak AD-H column (HPLC: AD-H, 254 nm, hexane/isopropanol = 90:10, flow rate 0.5 mL/min, 25 °C. Major diastereoisomer t_r (minor) = 80.5 min, t_r (major) = 117.4 min); $[\alpha]_D^{20} = -30.5^\circ$ (c 1.0, CH_2Cl_2 , 92% ee).

Dibenzyl 1-((2*S*,3*S*)-4,4-dicyano-3-methyl-1-(1-methyl-1*H*-imidazol-2-yl)-1-oxobutan-2-yl)hydrazine-1,2-dicarboxylate (**6**)



^1H NMR (300 MHz, CDCl_3) δ 7.25–6.72 (m, 12H), 5.22–4.60 (m, 6H), 3.77 (s, 3H), 3.10–2.95 (m, 1H), 1.29 (s, 3H). (major diastereoisomer)

^{13}C NMR (75 MHz, CDCl_3) δ 155.7, 141.3, 135.4, 135.3, 128.8, 128.6, 128.5, 128.4, 128.2, 128.1, 128.0,

127.9, 113.3, 111.7, 69.1, 68.3, 53.5, 36.2, 35.4, 26.9. (major diastereoisomer)

IR (film): ν (cm⁻¹) 3260, 2958, 2925, 2254, 1726, 1677, 1454, 1396, 1241, 1207, 1156, 1079, 1040, 986, 959, 918, 852, 795, 740, 697, 641, 567, 506, 475, 403.

HRMS (ESI, m/z) calcd for C₂₇H₂₆N₆O₅Na [M+Na]⁺: 537.1856, found: 537.1848.

5.2.3 Investigation of the Stability of Rhodium Catalyst Δ -/ Δ -RhO

1) Catalyst stability investigated by ¹H NMR

The rhodium complex Δ -RhO (5.0 mg) was dissolved in CD₂Cl₂ and kept in the NMR tube at room temperature under reduced light. ¹H NMR spectra were recorded after 2, 4, 6 and 8 days (Figure 83).

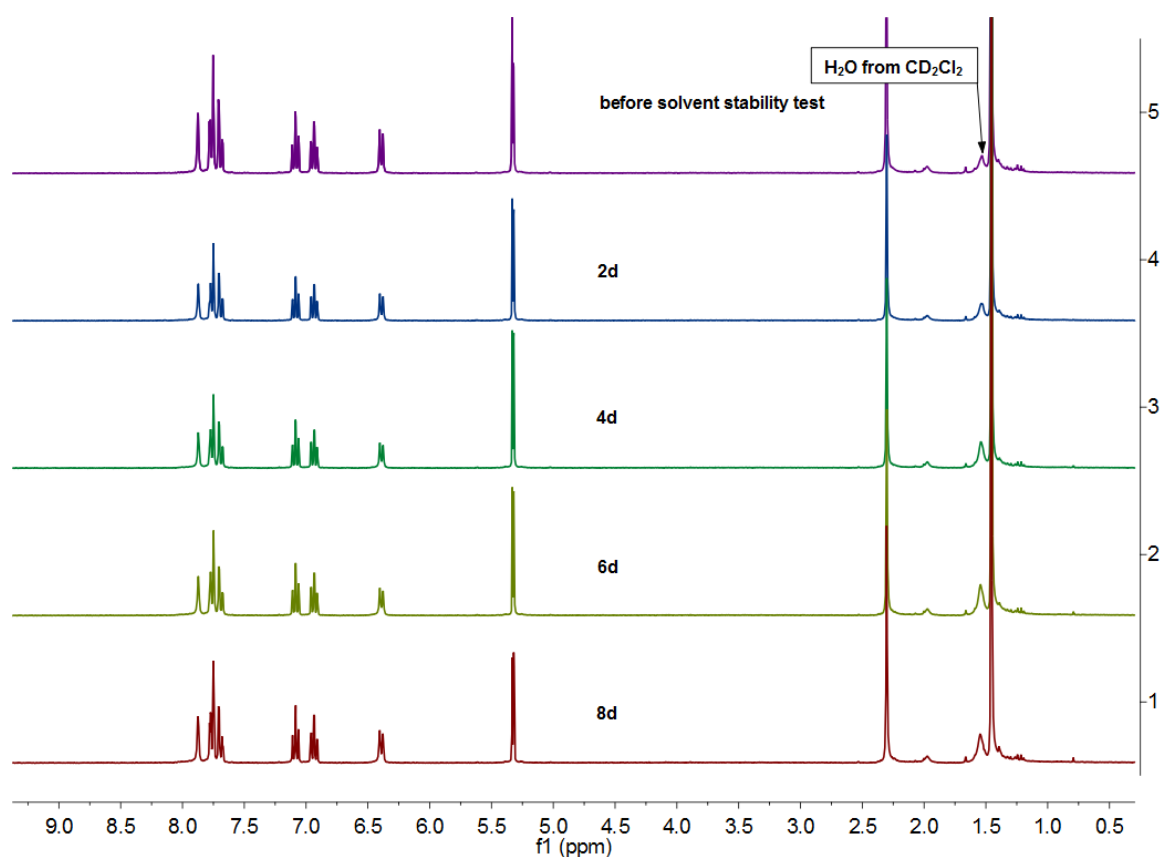


Figure 83 ¹H NMR of Δ -RhO recorded in CD₂Cl₂ over 8 days.

2) Catalyst stability investigated by chiral HPLC

Enantiopure pure rhodium complex Δ -**RhO** (2.0 mg) was dissolved in CH_2Cl_2 (1.0 mL, HPLC grade) and kept in a brown glass vial at room temperature. The HPLC spectra were collected after 2-8 days. HPLC conditions: Daicel Chiralpak IB (250 \times 4.6 mm) HPLC column, the column temperature was 25 $^\circ\text{C}$ and UV-absorption was measured at 254 nm. Solvent A = 0.1% TFA, solvent B = MeCN with a linear gradient of 30% to 41% B in 60 min at a flow rate = 0.6 mL/min.

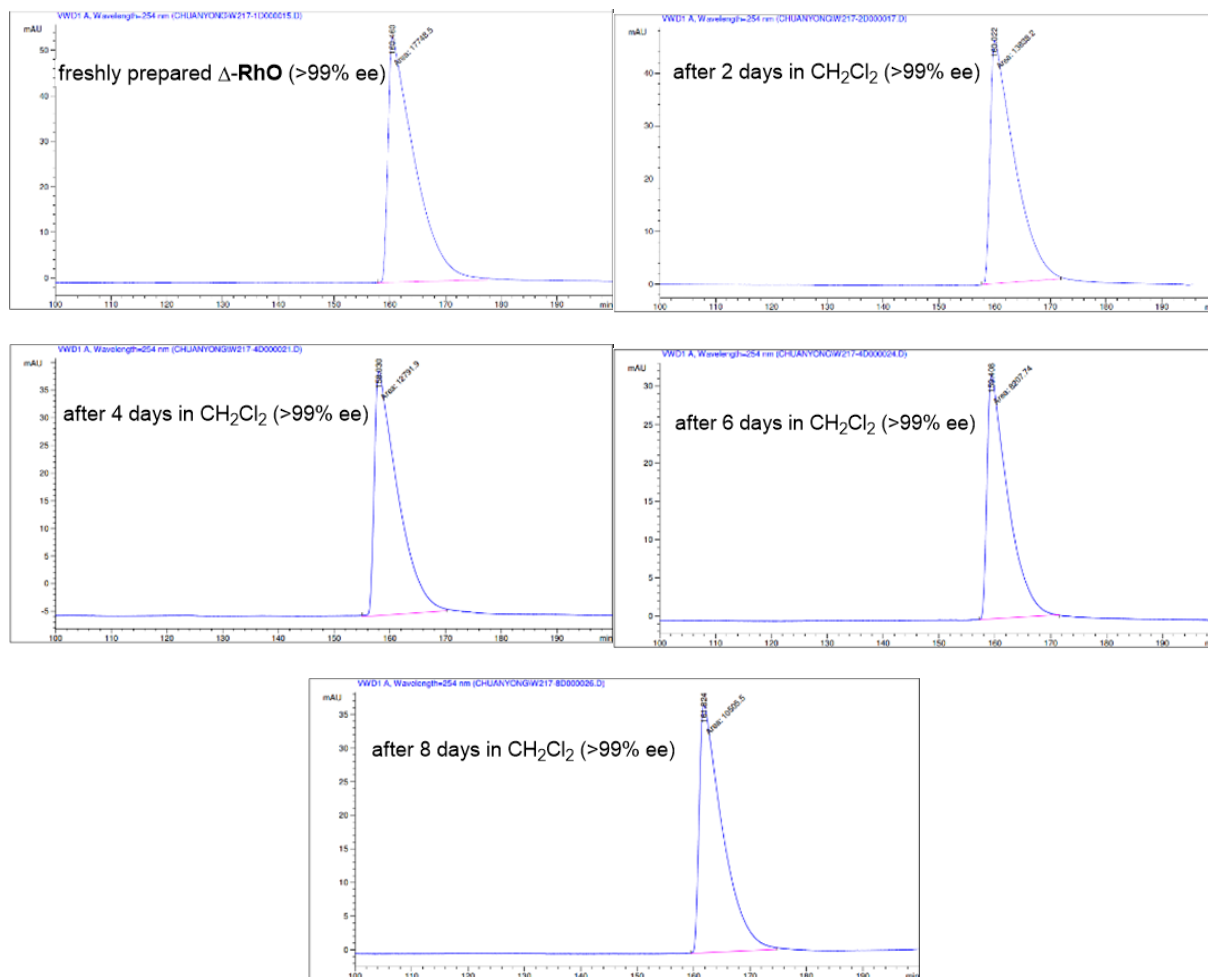


Figure 84 HPLC traces of the freshly prepared Δ -**RhO** in CH_2Cl_2 (>99% ee) and after 2-8 days in CH_2Cl_2 (>99% ee).

5.2.4 Investigation of the Proposed Catalyst-Coordinated Substrate Intermediate

To a solution of Δ -RhO (10.0 mg, 0.012 mmol) in CD_2Cl_2 (0.70 mL) at room temperature was added substrate **4a** (9.5 mg, 0.063 mmol). The mixture was stirred at room temperature for 20 min and then analyzed by ^1H NMR spectroscopy. The ^1H NMR analysis is consistent with a fast bidentate coordination of **4a** to Δ -RhO under release of the coordinated acetonitrile ligands.

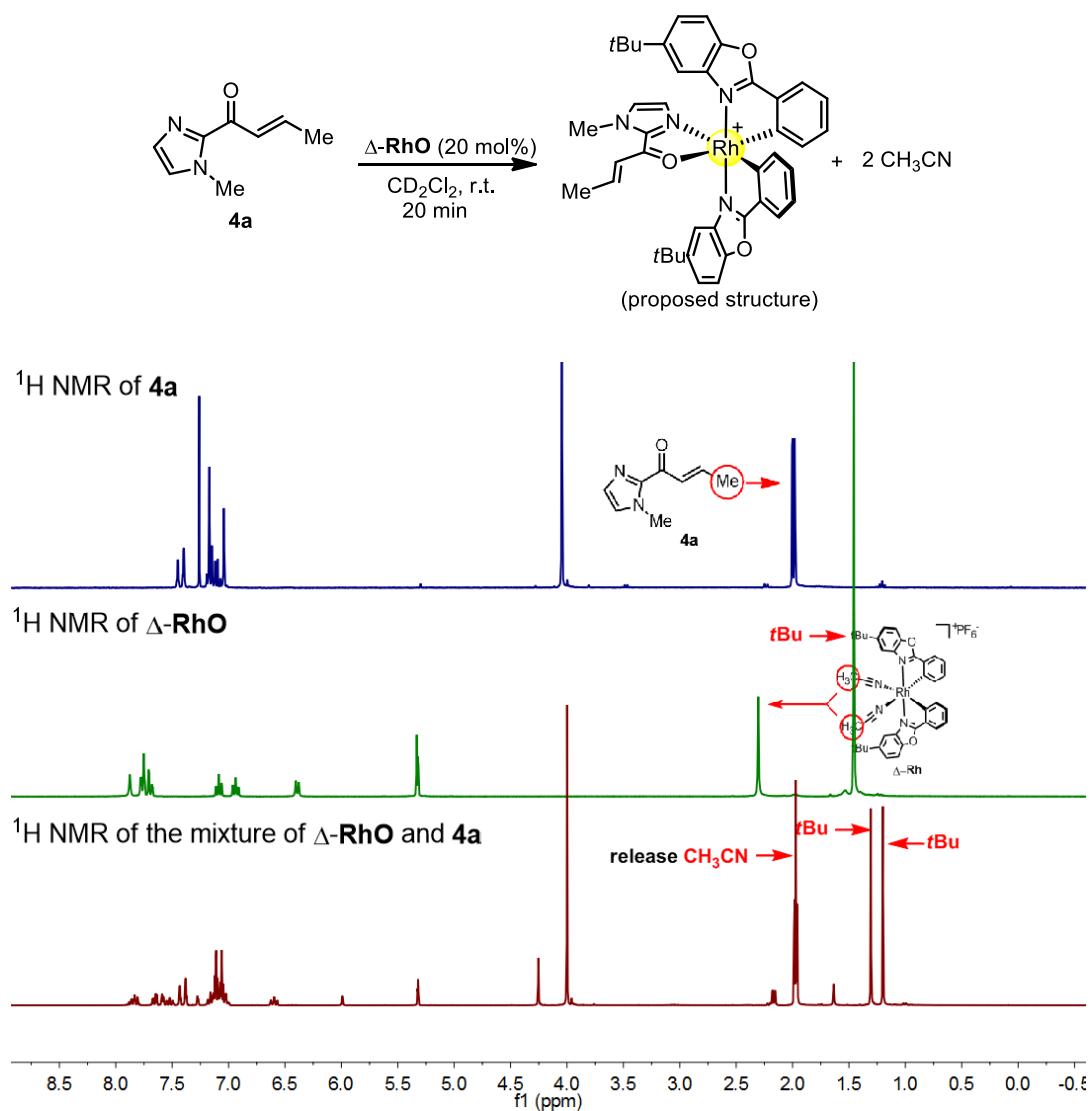


Figure 85 ^1H NMR spectra of substrate **4a**, catalyst Δ -RhO, and a mixture of **4a** and Δ -RhO.

5.2.5 The Acetonitrile Exchange Rates: Δ -RhO vs. Δ -IrO

To a solution of Δ -RhO (5.0 mg, 0.006 mmol) or Δ -IrO (5.5 mg, 0.006 mmol) in CD_2Cl_2 (3 mL) at room temperature was added bipyridine (1.64 mg, 0.0105 mmol). The ^1H NMR spectra were collected after the indicated time. The conversion was calculated by area integration ratio of two different *tert*-butyl groups, which reveal that the acetonitrile exchange rates are faster in Δ -RhO compared to Δ -IrO.

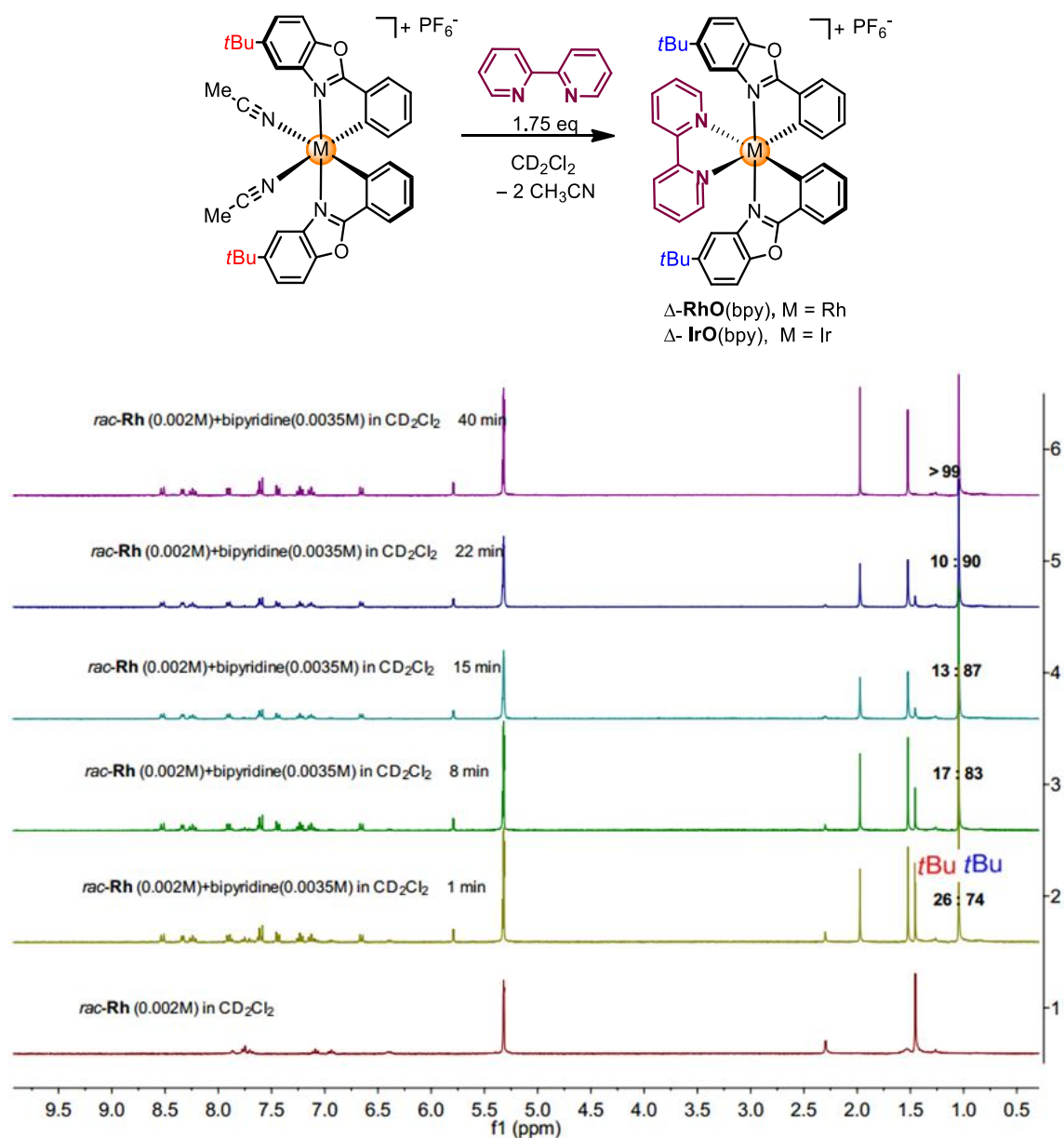


Figure 86 ^1H NMR spectra of Δ -RhO and the mixture of Δ -RhO and bipyridine in CD_2Cl_2 .

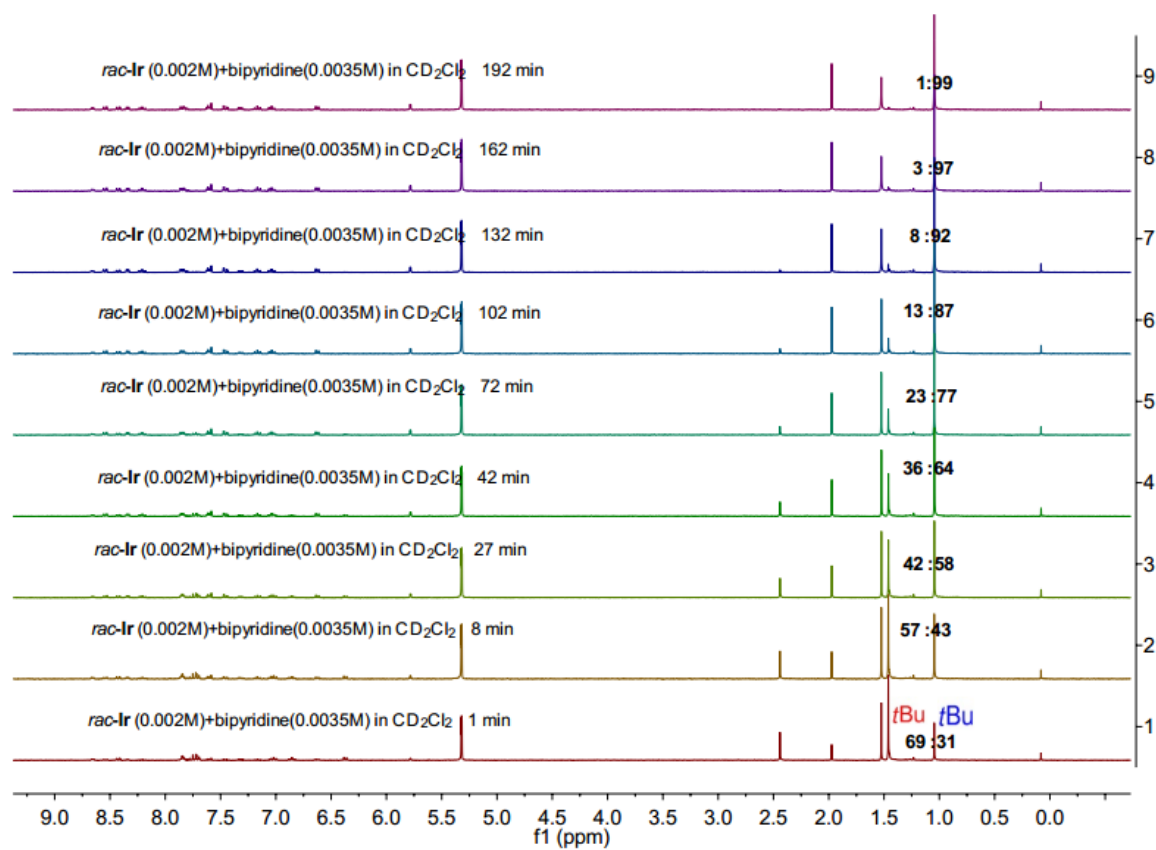


Figure 87 ^1H NMR spectra of the mixture of $\Delta\text{-IrO}$ and bipyridine in CD_2Cl_2 .

5.2.6 Single Crystal X-Ray Diffraction

Crystals of Δ -(*R*)-**3** and Δ -**RhO** were obtained by slow diffusion from a solution of the compounds in CH₂Cl₂ layered with Et₂O at room temperature for several weeks. Crystals of **5d**, racemic **5f** and **6** were obtained by slow diffusion from a solution of the compounds in CH₂Cl₂ layered with hexane at 5 °C for several days. Single crystals suitable for X-ray diffraction of the substrate coordinated rhodium catalyst (here denoted as **RhO-I**) were obtained by reacting **4b** (0.06 mmol) with Δ/Λ -**RhO** (0.06 mmol) overnight at room temperature in CH₂Cl₂ (2.0 mL). After the slow addition of hexane (5.0 mL), crystals were collected after several days (70% yield).

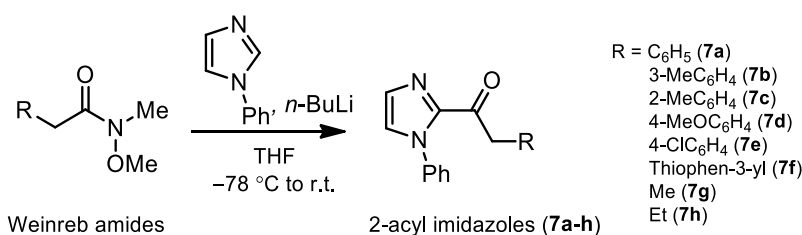
Crystal data and details of the structure determination are presented in Appendices 6.7. In the packing of **RhO-I** there are holes present that contain diffuse electron density that may belong to heavily disordered solvent molecules. This was taken into account using the “squeeze” procedure in the PLATON program system. The determination of the absolute configuration of the light atom structure **5d** by means of refining the “Flack parameter” was not possible. The absolute configurations of compounds Δ -(*R*)-**3** and Δ -**RhO** have been determined.

5.3 Merger of Visible Light Induced Oxidation and Enantioselective Alkylation with Chiral Iridium Catalyst

5.3.1 Synthesis of Substrates

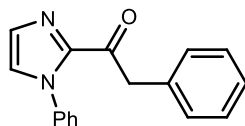
1) Synthesis of 2-acyl imidazoles

2-Acyl imidazoles **7a'**, **7a''** and Weinreb amides were synthesized following our recently published procedures.¹² 2-Acyl imidazoles **7a-h** were synthesized following the route shown below.



General procedure for the preparation of the 2-acyl imidazoles. All 2-acyl imidazoles were synthesized according to reported procedures with some modifications.¹³ To a solution of *N*-phenylimidazole (1.1 eq.) in THF (0.4 M) at $-78\text{ }^{\circ}\text{C}$ was added *n*-BuLi (1.1 eq.) dropwise. The reaction was stirred at $-78\text{ }^{\circ}\text{C}$ for 30 min, then stirred at room temperature for 30 min. The corresponding Weinreb amides (1.0 eq.) was added to the flask after the reaction was cooled back down to $-78\text{ }^{\circ}\text{C}$. The reaction was allowed to slowly warm to room temperature and stirred overnight. The reaction was quenched with AcOH (6.0 eq.) and extracted with EtOAc. The organic layer was washed with aqueous saturated NaHCO₃ and brine. The combined organic layers were dried over anhydrous Na₂SO₄, and concentrated under reduced pressure. The residue was purified by flash chromatography on silica gel (EtOAc/hexane = 1:3) to provide the 2-acyl imidazoles **7a-h**.

2-Phenyl-1-(1-phenyl-1*H*-imidazol-2-yl)ethanone (**7a**)

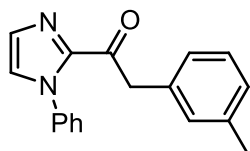


Following the general procedure, *N*-methoxy-*N*-methyl-2-phenylacetamide (1.797 g, 10.0 mmol) was converted to 2-acyl imidazole **7a** (1.709 g, 6.5 mmol, yield: 65%) as a white solid.

¹H NMR (300 MHz, CDCl₃) δ 7.46–7.37 (m, 3H), 7.34–7.20 (m, 8H), 7.19 (d, *J* = 1.0 Hz, 1H), 4.45 (s, 2H).

All spectroscopic data are in agreement with the literature.¹³

1-(1-Phenyl-1H-imidazol-2-yl)-2-*meta*-tolylethanone (7b)



Following the general procedure, *N*-methoxy-*N*-methyl-2-(*m*-tolyl)acetamide (1.544 g, 8.0 mmol) was converted to 2-acyl imidazole **7b** (1.186 g, 4.3 mmol, yield: 54%) as a white solid.

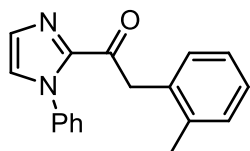
¹H NMR (300 MHz, CDCl₃) δ 7.45–7.38 (m, 3H), 7.33 (d, *J* = 1.0 Hz, 1H), 7.25–7.20 (m, 2H), 7.20–7.09 (m, 4H), 7.07–7.01 (m, 1H), 4.42 (s, 2H), 2.32 (s, 3H).

¹³C NMR (75 MHz, CDCl₃) δ 188.5, 142.8, 138.3, 138.0, 134.2, 130.7, 129.6, 128.9, 128.6, 128.3, 127.5, 127.3, 126.9, 125.8, 45.5, 21.3.

IR (film): ν (cm⁻¹) 3125, 3109, 1681, 1597, 1500, 1448, 1393, 1245, 1209, 1176, 1160, 1094, 963, 913, 894, 880, 842, 798, 767, 652, 543.

HRMS (ESI, *m/z*) calcd for C₁₈H₁₇N₂O [M+H]⁺: 277.1333, found: 277.1335.

1-(1-Phenyl-1H-imidazol-2-yl)-2-*ortho*-tolylethanone (7c)



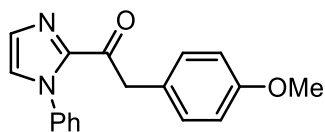
Following the general procedure, *N*-methoxy-*N*-methyl-2-(*o*-tolyl)acetamide (1.544 g, 8.0 mmol) was converted to 2-acyl imidazole **7c** (1.450 g, 5.3 mmol, yield: 66%) as a white solid.

¹H NMR (300 MHz, CDCl₃) δ 7.44–7.38 (m, 3H), 7.33 (d, *J* = 1.0 Hz, 1H), 7.29–7.22 (m, 2H), 7.22–7.19 (m, 2H), 7.17–7.10 (m, 3H), 4.53 (s, 2H), 2.29 (s, 3H).

¹³C NMR (75 MHz, CDCl₃) δ 188.4, 142.9, 138.2, 137.1, 133.1, 130.8, 130.2, 129.5, 128.9, 128.7, 127.3, 127.1, 125.87, 125.85, 43.5, 19.8.

IR (film): ν (cm⁻¹) 3104, 2936, 2911, 1691, 1594, 1490, 1407, 1393, 1340, 1326, 1208, 1189, 1142, 1076, 964, 942, 868, 806, 773, 738, 706, 693, 607, 556.

HRMS (ESI, *m/z*) calcd for C₁₈H₁₇N₂O [M+H]⁺: 277.1335, found: 277.1333.

2-(4-Methoxyphenyl)-1-(1-phenyl-1*H*-imidazol-2-yl)ethanone (7d)

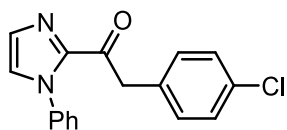
Following the general procedure, *N*-methoxy-2-(4-methoxyphenyl)-*N*-methylacetamide (1.674 g, 8.0 mmol) was converted to 2-acyl imidazole **7d** (1.682 g, 5.8 mmol, yield: 72%) as a white solid.

¹H NMR (300 MHz, CDCl₃) δ 7.48–7.41 (m, 3H), 7.35 (d, *J* = 1.0 Hz, 1H), 7.31–7.23 (m, 4H), 7.22 (d, *J* = 1.0 Hz, 1H), 6.92–6.87 (m, 1H), 6.87–6.84 (m, 1H), 4.43 (s, 2H), 3.80 (s, 3H).

¹³C NMR (75 MHz, CDCl₃) δ 188.7, 158.5, 142.7, 138.3, 130.9, 129.6, 128.9, 128.6, 127.3, 126.4, 125.8, 113.9, 55.2, 44.7.

IR (film): ν (cm⁻¹) 3129, 2949, 2828, 1668, 1602, 1505, 1450, 1393, 1345, 1302, 1244, 1170, 1141, 1032, 967, 910, 853, 823, 791, 763, 689, 610, 584, 520.

HRMS (ESI, *m/z*) calcd for C₁₈H₁₇N₂O₂ [M+H]⁺: 293.1285, found: 293.1283.

2-(4-Chlorophenyl)-1-(1-phenyl-1*H*-imidazol-2-yl)ethanone (7e)

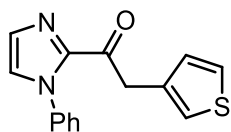
Following the general procedure, 2-(4-chlorophenyl)-*N*-methoxy-*N*-methylacetamide (1.764 g, 8.3 mmol) was converted to 2-acyl imidazole **7e** (1.536 g, 5.2 mmol, yield: 63%) as a colorless oil.

¹H NMR (300 MHz, CDCl₃) δ 7.47–7.40 (m, 3H), 7.33 (d, *J* = 1.0 Hz, 1H), 7.28–7.18 (m, 7H), 4.43 (s, 2H).

¹³C NMR (75 MHz, CDCl₃) δ 187.9, 142.5, 138.2, 132.8, 132.7, 131.3, 129.8, 129.0, 128.8, 128.5, 127.6, 125.8, 44.8.

IR (film): ν (cm⁻¹) 3012, 1682, 1594, 1492, 1446, 1397, 1307, 1148, 1092, 1041, 965, 862, 805, 764, 689, 659, 578, 547.

HRMS (ESI, *m/z*) calcd for C₁₇H₁₄ClN₂O [M+H]⁺: 297.0789, found: 297.0788.

1-(1-Phenyl-1*H*-imidazol-2-yl)-2-(thiophen-3-yl)ethanone (7f)

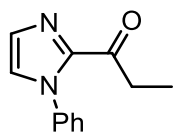
Following the general procedure, *N*-methoxy-*N*-methyl-2-(thiophen-3-yl)acetamide (1.482 g, 8.0 mmol) was converted to 2-acyl imidazole **7f** (1.256 g, 4.7 mmol, yield: 59%) as a white solid.

¹H NMR (300 MHz, CDCl₃) δ 7.46–7.40 (m, 3H), 7.32 (d, *J* = 1.0 Hz, 1H), 7.28–7.22 (m, 3H), 7.21–7.16 (m, 2H), 7.06 (dd, *J* = 4.9, 1.3 Hz, 1H), 4.50 (s, 2H).

¹³C NMR (75 MHz, CDCl₃) δ 187.8, 142.6, 138.2, 133.9, 129.7, 129.0, 128.9, 128.7, 127.4, 125.8, 125.3, 123.2, 40.1.

IR (film): ν (cm⁻¹) 3122, 3094, 1698, 1593, 1490, 1407, 1387, 1317, 1295, 1149, 1038, 969, 880, 823, 805, 763, 696, 669, 610, 589.

HRMS (ESI, *m/z*) calcd for C₁₅H₁₃N₂OS [M+H]⁺: 269.0743, found: 269.0743.

1-(1-Phenyl-1*H*-imidazol-2-yl)propan-1-one (7g)

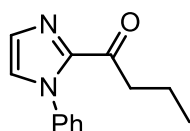
Following the general procedure, *N*-methoxy-*N*-methylpropionamide (874 mg, 7.5 mmol) was converted to 2-acyl imidazole **7g** (1.071 g, 5.3 mmol, yield: 71%) as a white solid.

¹H NMR (300 MHz, CDCl₃) δ 7.48–7.41 (m, 3H), 7.31–7.23 (m, 3H), 7.16 (d, *J* = 1.0 Hz, 1H), 3.17 (q, *J* = 7.3 Hz, 2H), 1.13 (t, *J* = 7.3 Hz, 3H).

¹³C NMR (75 MHz, CDCl₃) δ 192.0, 142.9, 138.5, 129.3, 128.9, 128.7, 126.8, 125.9, 32.4, 7.8.

IR (film): ν (cm⁻¹) 3123, 2972, 1686, 1593, 1491, 1450, 1407, 1346, 1215, 1149, 1034, 976, 936, 879, 801, 769, 693, 608, 565.

HRMS (ESI, *m/z*) calcd for C₁₂H₁₃N₂O [M+H]⁺: 201.1022, found: 201.1023.

1-(1-Phenyl-1*H*-imidazol-2-yl)butan-1-one (7h)

Following the general procedure, *N*-methoxy-*N*-methylbutyramide (1.495 g, 11.4 mmol) was converted to 2-acyl imidazole **7h** (1.305 g, 6.1 mmol, yield: 54%) as a white solid.

¹H NMR (300 MHz, CDCl₃) δ 7.51–7.43 (m, 3H), 7.32–7.25 (m, 3H), 7.18 (d, *J* = 1.0 Hz, 1H), 3.14 (t, *J* = 7.2 Hz, 2H), 1.82–1.60 (m, 2H), 0.98 (t, *J* = 7.4 Hz, 3H).

¹³C NMR (75 MHz, CDCl₃) δ 191.5, 143.1, 138.5, 129.3, 128.9, 128.7, 126.9, 125.9, 41.1, 17.4, 13.7.

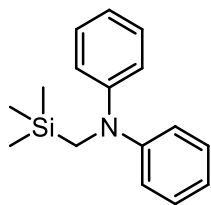
IR (film): ν (cm⁻¹) 3095, 2966, 2930, 2877, 1683, 1594, 1449, 1339, 1328, 1265, 1112, 1072, 961, 914, 891, 814, 796, 691, 542.

HRMS (ESI, *m/z*) calcd for C₁₃H₁₅N₂O [M+H]⁺: 215.1179, found: 215.1180.

2) Synthesis of α-silylamines

All α-silylamines were synthesized according to reported procedures with some modifications.¹⁴ To a solution of amines (1.0 eq.) in THF (0.4 M) under nitrogen atmosphere at 0 °C was added *n*-BuLi (1.0 eq.) dropwise. The reaction was stirred at 0 °C for 30 min, then stirred at room temperature for further 1 h. (Iodomethyl)trimethylsilane (1.5 eq.) was added slowly to the flask after the reaction was cooled back down to 0 °C, and the resulting solution was stirred at room temperature (**9a-b**) or 60 °C (**9c-e**) overnight. Afterwards, the reaction was quenched with water and extracted with *n*-hexane. The combined organic layers were dried (Na₂SO₄) and concentrated under reduced pressure. The residue was purified by flash chromatography on silica gel (100% *n*-hexane) to produce **9a-e**. The new synthesized α-silylamines were stored at -20 °C under nitrogen atmosphere.

N-Phenyl-*N*-((trimethylsilyl)methyl)aniline (**9a**)



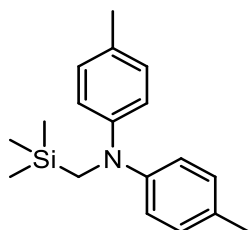
Following the general procedure, diphenylamine (1.690 g, 10.0 mmol) was converted to α-silylamine **9a** (1.788 g, 7.0 mmol, yield: 70%) as a colorless oil.

¹H NMR (300 MHz, CDCl₃) δ 7.33–7.23 (m, 4H), 7.06–7.00 (m, 4H), 6.98–6.92 (m, 2H), 3.34 (s, 2H), -0.01 (s, 9H).

¹³C NMR (75 MHz, CDCl₃) δ 149.6, 129.1, 121.1, 120.9, 43.7, -1.3.

All spectroscopic data are in agreement with the literature.¹⁴

4-Methyl-*N-p*-tolyl-*N*-((trimethylsilyl)methyl)aniline (**9b**)



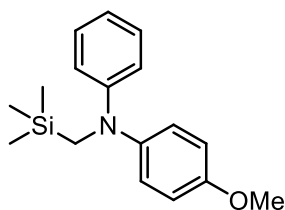
Following the general procedure, di-*p*-tolylamine (1.479g, 7.5 mmol) was converted to α -silylamine **9b** (1.381 g, 4.9 mmol, yield: 65%) as a pale yellow oil.

¹H NMR (300 MHz, CDCl₃) δ 7.04 (d, J = 8.3 Hz, 4H), 6.86 (d, J = 8.4 Hz, 4H), 3.23 (s, 2H), 2.29 (s, 6H), -0.05 (s, 9H).

¹³C NMR (75 MHz, CDCl₃) δ 147.4, 130.6, 129.6, 121.1, 44.2, 20.6, -1.3.

All spectroscopic data were in agreement with the literature.¹⁴

4-Methoxy-*N*-phenyl-*N*-((trimethylsilyl)methyl)aniline (**9c**)



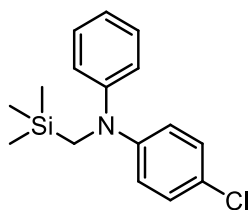
Following the general procedure, 4-methoxy-*N*-phenylaniline (1.374 g, 6.9 mmol) was converted to α -silylamine **9c** (0.925 g, 3.2 mmol, yield: 47%) as a white solid.

¹H NMR (300 MHz, CDCl₃) δ 7.26–7.05 (m, 4H), 6.98–6.68 (m, 5H), 3.87 (s, 3H), 3.27 (s, 2H), 0.00 (s, 9H).

¹³C NMR (75 MHz, CDCl₃) δ 156.5, 150.9, 142.1, 128.7, 127.6, 117.5, 115.7, 114.7, 55.5, 43.9, -1.38.

IR (film): ν (cm⁻¹) 3036, 2950, 2833, 1595, 1574, 1494, 1463, 1341, 1296, 1237, 1179, 1130, 1088, 868, 832, 790, 692, 555, 516.

HRMS (ESI, m/z) calcd for C₁₇H₂₄NOSi [M+H]⁺: 286.1622, found: 286.1624.

4-Chloro-*N*-phenyl-*N*-((trimethylsilyl)methyl)aniline (9d)

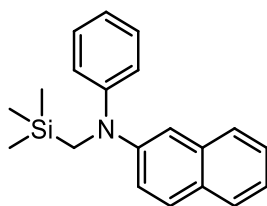
Following the general procedure, 4-chloro-*N*-phenylaniline (0.713 g, 3.5 mmol) was converted to α -silylamine **9d** (0.639 g, 2.2 mmol, yield: 63%) as a colorless oil.

^1H NMR (300 MHz, CDCl_3) δ 7.36–7.27 (m, 2H), 7.23–7.17 (m, 2H), 7.09–6.98 (m, 3H), 6.93–6.85 (m, 2H), 3.31 (s, 2H), 0.00 (s, 9H).

^{13}C NMR (75 MHz, CDCl_3) δ 149.1, 148.3, 129.3, 128.9, 124.9, 122.4, 122.2, 120.8, 43.9, –1.3.

IR (film): ν (cm^{-1}) 2952, 1585, 1487, 1429, 1354, 1248, 1188, 1095, 901, 839, 815, 746, 697, 627, 510.

HRMS (ESI, m/z) calcd for $\text{C}_{16}\text{H}_{21}\text{ClN}_2\text{Si}$ $[\text{M}+\text{H}]^+$: 290.1126, found: 290.1129.

***N*-Phenyl-*N*-((trimethylsilyl)methyl)naphthalen-2-amine (9e)**

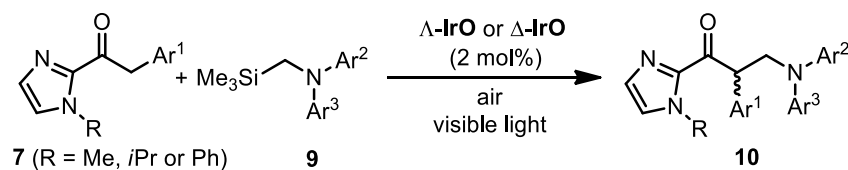
Following the general procedure, *N*-phenylnaphthalen-2-amine (2.192 g, 10.0 mmol) was converted to α -silylamine **9e** (1.832 g, 6.0 mmol, yield: 60%) as a colorless oil.

^1H NMR (300 MHz, CDCl_3) δ 7.75–7.61 (m, 3H), 7.44–7.36 (m, 1H), 7.33–7.24 (m, 4H), 7.17 (dd, $J = 8.9, 2.4$ Hz, 1H), 7.10–7.05 (m, 2H), 7.03–6.95 (m, 1H), 3.44 (s, 2H), 0.00 (s, 9H).

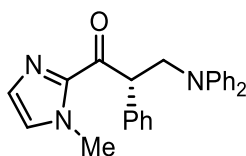
^{13}C NMR (75 MHz, CDCl_3) δ 149.6, 147.0, 134.7, 129.2, 128.9, 128.4, 127.5, 126.6, 126.2, 123.4, 122.1, 121.8, 114.9, 44.2, –1.2.

All spectroscopic data are in agreement with the literature.¹⁴

5.3.2 Iridium-Catalyzed Photoredox Reactions

1) Reaction of 2-acyl imidazoles with *N,N*-diaryl-*N*-(trimethylsilyl)methylamines

General catalysis procedure. To a solution of catalyst Λ - or Δ -IrO (2 mol% or 4 mol%) in distilled, anhydrous CH₂Cl₂ (0.50 mL, 0.4 M) in a 10 mL test tube, was added the 2-acyl imidazole (0.20 mmol). After being stirred at room temperature for 20 min, the α -silylamine (0.60 mmol) was added. The tube was positioned approximately 2 cm away from a 12 W white light energy saving lamp. The reaction was stirred at room temperature for the indicated time (monitored by TLC) under an atmosphere of air (air balloon). Afterwards, the solvent was concentrated under reduced pressure. The residue was purified by flash chromatography on silica gel (EtOAc/*n*-hexane = 1:20) to afford the non-racemic product. The enantiomeric excess was determined by chiral HPLC analysis. The absolute configuration of the product (*R*)-10e was determined by X-ray crystallography and used to assign the configuration of all other compounds. Racemic samples were obtained by carrying out the analogous reactions with the racemic catalyst *rac*-IrO.

(S)-3-(Diphenylamino)-1-(1-methyl-1*H*-imidazol-2-yl)-2-phenylpropan-1-one (10a'')

Using Λ -IrO (2 mol%) as catalyst, starting from 2-acyl imidazole **7a''** (40.0 mg, 0.20 mmol) and α -silylamine **9a** (153.2 mg, 0.60 mmol) according to the general procedure to give **10a''** as a pale yellow oil (25.9 mg, 0.068 mmol, yield: 34%). Enantiomeric excess established by HPLC analysis using a Chiralpak AD-H column, *ee* = 91% (HPLC: AD-H, 254 nm, hexane/isopropanol = 85:15, flow rate 0.5 mL/min, 25 °C, *t_r* (minor) = 13.2 min, *t_r* (major) = 13.9 min).

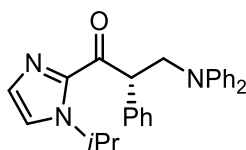
¹H NMR (300 MHz, CD₂Cl₂) δ 7.45–7.38 (m, 2H), 7.34–7.25 (m, 3H), 7.24–7.20 (m, 3H), 7.19–7.16 (m, 1H), 7.05 (d, *J* = 0.9 Hz, 1H), 7.00–6.97 (m, 1H), 6.97–6.90 (m, 2H), 6.90–6.84 (m, 4H), 5.66 (dd, *J* = 8.8, 4.9 Hz, 1H), 4.73–4.62 (dd, *J* = 14.5, 8.7 Hz, 1H), 4.02 (dd, *J* = 14.5, 4.9 Hz, 1H), 3.80 (s, 3H).

^{13}C NMR (75 MHz, CD_2Cl_2) δ 191.4, 148.5, 143.5, 138.3, 129.6, 129.5, 129.1, 129.0, 127.9, 127.6, 121.9, 121.8, 55.8, 51.8, 36.3.

IR (film): ν (cm^{-1}) 3059, 2923, 2853, 1668, 1587, 1491, 1453, 1364, 1288, 1207, 1185, 1154, 1029, 990, 950, 909, 862, 772, 745, 693, 630, 506.

HRMS (ESI, m/z) calcd for $\text{C}_{25}\text{H}_{24}\text{N}_3\text{O}$ $[\text{M}+\text{H}]^+$: 382.1914, found: 382.1916.

(S)-3-(Diphenylamino)-1-(1-isopropyl-1H-imidazol-2-yl)-2-phenylpropan-1-one (10a')



Using Δ -**IrO** (2 mol%) as catalyst, starting from 2-acyl imidazole **7a'** (45.7 mg, 0.20 mmol) and α -silylamine **9a** (153.2 mg, 0.60 mmol) according to the general procedure to give **10a'** as a pale yellow oil (39.3 mg, 0.096 mmol, yield: 48%). Enantiomeric excess established by HPLC analysis using a Chiralpak AD-H column, $ee = 90\%$ (HPLC: AD-H, 254 nm, hexane/isopropanol = 85:15, flow rate 0.5 mL/min, 25 °C, t_r (major) = 10.0 min, t_r (minor) = 10.8 min).

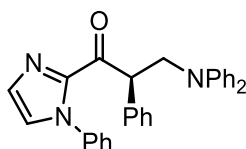
^1H NMR (300 MHz, CD_2Cl_2) δ 7.45–7.38 (m, 3H), 7.33–7.26 (m, 3H), 7.24–7.17 (m, 5H), 7.09 (d, $J = 0.8$ Hz, 1H), 6.97–6.86 (m, 5H), 5.72 (dd, $J = 8.8, 4.9$ Hz, 1H), 5.36–5.26 (m, 1H), 4.68 (dd, $J = 14.5, 8.8$ Hz, 1H), 4.00 (dd, $J = 14.5, 4.9$ Hz, 1H), 1.34 (d, $J = 6.7$ Hz, 3H), 1.30 (d, $J = 6.7$ Hz, 3H).

^{13}C NMR (75 MHz, CD_2Cl_2) δ 191.4, 161.9, 148.5, 138.5, 130.0, 129.5, 129.1, 129.0, 127.5, 127.3, 127.2, 126.7, 125.5, 122.1, 121.9, 121.8, 55.9, 52.3, 49.7, 23.6, 23.5.

IR (film): ν (cm^{-1}) 3060, 3030, 2979, 2931, 2870, 1687, 1670, 1589, 1492, 1392, 1298, 1254, 1194, 1029, 990, 947, 910, 862, 846, 745, 720, 695, 647, 577, 543.

HRMS (ESI, m/z) calcd for $\text{C}_{27}\text{H}_{27}\text{N}_3\text{ONa}$ $[\text{M}+\text{Na}]^+$: 432.2046, found: 432.2052.

(R)-3-(Diphenylamino)-2-phenyl-1-(1-phenyl-1H-imidazol-2-yl)propan-1-one (10a)



Using Δ -**IrO** (2 mol%) as catalyst, starting from 2-acyl imidazole **7a** (52.4 mg, 0.20 mmol) and α -silylamine **9a** (153.2 mg, 0.60 mmol) according to the general procedure to give **10a** as a pale yellow oil (79.7 mg, 0.184 mmol, yield: 92%). Enantiomeric excess established by HPLC analysis using a

Chiralpak AD-H column, $ee = 97\%$ (HPLC: AD-H, 254 nm, hexane/isopropanol = 97:3, flow rate 0.5 mL/min, 25 °C, t_r (major) = 20.8 min, t_r (minor) = 24.4 min). $[\alpha]_D^{20} = +76.4^\circ$ (c 0.6, CH_2Cl_2).

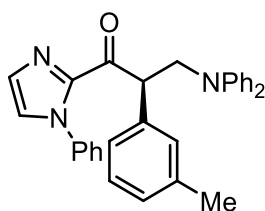
^1H NMR (300 MHz, CD_2Cl_2) δ 7.47–7.36 (m, 5H), 7.34–7.27 (m, 3H), 7.26–7.19 (m, 5H), 7.14 (d, $J = 0.9$ Hz, 1H), 7.10–7.03 (m, 2H), 7.00–6.93 (m, 2H), 6.93–6.86 (m, 4H), 5.68 (dd, $J = 8.7, 5.0$ Hz, 1H), 4.62 (dd, $J = 14.6, 8.7$ Hz, 1H), 3.97 (dd, $J = 14.6, 5.0$ Hz, 1H).

^{13}C NMR (75 MHz, CDCl_3) δ 189.7, 161.6, 147.9, 142.7, 138.2, 137.4, 129.8, 129.6, 129.1, 128.7, 128.6, 128.5, 127.2, 127.0, 126.8, 126.0, 125.7, 125.0, 121.5, 121.4, 55.3, 51.7.

IR (film): ν (cm^{-1}) 3059, 2924, 2854, 1681, 1588, 1490, 1452, 1398, 1339, 1304, 1266, 1247, 1150, 1095, 990, 970, 908, 862, 744, 665, 621.

HRMS (ESI, m/z) calcd for $\text{C}_{30}\text{H}_{25}\text{N}_3\text{ONa}$ $[\text{M}+\text{Na}]^+$: 466.1890, found: 466.1893.

(*R*)-3-(Diphenylamino)-1-(1-phenyl-1*H*-imidazol-2-yl)-2-*m*-tolylpropan-1-one (10b)



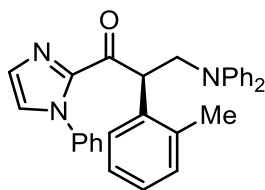
Using Δ -**IrO** (2 mol%) as catalyst, starting from 2-acyl imidazole **7b** (55.3 mg, 0.20 mmol) and α -silylamine **9a** (153.2 mg, 0.60 mmol) according to the general procedure to give **10b** as a pale yellow oil (75.0 mg, 0.164 mmol, yield: 82%). Enantiomeric excess established by HPLC analysis using a Chiralpak OD-H column, $ee = 96\%$ (HPLC: OD-H, 254 nm, hexane/isopropanol = 99:1, flow rate 0.5 mL/min, 25 °C, t_r (major) = 23.5 min, t_r (minor) = 25.9 min). $[\alpha]_D^{20} = +82.7^\circ$ (c 0.6, CH_2Cl_2).

^1H NMR (300 MHz, CD_2Cl_2) δ 7.47–7.39 (m, 4H), 7.34–7.30 (m, 1H), 7.29–7.23 (m, 3H), 7.22–7.18 (m, 5H), 7.14 (d, $J = 1.0$ Hz, 1H), 7.10–7.05 (m, 2H), 7.01–6.94 (m, 2H), 6.94–6.90 (m, 3H), 5.66 (dd, $J = 8.9, 4.8$ Hz, 1H), 4.62 (dd, $J = 14.5, 8.9$ Hz, 1H), 3.97 (dd, $J = 14.5, 4.9$ Hz, 1H), 2.32 (s, 3H).

^{13}C NMR (75 MHz, CD_2Cl_2) δ 190.0, 161.9, 148.5, 143.4, 138.9, 137.8, 130.1, 130.0, 129.8, 129.5, 129.1, 128.9, 128.8, 128.4, 127.9, 127.3, 127.2, 126.7, 126.2, 125.5, 121.9, 121.8, 55.7, 52.0, 21.5.

IR (film): ν (cm^{-1}) 3035, 2920, 1682, 1590, 1491, 1448, 1399, 1305, 1261, 1147, 1067, 1031, 943, 905, 865, 750, 693, 578, 547.

HRMS (ESI, m/z) calcd for $\text{C}_{31}\text{H}_{27}\text{N}_3\text{ONa}$ $[\text{M}+\text{Na}]^+$: 480.2046, found: 480.2049.

(R)-3-(Diphenylamino)-1-(1-phenyl-1*H*-imidazol-2-yl)-2-*o*-tolylpropan-1-one (10c)

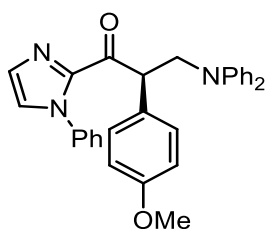
Using Δ -**IrO** (2 mol%) as catalyst, starting from 2-acyl imidazole **7c** (55.3 mg, 0.20 mmol) and α -silylamine **9a** (153.2 mg, 0.60 mmol) according to the general procedure to give **10c** as a pale yellow oil (70.5 mg, 0.154 mmol, yield: 77%). Enantiomeric excess established by HPLC analysis using a Chiralpak AD-H column, $ee = 96\%$ (HPLC: AD-H, 254 nm, hexane/isopropanol = 98:2, flow rate 0.5 mL/min, 25 °C, t_r (minor) = 16.7 min, t_r (major) = 17.3 min). $[\alpha]_D^{20} = +144.9^\circ$ (c 0.8, CH_2Cl_2).

^1H NMR (300 MHz, CDCl_3) δ 7.45–7.36 (m, 3H), 7.33–7.28 (m, 1H), 7.25–7.15 (m, 6H), 7.14–7.08 (m, 2H), 7.08–7.03 (m, 3H), 6.98–6.93 (m, 2H), 6.92–6.86 (m, 4H), 5.94 (dd, $J = 7.9, 5.6$ Hz, 1H), 4.66 (dd, $J = 14.6, 7.9$ Hz, 1H), 3.93 (dd, $J = 14.6, 5.6$ Hz, 1H), 2.52 (s, 3H).

^{13}C NMR (75 MHz, CDCl_3) δ 190.4, 148.1, 143.2, 138.3, 137.8, 135.9, 130.7, 129.8, 129.1, 128.8, 128.5, 127.6, 127.13, 127.10, 126.0, 125.7, 121.5, 121.4, 55.6, 47.5, 20.0.

IR (film): ν (cm^{-1}) 3059, 2924, 1679, 1587, 1490, 1399, 1308, 1271, 1218, 1149, 1072, 991, 908, 869, 731, 658, 648.

HRMS (ESI, m/z) calcd for $\text{C}_{31}\text{H}_{27}\text{N}_3\text{ONa}$ $[\text{M}+\text{Na}]^+$: 480.2046, found: 480.2052.

(R)-3-(Diphenylamino)-2-(4-methoxyphenyl)-1-(1-phenyl-1*H*-imidazol-2-yl)propan-1-one (10d)

Using Δ -**IrO** (4 mol%) as catalyst, starting from 2-acyl imidazole **7d** (58.5 mg, 0.20 mmol) and α -silylamine **9a** (153.2 mg, 0.60 mmol) according to the general procedure to give **10d** as a pale yellow oil (57.8 mg, 0.122 mmol, yield: 61%). Enantiomeric excess established by HPLC analysis using a Chiralpak AD-H column, $ee = 90\%$ (HPLC: AD-H, 254 nm, hexane/isopropanol = 95:5, flow rate 0.5 mL/min, 25 °C, t_r (major) = 24.4 min, t_r (minor) = 28.7 min). $[\alpha]_D^{20} = +88.2^\circ$ (c 0.6, CH_2Cl_2).

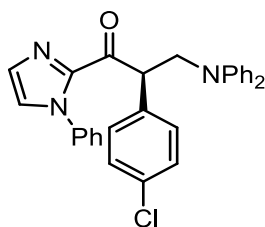
^1H NMR (300 MHz, CD_2Cl_2) δ 7.45–7.37 (m, 3H), 7.31–7.23 (m, 4H), 7.23–7.18 (m, 4H), 7.13 (d, J = 1.0 Hz, 1H), 7.08–7.03 (m, 2H), 6.99–6.93 (m, 2H), 6.92–6.87 (m, 3H), 6.86–6.82 (m, 2H), 5.60 (dd, J = 8.7, 5.1 Hz, 1H), 4.56 (dd, J = 14.5, 8.7 Hz, 1H), 3.93 (dd, J = 14.5, 5.1 Hz, 1H), 3.76 (s, 3H).

^{13}C NMR (75 MHz, CD_2Cl_2) δ 190.2, 159.4, 148.5, 143.3, 138.8, 130.2, 130.1, 130.0, 129.8, 129.6, 129.5, 129.4, 129.1, 128.9, 127.8, 126.2, 122.0, 121.9, 121.8, 114.4, 55.62, 55.60, 51.1.

IR (film): ν (cm^{-1}) 3062, 2931, 2835, 1679, 1587, 1443, 1398, 1244, 1094, 973, 908, 864, 829, 747, 728, 689, 531.

HRMS (ESI, m/z) calcd for $\text{C}_{31}\text{H}_{27}\text{N}_3\text{O}_2\text{Na}$ [$\text{M}+\text{Na}$] $^+$: 496.1995, found: 496.2000.

(*R*)-2-(4-Chlorophenyl)-3-(diphenylamino)-1-(1-phenyl-1*H*-imidazol-2-yl)propan-1-one (10e)



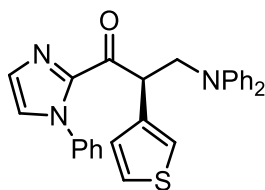
Using Δ -**IrO** (2 mol%) as catalyst, starting from 2-acyl imidazole **7e** (59.3 mg, 0.20 mmol) and α -silylamine **9a** (153.2 mg, 0.60 mmol) according to the general procedure to give **10e** as a white solid (66.9 mg, 0.140 mmol, yield: 70%). Enantiomeric excess established by HPLC analysis using a Chiralpak AD-H column, ee = 98% (HPLC: AD-H, 254 nm, hexane/isopropanol = 97:3, flow rate 0.5 mL/min, 25 °C, t_r (major) = 21.7 min, t_r (minor) = 27.3 min). $[\alpha]_D^{20}$ = +118.0° (c 0.8, CH_2Cl_2).

^1H NMR (300 MHz, CDCl_3) δ 7.32–7.18 (m, 5H), 7.14–7.04 (m, 7H), 6.97 (d, J = 0.8 Hz, 1H), 6.94–6.87 (m, 2H), 6.86–6.81 (m, 2H), 6.80–6.74 (m, 4H), 5.59 (dd, J = 8.1, 5.7 Hz, 1H), 4.49 (dd, J = 14.6, 8.1 Hz, 1H), 3.88 (dd, J = 14.6, 5.6 Hz, 1H).

^{13}C NMR (75 MHz, CDCl_3) δ 189.3, 147.8, 142.5, 138.1, 135.9, 133.2, 130.2, 129.9, 129.1, 128.8, 128.7, 128.6, 127.4, 125.7, 121.6, 121.4, 55.2, 51.1.

IR (film): ν (cm^{-1}) 3034, 2910, 1673, 1587, 1455, 1396, 1269, 1185, 1105, 1034, 992, 938, 859, 830, 746, 731, 690, 645, 617, 589, 558, 526.

HRMS (ESI, m/z) calcd for $\text{C}_{30}\text{H}_{24}\text{ClN}_3\text{ONa}$ [$\text{M}+\text{Na}$] $^+$: 500.1500, found: 500.1506.

(R)-3-(Diphenylamino)-1-(1-phenyl-1H-imidazol-2-yl)-2-(thiophen-3-yl)propan-1-one (10f)

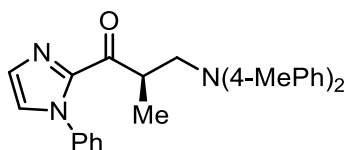
Using Δ -**IrO** (2 mol%) as catalyst, starting from 2-acyl imidazole **7f** (53.7 mg, 0.20 mmol) and α -silylamine **9a** (153.2 mg, 0.60 mmol) according to the general procedure to give **10f** as a pale yellow oil (55.7 mg, 0.124 mmol, yield: 62%). Enantiomeric excess established by HPLC analysis using a Chiralpak AD-H column, $ee = 94\%$ (HPLC: AD-H, 254 nm, hexane/isopropanol = 97:3, flow rate 0.5 mL/min, 25 °C, t_r (major) = 25.9 min, t_r (minor) = 38.1 min). $[\alpha]_D^{20} = +54.5^\circ$ (c 0.5, CH_2Cl_2).

^1H NMR (300 MHz, CD_2Cl_2) δ 7.46–7.39 (m, 3H), 7.29–7.25 (m, 2H), 7.25–7.19 (m, 5H), 7.17 (d, $J = 1.0$ Hz, 1H), 7.13–7.06 (m, 3H), 7.01–6.95 (m, 2H), 6.94–6.89 (m, 4H), 5.87 (dd, $J = 8.7, 5.3$ Hz, 1H), 4.58 (dd, $J = 14.5, 8.7$ Hz, 1H), 3.99 (dd, $J = 14.5, 5.3$ Hz, 1H).

^{13}C NMR (75 MHz, CD_2Cl_2) δ 189.7, 148.4, 143.2, 138.7, 138.0, 130.2, 129.5, 129.1, 128.9, 128.1, 128.0, 126.2, 126.0, 123.2, 122.0, 121.7, 55.6, 47.5.

IR (film): ν (cm^{-1}) 3059, 2922, 1681, 1587, 1490, 1445, 1364, 1341, 1244, 1188, 1148, 1095, 907, 859, 841, 747, 690, 654, 575, 547.

HRMS (ESI, m/z) calcd for $\text{C}_{28}\text{H}_{23}\text{N}_3\text{OSNa}$ [$\text{M}+\text{Na}$] $^+$: 472.1454, found: 472.1457.

(R)-3-(Di-*p*-tolylamino)-2-methyl-1-(1-phenyl-1H-imidazol-2-yl)propan-1-one (10g)

Using Δ -**IrO** (4 mol%) as catalyst, starting from 2-acyl imidazole **7g** (40.0 mg, 0.20 mmol) and α -silylamine **9b** (170.0 mg, 0.60 mmol) according to the general procedure to give **10g** as a pale yellow oil (76.2 mg, 0.186 mmol, yield: 93%). Enantiomeric excess established by HPLC analysis using a Chiralpak AD-H column, $ee = 96\%$ (HPLC: AD-H, 254 nm, hexane/isopropanol = 97:3, flow rate 0.5 mL/min, 25 °C, t_r (major) = 21.7 min, t_r (minor) = 29.3 min). $[\alpha]_D^{20} = -108.2^\circ$ (c 0.8, CH_2Cl_2).

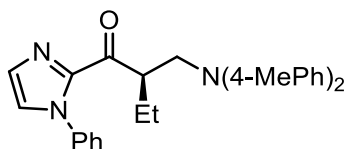
^1H NMR (300 MHz, CD_2Cl_2) δ 7.45–7.40 (m, 2H), 7.25–7.16 (m, 3H), 7.14–7.08 (m, 2H), 7.07–7.00 (m, 4H), 6.89–6.81 (m, 4H), 4.53–4.31 (m, 1H), 4.15 (dd, $J = 14.4, 8.0$ Hz, 1H), 3.66 (dd, $J = 14.4, 6.0$ Hz, 1H), 2.30 (s, 6H), 1.20 (d, $J = 7.0$ Hz, 3H).

^{13}C NMR (75 MHz, CD_2Cl_2) δ 194.3, 161.9, 146.6, 143.3, 139.0, 131.1, 130.5, 130.0, 129.9, 129.1, 128.8, 127.7, 126.4, 126.3, 125.3, 121.6, 56.2, 41.2, 20.7, 15.7.

IR (film): ν (cm^{-1}) 3052, 2922, 1679, 1606, 1596, 1505, 1492, 1444, 1366, 1263, 1225, 1074, 949, 910, 810, 758, 727, 691, 664, 578, 539.

HRMS (ESI, m/z) calcd for $\text{C}_{27}\text{H}_{27}\text{N}_3\text{ONa}$ [$\text{M}+\text{Na}$] $^+$: 432.2046, found: 432.2049.

(*R*)-2-((Di-*p*-tolylamino)methyl)-1-(1-phenyl-1*H*-imidazol-2-yl)butan-1-one (10h)



Using Δ -**IrO** (4 mol%) as catalyst, starting from 2-acyl imidazole **7h** (42.9 mg, 0.20 mmol) and α -silylamine **9b** (170.0 mg, 0.60 mmol) according to the general procedure to give **10h** as a pale yellow oil (55.0 mg, 0.130 mmol, yield: 65%). Enantiomeric excess established by HPLC analysis using a Chiralpak AD-H column, $ee = 96\%$ (HPLC: AD-H, 254 nm, hexane/isopropanol = 97:3, flow rate 0.5 mL/min, 25 °C, t_r (major) = 18.5 min, t_r (minor) = 22.9 min). $[\alpha]_{\text{D}}^{20} = -84.4^\circ$ (c 0.7, CH_2Cl_2).

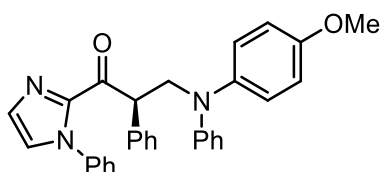
^1H NMR (300 MHz, CD_2Cl_2) δ 7.45–7.38 (m, 2H), 7.24–7.15 (m, 3H), 7.10–7.00 (m, 6H), 6.85–6.76 (m, 4H), 4.45–4.29 (m, 1H), 4.11 (dd, $J = 14.4, 8.8$ Hz, 1H), 3.73 (dd, $J = 14.4, 5.1$ Hz, 1H), 2.30 (s, 6H), 1.86–1.56 (m, 2H), 0.91 (t, $J = 7.5$ Hz, 3H).

^{13}C NMR (75 MHz, CD_2Cl_2) δ 194.4, 161.9, 146.6, 144.1, 139.0, 131.0, 130.5, 130.0, 129.9, 129.0, 128.7, 127.6, 126.4, 126.3, 125.3, 121.6, 55.3, 47.9, 24.3, 20.7, 11.9.

IR (film): ν (cm^{-1}) 3027, 2962, 2920, 2860, 1676, 1607, 1569, 1506, 1456, 1367, 1277, 1187, 1074, 952, 812, 760, 726, 708, 692, 665, 556.

HRMS (ESI, m/z) calcd for $\text{C}_{28}\text{H}_{29}\text{N}_3\text{ONa}$ [$\text{M}+\text{Na}$] $^+$: 446.2203, found: 446.2208.

(*R*)-3-((4-Methoxyphenyl)(phenyl)amino)-2-phenyl-1-(1-phenyl-1*H*-imidazol-2-yl)propan-1-one (10i)



Using Δ -**IrO** (2 mol%) as catalyst, starting from 2-acyl imidazole **7a** (52.4 mg, 0.20 mmol) and α -silylamine **9c** (171.3 mg, 0.60 mmol) according to the general procedure to give **10i** as a pale yellow oil (85.2 mg, 0.180 mmol, yield: 90%). Enantiomeric excess established by HPLC analysis using a Chiralpak AD-H column, $ee = 95\%$ (HPLC: AD-H, 254 nm, hexane/isopropanol = 95:5, flow rate 0.5 mL/min, 25 °C, t_r (major) = 22.6 min, t_r (minor) = 25.4 min). $[\alpha]_D^{20} = +31.3^\circ$ (c 0.6, CH_2Cl_2).

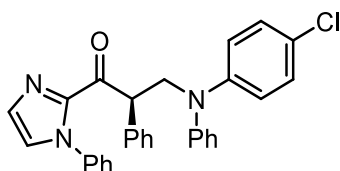
^1H NMR (300 MHz, CD_2Cl_2) δ 7.48–7.38 (m, 5H), 7.35–7.26 (m, 3H), 7.22 (d, $J = 1.0$ Hz, 1H), 7.21–7.13 (m, 3H), 7.11–7.06 (m, 2H), 6.95–6.88 (m, 2H), 6.87–6.80 (m, 2H), 6.79–6.71 (m, 3H), 5.68 (dd, $J = 8.8, 4.8$ Hz, 1H), 4.57 (dd, $J = 14.4, 8.8$ Hz, 1H), 3.92 (dd, $J = 14.4, 4.8$ Hz, 1H), 3.81 (s, 3H).

^{13}C NMR (75 MHz, CD_2Cl_2) δ 190.0, 157.1, 149.5, 143.4, 140.9, 138.9, 138.1, 130.1, 129.3, 129.2, 129.1, 129.0, 128.9, 127.94, 127.91, 127.7, 126.2, 118.9, 116.7, 115.0, 55.9, 55.8, 52.2.

IR (film): ν (cm^{-1}) 3059, 3031, 2931, 2835, 1734, 1681, 1595, 1506, 1492, 1453, 1398, 1371, 1340, 1307, 1273, 1180, 1072, 990, 965, 869, 760, 692.

HRMS (ESI, m/z) calcd for $\text{C}_{31}\text{H}_{27}\text{N}_3\text{O}_2\text{Na}$ $[\text{M}+\text{Na}]^+$: 496.1995, found: 496.1999.

(R)-3-((4-Chlorophenyl)(phenyl)amino)-2-phenyl-1-(1-phenyl-1H-imidazol-2-yl)propan-1-one
(10j)



Using Δ -**IrO** (2 mol%) as catalyst, starting from 2-acyl imidazole **7a** (52.4 mg, 0.20 mmol) and α -silylamine **9d** (174.0 mg, 0.60 mmol) according to the general procedure to give **10j** as a pale yellow oil (62.1 mg, 0.130 mmol, yield: 65%). Enantiomeric excess established by HPLC analysis using a Chiralpak AD-H column, $ee = 95\%$ (HPLC: AD-H, 254 nm, hexane/isopropanol = 97:3, flow rate 0.5 mL/min, 25 °C, t_r (major) = 17.6 min, t_r (minor) = 19.5 min). $[\alpha]_D^{20} = +54.3^\circ$ (c 0.8, CH_2Cl_2).

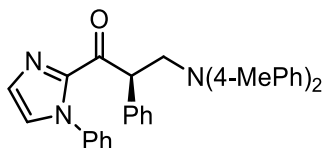
^1H NMR (300 MHz, CDCl_3) δ 7.46–7.38 (m, 5H), 7.33–7.24 (m, 5H), 7.22–7.17 (m, 2H), 7.16–7.14 (m, 2H), 7.10–7.05 (m, 2H), 7.05–6.98 (m, 1H), 6.96–6.90 (m, 2H), 6.87–6.80 (m, 2H), 5.69 (dd, $J = 8.6, 5.1$ Hz, 1H), 4.61 (dd, $J = 14.6, 8.7$ Hz, 1H), 3.96 (dd, $J = 14.6, 5.1$ Hz, 1H).

^{13}C NMR (75 MHz, CD_2Cl_2) δ 189.8, 148.0, 147.3, 143.2, 138.8, 137.8, 130.2, 129.7, 129.4, 129.2, 129.14, 129.12, 129.0, 128.0, 127.8, 127.7, 126.2, 122.8, 122.6, 122.3, 55.7, 52.0.

IR (film): ν (cm⁻¹) 3065, 2929, 1682, 1587, 1488, 1454, 1399, 1218, 1181, 1133, 1030, 938, 909, 865, 830, 759, 692, 541.

HRMS (ESI, m/z) calcd for C₃₀H₂₄CIN₃ONa [M+Na]⁺: 500.1500, found: 500.1504.

(R)-3-(Di-*p*-tolylamino)-2-phenyl-1-(1-phenyl-1*H*-imidazol-2-yl)propan-1-one (10k)



Using Δ -**IrO** (2 mol%) as catalyst, starting from 2-acyl imidazole **7a** (52.4 mg, 0.20 mmol) and α -silylamine **9b** (170.0 mg, 0.60 mmol) according to the general procedure to give **10k** as a pale yellow oil (84.0 mg, 0.178 mmol, yield: 89%). Enantiomeric excess established by HPLC analysis using a Chiralpak AD-H column, $ee = 91\%$ (HPLC: AD-H, 254 nm, hexane/isopropanol = 97:3, flow rate 0.5 mL/min, 25 °C, t_r (major) = 22.6 min, t_r (minor) = 25.3 min). $[\alpha]_D^{20} = +54.5^\circ$ (c 0.8, CH₂Cl₂).

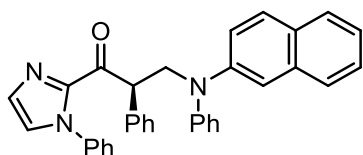
¹H NMR (300 MHz, CD₂Cl₂) δ 7.46–7.36 (m, 5H), 7.35–7.24 (m, 3H), 7.23–7.17 (m, 2H), 7.13 (d, $J = 1.0$ Hz, 1H), 7.08–7.04 (m, 3H), 7.03–7.00 (m, 2H), 6.81–6.74 (m, 4H), 5.65 (dd, $J = 8.9, 4.7$ Hz, 1H), 4.56 (dd, $J = 14.4, 8.9$ Hz, 1H), 3.90 (dd, $J = 14.4, 4.7$ Hz, 1H), 2.30 (s, 6H).

¹³C NMR (75 MHz, CD₂Cl₂) δ 190.0, 161.9, 146.3, 143.3, 138.8, 138.1, 131.3, 130.5, 130.1, 130.03, 130.00, 129.10, 129.09, 129.00, 128.9, 127.9, 127.6, 126.4, 126.2, 125.3, 121.6, 55.9, 52.0, 20.7.

IR (film): ν (cm⁻¹) 3027, 2919, 2858, 1681, 1598, 1507, 1445, 1399, 1263, 1247, 1148, 1073, 938, 909, 869, 848, 759, 735, 693, 610, 547.

HRMS (ESI, m/z) calcd for C₃₂H₂₉N₃ONa [M+Na]⁺: 494.2203, found: 494.2206.

(R)-3-(Naphthalen-2-yl(phenyl)amino)-2-phenyl-1-(1-phenyl-1*H*-imidazol-2-yl)propan-1-one (10l)



Using Δ -**IrO** (2 mol%) as catalyst, starting from 2-acyl imidazole **7a** (52.4 mg, 0.20 mmol) and α -silylamine **9e** (183.3 mg, 0.60 mmol) according to the general procedure to give **10l** as a white solid (62.2 mg, 0.126 mmol, yield: 63%). Enantiomeric excess established by HPLC analysis using a

Chiralpak AD-H column, *ee* = 97% (HPLC: AD-H, 254 nm, hexane/isopropanol = 97:3, flow rate 0.5 mL/min, 25 °C, *t_r* (minor) = 34.8 min, *t_r* (major) = 37.3 min). $[\alpha]_{\text{D}}^{20} = +29.2^{\circ}$ (*c* 0.5, CH₂Cl₂).

¹H NMR (300 MHz, CD₂Cl₂) δ 7.77 (d, *J* = 7.9 Hz, 1H), 7.62 (t, *J* = 8.9 Hz, 2H), 7.48–7.40 (m, 4H), 7.40–7.30 (m, 7H), 7.28–7.22 (m, 2H), 7.19 (d, *J* = 0.9 Hz, 1H), 7.10 (td, *J* = 5.1, 2.4 Hz, 2H), 7.05–6.90 (m, 5H), 5.80 (dd, *J* = 8.6, 4.9 Hz, 1H), 4.77 (dd, *J* = 14.6, 8.6 Hz, 1H), 4.09 (dd, *J* = 14.6, 4.9 Hz, 1H).

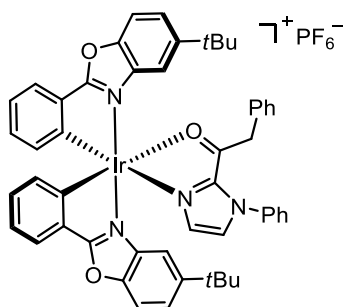
¹³C NMR (75 MHz, CD₂Cl₂) δ 189.8, 148.4, 145.8, 143.2, 138.7, 138.1, 135.0, 130.1, 129.9, 129.6, 129.2, 129.10, 129.07, 129.00, 128.8, 128.0, 127.8, 127.7, 127.2, 126.6, 126.1, 124.4, 123.3, 122.2, 122.0, 117.1, 55.9, 51.8.

IR (film): ν (cm⁻¹) 3056, 2924, 2853, 1734, 1681, 1627, 1592, 1491, 1469, 1397, 1371, 1303, 1263, 1182, 1147, 1044, 938, 902, 846, 814, 742, 691, 663, 521, 503.

HRMS (ESI, *m/z*) calcd for C₃₄H₂₇N₃ONa [M+Na]⁺: 516.2046, found: 516.2050.

5.3.3 Substrate-Coordinated Iridium Complex (Proposed Intermediate A)

1) Synthesis of complex A



The racemic complex **A** was obtained by reacting substrate **7a** (13.0 mg, 0.049 mmol) with racemic Δ/Λ -**IrO** (40.0 mg, 0.043 mmol) at room temperature overnight in CH₂Cl₂ (1.0 mL). After the slow addition of hexane (5.0 mL), crystals were collected after several days (32.2 mg, yield: 68%).

¹H NMR (300 MHz, CD₂Cl₂) δ 7.90–7.80 (m, 2H), 7.78–7.71 (m, 3H), 7.70–7.68 (m, 1H), 7.67–7.47 (m, 4H), 7.28 (t, *J* = 1.8 Hz, 2H), 7.22–7.07 (m, 3H), 7.05–6.96 (m, 3H), 6.95–6.93 (m, 1H), 6.69 (t, *J* = 7.8 Hz, 2H), 6.62 (d, *J* = 7.7 Hz, 2H), 6.12–6.07 (m, 2H), 6.06–6.04 (m, 1H), 4.15 (d, *J* = 14.7 Hz, 1H), 3.98 (d, *J* = 14.7 Hz, 1H), 1.36 (s, 9H), 1.13 (s, 9H).

¹³C NMR (75 MHz, CD₂Cl₂) δ 197.0, 178.9, 176.8, 151.3, 151.2, 148.9, 148.8, 147.3, 145.8, 137.6, 137.5, 135.9, 134.8, 134.4, 133.7, 133.3, 133.1, 133.0, 132.9, 132.8, 132.5, 131.2, 130.6, 130.2, 129.3,

129.1, 128.5, 128.3, 126.9, 126.5, 124.8, 124.6, 124.0, 123.6, 112.4, 112.3, 111.5, 111.0, 45.4, 35.5, 35.4, 31.8, 31.7.

2) Absorption and emission spectra of complex A

UV/Vis-absorbance and photoluminescence ($\lambda_{\text{ex}} = 390 \text{ nm}$) spectra of complex A were performed in CH_2Cl_2 at a concentration of 0.1 mM using a Spectra Max M5 microplate reader with a 10 mm quartz cuvette.

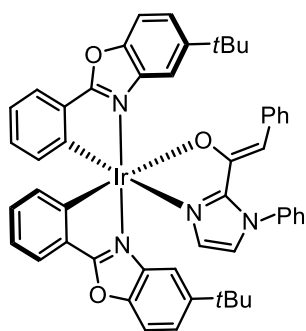
3) Stern-volmer-plot with complex A

Performed in CH_2Cl_2 at a concentration of 0.1 mM of complex A (volume of 1.0 mL) and different concentrations of amine **9a**. Emission intensities were recorded with a Spectra Max M5 microplate reader in a 10 mm quartz cuvette with a cap upon excitation at 390 nm. A concentrated stock solution (100 mM in CH_2Cl_2) of amine **9a** was titrated in 5.0 μL steps. After the additions, the solutions were shaken once in a while over a period of 5 min and thereafter the emission quenching measured.

4) Cyclovoltammetry with complex A

Cyclic voltammetry was carried out on a BAS C3 Cell Strand and a BAS 100 series Electrochemical Analyzer using a platinum disk working electrode (2.0 mm diameter) and a platinum wire counter electrode (0.5 mm diameter) at room temperature in THF containing Bu_4NBF_4 (0.1 M). Potentials were referred to a saturated Ag/AgCl reference electrode. Before each experiment, the surface of the working electrode was polished followed by thorough rinsing with distilled water. The solution was purged with nitrogen before each measurement.

5.3.4 Synthesis of the Proposed Intermediate Iridium Enolate Complex B



To a solution of racemic catalyst Δ/Λ -**IrO** (40.0 mg, 0.043 mmol) in CH_2Cl_2 (1.5 mL) was added 2-acyl imidazole **7a** (33.8 mg, 0.129 mmol). The reaction mixture was concentrated after around 16 h. The residue was purified by flash chromatography on silica gel ($\text{CH}_2\text{Cl}_2/\text{EtOAc} = 50:1$) to afford the enolate complex **B** as a red solid (34.9 mg, 0.036 mmol, yield: 85%).

^1H NMR (300 MHz, CD_2Cl_2) δ 7.86 (d, $J = 1.5$ Hz, 1H), 7.78–7.69 (m, 2H), 7.61 (dt, $J = 4.5, 2.2$ Hz, 1H), 7.56–7.49 (m, 4H), 7.48–7.38 (m, 4H), 7.37–7.32 (m, 2H), 7.05–6.97 (m, 4H), 6.94 (dd, $J = 7.5, 1.1$ Hz, 1H), 6.88 (dd, $J = 7.5, 1.5$ Hz, 1H), 6.85–6.73 (m, 3H), 6.71–6.65 (m, 3H), 4.75 (s, 1H), 1.26 (s, 9H), 0.95 (s, 9H).

^{13}C NMR (75 MHz, CD_2Cl_2) δ 179.1, 178.1, 155.5, 155.4, 153.3, 150.8, 150.0, 149.0, 148.8, 148.1, 139.9, 139.0, 138.9, 138.4, 134.7, 134.1, 131.7, 131.6, 131.02, 131.01, 129.9, 127.9, 127.5, 127.4, 126.8, 126.1, 126.0, 124.8, 123.5, 123.1, 122.6, 121.3, 120.9, 115.6, 112.7, 111.3, 110.3, 103.9, 35.5, 35.2, 32.0, 31.4.

5.3.5 Control Reactions

1) Evaluating the catalytic activities of complexes A and B

Using complex **A** (2 mol%) as catalyst, starting from 2-acyl imidazole **7a** (52.4 mg, 0.20 mmol) and α -silylamine **9a** (153.2 mg, 0.60 mmol) according to the general procedure of synthesizing **10a-l** to give **10a** (92% yield, 7.5 h). When use complex **B** (2 mol%) as catalyst instead, the product **10a** could not be observed.

2) Trapping experiment with dibenzyl diazodicarboxylate

To a solution of catalyst Δ -**IrO** (2 mol%) in anhydrous CH_2Cl_2 (0.50 mL, 0.4 M) was added the 2-acyl imidazole **7a** (52.4 mg, 0.2 mmol) in a 10 mL test tube. After being stirred at room temperature for 20

min, dibenzyl diazodicarboxylate (298.3 mg, 1.0 mmol) was added. The reaction was stirred at room temperature for 7 h under air atmosphere. Afterwards, the solvent was concentrated under reduced pressure. The residue was purified by flash chromatography on silica gel (EtOAc/hexane = 1:2) to afford the product **13** (97.5 mg, 0.174 mmol, yield: 87%) as a white oil. Enantiomeric excess established by HPLC analysis using a Chiralpak AD-H column, *ee* = 89% (HPLC: AD-H, 254 nm, hexane/isopropanol = 60:40, flow rate 1.0 mL/min, 40 °C, *t_r* (minor) = 9.0 min, *t_r* (major) = 15.8 min).

¹H NMR (300 MHz, CD₂Cl₂) δ 7.55–7.45 (m, 3H), 7.43–7.36 (m, 2H), 7.35–7.24 (m, 12H), 7.23–7.18 (m, 3H), 7.13–6.97 (m, 3H), 5.28–4.30 (m, 5H).

¹³C NMR (75 MHz, CD₂Cl₂) δ 171.2, 138.4, 136.4, 133.2, 130.9, 130.8, 130.6, 129.4, 129.2, 129.0, 128.8, 128.7, 128.4, 128.04, 128.02, 127.9, 126.2, 120.4, 68.6, 67.3, 60.6.

IR (film): ν (cm⁻¹) 3300, 3029, 2953, 1691, 1594, 1492, 1448, 1397, 1338, 1213, 1117, 1051, 969, 912, 844, 740, 693, 647, 591, 547.

HRMS (ESI, *m/z*) calcd for C₃₃H₂₈N₄O₅Na [M+Na]⁺: 583.1952, found: 583.1946.

3) Dark reaction with the oxidant *t*BuOOH

To a solution of catalyst Δ -**IrO** (5 mol%) in anhydrous CH₂Cl₂ (0.50 mL, 0.4 M) was added the 2-acyl imidazole **7a** (52.4 mg, 0.2 mmol) in a 10 mL test tube. After being stirred at room temperature for 20 min, **9a** (153.2 mg, 0.60 mmol) and *tert*-butyl hydroperoxide (36.0 mg, 0.40 mmol) were added. The reaction was stirred at room temperature for 24 h in the dark under air atmosphere. Afterwards, the resulting reaction mixture was purified to afford the product **10a** (54.0 mg, 0.121 mmol, yield: 61%, *ee*: 97%).

5.3.6 Single-Crystal X-Ray Diffraction Studies

Single crystals of the intermediate iridium enolate complex **B** suitable for X-ray diffraction were obtained after several days from a solution of the compound in CH₂Cl₂ layered with *n*-hexane. Crystals of **10e** were obtained from a solution of the compound in methanol at 5 °C after several days. Crystal data and details of the structure determination are presented in Appendices 6.7. The absolute configuration was determined

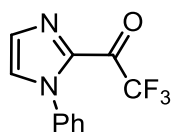
5.4 Asymmetric Radical-Radical Cross-Coupling through Visible Light Activated Iridium Catalysis

5.4.1 Synthesis of Substrates

1) Synthesis of 2-acyl imidazoles

2-Acyl imidazoles **14a**, **14b'-d'** were synthesized according to a reported procedure with some modifications.¹⁵ To a solution of the corresponding 1-substituted-1*H*-imidazole (1.0 eq.) in toluene (0.1 M) at -20 °C was added trifluoroacetic anhydride (1.2 eq.) dropwise. After that, triethylamine (1.2 eq.) was added dropwise to the flask. The reaction was allowed to slowly warm to room temperature and stirred overnight. Removal of the solvent in vacuo and the residue was purified by flash chromatography on silica gel (EtOAc/hexane = 1:3) to provide the 2-acyl imidazole **14a**, **14b'-d'**.

2,2,2-Trifluoro-1-(1-phenyl-1*H*-imidazol-2-yl)ethanone (**14a**)



Following the general procedure, 1-phenyl-1*H*-imidazole (1.440 g, 10.0 mmol) was converted to 2-acyl imidazole **14a** (1.801 g, 7.5 mmol, yield: 75%) as a white solid.

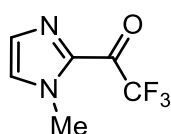
¹H NMR (300 MHz, CDCl₃) δ 7.56–7.47 (m, 4H), 7.39–7.35 (m, 1H), 7.34–7.28 (m, 2H).

¹³C NMR (75 MHz, CDCl₃) δ 169.8 (q, *J* = 36.7 Hz), 137.9, 137.0, 132.3, 129.6, 129.3, 129.2, 125.7, 116.3 (q, *J* = 288.5 Hz).

¹⁹F NMR (282 MHz, CDCl₃) δ -73.40 (s, 3F).

IR (film): ν (cm⁻¹) 3255, 3095, 2918, 2357, 1769, 1704, 1595, 1498, 1408, 1312, 1269, 1188, 1135, 1063, 1006, 906, 819, 757, 691, 649, 528.

2,2,2-Trifluoro-1-(1-methyl-1*H*-imidazol-2-yl)ethanone (**14b'**)



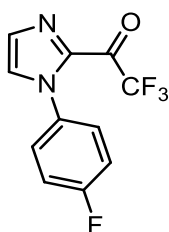
Following the general procedure, 1-methyl-1*H*-imidazole (0.821 g, 10.0 mmol) was converted to 2-acyl imidazole **14b'** (1.478, 8.3 mmol, yield: 83%) as a white solid.

¹H NMR (300 MHz, CDCl₃) δ 7.37 (d, *J* = 0.9 Hz, 1H), 7.23 (d, *J* = 0.9 Hz, 1H), 4.07 (s, 3H).

¹³C NMR (75 MHz, CDCl₃) δ 170.2 (q, *J* = 35.3 Hz), 137.8, 131.7, 129.5, 116.2 (q, *J* = 288.7 Hz), 36.3.

All spectroscopic data were in agreement with the literature.¹⁵

2,2,2-Trifluoro-1-(1-(4-fluorophenyl)-1*H*-imidazol-2-yl)ethanone (**14c'**)



Following the general procedure, 1-(4-fluorophenyl)-1*H*-imidazole (1.622 g, 10.0 mmol) was converted to 2-acyl imidazole **14c'** (2.065 g, 8.0 mmol, yield: 80%) as a white solid.

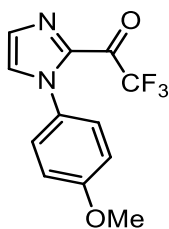
¹H NMR (300 MHz, CDCl₃) δ 7.53 (d, *J* = 0.9 Hz, 1H), 7.37 (d, *J* = 0.9 Hz, 1H), 7.35–7.27 (m, 2H), 7.26–7.17 (m, 2H).

¹³C NMR (75 MHz, CDCl₃) δ 169.6 (q, *J* = 36.5 Hz), 164.5, 161.2, 137.8, 132.9, 132.8, 132.2, 129.3, 127.6, 127.5, 116.4, 116.2 (q, *J* = 288.5 Hz), 116.1.

¹⁹F NMR (282 MHz, CDCl₃) δ -73.45 (s, 3F), -111.49 (s, 1F).

IR (film): ν (cm⁻¹) 3102, 1711, 1604, 1509, 1458, 1408, 1350, 1194, 1140, 898, 815, 740, 682, 633, 528.

2,2,2-Trifluoro-1-(1-(4-methoxyphenyl)-1*H*-imidazol-2-yl)ethanone (**14d'**)



Following the general procedure, 1-(4-methoxyphenyl)-1*H*-imidazole (1.742 g, 10.0 mmol) was converted to 2-acyl imidazole **14d'** (0.811 g, 3.0 mmol, yield: 30%) as a white solid.

¹H NMR (300 MHz, CDCl₃) δ 7.47 (d, *J* = 0.9 Hz, 1H), 7.33 (d, *J* = 0.9 Hz, 1H), 7.25–7.18 (m, 2H), 7.01–6.94 (m, 2H), 3.87 (s, 3H).

^{13}C NMR (75 MHz, CDCl_3) δ 169.6 (q, $J = 36.0$ Hz), 160.2, 137.8, 132.0, 129.6, 129.5, 126.8, 118.2 (q, $J = 288.8$ Hz), 114.9, 55.5.

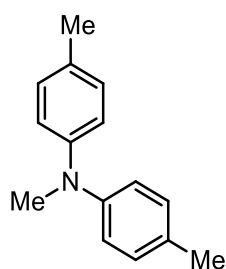
^{19}F NMR (282 MHz, CDCl_3) δ -73.37 (s, 3F).

IR (film): ν (cm^{-1}) 3208, 3154, 2942, 2841, 1699, 1605, 1510, 1456, 1355, 1252, 1134, 1073, 933, 828, 777, 633, 538.

2) Synthesis of tertiary amines

2-Aryl-1,2,3,4-tetrahydroisoquinolines **17a-e** were synthesized according to a reported procedure without any further change.¹⁶ All *N*-methyldiarylamines were synthesized according to a reported procedure with some modifications.¹⁷ To a solution of the corresponding diarylamines (1.0 eq.) in THF (0.4 M) under nitrogen atmosphere at 0 °C was added *n*-BuLi (1.1 eq.) dropwise. The reaction was stirred at 0 °C for 30 min, then stirred at room temperature for an additional 1 h. Methyl iodide (1.5 eq.) was added slowly to the flask after the reaction was cooled back down to 0 °C, and the resulting solution was stirred at room temperature overnight. Afterwards, the reaction was quenched with water and extracted with CH_2Cl_2 . The combined organic layers were dried over anhydrous Na_2SO_4 and concentrated under reduced pressure. The residue was purified by flash chromatography on silica gel (EtOAc/hexane = 1:100) to produce **15a-h**.

N,4-Dimethyl-*N*-(*p*-tolyl)aniline (**15a**)

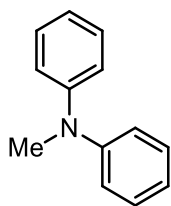


Following the general procedure, di(*p*-tolyl)amine (3.946 g, 20.0 mmol) was converted to amine **15a** (3.676 g, 17.4 mmol, yield: 87%) as a white solid.

^1H NMR (300 MHz, CDCl_3) δ 7.14–7.06 (m, 4H), 6.98–6.86 (m, 4H), 3.29 (s, 3H), 2.33 (s, 6H).

^{13}C NMR (75 MHz, CDCl_3) δ 147.1, 130.4, 129.7, 120.4, 40.4, 20.6.

All spectroscopic data were in agreement with the literature.¹⁸

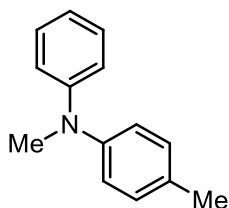
***N*-Methyl-*N*-phenylaniline (15b)**

Following the general procedure, diphenylamine (1.692 g, 10.0 mmol) was converted to amine **15b** (1.557 g, 8.5 mmol, yield: 85%) as a colorless oil.

^1H NMR (300 MHz, CDCl_3) δ 7.37–7.26 (m, 4H), 7.11–7.04 (m, 4H), 7.00 (ddt, $J = 8.4, 7.5, 1.1$ Hz, 2H), 3.37 (s, 3H).

^{13}C NMR (75 MHz, CDCl_3) δ 149.1, 129.2, 121.3, 120.5, 40.2.

All spectroscopic data were in agreement with the literature.¹⁷

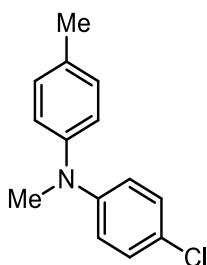
***N*,4-Dimethyl-*N*-phenylaniline (15c)**

Following the general procedure, 4-methyl-*N*-phenylaniline (1.410 g, 7.7 mmol) was converted to amine **15c** (1.184 g, 6.0 mmol, yield: 78%) as a colorless oil.

^1H NMR (300 MHz, CDCl_3) δ 7.32–7.25 (m, 2H), 7.20–7.14 (m, 2H), 7.08–7.04 (m, 2H), 7.01–6.95 (m, 2H), 6.94–6.87 (m, 1H), 3.34 (s, 3H), 2.38 (s, 3H)

^{13}C NMR (75 MHz, CDCl_3) δ 149.4, 146.6, 132.0, 129.9, 129.0, 122.5, 119.8, 118.3, 40.3, 20.7.

All spectroscopic data were in agreement with the literature.¹⁸

4-Chloro-*N*-methyl-*N*-(*p*-tolyl)aniline (15d)

Following the general procedure, 4-chloro-*N*-(*p*-tolyl)aniline (0.860 g, 3.9 mmol) was converted to amine **15d** (0.730 g, 3.1 mmol, yield: 80%) as a white solid.

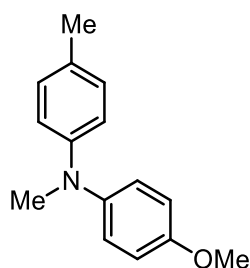
¹H NMR (300 MHz, CDCl₃) δ 7.20–7.08 (m, 4H), 7.00 (d, *J* = 8.4 Hz, 2H), 6.81 (d, *J* = 9.0 Hz, 2H), 3.26 (s, 3H), 2.34 (s, 3H).

¹³C NMR (75 MHz, CDCl₃) δ 148.0, 146.2, 132.9, 130.1, 128.8, 124.2, 123.2, 118.6, 40.4, 20.8.

IR (film): ν (cm⁻¹) 3026, 2917, 2814, 1706, 1589, 1507, 1498, 1411, 1333, 1251, 1068, 937, 868, 748, 716, 641, 607, 546.

HRMS (FD, *m/z*) calcd for C₁₄H₁₄ClN: 231.08148, found: 231.08143.

4-Methoxy-*N*-methyl-*N*-(*p*-tolyl)aniline (**15e**)



Following the general procedure, 4-methoxy-*N*-(*p*-tolyl)aniline (1.826 g, 8.5 mmol) was converted to amine **15e** (1.642 g, 7.2 mmol, yield: 85%) as a white solid.

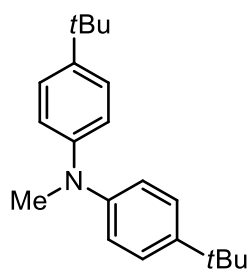
¹H NMR (300 MHz, CDCl₃) δ 7.08–6.97 (m, 4H), 6.91–6.84 (m, 2H), 6.81–6.75 (m, 2H), 3.81 (s, 3H), 3.25 (s, 3H), 2.29 (s, 3H).

¹³C NMR (75 MHz, CDCl₃) δ 155.5, 147.6, 142.9, 129.5, 128.6, 124.5, 117.5, 114.7, 55.5, 40.7, 20.4.

IR (film): ν (cm⁻¹) 2906, 2824, 1606, 1501, 1331, 1236, 1179, 1113, 1029, 870, 816, 763, 716, 650, 552.

HRMS (FD, *m/z*) calcd for C₁₅H₁₇NO: 227.13101, found: 227.13108.

4-(*tert*-Butyl)-*N*-(4-(*tert*-butyl)phenyl)-*N*-methylaniline (**15f**)



Following the general procedure, bis(4-(*tert*-butyl)phenyl)amine (2.814 g, 10.0 mmol) was converted to amine **15f** (2.393 g, 8.1 mmol, yield: 81%) as a white solid.

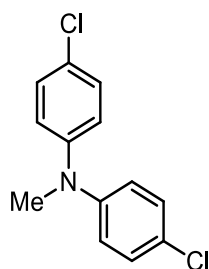
^1H NMR (300 MHz, CDCl_3) δ 7.35–7.22 (m, 4H), 7.02–6.90 (m, 4H), 3.30 (s, 3H), 1.33 (s, 18H).

^{13}C NMR (75 MHz, CDCl_3) δ 146.6, 143.8, 125.9, 119.8, 40.2, 34.1, 31.5.

IR (film): ν (cm^{-1}) 3032, 2952, 2868, 1604, 1565, 1340, 1252, 1194, 1073, 874, 820, 766, 556.

HRMS (FD, m/z) calcd for $\text{C}_{21}\text{H}_{29}\text{N}$: 295.23000, found: 295.23011.

4-Chloro-*N*-(4-chlorophenyl)-*N*-methylaniline (15g)



Following the general procedure, bis(4-chlorophenyl)amine (1.520 g, 6.4 mmol) was converted to amine **15g** (1.290 g, 5.1 mmol, yield: 80%) as a white solid.

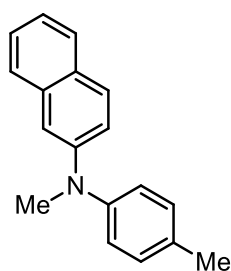
^1H NMR (300 MHz, CDCl_3) δ 7.33–7.17 (m, 4H), 7.00–6.86 (m, 4H), 3.29 (s, 3H).

^{13}C NMR (75 MHz, CDCl_3) δ 147.3, 129.2, 126.6, 121.7, 40.4.

IR (film): ν (cm^{-1}) 3082, 2894, 1580, 1481, 1328, 1246, 1176, 999, 815, 757, 673, 579.

HRMS (ESI, m/z) calcd for $\text{C}_{13}\text{H}_{12}\text{Cl}_2\text{N}$ $[\text{M}+\text{H}]^+$: 252.0341, found: 252.0341.

N-Methyl-*N*-(*p*-tolyl)naphthalen-2-amine (15h)



Following the general procedure, *N*-(*p*-tolyl)naphthalen-2-amine (1.353 g, 5.8 mmol) was converted to amine **15h** (1.112 g, 4.5 mmol, yield: 77%) as a white solid.

^1H NMR (300 MHz, CDCl_3) δ 7.65–7.57 (m, 2H), 7.56–7.51 (m, 1H), 7.34–7.26 (m, 1H), 7.20–7.15 (m, 1H), 7.14–7.11 (m, 1H), 7.08–7.01 (m, 3H), 7.00–6.94 (m, 2H), 3.31 (s, 3H), 2.26 (s, 3H).

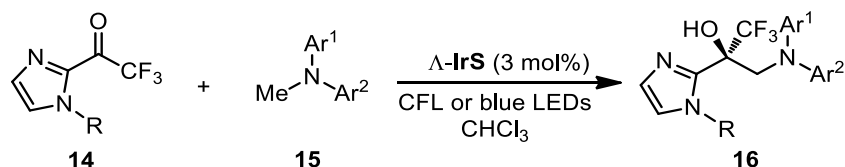
^{13}C NMR (75 MHz, CDCl_3) δ 147.0, 146.7, 134.8, 132.5, 130.0, 128.5, 128.3, 127.5, 126.5, 126.2, 123.2, 123.1, 120.7, 112.1, 40.7, 20.8.

IR (film): ν (cm^{-1}) 3020, 2907, 1607, 1496, 1369, 1275, 1121, 946, 820, 776, 646, 555.

HRMS (FD, m/z) calcd for $C_{18}H_{17}N$: 247.13610, found: 247.13579.

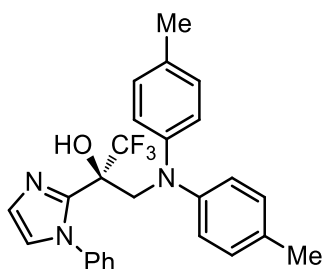
5.4.2 Iridium-Catalyzed Photoredox Reactions

1) Reactions of 2-acyl imidazoles with *N*-methyldiarylamines



General catalysis procedure. A dried 10 mL Schlenk tube was charged with the catalyst Δ -IrS¹² (3 mol%), 2-acyl imidazoles **14a**, **14b'-d'** (0.20 mmol, 1.0 eq.) and the corresponding amine **15a-h** (0.60 mmol, 3.0 eq.). The tube was purged with nitrogen and $CHCl_3$ (0.4 mL) was added *via* syringe. The reaction mixture was degassed *via* freeze-pump-thaw for three cycles. After the mixture was thoroughly degassed, the vial was sealed and positioned approximately 5 cm from a 23 W CFL or approximately 8 cm from a 24 W blue LEDs. The reaction was stirred at room temperature for the indicated time (monitored by TLC) under nitrogen atmosphere. Afterwards, the mixture was diluted with CH_2Cl_2 (4 mL). The combined organic layers were concentrated under reduced pressure. The residue was purified by flash chromatography on silica gel (EtOAc/hexane = 1:20 to 1:10) to afford the products **16a-h**. Racemic samples were obtained by carrying out the reactions with *rac*-IrS. The enantiomeric excess was determined by chiral HPLC analysis.

(*S*)-3-(Di-*p*-tolylamino)-1,1,1-trifluoro-2-(1-phenyl-1*H*-imidazol-2-yl)propan-2-ol (**16a**)



Starting from 2-acyl imidazole **14a** (48.0 mg, 0.20 mmol) and amine **15a** (126.8 mg, 0.60 mmol) according to the general procedure to give **16a** as a colorless oil (74.0 mg, 0.164 mmol, yield: 82%). Enantiomeric excess established by HPLC analysis using a Chiralpak AD-H column, $ee = 99\%$ (HPLC:

AD-H, 254 nm, hexane/isopropanol = 95:5, flow rate 0.5 mL/min, 25 °C, t_r (minor) = 14.7 min, t_r (major) = 20.0 min). $[\alpha]_D^{20} = -63.9^\circ$ (c 0.7, CH_2Cl_2).

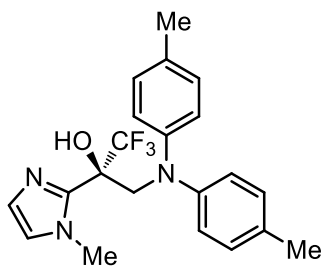
^1H NMR (300 MHz, CDCl_3) δ 7.41–7.27 (m, 3H), 7.07 (d, $J = 1.2$ Hz, 1H), 7.05–6.98 (m, 4H), 6.94–6.86 (m, 2H), 6.78 (d, $J = 1.3$ Hz, 1H), 6.75–6.66 (m, 4H), 4.86 (d, $J = 15.1$ Hz, 1H), 4.27 (d, $J = 15.1$ Hz, 1H), 4.14 (s, 1H), 2.28 (s, 6H).

^{13}C NMR (75 MHz, CDCl_3) δ 146.2, 142.7, 139.0, 132.4, 129.8, 128.5, 128.3, 127.4, 126.9, 124.7, 122.0, 74.8 (q, $J = 28.5$ Hz), 58.1, 20.5.

^{19}F NMR (282 MHz, CDCl_3) δ -78.00 (s, 3F).

IR (film): ν (cm^{-1}) 3336, 3029, 2922, 2864, 1684, 1607, 1505, 1360, 1161, 1052, 983, 811, 761, 738, 693, 643, 570, 530.

(S)-3-(Di-*p*-tolylamino)-1,1,1-trifluoro-2-(1-methyl-1*H*-imidazol-2-yl)propan-2-ol (16b')



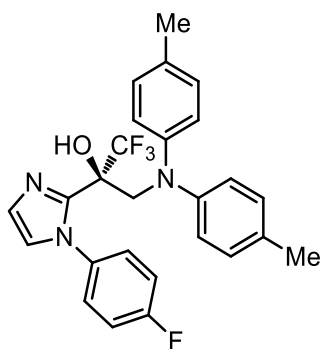
Starting from 2-acyl imidazole **14b'** (35.6 mg, 0.20 mmol) and amine **15a** (126.8 mg, 0.60 mmol) according to the general procedure to give **16b'** as a white solid (30.8 mg, 0.079 mmol, yield: 40%). Enantiomeric excess established by HPLC analysis using a Chiralpak AD-H column, $ee = 98\%$ (HPLC: AD-H, 254 nm, hexane/isopropanol = 95:5, flow rate 0.5 mL/min, 25 °C, t_r (minor) = 18.9 min, t_r (major) = 23.9 min). $[\alpha]_D^{20} = -145.0^\circ$ (c 0.3, CH_2Cl_2).

^1H NMR (300 MHz, CDCl_3) δ 7.04–6.98 (m, 4H), 6.94 (d, $J = 1.1$ Hz, 1H), 6.79–6.73 (m, 4H), 6.71 (d, $J = 1.1$ Hz, 1H), 5.10 (s, 1H), 4.81 (d, $J = 15.5$ Hz, 1H), 4.50 (d, $J = 15.5$ Hz, 1H), 3.56 (s, 3H), 2.28 (s, 6H).

^{13}C NMR (75 MHz, CDCl_3) δ 146.6, 141.9, 132.4, 129.9, 126.9, 126.3, 124.3, 122.0, 74.4 (q, $J = 29.2$ Hz), 57.1, 34.9, 20.6.

^{19}F NMR (282 MHz, CDCl_3) δ -78.86 (s, 3F).

IR (film): ν (cm^{-1}) 3359, 3112, 2933, 2851, 1654, 1581, 1453, 1336, 1208, 1154, 1029, 950, 910, 862, 745, 693, 663, 586.

(S)-3-(Di-*p*-tolylamino)-1,1,1-trifluoro-2-(1-(4-fluorophenyl)-1*H*-imidazol-2-yl)propan-2-ol (16c')

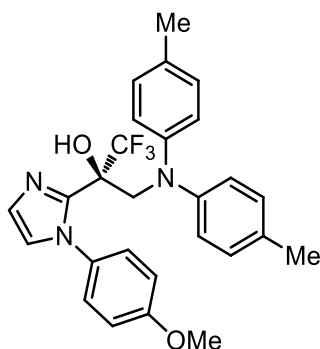
Starting from 2-acyl imidazole **14c'** (51.6 mg, 0.20 mmol) and amine **15a** (126.8 mg, 0.60 mmol) according to the general procedure to give **16c'** as a colorless oil (62.1 mg, 0.132 mmol, yield: 66%). Enantiomeric excess established by HPLC analysis using a Chiralpak AD-H column, *ee* = 90% (HPLC: AD-H, 254 nm, hexane/isopropanol = 90:10, flow rate 0.5 mL/min, 25 °C, *t_r* (minor) = 12.9 min, *t_r* (major) = 17.0 min). $[\alpha]_D^{20} = -51.4^\circ$ (*c* 0.6, CH₂Cl₂).

¹H NMR (300 MHz, CDCl₃) δ 7.08 (d, *J* = 1.2 Hz, 1H), 7.05–6.99 (m, 4H), 6.99–6.93 (m, 2H), 6.88–6.81 (m, 2H), 6.76 (d, *J* = 1.2 Hz, 1H), 6.75–6.69 (m, 4H), 4.88 (d, *J* = 15.1 Hz, 1H), 4.25 (d, *J* = 15.1 Hz, 1H), 4.19 (s, 1H), 2.28 (s, 6H).

¹³C NMR (75 MHz, CDCl₃) δ 163.9, 160.6, 146.2, 142.9, 135.0, 132.6, 129.8, 128.6, 128.5, 127.7, 126.3, 125.9, 125.3, 124.7, 122.5, 122.0, 115.8, 115.5, 115.3, 115.0, 74.6 (q, *J* = 28.5 Hz), 58.1, 20.6.

¹⁹F NMR (282 MHz, CDCl₃) δ -73.05 (s, 1F), -79.01 (s, 3F).

IR (film): ν (cm⁻¹) 3305, 3121, 3025, 2923, 1612, 1504, 1445, 1356, 1213, 1152, 959, 823, 769, 707, 628, 523.

(S)-3-(Di-*p*-tolylamino)-1,1,1-trifluoro-2-(1-(4-methoxyphenyl)-1*H*-imidazol-2-yl)propan-2-ol (16d')

Starting from 2-acyl imidazole **14d'** (54.0 mg, 0.20 mmol) and amine **15a** (126.8 mg, 0.60 mmol) according to the general procedure to give **16d'** as a white solid (64.5 mg, 0.134 mmol, yield: 67%). Enantiomeric excess established by HPLC analysis using a Chiralpak AD-H column, *ee* = 92% (HPLC: AD-H, 254 nm, hexane/isopropanol = 90:10, flow rate 0.5 mL/min, 25 °C, t_r (minor) = 11.7 min, t_r (major) = 18.1 min). $[\alpha]_D^{20} = -73.2^\circ$ (*c* 0.6, CH₂Cl₂).

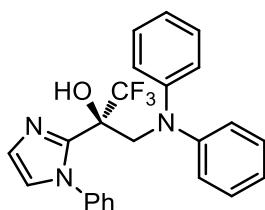
¹H NMR (300 MHz, CDCl₃) δ 7.00–6.87 (m, 5H), 6.77–6.52 (m, 9H), 4.70 (d, *J* = 15.1 Hz, 1H), 4.28–4.12 (m, 2H), 3.72 (s, 3H), 2.19 (s, 6H).

¹³C NMR (75 MHz, CDCl₃) δ 159.5, 146.3, 142.9, 132.3, 131.6, 129.8, 128.0, 127.2, 125.1, 122.0, 113.4, 74.9 (q, *J* = 28.5 Hz), 57.9, 55.4, 20.6.

¹⁹F NMR (282 MHz, CDCl₃) δ -78.85 (s, 3F).

IR (film): ν (cm⁻¹) 3344, 3020, 2925, 1610, 1508, 1455, 1365, 1247, 1164, 1114, 1038, 980, 887, 813, 743, 628, 568, 515.

(S)-3-(Diphenylamino)-1,1,1-trifluoro-2-(1-phenyl-1H-imidazol-2-yl)propan-2-ol (16b)



Starting from 2-acyl imidazole **14a** (48.0 mg, 0.20 mmol) and amine **15b** (109.9 mg, 0.60 mmol) according to the general procedure to give **16b** as a pale yellow oil (50.8 mg, 0.12 mmol, yield: 60%). Enantiomeric excess established by HPLC analysis using a Chiralpak AD-H column, *ee* = 98% (HPLC: AD-H, 254 nm, hexane/isopropanol = 98:2, flow rate 0.5 mL/min, 25 °C, t_r (major) = 20.4 min, t_r (minor) = 33.0 min). $[\alpha]_D^{20} = -67.6^\circ$ (*c* 0.3, CH₂Cl₂).

¹H NMR (300 MHz, CDCl₃) δ 7.47–7.40 (m, 1H), 7.37–7.27 (m, 2H), 7.26–7.22 (m, 1H), 7.21–7.16 (m, 3H), 7.04 (d, *J* = 1.2 Hz, 1H), 6.98 (ddt, *J* = 8.5, 6.9, 1.2 Hz, 2H), 6.89–6.79 (m, 6H), 6.74 (d, *J* = 1.2 Hz, 1H), 4.89 (d, *J* = 15.2 Hz, 1H), 4.31 (d, *J* = 15.2 Hz, 1H), 4.06 (s, 1H).

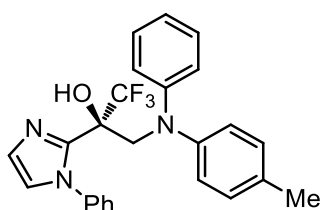
¹³C NMR (75 MHz, CDCl₃) δ 148.3, 142.5, 138.9, 129.3, 128.9, 128.64, 128.57, 128.4, 127.4, 126.9, 125.8, 125.2, 124.9, 124.3 (q, *J* = 284.2 Hz), 123.0, 122.1, 75.1 (q, *J* = 28.5 Hz), 57.7.

¹⁹F NMR (282 MHz, CDCl₃) δ -78.50 (s, 3F).

IR (film): ν (cm⁻¹) 3335, 3059, 2923, 1592, 1493, 1452, 1365, 1307, 1258, 1162, 970, 917, 835, 752, 688, 589, 500.

HRMS (ESI, m/z) calcd for C₂₄H₂₀F₃N₃ONa [M+Na]⁺: 446.1462, found: 446.1453.

(S)-1,1,1-Trifluoro-3-(phenyl(*p*-tolyl)amino)-2-(1-phenyl-1*H*-imidazol-2-yl)propan-2-ol (16c)



Starting from 2-acyl imidazole **14a** (48.0 mg, 0.20 mmol) and amine **15c** (118.4 mg, 0.60 mmol) according to the general procedure to give **16c** as a colorless oil (52.5 mg, 0.12 mmol, yield: 60%). Enantiomeric excess established by HPLC analysis using a Chiralpak AD-H column, $ee = 96\%$ (HPLC: AD-H, 254 nm, hexane/isopropanol = 98:2, flow rate 0.5 mL/min, 25 °C, t_r (major) = 23.5 min, t_r (minor) = 27.6 min). $[\alpha]_D^{20} = -78.3^\circ$ (c 0.3, CH₂Cl₂).

¹H NMR (300 MHz, CDCl₃) δ 7.42–7.25 (m, 3H), 7.23–7.14 (m, 2H), 7.10–7.01 (m, 3H), 6.98–6.85 (m, 3H), 6.83–6.70 (m, 5H), 4.87 (d, $J = 15.1$ Hz, 1H), 4.31 (d, $J = 15.1$ Hz, 1H), 4.12 (s, 1H), 2.30 (s, 3H).

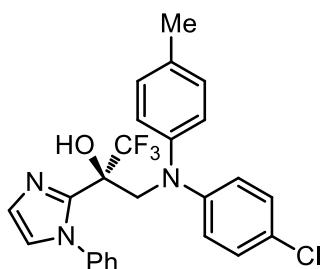
¹³C NMR (75 MHz, CDCl₃) δ 149.0, 145.6, 142.6, 139.0, 133.5, 130.0, 129.1, 128.6, 128.4, 127.4, 126.9, 124.9, 124.3 (q, $J = 284.2$ Hz), 123.7, 121.9, 120.4, 75.0 (q, $J = 28.5$ Hz), 57.9, 20.7.

¹⁹F NMR (282 MHz, CDCl₃) δ -78.58 (s, 3F).

IR (film): ν (cm⁻¹) 3330, 3034, 2924, 1594, 1498, 1454, 1364, 1258, 1166, 1117, 1050, 980, 884, 821, 754, 690, 591.

HRMS (ESI, m/z) calcd for C₂₅H₂₂F₃N₃ONa [M+Na]⁺: 460.1618, found: 460.1609.

(S)-3-((4-Chlorophenyl)(*p*-tolyl)amino)-1,1,1-trifluoro-2-(1-phenyl-1*H*-imidazol-2-yl)propan-2-ol (16d)



Starting from 2-acyl imidazole **14a** (48.0 mg, 0.20 mmol) and amine **15d** (139.0 mg, 0.60 mmol) according to the general procedure to give **16d** as a pale yellow oil (75.5 mg, 0.16 mmol, yield: 80%). Enantiomeric excess established by HPLC analysis using a Chiralpak AD-H column, $ee = 94\%$ (HPLC: AD-H, 254 nm, hexane/isopropanol = 95:5, flow rate 0.5 mL/min, 25 °C, t_r (minor) = 15.0 min, t_r (major) = 16.7 min). $[\alpha]_D^{20} = -95.4^\circ$ (c 0.7, CH_2Cl_2).

^1H NMR (300 MHz, CDCl_3) δ 7.43–7.28 (m, 3H), 7.15–7.11 (m, 1H), 7.10–7.06 (m, 4H), 6.92–6.85 (m, 2H), 6.81 (d, $J = 1.2$ Hz, 1H), 6.79–6.73 (m, 2H), 6.72–6.65 (m, 2H), 4.71 (d, $J = 15.2$ Hz, 1H), 4.28 (d, $J = 15.2$ Hz, 1H), 4.22 (s, 1H), 2.32 (s, 3H).

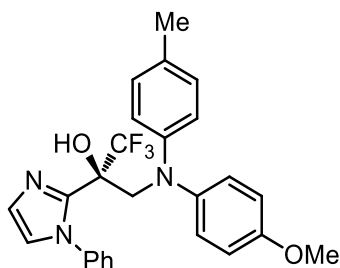
^{13}C NMR (75 MHz, CDCl_3) δ 147.9, 145.1, 142.4, 138.6, 134.4, 130.2, 128.9, 128.8, 128.5, 127.3, 126.9, 126.3, 125.2, 124.6, 124.2 (q, $J = 284.2$ Hz), 120.5, 75.3 (q, $J = 28.5$ Hz), 57.5, 20.7.

^{19}F NMR (282 MHz, CDCl_3) δ -78.26 (s, 3F).

IR (film): ν (cm^{-1}) 3300, 3050, 2928, 1686, 1594, 1491, 1366, 1257, 1166, 1122, 921, 809, 758, 697, 625, 530.

HRMS (ESI, m/z) calcd for $\text{C}_{25}\text{H}_{21}\text{ClF}_3\text{N}_3\text{O}_2\text{Na}$ $[\text{M}+\text{Na}]^+$: 494.1228, found: 494.1221.

(S)-1,1,1-Trifluoro-3-((4-methoxyphenyl)(*p*-tolyl)amino)-2-(1-phenyl-1*H*-imidazol-2-yl)propan-2-ol (16e)



Starting from 2-acyl imidazole **14a** (48.0 mg, 0.20 mmol) and amine **15e** (136.4 mg, 0.60 mmol) according to the general procedure to give **16e** as a pale yellow oil (66.4 mg, 0.142 mmol, yield: 71%). Enantiomeric excess established by HPLC analysis using a Chiralpak AD-H column, $ee = 97\%$ (HPLC: AD-H, 254 nm, hexane/isopropanol = 90:10, flow rate 0.5 mL/min, 25 °C, t_r (minor) = 14.1 min, t_r (major) = 15.5 min). $[\alpha]_D^{20} = -55.0^\circ$ (c 0.5, CH_2Cl_2).

^1H NMR (300 MHz, CDCl_3) δ 7.42–7.27 (m, 3H), 7.08 (d, $J = 1.2$ Hz, 1H), 7.02–6.90 (m, 4H), 6.87–6.76 (m, 5H), 6.68–6.60 (m, 2H), 4.83 (d, $J = 15.0$ Hz, 1H), 4.44 (br s, 1H), 4.24 (d, $J = 15.0$ Hz, 1H), 3.78 (s, 3H), 2.25 (s, 3H).

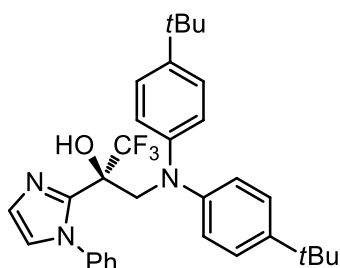
^{13}C NMR (75 MHz, CDCl_3) δ 156.5, 147.3, 142.7, 141.1, 138.9, 131.0, 129.6, 128.6, 128.4, 127.3, 126.9, 125.9, 124.8, 124.3 (q, $J = 284.2$ Hz), 119.4, 114.7, 74.8 (q, $J = 28.5$ Hz), 58.3, 55.5, 20.4.

^{19}F NMR (282 MHz, CDCl_3) δ -78.63 (s, 3F).

IR (film): ν (cm^{-1}) 3313, 3117, 2928, 2842, 1676, 1605, 1503, 1454, 1359, 1241, 1165, 1035, 886, 814, 757, 693, 643, 576.

HRMS (ESI, m/z) calcd for $\text{C}_{26}\text{H}_{24}\text{F}_3\text{N}_3\text{O}_2\text{Na}$ $[\text{M}+\text{Na}]^+$: 490.1724, found: 490.1715.

(S)-3-(Bis(4-(*tert*-butyl)phenyl)amino)-1,1,1-trifluoro-2-(1-phenyl-1*H*-imidazol-2-yl)propan-2-ol (16f)



Starting from 2-acyl imidazole **14a** (48.0 mg, 0.20 mmol) and amine **15f** (177.3 mg, 0.60 mmol) according to the general procedure to give **16f** as a white solid (80.3 mg, 0.15 mmol, yield: 75%). Enantiomeric excess established by HPLC analysis using a Chiralpak IC column, $ee = 95\%$ (HPLC: IC, 254 nm, hexane/isopropanol = 98:2, flow rate 0.5 mL/min, 25 °C, t_r (minor) = 8.7 min, t_r (major) = 9.4 min). $[\alpha]_D^{20} = -69.4^\circ$ (c 0.8, CH_2Cl_2).

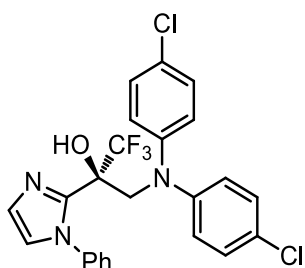
^1H NMR (300 MHz, CDCl_3) δ 7.40–7.18 (m, 7H), 7.05 (d, $J = 1.2$ Hz, 1H), 6.86–6.78 (m, 6H), 6.73 (d, $J = 1.2$ Hz, 1H), 4.91 (d, $J = 15.0$ Hz, 1H), 4.29 (d, $J = 15.0$ Hz, 1H), 4.12 (s, 1H), 1.31 (s, 18H).

^{13}C NMR (75 MHz, CDCl_3) δ 145.8, 145.6, 142.7, 139.0, 128.5, 128.3, 127.5, 126.8, 126.1, 124.6, 124.3 (q, $J = 283.5$ Hz), 121.6, 74.9 (q, $J = 28.5$ Hz), 58.0, 34.2, 31.4.

^{19}F NMR (282 MHz, CDCl_3) δ -78.65 (s, 3F).

IR (film): ν (cm^{-1}) 3304, 3043, 2956, 1601, 1503, 1366, 1168, 1117, 979, 827, 755, 696, 629, 555.

HRMS (ESI, m/z) calcd for $\text{C}_{32}\text{H}_{37}\text{F}_3\text{N}_3\text{O}$ $[\text{M}+\text{H}]^+$: 536.2894, found: 536.2892.

(S)-3-(Bis(4-chlorophenyl)amino)-1,1,1-trifluoro-2-(1-phenyl-1H-imidazol-2-yl)propan-2-ol (16g)

Starting from 2-acyl imidazole **14a** (48.0 mg, 0.20 mmol) and amine **15g** (151.3 mg, 0.60 mmol) according to the general procedure to give **16g** as a white solid (62.0 mg, 0.126 mmol, yield: 63%). Enantiomeric excess established by HPLC analysis using a Chiralpak AD-H column, *ee* = 91% (HPLC: AD-H, 254 nm, hexane/isopropanol = 99:1, flow rate 0.5 mL/min, 25 °C, t_r (major) = 33.6 min, t_r (minor) = 36.2 min). $[\alpha]_D^{20} = -105.0^\circ$ (*c* 0.5, CH₂Cl₂).

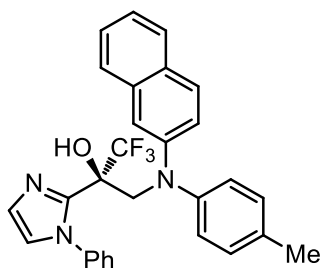
¹H NMR (300 MHz, CDCl₃) δ 7.49–7.43 (m, 1H), 7.42–7.38 (m, 1H), 7.36–7.31 (m, 1H), 7.22–7.18 (m, 2H), 7.17–7.13 (m, 2H), 7.07 (d, *J* = 1.3 Hz, 1H), 6.95–6.90 (m, 2H), 6.83 (d, *J* = 1.2 Hz, 1H), 6.78–6.72 (m, 4H), 4.68 (d, *J* = 15.3 Hz, 1H), 4.27 (d, *J* = 15.3 Hz, 1H), 4.09 (s, 1H).

¹³C NMR (75 MHz, CDCl₃) δ 146.7, 142.1, 138.3, 129.4, 129.0, 128.9, 128.7, 128.6, 128.4, 127.3, 126.9, 126.8, 125.8, 125.5, 125.2, 124.1 (q, *J* = 285.0 Hz), 123.3, 75.6 (q, *J* = 28.5 Hz), 57.2.

¹⁹F NMR (282 MHz, CDCl₃) δ -78.10 (s, 3F).

IR (film): ν (cm⁻¹) 3312, 3049, 2921, 1684, 1592, 1488, 1359, 1317, 1252, 1120, 1048, 937, 896, 754, 684, 618, 533.

HRMS (ESI, *m/z*) calcd for C₂₄H₁₉Cl₂F₃N₃O [M+H]⁺: 492.0852, 494.0822, found: 492.0855, 494.0824.

(S)-1,1,1-Trifluoro-3-(naphthalen-2-yl(*p*-tolyl)amino)-2-(1-phenyl-1H-imidazol-2-yl)propan-2-ol (16h)

Starting from 2-acyl imidazole **14a** (48.0 mg, 0.20 mmol) and amine **15h** (148.4 mg, 0.60 mmol) according to the general procedure to give **16h** as a white solid (59.5 mg, 0.122 mmol, yield: 61%). Enantiomeric excess established by HPLC analysis using a Chiralpak AD-H column, *ee* = 95% (HPLC:

AD-H, 254 nm, hexane/isopropanol = 90:10, flow rate 0.5 mL/min, 25 °C, t_r (minor) = 15.3 min, t_r (major) = 23.2 min). $[\alpha]_D^{20} = -67.0^\circ$ (c 0.3, CH_2Cl_2).

^1H NMR (300 MHz, CDCl_3) δ 7.62 (d, $J = 7.9$ Hz, 1H), 7.55 (d, $J = 8.9$ Hz, 1H), 7.48 (d, $J = 8.1$ Hz, 1H), 7.39–7.29 (m, 1H), 7.28–7.21 (m, 2H), 7.20–7.13 (m, 2H), 7.03–6.90 (m, 5H), 6.79–6.68 (m, 4H), 6.65–6.62 (m, 1H), 4.94 (d, $J = 15.1$ Hz, 1H), 4.28 (d, $J = 15.1$ Hz, 1H), 4.00 (s, 1H), 2.23 (s, 3H).

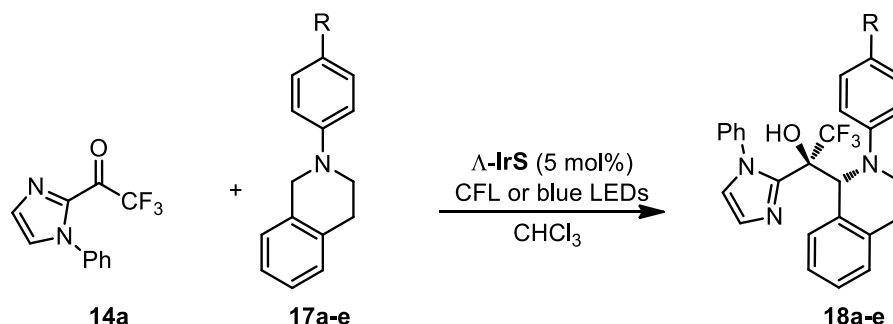
^{13}C NMR (75 MHz, CDCl_3) δ 145.9, 145.8, 142.8, 138.9, 134.2, 133.7, 130.1, 129.4, 128.8, 128.6, 128.5, 128.3, 127.5, 127.4, 127.1, 126.8, 126.4, 124.9, 124.4, 124.3 (q, $J = 284.3$ Hz), 123.7, 121.6, 116.3, 74.9 (q, $J = 29.2$ Hz), 57.9, 20.7.

^{19}F NMR (282 MHz, CDCl_3) δ -78.86 (s, 3F).

IR (film): ν (cm^{-1}) 3342, 3051, 2924, 1598, 1502, 1458, 1375, 1262, 1164, 1054, 957, 819, 750, 692, 534.

HRMS (ESI, m/z) calcd for $\text{C}_{29}\text{H}_{25}\text{F}_3\text{N}_3\text{O}$ $[\text{M}+\text{H}]^+$: 488.1944, found: 488.1946.

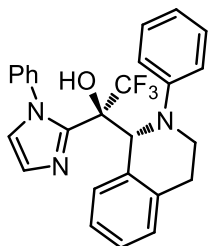
2) Reactions of 2-acyl imidazole **14a** with 2-aryl-1,2,3,4-tetrahydroisoquinolines



General catalysis procedure. A dried 10 mL Schlenk tube was charged with the catalyst $\Delta\text{-IrS}$ (5 mol%), 2-acyl imidazole **14a** (0.20 mmol, 1.0 eq.), and the corresponding 2-aryl-1,2,3,4-tetrahydroisoquinolines **17a-e** (0.60 mmol, 3.0 eq.). The tube was purged with nitrogen and CHCl_3 (0.40 mL) was added *via* syringe. The reaction mixture was degassed *via* freeze-pump-thaw for three cycles. After the mixture was thoroughly degassed, the vial was sealed and positioned approximately 8 cm from 24 W blue LEDs (**18a**) or approximately 5 cm from a 23 W CFL (**18b-e**). The reaction was stirred at room temperature for the indicated time (monitored by TLC) under nitrogen atmosphere. Afterwards, the mixture was diluted with CH_2Cl_2 (4 mL). The combined organic layers were concentrated under reduced pressure. The residue was purified by flash chromatography on silica gel (EtOAc/hexane = 1:20 to 1:10) to afford the products **18a-e**. Racemic samples were obtained by carrying out the reactions with

rac-**IrS**. The enantiomeric excess was determined by chiral HPLC analysis and *dr* values were determined by ^1H NMR analysis of the crude product. Shown below is an example for the calculation of *dr* value (Figure 88).

(S)-2,2,2-Trifluoro-1-((R)-2-phenyl-1,2,3,4-tetrahydroisoquinolin-1-yl)-1-(1-phenyl-1*H*-imidazol-2-yl)ethanol (18a**)**



Starting from 2-acyl imidazole **14a** (48.0 mg, 0.20 mmol) and 2-aryl-1,2,3,4-tetrahydroisoquinoline **17a** (125.6 mg, 0.60 mmol) according to the general procedure to give **18a** as a white solid (82.7 mg, 0.184 mmol, yield: 92%, *dr*: 8:1). Enantiomeric excess established by HPLC analysis using a Chiralpak AD-H column, *ee* = 94% (major product) (HPLC: AD-H, 254 nm, hexane/isopropanol = 90:10, flow rate 0.5 mL/min, 25 °C, t_r (minor) = 10.7 min, t_r (major) = 17.1 min). $[\alpha]_{\text{D}}^{20} = +15.3^\circ$ (c 0.5, CH_2Cl_2). The *dr* value was determined by crude ^1H NMR as shown below.

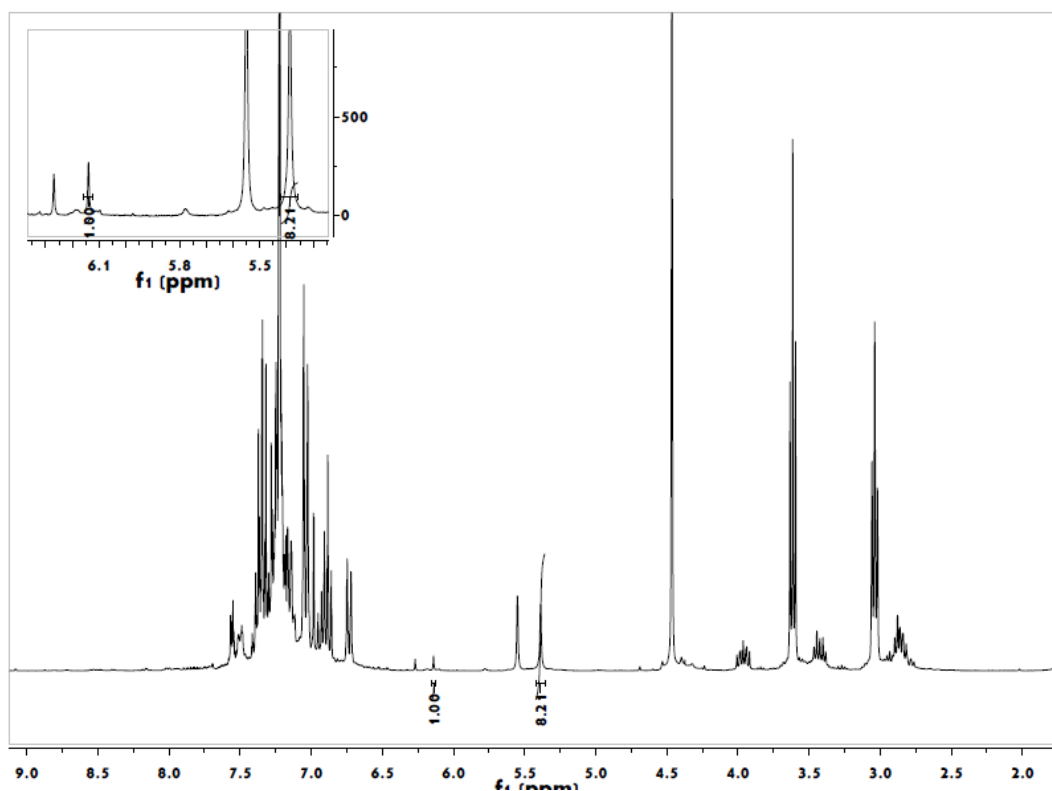


Figure 88 ^1H NMR of the crude product **18a** and its diastereomer **18a'**. Calculated *dr* = 8:1.

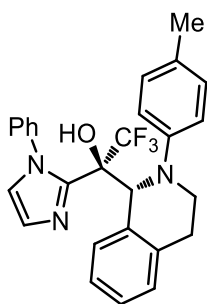
^1H NMR (300 MHz, CDCl_3) δ 7.40–7.32 (m, 1H), 7.30–7.22 (m, 1H), 7.19–7.16 (m, 1H), 7.16–7.04 (m, 6H), 7.03–6.97 (m, 3H), 6.85 (d, $J = 1.3$ Hz, 1H), 6.83–6.76 (m, 1H), 6.65–6.55 (m, 2H), 5.41 (s, 1H), 5.25 (br s, 1H), 3.84 (ddd, $J = 13.2, 7.9, 5.6$ Hz, 1H), 3.30 (dt, $J = 12.4, 6.0$ Hz, 1H), 2.88–2.55 (m, 2H).

^{13}C NMR (75 MHz, CDCl_3) δ 150.4, 144.7, 138.5, 136.5, 131.6, 129.8–129.6 (m), 129.1, 128.7, 128.3, 128.1, 127.7, 127.5, 126.9, 125.6, 125.5, 124.0 (q, $J = 285.8$ Hz), 121.0, 118.4, 79.9 (q, $J = 27.0$ Hz), 63.8, 46.2, 26.0.

^{19}F NMR (282 MHz, CDCl_3) δ -71.23 (s, 3F).

IR (film): ν (cm^{-1}) 3341, 3018, 2974, 2738, 1688, 1593, 1492, 1454, 1385, 1309, 1250, 1162, 1110, 918, 823, 754, 690, 593, 549.

(S)-2,2,2-Trifluoro-1-(1-phenyl-1H-imidazol-2-yl)-1-((R)-2-(p-tolyl)-1,2,3,4-tetrahydroisoquinolin-1-yl)ethanol (18b)



Starting from 2-acyl imidazole **14a** (48.0 mg, 0.20 mmol) and 2-aryl-1,2,3,4-tetrahydroisoquinoline **17b** (134.0 mg, 0.60 mmol) according to the general procedure to give **18b** as a colorless oil (52.8 mg, 0.114 mmol, yield: 57%, *dr*: 4:1 (determined by the isolated yield of each isomer)). Enantiomeric excess established by HPLC analysis using a Chiralpak AD-H column, *ee* = 97% (major product) (HPLC: AD-H, 254 nm, hexane/isopropanol = 90:10, flow rate 0.5 mL/min, 25 °C, t_r (minor) = 10.5 min, t_r (major) = 14.9 min). $[\alpha]_D^{20} = +28.7^\circ$ (c 0.5, CH_2Cl_2).

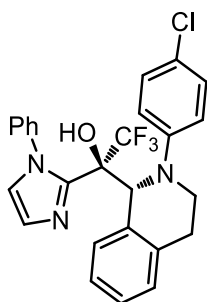
^1H NMR (300 MHz, CDCl_3) δ 7.60–7.51 (m, 1H), 7.46–7.38 (m, 1H), 7.35–7.24 (m, 5H), 7.23–7.14 (m, 3H), 7.07–6.98 (m, 3H), 6.72–6.62 (m, 2H), 5.63 (s, 1H), 5.55 (s, 1H), 3.93 (ddd, $J = 13.1, 7.9, 5.5$ Hz, 1H), 3.39 (dt, $J = 12.4, 5.9$ Hz, 1H), 2.95–2.76 (m, 2H), 2.33 (s, 3H).

^{13}C NMR (75 MHz, CDCl_3) δ 148.2, 144.9, 138.7, 136.5, 131.6, 130.9, 129.9–129.7 (m), 129.6, 128.6, 128.3, 128.1, 127.6, 127.5, 127.0, 125.6, 125.3, 124.1 (q, $J = 285.8$ Hz), 119.1, 79.4 (q, $J = 27.0$ Hz), 64.5, 46.6, 26.0, 20.4.

^{19}F NMR (282 MHz, CDCl_3) δ -70.53 (s, 3F).

IR (film): ν (cm⁻¹) 3279, 3030, 2921, 2732, 1682, 1604, 1504, 1456, 1302, 1165, 1020, 921, 812, 748, 690, 515.

(*S*)-1-((*R*)-2-(4-Chlorophenyl)-1,2,3,4-tetrahydroisoquinolin-1-yl)-2,2,2-trifluoro-1-(1-phenyl-1*H*-imidazol-2-yl)ethanol (**18c**)



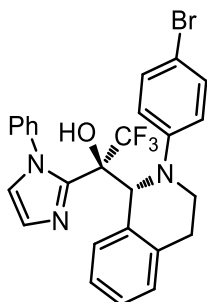
Starting from 2-acyl imidazole **14a** (48.0 mg, 0.20 mmol) and 2-aryl-1,2,3,4-tetrahydroisoquinoline **17c** (146.2 mg, 0.60 mmol) according to the general procedure to give **18c** as a white solid (86.7 mg, 0.180 mmol, yield: 90%, *dr*: 8:1). Enantiomeric excess established by HPLC analysis using a Chiralpak AD-H column, *ee* = 98% (major product) (HPLC: AD-H, 254 nm, hexane/isopropanol = 90:10, flow rate 0.5 mL/min, 25 °C, *t_r* (minor) = 11.8 min, *t_r* (major) = 16.3 min). $[\alpha]_D^{20} = +11.4^\circ$ (*c* 0.6, CH₂Cl₂).

¹H NMR (300 MHz, CDCl₃) δ 7.45–7.35 (m, 2H), 7.33–7.19 (m, 5H), 7.17–7.12 (m, 2H), 7.11–7.07 (m, 3H), 6.96 (d, *J* = 1.3 Hz, 1H), 6.69–6.58 (m, 2H), 5.38 (s, 1H), 5.09 (s, 1H), 3.96 (ddd, *J* = 13.4, 8.0, 5.8 Hz, 1H), 3.35 (dt, *J* = 12.5, 6.0 Hz, 1H), 2.95–2.60 (m, 2H).

¹³C NMR (75 MHz, CDCl₃) δ 149.0, 144.2, 138.3, 136.4, 131.1, 129.6–129.5 (m), 128.94, 128.89, 128.5, 128.3, 127.9, 127.5, 126.9, 125.7, 125.6, 125.5, 123.9 (q, *J* = 285.8 Hz), 119.2, 80.4 (q, *J* = 27.0 Hz), 63.1, 45.9, 25.8.

¹⁹F NMR (282 MHz, CDCl₃) δ -70.53 (s, 3F).

IR (film): ν (cm⁻¹) 3298, 3057, 2921, 1673, 1593, 1488, 1393, 1250, 1166, 1005, 918, 818, 749, 691, 508.

(S)-1-((R)-2-(4-Bromophenyl)-1,2,3,4-tetrahydroisoquinolin-1-yl)-2,2,2-trifluoro-1-(1-phenyl-1H-imidazol-2-yl)ethanol (18d)

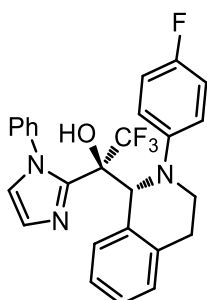
Starting from 2-acyl imidazole **14a** (48.0 mg, 0.20 mmol) and 2-aryl-1,2,3,4-tetrahydroisoquinoline **17d** (172.9 mg, 0.60 mmol) according to the general procedure to give **18d** as a white solid (102.5 mg, 0.194 mmol, yield: 97%, *dr*: 10:1). Enantiomeric excess established by HPLC analysis using a Chiralpak AD-H column, *ee* = 98% (major product) (HPLC: AD-H, 254 nm, hexane/isopropanol = 90:10, flow rate 0.5 mL/min, 25 °C, t_r (minor) = 12.4 min, t_r (major) = 17.4 min). $[\alpha]_D^{20} = +9.9^\circ$ (*c* 0.6, CH₂Cl₂).

¹H NMR (300 MHz, CDCl₃) δ 7.43–7.33 (m, 2H), 7.31–7.23 (m, 4H), 7.22–7.18 (m, 3H), 7.15–7.07 (m, 3H), 6.96 (d, *J* = 1.2 Hz, 1H), 6.66–6.48 (m, 2H), 5.38 (s, 1H), 5.02 (s, 1H), 3.96 (ddd, *J* = 13.4, 8.0, 5.8 Hz, 1H), 3.36 (dt, *J* = 12.6, 6.0 Hz, 1H), 2.98–2.65 (m, 2H).

¹³C NMR (75 MHz, CDCl₃) δ 149.4, 144.1, 138.3, 136.4, 131.9, 131.1, 129.6–129.5 (m), 128.9, 128.5, 128.3, 128.0, 127.5, 126.8, 125.7, 125.6, 123.9 (q, *J* = 285.8 Hz), 119.5, 112.8, 80.4 (q, *J* = 27.0 Hz), 63.0, 45.7, 25.8.

¹⁹F NMR (282 MHz, CDCl₃) δ -70.67 (s, 3F).

IR (film): ν (cm⁻¹) 3352, 3062, 2922, 2856, 1671, 1591, 1490, 1396, 1302, 1254, 1167, 918, 814, 751, 691, 507.

(S)-2,2,2-Trifluoro-1-((R)-2-(4-fluorophenyl)-1,2,3,4-tetrahydroisoquinolin-1-yl)-1-(1-phenyl-1H-imidazol-2-yl)ethanol (18e)

Starting from 2-acyl imidazole **14a** (48.0 mg, 0.20 mmol) and 2-aryl-1,2,3,4-tetrahydroisoquinoline **17e** (136.4 mg, 0.60 mmol) according to the general procedure to give **18e** as a white solid (83.0 mg, 0.178 mmol, yield: 89%, *dr*: 8:1). Enantiomeric excess established by HPLC analysis using a Chiralpak AD-H column, *ee* = 97% (major product) (HPLC: AD-H, 254 nm, hexane/isopropanol = 90:10, flow rate 0.5 mL/min, 25 °C, *t_r* (minor) = 10.7 min, *t_r* (major) = 15.3 min). $[\alpha]_{\text{D}}^{20} = +17.7^{\circ}$ (*c* 0.8, CH₂Cl₂).

¹H NMR (300 MHz, CDCl₃) δ 7.40–7.31 (m, 2H), 7.27–7.14 (m, 5H), 7.13–7.06 (m, 3H), 6.93 (d, *J* = 1.2 Hz, 1H), 6.89–6.80 (m, 2H), 6.69–6.60 (m, 2H), 5.42 (s, 1H), 5.33 (s, 1H), 3.89 (ddd, *J* = 12.9, 8.3, 5.5 Hz, 1H), 3.26 (dt, *J* = 12.3, 5.8 Hz, 1H), 2.92–2.59 (m, 2H).

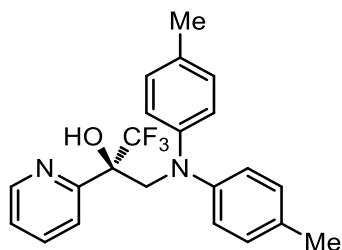
¹³C NMR (75 MHz, CDCl₃) δ 159.4, 156.2, 147.03, 147.00, 144.5, 138.3, 136.5, 131.1, 129.6–129.4 (m), 128.8, 128.4, 128.3, 127.7, 127.4, 126.6, 125.7, 125.5, 123.9 (q, *J* = 285.8 Hz), 121.0, 120.9, 115.7, 115.4, 80.9 (q, *J* = 27.8 Hz), 64.0, 47.2, 25.8.

¹⁹F NMR (282 MHz, CDCl₃) δ -73.1 (s, 3F), -123.1 (s, 1F).

IR (film): ν (cm⁻¹) 3340, 3039, 2922, 2710, 1682, 1598, 1501, 1385, 1162, 1108, 921, 823, 749, 692, 516.

3) Reactions of 2-acyl pyridines with amine **15a**

General catalysis procedure. A dried 10 mL Schlenk tube was charged with the catalyst Λ -**IrS** (3 or 5 mol%), 2-acyl pyridines¹⁹ **19a-c** (0.20 mmol, 1.0 eq.) and amine **15a** (0.60 mmol, 3.0 eq.). The tube was purged with nitrogen and CHCl₃ (0.4 mL) was added *via* syringe. The reaction mixture was degassed *via* freeze-pump-thaw for three cycles. After the mixture was thoroughly degassed, the vial was sealed and positioned approximately 8 cm from a 24 W blue LEDs. The reaction was stirred at room temperature for the indicated time (monitored by TLC) under nitrogen atmosphere. Afterwards, the mixture was diluted with CH₂Cl₂ (4 mL). The combined organic layers were concentrated under reduced pressure. The residue was purified by flash chromatography on silica gel (EtOAc/hexane = 1:50) to afford the products **20a-c**. Racemic samples were obtained by carrying out the reactions with *rac*-**IrS**. The enantiomeric excess was determined by chiral HPLC analysis.

(S)-3-(Di-*p*-tolylamino)-1,1,1-trifluoro-2-(pyridin-2-yl)propan-2-ol (20a)

Starting from 2-acyl pyridine **19a** (35.0 mg, 0.20 mmol) and amine **15a** (126.6 mg, 0.60 mmol) according to the general procedure to give **20a** as a white solid (57.2 mg, 0.148 mmol, yield: 74%). Enantiomeric excess established by HPLC analysis using a Chiralpak AD-H column, *ee* = 93% (HPLC: AD-H, 254 nm, hexane/isopropanol = 98:2, flow rate 0.5 mL/min, 25 °C, *t_r* (major) = 16.8 min, *t_r* (minor) = 18.9 min). $[\alpha]_D^{20} = -266.0^\circ$ (*c* 0.3, CH₂Cl₂).

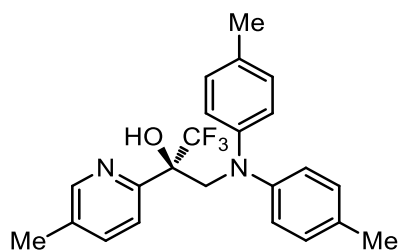
¹H NMR (300 MHz, CDCl₃) δ 8.52–8.43 (m, 1H), 7.43–7.29 (m, 1H), 7.23–7.09 (m, 2H), 6.93–6.84 (m, 4H), 6.72–6.60 (m, 5H), 4.56 (s, 2H), 2.23 (s, 6H).

¹³C NMR (75 MHz, CDCl₃) δ 152.5, 146.9, 146.8, 136.3, 131.0, 129.5, 125.1 (q, *J* = 285 Hz), 123.4, 122.3–122.1 (m), 121.5, 77.4 (q, *J* = 26.3 Hz), 56.7, 20.5.

¹⁹F NMR (282 MHz, CDCl₃) δ -78.69 (s, 3F).

IR (film): ν (cm⁻¹) 3292, 3023, 2925, 2863, 1605, 1508, 1412, 1367, 1258, 1169, 1052, 988, 916, 857, 815, 769, 708, 661, 572, 520.

HRMS (ESI, *m/z*) calcd for C₂₂H₂₂F₃N₂O [M+H]⁺: 387.1679, found: 387.1677.

(S)-3-(Di-*p*-tolylamino)-1,1,1-trifluoro-2-(5-methylpyridin-2-yl)propan-2-ol (20b)

Starting from 2-acyl pyridine **19b** (37.8 mg, 0.20 mmol) and amine **15a** (126.6 mg, 0.60 mmol) according to the general procedure to give **20b** as a white solid (52.2 mg, 0.130 mmol, yield: 65%).

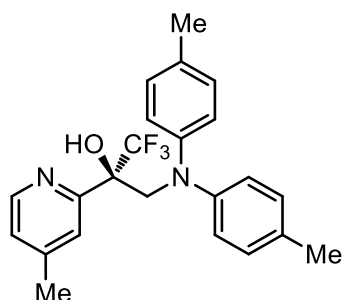
Enantiomeric excess established by HPLC analysis using a Chiralpak AD-H column, *ee* = 90% (HPLC:

AD-H, 254 nm, hexane/isopropanol = 98:2, flow rate 0.5 mL/min, 25 °C, t_r (major) = 15.7 min, t_r (minor) = 18.0 min).

^1H NMR (300 MHz, CDCl_3) δ 8.18 (dd, J = 2.0, 1.1 Hz, 1H), 7.05 (dd, J = 8.2, 2.1 Hz, 1H), 6.98–6.90 (m, 1H), 6.85–6.77 (d, J = 8.3 Hz, 4H), 6.61–6.54 (m, 4H), 4.44 (s, 2H), 2.20 (s, 3H), 2.15 (s, 6H).

^{13}C NMR (75 MHz, CDCl_3) δ 149.7, 147.0, 146.8, 136.9, 133.3, 130.9, 129.4, 121.7, 121.63, 121.58, 56.8, 20.5, 17.9.

(S)-3-(Di-*p*-tolylamino)-1,1,1-trifluoro-2-(pyridin-2-yl)propan-2-ol (**20c**)

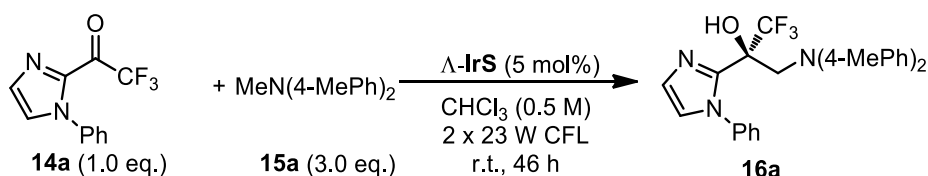


Starting from 2-acyl pyridine **19c** (37.8 mg, 0.20 mmol) and amine **15a** (126.6 mg, 0.60 mmol) according to the general procedure to give **20c** as a white solid (49.5 mg, 0.124 mmol, yield: 62%). Enantiomeric excess established by HPLC analysis using a Chiralpak AD-H column, ee = 90% (HPLC: AD-H, 254 nm, hexane/isopropanol = 99:1, flow rate 0.5 mL/min, 25 °C, t_r (minor) = 12.1 min, t_r (major) = 18.4 min).

^1H NMR (300 MHz, CDCl_3) δ 8.29 (dd, J = 5.1, 0.9 Hz, 1H), 6.98–6.93 (m, 1H), 6.92–6.89 (m, 5H), 6.71–6.63 (m, 4H), 4.64–4.45 (m, 2H), 2.23 (s, 6H), 2.05 (s, 3H).

^{19}F NMR (282 MHz, CDCl_3) δ -78.90 (s, 3F).

4) Reaction of 2-acyl imidazole **14a** with amine **15a** on gram scale



A dried 25 mL Schlenk tube was charged with catalyst Λ -IrS (5 mol%), 2-acyl imidazole **14a** (0.818 g, 3.4 mmol), and amine **15a** (2.152 g, 10.2 mmol). The tube was purged with nitrogen and CHCl_3 (6.8 mL) was added *via* syringe. The reaction mixture was degassed *via* freeze-pump-thaw for three cycles.

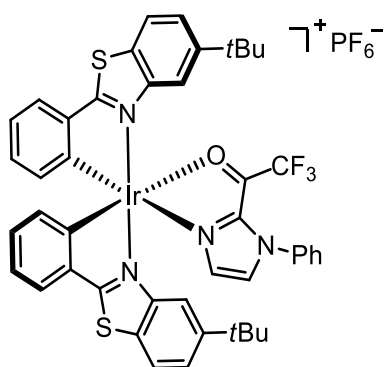
After the mixture was thoroughly degassed, the vial was sealed and positioned approximately 5 cm away from two 23 W CFL. The reaction was stirred at room temperature for 46 h under nitrogen atmosphere. Afterwards, the mixture was diluted with CH_2Cl_2 . The combined organic layers were concentrated under reduced pressure. The residue was purified by flash chromatography on silica gel (EtOAc/hexane = 1:15) to afford the product **16a** (0.915 g, 2.05 mmol, 60% yield with 98% *ee*) and unreacted starting material **14a** was recollected in a yield of 25%.

Reaction setup:



5.4.3 Mechanistic Investigations

1) Substrate-coordinated iridium complex IrS-I



The racemic substrate-coordinated iridium complex was obtained by reacting substrate **14a** (12.1 mg, 0.050 mmol) with racemic Δ/Λ -IrS (40.0 mg, 0.042 mmol) at 50 °C overnight in CHCl_3 (5.0 mL). After the slow addition of hexane (5.0 mL), crystals were collected after several days (32.2 mg, yield: 69%). ^1H NMR (300 MHz, CD_2Cl_2) δ 8.12–8.04 (m, 1H), 7.95 (d, $J = 8.5$ Hz, 1H), 7.88 (d, $J = 8.6$ Hz, 1H), 7.83–7.72 (m, 2H), 7.57 (td, $J = 8.7, 1.9$ Hz, 2H), 7.44–7.25 (m, 5H), 7.12 (d, $J = 1.5$ Hz, 1H), 7.08–6.95 (m, 2H), 6.94–6.77 (m, 3H), 6.58–6.45 (m, 2H), 6.29 (d, $J = 7.6$ Hz, 1H), 1.26 (s, 9H), 1.11 (s, 9H).

^{13}C NMR (75 MHz, CD_2Cl_2) δ 183.1, 178.1, 151.7, 150.8, 150.2, 149.5, 147.2, 146.2, 143.2, 140.6, 138.2, 136.5, 134.5, 134.3, 130.2, 129.8, 129.5, 129.1, 128.8, 128.4, 128.2, 127.4, 126.32, 126.29, 125.7, 125.6, 124.8, 124.4, 123.5, 122.5, 122.2, 121.9, 121.7, 117.4, 115.7, 34.83, 34.79, 31.3, 30.6.

2) Control reactions

Performed in analogy to entry 8 of Table 7 (chapter 3.3), but in the presence of air. The reaction was performed in a 10 mL test tube under an atmosphere of air (air balloon). No product **16a** could be detected by crude ^1H NMR.

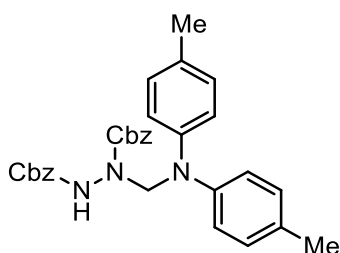
3) Trapping experiments with alkenes and a diazodicarboxylate

Starting from 2-acyl imidazole **14a** (48.0 mg, 0.20 mmol), amine **15a** (21.1 mg, 0.20 mmol) and (*E*)-dibenzyl diazene-1,2-dicarboxylate (298.3 mg, 1.0 mol) according to the general procedure of synthesizing **16a-h** to give **21** (88.2 mg, 0.172 mmol, yield: 86%) and product *rac*-**16a** was not observed.

Starting from 2-acyl imidazole **14a** (48.0 mg, 0.20 mmol), amine **15a** (21.1 mg, 0.20 mmol), and ethyl acrylate (0.054 mL, 0.60 mol) according to the general procedure of synthesizing **16a-h** to give **22a** (30.0 mg, 0.101 mmol, yield: 51%) and *rac*-**16a** (24.6 mg, 0.054 mmol, yield: 27%).

Starting from 2-acyl imidazole **14a** (48.0 mg, 0.20 mmol), amine **15a** (21.1 mg, 0.20 mmol), and acrylonitrile (0.066 mL, 1.0 mol) according to the general procedure of synthesizing **16a-h** to give **22b** (23.1 mg, 0.088 mmol, yield: 44%) and *rac*-**16a** (yield <10%).

Dibenzyl 1-((di-*p*-tolylamino)methyl)hydrazine-1,2-dicarboxylate (**21**)

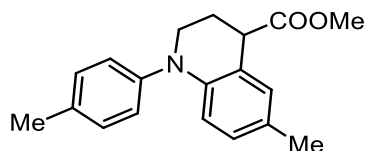


^1H NMR (300 MHz, CDCl_3) δ 7.31–7.10 (m, 11H), 6.98–6.85 (m, 4H), 6.83–6.70 (m, 3H), 5.43–4.72 (m, 6H), 2.17 (s, 6H).

^{13}C NMR (75 MHz, CDCl_3) δ 155.5, 144.4, 135.6, 131.6, 129.8, 129.3, 128.6, 128.47, 128.45, 128.2, 128.0, 125.7, 121.0, 67.6, 20.6.

HRMS (ESI, m/z) calcd for $\text{C}_{31}\text{H}_{31}\text{N}_3\text{O}_4\text{Na}$ $[\text{M}+\text{Na}]^+$: 532.2207, found: 532.2210.

Methyl 6-methyl-1-(*p*-tolyl)-1,2,3,4-tetrahydroquinoline-4-carboxylate (22a)

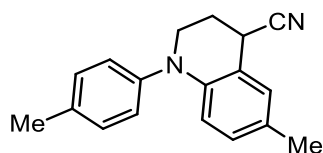


^1H NMR (300 MHz, CDCl_3) δ 7.20–7.08 (m, 4H), 7.00–6.96 (m, 1H), 6.80 (dd, $J = 8.4, 2.2$ Hz, 1H), 6.63–6.55 (m, 1H), 3.84 (t, $J = 5.2$ Hz, 1H), 3.75 (s, 3H), 3.73–3.65 (m, 1H), 3.59–3.50 (m, 1H), 2.39–2.28 (m, 4H), 2.23 (s, 3H), 2.21–2.07 (m, 1H).

^{13}C NMR (75 MHz, CDCl_3) δ 174.7, 145.8, 142.4, 133.8, 130.2, 130.1, 128.5, 127.1, 125.3, 119.9, 116.1, 52.1, 48.2, 42.6, 25.3, 20.9, 20.4.

HRMS (ESI, m/z) calcd for $\text{C}_{19}\text{H}_{22}\text{NO}_2$ $[\text{M}+\text{H}]^+$: 296.1645, found: 296.1645.

6-Methyl-1-(*p*-tolyl)-1,2,3,4-tetrahydroquinoline-4-carbonitrile (22b)



^1H NMR (300 MHz, CDCl_3) δ 7.23–7.16 (m, 2H), 7.14–7.07 (m, 3H), 6.84 (dd, $J = 8.5, 2.1$ Hz, 1H), 6.56 (d, $J = 8.4$ Hz, 1H), 4.03 (t, $J = 5.9$ Hz, 1H), 3.82–3.70 (m, 1H), 3.67–3.53 (m, 1H), 2.42–2.29 (m, 5H), 2.25 (s, 3H).

^{13}C NMR (75 MHz, CDCl_3) δ 144.9, 142.0, 134.6, 130.3, 129.6, 129.4, 127.9, 125.4, 121.2, 116.2, 116.1, 48.4, 29.3, 26.4, 20.9, 20.2.

HRMS (ESI, m/z) calcd for $\text{C}_{18}\text{H}_{19}\text{N}_2$ $[\text{M}+\text{H}]^+$: 263.1543, found: 263.1543.

4) Trapping experiments with single electron oxidants

A dried 10 mL Schlenk tube was charged with the catalyst $\Delta/\Lambda\text{-IrS}$ (3 mol%), 2-acyl imidazole **14a** (0.20 mmol, 1.0 eq), amine **15a** (0.60 mmol, 3.0 eq), and the corresponding single electron oxidant (5 mol% or 1.0 eq). The tube was purged with nitrogen and CHCl_3 (0.40 mL) was added *via* syringe. The

reaction mixture was degassed *via* freeze-pump-thaw for three cycles. After the mixture was thoroughly degassed, the vial was sealed and positioned in the dark. The reaction was stirred at room temperature for 22 h under nitrogen atmosphere.

No product **16b** could be detected by ¹H NMR when Cp₂FePF₆ or (BrC₆H₄)₃NSbCl₆ or Ce(NH₄)₂(NO₃)₆ (5 mol% or 1.0 eq.) was used as single electron oxidant.

5) Quantum yield measurement

The quantum yield was measured by standard ferrioxalate actinometry.²⁰ A 150 W Xenon lamp (50% of light intensity, 420±5 nm bandpass filter high transmittance) was used as the light source. The measured method was designed according to published procedures with modifications.^{21, 22}

The solutions were prepared under the red light (1.1 W red LEDs) and stored in the dark:

Potassium ferrioxalate solution (0.15 M): 736.9 mg of potassium ferrioxalate hydrate was dissolved in 10 mL of 0.05 M H₂SO₄.

Buffered solution of phenanthroline: 50 mg of 1,10-phenanthroline and 11.25 g of sodium acetate were dissolved in 50 mL of 0.5 M H₂SO₄.

a) Measurement of light intensity at 420 nm

1 mL of the ferrioxalate solution was added to a quartz cuvette (l = 10 mm). The actinometry solution was irradiated with 150 W Xenon lamp (50% of light intensity, 420 nm ± 5 nm bandpass filter high transmittance) for specified time intervals (30s, 60s, 90s, 120s). After irradiation, 175 μL of the phenanthroline solution was added to the cuvette. The solution was kept in dark for 30 min to make sure the complete coordination. The absorbance of the actinometry solution was monitored at 510 nm. The absorbance of a non-irradiated (in dark) sample was also measured at 510 nm.

<i>t/s</i>	<i>30</i>	<i>60</i>	<i>90</i>	<i>120</i>
<i>ΔA/a.u.</i>	<i>0.350</i>	<i>0.738</i>	<i>1.108</i>	<i>1.399</i>

The moles of Fe²⁺ formed were determined using Beer's Law (eq 1):

$$\text{mol Fe}^{2+} = \frac{V \times \Delta A(510 \text{ nm})}{l \times \epsilon(510 \text{ nm})} \quad (1)$$

V is the final volume (0.01175 L) after complexation with phenanthroline;

- ΔA (510 nm) is the optical difference in absorbance between the irradiated and non-irradiated solutions;
- l is the path length (1 cm);
- $\epsilon(510 \text{ nm})$ is the molar absorptivity of $\text{Fe}(\text{phen})_3^{2+}$ ($11100 \text{ L} \cdot \text{mol}^{-1} \cdot \text{cm}^{-1}$).

The photon flux (defined as the number of photons per second per unit area) can be calculated (eq 2):

$$\text{photon flux} = \frac{d(\text{mol Fe}^{2+})/dt}{\Phi \times f} \quad (2)$$

$$f = 1 - 10^{-A} \quad (3)$$

- Φ is the quantum yield for the ferrioxalate actinometer (1.05 for a 0.15 M solution at 412 nm; 1.04 for a 0.15 M solution at 422 nm; 1.03 for a 0.15 M solution at 433 nm);²⁰
- f is the fraction of light absorbed which was calculated using eq 3, where A is the absorbance of above ferrioxalate solution at 420 nm (as shown in Figure 90, $A > 3$, indicating $f > 0.999 \approx 1$).

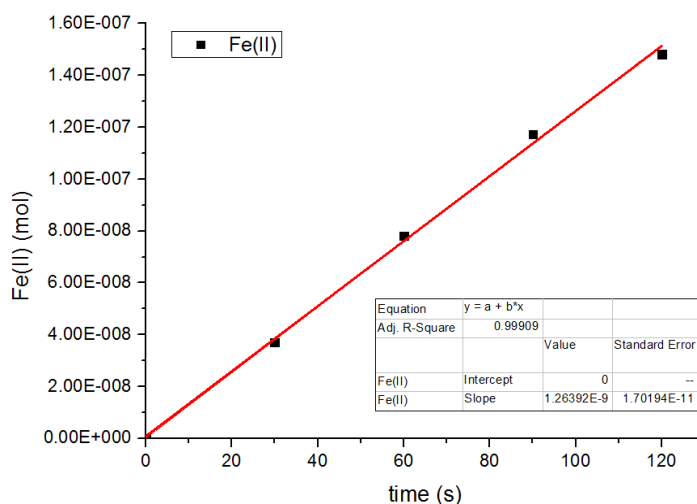


Figure 89 The moles of Fe^{2+} are plotted as a function of time.

According to the equation, photon flux can be calculated as follows:

$$\text{photon flux} = \frac{1.26 \times 10^{-9}}{1.04 \times 1} = 1.22 \times 10^{-9} \text{ einstein} \cdot \text{s}^{-1}$$

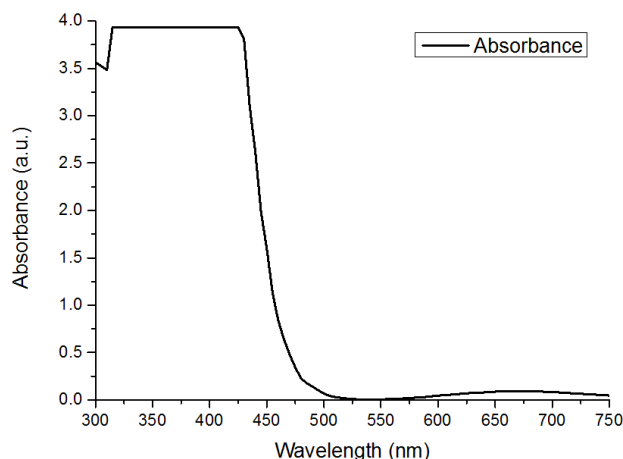
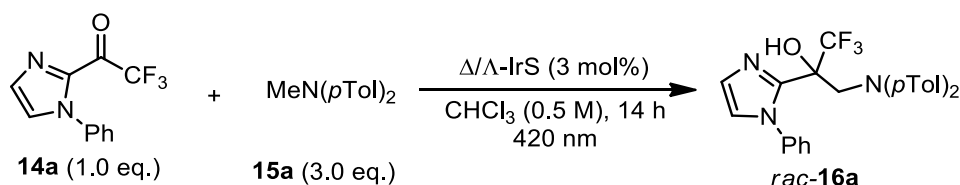


Figure 90 Absorbance of the ferrioxalate actinometer solution (0.15 M).

b) Measurement of quantum yield

Model reaction:



A screw-top cuvette (10.0 mm) was charged with the catalyst *rac*-IrS (3 mol%), 2-acyl imidazole **14a** (96.0 mg, 0.40 mmol), amine **15a** (253.6 mg, 1.20 mmol), 0.8 mL CHCl₃ (0.5 M), and a small magnetic stir bar. The cuvette was degassed with a nitrogen stream for 10 min. After thoroughly degassed, the reaction mixture was stirred and irradiated with 150 W Xenon lamp (50% of light intensity, 420 nm ± 5 nm bandpass filter high transmittance) for 50400 s (14 h). After irradiation, the reaction mixture was passed through a short silica gel column. The yield of product formed was measured by ¹H NMR with trimethyl(phenyl)silane as internal standard. The quantum yield calculation is then as following:

$$\Phi = \frac{\text{mole of product formed}}{\text{mole of photon absorbed}} = \frac{0.4 \times 10^{-3} \times 0.014}{1.22 \times 10^{-9} \times 14 \times 3600 \times 1} = 0.09$$

5.4.4 Single-Crystal X-Ray Diffraction Studies

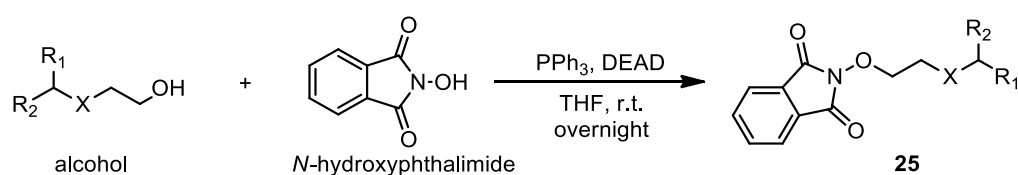
Crystals of the (*S*)-**16g** and (*S,R*)-**18a** were obtained from a solution of the compound in CH₂Cl₂ layered with n-hexane. Crystal data and details of the structure determination are presented in Appendices 6.7. The absolute configuration was determined.

5.5 Catalytic Asymmetric C(sp³)-H Functionalization under Photoredox Conditions by Radical Translocation and Stereocontrolled Alkene Addition

5.5.1 Synthesis of Substrates

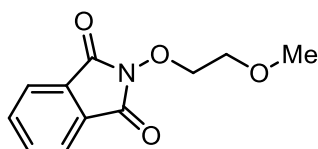
α,β -Unsaturated 2-acyl pyrazoles **24a-l**²³, *N*-alkoxyphthalimides **25i** and **25j**²⁴ were synthesized according to published procedures without any further change, while *N*-alkoxyphthalimides **25a-h**, **25k** and **25l** were synthesized according to the procedure with some modifications.²⁴

General procedure for the synthesis of *N*-alkoxyphthalimides.



To a solution of the corresponding alcohol (1.0 eq.), PPh₃ (1.2 eq.) and *N*-hydroxyphthalimide (1.2 eq.) in THF (0.2 M) was added diisopropyl azodicarboxylate (2.2 M in toluene, 1.2 eq.) over 5 min at room temperature under nitrogen atmosphere. The reaction mixture was stirred overnight at ambient temperature. Afterwards, the reaction was quenched with aqueous saturated NaHCO₃ and extracted with EtOAc. The organic layer was washed with brine. The combined organic layers were dried over anhydrous Na₂SO₄, and concentrated under reduced pressure. The residue was purified by flash chromatography on silica gel (EtOAc/hexane = 1:10 to 1:5) to produce the *N*-alkoxyphthalimides **25a-h**, **25k** and **25l**.

2-(2-Methoxyethoxy)isoindoline-1,3-dione (**25a**)



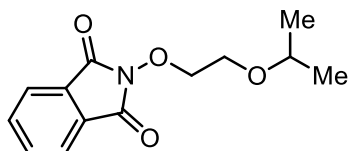
Following the general procedure, 2-methoxyethanol (0.761 g, 10.0 mmol) was converted to *N*-alkoxyphthalimide **25a** (1.858 g, 8.4 mmol, yield: 84%) as a white solid.

¹H NMR (300 MHz, CDCl₃) δ 7.83 (dd, *J* = 5.5, 3.1 Hz, 2H), 7.74 (dd, *J* = 5.5, 3.1 Hz, 2H), 4.39–4.31 (m, 2H), 3.80–3.72 (m, 2H), 3.37 (s, 3H).

¹³C NMR (75 MHz, CDCl₃) δ 163.4, 134.4, 129.0, 123.5, 70.4, 59.1.

All spectroscopic data were in agreement with the literature.²⁴

2-(2-Isopropoxyethoxy)isoindoline-1,3-dione (**25b**)



Following the general procedure, 2-isopropoxyethanol (0.520 g, 5.0 mmol) was converted to *N*-alkoxyphthalimide **25b** (1.122 g, 4.5 mmol, yield: 90%) as a white solid.

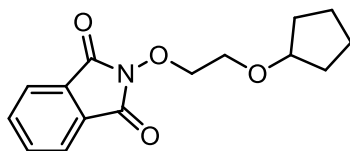
¹H NMR (300 MHz, CDCl₃) δ 7.83 (dd, $J = 5.5, 3.1$ Hz, 2H), 7.73 (dd, $J = 5.5, 3.1$ Hz, 2H), 4.40–4.32 (m, 2H), 3.83–3.70 (m, 2H), 3.59 (p, $J = 6.1$ Hz, 1H), 1.05 (d, $J = 6.1$ Hz, 6H).

¹³C NMR (75 MHz, CDCl₃) δ 163.5, 134.3, 129.1, 123.4, 72.1, 66.4, 21.8.

IR (film): ν (cm⁻¹) 2969, 2875, 1787, 1726, 1611, 1464, 1417, 1373, 1329, 1283, 1230, 1184, 1127, 1091, 979, 876, 787, 695, 624, 569, 516.

HRMS (ESI, m/z) calcd for C₁₃H₁₅NO₄Na [M+Na]⁺: 272.0893, found: 272.0894.

2-(2-(Cyclopentyloxy)ethoxy)isoindoline-1,3-dione (**25c**)



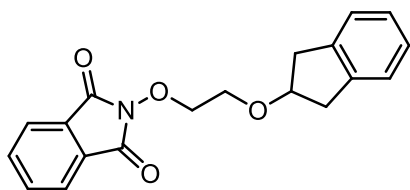
Following the general procedure, 2-(cyclopentyloxy)ethanol (0.978 g, 5.0 mmol) was converted to *N*-alkoxyphthalimide **25c** (1.211 g, 4.4 mmol, yield: 88%) as a white solid.

¹H NMR (300 MHz, CDCl₃) δ 7.83 (dd, $J = 5.5, 3.1$ Hz, 2H), 7.73 (dd, $J = 5.5, 3.1$ Hz, 2H), 4.42–4.29 (m, 2H), 3.95–3.82 (m, 1H), 3.80–3.69 (m, 2H), 1.73–1.31 (m, 8H).

¹³C NMR (75 MHz, CDCl₃) δ 163.5, 134.3, 129.1, 123.4, 82.1, 67.2, 32.0, 23.5.

IR (film): ν (cm⁻¹) 2951, 2868, 1788, 1727, 1611, 1462, 1369, 1290, 1235, 1183, 1116, 1026, 876, 786, 700, 518.

HRMS (ESI, m/z) calcd for C₁₅H₁₇NO₄Na [M+Na]⁺: 298.1050, found: 298.1050.

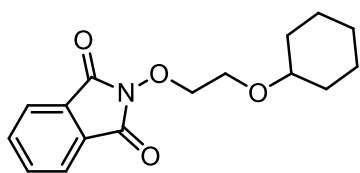
2-(2-((2,3-Dihydro-1*H*-inden-2-yl)oxy)ethoxy)isoindoline-1,3-dione (25d)

Following the general procedure, 2-((1-tosylazetid-3-yl)oxy)ethanol (0.660 g, 3.7 mmol) was converted to *N*-alkoxyphthalimide **25d** (1.135 g, 3.5 mmol, yield: 95%) as a white solid.

¹H NMR (300 MHz, CDCl₃) δ 7.90–7.62 (m, 4H), 7.19–7.05 (d, *J* = 1.5 Hz, 4H), 4.49–4.29 (m, 3H), 3.96–3.77 (m, 2H), 3.09 (dd, *J* = 16.2, 6.6 Hz, 2H), 2.87 (dd, *J* = 16.2, 4.6 Hz, 2H).

¹³C NMR (75 MHz, CDCl₃) δ 163.4, 140.7, 134.3, 128.9, 126.4, 124.6, 123.4, 81.0, 67.5, 39.0.

All spectroscopic data were in agreement with the literature.²⁴

2-(2-(Cyclohexyloxy)ethoxy)isoindoline-1,3-dione (25e)

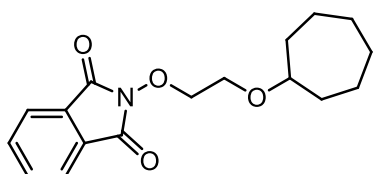
Following the general procedure, 2-(cyclohexyloxy)ethanol (0.596 g, 4.1 mmol) was converted to *N*-alkoxyphthalimide **25e** (0.664 g, 2.3 mmol, yield: 56%) as a white solid.

¹H NMR (300 MHz, CDCl₃) δ 7.82 (dd, *J* = 5.5, 3.1 Hz, 2H), 7.73 (dd, *J* = 5.5, 3.1 Hz, 2H), 4.42–4.28 (m, 2H), 3.88–3.65 (m, 2H), 3.35–3.15 (m, 1H), 1.77 (dq, *J* = 13.1, 8.4, 6.3 Hz, 2H), 1.68–1.57 (m, 2H), 1.52–1.36 (m, 1H), 1.30–1.01 (m, 5H).

¹³C NMR (75 MHz, CDCl₃) δ 163.4, 134.3, 129.1, 123.4, 77.9, 66.1, 31.8, 25.7, 23.9.

IR (film): ν (cm⁻¹) 2928, 2853, 1784, 1720, 1609, 1453, 1369, 1241, 1181, 1119, 1027, 983, 951, 851, 790, 698, 693, 609, 513.

HRMS (ESI, *m/z*) calcd for C₁₆H₁₉NO₄Na [M+Na]⁺: 312.1206, found: 312.1206.

2-(2-(Cycloheptyloxy)ethoxy)isoindoline-1,3-dione (25f)

Following the general procedure, 2-(cycloheptyloxy)ethanol (0.316 g, 2.0 mmol) was converted to *N*-alkoxyphthalimide **25f** (0.371 g, 1.2 mmol, yield: 61%) as a white solid.

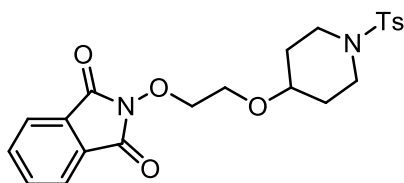
$^1\text{H NMR}$ (300 MHz, CDCl_3) δ 7.86–7.78 (m, 2H), 7.75–7.68 (m, 2H), 4.40–4.29 (m, 2H), 3.79–3.70 (m, 2H), 3.50–3.35 (m, 1H), 1.88–1.71 (m, 2H), 1.60–1.38 (m, 8H), 1.34–1.18 (m, 2H).

$^{13}\text{C NMR}$ (75 MHz, CDCl_3) δ 163.4, 134.3, 129.1, 123.3, 80.6, 77.3, 66.6, 33.5, 28.3, 22.8.

IR (film): ν (cm^{-1}) 2920, 2876, 1723, 1609, 1441, 1360, 1228, 1177, 1110, 1025, 1000, 987, 851, 789, 690, 610, 513.

HRMS (ESI, m/z) calcd for $\text{C}_{17}\text{H}_{21}\text{NO}_4\text{Na}$ $[\text{M}+\text{Na}]^+$: 326.1363, found: 326.1363.

2-(2-((1-Tosylpiperidin-4-yl)oxy)ethoxy)isoindoline-1,3-dione (**25g**)



Following the general procedure, 2-((1-tosylpiperidin-4-yl)oxy)ethanol (0.596 g, 4.0 mmol) was converted to *N*-alkoxyphthalimide **25g** (1.422 g, 3.2 mmol, yield: 80%) as a white solid.

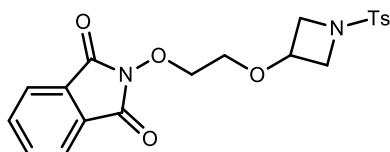
$^1\text{H NMR}$ (300 MHz, CDCl_3) δ 7.83–7.71 (m, 4H), 7.61 (d, $J = 8.2$ Hz, 2H), 7.30 (d, $J = 8.0$ Hz, 2H), 4.31–4.26 (m, 2H), 3.79–3.67 (m, 2H), 3.46–3.34 (m, 1H), 3.26–3.10 (m, 2H), 2.90–2.74 (m, 2H), 2.42 (s, 3H), 1.92–1.74 (m, 2H), 1.68–1.54 (m, 2H).

$^{13}\text{C NMR}$ (75 MHz, CDCl_3) δ 163.3, 143.4, 134.4, 133.5, 129.6, 128.9, 127.6, 123.4, 77.2, 73.5, 66.4, 43.1, 30.1, 21.5.

IR (film): ν (cm^{-1}) 2953, 2860, 1833, 1786, 1726, 1599, 1460, 1374, 1332, 1249, 1149, 1112, 1031, 938, 878, 800, 698, 647, 543.

HRMS (ESI, m/z) calcd for $\text{C}_{22}\text{H}_{24}\text{N}_2\text{O}_6\text{SNa}$ $[\text{M}+\text{Na}]^+$: 467.1247, found: 467.1244.

2-(2-((1-Tosylazetidid-3-yl)oxy)ethoxy)isoindoline-1,3-dione (**25h**)



Following the general procedure, 2-((1-tosylazetidid-3-yl)oxy)ethanol (0.600 g, 2.2 mmol) was converted to *N*-alkoxyphthalimide **25h** (0.559 g, 1.3 mmol, yield: 61%) as a white solid.

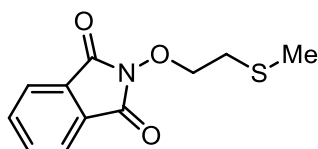
^1H NMR (300 MHz, CDCl_3) δ 7.89–7.77 (m, 4H), 7.74 (d, $J = 8.3$ Hz, 2H), 7.38 (d, $J = 8.0$ Hz, 2H), 4.32–4.19 (m, 3H), 4.03–3.92 (m, 2H), 3.72–3.67 (m, 2H), 3.66–3.58 (m, 2H), 2.48 (s, 3H).

^{13}C NMR (75 MHz, CDCl_3) δ 163.3, 144.0, 134.6, 131.7, 129.7, 128.8, 128.4, 123.6, 67.4, 67.3, 57.9, 21.6.

IR (film): ν (cm^{-1}) 3046, 2998, 2951, 2873, 1791, 1721, 1600, 1463, 1367, 1336, 1296, 1155, 1125, 1090, 1004, 956, 923, 872, 809, 748, 700, 665, 601, 745, 513.

HRMS (ESI, m/z) calcd for $\text{C}_{20}\text{H}_{20}\text{N}_2\text{O}_6\text{SNa}$ [$\text{M}+\text{Na}$] $^+$: 439.0931, found: 439.0934.

2-(2-(Methylthio)ethoxy)isoindoline-1,3-dione (25k)



Following the general procedure, 2-(methylthio)ethanol (0.461 g, 5.0 mmol) was converted to *N*-alkoxyphthalimide **25k** (1.103 g, 4.65 mmol, yield: 93%) as a white solid.

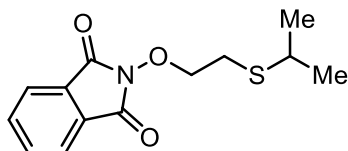
^1H NMR (300 MHz, CDCl_3) δ 7.85–7.60 (m, 4H), 4.27 (t, $J = 7.2$ Hz, 2H), 2.80 (t, $J = 7.2$ Hz, 2H), 2.10 (s, 3H).

^{13}C NMR (75 MHz, CDCl_3) δ 163.2, 134.3, 128.6, 123.3, 76.9, 31.3, 15.7.

IR (film): ν (cm^{-1}) 2922, 1780, 1721, 1611, 1458, 1362, 1293, 1181, 1118, 1075, 1021, 980, 872, 793, 759, 699, 597, 553, 515.

HRMS (ESI, m/z) calcd for $\text{C}_{11}\text{H}_{11}\text{NO}_3\text{SNa}$ [$\text{M}+\text{Na}$] $^+$: 260.0352, found: 260.0352.

2-(2-(Isopropylthio)ethoxy)isoindoline-1,3-dione (25l)



Following the general procedure, 2-(isopropylthio)ethanol (0.601 g, 5.0 mmol) was converted to *N*-alkoxyphthalimide **25l** (1.035 g, 3.9 mmol, yield: 78%) as a white solid.

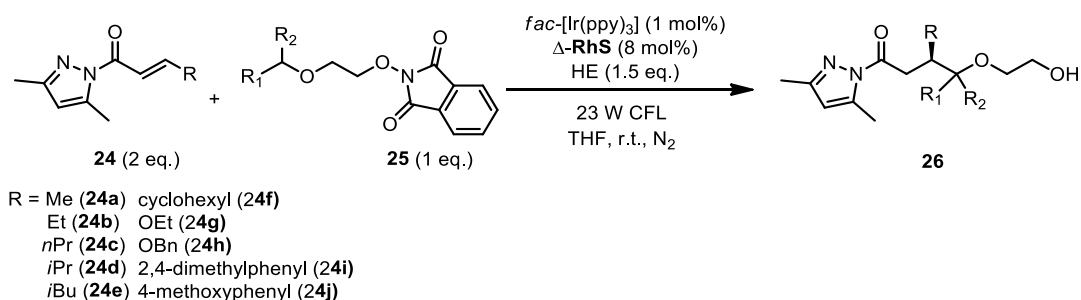
^1H NMR (300 MHz, CDCl_3) δ 7.92–7.80 (m, 2H), 7.78–7.70 (m, 2H), 4.32 (t, $J = 7.5$ Hz, 2H), 3.10–2.85 (m, 3H), 1.28 (d, $J = 6.7$ Hz, 6H).

^{13}C NMR (75 MHz, CDCl_3) δ 163.5, 134.5, 128.9, 123.6, 77.6, 35.4, 28.1, 23.5.

IR (film): ν (cm⁻¹) 2960, 2920, 2864, 1781, 1717, 1610, 1459, 1366, 1288, 1231, 1181, 1124, 1077, 1014, 976, 872, 784, 696, 606, 550, 515.

HRMS (ESI, m/z) calcd for C₁₃H₁₅NO₃SNa [M+Na]⁺: 288.0665, found: 288.0665.

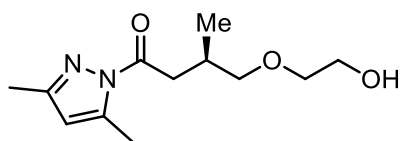
5.5.2 Rhodium-Catalyzed Photoredox Reactions



General catalysis procedure. A dried 10 mL Schlenk tube was charged with the catalyst *fac*-[Ir(ppy)₃] (1 mol%), Δ -RhS (8 mol%), Hantzsch ester (0.30 mmol, 1.5 eq.), 2-acyl pyrazoles **24a-j** (0.40 mmol, 2.0 eq.), and the corresponding *N*-alkoxyphthalimides **25a-l** (0.20 mmol, 1.0 eq.). The tube was purged with nitrogen and THF (1.0 mL) was added *via* syringe. The reaction mixture was degassed *via* freeze-pump-thaw for three cycles. After the mixture was thoroughly degassed, the tube was sealed and positioned approximately 5 cm from a 23 W compact fluorescent lamp (CFL). The reaction was stirred at room temperature for the indicated time (monitored by TLC) under nitrogen atmosphere. Afterwards, the mixture was diluted with DCM (2 mL). The combined organic layers were concentrated under reduced pressure. The residue was purified by flash chromatography on silica gel (EtOAc/hexane = 1:10 to 1:5) to afford the products **26a-j**, **26m-y**. Racemic samples were obtained by carrying out the reactions with *rac*-RhS. The enantiomeric excess was determined by chiral HPLC analysis.

Exemplary reaction setup:



(R)-1-(3,5-Dimethyl-1H-pyrazol-1-yl)-4-(2-hydroxyethoxy)-3-methylbutan-1-one (26a)

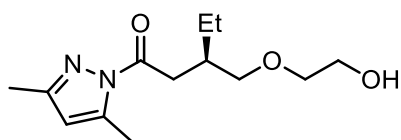
Starting from 2-acyl pyrazole **24a** (65.7 mg, 0.40 mmol) and *N*-alkoxyphthalimide **25a** (44.2 mg, 0.20 mmol) according to the general procedure to give **26a** as a pale yellow oil (33.6 mg, 0.140 mmol, yield: 70%). Enantiomeric excess established by HPLC analysis using a Chiralpak OD-H column, *ee* = 92% (HPLC: OD-H, 254 nm, hexane/isopropanol = 95:5, flow rate 1.0 mL/min, 25 °C, *t_r* (major) = 8.1 min, *t_r* (minor) = 8.7 min). $[\alpha]_{\text{D}}^{25} = +14.5^{\circ}$ (*c* 0.4, CH₂Cl₂).

¹H NMR (300 MHz, CDCl₃) δ 5.94 (s, 1H), 3.68–3.60 (m, 2H), 3.56–3.46 (m, 2H), 3.44–3.32 (m, 2H), 3.24 (dd, *J* = 15.9, 6.8 Hz, 1H), 2.90 (dd, *J* = 15.9, 6.8 Hz, 1H), 2.56–2.46 (m, 4H), 2.44–2.37 (m, 1H), 2.22 (s, 3H), 1.02 (d, *J* = 6.8 Hz, 3H).

¹³C NMR (75 MHz, CDCl₃) δ 173.5, 151.8, 144.0, 111.0, 75.8, 72.1, 61.7, 39.5, 30.6, 17.2, 14.6, 13.7.

IR (film): ν (cm⁻¹) 3477, 2993, 2923, 2861, 1724, 1582, 1479, 1445, 1384, 1345, 1251, 1212, 1117, 1064, 1028, 995, 968, 893, 845, 738, 695, 614, 589, 554, 507.

HRMS (ESI, *m/z*) calcd for C₁₂H₂₀N₂O₃Na [M+Na]⁺: 263.1366, found: 263.1367.

(R)-1-(3,5-Dimethyl-1H-pyrazol-1-yl)-3-((2-hydroxyethoxy)methyl)pentan-1-one (26b)

Starting from 2-acyl pyrazole **24b** (71.3 mg, 0.40 mmol) and *N*-alkoxyphthalimide **25a** (44.2 mg, 0.20 mmol) according to the general procedure to give **26b** as a pale yellow oil (34.1 mg, 0.134 mmol, yield: 67%). Enantiomeric excess established by HPLC analysis using a Chiralpak OD-H column, *ee* = 93% (HPLC: OD-H, 254 nm, hexane/isopropanol = 95:5, flow rate 1.0 mL/min, 25 °C, *t_r* (major) = 7.1 min, *t_r* (minor) = 7.7 min). $[\alpha]_{\text{D}}^{25} = +14.0^{\circ}$ (*c* 0.3, CH₂Cl₂).

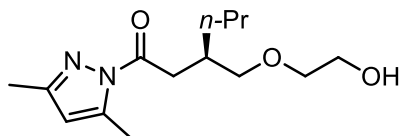
¹H NMR (300 MHz, CDCl₃) δ 5.95 (s, 1H), 3.65–3.56 (m, 2H), 3.54–3.35 (m, 4H), 3.22 (dd, *J* = 15.9, 8.0 Hz, 1H), 2.99 (dd, *J* = 15.9, 5.4 Hz, 1H), 2.53 (s, 3H), 2.41–2.26 (m, 2H), 2.22 (s, 3H), 1.55–1.35 (m, 2H), 0.95 (t, *J* = 7.5 Hz, 3H).

¹³C NMR (75 MHz, CDCl₃) δ 173.9, 151.8, 144.0, 111.1, 73.7, 72.1, 61.7, 37.5, 37.3, 24.5, 14.6, 13.7, 11.4.

IR (film): ν (cm⁻¹) 3404, 2925, 2867, 1721, 1581, 1457, 1378, 1337, 1257, 1119, 1063, 999, 964, 890, 804, 744, 652, 588.

HRMS (ESI, m/z) calcd for C₁₃H₂₂N₂O₃Na [M+Na]⁺: 277.1523, found: 277.1523.

(R)-1-(3,5-Dimethyl-1H-pyrazol-1-yl)-3-((2-hydroxyethoxy)methyl)hexan-1-one (26c)



Starting from 2-acyl pyrazole **24c** (76.9 mg, 0.40 mmol) and *N*-alkoxyphthalimide **25a** (44.2 mg, 0.20 mmol) according to the general procedure to give **26c** as a pale yellow oil (35.0 mg, 0.130 mmol, yield: 65%). Enantiomeric excess established by HPLC analysis using a Chiralpak OD-H column, *ee* = 92% (HPLC: OD-H, 254 nm, hexane/isopropanol = 95:5, flow rate 1.0 mL/min, 25 °C, t_r (major) = 6.5 min, t_r (minor) = 6.8 min). $[\alpha]_D^{25} = +27.5^\circ$ (*c* 0.2, CH₂Cl₂).

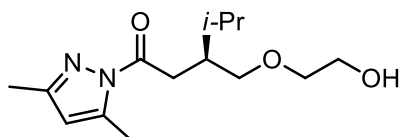
¹H NMR (300 MHz, CDCl₃) δ 5.95 (s, 1H), 3.64–3.51 (m, 2H), 3.53–3.44 (m, 3H), 3.43–3.35 (m, 4H), 3.21 (dd, *J* = 15.8, 8.1 Hz, 1H), 2.99 (dd, *J* = 15.8, 5.2 Hz, 1H), 2.53 (s, 3H), 2.48–2.28 (m, 2H), 2.22 (s, 3H), 1.43–1.32 (m, 4H), 0.96–0.87 (m, 3H).

¹³C NMR (75 MHz, CDCl₃) 174.0, 151.8, 144.0, 111.1, 74.2, 72.1, 61.7, 37.9, 35.5, 34.0, 20.1, 14.6, 14.2, 13.7.

IR (film): ν (cm⁻¹) 3433, 2955, 2926, 2866, 1721, 1581, 1458, 1409, 1378, 1333, 1257, 1174, 1119, 1061, 992, 963, 890, 802, 742, 649, 589, 530.

HRMS (ESI, m/z) calcd for C₁₄H₂₄N₂O₃Na [M+Na]⁺: 291.1679, found: 291.1680.

(S)-1-(3,5-Dimethyl-1H-pyrazol-1-yl)-3-((2-hydroxyethoxy)methyl)-4-methylpentan-1-one (26d)



Starting from 2-acyl pyrazole **24d** (78.9 mg, 0.40 mmol) and *N*-alkoxyphthalimide **25a** (44.2 mg, 0.20 mmol) according to the general procedure to give **26d** as a pale yellow oil (33.3 mg, 0.124 mmol, yield: 62%). Enantiomeric excess established by HPLC analysis using a Chiralpak OD-H column, *ee* = 94% (HPLC: OD-H, 254 nm, hexane/isopropanol = 95:5, flow rate 1.0 mL/min, 25 °C, t_r (major) = 6.8 min, t_r (minor) = 7.5 min). $[\alpha]_D^{25} = -8.4^\circ$ (*c* 0.3, CH₂Cl₂).

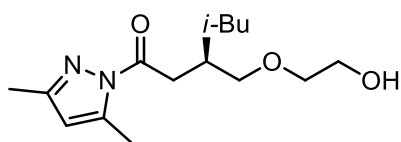
^1H NMR (300 MHz, CDCl_3) δ 5.94 (s, 1H), 3.61–3.38 (m, 6H), 3.20 (dd, $J = 15.7, 8.8$ Hz, 1H), 2.98 (dd, $J = 15.7, 4.4$ Hz, 1H), 2.52 (s, 3H), 2.45–2.26 (m, 2H), 2.22 (s, 3H), 1.91–1.73 (m, 1H), 0.95 (d, $J = 6.9$ Hz, 6H).

^{13}C NMR (75 MHz, CDCl_3) δ 174.4, 151.8, 144.0, 111.1, 72.6, 72.1, 61.6, 41.5, 35.2, 29.1, 19.8, 19.6, 14.6, 13.7.

IR (film): ν (cm^{-1}) 3435, 2950, 2923, 2876, 1725, 1578, 1467, 1411, 1389, 1333, 1257, 1170, 1119, 1065, 998, 956, 891, 802, 743, 649, 530.

HRMS (ESI, m/z) calcd for $\text{C}_{14}\text{H}_{24}\text{N}_2\text{O}_3\text{Na}$: $[\text{M}+\text{Na}]^+$: 291.1679, found: 291.1680.

(R)-1-(3,5-Dimethyl-1H-pyrazol-1-yl)-3-((2-hydroxyethoxy)methyl)-5-methylhexan-1-one (26e)



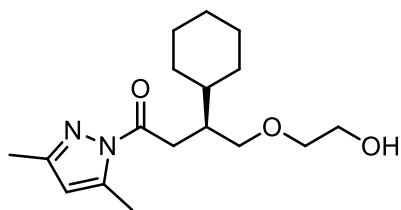
Starting from 2-acyl pyrazole **24e** (82.5 mg, 0.40 mmol) and *N*-alkoxyphthalimide **25a** (44.2 mg, 0.20 mmol) according to the general procedure to give **26e** as a pale yellow solid (35.0 mg, 0.124 mmol, yield: 62%). Enantiomeric excess established by HPLC analysis using a Chiralpak OD-H column, $ee = 91\%$ (HPLC: OD-H, 254 nm, hexane/isopropanol = 98:2, flow rate 0.5 mL/min, 25 °C, t_r (major) = 18.9 min, t_r (minor) = 19.6 min). $[\alpha]_{\text{D}}^{25} = +8.0^\circ$ (c 0.4, CH_2Cl_2).

^1H NMR (300 MHz, CDCl_3) δ 5.95 (s, 1H), 3.66–3.55 (m, 2H), 3.53–3.41 (m, 3H), 3.40–3.31 (m, 1H), 3.17 (dd, $J = 15.5, 8.5$ Hz, 1H), 2.99 (dd, $J = 15.5, 4.7$ Hz, 1H), 2.58–2.32 (m, 5H), 2.22 (s, 3H), 1.77–1.58 (m, $J = 6.7$ Hz, 1H), 1.24 (t, $J = 7.1$ Hz, 2H), 0.92 (d, $J = 6.6$ Hz, 6H).

^{13}C NMR (75 MHz, CDCl_3) δ 174.1, 151.8, 144.0, 111.1, 74.5, 72.2, 61.7, 41.2, 38.4, 33.8, 25.4, 22.8, 22.6, 14.6, 13.7.

IR (film): ν (cm^{-1}) 3435, 2953, 2927, 2868, 1722, 1622, 1580, 1464, 1410, 1377, 1333, 1258, 1170, 1119, 1058, 1000, 962, 888, 803, 746, 648, 588, 550.

HRMS (ESI, m/z) calcd for $\text{C}_{15}\text{H}_{26}\text{N}_2\text{O}_3\text{Na}$ $[\text{M}+\text{Na}]^+$: 305.1836, found: 305.1837.

(S)-3-Cyclohexyl-1-(3,5-dimethyl-1H-pyrazol-1-yl)-4-(2-hydroxyethoxy)butan-1-one (26f)

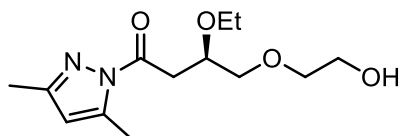
Starting from 2-acyl pyrazole **24f** (92.9 mg, 0.40 mmol) and *N*-alkoxyphthalimide **25a** (44.2 mg, 0.20 mmol) according to the general procedure to give **26f** as a white solid (45.6 mg, 0.148 mmol, yield: 74%). Enantiomeric excess established by HPLC analysis using a Chiralpak OD-H column, *ee* = 91% (HPLC: OD-H, 254 nm, hexane/isopropanol = 95:5, flow rate 1.0 mL/min, 25 °C, t_r (major) = 6.1 min, t_r (minor) = 6.8 min). $[\alpha]_D^{25} = -4.3^\circ$ (*c* 0.5, CH₂Cl₂).

¹H NMR (300 MHz, CDCl₃) δ 5.94 (s, 1H), 3.62–3.49 (m, 3H), 3.48–3.42 (m, 2H), 3.22 (dd, *J* = 15.8, 8.7 Hz, 1H), 3.00 (dd, *J* = 15.8, 4.5 Hz, 1H), 2.52 (s, 3H), 2.46–2.27 (m, 2H), 2.22 (s, 3H), 1.81–1.59 (m, 5H), 1.54–1.38 (m, 1H), 1.34–0.98 (m, 6H).

¹³C NMR (75 MHz, CDCl₃) δ 174.5, 151.8, 144.0, 111.0, 72.5, 72.1, 61.6, 40.9, 39.5, 35.6, 30.3, 30.2, 26.63, 26.61, 26.5, 14.6, 13.7.

IR (film): ν (cm⁻¹) 3424, 2922, 2853, 1723, 1581, 1446, 1410, 1378, 1333, 1237, 1172, 1118, 1057, 963, 889, 801, 748, 649, 588.

HRMS (ESI, *m/z*) calcd for C₁₇H₂₈N₂O₃Na [M+Na]⁺: 331.1992, found: 331.1994.

(R)-1-(3,5-Dimethyl-1H-pyrazol-1-yl)-3-ethoxy-4-(2-hydroxyethoxy)butan-1-one (26g)

Starting from 2-acyl pyrazole **24g** (77.7 mg, 0.40 mmol) and *N*-alkoxyphthalimide **25a** (44.2 mg, 0.20 mmol) according to the general procedure to give **26g** as a pale yellow oil (43.2 mg, 0.160 mmol, yield: 80%). Enantiomeric excess established by HPLC analysis using a Chiralpak IC column, *ee* = 97% (HPLC: IC, 254 nm, hexane/isopropanol = 95:5, flow rate 1.0 mL/min, 25 °C, t_r (major) = 30.0 min, t_r (minor) = 32.3 min). $[\alpha]_D^{25} = -11.0^\circ$ (*c* 0.5, CH₂Cl₂).

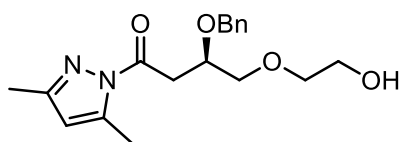
^1H NMR (300 MHz, CDCl_3) δ 5.94 (s, 1H), 4.21–4.05 (m, 1H), 3.72–3.66 (m, 2H), 3.64–3.55 (m, 5H), 3.41 (dd, $J = 16.0, 6.5$ Hz, 1H), 3.29 (dd, $J = 16.1, 6.1$ Hz, 1H), 3.15 (q, $J = 7.3, 6.3$ Hz, 1H), 2.52 (s, 3H), 2.31–2.11 (m, 4H), 1.16 (t, $J = 7.0$ Hz, 3H).

^{13}C NMR (75 MHz, CDCl_3) δ 171.8, 152.0, 144.0, 111.2, 74.9, 72.8, 72.7, 65.5, 61.7, 38.2, 15.4, 14.4, 13.7.

IR (film): ν (cm^{-1}) 3414, 2971, 2925, 2873, 1721, 1582, 1440, 1380, 1335, 1249, 1121, 1063, 995, 963, 846, 747, 662, 592, 588.

HRMS (ESI, m/z) calcd for $\text{C}_{13}\text{H}_{22}\text{N}_2\text{O}_4\text{Na}$ [$\text{M}+\text{Na}$] $^+$: 293.1472, found: 293.1473.

(R)-3-(Benzyloxy)-1-(3,5-dimethyl-1H-pyrazol-1-yl)-4-(2-hydroxyethoxy)butan-1-one (26h)



Starting from 2-acyl pyrazole **24h** (102.5 mg, 0.40 mmol) and *N*-alkoxyphthalimide **25a** (44.2 mg, 0.20 mmol) according to the general procedure to give **26h** as a white solid (52.0 mg, 0.156 mmol, yield: 78%). Enantiomeric excess established by HPLC analysis using a Chiralpak AD-H column, $ee = 97\%$ (HPLC: AD-H, 254 nm, hexane/isopropanol = 94:6, flow rate 1.0 mL/min, 25 °C, t_r (minor) = 20.0 min, t_r (major) = 22.0 min). $[\alpha]_D^{25} = -6.1^\circ$ (c 0.5, CH_2Cl_2).

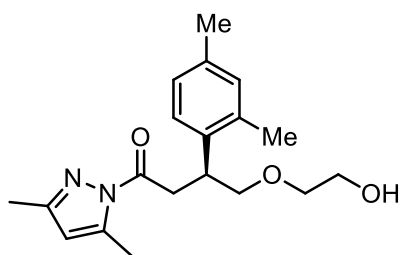
^1H NMR (300 MHz, CDCl_3) δ 7.41–7.20 (m, 5H), 5.99 (s, 1H), 4.78–4.64 (m, 2H), 4.36–4.25 (m, 1H), 3.75–3.65 (m, 4H), 3.64–3.58 (m, 2H), 3.53 (dd, $J = 15.9, 6.7$ Hz, 1H), 3.39 (dd, $J = 15.9, 6.0$ Hz, 1H), 2.74–2.62 (m, 1H), 2.56 (s, 3H), 2.25 (s, 3H).

^{13}C NMR (75 MHz, CDCl_3) δ 171.6, 152.1, 144.0, 138.3, 128.3, 127.8, 127.6, 111.2, 74.8, 72.8, 72.6, 72.2, 61.7, 38.3, 14.5, 13.7.

IR (film): ν (cm^{-1}) 3477, 2993, 2923, 2861, 1724, 1582, 1479, 1445, 1384, 1345, 1251, 1212, 1117, 1064, 1028, 995, 968, 893, 845, 738, 695, 614, 589, 554, 507.

HRMS (ESI, m/z) calcd for $\text{C}_{18}\text{H}_{24}\text{N}_2\text{O}_4\text{Na}$ [$\text{M}+\text{Na}$] $^+$: 355.1628, found: 355.1625.

(S)-1-(3,5-Dimethyl-1H-pyrazol-1-yl)-3-(2,4-dimethylphenyl)-4-(2-hydroxyethoxy)butan-1-one
(26i)



Starting from 2-acyl pyrazole **24i** (101.7 mg, 0.40 mmol) and *N*-alkoxyphthalimide **25a** (44.2 mg, 0.20 mmol) according to the general procedure to give **26i** as a white solid (33.7 mg, 0.102 mmol, yield: 51%). Enantiomeric excess established by HPLC analysis using a Chiralpak OD-H column, *ee* = 91% (HPLC: OD-H, 254 nm, hexane/isopropanol = 95:5, flow rate 1.0 mL/min, 25 °C, *t_r* (minor) = 8.9 min, *t_r* (major) = 12.1 min). $[\alpha]_D^{25} = -24.6^\circ$ (*c* 0.3, CH₂Cl₂).

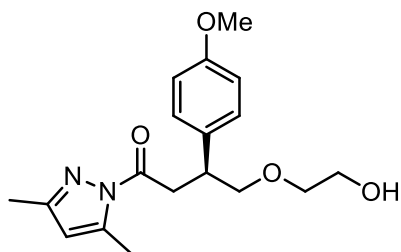
¹H NMR (300 MHz, CDCl₃) δ 7.14 (d, *J* = 7.7 Hz, 1H), 7.05–6.91 (m, 2H), 5.95 (s, 1H), 4.05–3.87 (m, 1H), 3.69–3.42 (m, 7H), 3.37 (dd, *J* = 15.9, 6.3 Hz, 1H), 2.50 (s, 3H), 2.42 (s, 3H), 2.33–2.21 (d, *J* = 10.3 Hz, 7H).

¹³C NMR (75 MHz, CDCl₃) δ 173.1, 151.9, 144.0, 136.7, 136.1, 136.0, 131.3, 126.8, 126.1, 111.0, 75.0, 72.2, 61.6, 39.1, 37.0, 20.9, 19.6, 14.5, 13.7.

IR (film): ν (cm⁻¹) 3429, 2923, 2863, 1722, 1616, 1580, 1501, 1445, 1409, 1377, 1339, 1256, 1169, 1118, 1056, 1000, 961, 884, 813, 739, 702, 654, 579.

HRMS (ESI, *m/z*) calcd for C₁₉H₂₆N₂O₃Na [M+Na]⁺: 353.1836, found: 353.1832.

(S)-1-(3,5-Dimethyl-1H-pyrazol-1-yl)-4-(2-hydroxyethoxy)-3-(4-methoxyphenyl)butan-1-one
(26j)



Starting from 2-acyl pyrazole **2j** (102.5 mg, 0.40 mmol) and *N*-alkoxyphthalimide **25a** (44.2 mg, 0.20 mmol) according to the general procedure to give **26j** as a white solid (37.9 mg, 0.114 mmol, yield: 57%). Enantiomeric excess established by HPLC analysis using a Chiralpak OD-H column, *ee* = 82%

(HPLC: OD-H, 254 nm, hexane/isopropanol = 95:5, flow rate 1.0 mL/min, 25 °C, t_r (major) = 17.3 min, t_r (minor) = 20.2 min). $[\alpha]_D^{25} = -8.0^\circ$ (c 0.4, CH_2Cl_2).

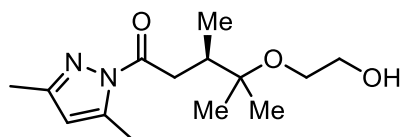
^1H NMR (300 MHz, CDCl_3) δ 7.22 (d, $J = 8.7$ Hz, 2H), 6.84 (d, $J = 8.7$ Hz, 2H), 5.93 (s, 1H), 3.77 (s, 3H), 3.69–3.58 (m, 6H), 3.54–3.47 (m, 2H), 3.44–3.30 (m, 1H), 2.48 (s, 3H), 2.38–2.28 (m, 1H), 2.24 (s, 3H).

^{13}C NMR (75 MHz, CDCl_3) δ 172.8, 158.4, 151.9, 144.1, 133.7, 128.7, 113.9, 111.1, 75.3, 72.1, 61.6, 55.2, 41.1, 38.8, 14.5, 13.8.

IR (film): ν (cm^{-1}) 3450, 2924, 2880, 1726, 1610, 1582, 1501, 1453, 1375, 1324, 1242, 1175, 1112, 1032, 960, 891, 823, 745, 634, 561, 527.

HRMS (ESI, m/z) calcd for $\text{C}_{18}\text{H}_{24}\text{N}_2\text{O}_4\text{Na}$ $[\text{M}+\text{Na}]^+$: 355.1625, found: 355.1624.

(*R*)-1-(3,5-Dimethyl-1*H*-pyrazol-1-yl)-4-(2-hydroxyethoxy)-3,4-dimethylpentan-1-one (26m)



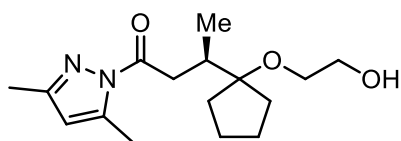
Starting from 2-acyl pyrazole **24a** (65.7 mg, 0.40 mmol) and *N*-alkoxyphthalimide **25b** (49.9 mg, 0.20 mmol) according to the general procedure to give **26m** as a white solid (45.1 mg, 0.168 mmol, yield: 84%). Enantiomeric excess established by HPLC analysis using a Chiralpak OD-H column, $ee = 91\%$ (HPLC: OD-H, 254 nm, hexane/isopropanol = 95:5, flow rate 1.0 mL/min, 25 °C, t_r (major) = 6.3 min, t_r (minor) = 6.7 min). $[\alpha]_D^{25} = +25.2^\circ$ (c 0.5, CH_2Cl_2).

^1H NMR (300 MHz, CDCl_3) δ 5.93 (s, 1H), 3.63–3.53 (m, 2H), 3.50–3.36 (m, 3H), 2.70 (dd, $J = 15.5$, 8.4 Hz, 1H), 2.52 (s, 3H), 2.49–2.35 (m, 2H), 2.22 (s, 3H), 1.16 (d, $J = 14.2$ Hz, 6H), 0.98 (d, $J = 6.9$ Hz, 3H).

^{13}C NMR (75 MHz, CDCl_3) δ 174.4, 151.7, 144.0, 111.0, 77.2, 62.2, 62.1, 38.7, 37.6, 23.7, 20.6, 15.9, 14.6, 13.7.

IR (film): ν (cm^{-1}) 3425, 2974, 2873, 1721, 1581, 1514, 1461, 1376, 1326, 1246, 1153, 1049, 992, 960, 927, 888, 801, 757, 707, 657, 561, 524.

HRMS (ESI, m/z) calcd for $\text{C}_{14}\text{H}_{24}\text{N}_2\text{O}_3\text{Na}$ $[\text{M}+\text{Na}]^+$: 291.1679, found: 291.1680.

(R)-1-(3,5-Dimethyl-1H-pyrazol-1-yl)-3-(1-(2-hydroxyethoxy)cyclopentyl)butan-1-one (26n)

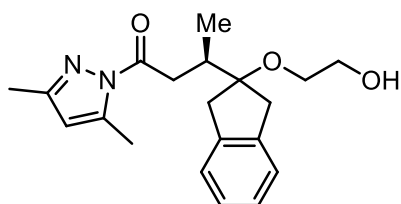
Starting from 2-acyl pyrazole **24a** (65.7 mg, 0.40 mmol) and *N*-alkoxyphthalimide **25c** (55.1 mg, 0.20 mmol) according to the general procedure to give **26n** as a pale yellow oil (43.0 mg, 0.146 mmol, yield: 73%). Enantiomeric excess established by HPLC analysis using a Chiralpak OD-H column, *ee* = 93% (HPLC: OD-H, 254 nm, hexane/isopropanol = 95:5, flow rate 1.0 mL/min, 25 °C, *t_r* (major) = 6.7 min, *t_r* (minor) = 7.7 min). $[\alpha]_{\text{D}}^{25} = +24.5^{\circ}$ (*c* 0.2, CH₂Cl₂).

¹H NMR (300 MHz, CDCl₃) δ 5.94 (s, 1H), 3.71–3.63 (m, 2H), 3.55–3.47 (m, 1H), 3.46–3.35 (m, 2H), 2.81 (dd, *J* = 15.6, 9.7 Hz, 1H), 2.68–2.57 (m, 1H), 2.53 (s, 3H), 2.45–2.28 (m, 1H), 2.22 (s, 3H), 1.83–1.52 (m, 8H), 0.99 (d, *J* = 6.8 Hz, 3H).

¹³C NMR (75 MHz, CDCl₃) δ 174.2, 151.8, 144.0, 111.0, 89.6, 62.43, 62.36, 38.3, 34.6, 32.8, 32.5, 24.7, 24.6, 15.7, 14.6, 13.7.

IR (film): ν (cm⁻¹) 3422, 2957, 2870, 1721, 1581, 1456, 1409, 1377, 1326, 1243, 1180, 1139, 1055, 965, 893, 803, 755, 658, 613, 553.

HRMS (ESI, *m/z*) calcd for C₁₆H₂₆N₂O₃Na [M+Na]⁺: 317.1836, found: 317.1838.

(R)-1-(3,5-Dimethyl-1H-pyrazol-1-yl)-3-(2-(2-hydroxyethoxy)-2,3-dihydro-1H-inden-2-yl)butan-1-one (26o)

Starting from 2-acyl pyrazole **24a** (65.7 mg, 0.40 mmol) and *N*-alkoxyphthalimide **25d** (64.7 mg, 0.20 mmol) according to the general procedure to give **26o** as a pale yellow oil (52.0 mg, 0.152 mmol, yield: 76%). Enantiomeric excess established by HPLC analysis using a Chiralpak OD-H column, *ee* = 94% (HPLC: OD-H, 254 nm, hexane/isopropanol = 95:5, flow rate 1.0 mL/min, 25 °C, *t_r* (major) = 13.7 min, *t_r* (minor) = 15.8 min). $[\alpha]_{\text{D}}^{25} = +4.8^{\circ}$ (*c* 0.6, CH₂Cl₂).

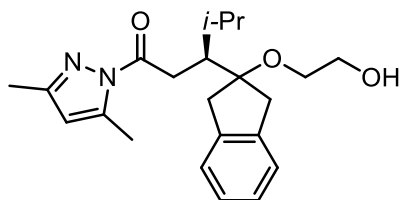
^1H NMR (300 MHz, CDCl_3) δ 7.24–7.09 (m, 4H), 5.96 (s, 1H), 3.56–3.41 (m, 3H), 3.36–3.20 (m, 2H), 3.19–3.04 (m, 4H), 2.96 (dd, $J = 15.7, 8.6$ Hz, 1H), 2.75–2.60 (m, 1H), 2.55 (s, 3H), 2.42–2.30 (m, 1H), 2.24 (s, 3H), 1.06 (d, $J = 6.8$ Hz, 3H).

^{13}C NMR (75 MHz, CDCl_3) δ 174.0, 151.8, 144.0, 141.5, 141.3, 126.59, 126.55, 124.04, 124.01, 111.1, 88.7, 63.9, 62.2, 41.3, 40.4, 38.3, 38.2, 16.0, 14.6, 13.8.

IR (film): ν (cm^{-1}) 3426, 2928, 2871, 1721, 1581, 1514, 1460, 1410, 1377, 1326, 1289, 1217, 1092, 1044, 964, 888, 802, 740, 655, 582, 551.

HRMS (ESI, m/z) calcd for $\text{C}_{20}\text{H}_{26}\text{N}_2\text{O}_3\text{Na}$ $[\text{M}+\text{Na}]^+$: 365.1836, found: 365.1835.

(S)-1-(3,5-Dimethyl-1H-pyrazol-1-yl)-3-(2-(2-hydroxyethoxy)-2,3-dihydro-1H-inden-2-yl)-4-methylpentan-1-one (26p)



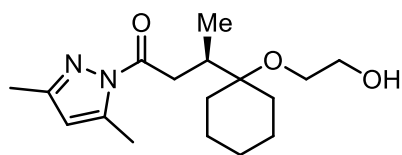
Starting from 2-acyl pyrazole **24d** (78.9 mg, 0.40 mmol) and *N*-alkoxyphthalimide **25d** (64.7 mg, 0.20 mmol) according to the general procedure to give **26p** as a pale yellow oil (58.1 mg, 0.170 mmol, yield: 85%). Enantiomeric excess established by HPLC analysis using a Chiralpak OD-H column, $ee = 97\%$ (HPLC: OD-H, 254 nm, hexane/isopropanol = 95:5, flow rate 1.0 mL/min, 25 °C, t_r (major) = 9.3 min, t_r (minor) = 10.8 min). $[\alpha]_{\text{D}}^{25} = -9.1^\circ$ (c 0.6, CH_2Cl_2).

^1H NMR (300 MHz, CDCl_3) δ 7.21–7.09 (m, 4H), 5.98 (s, 1H), 3.60–3.39 (m, 3H), 3.22–3.09 (m, 5H), 3.05–2.93 (m, 2H), 2.65–2.58 (m, 1H), 2.56 (s, 3H), 2.48–2.39 (m, 1H), 2.26 (s, 3H), 2.20–2.09 (m, 1H), 1.00 (d, $J = 6.9$ Hz, 6H).

^{13}C NMR (75 MHz, CDCl_3) δ 175.3, 152.0, 144.1, 141.6, 141.4, 126.6, 126.5, 123.83, 123.79, 111.2, 89.5, 64.0, 62.2, 49.0, 42.6, 41.5, 31.5, 28.4, 23.6, 18.7, 14.7, 13.8.

IR (film): ν (cm^{-1}) 3445, 2929, 2871, 1722, 1581, 1461, 1411, 1379, 1314, 1279, 1234, 1173, 1094, 1053, 989, 961, 803, 737, 674, 583, 540.

HRMS (ESI, m/z) calcd for $\text{C}_{22}\text{H}_{30}\text{N}_2\text{O}_3\text{Na}$ $[\text{M}+\text{Na}]^+$: 393.2149, found: 393.2149.

(R)-1-(3,5-Dimethyl-1H-pyrazol-1-yl)-3-(1-(2-hydroxyethoxy)cyclohexyl)butan-1-one (26q)

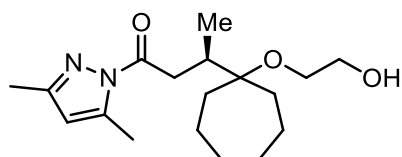
Starting from 2-acyl pyrazole **24a** (65.7 mg, 0.40 mmol) and *N*-alkoxyphthalimide **25e** (57.9 mg, 0.20 mmol) according to the general procedure to give **26q** as a pale yellow oil (50.0 mg, 0.162 mmol, yield: 81%). Enantiomeric excess established by HPLC analysis using a Chiralpak OD-H column, *ee* = 94% (HPLC: OD-H, 254 nm, hexane/isopropanol = 99:1, flow rate 1.0 mL/min, 25 °C, *t_r* (major) = 14.2 min, *t_r* (minor) = 15.5 min). $[\alpha]_{\text{D}}^{25} = +8.5^{\circ}$ (*c* 0.6, CH₂Cl₂).

¹H NMR (300 MHz, CDCl₃) δ 5.93 (s, 1H), 3.80–3.68 (m, 2H), 3.56–3.46 (m, 1H), 3.44–3.30 (m, 2H), 2.80 (dd, *J* = 15.8, 10.8 Hz, 1H), 2.58–2.36 (m, 5H), 2.21 (s, 3H), 1.72–1.33 (m, 9H), 1.22–1.07 (m, 1H), 0.94 (d, *J* = 6.9 Hz, 3H).

¹³C NMR (75 MHz, CDCl₃) δ 174.4, 151.7, 144.0, 111.0, 77.1, 62.6, 60.3, 37.0, 34.6, 30.1, 29.9, 25.8, 21.6, 21.4, 15.0, 14.6, 13.7.

IR (film): ν (cm⁻¹) 3424, 2930, 2860, 1722, 1581, 1449, 1410, 1377, 1327, 1218, 1146, 1055, 965, 899, 804, 755, 705, 659, 600, 548.

HRMS (ESI, *m/z*) calcd for C₁₇H₂₈N₂O₃Na [M+Na]⁺: 331.1992, found: 331.1993.

(R)-1-(3,5-Dimethyl-1H-pyrazol-1-yl)-3-(1-(2-hydroxyethoxy)cycloheptyl)butan-1-one (26r)

Starting from 2-acyl pyrazole **24a** (65.7 mg, 0.40 mmol) and *N*-alkoxyphthalimide **25f** (60.7 mg, 0.20 mmol) according to the general procedure to give **26r** as a pale yellow oil (40.0 mg, 0.124 mmol, yield: 62%). Enantiomeric excess established by HPLC analysis using a Chiralpak OD-H column, *ee* = 95% (HPLC: OD-H, 254 nm, hexane/isopropanol = 95:5, flow rate 1.0 mL/min, 25 °C, *t_r* (major) = 5.7 min, *t_r* (minor) = 6.3 min). $[\alpha]_{\text{D}}^{25} = +21.1^{\circ}$ (*c* 0.4, CH₂Cl₂).

¹H NMR (300 MHz, CDCl₃) δ 5.93 (s, 1H), 3.71 (t, *J* = 4.7 Hz, 2H), 3.57–3.48 (m, 1H), 3.45–3.37 (m, 1H), 3.32 (dd, *J* = 15.8, 2.6 Hz, 1H), 2.85 (dd, *J* = 15.8, 10.7 Hz, 1H), 2.57–2.39 (m, 5H), 2.21 (s, 3H), 1.82–1.40 (m, 12H), 0.95 (d, *J* = 6.8 Hz, 3H).

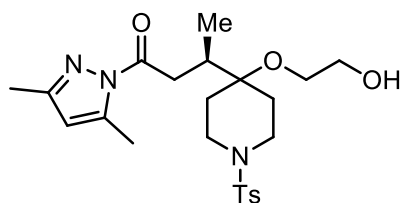
^{13}C NMR (75 MHz, CDCl_3) δ 174.3, 151.7, 144.0, 111.0, 80.7, 62.5, 61.0, 37.2, 36.7, 34.8, 34.5, 29.4, 29.3, 22.6, 22.5, 15.1, 14.6, 13.7.

IR (film): ν (cm^{-1}) 3430, 2925, 2860, 1723, 1581, 1460, 1410, 1379, 1331, 1218, 1171, 1048, 963, 892, 805, 751, 664, 593, 555.

HRMS (ESI, m/z) calcd for $\text{C}_{18}\text{H}_{30}\text{N}_2\text{O}_3\text{Na}$ $[\text{M}+\text{Na}]^+$: 345.2149, found: 345.2149.

(R)-1-(3,5-Dimethyl-1H-pyrazol-1-yl)-3-(4-(2-hydroxyethoxy)-1-tosylpiperidin-4-yl)butan-1-one

(26s)



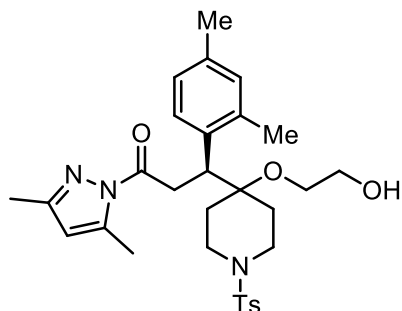
Starting from 2-acyl **24a** (65.7 mg, 0.40 mmol) and *N*-alkoxyphthalimide **25g** (88.9 mg, 0.20 mmol) according to the general procedure to give **26s** as a white solid (67.0 mg, 0.144 mmol, yield: 72%). Enantiomeric excess established by HPLC analysis using a Chiralpak OD-H column, *ee* = 93% (HPLC: OD-H, 254 nm, hexane/isopropanol = 80:20, flow rate 1.0 mL/min, 25 °C, t_r (major) = 10.6 min, t_r (minor) = 13.1 min). $[\alpha]_D^{25} = +25.6^\circ$ (*c* 0.8, CH_2Cl_2).

^1H NMR (300 MHz, CDCl_3) δ 7.63 (d, $J = 8.0$ Hz, 2H), 7.30 (d, $J = 7.9$ Hz, 2H), 5.93 (s, 1H), 3.70–3.49 (m, 4H), 3.47–3.38 (m, 1H), 3.35–3.17 (m, 2H), 2.74 (dd, $J = 15.7, 10.6$ Hz, 1H), 2.62 (td, $J = 11.9, 3.0$ Hz, 1H), 2.56–2.36 (d, $J = 25.5$ Hz, 8H), 2.18 (s, 3H), 2.12–1.98 (m, 1H), 1.90–1.61 (m, 4H), 0.90 (d, $J = 6.8$ Hz, 3H).

^{13}C NMR (75 MHz, CDCl_3) δ 173.5, 151.9, 144.0, 143.4, 133.4, 129.5, 127.6, 111.1, 74.8, 62.1, 60.7, 41.8, 41.7, 36.6, 33.7, 29.2, 28.8, 21.4, 14.8, 14.5, 13.6.

IR (film): ν (cm^{-1}) 3411, 2930, 2866, 1720, 1586, 1459, 1408, 1378, 1327, 1248, 1216, 1159, 1088, 1050, 968, 893, 846, 815, 762, 651, 545.

HRMS (ESI, m/z) calcd for $\text{C}_{23}\text{H}_{33}\text{N}_3\text{O}_5\text{SNa}$ $[\text{M}+\text{Na}]^+$: 486.2033, found: 486.2034.

(S)-1-(3,5-Dimethyl-1H-pyrazol-1-yl)-3-(2,4-dimethylphenyl)-3-(4-(2-hydroxyethoxy)-1-tosylpiperidin-4-yl)propan-1-one (26t)

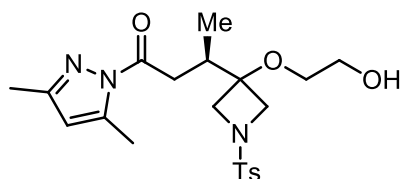
Starting from 2-acyl pyrazole **24i** (101.7 mg, 0.40 mmol) and *N*-alkoxyphthalimide **25g** (88.9 mg, 0.20 mmol) according to the general procedure to give **26t** as a white solid (60.0 mg, 0.108 mmol, yield: 54%). Enantiomeric excess established by HPLC analysis using a Chiralpak OD-H column, *ee* = 92% (HPLC: OD-H, 254 nm, hexane/isopropanol = 85:15, flow rate 1.0 mL/min, 25 °C, *t_r* (major) = 12.6 min, *t_r* (minor) = 18.9 min). $[\alpha]_D^{25} = -19.7^\circ$ (*c* 0.4, CH₂Cl₂).

¹H NMR (300 MHz, CDCl₃) δ 7.59 (d, *J* = 8.2 Hz, 2H), 7.29 (d, *J* = 8.1 Hz, 2H), 7.13 (d, *J* = 7.9 Hz, 1H), 7.00–6.89 (m, 2H), 5.87 (s, 1H), 4.11 (dd, *J* = 9.2, 5.2 Hz, 1H), 3.78–3.51 (m, 5H), 3.50–3.41 (m, 1H), 3.40–3.31 (m, 1H), 2.65 (td, *J* = 12.1, 3.1 Hz, 1H), 2.50–2.36 (m, 4H), 2.35–2.24 (m, 9H), 2.23–2.10 (m, 4H), 2.02 (td, *J* = 12.7, 4.7 Hz, 1H), 1.95–1.81 (m, 2H), 1.44–1.22 (m, 2H).

¹³C NMR (75 MHz, CDCl₃) δ 172.7, 151.8, 144.0, 143.9, 137.1, 136.3, 134.2, 133.3, 131.5, 129.5, 128.0, 127.6, 126.8, 110.9, 76.4, 62.2, 61.2, 41.9, 41.7, 39.7, 35.8, 30.7, 28.2, 21.5, 20.9, 20.4, 14.3, 13.7.

IR (film): ν (cm⁻¹) 3560, 2928, 2865, 1721, 1585, 1458, 1410, 1378, 1321, 1248, 1161, 1087, 1049, 992, 959, 811, 768, 726, 653, 585, 545.

HRMS (ESI, *m/z*) calcd for C₃₀H₃₉N₃O₅SNa [M+Na]⁺: 576.2503, found: 576.2507.

(R)-1-(3,5-Dimethyl-1H-pyrazol-1-yl)-3-(3-(2-hydroxyethoxy)-1-tosylazetidin-3-yl)butan-1-one (26u)

Starting from 2-acyl pyrazole **24a** (65.7 mg, 0.40 mmol) and *N*-alkoxyphthalimide **25h** (83.2 mg, 0.20 mmol) according to the general procedure to give **26u** as a white solid (50.0 mg, 0.114 mmol, yield:

57%). Enantiomeric excess established by HPLC analysis using a Chiralpak AD-H column, $ee = 86\%$ (HPLC: AD-H, 254 nm, hexane/isopropanol = 90:10, flow rate 1.0 mL/min, 25 °C, t_r (minor) = 27.8 min, t_r (major) = 30.8 min). $[\alpha]_D^{25} = +15.8^\circ$ (c 0.4, CH_2Cl_2).

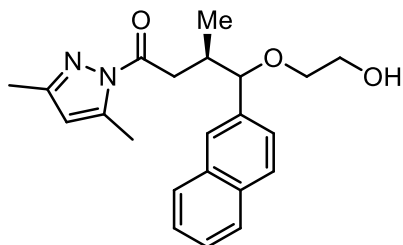
^1H NMR (300 MHz, CDCl_3) δ 7.73 (d, $J = 8.3$ Hz, 2H), 7.36 (d, $J = 7.8$ Hz, 2H), 5.94 (s, 1H), 3.86–3.68 (m, 4H), 3.52 (t, $J = 4.7$ Hz, 2H), 3.39 (ddd, $J = 9.0, 5.1, 3.7$ Hz, 1H), 3.34–3.25 (m, 1H), 3.11 (dd, $J = 15.6, 4.8$ Hz, 1H), 2.80 (dd, $J = 15.5, 8.3$ Hz, 1H), 2.49 (s, 3H), 2.46–2.34 (m, 4H), 2.25–2.08 (m, 4H), 0.95 (d, $J = 6.8$ Hz, 3H).

^{13}C NMR (75 MHz, CDCl_3) δ 172.9, 152.1, 144.3, 144.0, 131.6, 129.7, 128.3, 111.3, 64.4, 61.6, 57.8, 57.1, 56.7, 36.6, 35.3, 21.5, 14.5, 14.1, 13.7.

IR (film): ν (cm^{-1}) 3533, 2930, 2877, 1722, 1634, 1590, 1451, 1381, 1336, 1157, 1089, 966, 842, 756, 705, 667, 607, 548.

HRMS (ESI, m/z) calcd for $\text{C}_{21}\text{H}_{29}\text{N}_3\text{O}_5\text{SNa}$ $[\text{M}+\text{Na}]^+$: 458.1720, found: 458.1719.

(3R)-1-(3,5-Dimethyl-1H-pyrazol-1-yl)-4-(2-hydroxyethoxy)-3-methyl-4-(naphthalen-2-yl)butan-1-one (26v)



Starting from 2-acyl pyrazole **24a** (65.7 mg, 0.40 mmol) and *N*-alkoxyphthalimide **25i** (69.3 mg, 0.20 mmol) according to the general procedure to give **26v** as a pale yellow oil (52.0 mg, 0.142 mmol, yield: 71%, $dr = 3:1$). Enantiomeric excess established by HPLC analysis using a Chiralpak OJ-H column, $ee = 97\%$ (major product) (HPLC: OJ-H, 254 nm, hexane/isopropanol = 95:5, flow rate 1.0 mL/min, 25 °C, t_r (minor) = 16.7 min, t_r (major) = 27.3 min). The dr value was determined by ^1H NMR of **26v** (after purified by flash chromatography).

^1H NMR (300 MHz, CDCl_3) δ 7.84–7.78 (m, 3H), 7.74 (s, 1H), 7.48–7.42 (m, 3H), 5.90 (s, 1H), 4.48 (d, $J = 5.6$ Hz, 1H), 3.74–3.66 (m, 2H), 3.61–3.51 (m, 1H), 3.45–3.33 (m, 2H), 2.91 (dd, $J = 16.2, 6.8$ Hz, 1H), 2.78–2.66 (m, 1H), 2.64–2.58 (m, 1H), 2.47 (s, 3H), 2.23 (s, 3H), 1.07 (d, $J = 6.8$ Hz, 3H) (major product).

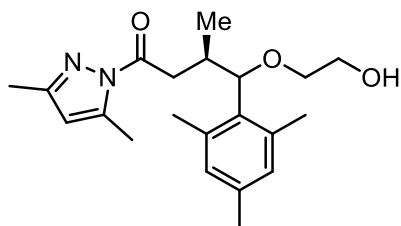
^{13}C NMR (75 MHz, CDCl_3) δ 173.3, 151.8, 143.9, 137.7, 133.04, 133.02, 128.0, 127.8, 127.6, 126.4, 126.0, 125.8, 125.0, 111.1, 85.2, 70.6, 62.0, 38.7, 36.7, 15.5, 14.5, 13.7 (major product).

IR (film): ν (cm^{-1}) 3431, 2963, 2927, 2868, 1720, 1582, 1460, 1410, 1377, 1328, 1270, 1168, 1105, 1058, 963, 898, 818, 740, 658, 588, 554.

HRMS (ESI, m/z) calcd for $\text{C}_{22}\text{H}_{26}\text{N}_2\text{O}_3\text{Na}$ $[\text{M}+\text{Na}]^+$: 389.1836, found: 389.1841.

(3R)-1-(3,5-Dimethyl-1H-pyrazol-1-yl)-4-(2-hydroxyethoxy)-4-mesityl-3-methylbutan-1-one

(26w)



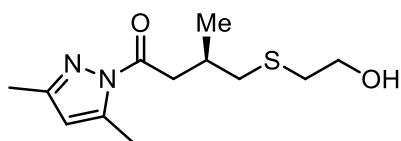
Starting from 2-acyl pyrazole **24a** (65.7 mg, 0.40 mmol) and *N*-alkoxyphthalimide **25j** (68.1 mg, 0.20 mmol) according to the general procedure to give **26w** as a pale yellow oil (45.1 mg, 0.126 mmol, yield: 63%, $dr = 3:1$). Enantiomeric excess established by HPLC analysis using a Chiralpak IC column, $ee = 97\%$ (major product) (HPLC: IC, 254 nm, hexane/isopropanol = 94:6, flow rate 0.7 mL/min, 25 °C, t_r (major) = 12.2 min, t_r (minor) = 16.0 min). The dr value was determined by ^1H NMR of **26w** (after purified by flash chromatography).

^1H NMR (300 MHz, CDCl_3) δ 6.78 (s, 1H), 6.66 (s, 1H), 5.86 (s, 1H), 4.54 (d, $J = 8.6$ Hz, 1H), 3.67 (t, $J = 4.6$ Hz, 2H), 3.41–3.25 (m, 2H), 3.02–2.86 (m, 2H), 2.81–2.70 (m, 1H), 2.51–2.37 (m, 7H), 2.27–2.14 (m, 9H), 1.21 (d, $J = 6.3$ Hz, 3H) (major product).

^{13}C NMR (75 MHz, CDCl_3) δ 172.8, 151.4, 143.8, 136.7, 132.3, 131.4, 131.2, 128.9, 128.8, 110.8, 83.1, 70.0, 62.2, 39.1, 34.7, 21.2, 20.7, 20.4, 17.9, 14.3, 13.7 (major product).

IR (film): ν (cm^{-1}) 3433, 2923, 1723, 1610, 1581, 1455, 1411, 1376, 1324, 1210, 1104, 1055, 964, 894, 854, 802, 746, 655, 586, 536.

HRMS (ESI, m/z) calcd for $\text{C}_{21}\text{H}_{30}\text{N}_2\text{O}_3\text{Na}$ $[\text{M}+\text{Na}]^+$: 381.2149, found: 381.2145.

(R)-1-(3,5-Dimethyl-1H-pyrazol-1-yl)-4-((2-hydroxyethyl)thio)-3-methylbutan-1-one (26x)

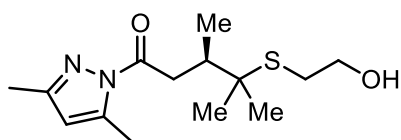
Starting from 2-acyl pyrazole **24a** (65.7 mg, 0.40 mmol) and *N*-alkoxyphthalimide **25k** (47.5 mg, 0.20 mmol) according to the general procedure to give **26x** as a pale yellow oil (25.1 mg, 0.098 mmol, yield: 49%). Enantiomeric excess established by HPLC analysis using a Chiralpak OD-H column, *ee* = 86% (HPLC: OD-H, 254 nm, hexane/isopropanol = 95:5, flow rate 1.0 mL/min, 25 °C, *t_r* (major) = 11.2 min, *t_r* (minor) = 12.5 min). $[\alpha]_{\text{D}}^{25} = +54.6^{\circ}$ (*c* 0.2, CH₂Cl₂).

¹H NMR (300 MHz, CDCl₃) δ 5.94 (s, 1H), 3.72 (t, *J* = 5.9 Hz, 2H), 3.32 (dd, *J* = 16.6, 6.2 Hz, 1H), 2.97 (dd, *J* = 16.6, 7.2 Hz, 1H), 2.73 (t, *J* = 5.9 Hz, 2H), 2.66–2.45 (m, 6H), 2.38 (dt, *J* = 13.4, 6.7 Hz, 1H), 2.22 (s, 3H), 1.10 (d, *J* = 6.7 Hz, 3H).

¹³C NMR (75 MHz, CDCl₃) δ 173.0, 151.9, 144.0, 111.1, 60.4, 41.1, 38.7, 35.7, 30.1, 19.7, 14.5, 13.7.

IR (film): ν (cm⁻¹) 3421, 2960, 2925, 2874, 1721, 1582, 1463, 1410, 1377, 1328, 1247, 1165, 1048, 998, 963, 903, 804, 747, 639, 586, 557.

HRMS (ESI, *m/z*) calcd for C₁₂H₂₀N₂O₂SNa [M+Na]⁺: 279.1138, found: 279.1139.

(R)-1-(3,5-Dimethyl-1H-pyrazol-1-yl)-4-((2-hydroxyethyl)thio)-3,4-dimethylpentan-1-one (26y)

Starting from 2-acyl pyrazole **24a** (65.7 mg, 0.40 mmol) and *N*-alkoxyphthalimide **25l** (53.1 mg, 0.20 mmol) according to the general procedure to give **26y** as a pale yellow oil (41.0 mg, 0.144 mmol, yield: 72%). Enantiomeric excess established by HPLC analysis using a Chiralpak OD-H column, *ee* = 93% (HPLC: OD-H, 254 nm, hexane/isopropanol = 95:5, flow rate 1.0 mL/min, 25 °C, *t_r* (major) = 9.3 min, *t_r* (minor) = 14.3 min). $[\alpha]_{\text{D}}^{25} = +55.6^{\circ}$ (*c* 0.4, CH₂Cl₂).

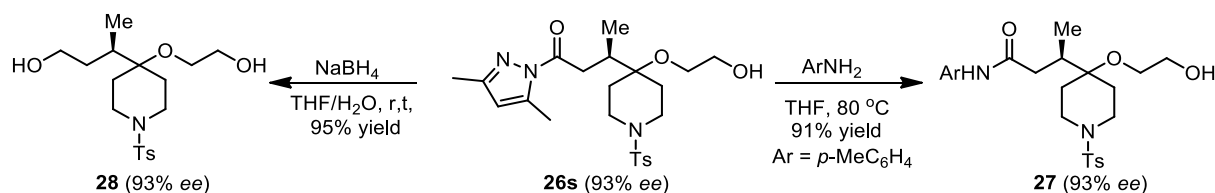
¹H NMR (300 MHz, CDCl₃) δ 5.94 (s, 1H), 3.73 (t, *J* = 6.1 Hz, 2H), 3.58 (dd, *J* = 16.4, 3.1 Hz, 1H), 2.98 (dd, *J* = 16.4, 10.1 Hz, 1H), 2.79 (td, *J* = 6.0, 2.2 Hz, 2H), 2.53 (s, 3H), 2.49–2.33 (m, 1H), 2.31–2.15 (s, 4H), 1.38 (s, 3H), 1.28 (s, 3H), 1.04 (d, *J* = 6.8 Hz, 3H).

¹³C NMR (75 MHz, CDCl₃) δ 173.9, 151.8, 144.0, 111.1, 61.4, 49.1, 38.7, 38.2, 31.4, 27.5, 24.9, 15.4, 14.6, 13.8.

IR (film): ν (cm⁻¹) 3403, 2928, 2876, 1721, 1582, 1458, 1410, 1377, 1324, 1289, 1240, 1170, 1136, 1107, 1042, 994, 963, 935, 805, 769, 736, 661, 627, 587.

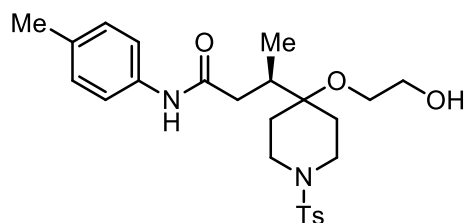
HRMS (ESI, m/z) calcd for C₁₄H₂₄N₂O₂SNa [M+Na]⁺: 307.1451, found: 307.1452.

5.5.3 Synthetic Transformations



To a solution of **26s** (46.4 mg, 0.10 mmol) in THF (0.5 mL) was added *p*-toluidine (107.2 mg, 1.0 mmol). The reaction mixture was heated to 80 °C for 65 h. After cooled to room temperature, the reaction residue was purified by flash silica gel column chromatography to afford **27** as a colorless oil (43.0 mg, 91%). Enantiomeric excess established by HPLC analysis using a Chiralpak AD-H column, *ee* = 93% (HPLC: AD-H, 254 nm, hexane/isopropanol = 80:20, flow rate 1.0 mL/min, 25 °C, t_r (minor) = 25.4 min, t_r (major) = 28.0 min). $[\alpha]_D^{25} = +8.7^\circ$ (c 0.4, CH₂Cl₂).

(*R*)-3-(4-(2-Hydroxyethoxy)-1-tosylpiperidin-4-yl)-*N*-(*p*-tolyl)butanamide (**27**)



¹H NMR (300 MHz, CDCl₃) δ 8.04 (s, 1H), 7.63 (d, J = 8.3 Hz, 2H), 7.39 (d, J = 8.4 Hz, 2H), 7.32 (d, J = 8.0 Hz, 2H), 7.07 (d, J = 8.1 Hz, 2H), 3.67–3.50 (m, 4H), 3.46–3.33 (m, 1H), 3.26–3.15 (m, 1H), 2.63 (ddd, J = 24.5, 12.9, 2.6 Hz, 2H), 2.52–2.40 (m, 4H), 2.39–2.20 (m, 5H), 1.90–1.77 (m, 1H), 1.76–1.56 (m, 3H), 1.44 (dd, J = 13.8, 2.7 Hz, 1H), 0.93 (d, J = 6.8 Hz, 3H).

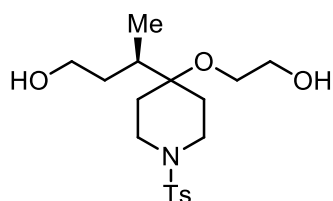
¹³C NMR (75 MHz, CDCl₃) δ 171.3, 143.6, 135.7, 133.7, 133.5, 129.6, 129.3, 127.6, 119.7, 74.8, 62.2, 60.8, 41.9, 41.7, 38.8, 35.0, 29.1, 28.9, 21.5, 20.8, 15.0.

IR (film): ν (cm⁻¹) 3502, 2928, 2870, 1664, 1601, 1526, 1457, 1405, 1325, 1246, 1160, 1086, 977, 930, 816, 725, 651, 551.

HRMS (ESI, m/z) calcd for C₂₅H₃₄N₂O₅SNa [M+Na]⁺: 497.2080, found: 497.2083.

To a solution of **26s** (46.4 mg, 0.10 mmol) in THF/H₂O (v/v = 4:1, 1.0 mL) at 0 °C was added NaBH₄ (37.3 mg, 1.0 mmol). The reaction mixture was stirred at room temperature overnight. The reaction was quenched with aqueous 2 N HCl and extracted with DCM. The combined organic layers were dried over anhydrous Na₂SO₄, filtered, and concentrated. The residue was purified by flash chromatography on silica gel (100% EtOAc) to afford **28** (35.3 mg, yield: 95%) as a colorless oil. Enantiomeric excess established by HPLC analysis using a Chiralpak AD-H column, *ee* = 93% (HPLC: AD-H, 254 nm, hexane/isopropanol = 60:40, flow rate 1.0 mL/min, 25 °C, *t_r* (minor) = 5.4 min, *t_r* (major) = 6.0 min). $[\alpha]_D^{25} = +25.5^\circ$ (*c* 0.4, CH₂Cl₂).

(R)-3-(4-(2-Hydroxyethoxy)-1-tosylpiperidin-4-yl)butan-1-ol (28)



¹H NMR (300 MHz, CDCl₃) δ 7.58 (d, *J* = 8.3 Hz, 2H), 7.25 (d, *J* = 8.0 Hz, 2H), 3.67 (td, *J* = 6.2, 3.1 Hz, 1H), 3.59–3.42 (m, 5H), 3.29 (dt, *J* = 9.9, 5.0 Hz, 1H), 3.11 (dt, *J* = 9.5, 4.0 Hz, 1H), 2.68–2.27 (m, 5H), 1.98–1.82 (m, 3H), 1.80–1.41 (m, 5H), 1.15–0.91 (m, 1H), 0.78 (d, *J* = 6.8 Hz, 3H).

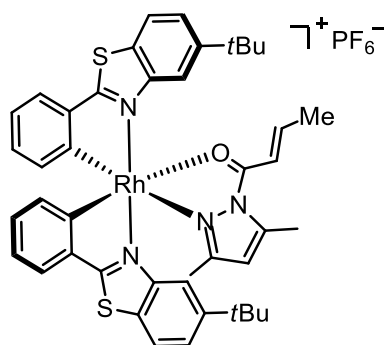
¹³C NMR (75 MHz, CDCl₃) δ 143.4, 133.5, 129.6, 127.6, 75.0, 62.2, 60.9, 60.4, 41.9, 41.8, 33.3, 33.1, 29.1, 29.0, 21.5, 14.1.

IR (film): ν (cm⁻¹) 3382, 2936, 2873, 1461, 1330, 1244, 1160, 1086, 1054, 977, 929, 894, 815, 725, 651, 573, 550.

HRMS (ESI, *m/z*) calcd for C₁₈H₂₉NO₅SNa [M+Na]⁺: 394.1659, found: 394.1659.

5.5.4 Mechanistic Investigations

1) Substrate-Coordinated Rhodium Complex RhS-I



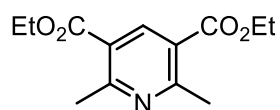
The racemic substrate-coordinated rhodium complex **RhS-I** was obtained by reacting substrate **24a** (11.5 mg, 0.070 mmol) with racemic Δ/Λ -**RhS** (50.0 mg, 0.058 mmol) overnight in DCM (1.5 mL) at room temperature. After the slow addition of hexane (5.0 mL), crystals were collected after several days (39.4 mg, yield: 72%).

^1H NMR (300 MHz, CD_2Cl_2) δ 7.95 (d, $J = 8.8$ Hz, 2H), 7.84–7.69 (m, 3H), 7.64–7.55 (m, 3H), 7.12 (tdd, $J = 7.5, 2.4, 1.0$ Hz, 2H), 6.98–6.86 (m, 3H), 6.73 (dq, $J = 14.9, 1.6$ Hz, 1H), 6.44–6.37 (m, 2H), 6.26 (d, $J = 7.8$ Hz, 1H), 2.66 (s, 3H), 2.10 (dd, $J = 7.1, 1.6$ Hz, 3H), 1.76 (s, 3H), 1.27 (s, 9H), 1.16 (s, 9H).

^{13}C NMR (75 MHz, CD_2Cl_2) δ 168.5, 161.3, 160.6, 160.2, 159.9, 159.6, 152.5, 152.4, 149.6, 149.4, 145.7, 140.4, 139.8, 133.89, 133.80, 131.24, 131.22, 131.10, 131.08, 128.94, 128.93, 128.86, 128.84, 126.6, 126.2, 124.9, 124.5, 124.2, 122.81, 122.78, 118.5, 117.3, 115.1, 114.5, 35.0, 34.8, 31.2, 31.1, 19.5, 15.6, 13.1.

2) Isolation of byproducts

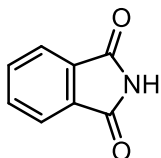
Performed the reaction under the conditions of entry 5 in Table 8 (chapter 3.4), the expected byproducts isoindoline-1,3-dione **29** and diethyl 2,6-dimethylpyridine-3,5-dicarboxylate **30** were isolated.

Diethyl 2,6-dimethylpyridine-3,5-dicarboxylate (**29**)

^1H NMR (300 MHz, CDCl_3) δ 8.66 (s, 1H), 4.39 (q, $J = 7.1$ Hz, 4H), 2.84 (s, 6H), 1.41 (t, $J = 7.1$ Hz, 6H).

All spectroscopic data were in agreement with the literature.²⁵

Isoindoline-1,3-dione (30)



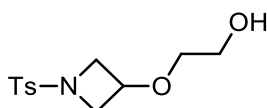
^1H NMR (300 MHz, DMSO-d_6) δ 11.31 (br s, 1H), 7.81 (s, 4H).

All spectroscopic data were in agreement with the literature.²⁶

3) Isolation of a side product

Starting from 2-acyl pyrazole **24a** (65.7 mg, 0.40 mmol) and *N*-alkoxyphthalimide **25h** (83.2 mg, 0.20 mmol) according to the general procedure by using *rac*-**RhS** to give **26t** as a white solid (51.0 mg, 0.117 mmol, yield: 59%) and a side product 2-((1-tosylazetid-3-yl)oxy)ethanol **31** (8.3 mg, 0.030 mmol, yield: 15%).

2-((1-Tosylazetid-3-yl)oxy)ethanol (31)



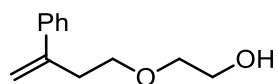
^1H NMR (300 MHz, CDCl_3) δ 7.73 (d, $J = 8.2$ Hz, 2H), 7.37 (d, $J = 8.0$ Hz, 2H), 4.23–4.05 (m, 1H), 4.03–3.89 (m, 2H), 3.67–3.56 (m, 4H), 3.38 (dd, $J = 5.2, 3.9$ Hz, 2H), 2.45 (s, 3H), 1.75 (s, 1H).

^{13}C NMR (75 MHz, CDCl_3) δ 144.2, 131.7, 129.7, 128.4, 70.0, 67.0, 61.5, 57.9, 21.6.

4) Trapping Experiments

a) Trapping experiment with ((2-phenylallyl)sulfonyl)benzene

Using Δ -**RhS** (8 mol%) and *fac*-[Ir(ppy)₃] (1 mol%) as dual catalysts, 2-acyl pyrazole **24a** (65.7 mg, 0.40 mmol), *N*-alkoxyphthalimide **25a** (44.2 mg, 0.20 mmol), Hantzsh ester (76.0 mg, 0.30 mmol) and ((2-phenylallyl)sulfonyl)benzene **32** (103.4 mg, 0.40 mmol)²⁷ according to the general procedure of synthesizing **26a-y** to give **26a** in 64% yield and 92% *ee* and **33** in 18% yield.

2-((3-Phenylbut-3-en-1-yl)oxy)ethanol (33)

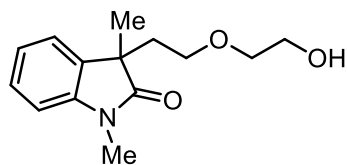
$^1\text{H NMR}$ (300 MHz, CDCl_3) δ 7.46–7.39 (m, 2H), 7.38–7.24 (m, 3H), 5.36 (d, $J = 1.4$ Hz, 1H), 5.14 (d, $J = 1.3$ Hz, 1H), 3.68 (q, $J = 4.5$ Hz, 2H), 3.61 (t, $J = 7.0$ Hz, 2H), 3.52 (dd, $J = 5.3, 3.8$ Hz, 2H), 2.83 (td, $J = 6.9, 1.2$ Hz, 2H), 2.06–1.95 (m, 1H).

$^{13}\text{C NMR}$ (75 MHz, CD_2Cl_2) δ 145.4, 140.9, 128.3, 127.5, 126.0, 113.9, 71.8, 70.0, 61.8, 35.6.

IR (film): ν (cm^{-1}) 3434, 2927, 2872, 1720, 1682, 1597, 1488, 1447, 1364, 1282, 1218, 1114, 1054, 892, 756, 698, 658, 576, 542.

b) Trapping experiment with *N*-methyl-*N*-phenylmethacrylamide

A dried 10 mL Schlenk tube was charged with the catalyst *fac*-[Ir(ppy) $_3$] (1 mol%), Δ/Λ -**RhS** (8 mol%), Hantzsch ester (0.30 mmol, 1.5 eq.), 2-acyl pyrazole **24a** (0.40 mmol, 2.0 eq.), *N*-alkoxyphthalimide **25a** (0.20 mmol, 1.0 eq.) and *N*-methyl-*N*-phenylmethacrylamide **34** (140.2 mg, 2.0 eq.)²⁸. The tube was purged with nitrogen and THF (1.0 mL) was added *via* syringe. The reaction mixture was degassed *via* freeze-pump-thaw for three cycles. After the mixture was thoroughly degassed, the vial was sealed and positioned approximately 8 cm from 24 W blue LEDs. Afterwards, the mixture was diluted with DCM (2 mL). The combined organic layers were concentrated under reduced pressure. The residue was purified by flash chromatography on silica gel (EtOAc/hexane = 1:10) to afford the *rac*-**26a** in 85% yield and **35** in 18% yield.

3-(2-(2-Hydroxyethoxy)ethyl)-1,3-dimethylindolin-2-one (35)

$^1\text{H NMR}$ (300 MHz, CDCl_3) δ 7.32–7.24 (m, 1H), 7.20–7.15 (m, 1H), 7.07 (td, $J = 7.5, 1.0$ Hz, 1H), 6.87–6.84 (m, 1H), 3.51 (t, $J = 4.4$ Hz, 2H), 3.36–3.27 (m, 1H), 3.26–3.10 (m, 6H), 2.50–2.34 (m, 1H), 2.26–2.10 (m, 1H), 1.96 (dt, $J = 14.1, 4.8$ Hz, 1H), 1.38 (s, 3H).

$^{13}\text{C NMR}$ (75 MHz, CDCl_3) δ 181.0, 143.4, 133.5, 127.9, 122.6, 122.4, 108.0, 72.0, 67.5, 61.8, 46.8, 37.7, 26.2, 24.7.

IR (film): ν (cm⁻¹) 3434, 2926, 2870, 1692, 1610, 1466, 1425, 1377, 1349, 1308, 1247, 1163, 1121, 1064, 889, 753, 697, 640, 544.

HRMS (ESI, m/z) calcd for C₁₄H₁₉NO₃Na [M+Na]⁺: 272.1257, found: 272.1258.

5) The cross-over experiment

The reaction designed below is to explore the C(sp³)-H activation occurs through intramolecular or intermolecular 1,5-HAT. When the *N*-alkoxyphthalimide **25I** and alcohol were both subjected to the reaction conditions, the adduct **26y** was isolated with no loss any of yield or enantioselectivity, whereas the product **26m** was not formed in the reaction (Figure 91). It provides a good evidence that the C(sp³)-H activation occurs through intramolecular 1,5-HAT.

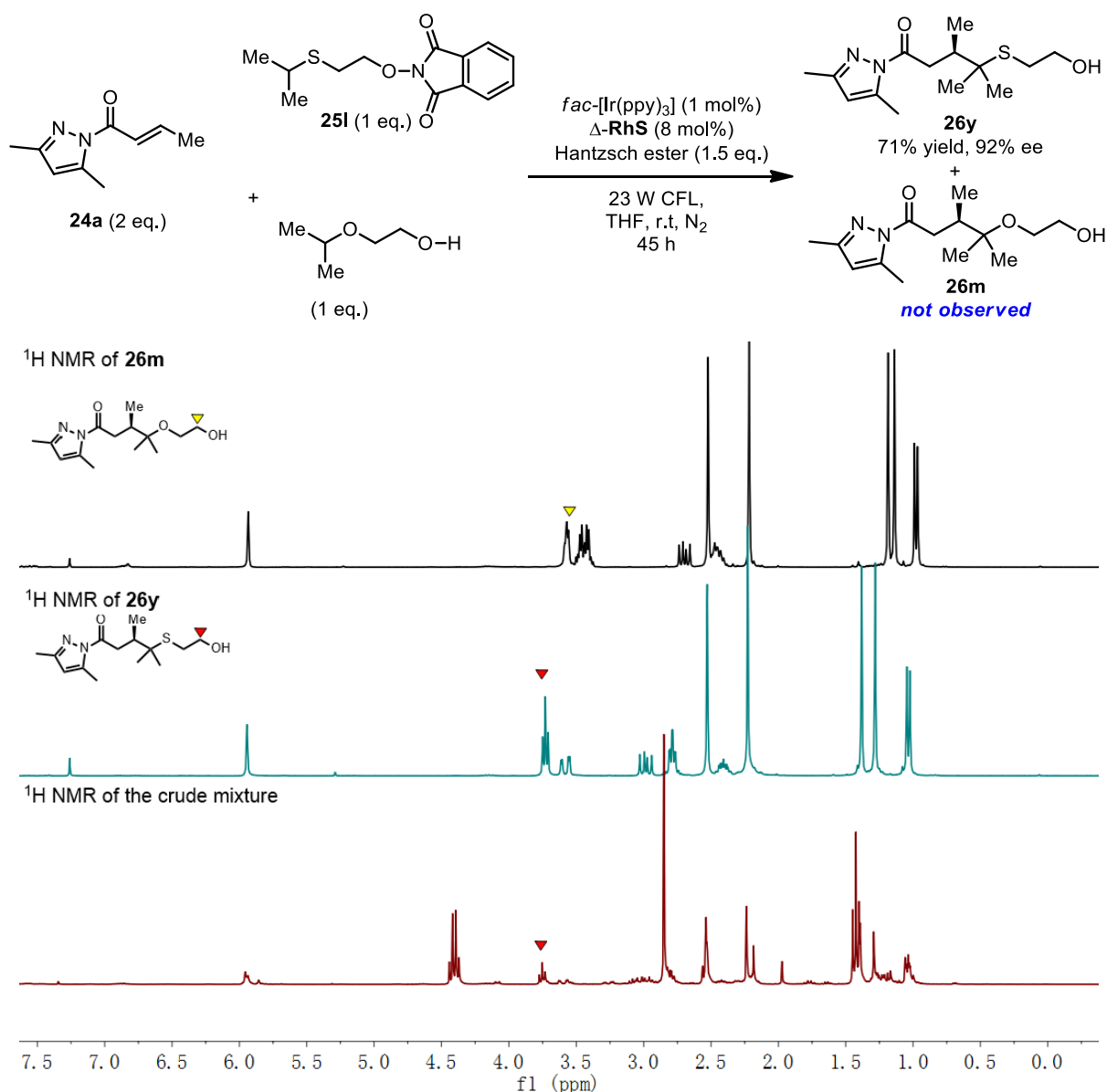


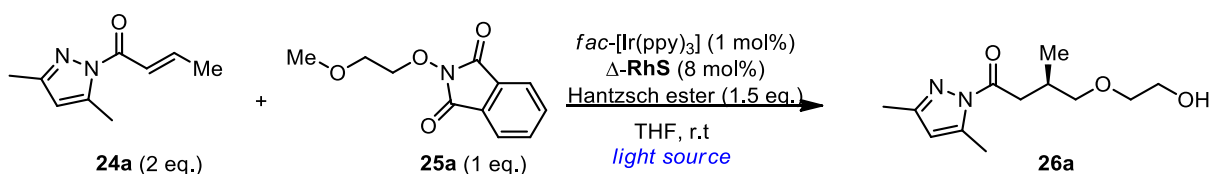
Figure 91 ¹H NMR spectra of **26m**, **26y** and crude mixture.

6) Luminescence quenching experiments

The luminescence quenching experiments with the photoredox catalyst were investigated both in the absence and presence of intermediate **RhS-I**. Emission intensities were recorded on a Spectra Max M5 microplate reader in a 10.0 mm quartz cuvette. All *fac*-[Ir(ppy)₃] solutions were excited at 370 nm and the emission was measured at 515 nm. The concentration of the photoredox catalyst solution (*fac*-[Ir(ppy)₃] and intermediate **RhS-I**) was 0.2 mM in THF. The concentration of the quencher (*N*-alkoxyphthalimide **25a** and Michael acceptor **24a**) stock solution was 10 mM in THF. For each quenching experiment, 5 μL of this stock solution were titrated to a solution (1 mL) of iridium complex in a screw-top 10.0 mm quartz cuvette. The addition of 5 μL stock solution refers to an increase of the quencher concentration of 0.05 mM. After degassing with an argon stream for 5 minutes, the emission intensity was collected.

7) Light source screening

Different light sources contain CFL and blue LEDs were tested in the following reaction. It is not obvious that light intensity or wavelength effect the enantioselectivity of the product **26a**. For example, the enantioselectivities obtained were almost the same when using 12 W or 2 × 20 W CFL as light source compared to 23 W CFL. However, it dropped to 86% and 76% *ee* when using 6 W and 24 W blue LEDs, respectively. The output wavelength of the used 6 W blue LEDs is shown in Figure 92.



	light source	yield	<i>ee</i>
1	12 W CFL (40 h)	42%	92%
2	23 W CFL (40 h)	70%	92%
3	2*20 W CFL (40 h)	68%	91%
4	24 W blue LEDs (20 h)	54%	76%
5	6 W blue LEDs (40 h)	69%	86%

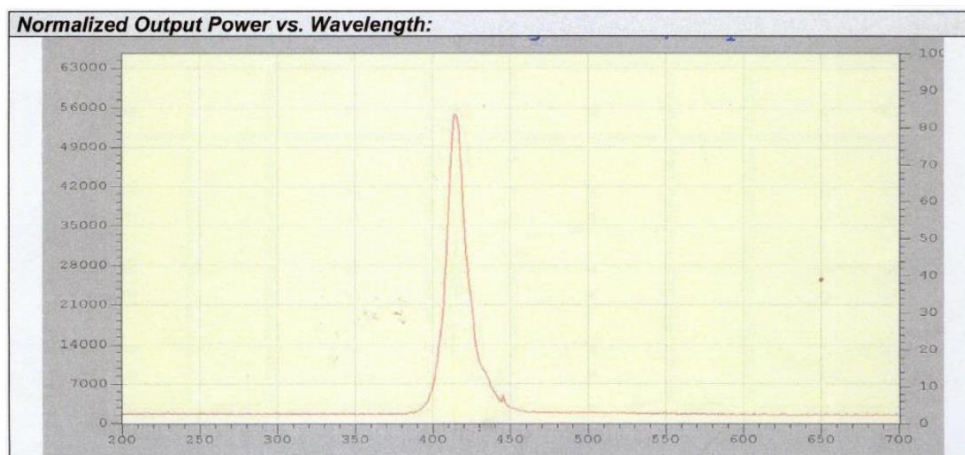


Figure 92 The output wavelength of the used 6 W blue LEDs ($420 \text{ nm} \pm 10 \text{ nm}$).

8) Quantum yield measurement

The quantum yield was measured by standard ferrioxalate actinometry.²⁰ A 150 W xenon lamp (50% of light intensity, $420 \pm 5 \text{ nm}$ bandpass filter) was used as the light source. The measured method was designed according to a published procedure with slight modifications.^{21,22} All the light sensitive operations were processed in the darkroom under red light.

The solutions were prepared and stored in the dark:

Potassium ferrioxalate solution (0.15 M): 736.9 mg of potassium ferrioxalate hydrate was dissolved in 10 mL of 0.05 M H_2SO_4 .

Buffered solution of phenanthroline: 50 mg of 1,10-phenanthroline and 11.25 g of sodium acetate were dissolved in 50 mL of 0.5 M H_2SO_4 .

a) Measurement of light intensity at 420 nm

1000 μL of the ferrioxalate solution was added to a quartz cuvette ($l = 10 \text{ mm}$). The actinometry solution was irradiated with 150 W Xenon Lamp (50% of light intensity, $420 \text{ nm} \pm 5 \text{ nm}$) for specified time intervals (30, 60, 90, 120 seconds). After irradiation, 175 μL of the phenanthroline solution was added to the cuvette. The solution was kept in dark for 30 min to make sure the complete coordination. The absorbance of the actinometry solution was monitored at 510 nm. The absorbance of a non-irradiated (in dark) sample was also measured at 510 nm.

The moles of Fe^{2+} formed was determined using Beer's Law:

Chapter 5: Experimental Part

$$\text{moles Fe}^{2+} = \frac{V_1 \times V_3 \times \Delta A(510 \text{ nm})}{10^3 \times V_2 \times l \times \varepsilon(510 \text{ nm})}$$

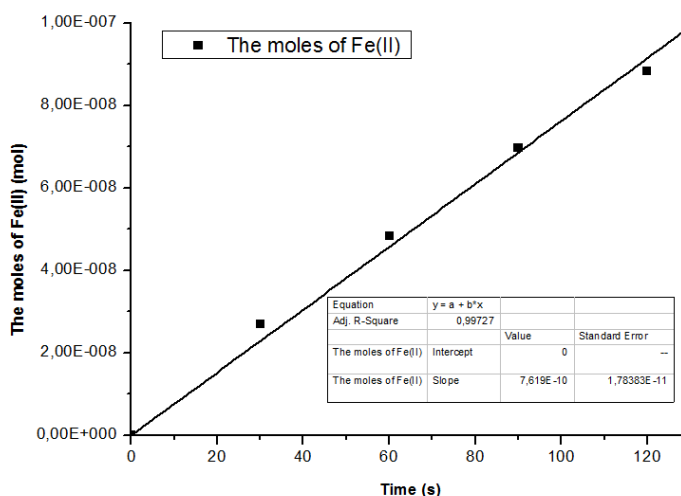
Where V_1 (1 mL) is the irradiated volume, V_2 (1mL) is the aliquot of the irradiated solution taken for the determination of the ferrous ions. V_3 (1.175 mL) is the final volume after complexation with phenanthroline (all in mL), l is the path length (1 cm), and $\Delta A(510 \text{ nm})$ is the optical difference in absorbance between the irradiated and non-irradiated solutions, $\varepsilon(510 \text{ nm})$ is the molar absorptivity of Fe(phen)_3^{2+} ($11100 \text{ L mol}^{-1}\text{cm}^{-1}$).

The moles of Fe^{2+} formed for each sample (30, 60, 90, 120 seconds) are shown below:

Irradiation time	30 s	60 s	90 s	120 s
ΔA	0.252	0.457	0.658	0.834
Fe^{2+} (10^{-8} mol)	2.668	4.838	6.965	8.828

The moles of Fe^{2+} formed are plotted as a function of time (t). The slope is shown as:

$$d(\text{moles Fe}^{2+})/dt = 7.619 \times 10^{-10}$$



The photon flux can be calculated as:

$$\text{photo flux (Einstein s}^{-1}\text{)} = \frac{\text{moles Fe}^{2+}}{\Phi \cdot t \cdot f} = \frac{d(\text{moles Fe}^{2+})/dt}{\Phi \cdot f} = \frac{7.619 \times 10^{-10}}{1.04 \times 1.0} = 7.32 \times 10^{-10}$$

Where Φ is the quantum yield for the ferrioxalate actinometer (1.05 for a 0.15 solution at 412 nm; 1.04 for a 0.15 solution at 422 nm; 1.03 for a 0.15 solution at 433 nm)²¹, t is the irradiated time, and f is the fraction of light absorbed at $\lambda = 420 \text{ nm}$ ($f = 1 - 10^{-A}$). The measurement of the fraction of the light at 420 nm for the ferrioxalate solution was shown in Figure 93. The absorbance of the ferrioxalate solution at 420 nm is >3 indicating f ($f = 1 - 10^{-A}$) is >0.999 .

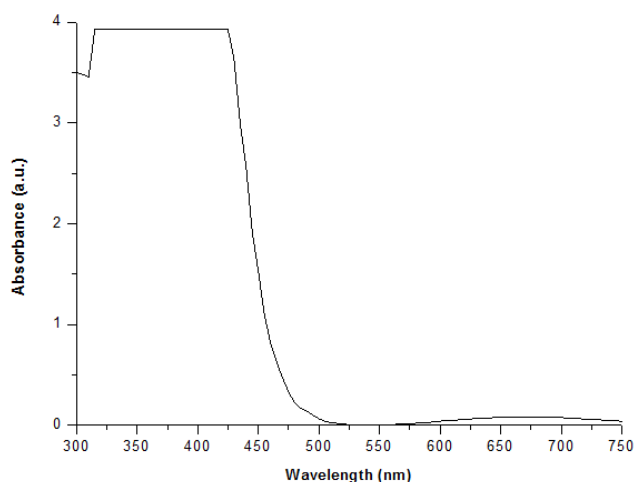
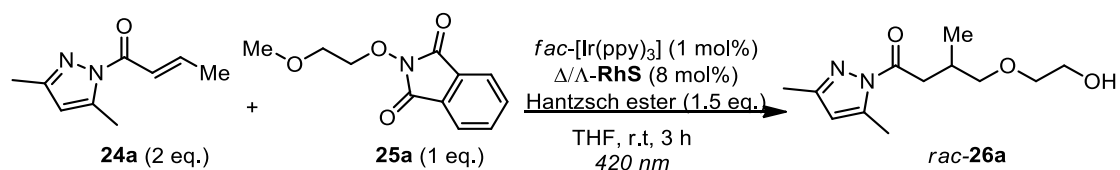


Figure 93 Absorbance of the ferrioxalate actinometer solution (0.15 M).

b) Measurement of quantum yield:

Model reaction:



A screw-top cuvette (10.0 mm) was charged with the catalyst *rac*-**RhS** (8 mol%), photosensitizer *fac*-[Ir(ppy)₃] (1 mol%), **24a** (0.4 mmol, 2.0 eq.), **25a** (0.2 mmol, 1 eq.), Hantzsch ester (0.3 mmol, 1.5 eq.), 1.0 mL THF and a small magnetic stir bar. The cuvette was degassed with an argon stream for 10 min. After the mixture was thoroughly degassed, the vial was sealed and fixed at the same position as the measurement of photon flux. The reaction mixture was stirred and irradiated with 150 W Xenon lamp (50% of light intensity, 420 nm ± 5 nm bandpass filter high transmittance) for 10800 s (3 h). After irradiation, the reaction mixture was passed through a short silica gel column. The moles of product formed was measured by GC analysis (FID detector, column: HP-5) using dodecane as internal standard. The quantum yield calculation is then as following:

$$\Phi = \frac{\text{moles of product}}{\text{moles of absorbed photons}} = \frac{\text{moles of product}}{\text{moles of incident photons} \times (1 - 10^{-A(420 \text{ nm})})}$$

$$= \frac{0.2 \times 10^{-3} \times 0.2\%}{7.32 \times 10^{-10} \times 3 \times 3600} = 0.05$$

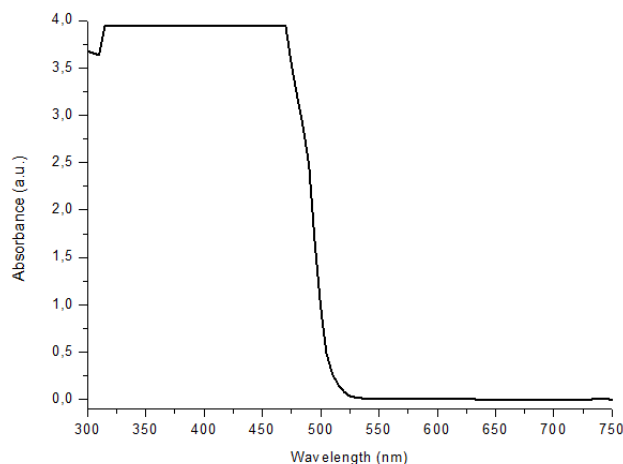


Figure 94 Absorbance of the reaction solution ($fac\text{-}[\text{Ir}(\text{ppy})_3] = 2 \text{ mM}$, $\text{RhS} = 16 \text{ mM}$). Absorbance at 420 nm (>3) demonstrating that the fraction of light absorbed is >0.999 ($f = 1 - 10^{-A(420 \text{ nm})}$).

5.5.5 Single-Crystal X-Ray Diffraction Studies

Single crystals of the rhodium intermediate complex **RhS-I** suitable for X-ray diffraction were obtained after one night from a solution of the compound in CH_2Cl_2 layered with n-hexane. Crystals of the (*R*)-**26t** were obtained by slow diffusion from a solution in CH_2Cl_2 layered with n-hexane. X-ray data of **RhS-I** and (*R*)-**26t** were collected with a Bruker 3 circuit D8 Quest diffractometer with $\text{MoK}\alpha$ radiation (microfocus tube with multilayer optics) and Photon 100 CMOS detector at 100 K. Crystal data and details of the structure determination of **RhS-I** and (*R*)-**26t** are presented in Appendices 6.7 The absolute configuration has been determined.

References

- 1 SADABS. *Bruker AXS area detector scaling and absorption correction*, Bruker AXS Inc., Madison, Wisconsin, USA, **2014**.
- 2 G. M. Sheldrick, *Acta Cryst. A*, **2015**, *71*, 3–8.
- 3 SHELXL-2013, G. M. Sheldrick, University of Göttingen, Germany, **2013**.
- 4 G. M. Sheldrick, *Acta Cryst. C*, **2015**, *71*, 3–8.
- 5 S. Parsons, H. Flack, T. Wagner, *Acta Cryst. B*, **2013**, *69*, 249–259.
- 6 Y.-X. Chen, L.-F. Qian, W. Zhang, B. Han, *Angew. Chem. Int. Ed.* **2008**, *47*, 9330–9333.
- 7 R.-G. Xing, Y.-N. Li, Q. Liu, Q.-Y. Meng, J. Li, X.-X. Shen, Z. Liu, B. Zhou, X. Yao, Z.-L. Liu, *Eur. J. Org. Chem.* **2010**, 6627–6632.
- 8 D. Ramlot, M. Rebarz, L. Volker, M. Ovaere, D. Beljonne, W. Dehaen, L. Van Meervelt, C. Moucheron, A. Kirsch-De Mesmaeker, *Eur. J. Inorg. Chem.* **2013**, 2031–2040.
- 9 R. Urban, R. Krämer, S. Mihan, K. Polborn, B. Wagner, W. Beck, *J. Organomet. Chem.* **1996**, *517*, 191–200.
- 10 H. Huo, C. Fu, K. Harms, E. Meggers, *J. Am. Chem. Soc.* **2014**, *136*, 2990–2993.
- 11 Y. Li, C. Wang, G. Jia, S. Lu, C. Li, *Tetrahedron* **2013**, *69*, 6585–6590.
- 12 H. Huo, X. Shen, C. Wang, L. Zhang, P. Röse, L.-A. Chen, K. Harms, M. Marsch, G. Hilt, E. Meggers, *Nature* **2014**, *515*, 100–103.
- 13 B. M. Trost, K. Lehr, D. J. Michaelis, J. Xu, A. K. Buckl, *J. Am. Chem. Soc.* **2010**, *132*, 8915–8917.
- 14 Y. Miyake, Y. Ashida, K. Nakajima, Y. Nishibayashi, *Chem. Eur. J.* **2014**, *20*, 6120–6125.
- 15 P. V. Khodakovskiy, D. M. Volochnyuk, D. M. Panov, I. I. Pervak, E. V. Zarudnitskii, O. V. Shishkin, A. A. Yurchenko, A. Shivanyuk, A. A. Tolmachev, *Synthesis* **2008**, 948–956.
- 16 J.-J. Zhong, Q.-Y. Meng, G.-X. Wang, Q. Liu, B. Chen, K. Feng, C.-H. Tung, L.-Z. Wu, *Chem. Eur. J.* **2013**, *19*, 6443–6450.
- 17 C. Hernandez-Perez, S. K. Collins, *Angew. Chem. Int. Ed.* **2013**, *52*, 12696–12700.
- 18 M. A. Topchiy, A. F. Asachenko, M. S. Nechaev, *Eur. J. Org. Chem.* **2014**, 3319–3322.
- 19 M. J. O'Connor, K. N. Boblak, M. J. Topinka, P. J. Kindelin, J. M. Briski, C. Zheng, D. A. Klumpp, *J. Am. Chem. Soc.* **2010**, *132*, 3266–3267.

- 20 S. L. Murov, I. Carmichael, G. L. Hug, *Handbook of photochemistry (2nd Edition)*, New York, **1993**.
- 21 M. A. Cismesia, T. P. Yoon, *Chem. Sci.* **2015**, *6*, 5426–5434.
- 22 Ł. Woźniak, J. J. Murphy, P. Melchiorre, *J. Am. Chem. Soc.* **2015**, *137*, 5678–5681.
- 23 Q. Yao, Z. Wang, Y. Zhang, X. Liu, L. Lin, X. Feng, *J. Org. Chem.* **2015**, *80*, 5704–5712.
- 24 J. Zhang, Y. Li, F. Zhang, C. Hu, Y. Chen, *Angew. Chem. Int. Ed.* **2016**, *55*, 1872–1875.
- 25 F. Saikh, R. De, S. Ghosh, *Tetrahedron Lett.* **2014**, *55*, 6171–6174.
- 26 M. A. Ali, S. M. Siddiki, K. Kon, J. Hasegawa, K. Shimizu, *Chem. Eur. J.* **2014**, *20*, 14256–14260.
- 27 A. Pudikova, N. P. Gerasimova, Yu. A. Moskvichev, E. M. Alov, A. S. Danilova, O. S. Kozlova, *Russ. J. Org. Chem.* **2010**, *46*, 352–354.
- 28 D. Zhang, F. Gao, Y. Nian, Y. Zhou, H. Jiang, H. Liu, *Chem. Commun.* **2015**, *51*, 7509–7511.

Chapter 6: Appendices

6.1 List of Abbreviations

^1H NMR	proton nuclear magnetic resonance spectroscopy
^{13}C NMR	carbon nuclear magnetic resonance spectroscopy
^9F NMR	fluorine nuclear magnetic resonance spectroscopy
δ	chemical shift
J	coupling constant
br	broad
s	singlet
d	doublet
t	triplet
q	quartet
m	multiplet
ppm	parts per million
AcOH	acetic acid
aq	aqueous
Ar	argon
bpy	2,2'-bipyridine
CD	circular dichroism
CH_2Cl_2 / DCM	dichloromethane
CD_2Cl_2	dideuteromethylenechloride
CHCl_3	chloroform
CDCl_3	deuteriochloroform
CH_3CN / MeCN	acetonitrile
conc	concentrated
DMAP	4-dimethylaminopyridine
DMF	dimethylformamide
DMSO	dimethyl sulfoxide
dr	diastereomeric ratio
EDA	electron donor-acceptor
EDC	1-ethyl-3-(3-dimethylaminopropyl)carbodiimide hydrochloride
ee	enantiomeric excesses
e.g.	exempli gratia (lat.: for example)
et al.	et alii (lat.: and others)
ESI	electrospray ionization
EtOH	ethanol
Et_2O	diethyl ether
Et_3N	triethyl amine
EtOAc	ethyl acetate
EWG	electron withdrawing group
HAT	hydrogen atom transfer

Chapter 6: Appendices

h	hour(s)
HPLC	high performance liquid chromatography
HRMS	high resolution mass spectrometry
Hz	Hertz
IR spectra	infrared spectra
Ir	iridium
L	liter(s)
M	mol/liter
<i>m</i>	meta-
min	minute(s)
mL	milliliter(s)
mmol	millimole
MS	mass spectroscopy
N ₂	nitrogen
Nu	nucleophile
PCET	proton-coupled electron transfer
Ph	phenyl
PPh ₃	triphenylphosphine
ppm	parts per million
ppy	2-phenylpyridine
PC	photoredox catalyst
<i>rac</i>	racemate
Rh	rhodium
rt	room temperature
SET	single-electron transfer
TEMPO	2,2,6,6-tetramethyl-1-piperidinyloxy
4-MeO-TEMPO	4-methoxy-2,2,6,6-tetramethyl-1-piperidinyloxy
TFA	trifluoroacetic acid
THF	tetrahydrofuran
TLC	thin layer chromatography
UV	ultraviolet

6.2 List of Figures

Figure 1 Structures of (<i>R</i>)-thalidomide and (<i>S</i>)-thalidomide.	1
Figure 2 Asymmetric catalysis by octahedral chiral-at-metal ruthenium(II) complexes.	2
Figure 3 Asymmetric Michael addition by a chiral-at-metal Werner complex.....	3
Figure 4 Asymmetric transfer hydrogenation catalyzed by a chiral-at-metal iridium(III) complex.....	4
Figure 5 Proposed transition state of Λ - Ir1 in asymmetric transfer hydrogenation.....	4
Figure 6 Asymmetric Friedel-Crafts alkylation catalyzed by a chiral-at-metal iridium(III) complex....	4
Figure 7 Asymmetric sulfa-Michael and aza-Henry reactions catalyzed by chiral Brønsted base catalysts.	5
Figure 8 Proposed ternary complex for the asymmetric sulfa-Michael addition catalyzed by Λ - Ir3	5
Figure 9 Asymmetric catalysis by enamine/H-bonding dual activation chiral-at-metal Iridium(III) catalyst.....	6
Figure 10 Proposed enamine/H-bonding mechanism model of the asymmetric α -amination catalyzed by iridium complex Λ - Ir5	6
Figure 11 Asymmetric Friedel-Crafts reaction by a simple chiral-at-metal Lewis acid catalyst.....	6
Figure 12 Proposed reaction model of enantioselective Friedel-Crafts addition with Λ - IrO	7
Figure 13 The common classic transition metal photocatalysts (<i>vs.</i> SCE).....	8
Figure 14 Enantioselective α -functionalization of aldehydes <i>via</i> dual photoredox enamine catalysis...	9
Figure 15 Asymmetric α -photoalkylation of β -ketocarboxyls with a combination of chiral primary amine and photoredox catalyst.	10
Figure 16 Asymmetric radical conjugate addition by photoredox iminium dual catalysis.....	10
Figure 17 Asymmetric α -acylation of tertiary amines by photoredox carbene dual catalysis.	11
Figure 18 Enantioselective aza-pinacol cyclizations by a chiral phosphoric acid catalyst and a photoredox catalyst.....	12
Figure 19 Asymmetric α -acylation of tertiary amines by photoredox hydrogen bonding dual catalysis.	13
Figure 20 Enantioselective radical coupling reaction with chiral arylaminophosphonium ion catalyst and iridium photoredox catalyst.	13
Figure 21 Enantioselective [2+2] photocycloadditions with a photoredox catalyst and a stereocontrolling Lewis acid.	14
Figure 22 Enantioselective radical addition with cooperative Lewis acid-photoredox catalysis.	15
Figure 23 Enantioselective C(sp ³)-C(sp ²) cross-coupling reaction by interfacing photoredox and nickel catalysis.	15
Figure 24 Visible light induced asymmetric α -alkylation of aldehydes <i>via</i> radical initiation step and chain process.	16
Figure 25 Photoinduced asymmetric [2+2] intramolecular cycloaddition <i>via</i> energy transfer process.	17
Figure 26 Enantioselective α -alkylation of 2-acyl imidazoles with a single chiral-at-metal iridium catalyst. PC = photoredox catalyst.	18
Figure 27 Enantioselective C-N cross-coupling with an in-situ chiral copper catalyst.....	19
Figure 28 Catalyst design for the chiral-at metal rhodium complex.	25
Figure 29 Crystal structure of Δ -(<i>R</i>)- 3 . Hydrogen atoms are omitted for clarity. ORTEP drawing with 50% probability thermal ellipsoids.....	27
Figure 30 CD spectra (0.2 mM in CH ₃ OH) of Λ - and Δ - RhO	27

Figure 31 Chiral HPLC traces demonstrating the enantiopurity of synthesized Λ - and Δ - RhO . HPLC conditions: Daicel Chiralpak IB (250 × 4.6 mm), flow rate = 0.6 mL/min, 0.1% aq. TFA with MeCN as eluent (30% to 41% in 60 min).	28
Figure 32 Crystal structures of Δ - RhO (left) and Δ - IrO (right). The hexafluorophosphate counteranion and hydrogen atoms are omitted for clarity. Selected bond lengths (Å): N1-Rh1 = 2.056(2), N20-Rh1 = 2.044(2), N39-Rh1 = 2.142(3), N42-Rh1 = 2.155(3); N1-Ir1 = 2.054(9), N20-Ir1 = 2.044(6), N39-Ir1 = 2.111(6), N42-Ir1 = 2.100(9).	28
Figure 33 Asymmetric Friedel-Crafts alkylation catalyzed by Δ - IrO and Δ - RhO	29
Figure 34 Reaction design of the asymmetric cascade reaction.	32
Figure 35 Proposed mechanism for Δ - RhO catalyzed asymmetric additions and reaction model for the asymmetric induction in the transition state in which one face of the alkene is shielded by the C ₂ -symmetrical ligand sphere.	35
Figure 36 Crystal structure of substrate-coordinated rhodium intermediate complex RhO-I . Hydrogen atoms and the hexafluorophosphate counteranion are omitted for clarity. ORTEP drawing with 50% probability thermal ellipsoids.	35
Figure 37 The acetonitrile exchange experiments of Δ - RhO and Δ - IrO in the presence of bipyridine.	36
Figure 38 Reaction design for photoactivated asymmetric catalysis with chiral iridium(III) Lewis acids.	39
Figure 39 Asymmetric photoactivated α -aminoalkylation of 2-acyl imidazole 7a'' with dimethylaniline.	40
Figure 40 Substrate scope of the asymmetric photoinduced α -aminoalkylation. ^a Catalyst loading of 4 mol%.	43
Figure 41 Some limitations of the substrate scope with respect to silyl methylamines. n.d. = not determined.	44
Figure 42 Plausible mechanism for the photoinduced asymmetric catalysis. PC = iridium photoredox catalyst, most likely intermediates A and C . [O] = oxidant in form of molecular oxygen and superoxide anion.	45
Figure 43 Crystal structure of the proposed complex B (left) and proposed model for the asymmetric photoinduced α -aminoalkylation (right).	46
Figure 44 Evaluating the catalytic activities of complexes A and B	47
Figure 45 UV/Vis-absorbance spectra of intermediate complex A and racemic catalyst Δ/Λ - IrO . Measured as solution in CH ₂ Cl ₂ . a.u. = absorbance units.	49
Figure 46 Stern-Volmer plots. I ₀ and I = luminescence intensities in the absence and presence of the indicated concentrations of the α -silylamine 9a , respectively. All experiments were performed in CH ₂ Cl ₂	50
Figure 47 Cyclic voltammograms (CV) and differential pulse voltammograms (DPV) of the complex A and the reference iridium complex [Ir(ppy) ₂ (dtbbpy)]PF ₆ in THF containing 0.1 M <i>n</i> Bu ₄ NBF ₄	51
Figure 48 Two possible pathways for α -C(sp ³)-H bond functionalization of tertiary amines by photoredox catalysis.	53
Figure 49 Linking (photoinduced) single electron transfer between a donor substrate and an acceptor substrate to asymmetric radical-radical recombination with a single iridium catalyst.	54
Figure 50 Substrate scope with respect to <i>N</i> -methyl diarylamines.	56
Figure 51 Some limitations of substrate scope with respect to amines.	57
Figure 52 Reaction condition screening of cyclic tertiary amines.	57

Chapter 6: Appendices

Figure 53 2-Aryl-1,2,3,4-tetrahydroisoquinolines as amine substrates for enantio- and diastereoselective reactions. Relative configurations are assigned based on a crystal structure of 18a . n.d. = not determined.....	58
Figure 54 Asymmetric C-C bond cross coupling with other coordination groups.....	58
Figure 55 Putative mechanism for the visible light activated catalytic asymmetric process.....	59
Figure 56 Evaluation of the catalytic activity of intermediate complex IrS-I	60
Figure 57 UV/Vis-absorbance spectra of Δ/Λ - IrS and intermediate complex IrS-I . Measured in solution of CHCl ₃ (0.2 mM). a.u. = absorbance units.....	60
Figure 58 Control experiment in the dark with chemical initiators.....	61
Figure 59 Trapping experiments of α -aminomethyl radical.....	62
Figure 60 Model for the asymmetric induction in the course of the radical-radical recombination shown for selected substrates.....	63
Figure 61 Reaction design of photoredox-mediated C-H functionalization with asymmetric catalysis.....	66
Figure 62 Initial experiments with two different Michael acceptors.....	67
Figure 63 Transition-state of alkoxy radicals.....	69
Figure 64 Substrate scope with respect to α,β -unsaturated 2-acyl pyrazoles.....	70
Figure 65 Substrate scope with respect to <i>N</i> -alkoxyphthalimides. Crystal structure of 26t was obtained to determine the absolute configuration of the products.....	71
Figure 66 Limitation with respect to <i>N</i> -alkoxyphthalimides.....	71
Figure 67 Some limitations for the construction of quaternary carbon stereocenters.....	72
Figure 68 Exemplary transformations starting with one <i>N</i> -acyl pyrazole.....	72
Figure 69 Proposed mechanism which is consistent with the observed product formation and the mechanistic experiments.....	73
Figure 70 Crystal structure of proposed intermediate RhS-I (left, hydrogen atoms and the hexafluorophosphate counteranion are omitted for clarity) and stereochemical model (right).....	74
Figure 71 UV/Vis-absorption spectra of the used photoredox catalyst, the Lewis acid catalyst RhS and intermediate RhS-I . Measured as solutions in THF (0.2 mM). a.u. = absorbance units.....	76
Figure 72 UV/Vis-absorption spectra of substrate 25a and Hantzsch ester. Measured as solutions in THF (2 mM). a.u. = absorbance units.....	77
Figure 73 Stern-Volmer plots. I_0 and I are respective luminescence intensities in the absence and presence of the indicated concentrations of the corresponding quencher.....	77
Figure 74 Emission spectra of the photoactive species. The photoactive species were measured as solutions in THF (0.2 mM). a.u. = arbitrary unit.....	78
Figure 75 An overview for the thesis.....	81
Figure 76 Enantiomers of a substitutionally labile yet configurationally stable chiral-at-metal rhodium(III) Lewis acids Λ - RhO and Δ - RhO	82
Figure 77 Synthesis of the enantiomerically pure Lewis acid complexes Λ - RhO and Δ - RhO	82
Figure 78 Catalytic asymmetric conjugate additions and cascade reaction catalyzed by Δ - IrO and Δ - RhO	83
Figure 79 Visible light activated asymmetric α -aminoalkylation of 2-acyl imidazoles with a chiral iridium complex Δ - IrO . PC = photoredox catalyst.....	84
Figure 80 Visible light activated asymmetric radical-radical cross-coupling with a chiral iridium complex Λ - IrS	85
Figure 81 Visible light activated asymmetric C(sp ³)-H functionalization with a chiral Lewis acid Δ - RhS	

Chapter 6: Appendices

and a photoredox catalyst <i>fac</i> -[Ir(ppy) ₃]	86
Figure 82 ¹ H NMR of the crude product 5f and its diastereomer 5f' . Calculated <i>dr</i> = 1:10	98
Figure 83 ¹ H NMR of Δ - RhO recorded in CD ₂ Cl ₂ over 8 days	100
Figure 84 HPLC traces of the freshly prepared Δ - RhO in CH ₂ Cl ₂ (>99% <i>ee</i>) and after 2-8 days in CH ₂ Cl ₂ (>99% <i>ee</i>)	101
Figure 85 ¹ H NMR spectra of substrate 4a , catalyst Δ - RhO , and a mixture of 4a and Δ - RhO	102
Figure 86 ¹ H NMR spectra of Δ - RhO and the mixture of Δ - RhO and bipyridine in CD ₂ Cl ₂	103
Figure 87 ¹ H NMR spectra of the mixture of Δ - IrO and bipyridine in CD ₂ Cl ₂	104
Figure 88 ¹ H NMR of the crude product 18a and its diastereomer 18a' . Calculated <i>dr</i> = 8:1	141
Figure 89 The moles of Fe ²⁺ are plotted as a function of time	152
Figure 90 Absorbance of the ferrioxalate actinometer solution (0.15 M)	153
Figure 91 ¹ H NMR spectra of 26m , 26y and crude mixture	180
Figure 92 The output wavelength of the used 6 W blue LEDs (420 nm \pm 10 nm)	182
Figure 93 Absorbance of the ferrioxalate actinometer solution (0.15 M)	184
Figure 94 Absorbance of the reaction solution (<i>fac</i> -[Ir(ppy) ₃] = 2 mM, RhS = 16 mM). Absorbance at 420 nm (>3) demonstrating that the fraction of light absorbed is >0.999 ($f = 1 - 10^{-A(420 \text{ nm})}$)	185
Figure 95 ¹ H NMR and ¹³ C NMR spectra of dimer <i>rac</i> - 2	204
Figure 96 ¹ H NMR and ¹³ C NMR spectra of Δ -(<i>R</i>)- 3	205
Figure 97 ¹ H NMR and ¹³ C NMR spectra of Δ - RhO	206
Figure 98 ¹ H NMR and ¹³ C NMR spectra of enolate complex B	207
Figure 99 ¹ H NMR and ¹³ C NMR spectra of intermediate A	208
Figure 100 ¹ H NMR and ¹³ C NMR spectra of intermediate IrS-I	209
Figure 101 ¹ H NMR and ¹³ C NMR spectra of intermediate RhS-I	210
Figure 102 CD spectrum of complex Δ -(<i>S</i>)- 3 recorded in CH ₃ OH (0.2 mM)	211
Figure 103 CD spectrum of complex Δ -(<i>R</i>)- 3 recorded in CH ₃ OH (0.2 mM)	211
Figure 104 CD spectra of complexes Δ - RhO and Δ - RhO recorded in CH ₃ OH (0.2 mM)	212
Figure 105 HPLC trace for the racemic reference complexes Δ / Δ - RhO , Δ - RhO and Δ - RhO . HPLC conditions: Daicel Chiralpak IB (250 \times 4.6 mm) HPLC column on an Agilent 1200 Series HPLC System. The column temperature was 25 °C and UV-absorption was measured at 254 nm. Solvent A = 0.1% TFA, solvent B = MeCN (Daicel Chiralpak IB, with a linear gradient of 30% to 41% B in 60 min, flow rate = 0.6 mL/min)	213
Figure 106 HPLC traces (Daicel Chiralpak IC column) of <i>rac</i> - 5a (reference) and (<i>R</i>)- 5a	214
Figure 107 HPLC traces (Daicel Chiralpak AD-H column) of <i>rac</i> - 5b (reference) and (<i>R</i>)- 5b	215
Figure 108 HPLC traces (Daicel Chiralpak AD-H column) of <i>rac</i> - 5c (reference) and (<i>R</i>)- 5c	216
Figure 109 HPLC traces (Daicel Chiralpak AD-H column) of <i>rac</i> - 5d (reference) and (<i>R</i>)- 5d	217
Figure 110 HPLC traces (Daicel Chiralpak AD-H column) of <i>rac</i> - 5e (reference) and (<i>R,R</i>)- 5e	218
Figure 111 HPLC traces (Daicel Chiralpak AD-H column) of <i>rac</i> - 5f (reference) and (<i>R,R</i>)- 5f	219
Figure 112 HPLC traces (Daicel Chiralpak AD-H column) of <i>rac</i> - 6 (reference) and (<i>S,S</i>)- 6	220
Figure 113 HPLC traces (Daicel Chiralpak AD-H column) of <i>rac</i> - 10a'' (reference) and (<i>S</i>)- 10a''	221
Figure 114 HPLC traces (Daicel Chiralpak AD-H column) of <i>rac</i> - 10a' (reference) and (<i>S</i>)- 10a'	222
Figure 115 HPLC traces (Daicel Chiralpak AD-H column) of <i>rac</i> - 10a (reference) and (<i>R</i>)- 10a	223
Figure 116 HPLC traces (Daicel Chiralpak OD-H column) of <i>rac</i> - 10b (reference) and (<i>R</i>)- 10b	224
Figure 117 HPLC traces (Daicel Chiralpak AD-H column) of <i>rac</i> - 10c (reference) and (<i>R</i>)- 10c	225
Figure 118 HPLC traces (Daicel Chiralpak AD-H column) of <i>rac</i> - 10d (reference) and (<i>R</i>)- 10d	226
Figure 119 HPLC traces (Daicel Chiralpak AD-H column) of <i>rac</i> - 10e (reference) and (<i>R</i>)- 10e	227

Figure 120	HPLC traces (Daicel Chiralpak AD-H column) of <i>rac</i> - 10f (reference) and (<i>R</i>)- 10f 228
Figure 121	HPLC traces (Daicel Chiralpak AD-H column) of <i>rac</i> - 10g (reference) and (<i>R</i>)- 10g 229
Figure 122	HPLC traces (Daicel Chiralpak AD-H column) of <i>rac</i> - 10h (reference) and (<i>R</i>)- 10h 230
Figure 123	HPLC traces (Daicel Chiralpak AD-H column) of <i>rac</i> - 10i (reference) and (<i>R</i>)- 10i 231
Figure 124	HPLC traces (Daicel Chiralpak AD-H column) of <i>rac</i> - 10j (reference) and (<i>R</i>)- 10j 232
Figure 125	HPLC traces (Daicel Chiralpak AD-H column) of <i>rac</i> - 10k (reference) and (<i>S</i>)- 10k 233
Figure 126	HPLC traces (Daicel Chiralpak AD-H column) of <i>rac</i> - 10l (reference) and (<i>R</i>)- 10l 234
Figure 127	HPLC traces (Daicel Chiralpak AD-H column) of <i>rac</i> - 16a (reference) and (<i>S</i>)- 16a 235
Figure 128	HPLC traces (Daicel Chiralpak AD-H column) of <i>rac</i> - 16b' (reference) and (<i>S</i>)- 16b' 236
Figure 129	HPLC traces (Daicel Chiralpak AD-H column) of <i>rac</i> - 16c' (reference) and (<i>S</i>)- 16c' 237
Figure 130	HPLC traces (Daicel Chiralpak AD-H column) of <i>rac</i> - 16d' (reference) and (<i>S</i>)- 16d' 238
Figure 131	HPLC traces (Daicel Chiralpak AD-H column) of <i>rac</i> - 16b (reference) and (<i>S</i>)- 16b 239
Figure 132	HPLC traces (Daicel Chiralpak AD-H column) of <i>rac</i> - 16c (reference) and (<i>S</i>)- 16c 240
Figure 133	HPLC traces (Daicel Chiralpak AD-H column) of <i>rac</i> - 16d (reference) and (<i>S</i>)- 16d 241
Figure 134	HPLC traces (Daicel Chiralpak AD-H column) of <i>rac</i> - 16e (reference) and (<i>S</i>)- 16e 242
Figure 135	HPLC traces (Daicel Chiralpak IC column) of <i>rac</i> - 16f (reference) and (<i>S</i>)- 16f 243
Figure 136	HPLC traces (Daicel Chiralpak AD-H column) of <i>rac</i> - 16g (reference) and (<i>S</i>)- 16g 244
Figure 137	HPLC traces (Daicel Chiralpak AD-H column) of <i>rac</i> - 16h (reference) and (<i>S</i>)- 16h 245
Figure 138	HPLC traces (Daicel Chiralpak AD-H column) of <i>rac</i> - 18a (reference) and (<i>S,R</i>)- 18a 246
Figure 139	HPLC traces (Daicel Chiralpak AD-H column) of <i>rac</i> - 18b (reference) and (<i>S,R</i>)- 18b 247
Figure 140	HPLC traces (Daicel Chiralpak AD-H column) of <i>rac</i> - 18c (reference) and (<i>S,R</i>)- 18c 248
Figure 141	HPLC traces (Daicel Chiralpak AD-H column) of <i>rac</i> - 18d (reference) and (<i>S,R</i>)- 18d 249
Figure 142	HPLC traces (Daicel Chiralpak AD-H column) of <i>rac</i> - 18e (reference) and (<i>S,R</i>)- 18e 250
Figure 143	HPLC traces (Daicel Chiralpak AD-H column) of <i>rac</i> - 20a (reference) and (<i>S</i>)- 20a 251
Figure 144	HPLC traces (Daicel Chiralpak OD-H column) of <i>rac</i> - 26a (reference) and (<i>R</i>)- 26a 252
Figure 145	HPLC traces (Daicel Chiralpak OD-H column) of <i>rac</i> - 26b (reference) and (<i>R</i>)- 26b 253
Figure 146	HPLC traces (Daicel Chiralpak OD-H column) of <i>rac</i> - 26c (reference) and (<i>R</i>)- 26c 254
Figure 147	HPLC traces (Daicel Chiralpak OD-H column) of <i>rac</i> - 26d (reference) and (<i>S</i>)- 26d 255
Figure 148	HPLC traces (Daicel Chiralpak OD-H column) of <i>rac</i> - 26e (reference) and (<i>R</i>)- 26e 256
Figure 149	HPLC traces (Daicel Chiralpak OD-H column) of <i>rac</i> - 26f (reference) and (<i>S</i>)- 26f 257
Figure 150	HPLC traces (Daicel Chiralpak IC column) of <i>rac</i> - 26g (reference) and (<i>R</i>)- 26g 258
Figure 151	HPLC traces (Daicel Chiralpak AD-H column) of <i>rac</i> - 26h (reference) and (<i>R</i>)- 26h 259
Figure 152	HPLC traces (Daicel Chiralpak OD-H column) of <i>rac</i> - 26i (reference) and (<i>S</i>)- 26i 260
Figure 153	HPLC traces (Daicel Chiralpak OD-H column) of <i>rac</i> - 26j (reference) and (<i>S</i>)- 26j 261
Figure 154	HPLC traces (Daicel Chiralpak OD-H column) of <i>rac</i> - 26m (reference) and (<i>R</i>)- 26m 262
Figure 155	HPLC traces (Daicel Chiralpak OD-H column) of <i>rac</i> - 26n (reference) and (<i>R</i>)- 26n 263
Figure 156	HPLC traces (Daicel Chiralpak OD-H column) of <i>rac</i> - 26o (reference) and (<i>R</i>)- 26o 264
Figure 157	HPLC traces (Daicel Chiralpak OD-H column) of <i>rac</i> - 26p (reference) and (<i>S</i>)- 26p 265
Figure 158	HPLC traces (Daicel Chiralpak OD-H column) of <i>rac</i> - 26q (reference) and (<i>R</i>)- 26q 266
Figure 159	HPLC traces (Daicel Chiralpak OD-H column) of <i>rac</i> - 26r (reference) and (<i>R</i>)- 26r 267
Figure 160	HPLC traces (Daicel Chiralpak OD-H column) of <i>rac</i> - 26s (reference) and (<i>R</i>)- 26s 268
Figure 161	HPLC traces (Daicel Chiralpak OD-H column) of <i>rac</i> - 26t (reference) and (<i>S</i>)- 26t 269
Figure 162	HPLC traces (Daicel Chiralpak AD-H column) of <i>rac</i> - 26u (reference) and (<i>R</i>)- 26u 270
Figure 163	HPLC traces (Daicel Chiralpak OJ-H column) of <i>rac</i> - 26v (reference) and (<i>R</i>)- 26v 271
Figure 164	HPLC traces (Daicel Chiralpak IC column) of <i>rac</i> - 26w (reference) and (<i>R</i>)- 26w 272

Chapter 6: Appendices

Figure 165 HPLC traces (Daicel Chiralpak OD-H column) of <i>rac</i> - 26x (reference) and (<i>R</i>)- 26x	273
Figure 166 HPLC traces (Daicel Chiralpak OD-H column) of <i>rac</i> - 26y (reference) and (<i>R</i>)- 26y	274
Figure 167 HPLC traces (Daicel Chiralpak AD-H column) of <i>rac</i> - 27 (reference) and (<i>R</i>)- 27	275
Figure 168 HPLC traces (Daicel Chiralpak AD-H column) of <i>rac</i> - 28 (reference) and (<i>R</i>)- 28	276
Figure 169 Crystal structure of Δ -(<i>R</i>)- 3 . ORTEP drawing with 50% probability thermal ellipsoids.	277
Figure 170 Crystal structure of Δ - RhO . ORTEP drawing with 50% probability thermal ellipsoids. The hexafluorophosphate counteranion is omitted for clarity.	279
Figure 171 Crystal structure of 5d . ORTEP drawing with 50% probability thermal ellipsoids.	281
Figure 172 Crystal structure of racemic 5f to verify the relative configuration. ORTEP drawing with 50% probability thermal ellipsoids.	283
Figure 173 Crystal structure of racemic 6 to verify the relative configuration. ORTEP drawing with 50% probability thermal ellipsoids.	285
Figure 174 Crystal structure of RhO-I . ORTEP drawing with 50% probability thermal ellipsoids. The hexafluorophosphate counteranion is omitted for clarity.	287
Figure 175 Crystal structure of an iridium enolate complex B . ORTEP drawing with 50% probability thermal ellipsoids.	289
Figure 176 Crystal structure of (<i>R</i>)- 10e . ORTEP drawing with 50% probability thermal ellipsoids.	291
Figure 177 Crystal structure of (<i>S</i>)- 16g . ORTEP drawing with 50% probability thermal ellipsoids.	293
Figure 178 Crystal structure of 18a . ORTEP drawing with 50% probability thermal ellipsoids.	295
Figure 179 Crystal structure of rhodium intermediate RhS-I . ORTEP drawing with 50% probability thermal ellipsoids. Hexafluorophosphate counterion, hydrogen atoms and one CH ₂ Cl ₂ molecular are omitted for clarity.	297
Figure 180 Crystal structure of (<i>R</i>)- 26t . ORTEP drawing with 50% probability thermal ellipsoids..	299

6.3 List of Schemes

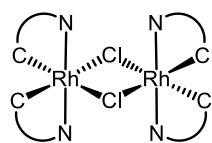
Scheme 1 Proline-mediated synthesis of the enantiomerically pure rhodium(III) complexes Λ - RhO and Δ - RhO	26
Scheme 2 Some limitations for asymmetric cascade reaction.	34
Scheme 3 Asymmetric photoactivated α -aminoalkylation of 2-acyl imidazole 7a'' with α -silylamine 9a	41
Scheme 4 The control experiment with dibenzyl diazodicarboxylate.	47
Scheme 5 The control experiments with <i>t</i> BuOOH in the dark or without air.....	48
Scheme 6 Control experiment in the presence of air.....	61
Scheme 7 Trapping experiment of ketyl radical in the presence of ethene-1,1-diylidibenzene.....	63
Scheme 8 Isolation of byproducts 29 and 30	74
Scheme 9 Isolation of a side product 31	75
Scheme 10 Probing radical pathway in the presence of air or BHT.	75
Scheme 11 Trapping experiments in the presence of alkene 32 or 34	76

6.4 List of Tables

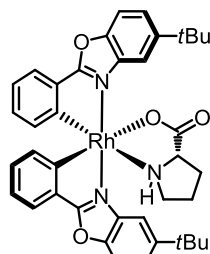
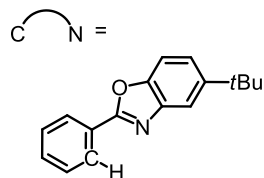
Table 1 Asymmetric addition of malononitrile ^a	30
Table 2 Asymmetric addition of Meldrum's acid ^a	31
Table 3 Asymmetric addition of β -ketoesters ^a	32
Table 4 Asymmetric cascade reaction ^a	33
Table 5 Optimization of the enantioselective photoactivated α -aminoalkylation of 2-acyl imidazoles. ^a	42
Table 6 Single versus dual catalysis for the photoactivated α -aminoalkylation of 2-acyl imidazoles. ^a	49
Table 7 Initial experiments and optimization of the visible light induced asymmetric C-C bond formation. ^a	55
Table 8 Reaction development. ^a	68
Table 9 Crystal data and structure refinement for Δ -(<i>R</i>)- 3	277
Table 10 Crystal data and structure refinement for Δ - RhO	279
Table 11 Crystal data and structure refinement for 5d	281
Table 12 Crystal data and structure refinement for 5f	283
Table 13 Crystal data and structure refinement for racemic 6	285
Table 14 Crystal data and structure refinement for RhO-I	287
Table 15 Crystal data and structure refinement for an iridium enolate complex B	289
Table 16 Crystal data and structure refinement for 10e	291
Table 17 Crystal data and structure refinement for 16g	293
Table 18 Crystal data and structure refinement for 18a	295
Table 19 Crystal data and structure refinement for RhS-I	297
Table 20 Crystal data and structure refinement for 26t	299

6.5 List of Synthesized Comounds

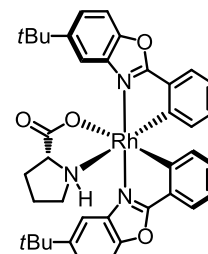
6.5.1 List of Iridium/Rhodium Complexes



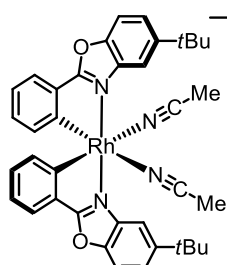
dimer-RhO



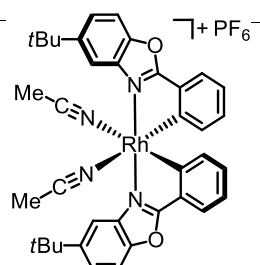
Δ-(S)-3



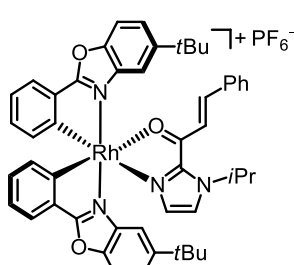
Δ-(R)-3



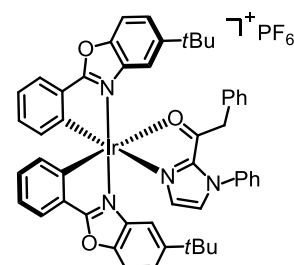
Δ-RhO



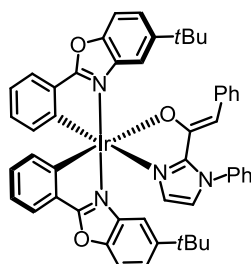
Δ-RhO



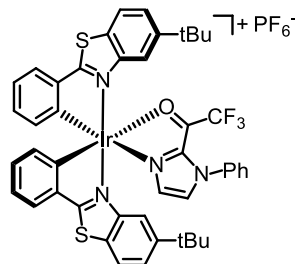
intermediate RhO-I



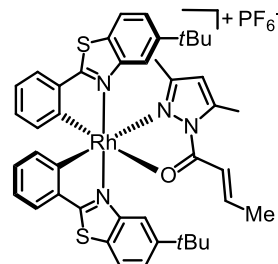
intermediate A



enolate complex B

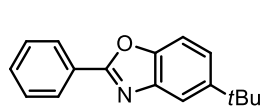


intermediate IrS-I

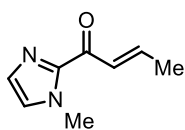


intermediate RhS-I

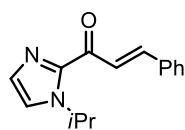
6.5.2 List of Organic Compounds



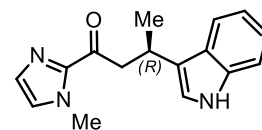
1



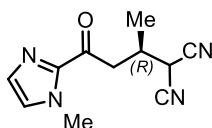
4a



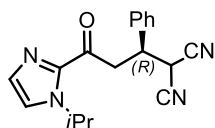
4b



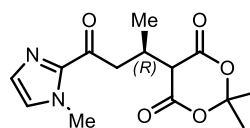
5a



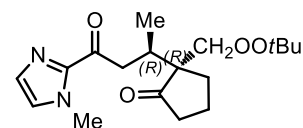
(R)-5b



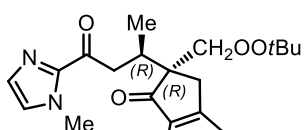
(R)-5c



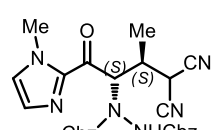
(R)-5d



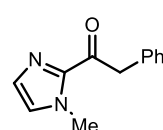
(R,R)-5e



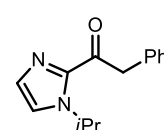
(R,R)-5f



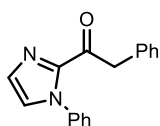
(S,S)-6



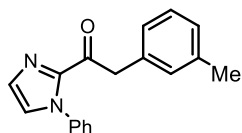
7a''



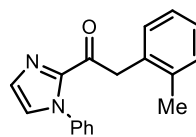
7a'



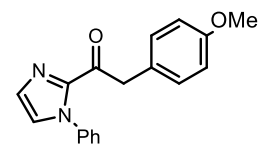
7a



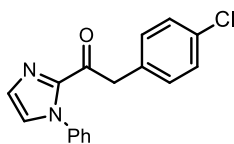
7b



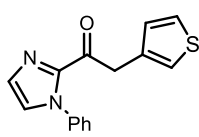
7c



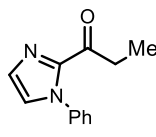
7d



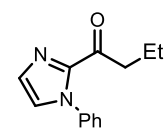
7e



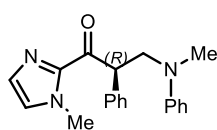
7f



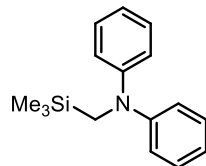
7g



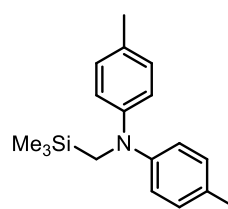
7h



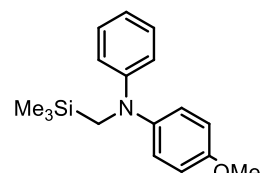
(R)-8



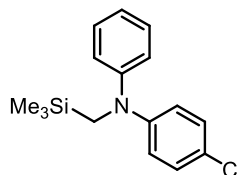
9a



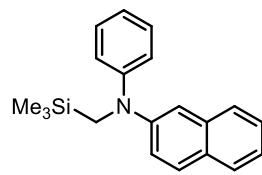
9b



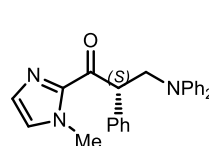
9c



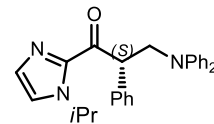
9d



9e

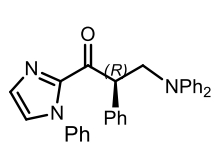


(S)-10a''

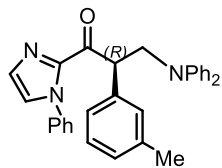


(S)-10a'

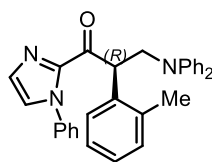
Chapter 6: Appendices



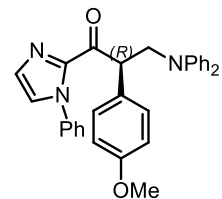
(R)-10a



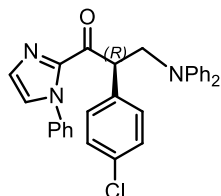
(R)-10b



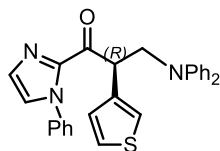
(R)-10c



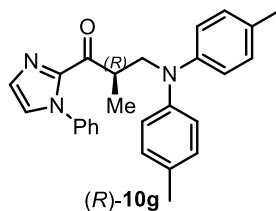
(R)-10d



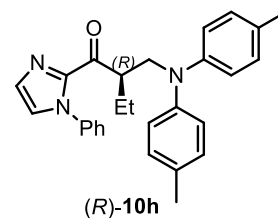
(R)-10e



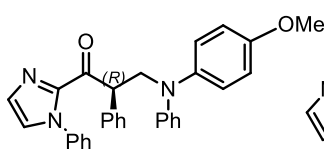
(R)-10f



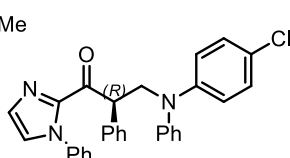
(R)-10g



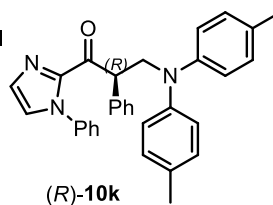
(R)-10h



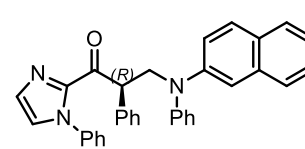
(R)-10i



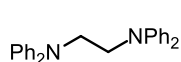
(R)-10j



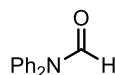
(R)-10k



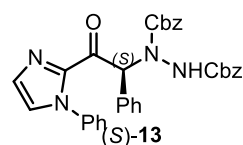
(R)-10l



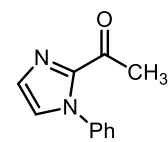
11



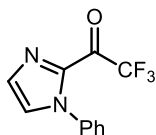
12



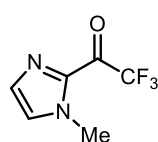
(S)-13



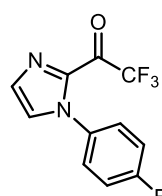
14a'



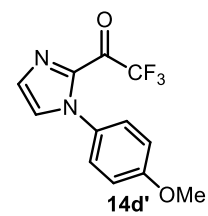
14a



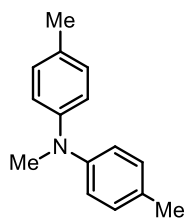
14b'



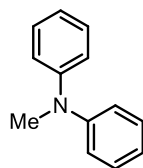
14c'



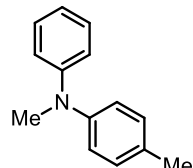
14d'



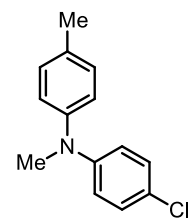
15a



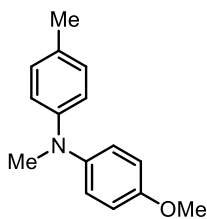
15b



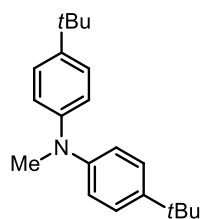
15c



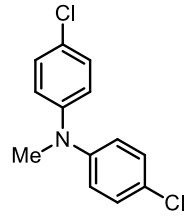
15d



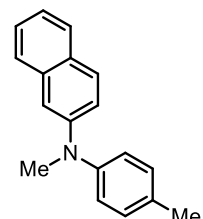
15e



15f

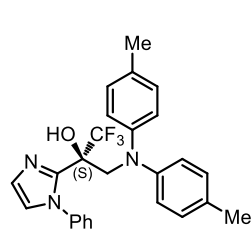


15g

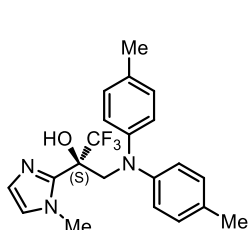


15h

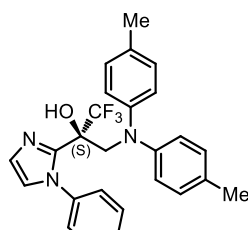
Chapter 6: Appendices



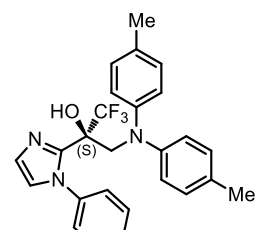
(S)-16a



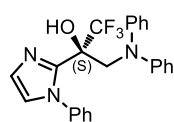
(S)-16b'



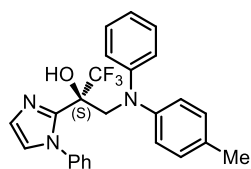
(S)-16c'



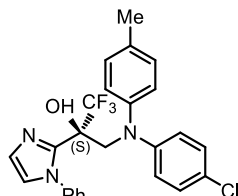
(S)-16d'



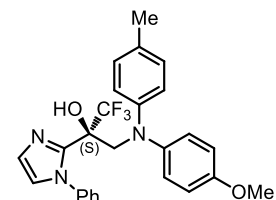
(S)-16b



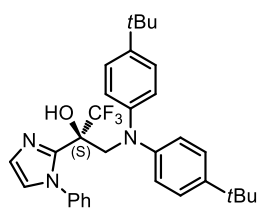
(S)-16c



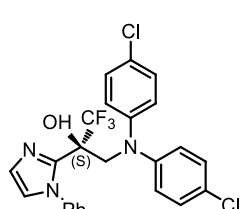
(S)-16d



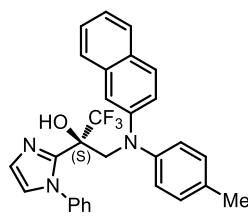
(S)-16e



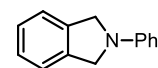
(S)-16f



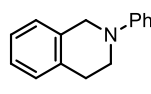
(S)-16g



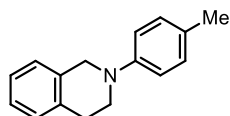
(S)-16h



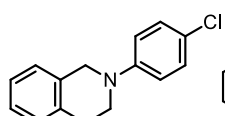
17a'



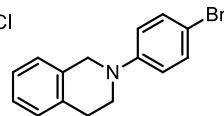
17a



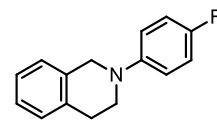
17b



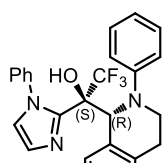
17c



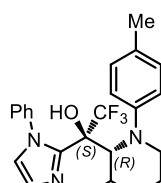
17d



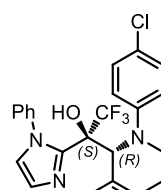
17e



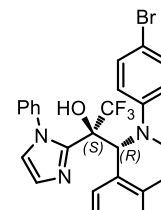
(S,R)-8a



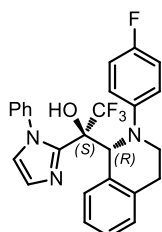
(S,R)-18b



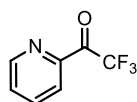
(S,R)-18c



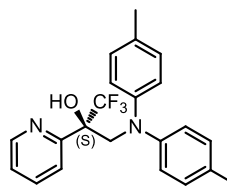
(S,R)-18d



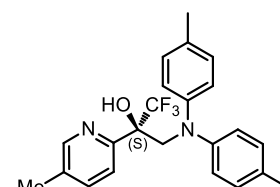
(S,R)-18e



19a

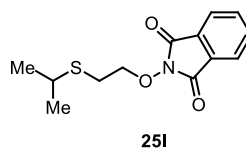
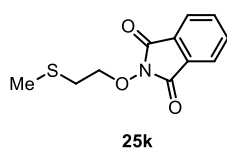
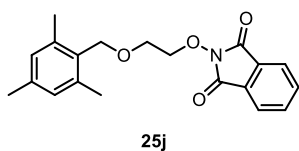
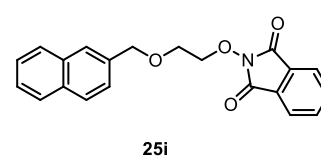
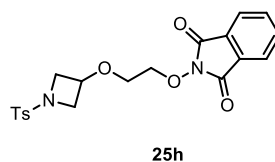
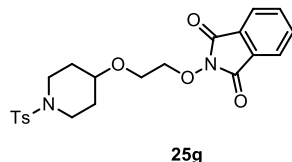
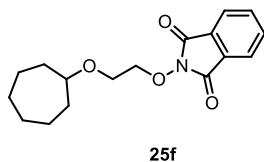
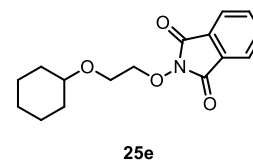
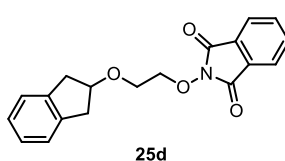
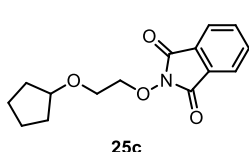
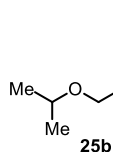
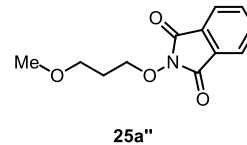
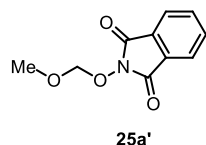
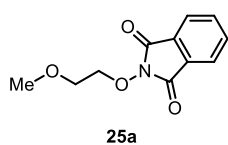
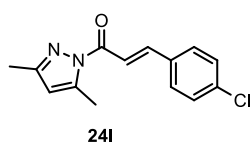
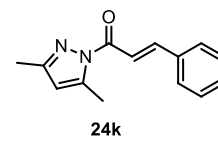
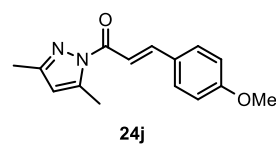
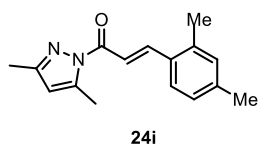
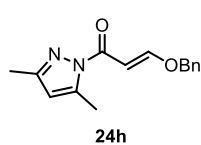
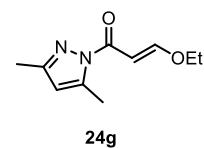
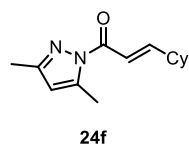
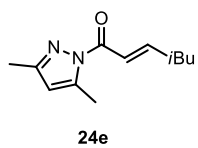
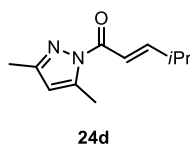
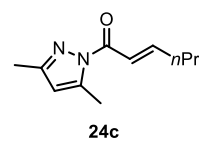
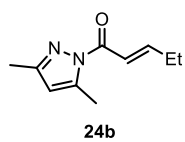
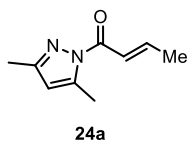
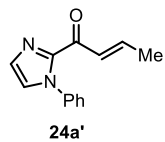
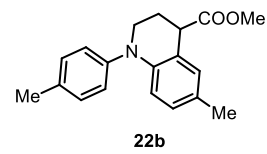
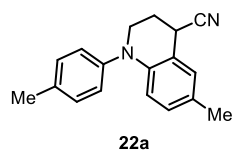
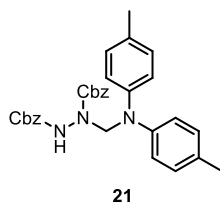
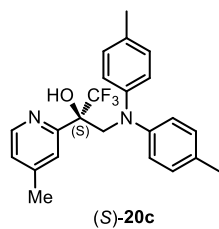


(S)-20a

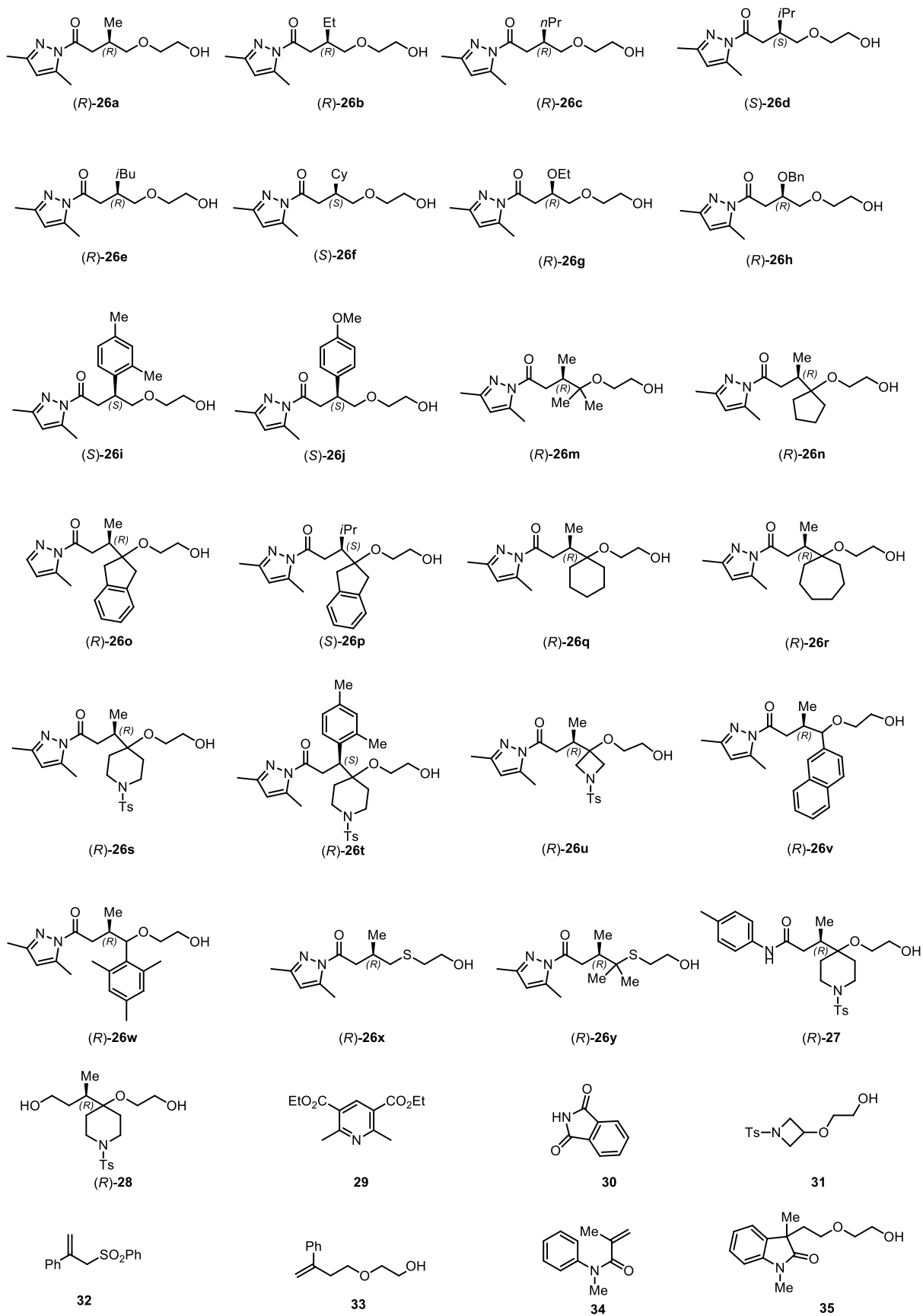


(S)-20b

Chapter 6: Appendices

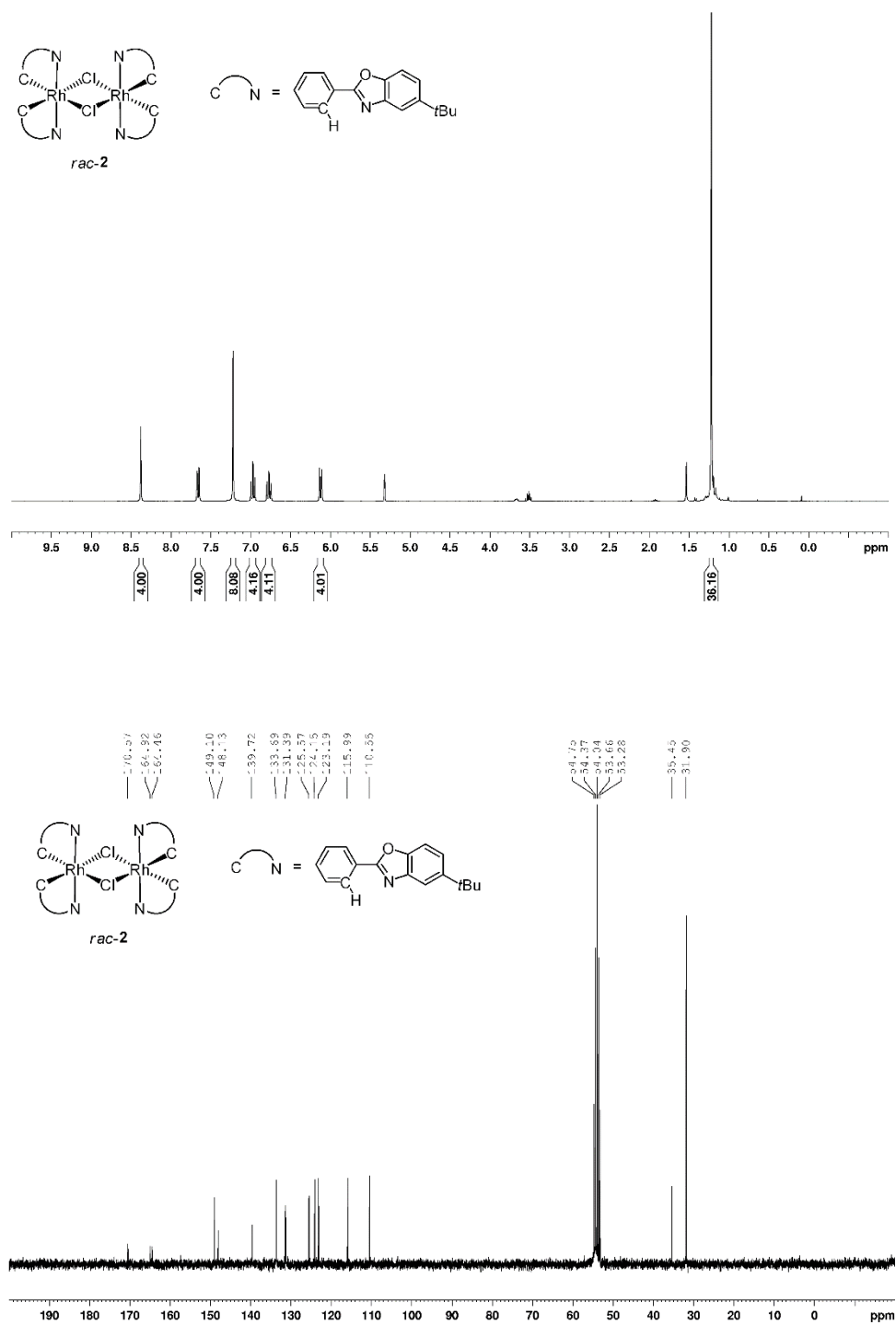


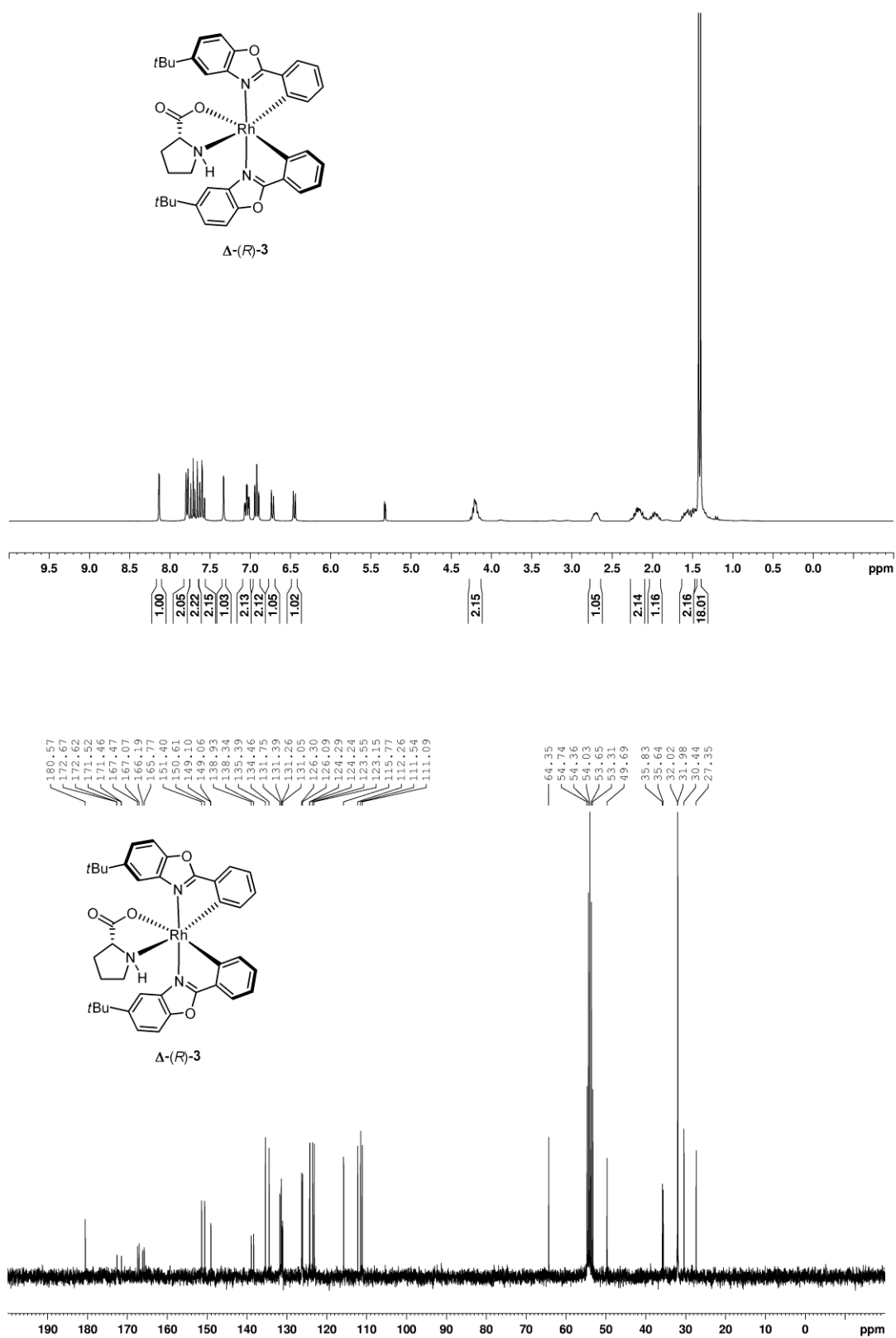
Chapter 6: Appendices

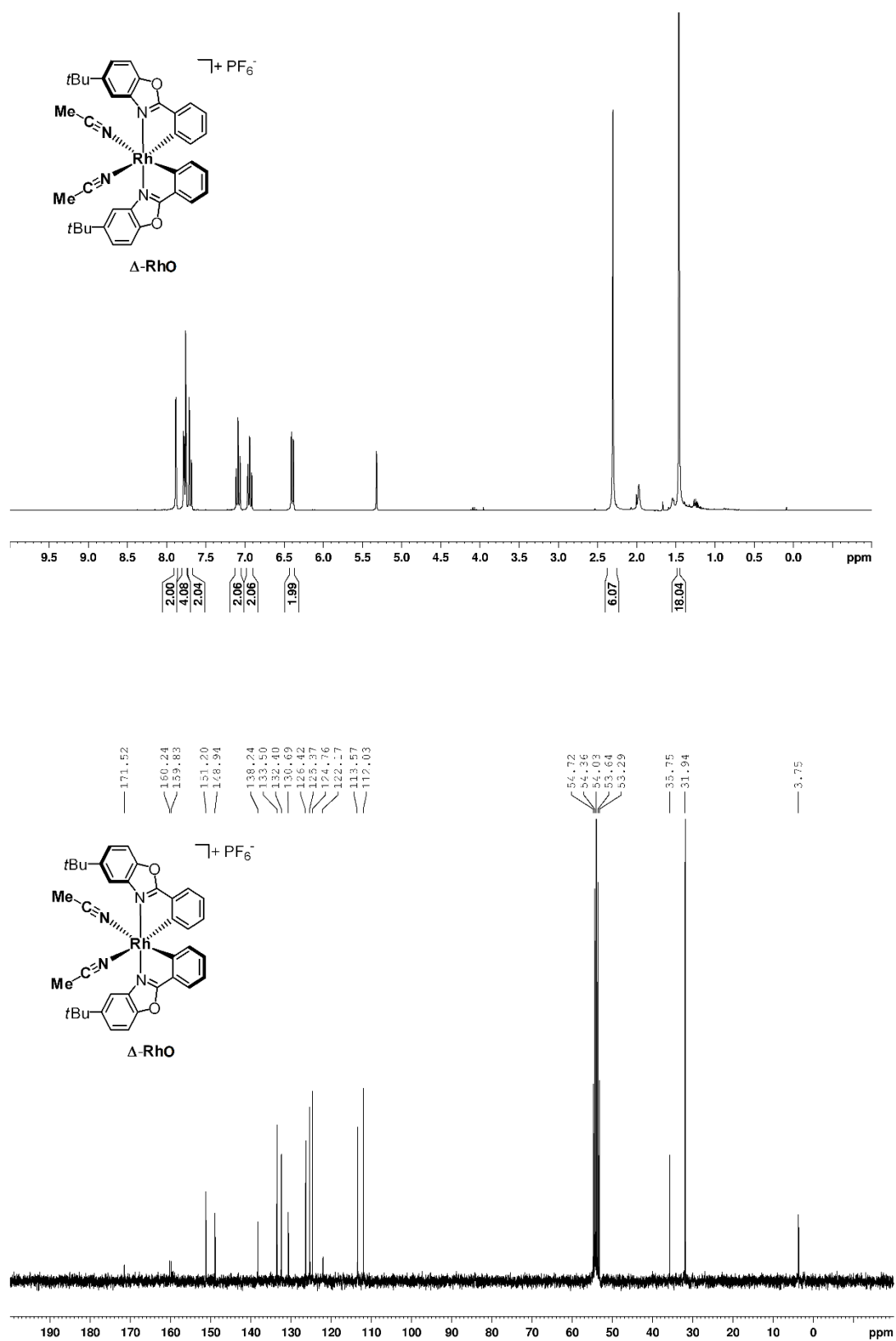


6.6 List of Spectra of Compounds

6.6.1 NMR spectra of Iridium/Rhodium Complexes

Figure 95 ^1H NMR and ^{13}C NMR spectra of dimer *rac-2*.

Figure 96 ^1H NMR and ^{13}C NMR spectra of Δ -(*R*)-3.

Figure 97 1H NMR and ^{13}C NMR spectra of Δ -RhO.

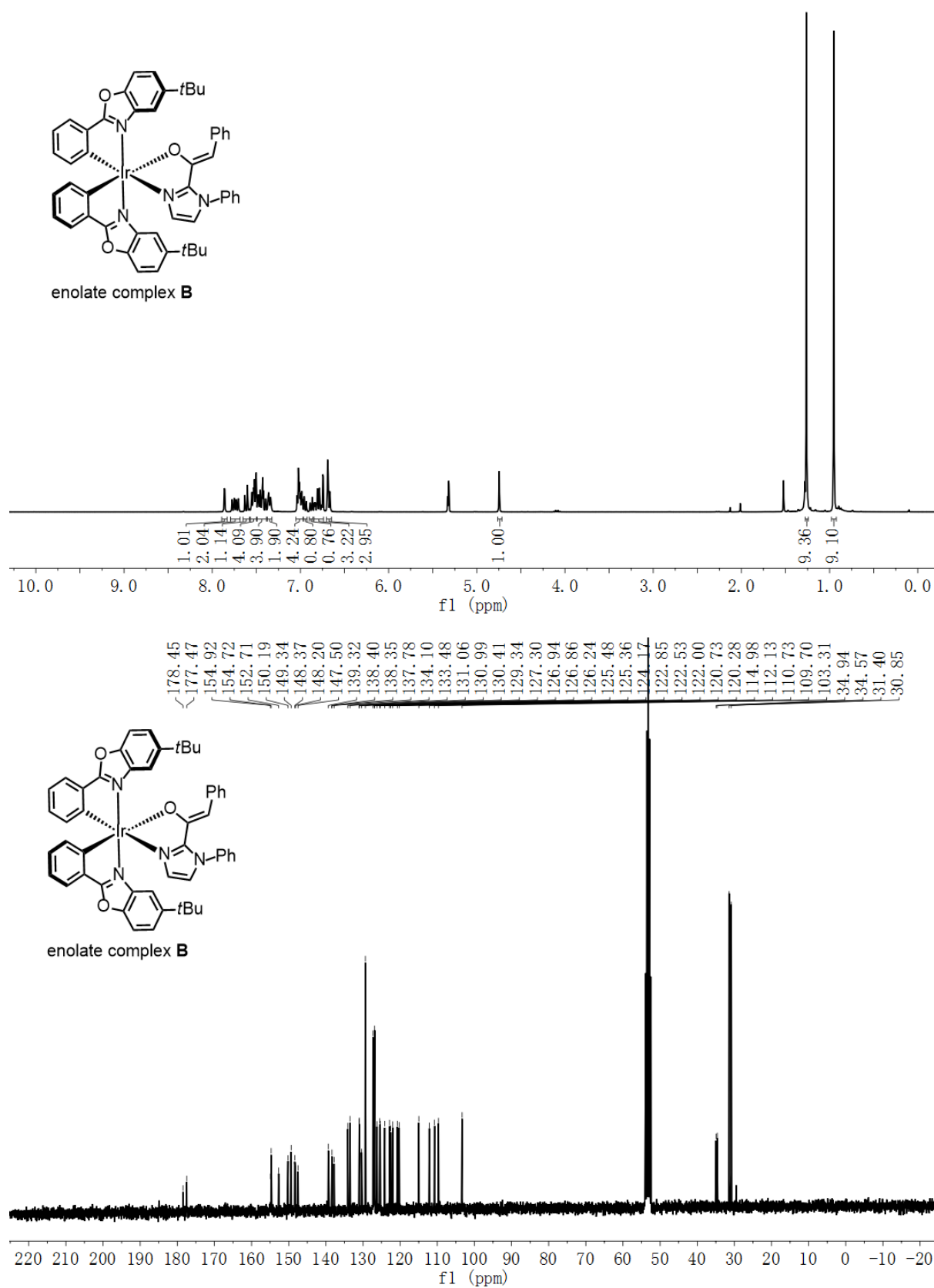


Figure 98 ^1H NMR and ^{13}C NMR spectra of enolate complex **B**.

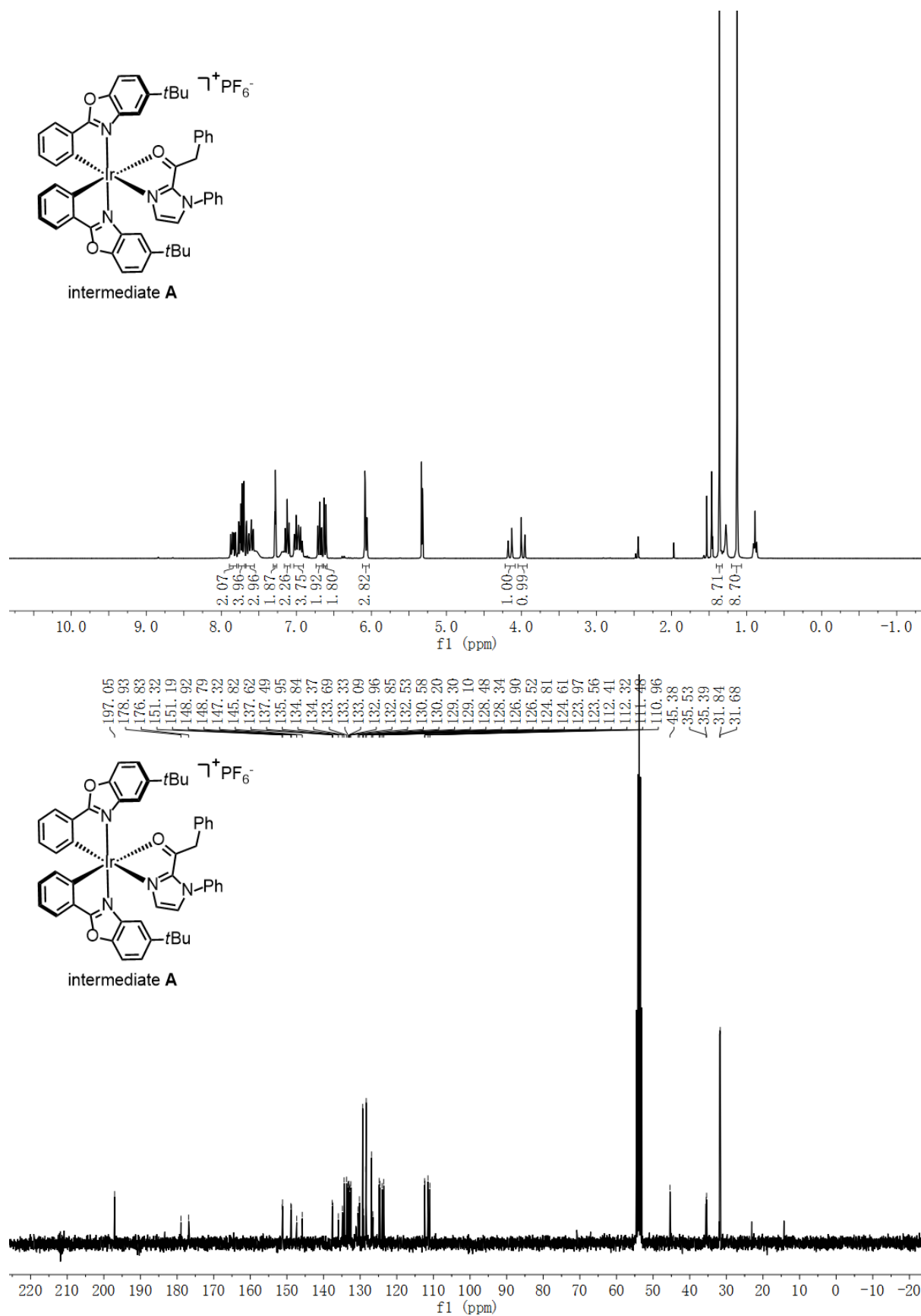


Figure 99 ^1H NMR and ^{13}C NMR spectra of intermediate A.

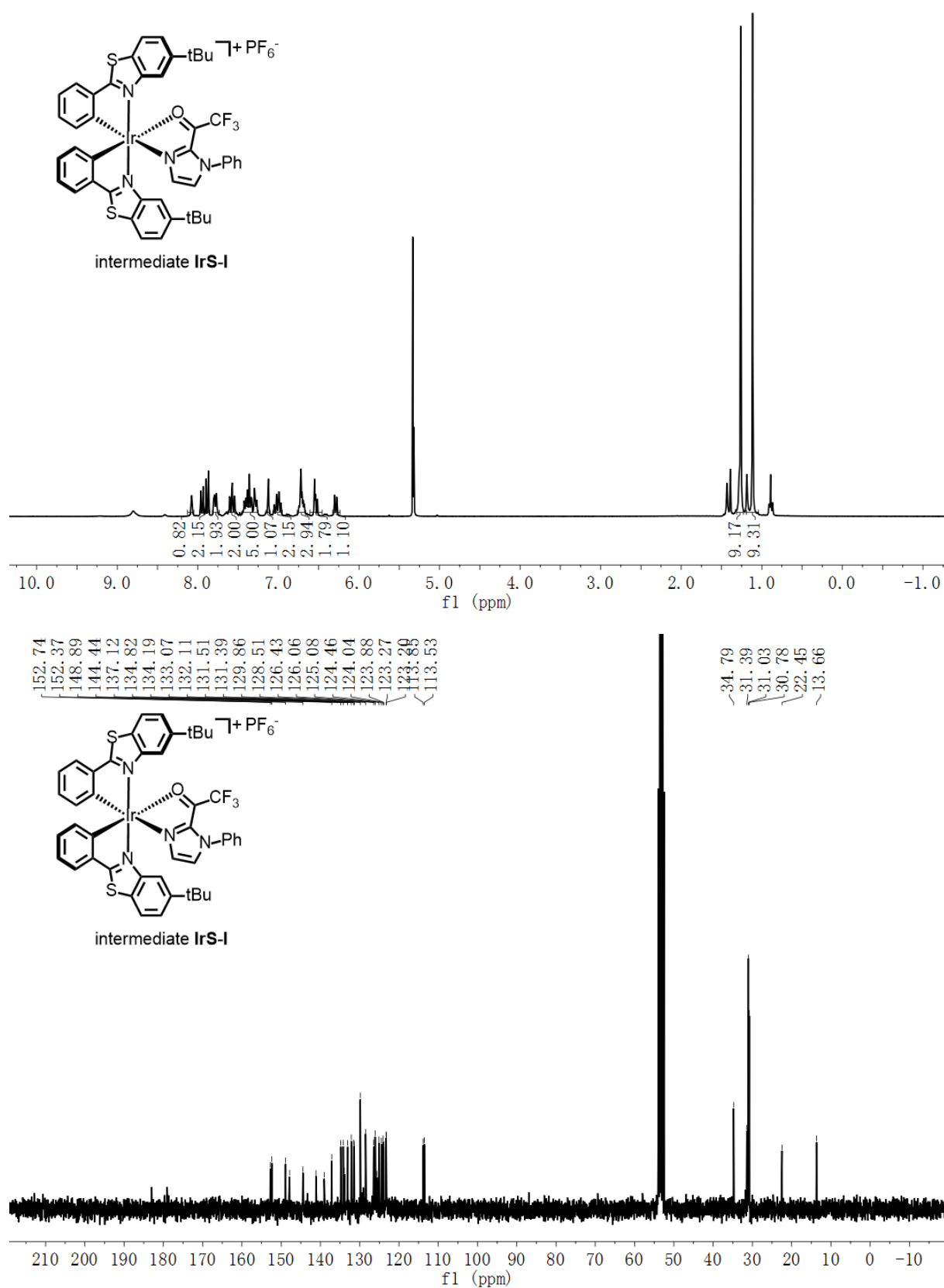


Figure 100 ^1H NMR and ^{13}C NMR spectra of intermediate IrS-I.

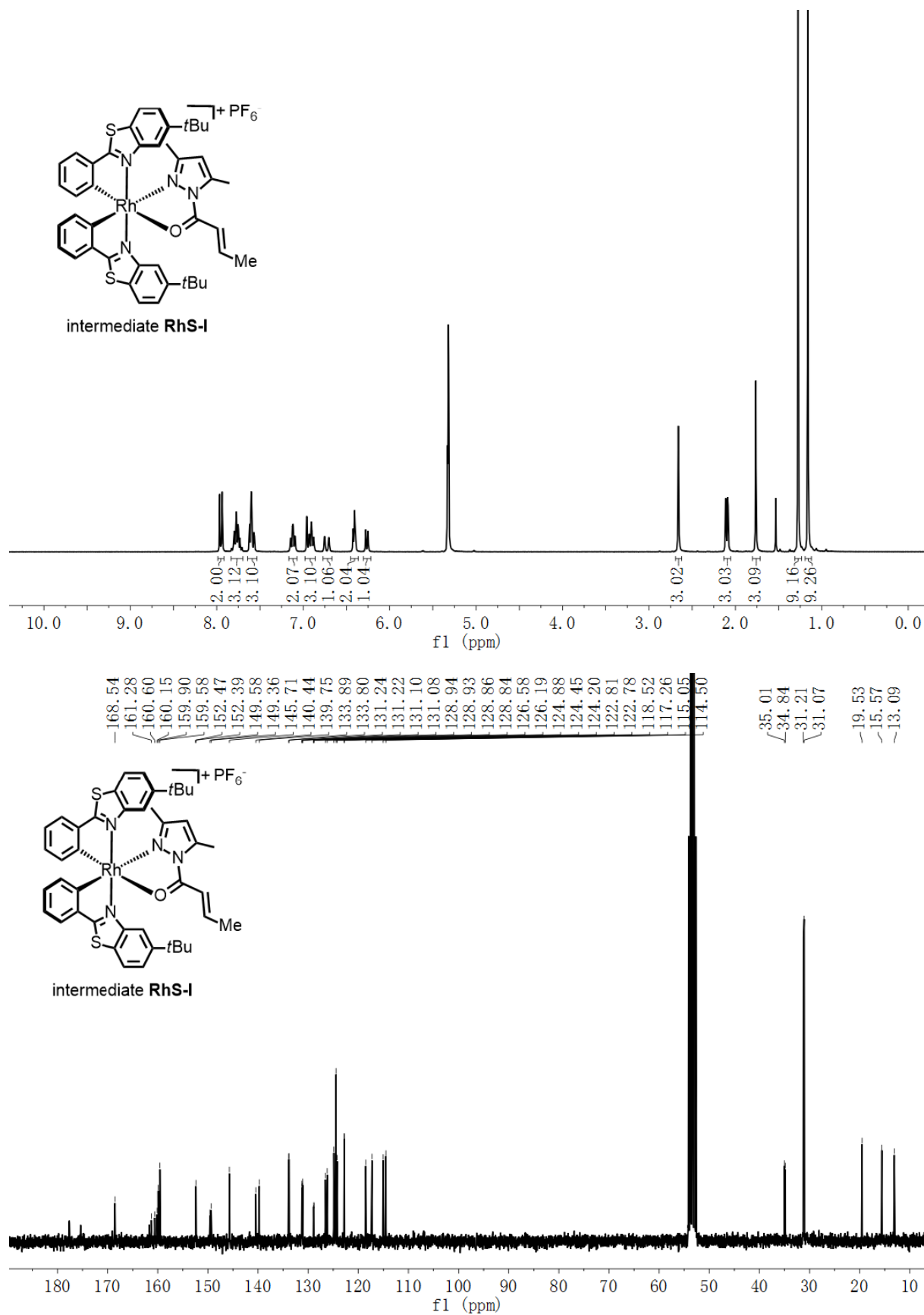


Figure 101 ^1H NMR and ^{13}C NMR spectra of intermediate **RhS-I**.

6.6.2 CD Spectra of Enantiopure Rhodium Complexes

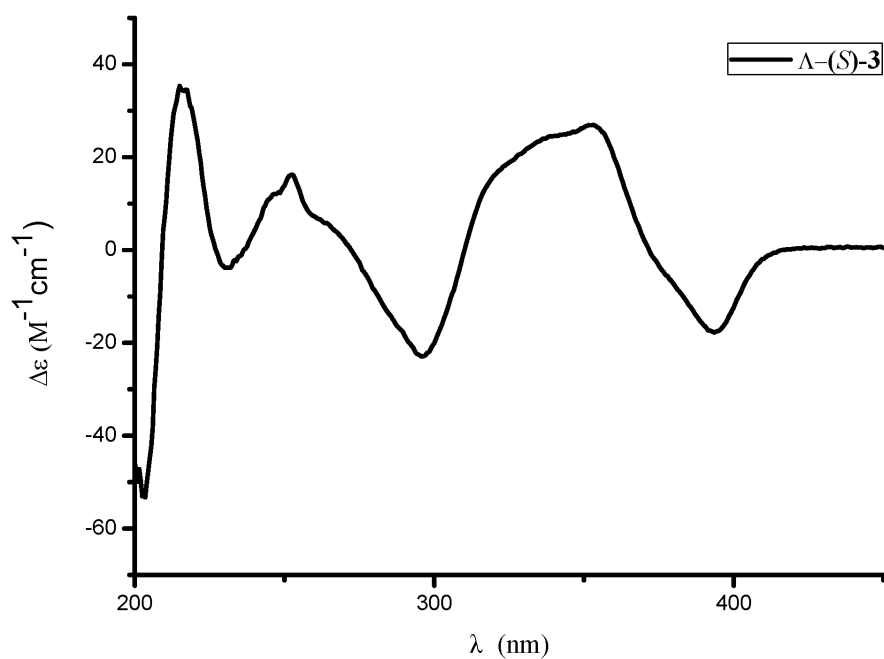


Figure 102 CD spectrum of complex $\Delta-(S)-3$ recorded in CH_3OH (0.2 mM).

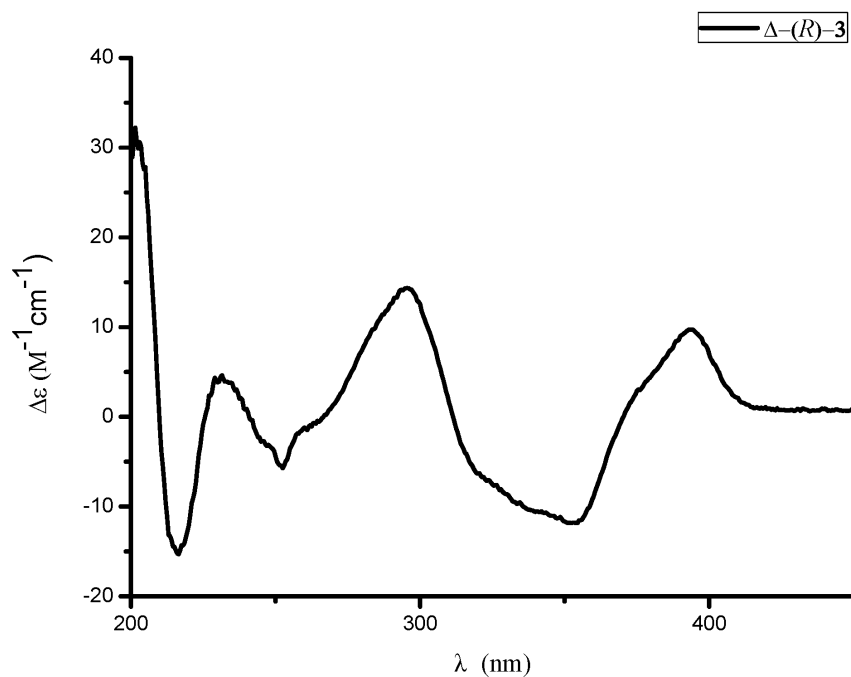


Figure 103 CD spectrum of complex $\Delta-(R)-3$ recorded in CH_3OH (0.2 mM).

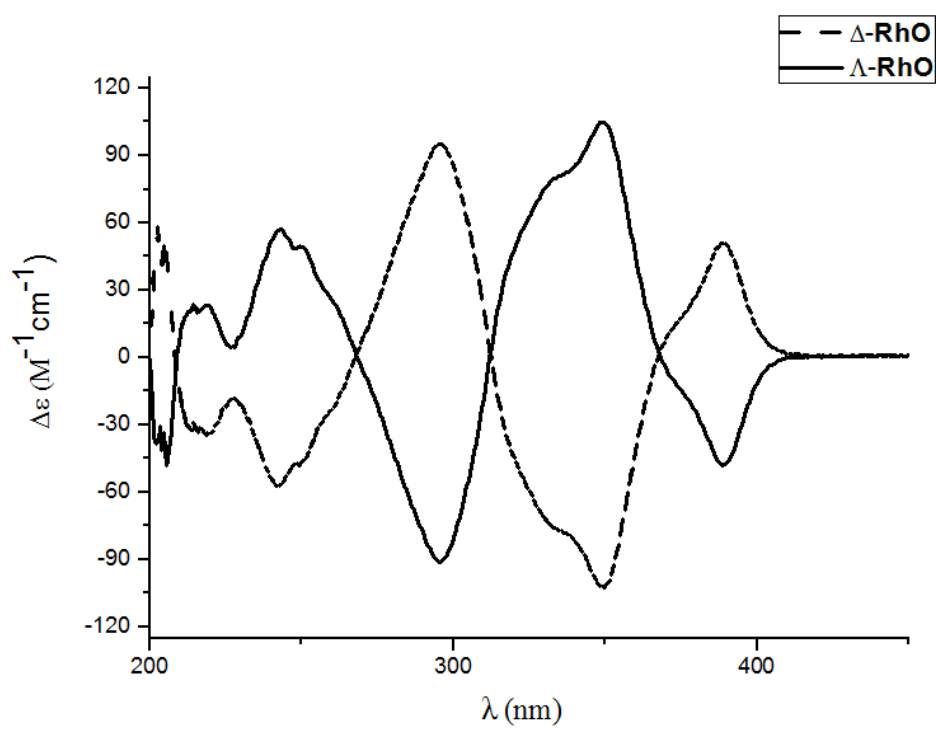


Figure 104 CD spectra of complexes Δ -RhO and Λ -RhO recorded in CH_3OH (0.2 mM).

6.6.3 HPLC Spectra of Compounds

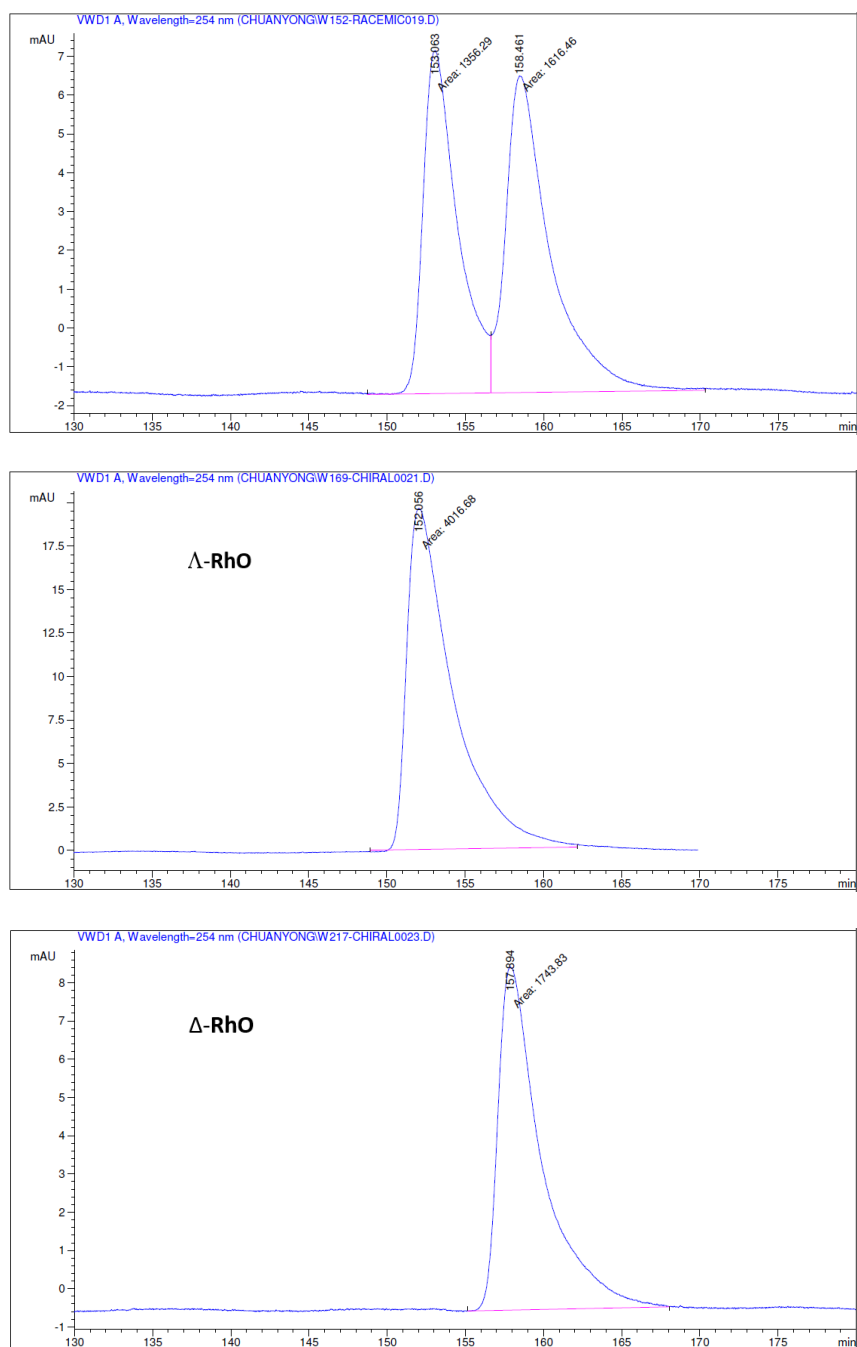


Figure 105 HPLC trace for the racemic reference complexes Δ/Λ -RhO, Δ -RhO and Λ -RhO. HPLC conditions: Daicel Chiralpak IB (250 \times 4.6 mm) HPLC column on an Agilent 1200 Series HPLC System. The column temperature was 25 °C and UV-absorption was measured at 254 nm. Solvent A = 0.1% TFA, solvent B = MeCN (Daicel Chiralpak IB, with a linear gradient of 30% to 41% B in 60 min, flow rate = 0.6 mL/min).

Chapter 6: Appendices

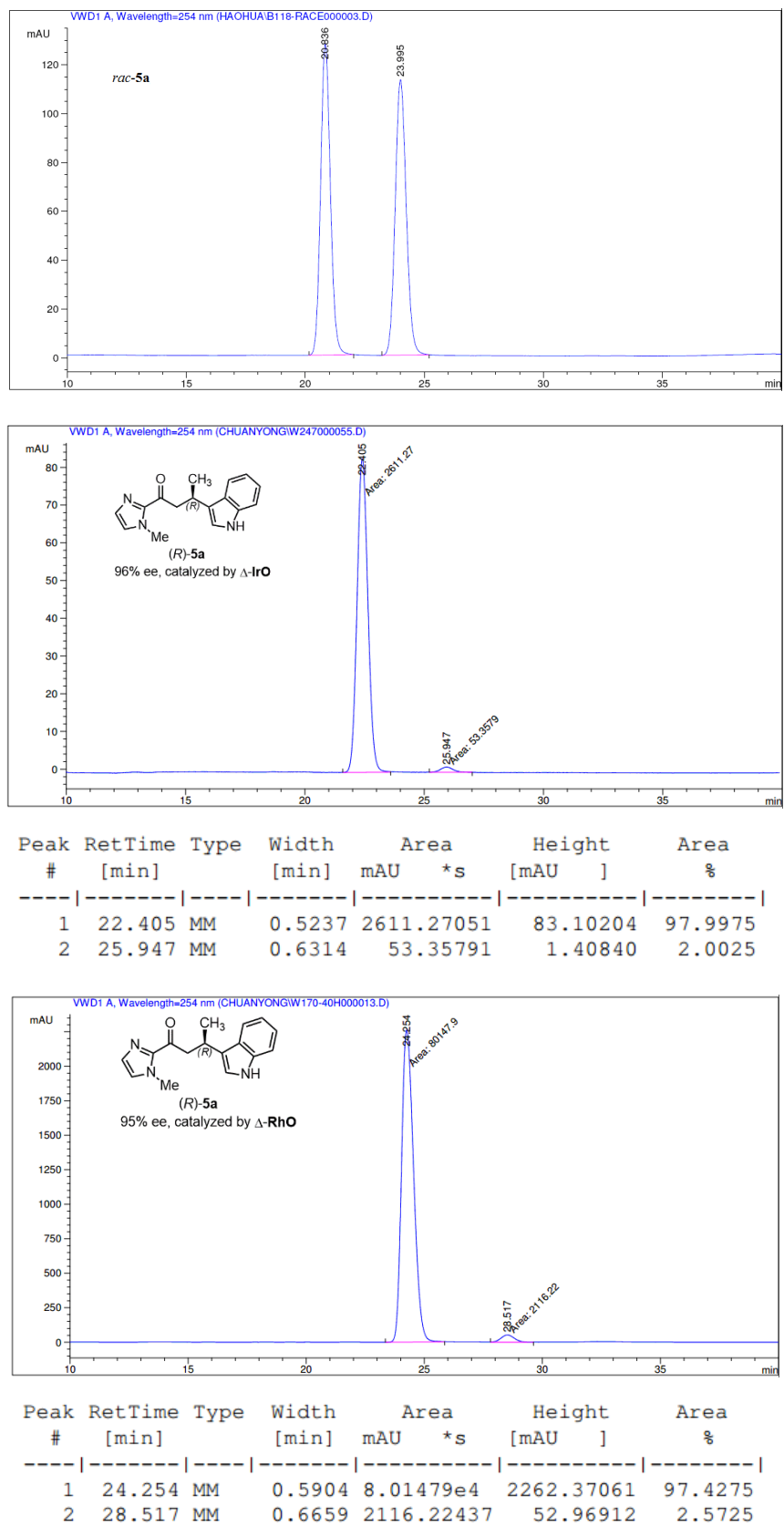
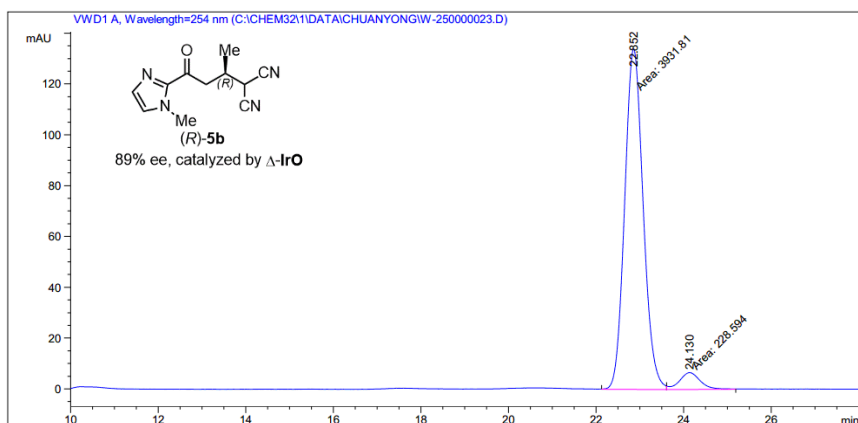
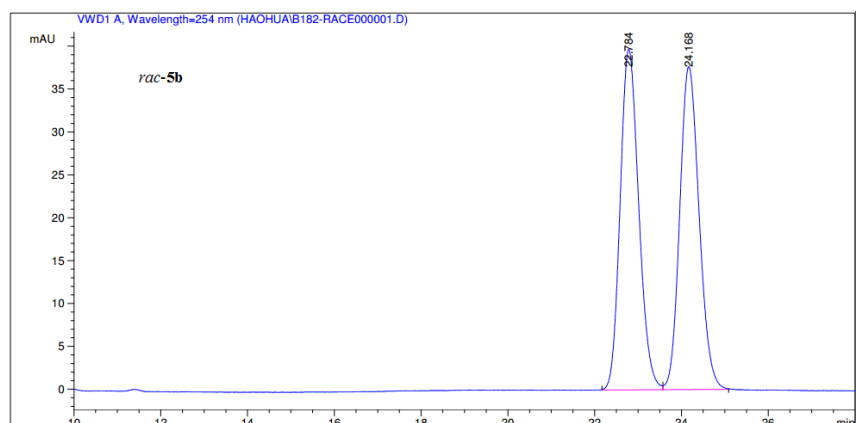
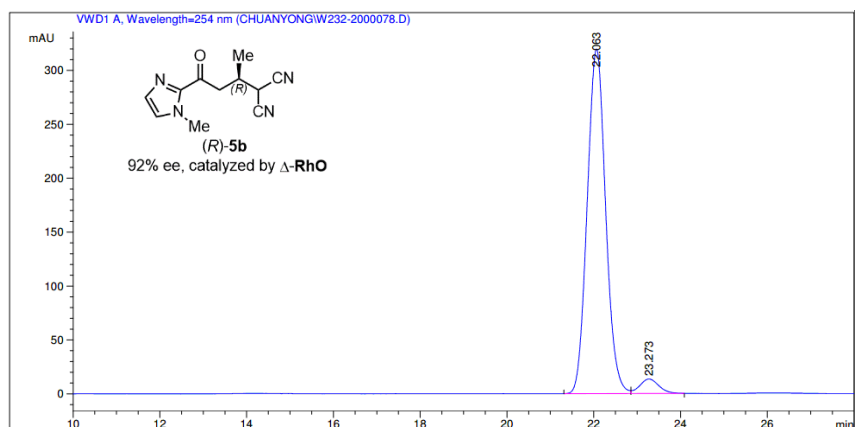


Figure 106 HPLC traces (Daicel Chiralpak IC column) of *rac*-**5a** (reference) and (*R*)-**5a**.

Chapter 6: Appendices



Peak #	RetTime [min]	Type	Width [min]	Area mAU	Height [mAU]	Area %
1	22.852	MM	0.4886	3931.80957	134.13013	94.5055
2	24.130	MM	0.5664	228.59448	6.72654	5.4945



Peak #	RetTime [min]	Type	Width [min]	Area mAU	Height [mAU]	Area %
1	22.063	BV	0.4589	9423.82324	319.67722	95.8346
2	23.273	VB	0.4681	409.60535	13.47748	4.1654

Figure 107 HPLC traces (Daicel Chiralpak AD-H column) of *rac*-**5b** (reference) and (*R*)-**5b**.

Chapter 6: Appendices

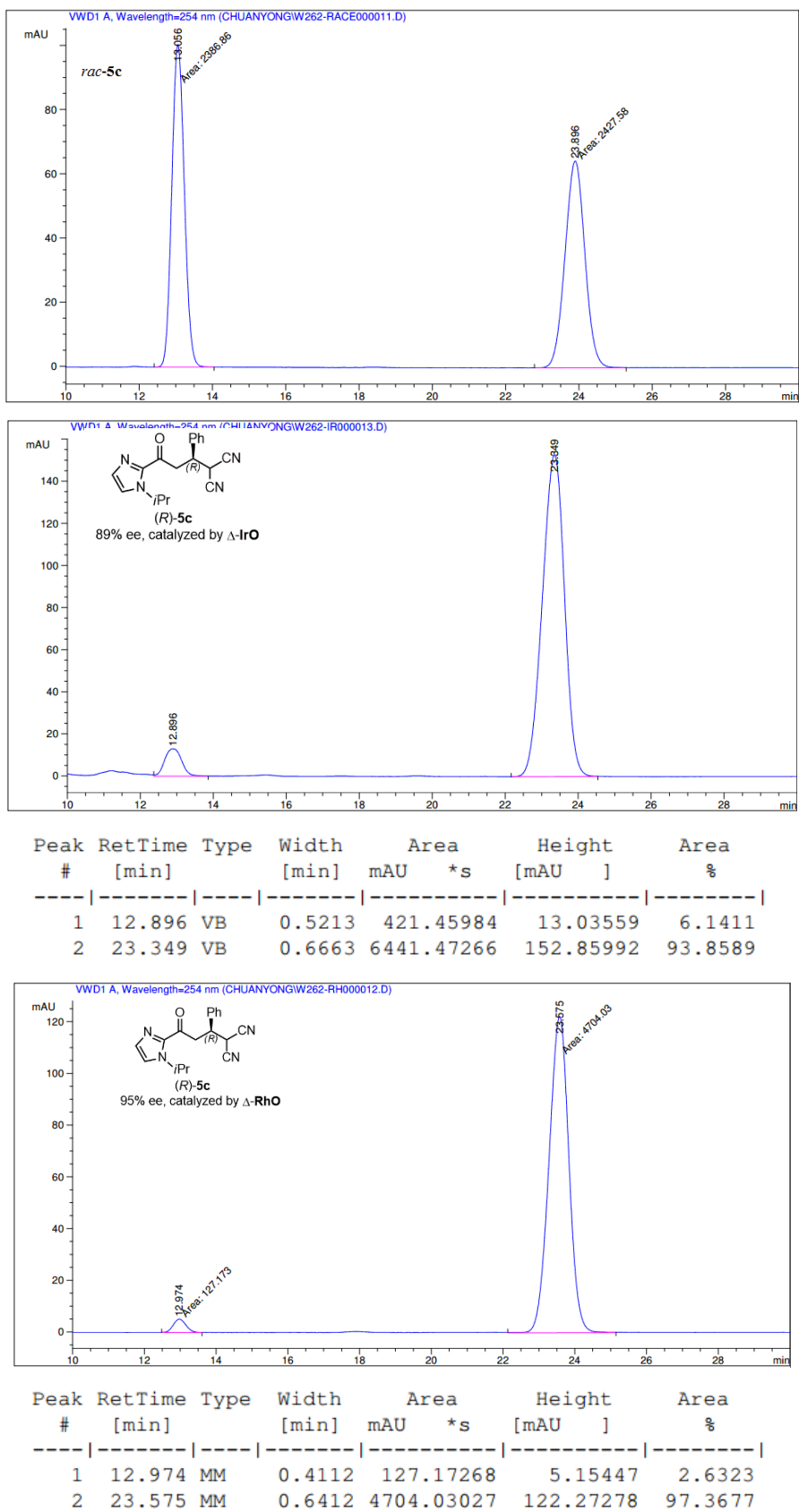


Figure 108 HPLC traces (Daicel Chiralpak AD-H column) of *rac*-5c (reference) and (*R*)-5c.

Chapter 6: Appendices

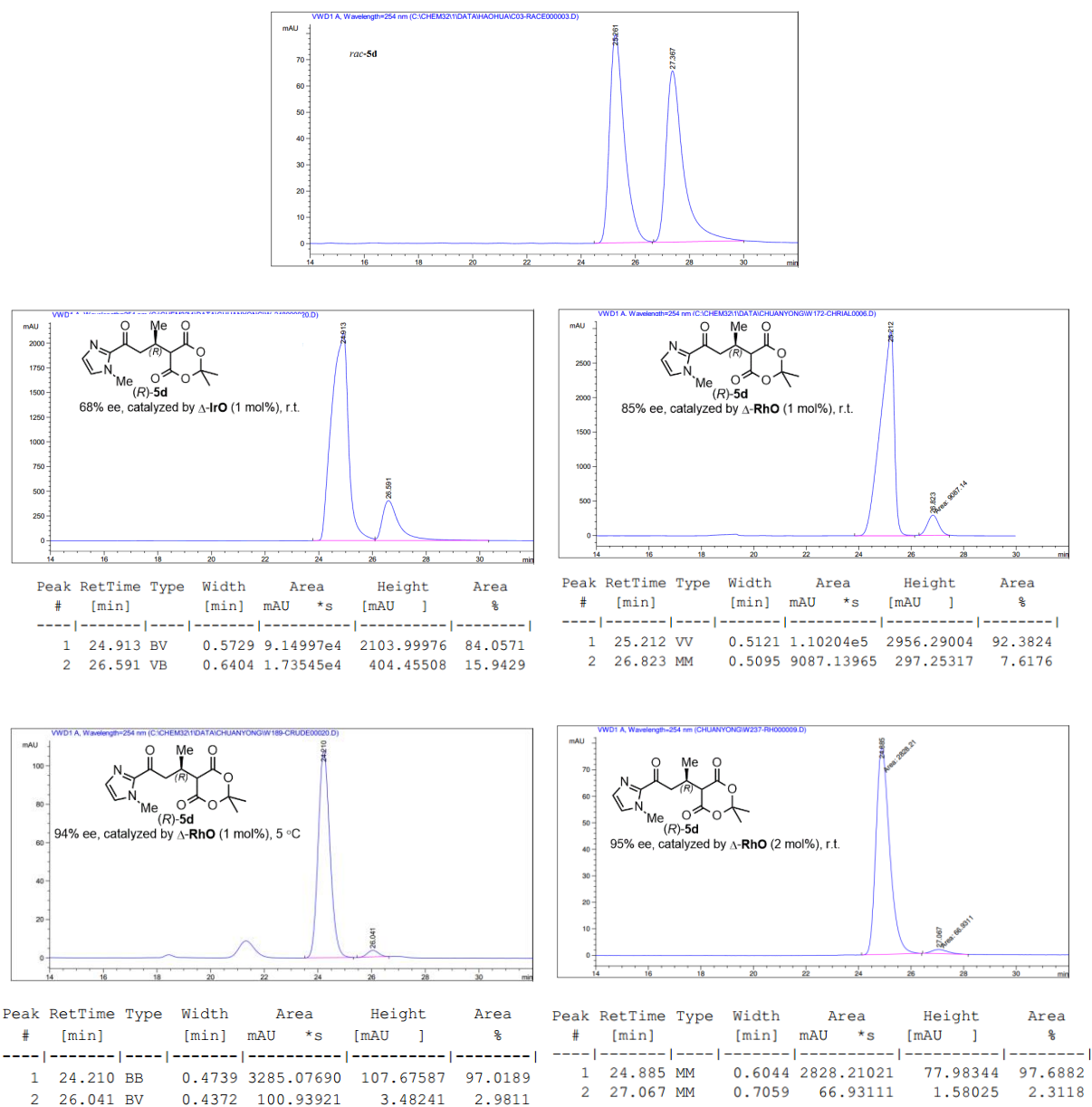


Figure 109 HPLC traces (Daicel Chiralpak AD-H column) of *rac*-5d (reference) and (*R*)-5d.

Chapter 6: Appendices

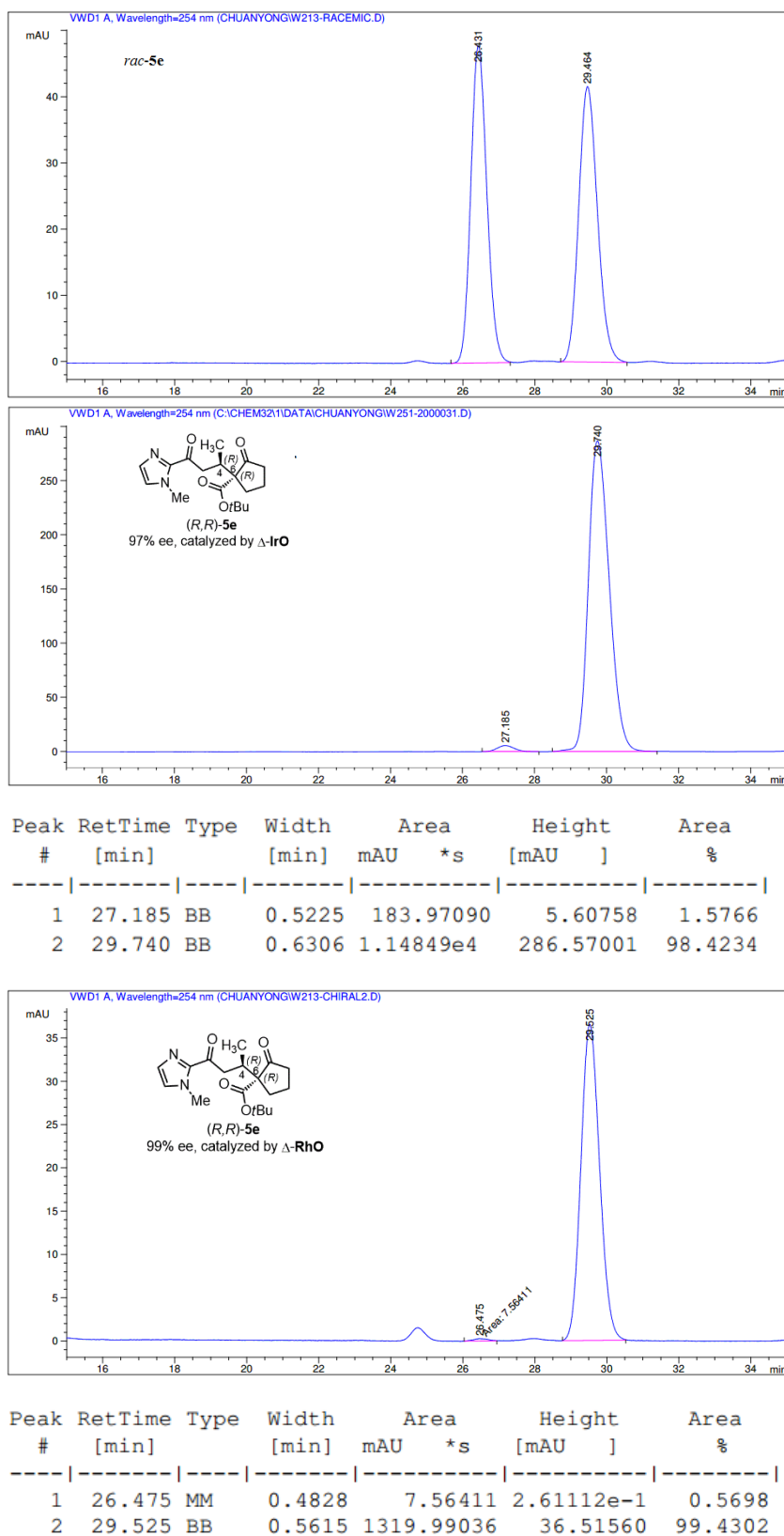
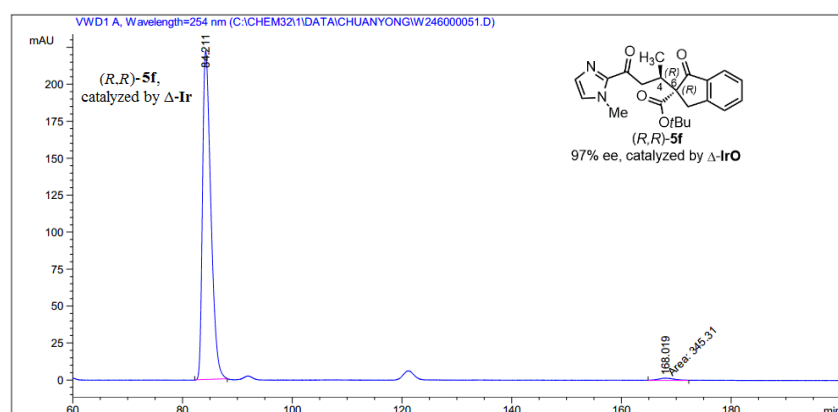
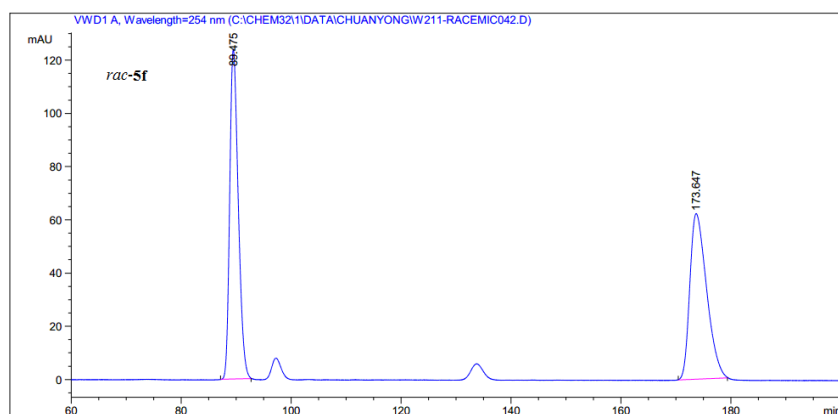
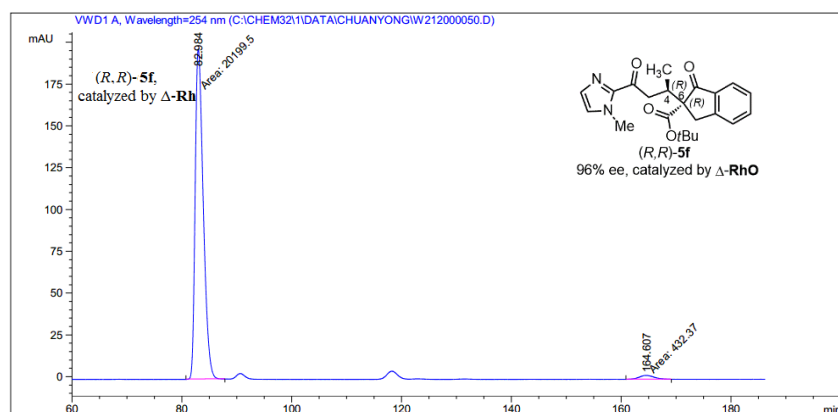


Figure 110 HPLC traces (Daicel Chiralpak AD-H column) of *rac*-5e (reference) and (*R,R*)-5e.

Chapter 6: Appendices



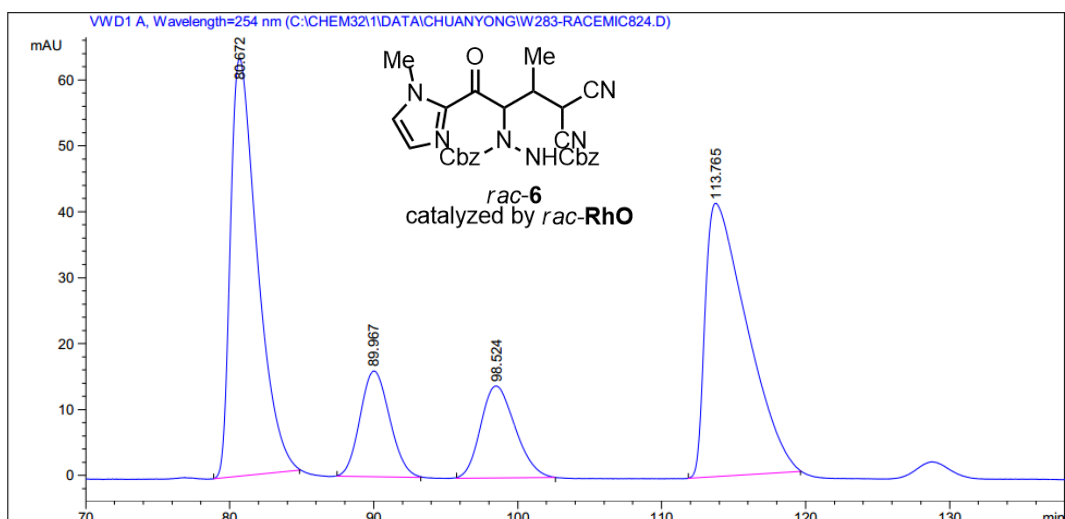
Peak #	RetTime [min]	Type	Width [min]	Area mAU	Height [mAU]	Area %
1	84.211	BB	1.5474	2.35205e4	222.56070	98.5531
2	168.019	MM	3.6661	345.30972	1.56983	1.4469



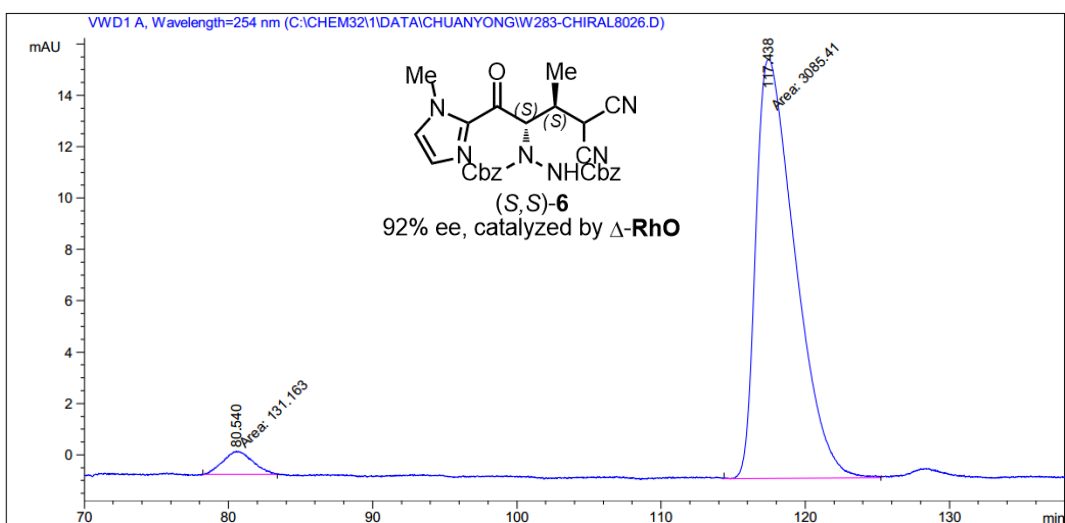
Peak #	RetTime [min]	Type	Width [min]	Area mAU	Height [mAU]	Area %
1	82.984	MM	1.7034	2.01995e4	197.64090	97.9044
2	164.607	MM	3.1124	432.37006	2.31528	2.0956

Figure 111 HPLC traces (Daicel Chiralpak AD-H column) of *rac*-**5f** (reference) and (*R,R*)-**5f**.

Chapter 6: Appendices



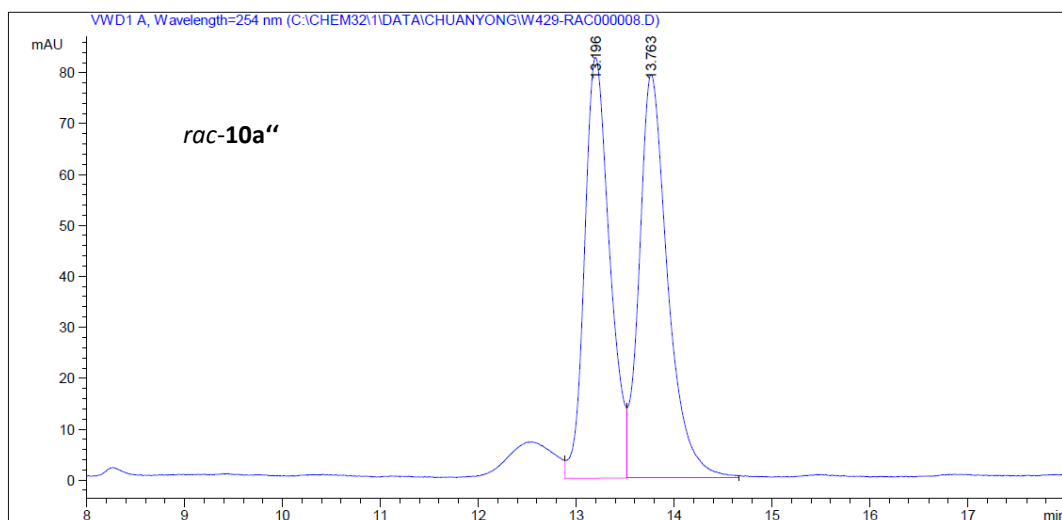
Peak #	RetTime [min]	Type	Width [min]	Area mAU *s	Height [mAU]	Area %
1	80.672	BB	1.5887	8230.40527	63.40287	38.7636
2	89.967	BV	1.6792	2299.65479	16.06056	10.8309
3	98.524	BV	1.9631	2344.05249	13.99327	11.0400
4	113.765	BB	2.3714	8358.17773	41.50156	39.3654



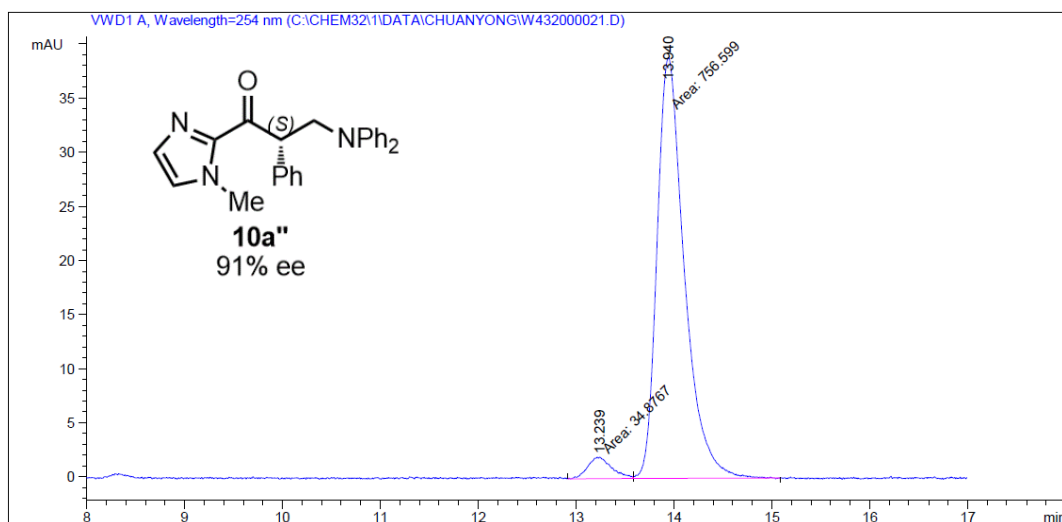
Peak #	RetTime [min]	Type	Width [min]	Area mAU *s	Height [mAU]	Area %
1	80.540	MM	2.4040	131.16324	9.09343e-1	4.0777
2	117.438	MM	3.1465	3085.41309	16.34288	95.9223

Figure 112 HPLC traces (Daicel Chiralpak AD-H column) of *rac-6* (reference) and (*S,S*)-6.

Chapter 6: Appendices



Peak #	RetTime [min]	Type	Width [min]	Area mAU *s	Height [mAU]	Area %
1	13.196	VV	0.2673	1476.68274	82.68617	47.8421
2	13.763	VV	0.2954	1609.89441	79.20117	52.1579



Peak #	RetTime [min]	Type	Width [min]	Area mAU *s	Height [mAU]	Area %
1	13.239	MF	0.2882	34.87672	2.01719	4.4065
2	13.940	FM	0.3241	756.59875	38.90553	95.5935

Figure 113 HPLC traces (Daicel Chiralpak AD-H column) of *rac-10a''* (reference) and (*S*)-**10a''**.

Chapter 6: Appendices

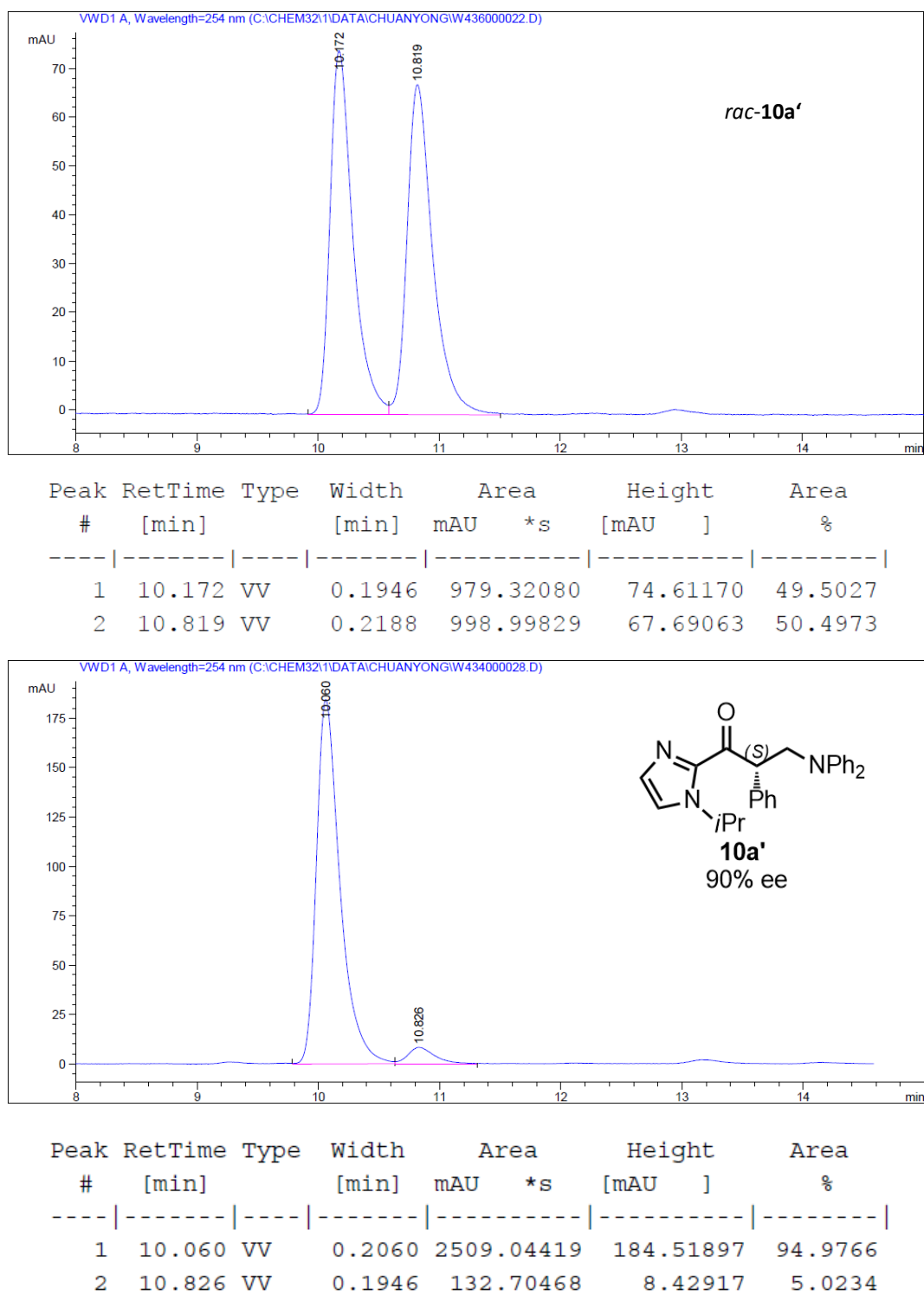


Figure 114 HPLC traces (Daicel Chiralpak AD-H column) of *rac-10a'* (reference) and (*S*)-**10a'**.

Chapter 6: Appendices

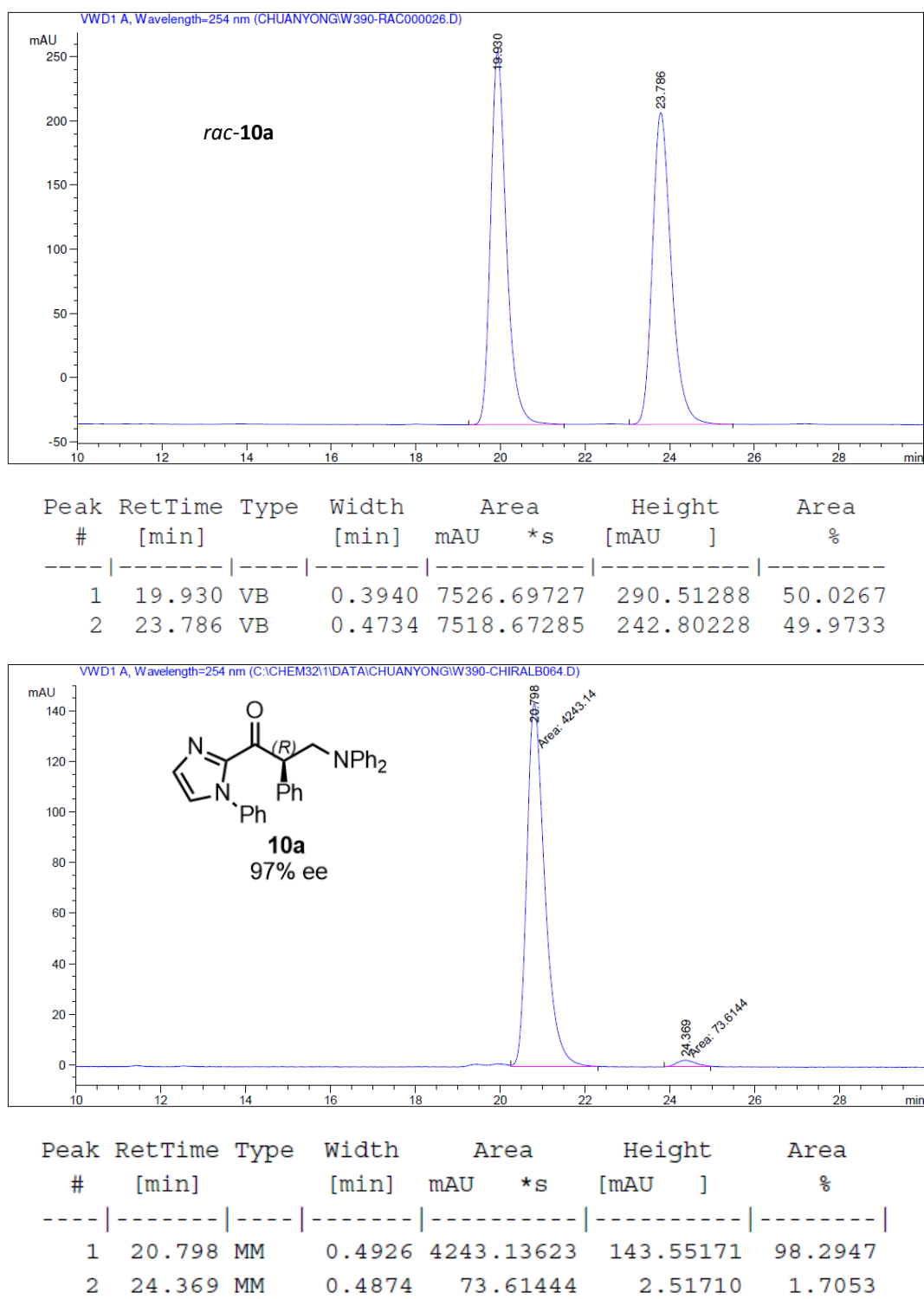
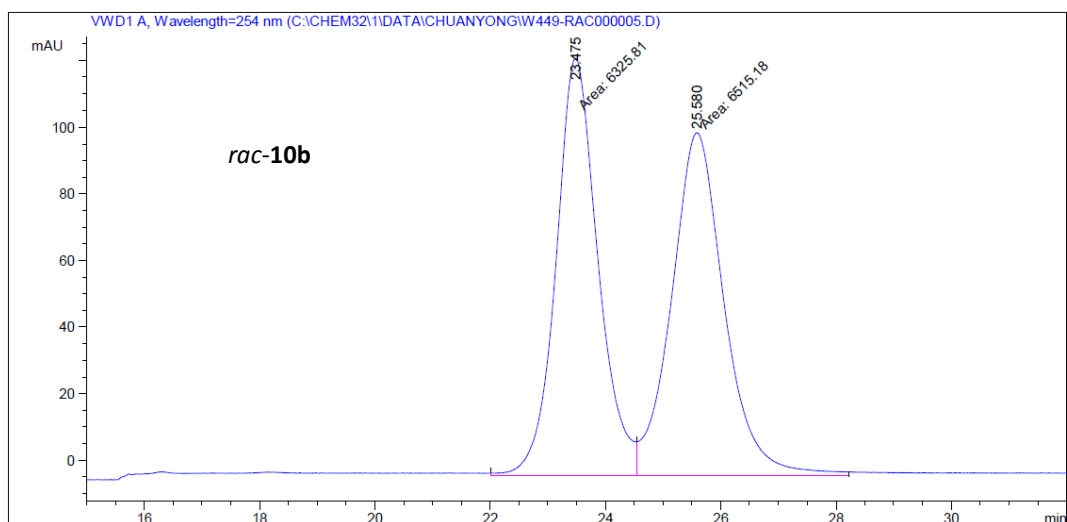
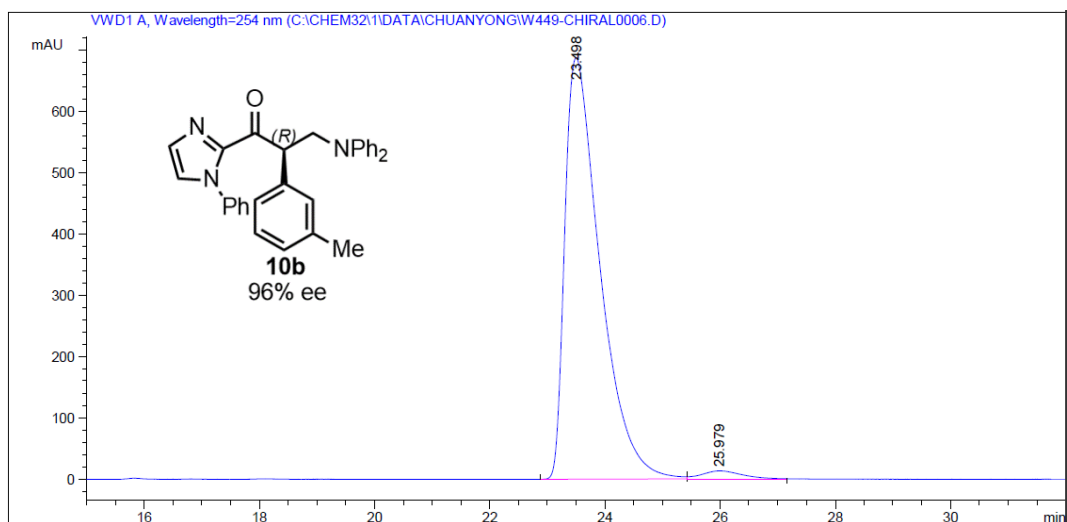


Figure 115 HPLC traces (Daicel Chiralpak AD-H column) of *rac*-**10a** (reference) and (*R*)-**10a**.

Chapter 6: Appendices



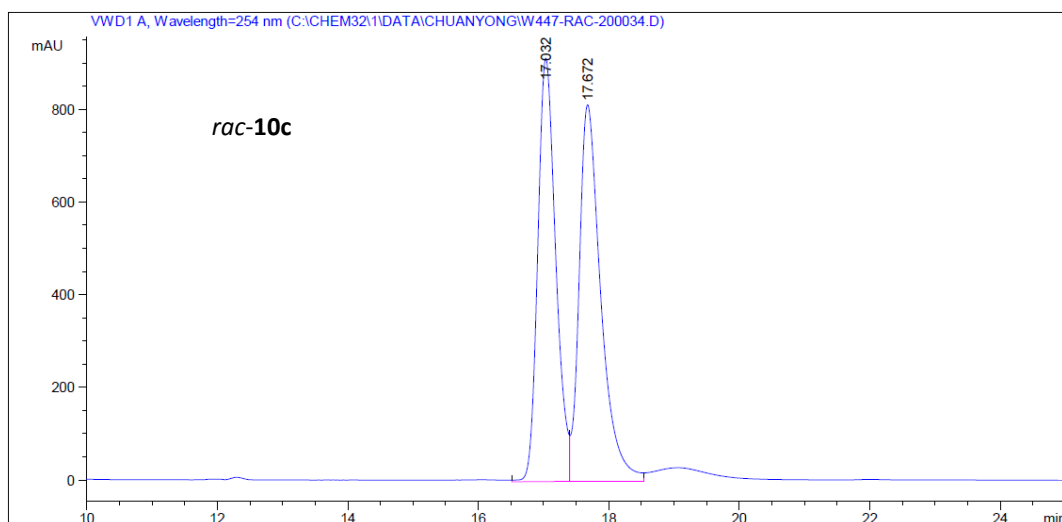
Peak #	RetTime [min]	Type	Width [min]	Area mAU *s	Height [mAU]	Area %
1	23.475	MF	0.8424	6325.81006	125.14971	49.2626
2	25.580	FM	1.0562	6515.17969	102.80542	50.7374



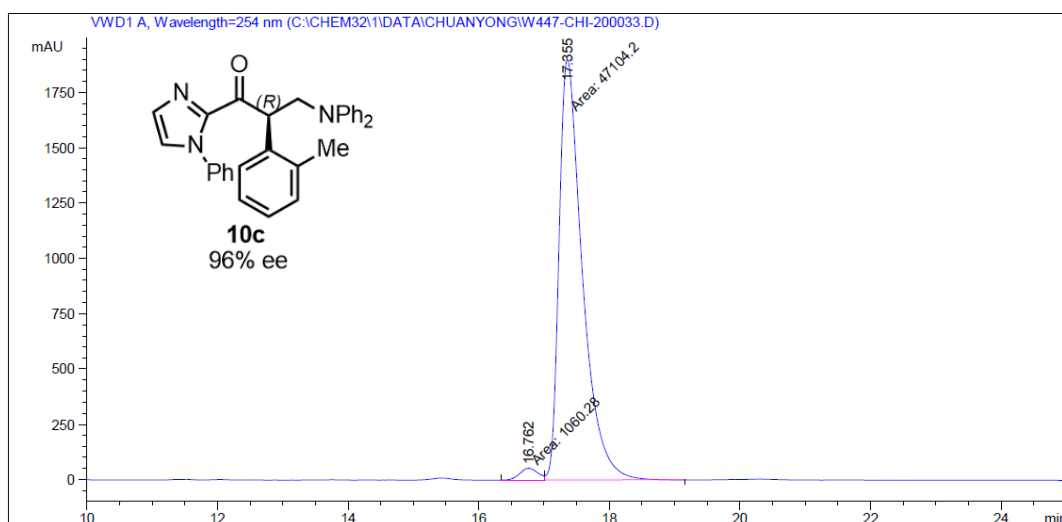
Peak #	RetTime [min]	Type	Width [min]	Area mAU *s	Height [mAU]	Area %
1	23.498	VV	0.5782	2.91600e4	688.01190	97.8213
2	25.979	VV	0.5712	649.47150	13.34978	2.1787

Figure 116 HPLC traces (Daicel Chiralpak OD-H column) of *rac*-**10b** (reference) and (*R*)-**10b**.

Chapter 6: Appendices



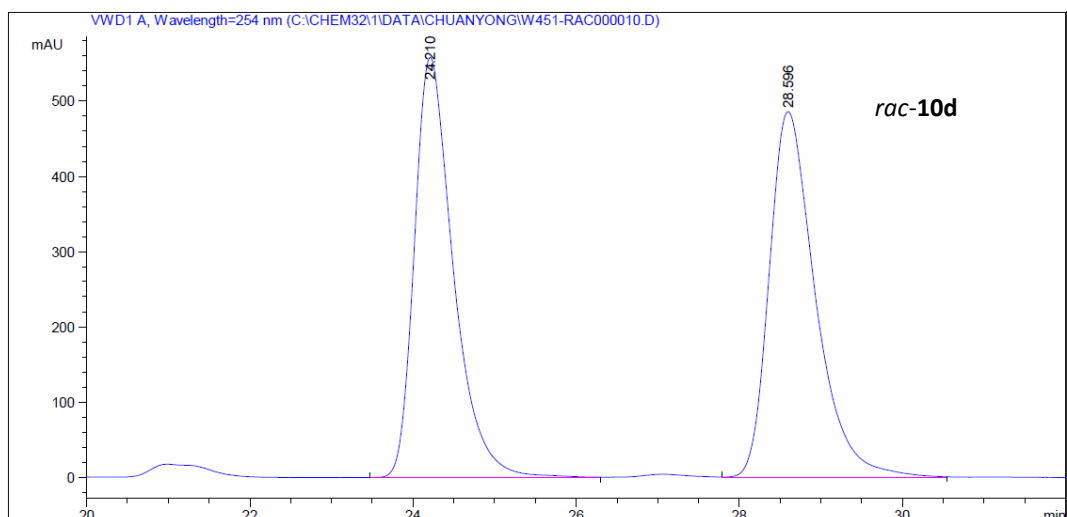
Peak #	RetTime [min]	Type	Width [min]	Area mAU *s	Height [mAU]	Area %
1	13.586	VV	0.2349	1928.50610	124.29128	46.4937
2	14.077	VB	0.2748	2219.38257	119.95074	53.5063



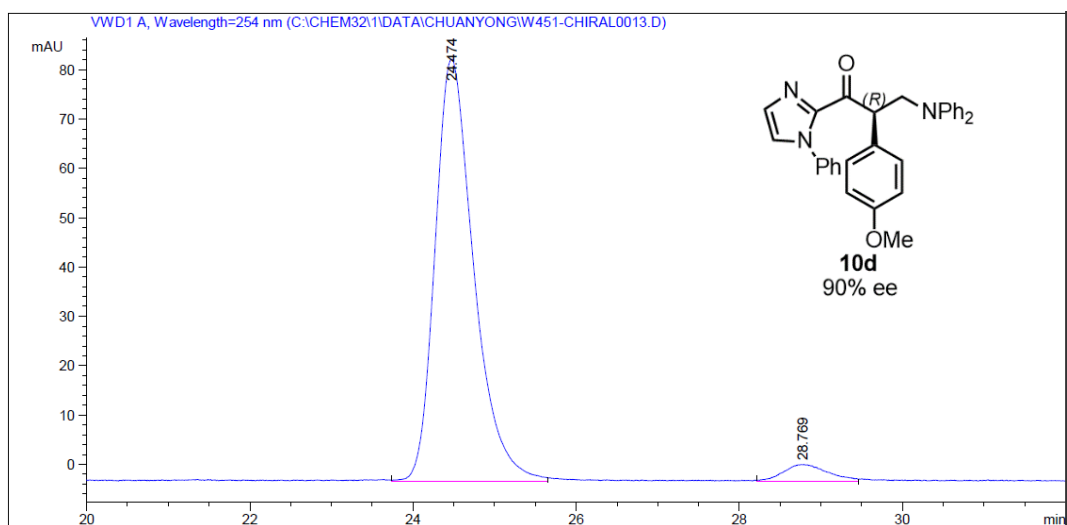
Peak #	RetTime [min]	Type	Width [min]	Area mAU *s	Height [mAU]	Area %
1	16.762	MF	0.3264	1060.27991	54.13697	2.2014
2	17.355	FM	0.4127	4.71042e4	1902.45703	97.7986

Figure 117 HPLC traces (Daicel Chiralpak AD-H column) of *rac-10c* (reference) and (*R*)-**10c**.

Chapter 6: Appendices



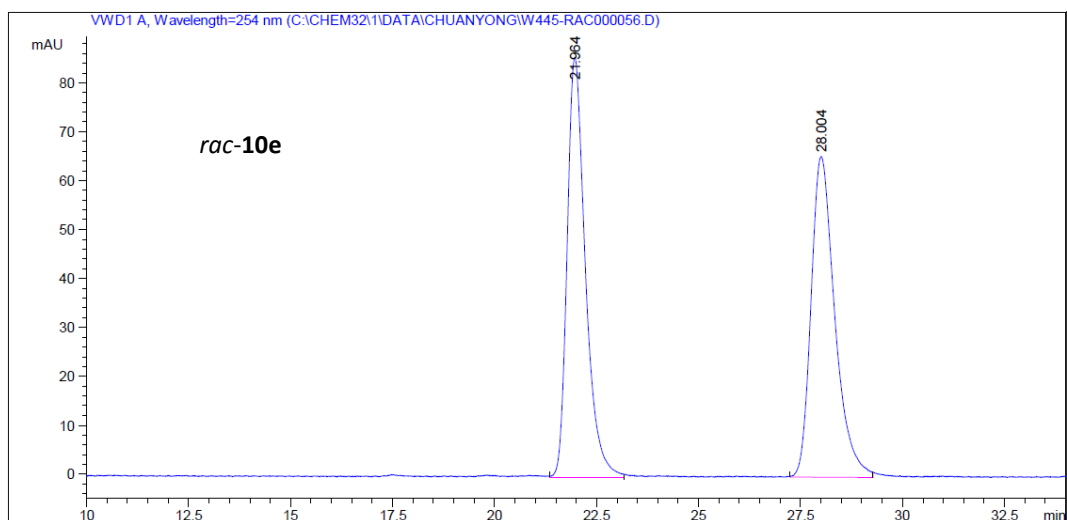
Peak #	RetTime [min]	Type	Width [min]	Area mAU *s	Height [mAU]	Area %
1	24.210	VB	0.4912	1.84991e4	557.57538	49.1619
2	28.596	VV	0.5476	1.91298e4	485.68527	50.8381



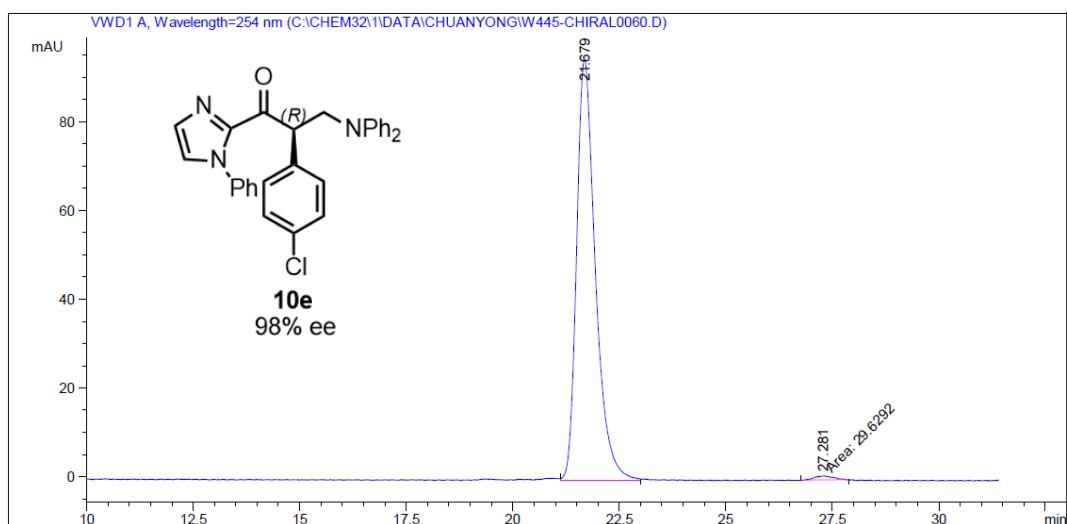
Peak #	RetTime [min]	Type	Width [min]	Area mAU *s	Height [mAU]	Area %
1	24.474	VV	0.4002	2821.40063	85.52086	95.6475
2	28.769	VV	0.4444	128.38893	3.39283	4.3525

Figure 118 HPLC traces (Daicel Chiralpak AD-H column) of *rac*-**10d** (reference) and (*R*)-**10d**.

Chapter 6: Appendices



Peak #	RetTime [min]	Type	Width [min]	Area mAU *s	Height [mAU]	Area %
1	21.964	VV	0.4228	2664.86475	85.79457	50.0815
2	28.004	VV	0.5027	2656.19312	65.63637	49.9185



Peak #	RetTime [min]	Type	Width [min]	Area mAU *s	Height [mAU]	Area %
1	21.679	VV	0.4291	2909.38184	94.88998	98.9919
2	27.281	MM	0.5000	29.62918	9.87632e-1	1.0081

Figure 119 HPLC traces (Daicel Chiralpak AD-H column) of *rac*-10e (reference) and (*R*)-10e.

Chapter 6: Appendices

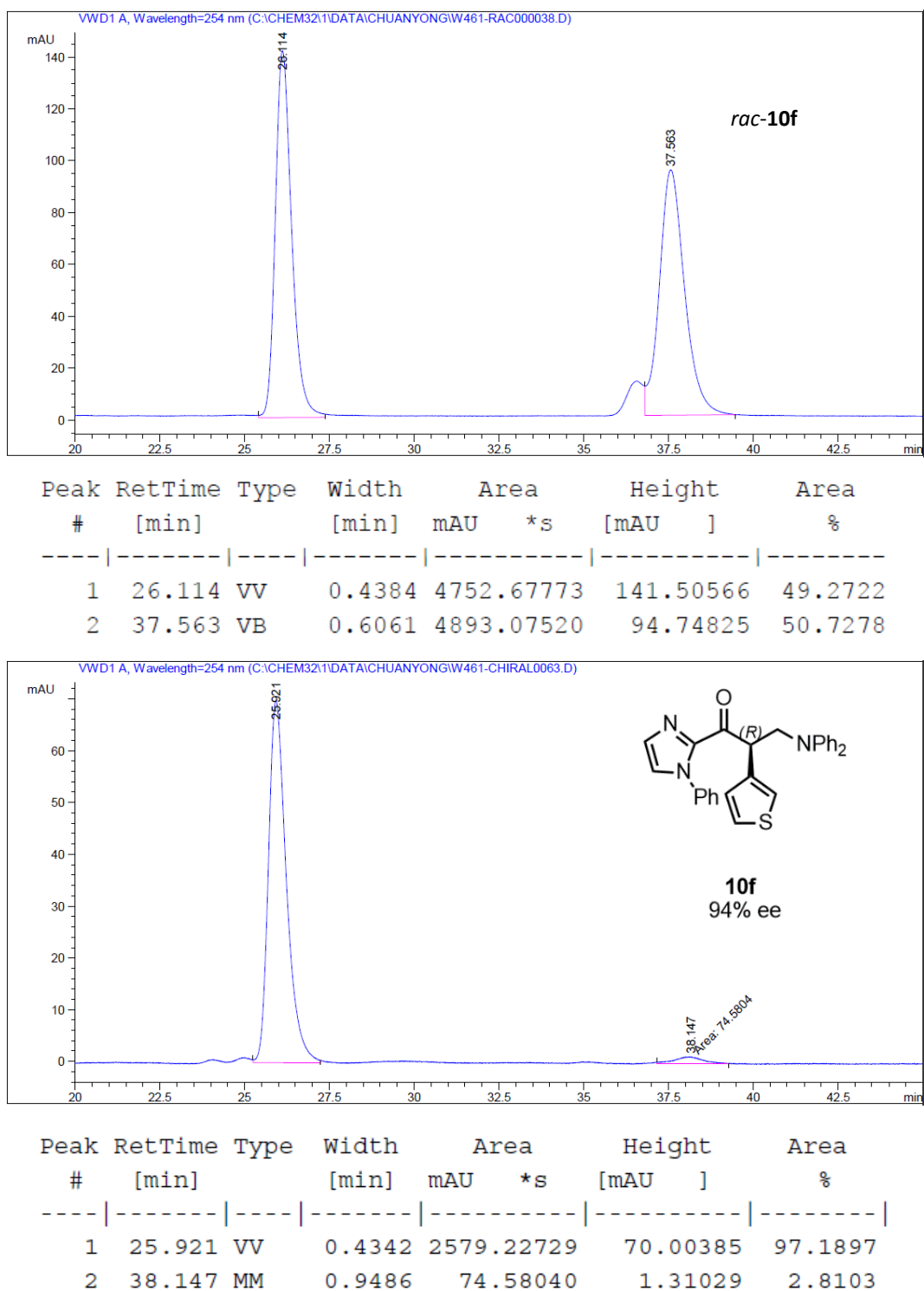
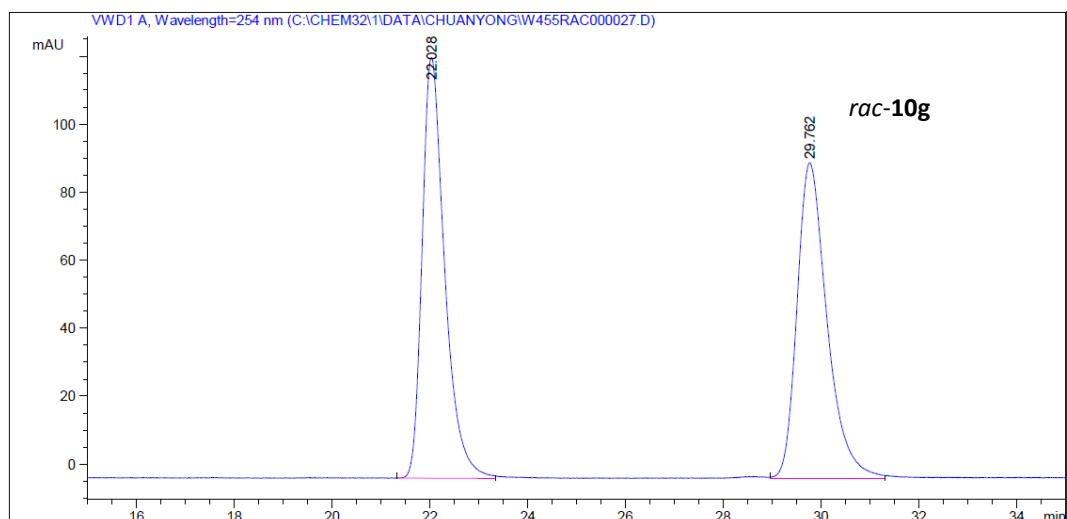
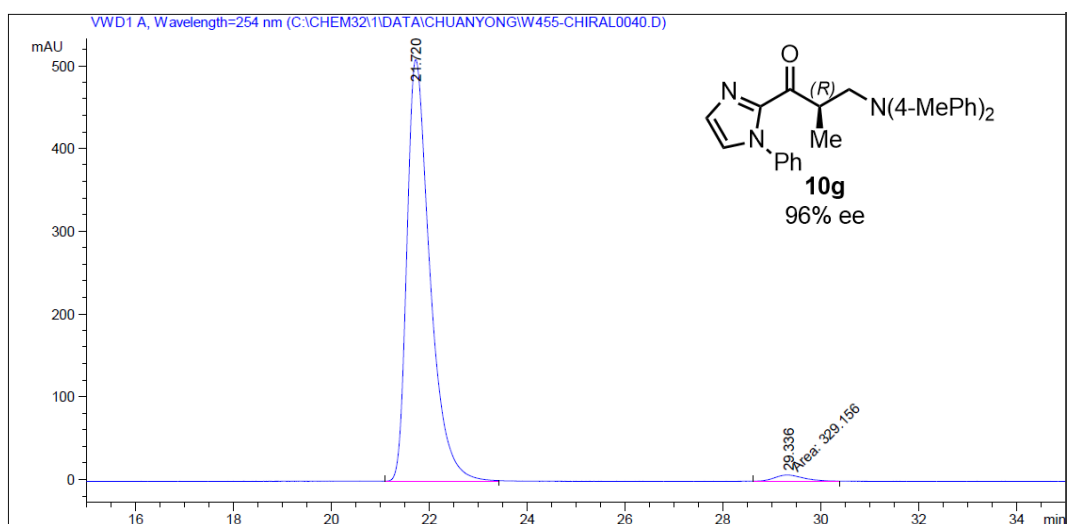


Figure 120 HPLC traces (Daicel Chiralpak AD-H column) of *rac*-**10f** (reference) and (*R*)-**10f**.

Chapter 6: Appendices



Peak #	RetTime [min]	Type	Width [min]	Area mAU *s	Height [mAU]	Area %
1	22.028	VV	0.4596	3966.41284	123.83491	49.9944
2	29.762	VV	0.5149	3967.29517	92.90932	50.0056



Peak #	RetTime [min]	Type	Width [min]	Area mAU *s	Height [mAU]	Area %
1	21.720	VV	0.4861	1.66585e4	509.71826	98.0624
2	29.336	MM	0.7108	329.15604	7.71824	1.9376

Figure 121 HPLC traces (Daicel Chiralpak AD-H column) of *rac-10g* (reference) and *(R)-10g*.

Chapter 6: Appendices

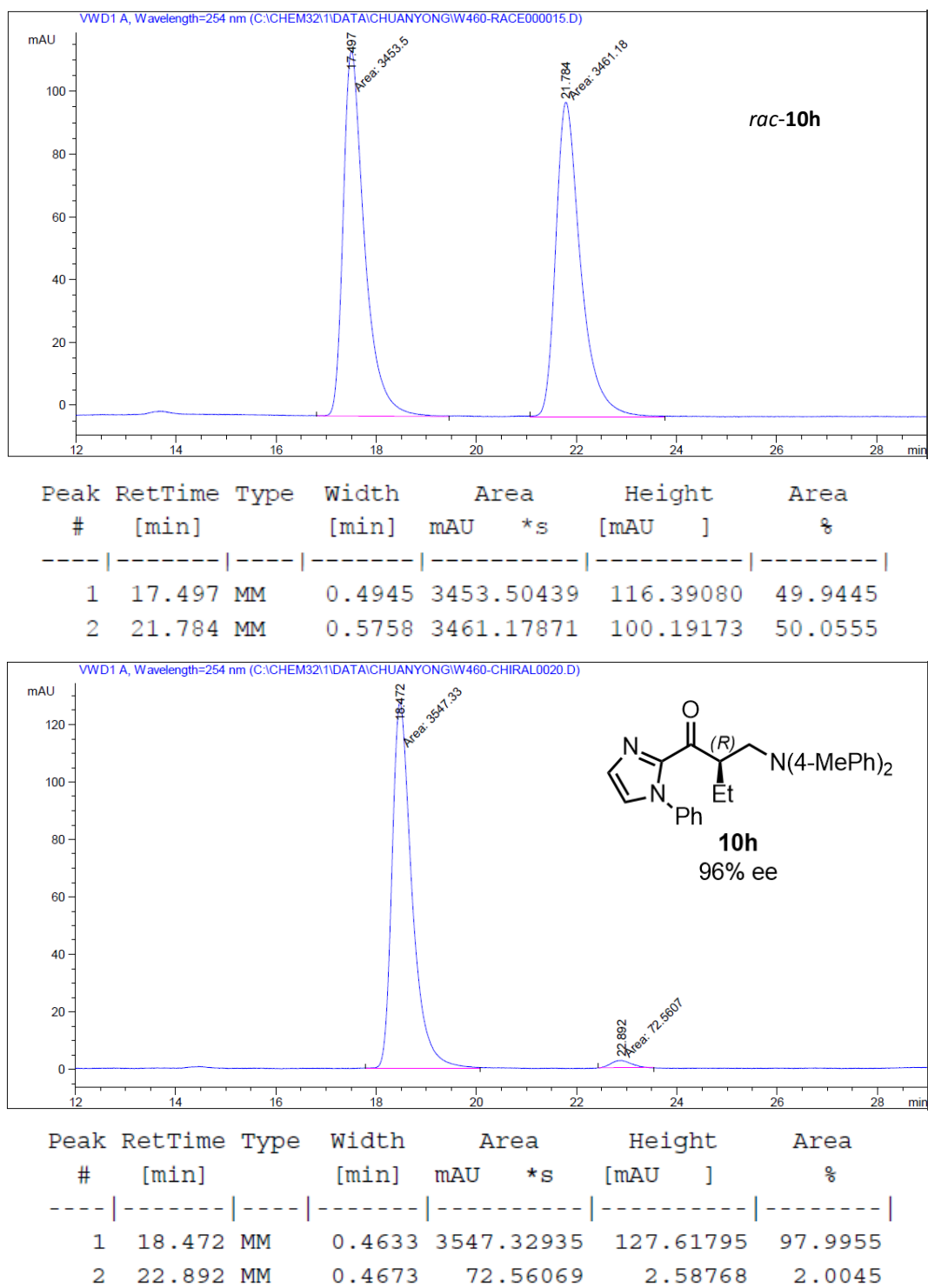
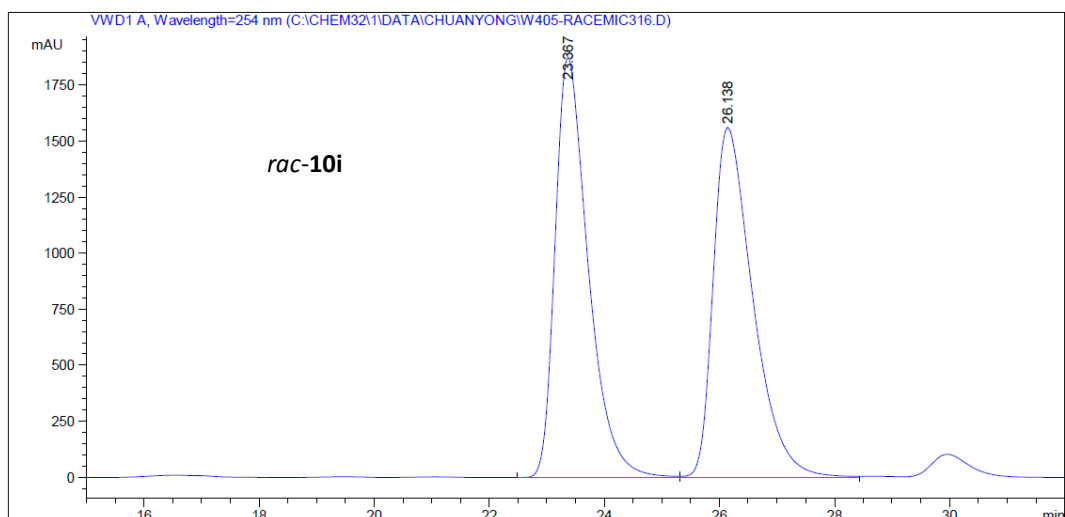
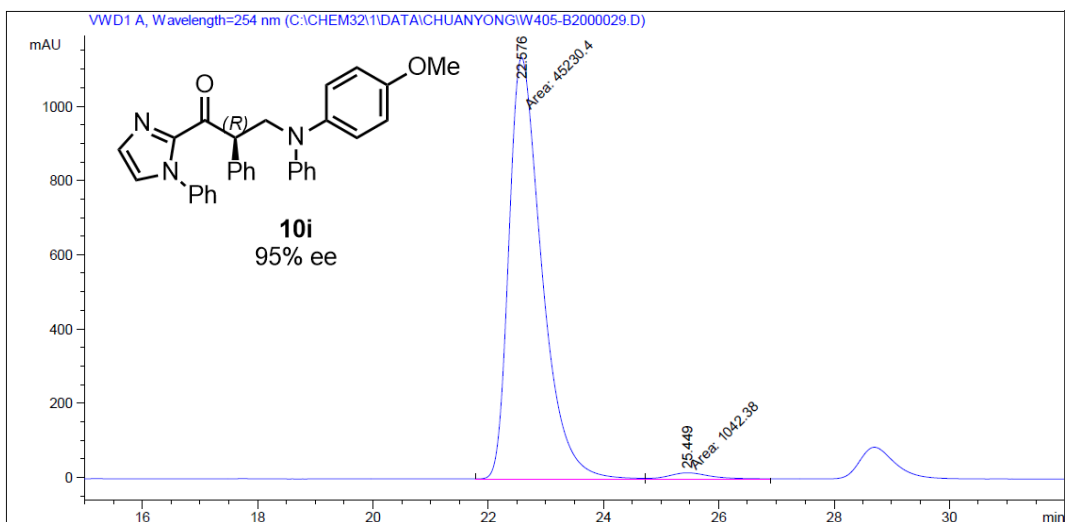


Figure 122 HPLC traces (Daicel Chiralpak AD-H column) of *rac*-**10h** (reference) and (*R*)-**10h**.

Chapter 6: Appendices



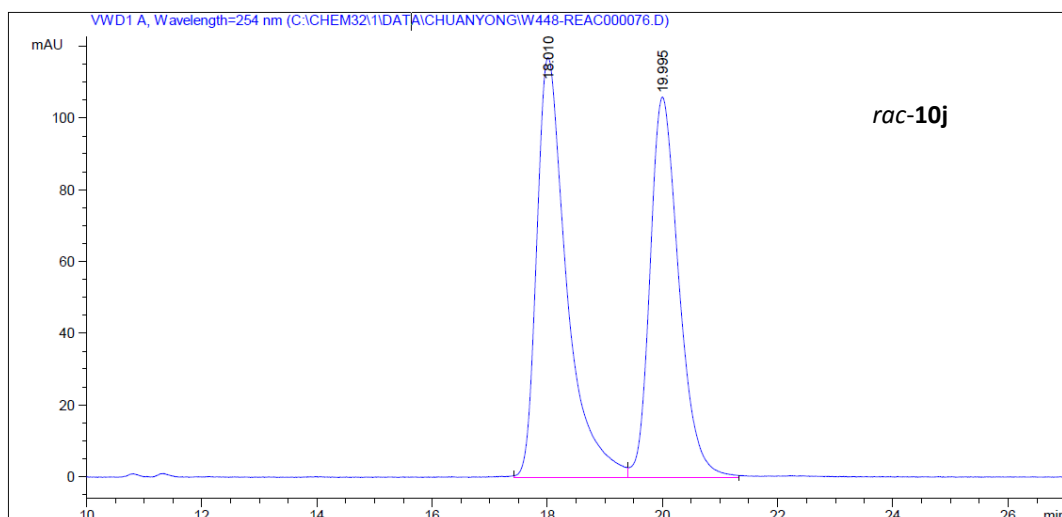
Peak #	RetTime [min]	Type	Width [min]	Area mAU *s	Height [mAU]	Area %
1	23.367	VV	0.4757	7.48852e4	1873.97351	50.0337
2	26.138	VV	0.5687	7.47845e4	1562.09912	49.9663



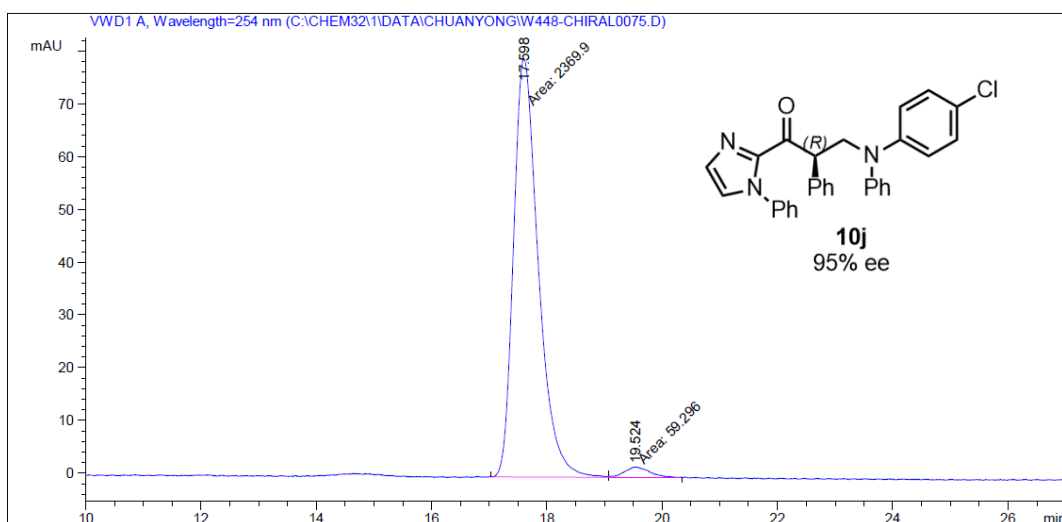
Peak #	RetTime [min]	Type	Width [min]	Area mAU *s	Height [mAU]	Area %
1	22.576	MF	0.6624	4.52304e4	1138.02124	97.7473
2	25.449	FM	0.9491	1042.38440	18.30458	2.2527

Figure 123 HPLC traces (Daicel Chiralpak AD-H column) of *rac*-10i (reference) and (*R*)-10i.

Chapter 6: Appendices



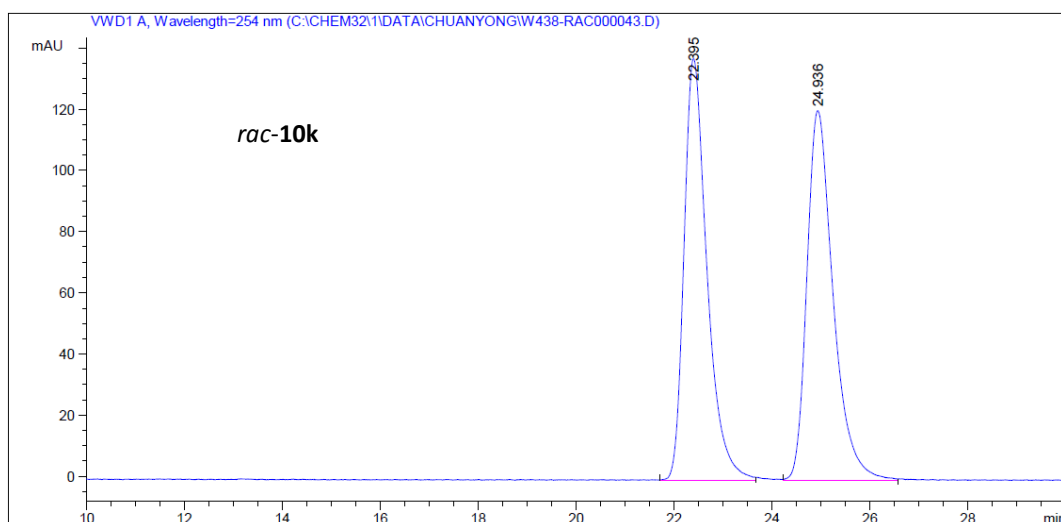
Peak #	RetTime [min]	Type	Width [min]	Area mAU *s	Height [mAU]	Area %
1	18.010	VV	0.4960	4224.42090	117.04946	53.3782
2	19.995	VV	0.4823	3689.71289	106.06081	46.6218



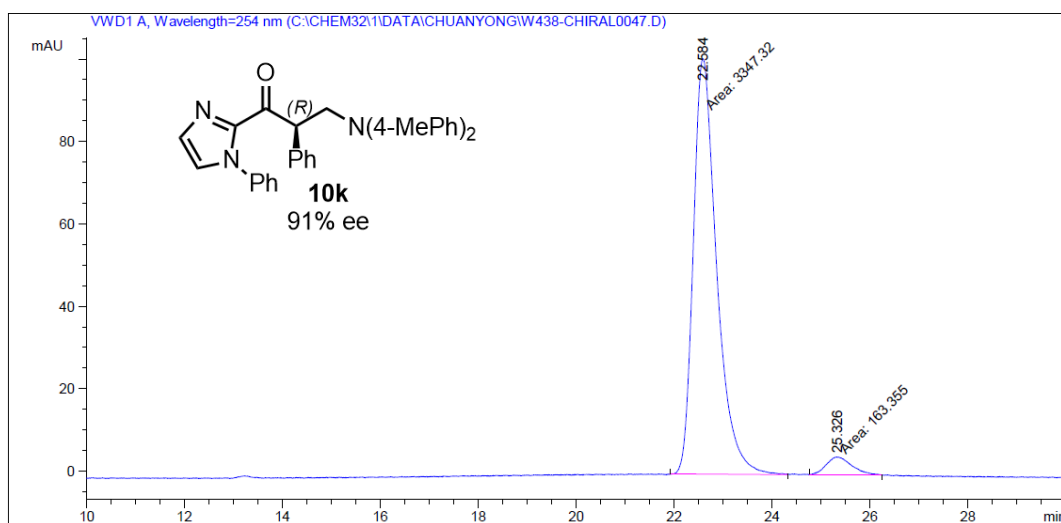
Peak #	RetTime [min]	Type	Width [min]	Area mAU *s	Height [mAU]	Area %
1	17.598	MF	0.4980	2369.89990	79.32042	97.5590
2	19.524	FM	0.5006	59.29604	1.97412	2.4410

Figure 124 HPLC traces (Daicel Chiralpak AD-H column) of *rac*-**10j** (reference) and (*R*)-**10j**.

Chapter 6: Appendices



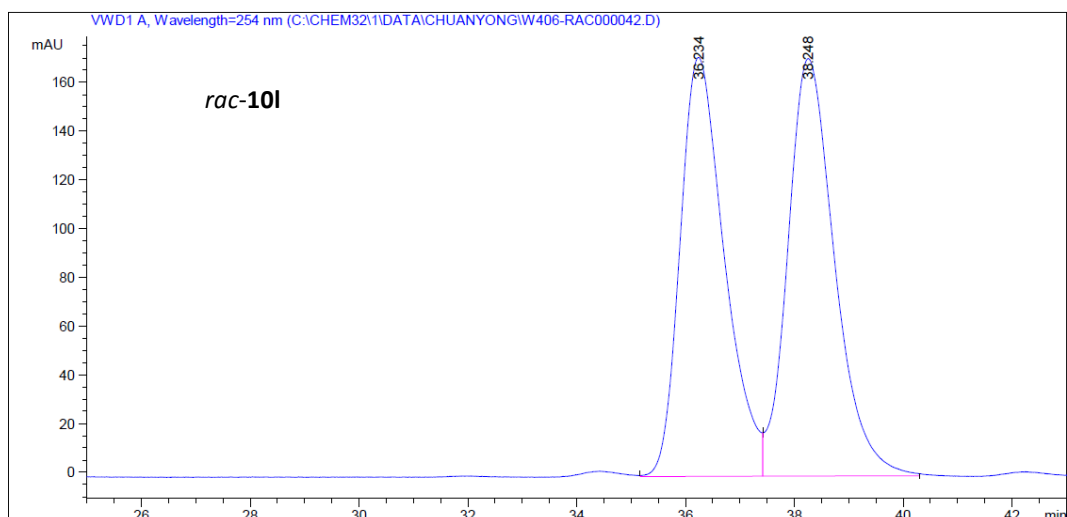
Peak #	RetTime [min]	Type	Width [min]	Area mAU *s	Height [mAU]	Area %
1	22.395	VV	0.4661	4493.14697	137.86949	49.9287
2	24.936	VV	0.4403	4505.97412	120.78177	50.0713



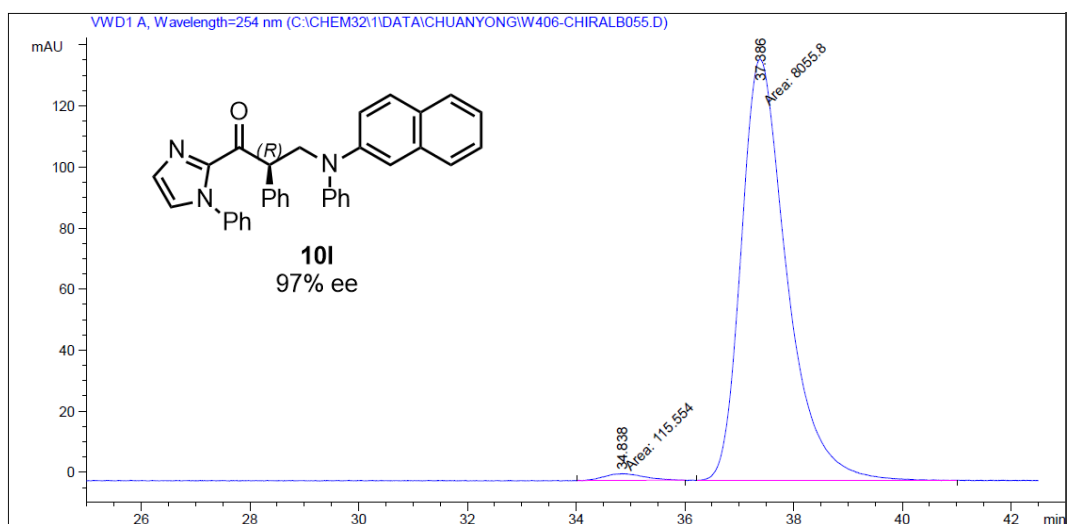
Peak #	RetTime [min]	Type	Width [min]	Area mAU *s	Height [mAU]	Area %
1	22.584	MM	0.5532	3347.32324	100.83930	95.3469
2	25.326	MM	0.6170	163.35477	4.41247	4.6531

Figure 125 HPLC traces (Daicel Chiralpak AD-H column) of *rac-10k* (reference) and (*S*)-**10k**.

Chapter 6: Appendices



Peak #	RetTime [min]	Type	Width [min]	Area mAU *s	Height [mAU]	Area %
1	36.234	VV	0.7064	9725.98437	171.98294	48.7249
2	38.248	VV	0.7032	1.02350e4	171.41588	51.2751



Peak #	RetTime [min]	Type	Width [min]	Area mAU *s	Height [mAU]	Area %
1	34.838	MM	0.8626	115.55431	2.23276	1.4141
2	37.386	MM	0.9735	8055.80273	137.92445	98.5859

Figure 126 HPLC traces (Daicel Chiralpak AD-H column) of *rac*-101 (reference) and (*R*)-101.

Chapter 6: Appendices

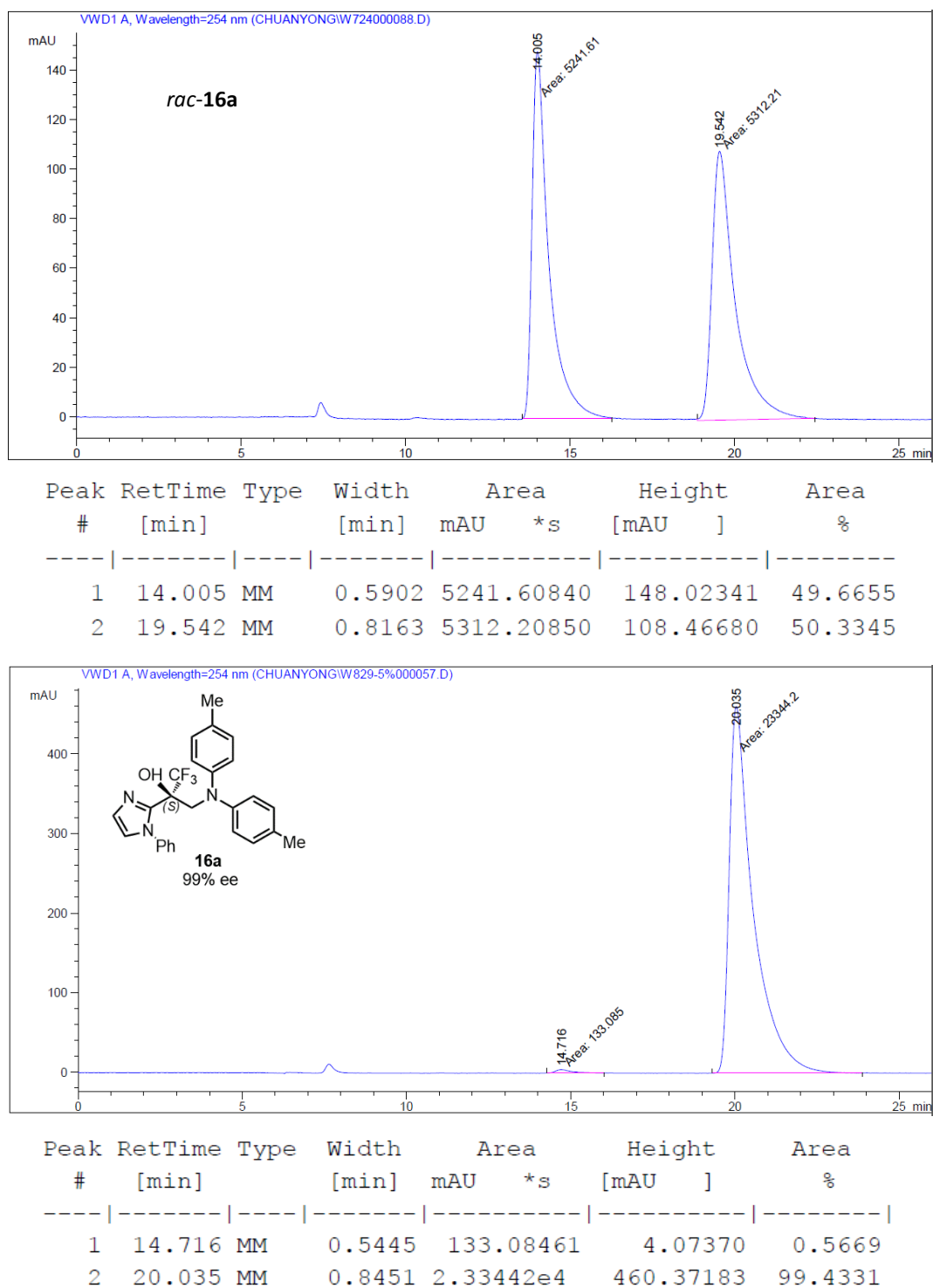
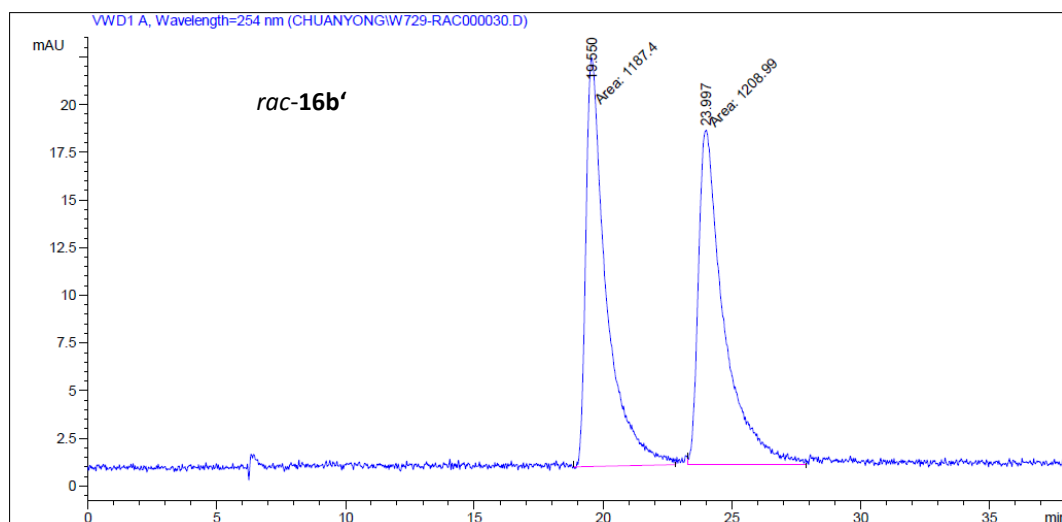
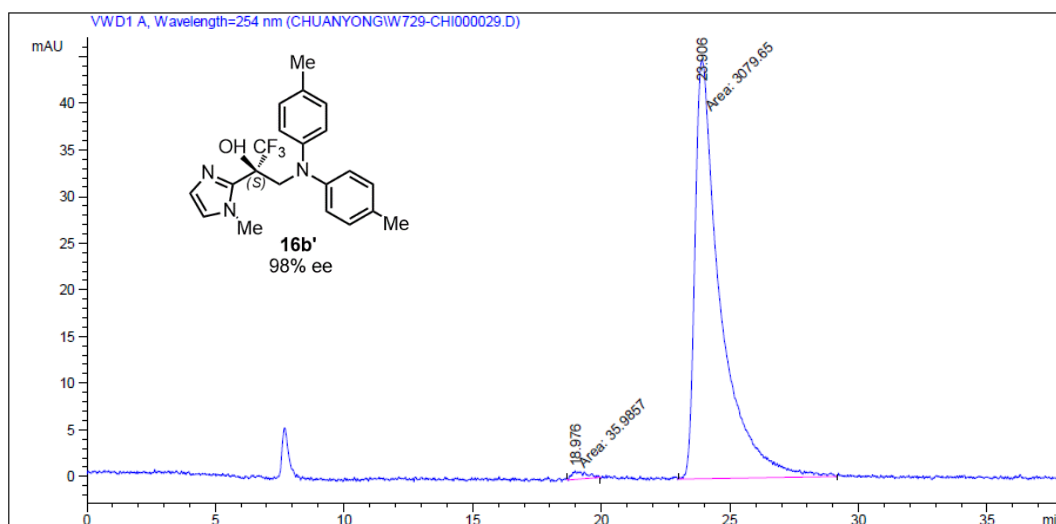


Figure 127 HPLC traces (Daicel Chiralpak AD-H column) of *rac*-**16a** (reference) and (*S*)-**16a**.

Chapter 6: Appendices



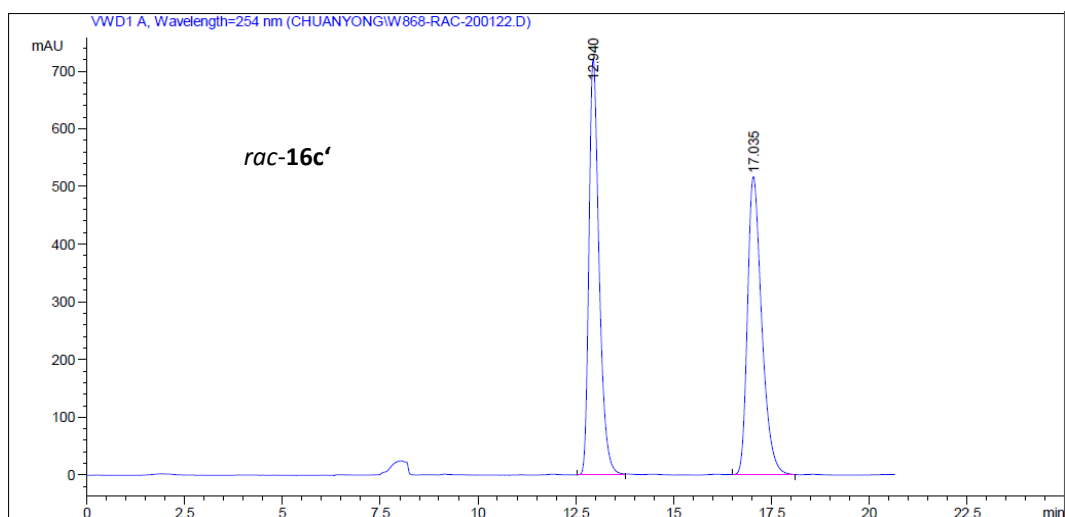
Peak #	RetTime [min]	Type	Width [min]	Area mAU *s	Height [mAU]	Area %
1	19.550	MM	0.9234	1187.39697	21.43205	49.5495
2	23.997	MM	1.1483	1208.98743	17.54687	50.4505



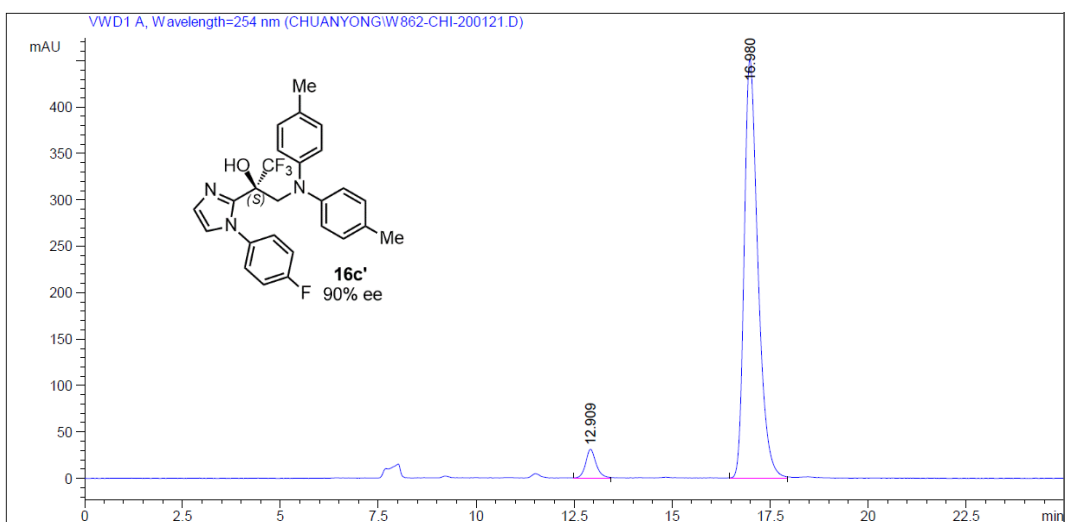
Peak #	RetTime [min]	Type	Width [min]	Area mAU *s	Height [mAU]	Area %
1	18.976	MM	0.6269	35.98571	9.56660e-1	1.1550
2	23.906	MM	1.1406	3079.65186	45.00161	98.8450

Figure 128 HPLC traces (Daicel Chiralpak AD-H column) of *rac-16b'* (reference) and (*S*)-**16b'**.

Chapter 6: Appendices



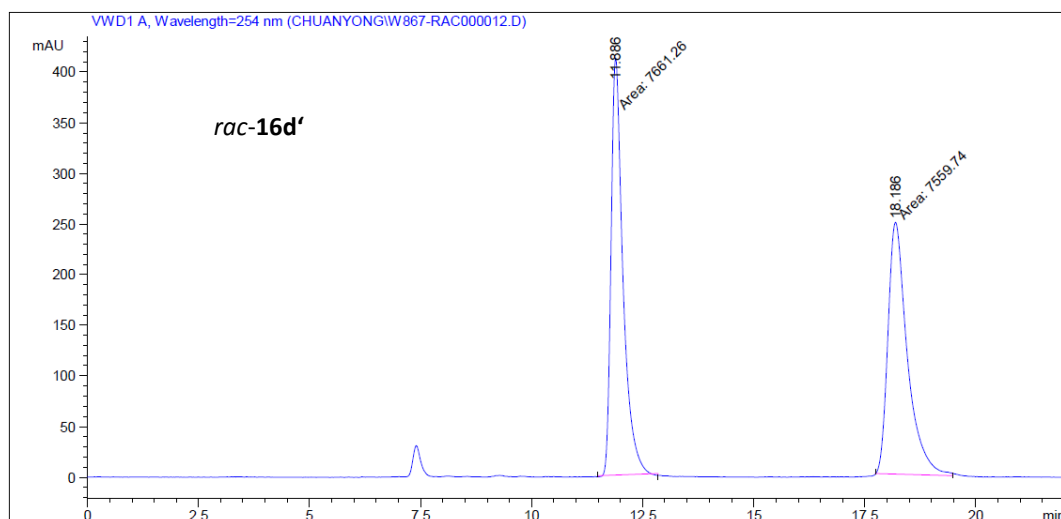
Peak #	RetTime [min]	Type	Width [min]	Area mAU *s	Height [mAU]	Area %
1	12.940	VV	0.2741	1.30969e4	722.61041	49.9074
2	17.035	VV	0.3867	1.31455e4	517.44623	50.0926



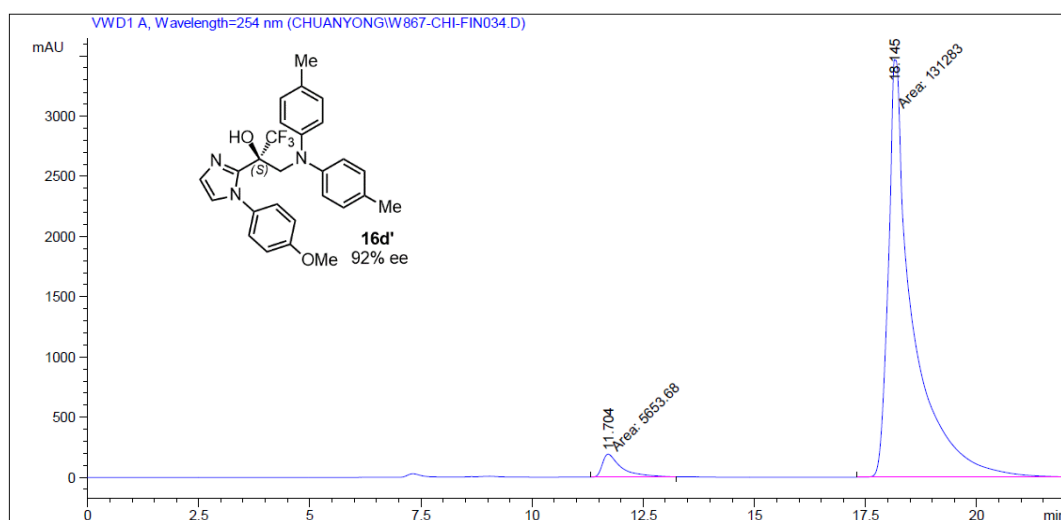
Peak #	RetTime [min]	Type	Width [min]	Area mAU *s	Height [mAU]	Area %
1	12.909	VV	0.2847	603.34113	31.48221	5.1896
2	16.980	VV	0.3676	1.10227e4	451.87784	94.8104

Figure 129 HPLC traces (Daicel Chiralpak AD-H column) of *rac-16c'* (reference) and *(S)-16c'*.

Chapter 6: Appendices



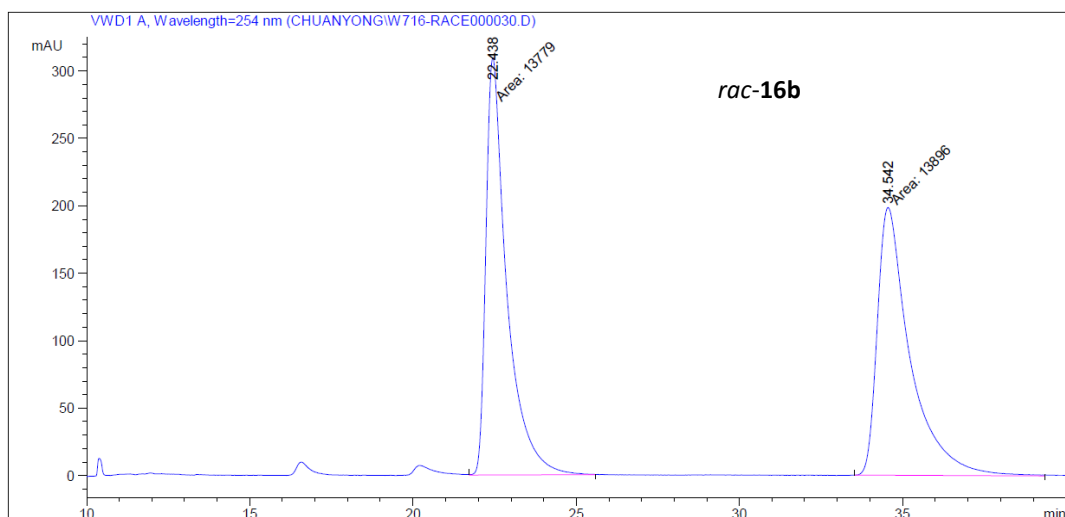
Peak #	RetTime [min]	Type	Width [min]	Area mAU *s	Height [mAU]	Area %
1	11.886	MM	0.3098	7661.26074	412.12961	50.3335
2	18.186	MM	0.5063	7559.73535	248.86792	49.6665



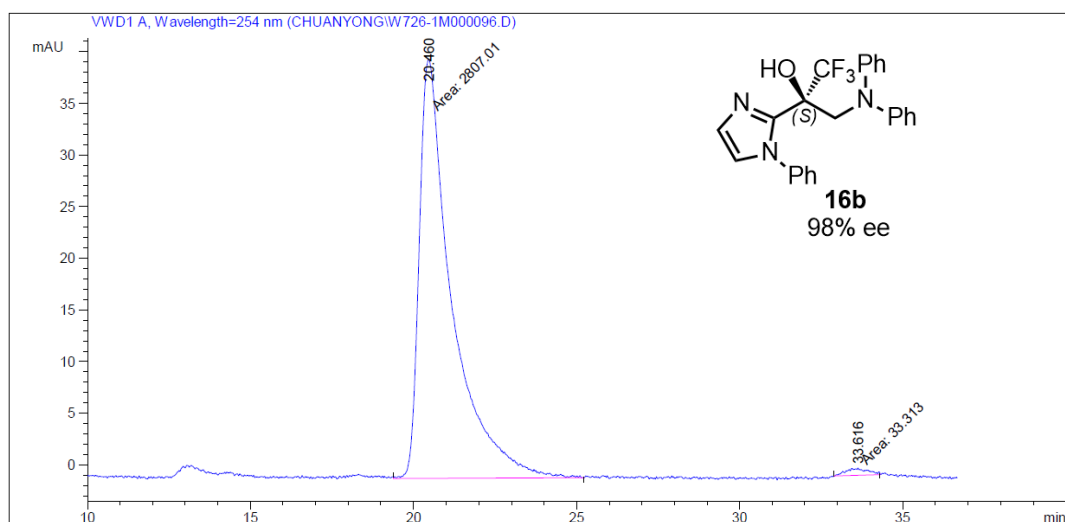
Peak #	RetTime [min]	Type	Width [min]	Area mAU *s	Height [mAU]	Area %
1	11.704	MM	0.4973	5653.67773	189.49368	4.1287
2	18.145	MM	0.6308	1.31283e5	3468.69238	95.8713

Figure 130 HPLC traces (Daicel Chiralpak AD-H column) of *rac-16d'* (reference) and *(S)-16d'*.

Chapter 6: Appendices



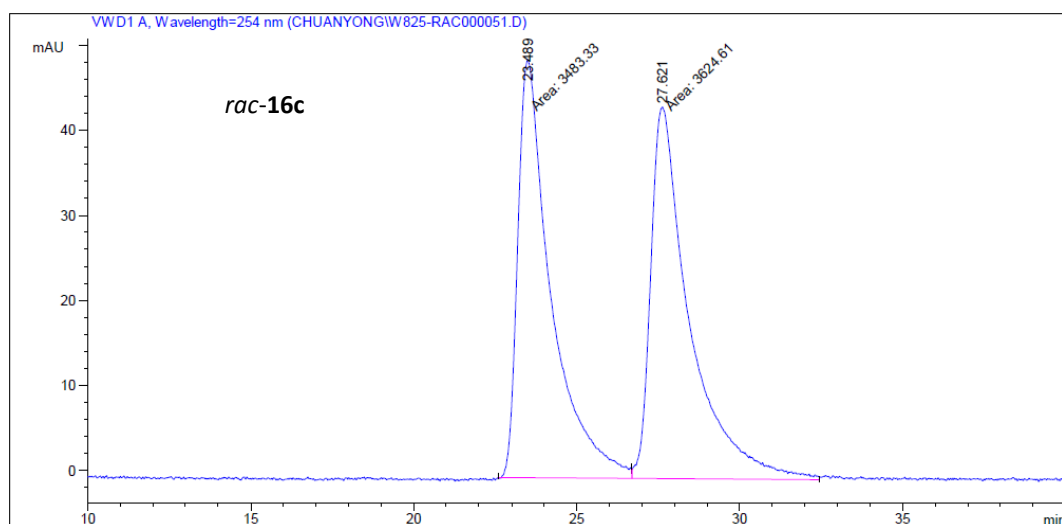
Peak #	RetTime [min]	Type	Width [min]	Area mAU *s	Height [mAU]	Area %
1	22.438	MM	0.7425	1.37790e4	309.30435	49.7886
2	34.542	MM	1.1663	1.38960e4	198.57458	50.2114



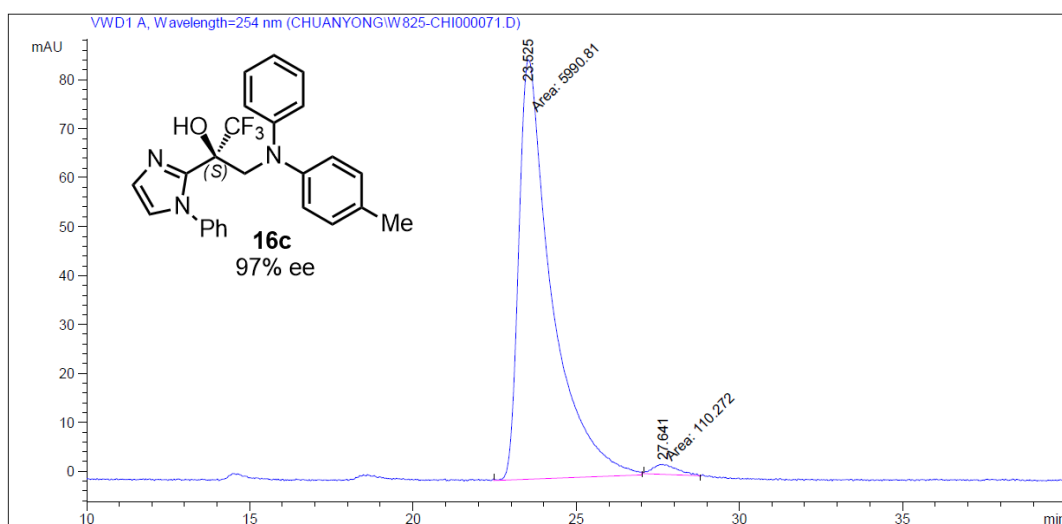
Peak #	RetTime [min]	Type	Width [min]	Area mAU *s	Height [mAU]	Area %
1	20.460	MM	1.1522	2807.00708	40.60313	98.8271
2	33.616	MM	0.7701	33.31297	7.20927e-1	1.1729

Figure 131 HPLC traces (Daicel Chiralpak AD-H column) of *rac*-**16b** (reference) and (*S*)-**16b**.

Chapter 6: Appendices



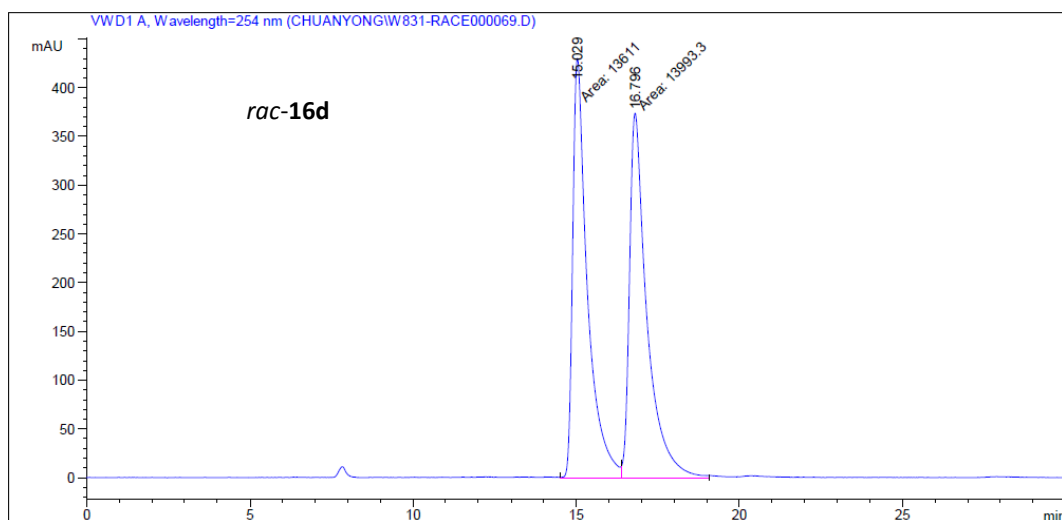
Peak #	RetTime [min]	Type	Width [min]	Area mAU *s	Height [mAU]	Area %
1	23.489	MF	1.1807	3483.33179	49.17051	49.0062
2	27.621	FM	1.3820	3624.61157	43.71193	50.9938



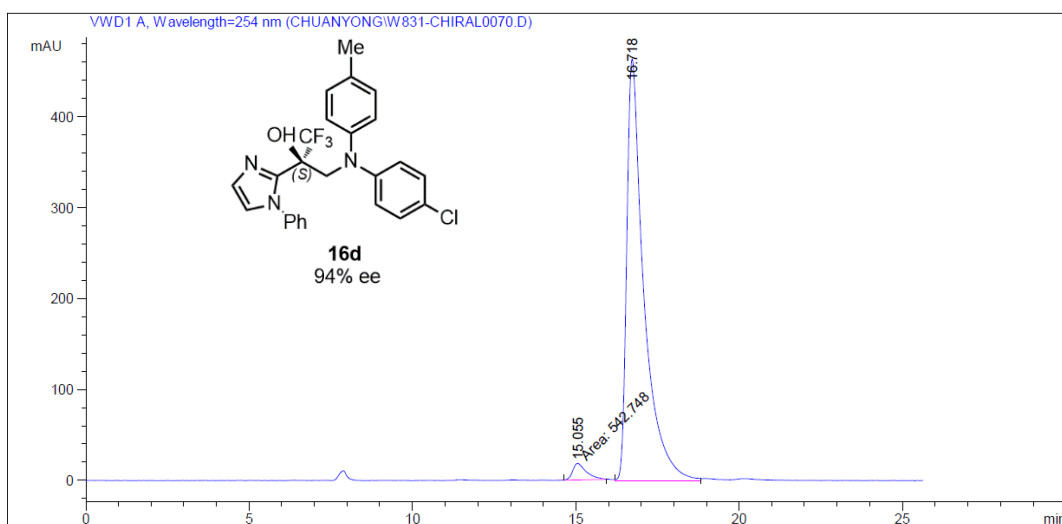
Peak #	RetTime [min]	Type	Width [min]	Area mAU *s	Height [mAU]	Area %
1	23.525	MM	1.1647	5990.80713	85.72684	98.1926
2	27.641	MM	0.8898	110.27168	2.06559	1.8074

Figure 132 HPLC traces (Daicel Chiralpak AD-H column) of *rac*-16c (reference) and (*S*)-16c.

Chapter 6: Appendices



Peak #	RetTime [min]	Type	Width [min]	Area mAU *s	Height [mAU]	Area %
1	15.029	MF	0.5262	1.36110e4	431.10709	49.3075
2	16.796	FM	0.6222	1.39933e4	374.84769	50.6925



Peak #	RetTime [min]	Type	Width [min]	Area mAU *s	Height [mAU]	Area %
1	15.055	MM	0.4924	542.74780	18.37232	3.1131
2	16.718	VV	0.5191	1.68914e4	464.27756	96.8869

Figure 133 HPLC traces (Daicel Chiralpak AD-H column) of *rac*-**16d** (reference) and (*S*)-**16d**.

Chapter 6: Appendices

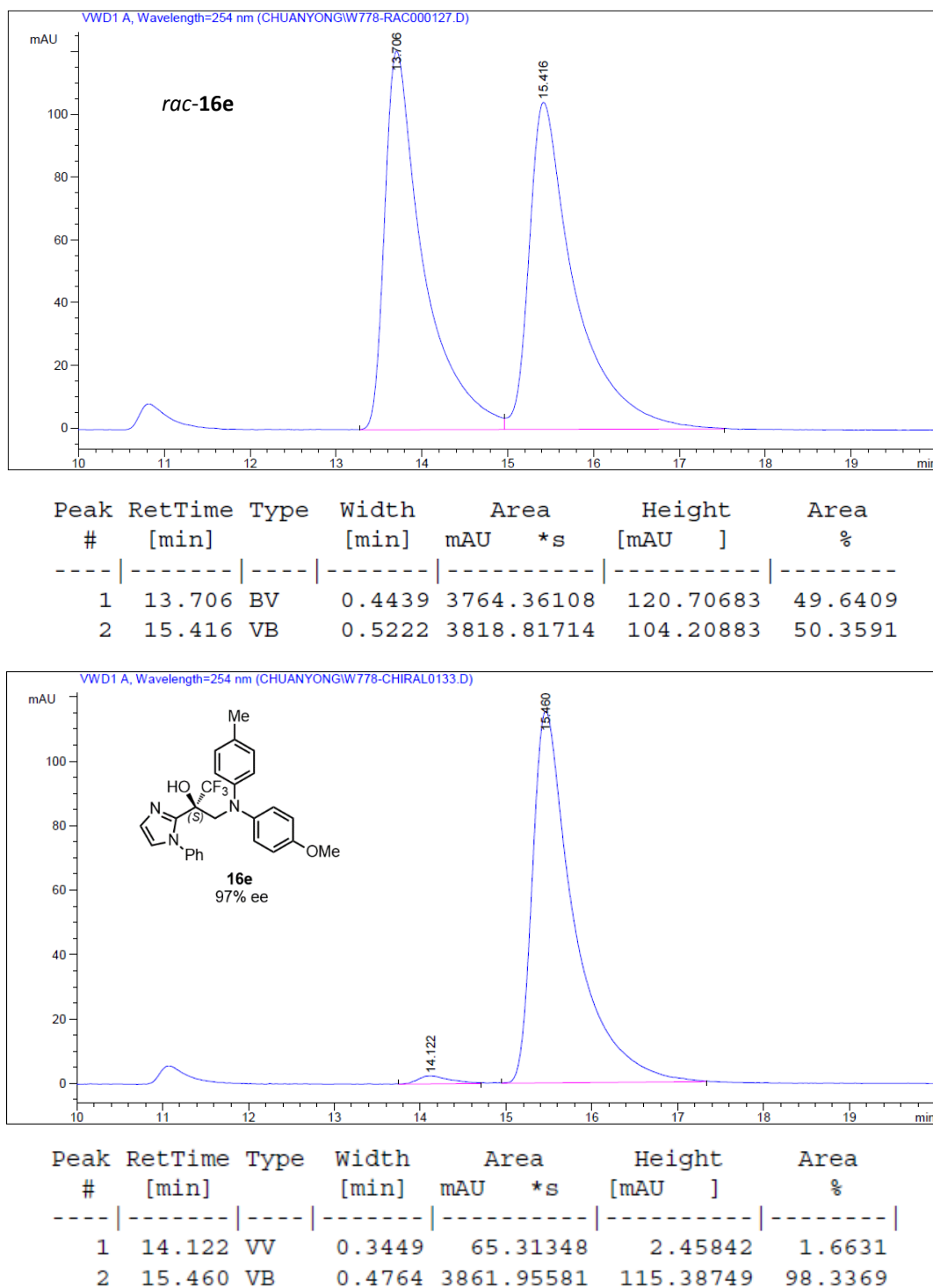


Figure 134 HPLC traces (Daicel Chiralpak AD-H column) of *rac*-**16e** (reference) and (*S*)-**16e**.

Chapter 6: Appendices

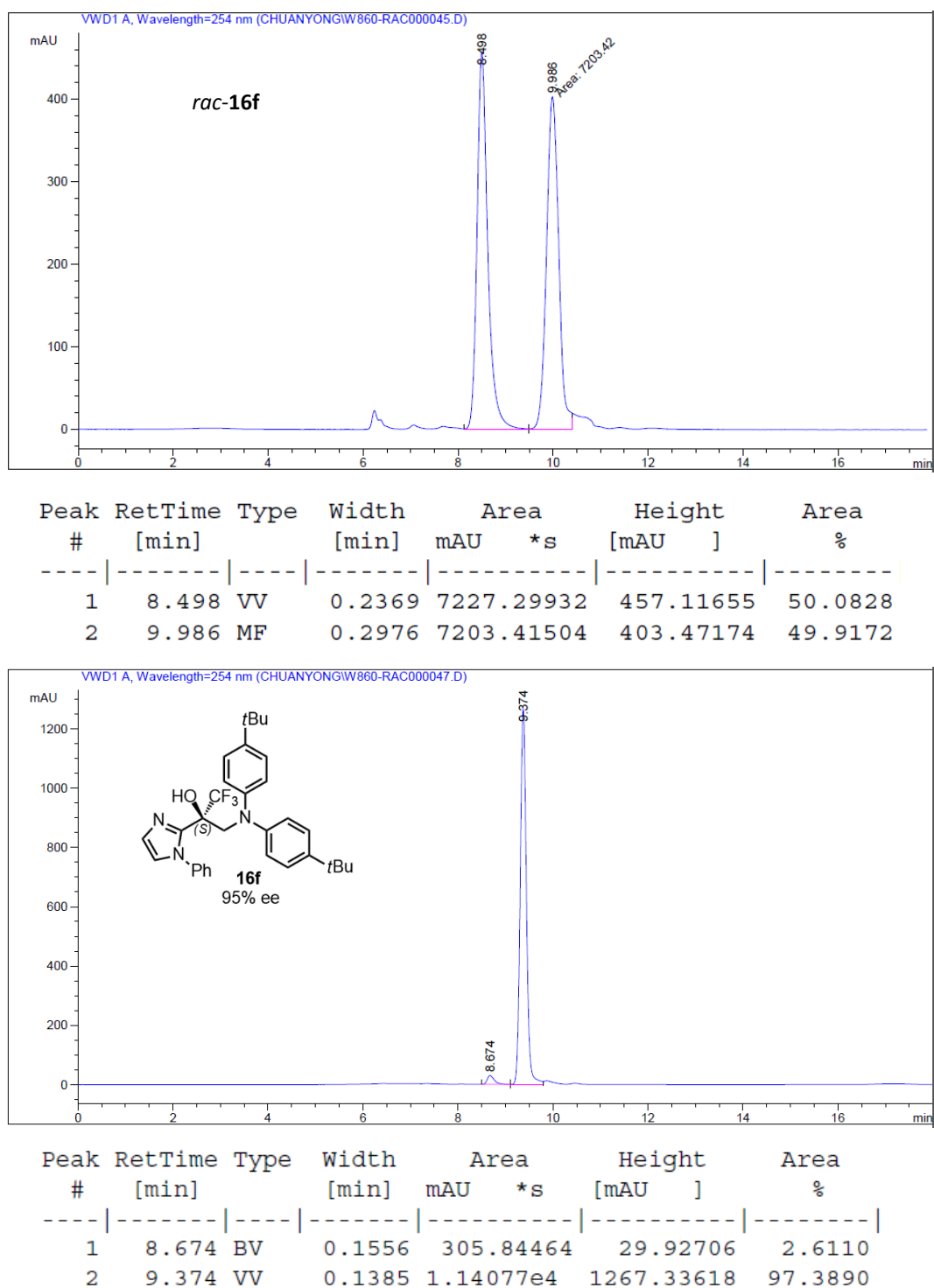
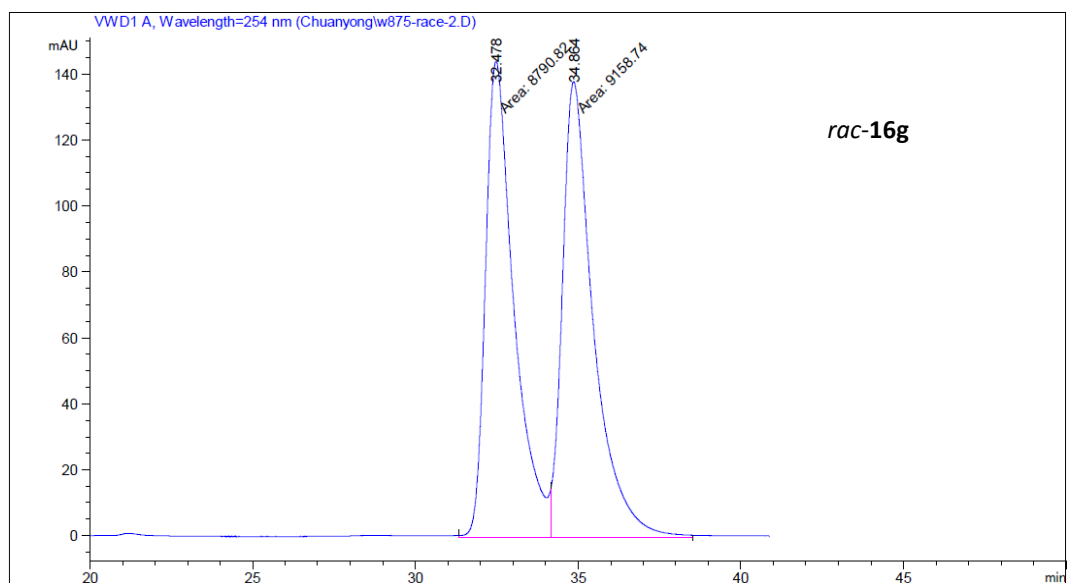
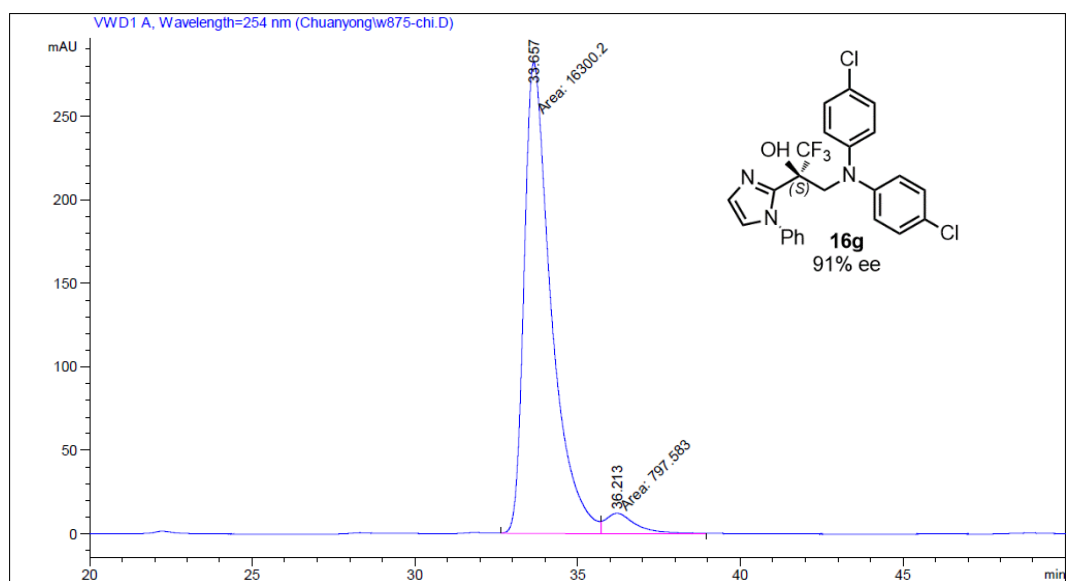


Figure 135 HPLC traces (Daicel Chiralpak IC column) of *rac*-**16f** (reference) and (*S*)-**16f**.

Chapter 6: Appendices



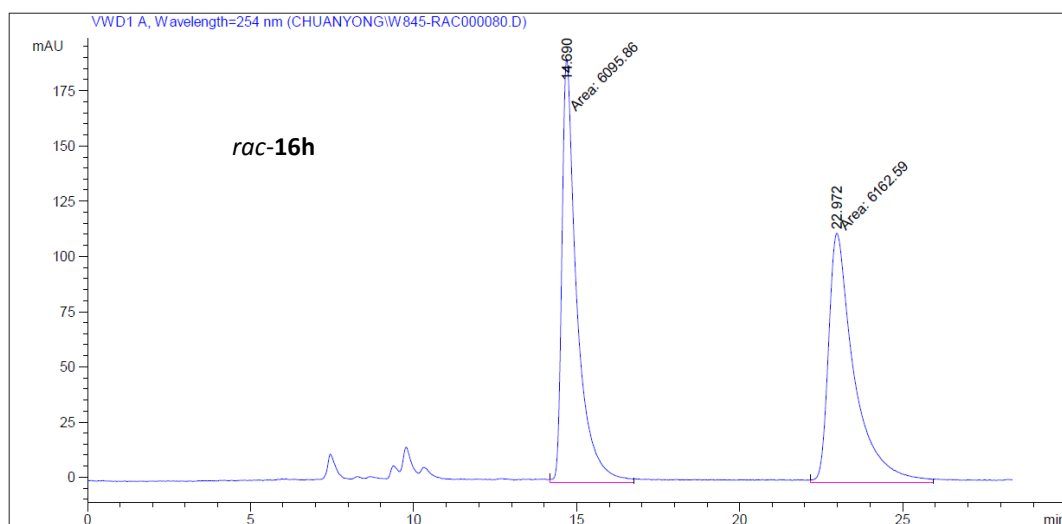
Peak #	RetTime [min]	Type	Width [min]	Area [mAU*s]	Height [mAU]	Area %
1	32.478	MF	1.0152	8790.82227	144.31926	48.9751
2	34.864	FM	1.1046	9158.74414	138.18967	51.0249



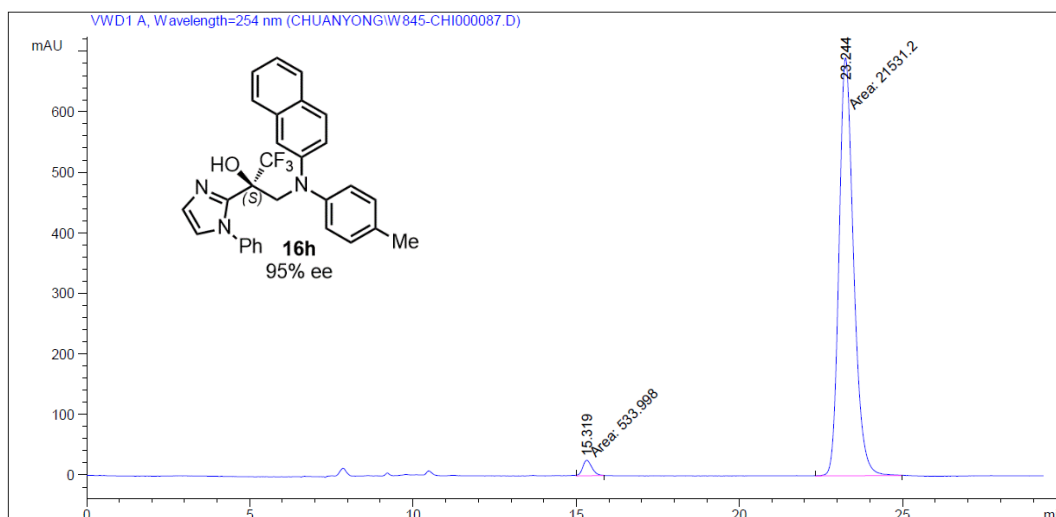
Peak #	RetTime [min]	Type	Width [min]	Area [mAU*s]	Height [mAU]	Area %
1	33.657	MF	0.9639	1.63002e4	281.85544	95.3352
2	36.213	FM	1.0922	797.58295	12.17051	4.6648

Figure 136 HPLC traces (Daicel Chiralpak AD-H column) of *rac*-**16g** (reference) and (*S*)-**16g**.

Chapter 6: Appendices



Peak #	RetTime [min]	Type	Width [min]	Area mAU *s	Height [mAU]	Area %
1	14.690	MM	0.5301	6095.86182	191.67450	49.7278
2	22.972	MM	0.9104	6162.59277	112.82057	50.2722

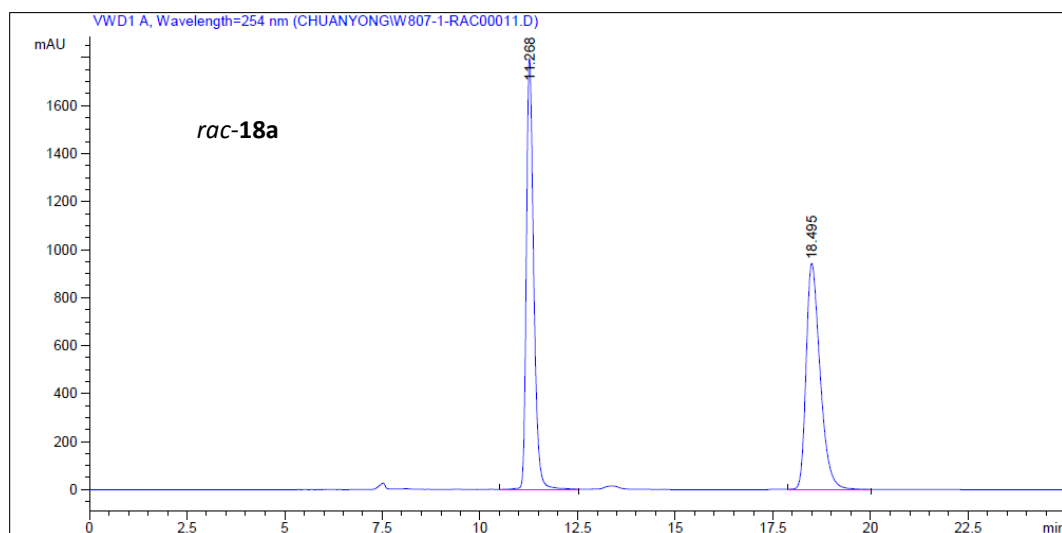


Peak #	RetTime [min]	Type	Width [min]	Area mAU *s	Height [mAU]	Area %
1	15.319	MM	0.3377	533.99762	26.35132	2.4201
2	23.244	MM	0.5192	2.15312e4	691.14276	97.5799

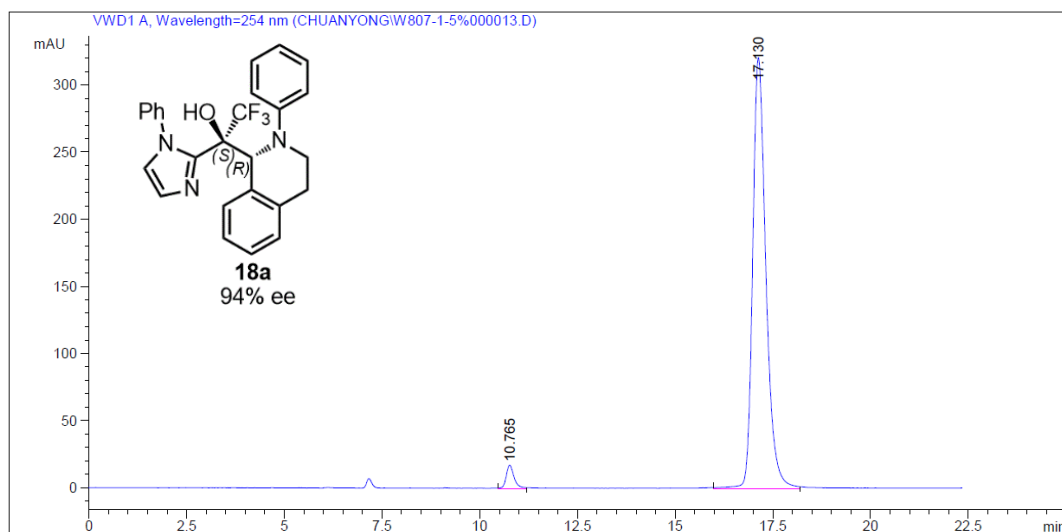
1

Figure 137 HPLC traces (Daicel Chiralpak AD-H column) of *rac*-**16h** (reference) and (*S*)-**16h**.

Chapter 6: Appendices



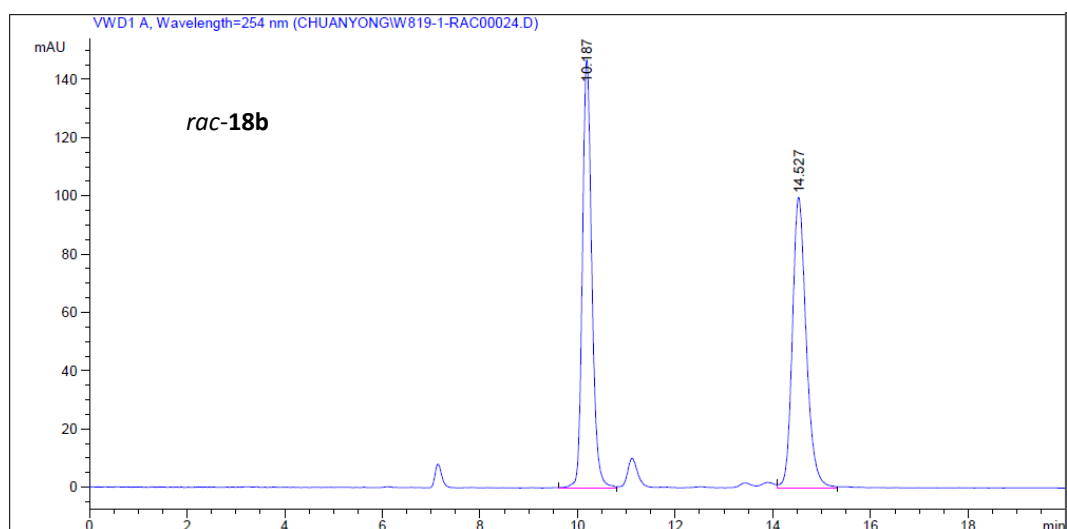
Peak #	RetTime [min]	Type	Width [min]	Area mAU *s	Height [mAU]	Area %
1	11.268	VB	0.1998	2.36111e4	1797.82593	50.1277
2	18.495	VB	0.3797	2.34909e4	942.25873	49.8723



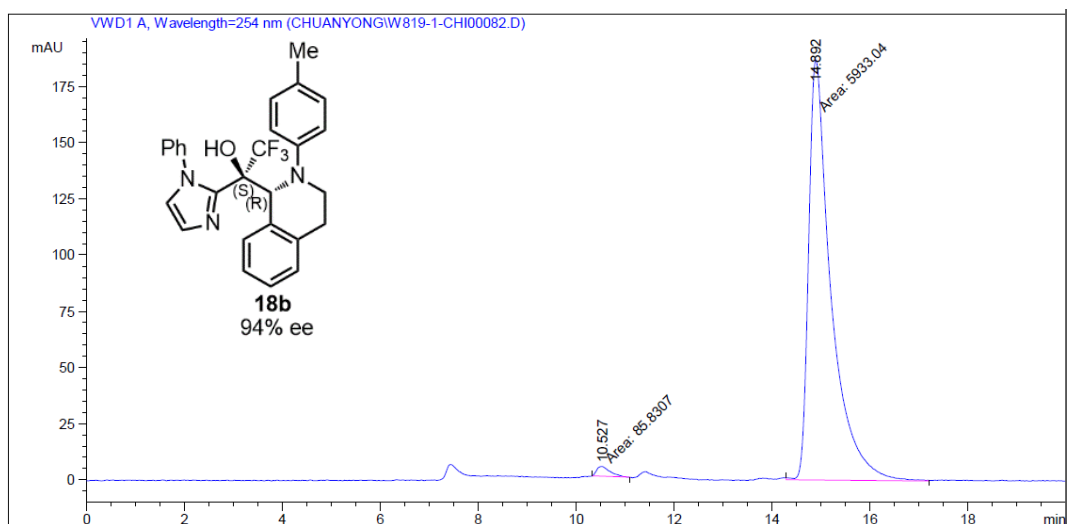
Peak #	RetTime [min]	Type	Width [min]	Area mAU *s	Height [mAU]	Area %
1	10.765	VV	0.2090	237.86102	17.24537	3.0575
2	17.130	VV	0.3558	7541.82080	320.82156	96.9425

Figure 138 HPLC traces (Daicel Chiralpak AD-H column) of *rac-18a* (reference) and (*S,R*)-**18a**.

Chapter 6: Appendices



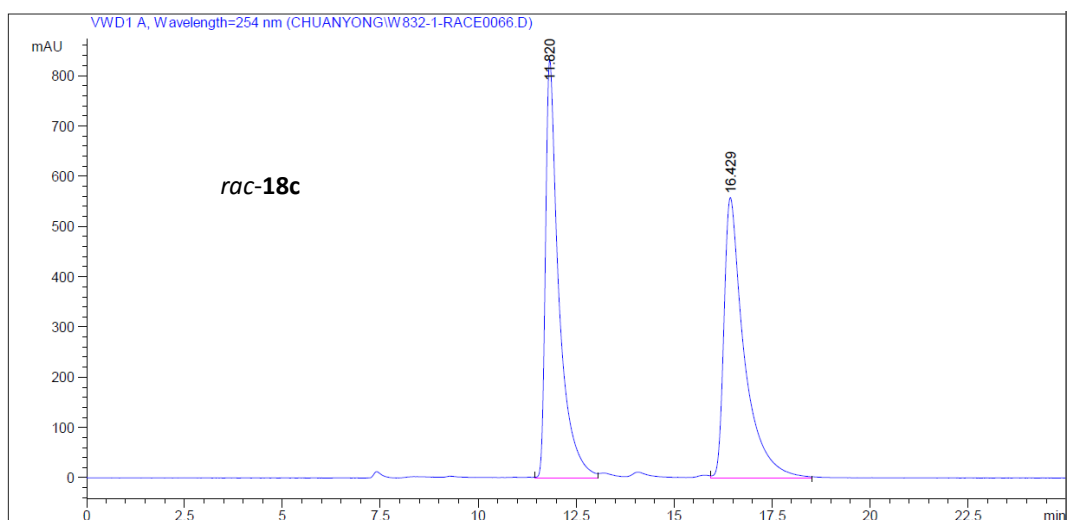
Peak #	RetTime [min]	Type	Width [min]	Area mAU *s	Height [mAU]	Area %
1	10.187	VV	0.2062	1973.62231	146.98195	50.0222
2	14.527	VV	0.3003	1971.87354	99.86518	49.9778



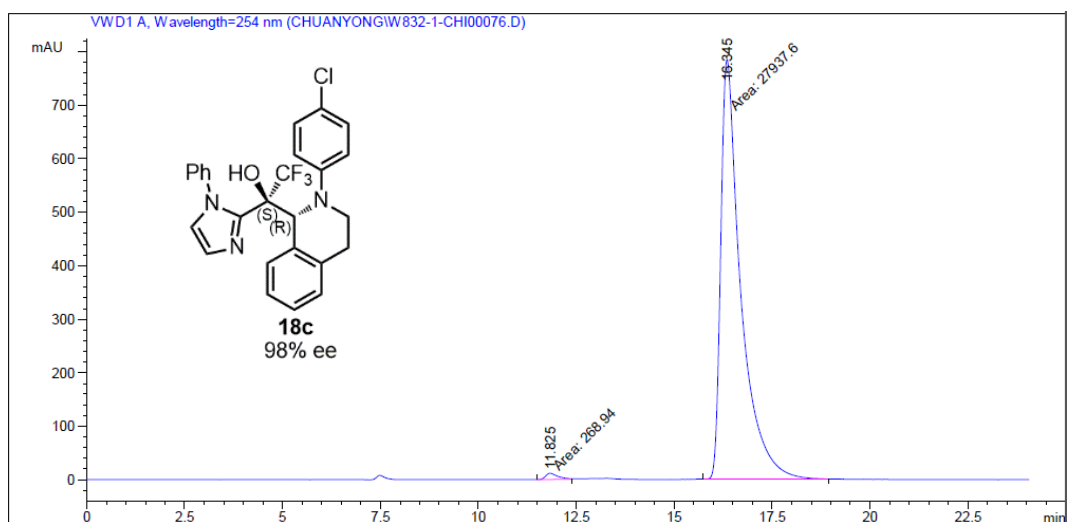
Peak #	RetTime [min]	Type	Width [min]	Area mAU *s	Height [mAU]	Area %
1	10.527	MM	0.3205	85.83068	4.46276	1.4260
2	14.892	MM	0.5294	5933.03613	186.79489	98.5740

Figure 139 HPLC traces (Daicel Chiralpak AD-H column) of *rac-18b* (reference) and (*S,R*)-**18b**.

Chapter 6: Appendices



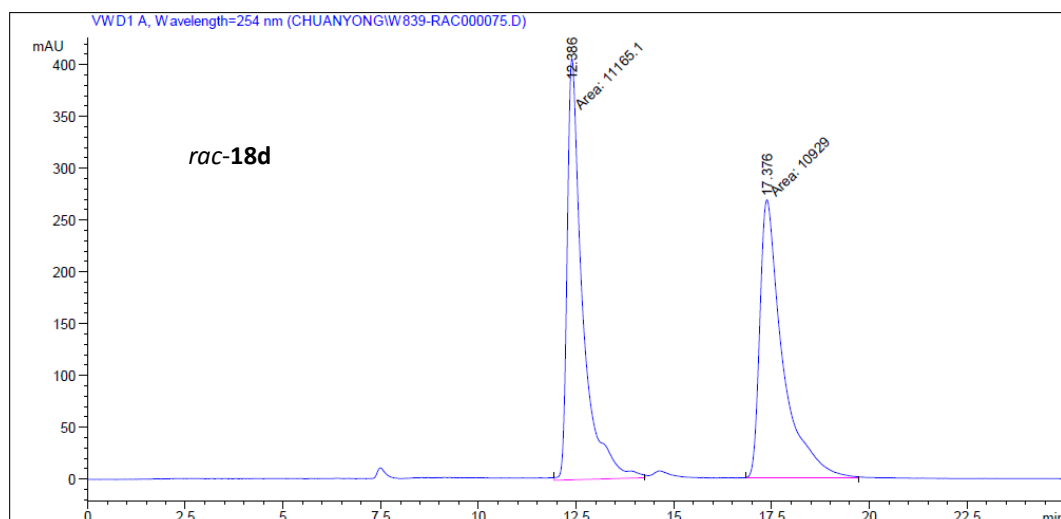
Peak #	RetTime [min]	Type	Width [min]	Area mAU *s	Height [mAU]	Area %
1	11.820	VV	0.3390	1.98400e4	833.17908	49.7752
2	16.429	VV	0.5100	2.00192e4	558.43201	50.2248



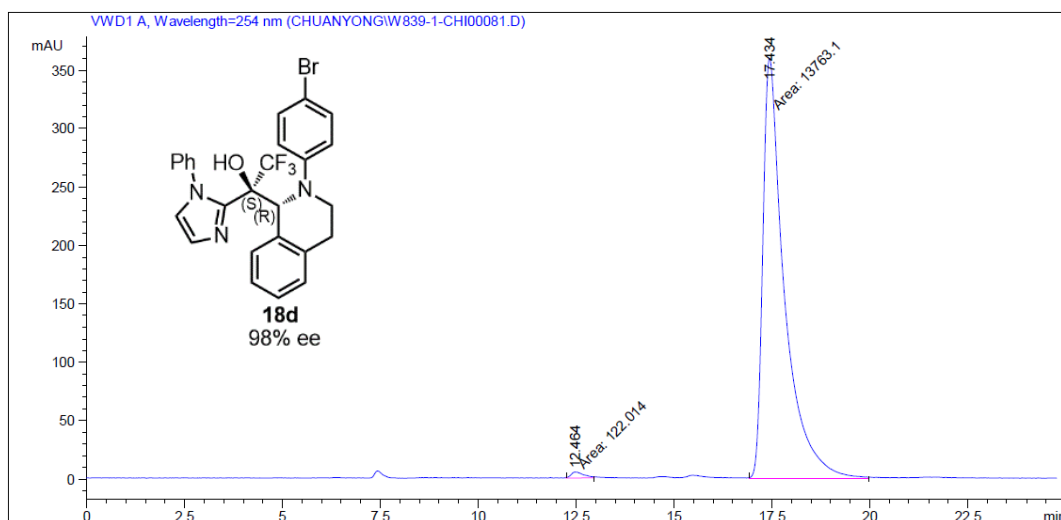
Peak #	RetTime [min]	Type	Width [min]	Area mAU *s	Height [mAU]	Area %
1	11.825	MM	0.3728	268.94019	12.02419	0.9535
2	16.345	MM	0.5932	2.79376e4	784.91852	99.0465

Figure 140 HPLC traces (Daicel Chiralpak AD-H column) of *rac*-**18c** (reference) and (*S,R*)-**18c**.

Chapter 6: Appendices



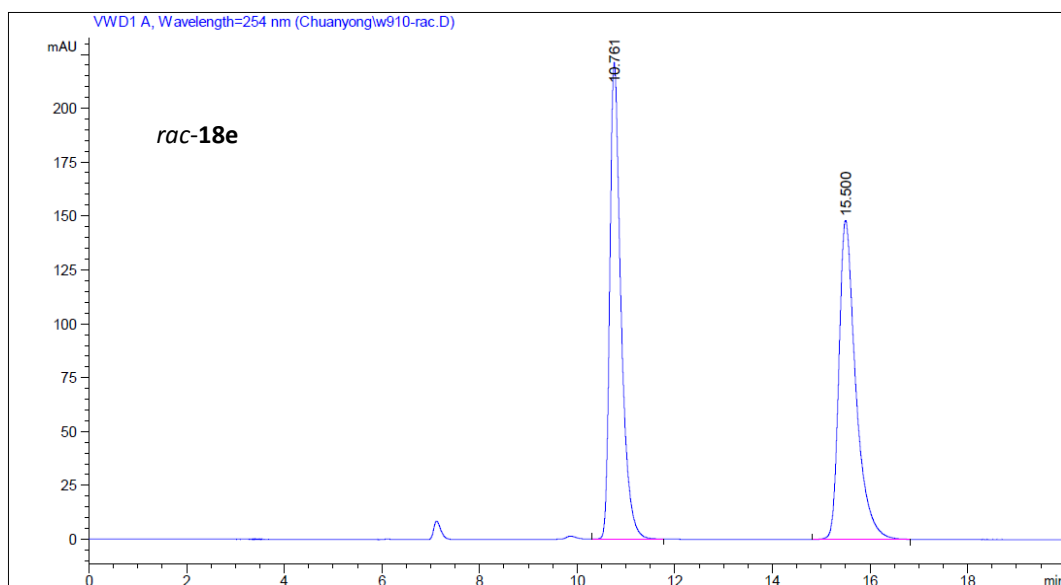
Peak #	RetTime [min]	Type	Width [min]	Area mAU *s	Height [mAU]	Area %
1	12.386	MM	0.4576	1.11651e4	406.68433	50.5343
2	17.376	MM	0.6783	1.09290e4	268.53183	49.4657



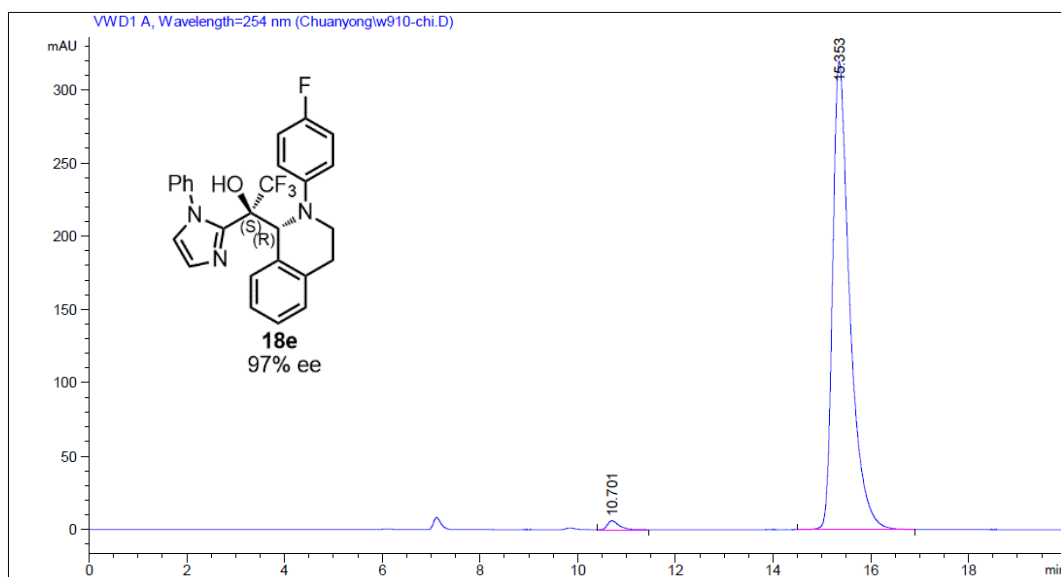
Peak #	RetTime [min]	Type	Width [min]	Area mAU *s	Height [mAU]	Area %
1	12.464	MM	0.3869	122.01412	5.25639	0.8787
2	17.434	MM	0.6377	1.37631e4	359.70395	99.1213

Figure 141 HPLC traces (Daicel Chiralpak AD-H column) of *rac*-**18d** (reference) and (*S,R*)-**18d**.

Chapter 6: Appendices



Peak #	RetTime [min]	Type	Width [min]	Area [mAU*s]	Height [mAU]	Area %
1	10.761	BV R	0.2399	3518.58008	221.45985	49.8482
2	15.500	BB	0.3424	3540.01318	148.10197	50.1518



Peak #	RetTime [min]	Type	Width [min]	Area [mAU*s]	Height [mAU]	Area %
1	10.701	BV R	0.1944	99.51356	6.14492	1.2681
2	15.353	VV R	0.3573	7748.07129	319.63849	98.7319

Figure 142 HPLC traces (Daicel Chiralpak AD-H column) of *rac-18e* (reference) and (*S,R*)-**18e**.

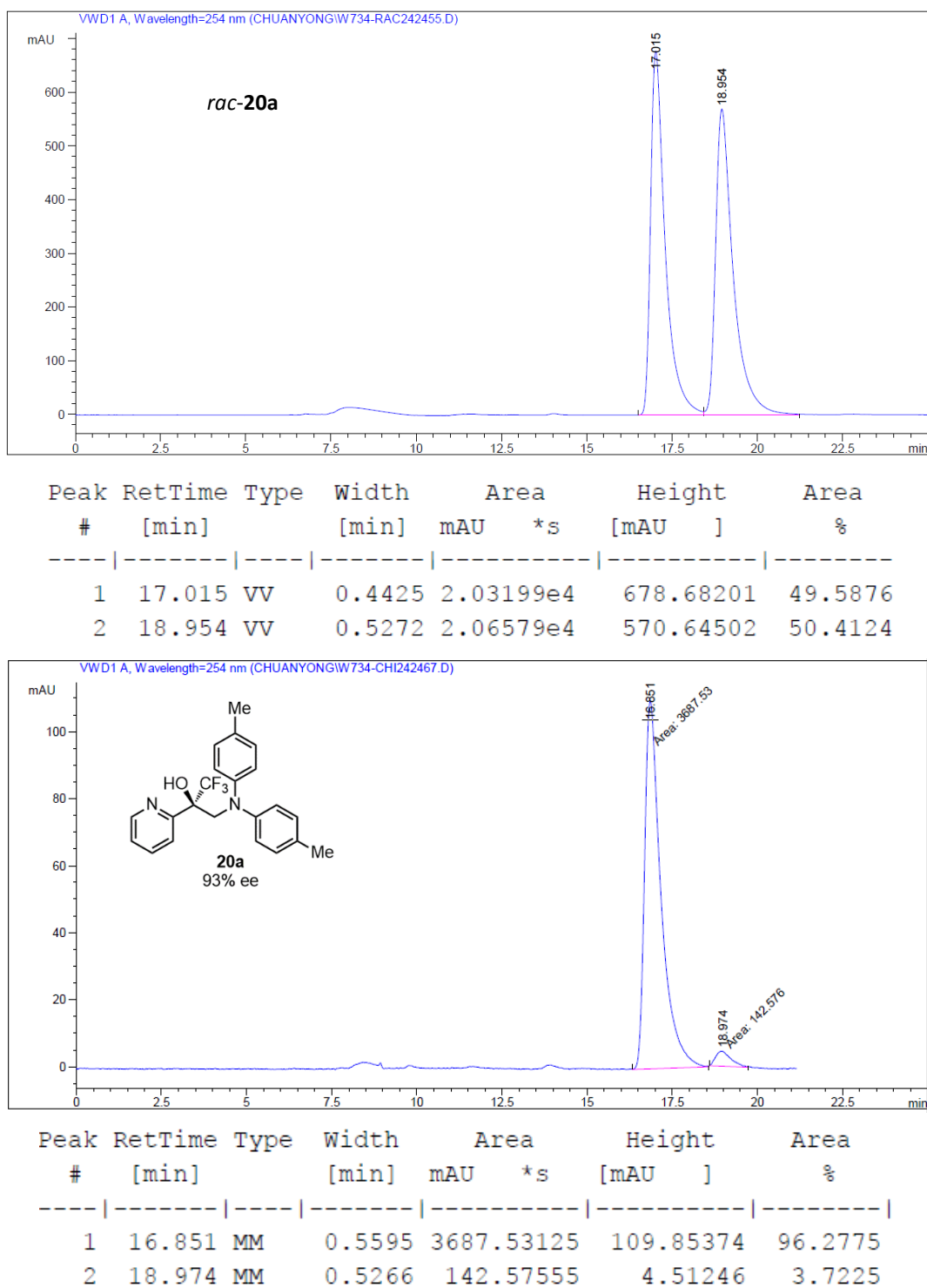
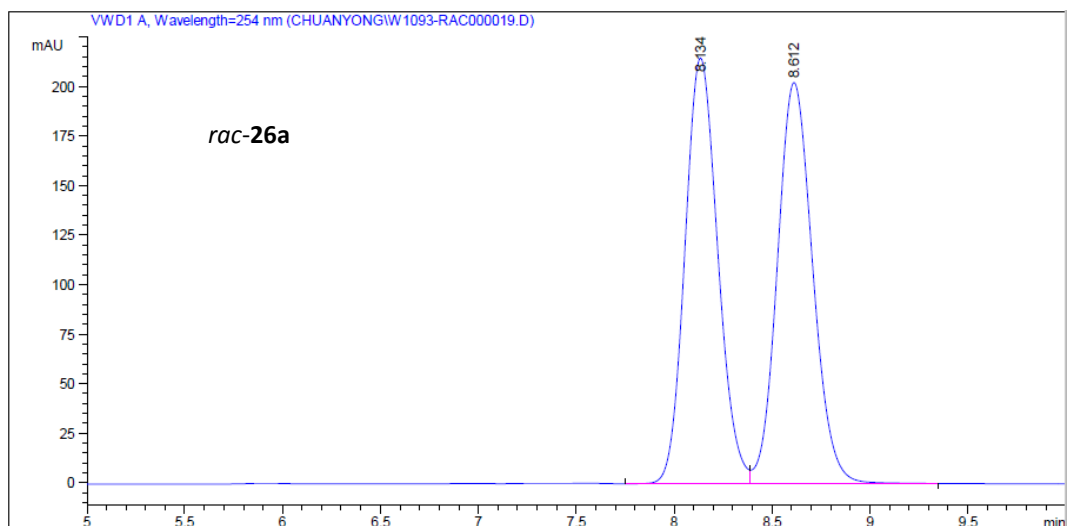
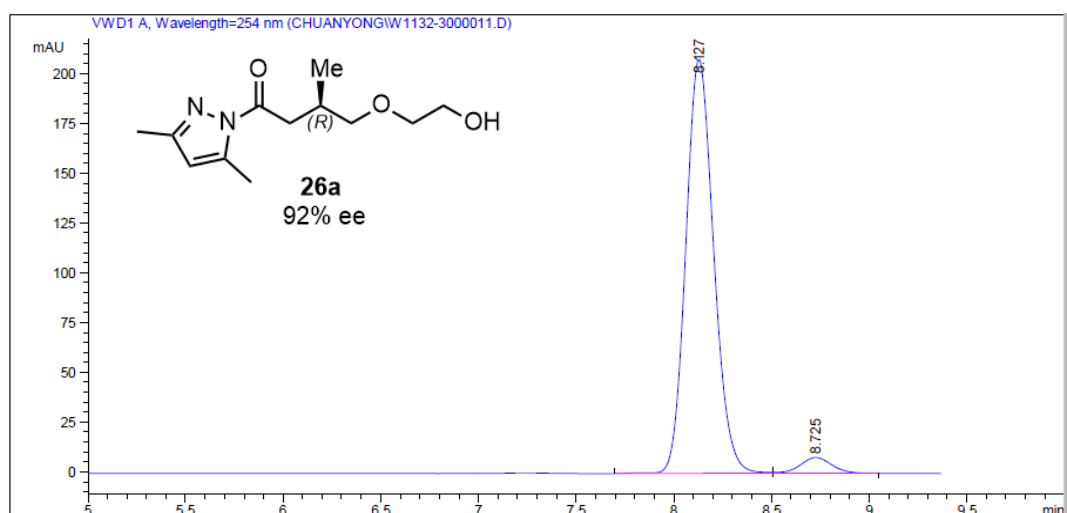


Figure 143 HPLC traces (Daicel Chiralpak AD-H column) of *rac-20a* (reference) and (*S*)-**20a**.

Chapter 6: Appendices



Peak #	RetTime [min]	Type	Width [min]	Area mAU *s	Height [mAU]	Area %
1	8.134	VV	0.1811	2503.54785	214.85976	49.3198
2	8.612	VB	0.1958	2538.54517	202.47427	50.0092



Peak #	RetTime [min]	Type	Width [min]	Area mAU *s	Height [mAU]	Area %
1	8.127	BV	0.1536	2063.95239	207.95863	95.7759
2	8.725	VB	0.1737	91.02784	7.99052	4.2241

Figure 144 HPLC traces (Daicel Chiralpak OD-H column) of *rac*-**26a** (reference) and (*R*)-**26a**.

Chapter 6: Appendices

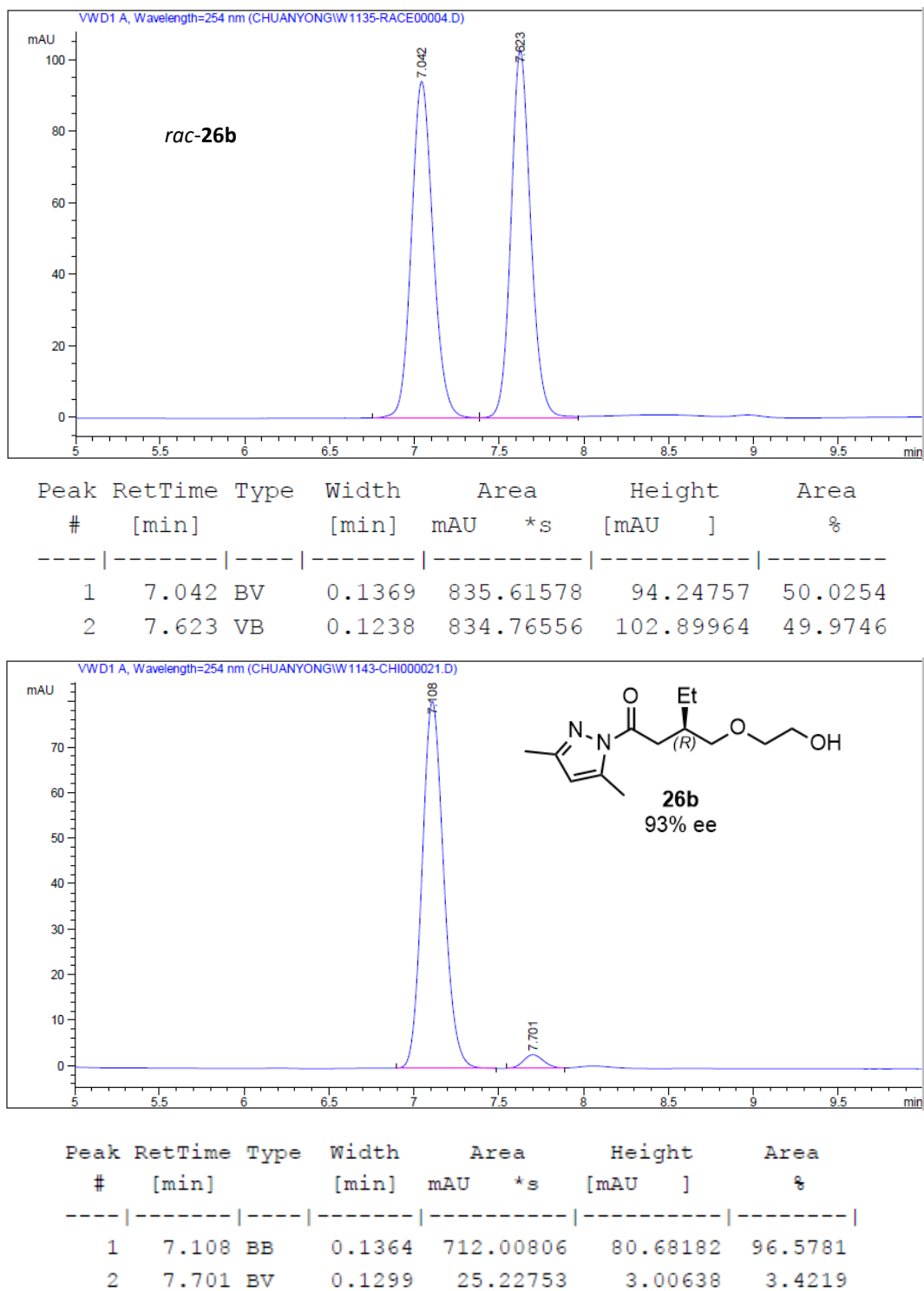
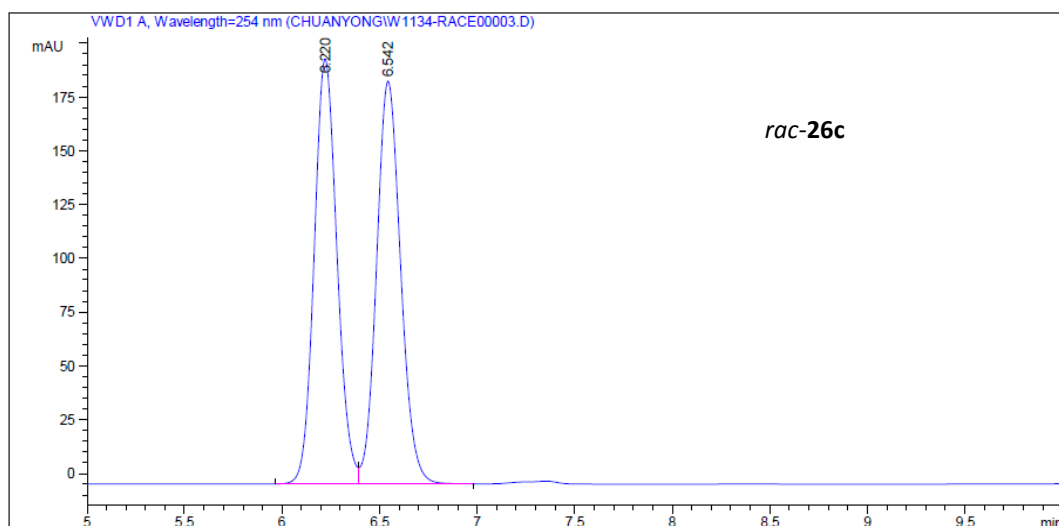
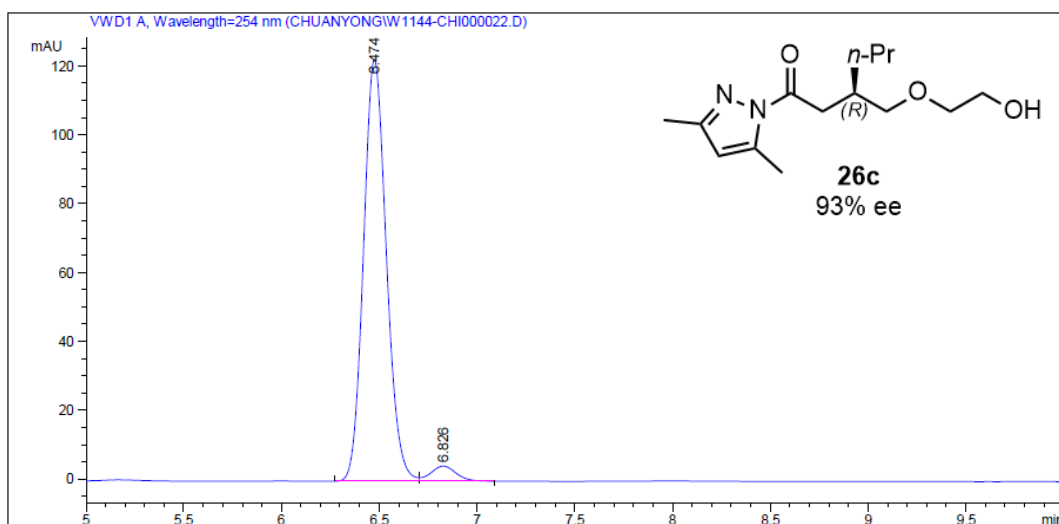


Figure 145 HPLC traces (Daicel Chiralpak OD-H column) of *rac-26b* (reference) and (*R*)-**26b**.

Chapter 6: Appendices



Peak #	RetTime [min]	Type	Width [min]	Area mAU *s	Height [mAU]	Area %
1	6.220	BV	0.1268	1606.02686	197.67368	49.9571
2	6.542	VB	0.1337	1608.78674	187.28456	50.0429



Peak #	RetTime [min]	Type	Width [min]	Area mAU *s	Height [mAU]	Area %
1	6.474	BV	0.1250	992.68506	122.63148	96.1521
2	6.826	VB	0.1374	39.72618	4.39941	3.8479

Figure 146 HPLC traces (Daicel Chiralpak OD-H column) of *rac-26c* (reference) and (*R*)-**26c**.

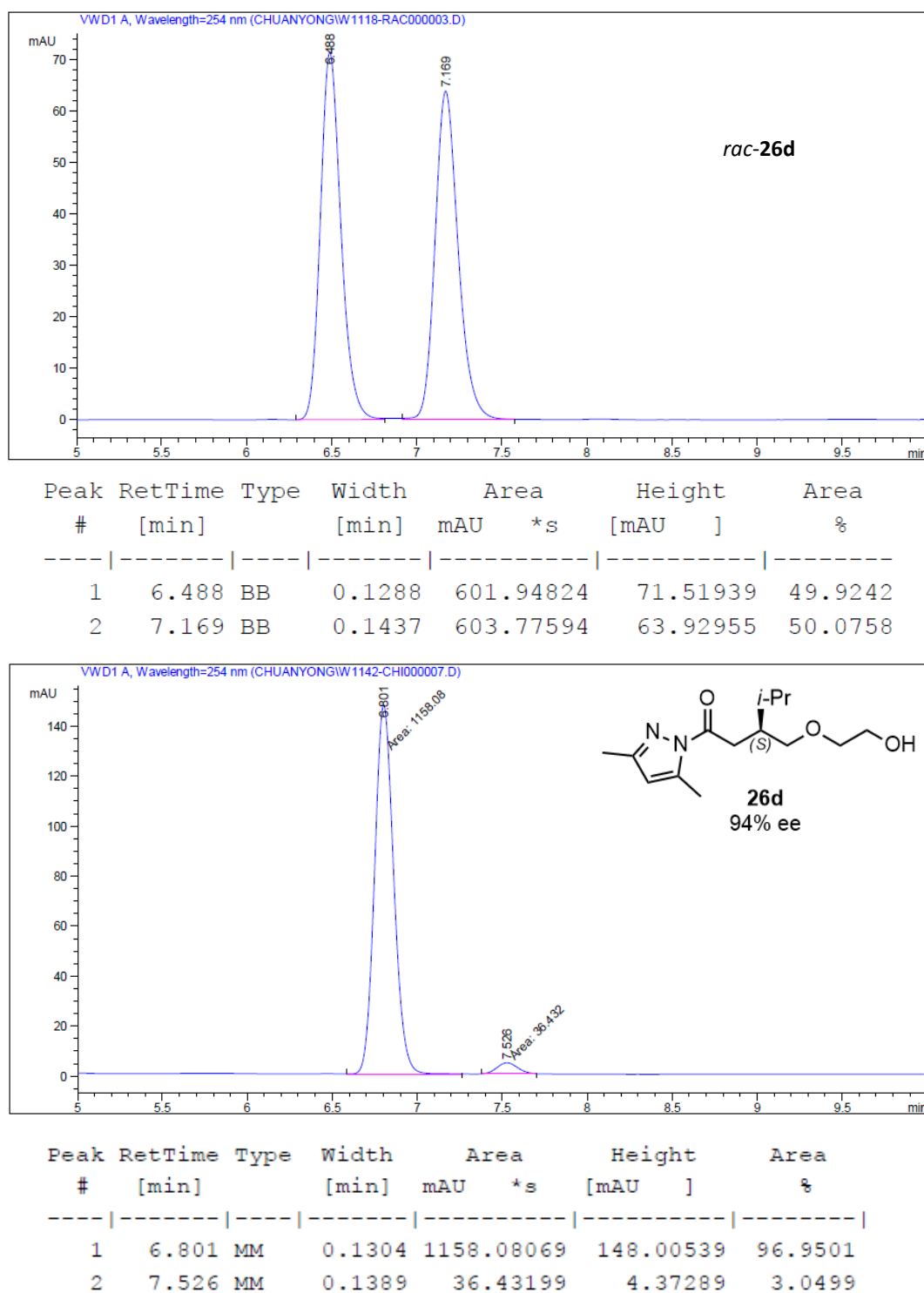
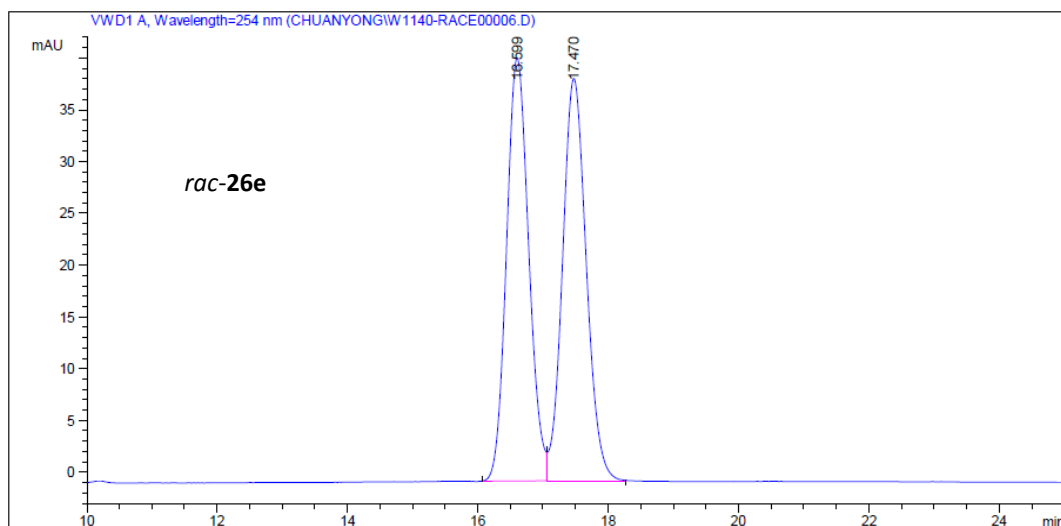
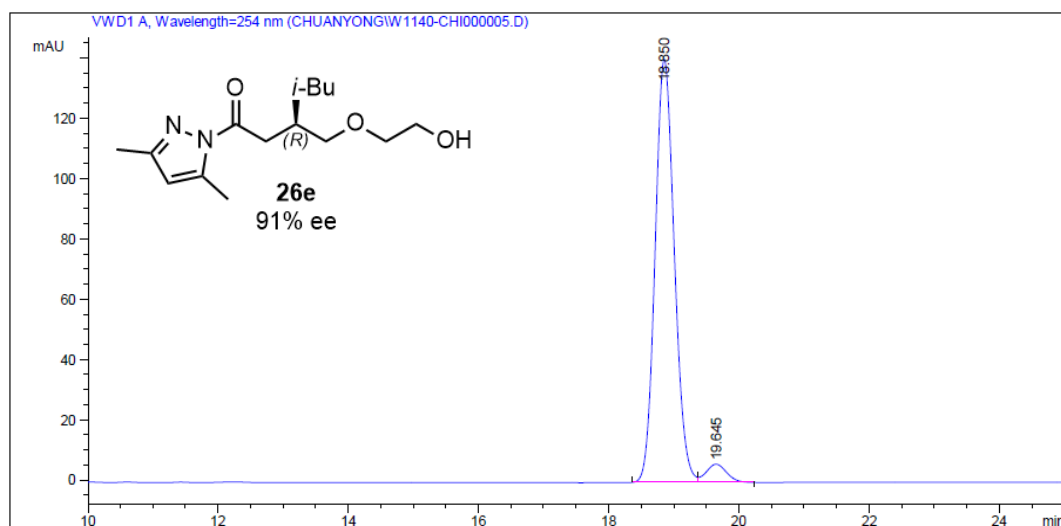


Figure 147 HPLC traces (Daicel Chiralpak OD-H column) of *rac-26d* (reference) and (*S*)-**26d**.

Chapter 6: Appendices



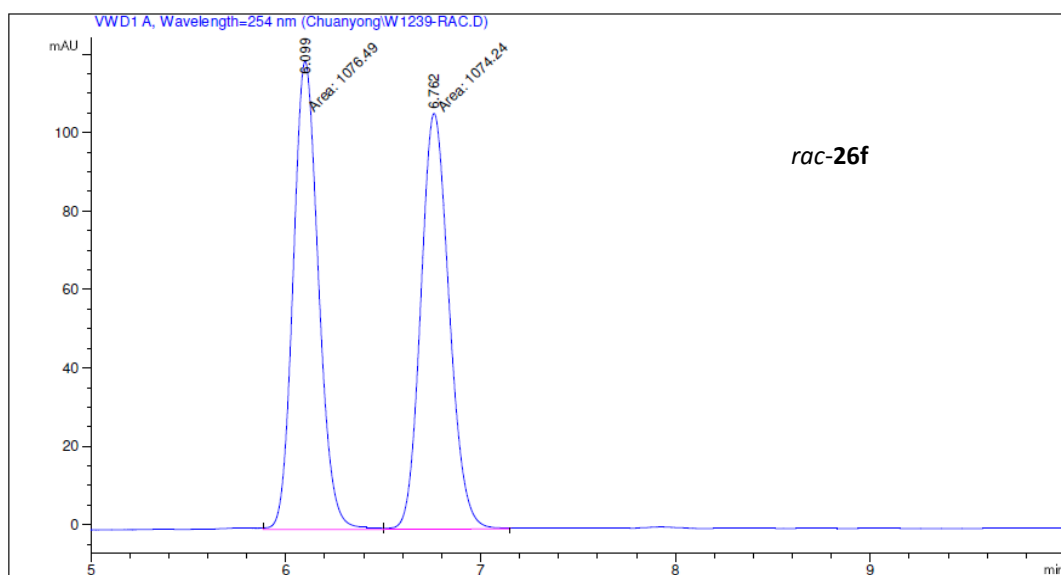
Peak #	RetTime [min]	Type	Width [min]	Area mAU *s	Height [mAU]	Area %
1	16.599	BV	0.3672	970.26538	40.87726	49.6314
2	17.470	VB	0.3917	984.67902	38.86379	50.3686



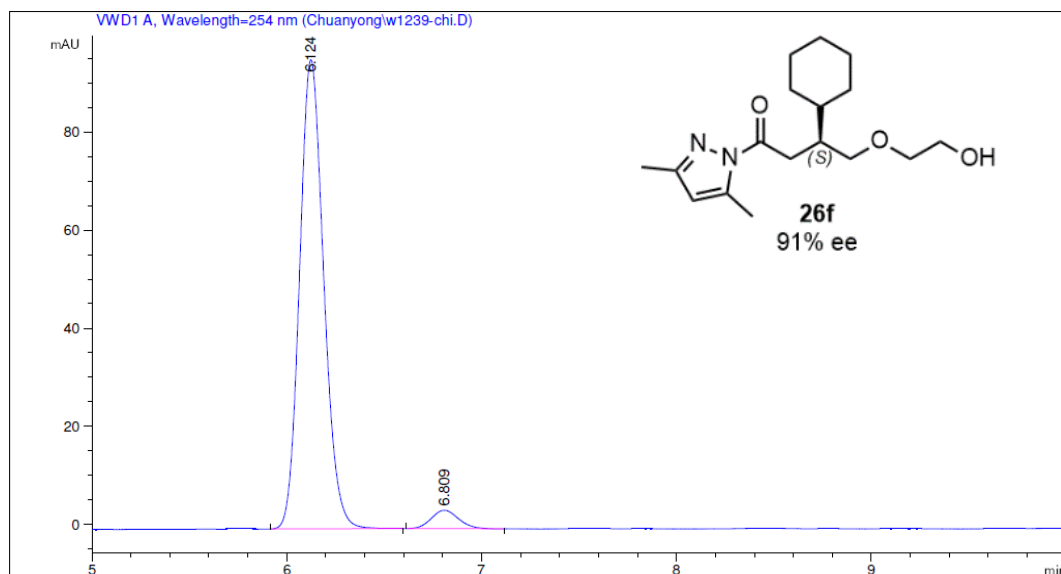
Peak #	RetTime [min]	Type	Width [min]	Area mAU *s	Height [mAU]	Area %
1	18.850	BV	0.3177	2876.42749	140.37120	95.5736
2	19.645	VB	0.3361	133.21835	6.07026	4.4264

Figure 148 HPLC traces (Daicel Chiralpak OD-H column) of *rac*-**26e** (reference) and (*R*)-**26e**.

Chapter 6: Appendices



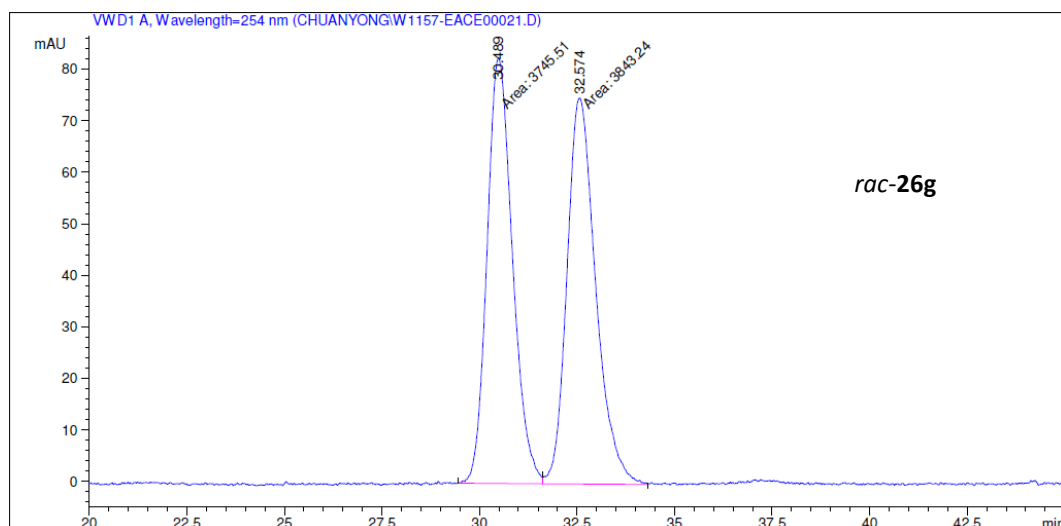
Peak #	RetTime [min]	Type	Width [min]	Area [mAU*s]	Height [mAU]	Area %
1	6.099	MF	0.1503	1076.49353	119.38616	50.0524
2	6.762	FM	0.1688	1074.24133	106.04774	49.9476



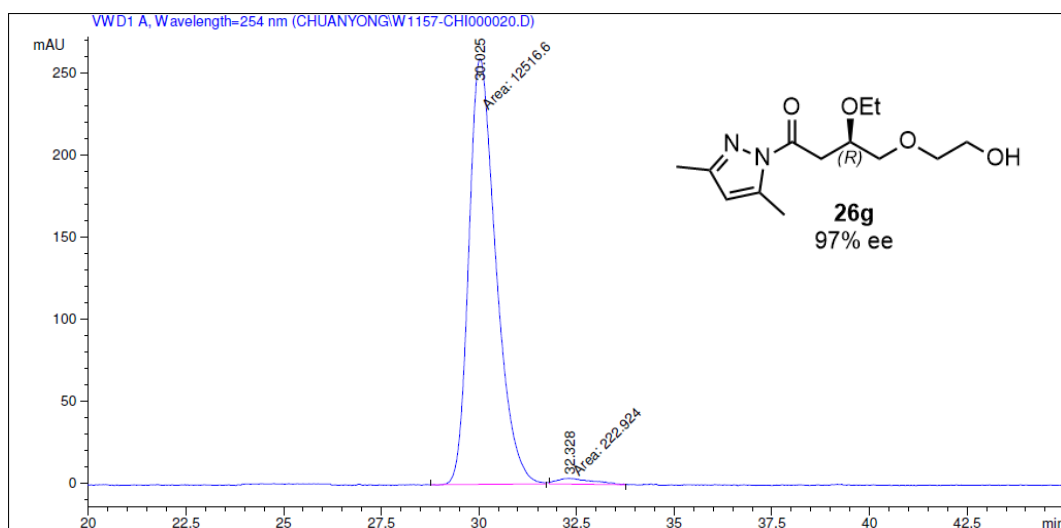
Peak #	RetTime [min]	Type	Width [min]	Area [mAU*s]	Height [mAU]	Area %
1	6.124	BB	0.1321	820.28455	95.59184	95.7285
2	6.809	BB	0.1190	36.60210	3.76359	4.2715

Figure 149 HPLC traces (Daicel Chiralpak OD-H column) of *rac*-26f (reference) and (*S*)-26f.

Chapter 6: Appendices



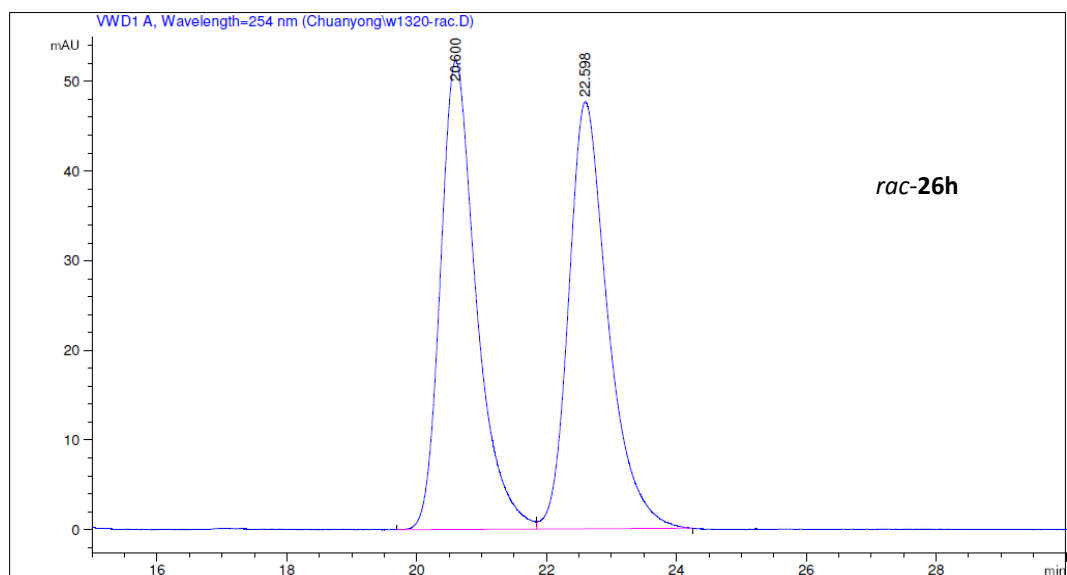
Peak #	RetTime [min]	Type	Width [min]	Area mAU *s	Height [mAU]	Area %
1	30.489	MF	0.7558	3745.51392	82.59969	49.3561
2	32.574	FM	0.8548	3843.24048	74.93472	50.6439



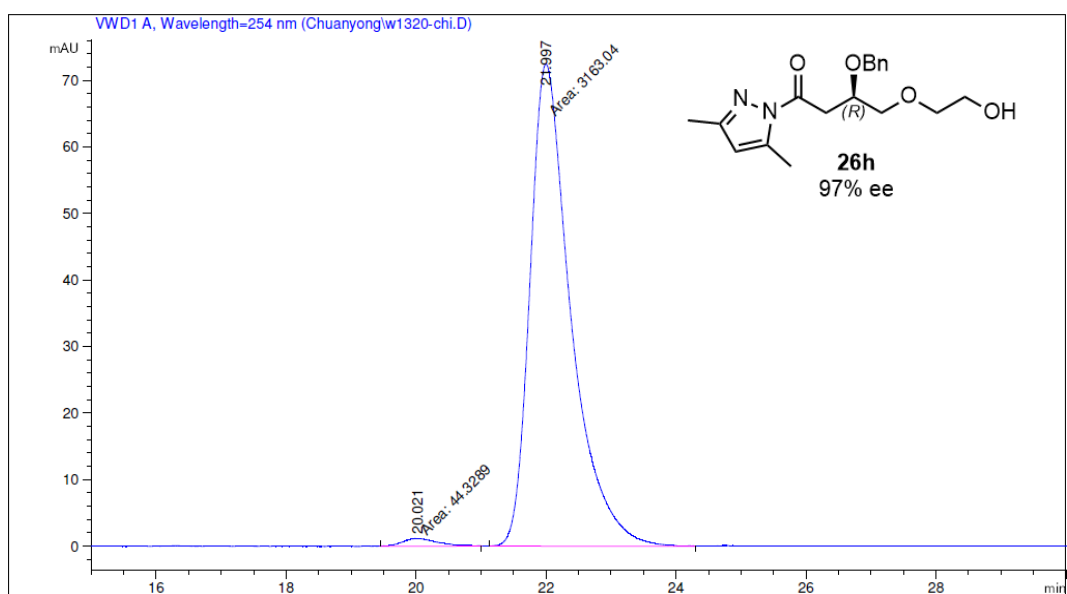
Peak #	RetTime [min]	Type	Width [min]	Area mAU *s	Height [mAU]	Area %
1	30.025	MM	0.8045	1.25166e4	259.29456	98.2501
2	32.328	MM	1.0498	222.92354	3.53899	1.7499

Figure 150 HPLC traces (Daicel Chiralpak IC column) of *rac*-**26g** (reference) and (*R*)-**26g**.

Chapter 6: Appendices



Peak #	RetTime [min]	Type	Width [min]	Area [mAU*s]	Height [mAU]	Area %
1	20.600	BV	0.4495	2005.38806	52.28069	50.0761
2	22.598	VV R	0.4949	1999.29309	47.65728	49.9239



Peak #	RetTime [min]	Type	Width [min]	Area [mAU*s]	Height [mAU]	Area %
1	20.021	MM	0.6285	44.32892	1.17552	1.3821
2	21.997	MM	0.7275	3163.03589	72.46577	98.6179

Figure 151 HPLC traces (Daicel Chiralpak AD-H column) of *rac*-**26h** (reference) and (*R*)-**26h**.

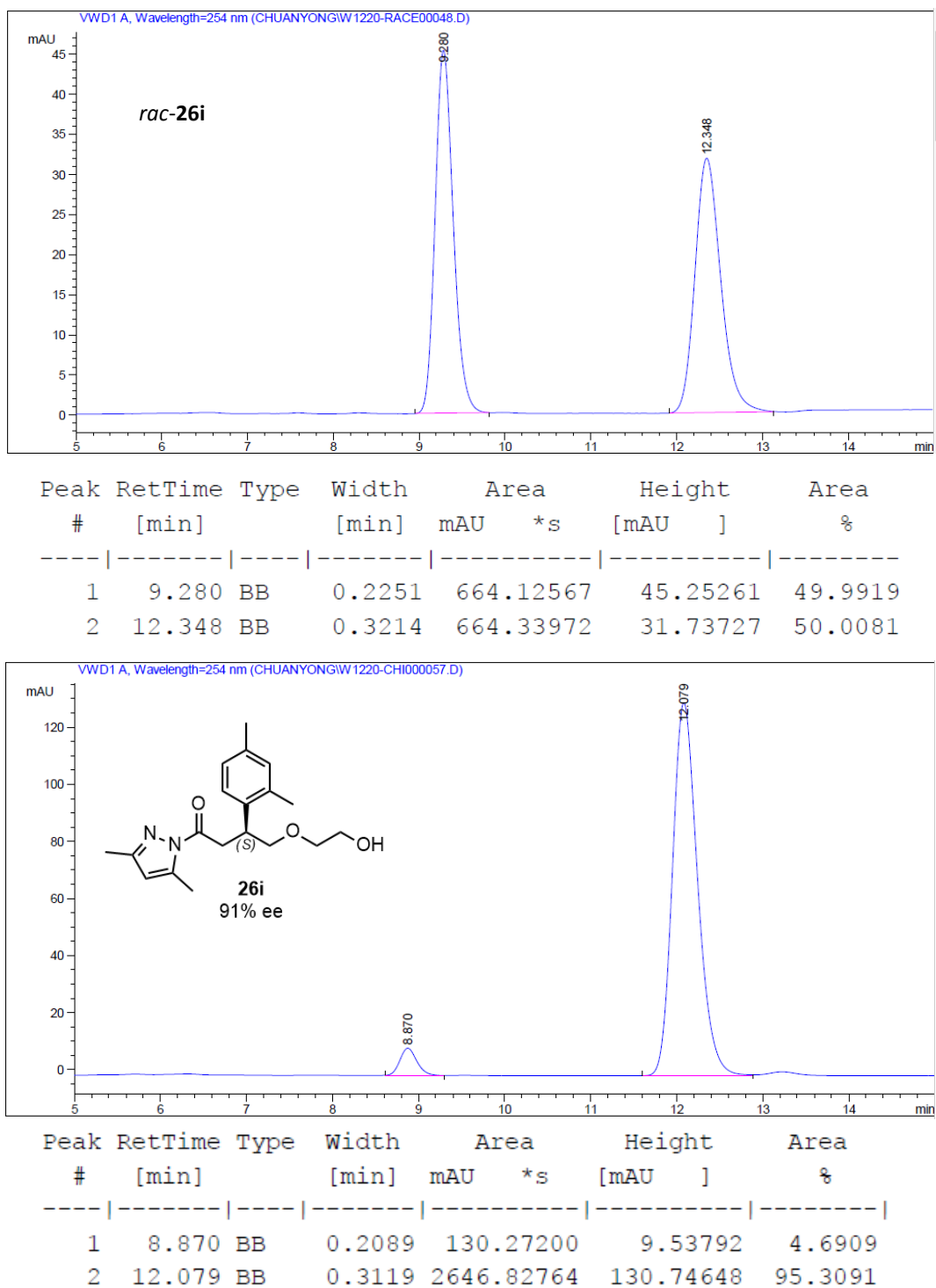


Figure 152 HPLC traces (Daicel Chiralpak OD-H column) of *rac-26i* (reference) and (*S*)-**26i**.

Chapter 6: Appendices

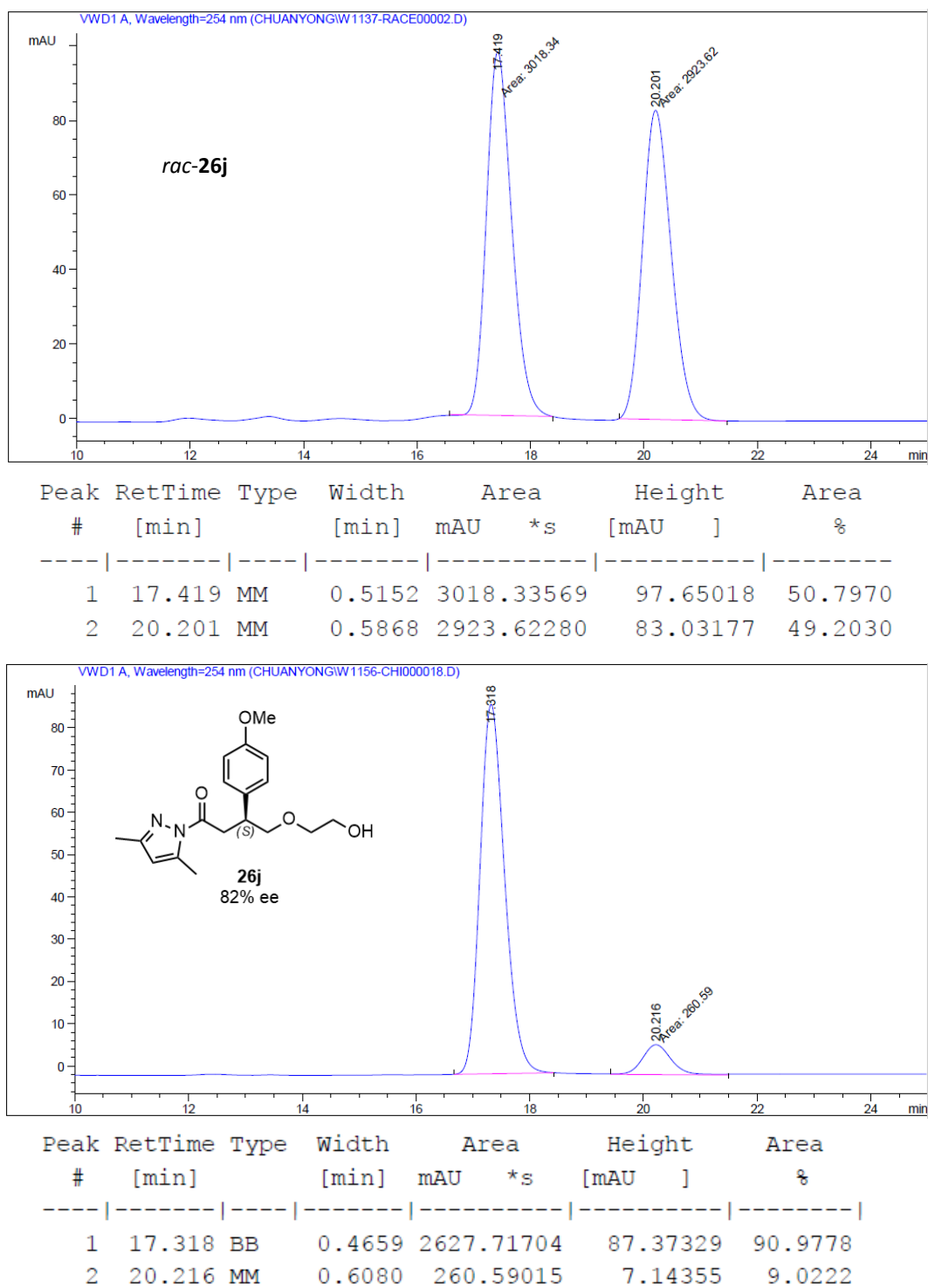


Figure 153 HPLC traces (Daicel Chiralpak OD-H column) of *rac*-26j (reference) and (*S*)-26j.

Chapter 6: Appendices

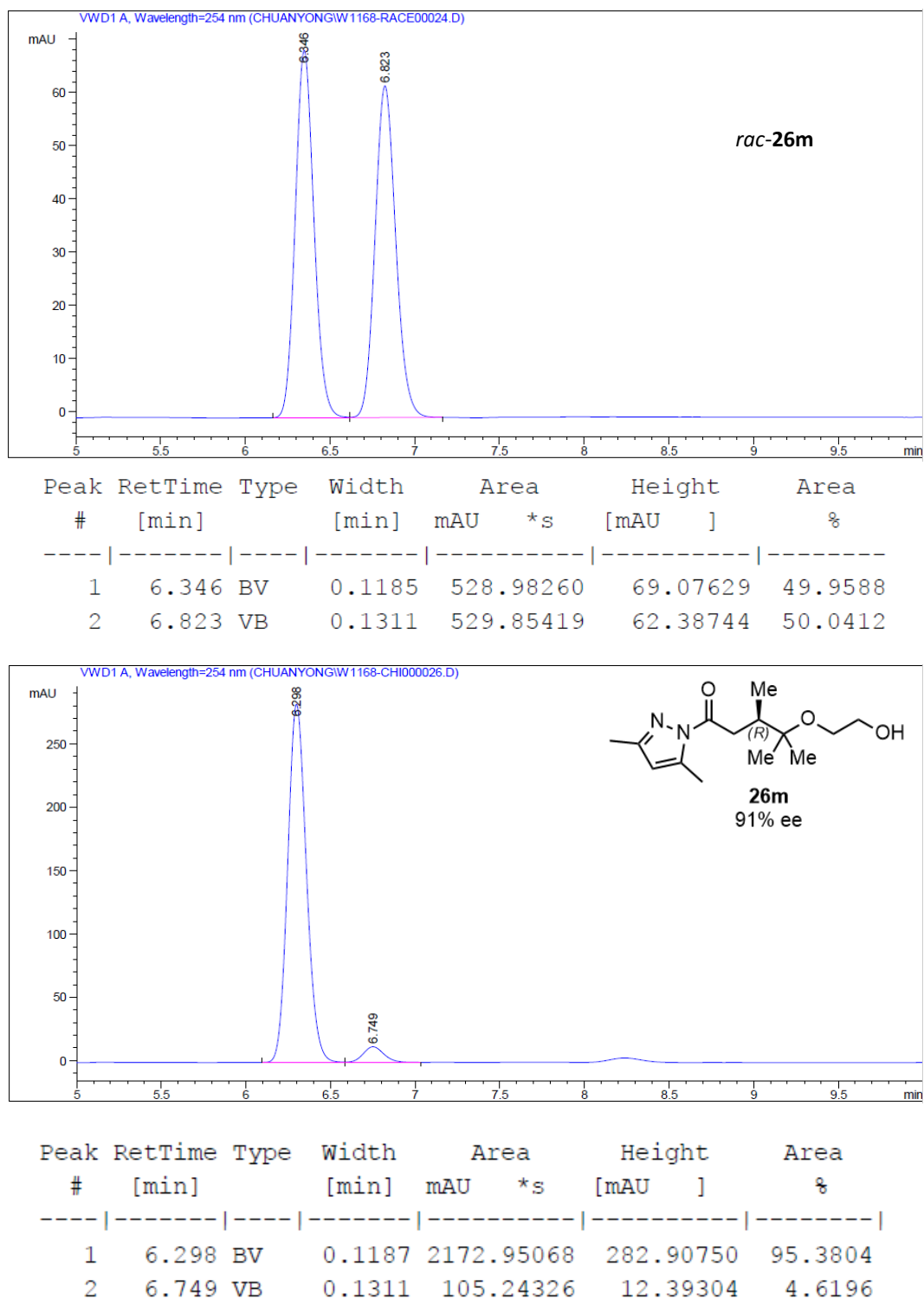


Figure 154 HPLC traces (Daicel Chiralpak OD-H column) of *rac*-**26m** (reference) and (*R*)-**26m**.

Chapter 6: Appendices

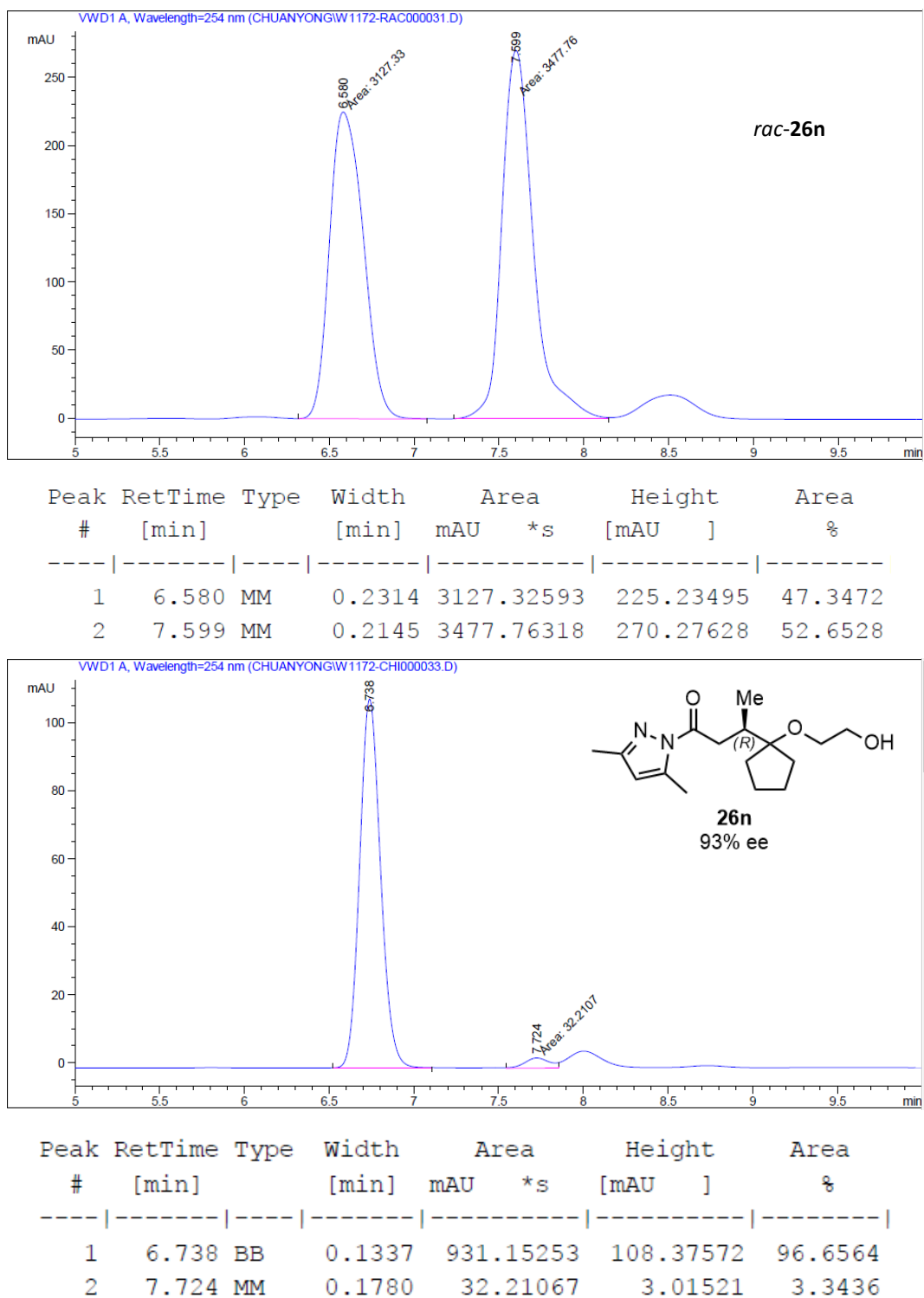
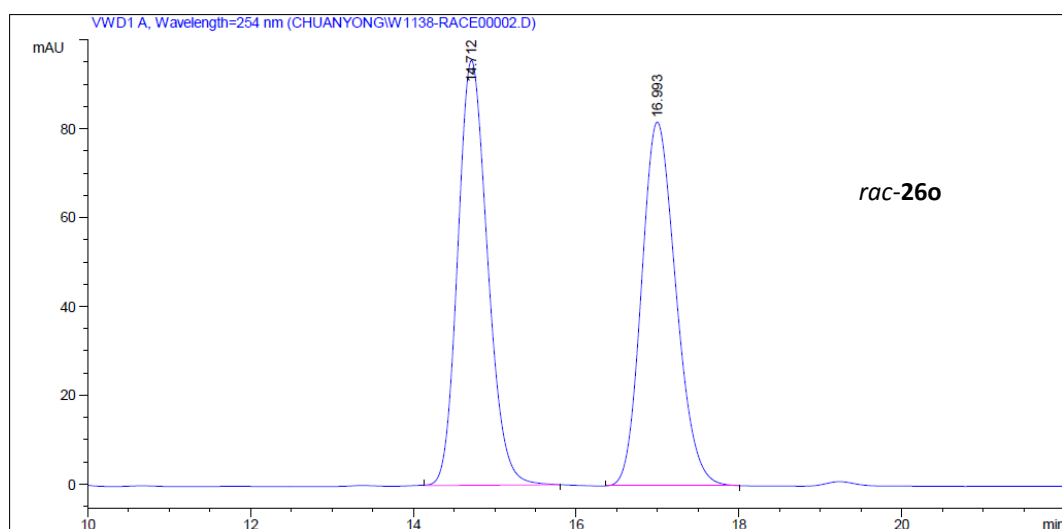
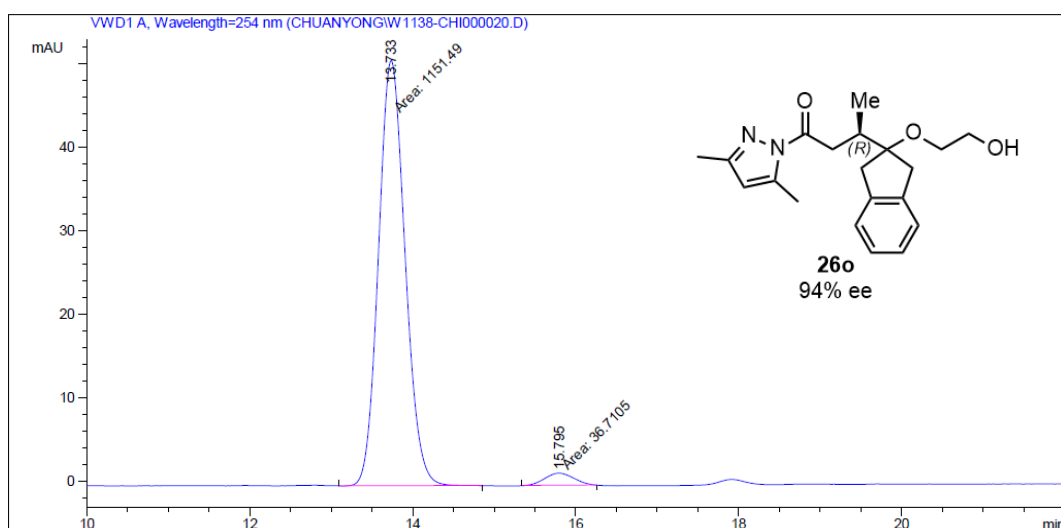


Figure 155 HPLC traces (Daicel Chiralpak OD-H column) of *rac-26n* (reference) and (*R*)-**26n**.

Chapter 6: Appendices



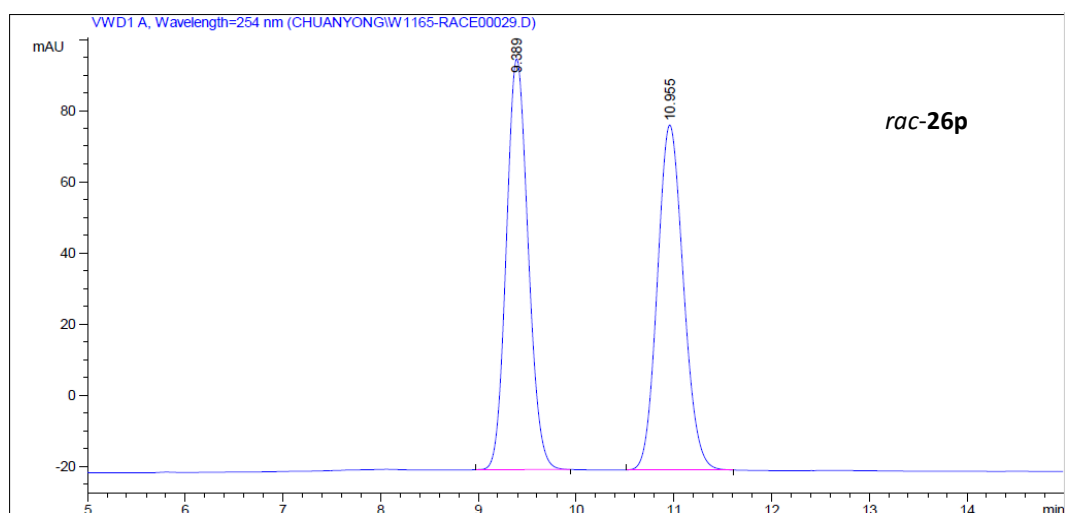
Peak #	RetTime [min]	Type	Width [min]	Area mAU *s	Height [mAU]	Area %
1	14.712	BB	0.3933	2438.32983	95.70654	50.3577
2	16.993	BB	0.4559	2403.68945	81.90963	49.6423



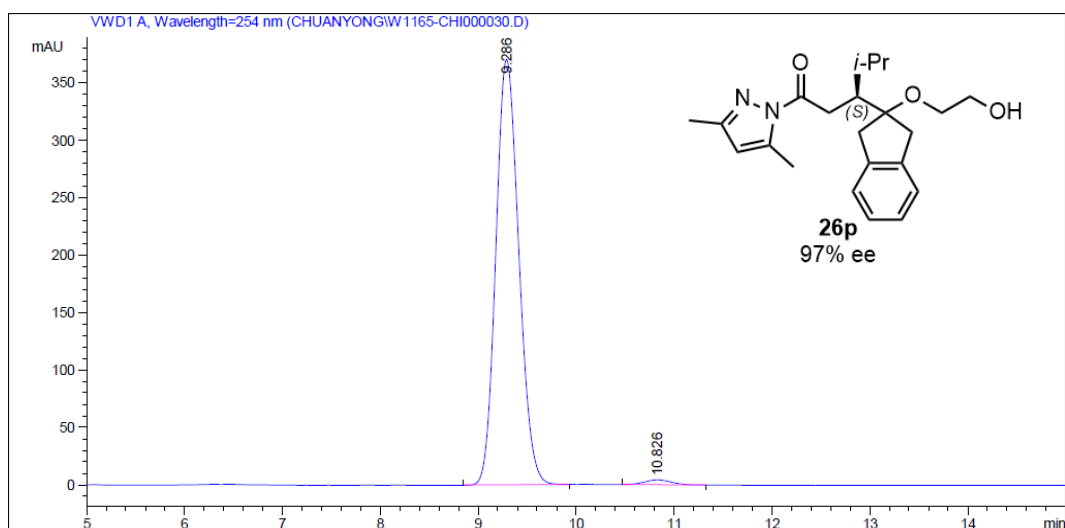
Peak #	RetTime [min]	Type	Width [min]	Area mAU *s	Height [mAU]	Area %
1	13.733	MM	0.3771	1151.48938	50.89389	96.9104
2	15.795	MM	0.4156	36.71046	1.47216	3.0896

Figure 156 HPLC traces (Daicel Chiralpak OD-H column) of *rac-26o* (reference) and (*R*)-**26o**.

Chapter 6: Appendices



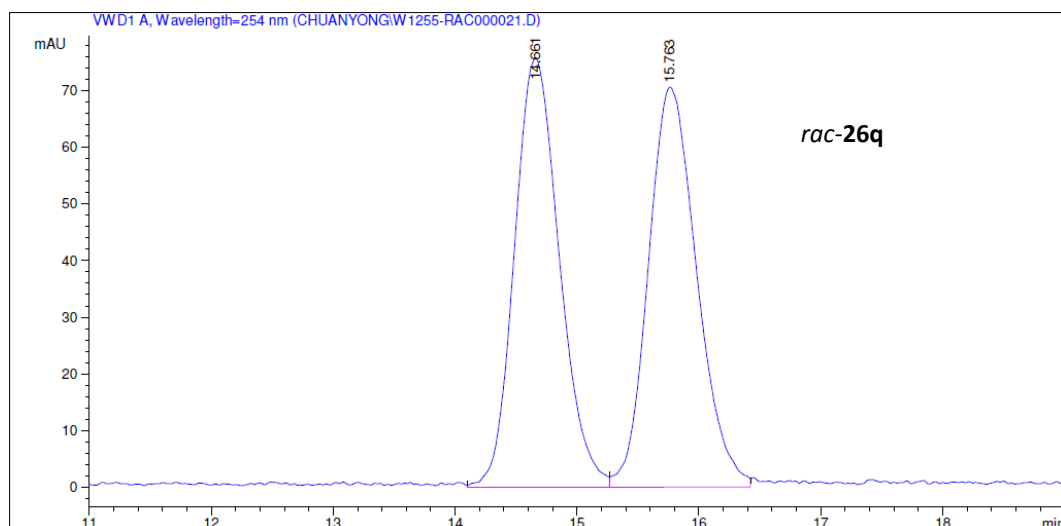
Peak #	RetTime [min]	Type	Width [min]	Area mAU *s	Height [mAU]	Area %
1	9.389	BB	0.2423	1793.49475	115.52425	49.9625
2	10.955	BB	0.2888	1796.18982	97.00903	50.0375



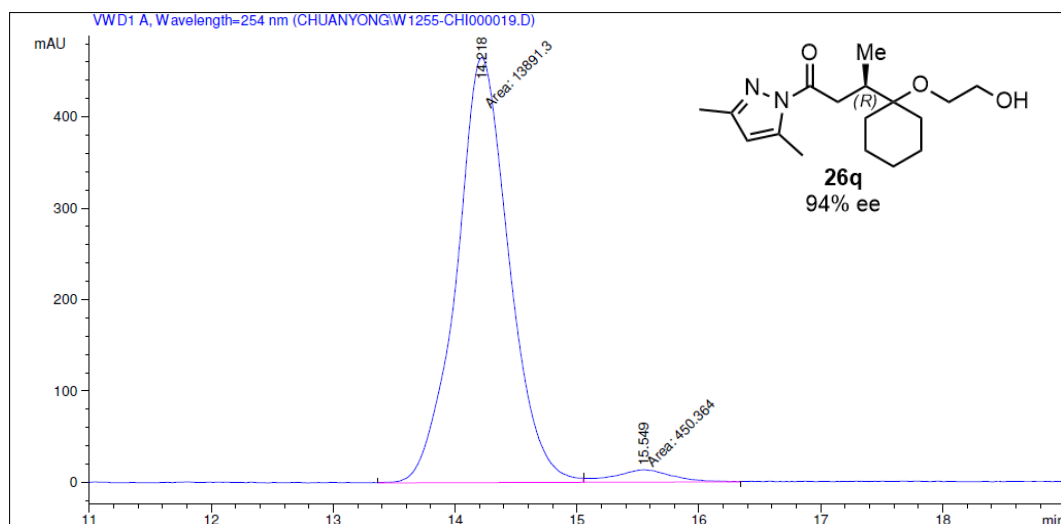
Peak #	RetTime [min]	Type	Width [min]	Area mAU *s	Height [mAU]	Area %
1	9.286	BB	0.2540	6030.62256	370.35068	98.7007
2	10.826	BB	0.2956	79.38618	4.18467	1.2993

Figure 157 HPLC traces (Daicel Chiralpak OD-H column) of *rac*-**26p** (reference) and (*S*)-**26p**.

Chapter 6: Appendices



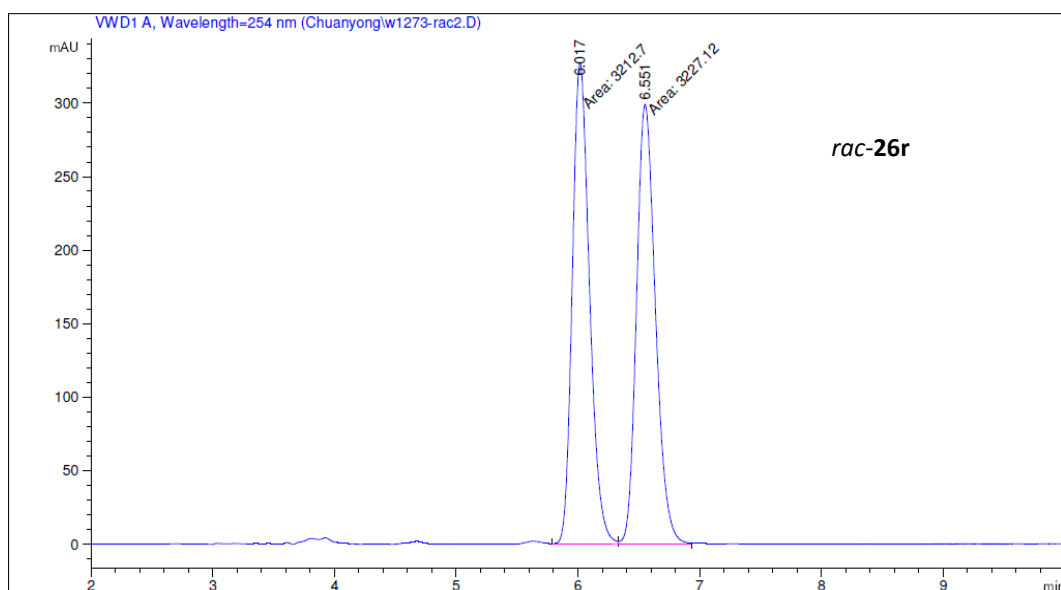
Peak #	RetTime [min]	Type	Width [min]	Area mAU *s	Height [mAU]	Area %
1	14.661	VV	0.3917	1936.57886	75.69459	49.9017
2	15.763	VV	0.4002	1944.20630	70.54542	50.0983



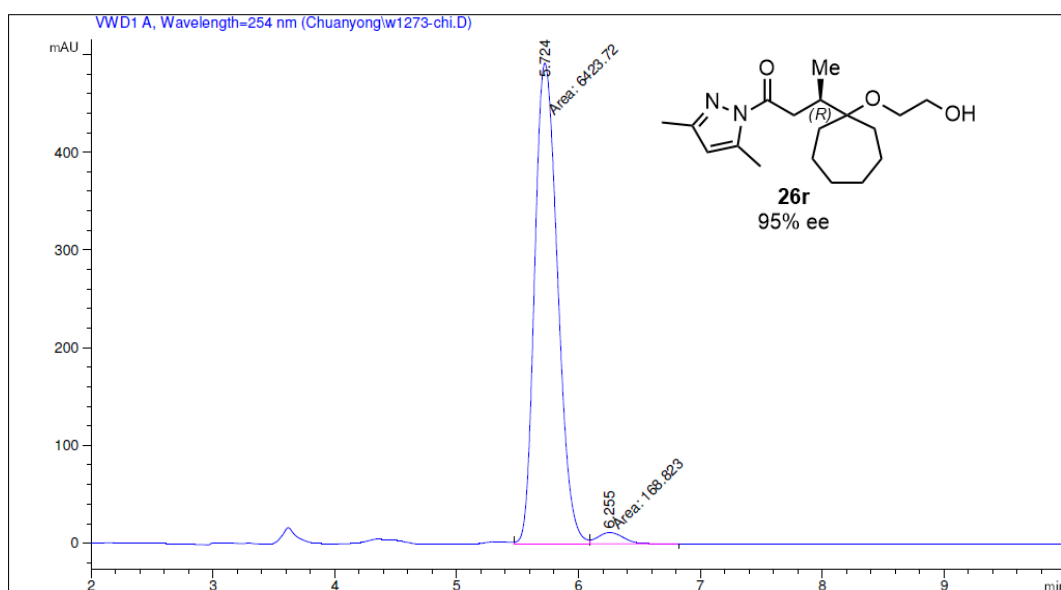
Peak #	RetTime [min]	Type	Width [min]	Area mAU *s	Height [mAU]	Area %
1	14.218	MF	0.4979	1.38913e4	464.99200	96.8598
2	15.549	FM	0.5558	450.36417	13.50606	3.1402

Figure 158 HPLC traces (Daicel Chiralpak OD-H column) of *rac*-**26q** (reference) and (*R*)-**26q**.

Chapter 6: Appendices



Peak #	RetTime [min]	Type	Width [min]	Area [mAU*s]	Height [mAU]	Area %
1	6.017	FM	0.1637	3212.70264	327.18060	49.8880
2	6.551	MF	0.1799	3227.12329	299.02869	50.1120



Peak #	RetTime [min]	Type	Width [min]	Area [mAU*s]	Height [mAU]	Area %
1	5.724	MF	0.2177	6423.72168	491.71777	97.4392
2	6.255	FM	0.2447	168.82259	11.49714	2.5608

Figure 159 HPLC traces (Daicel Chiralpak OD-H column) of *rac-26r* (reference) and (*R*)-**26r**.

Chapter 6: Appendices

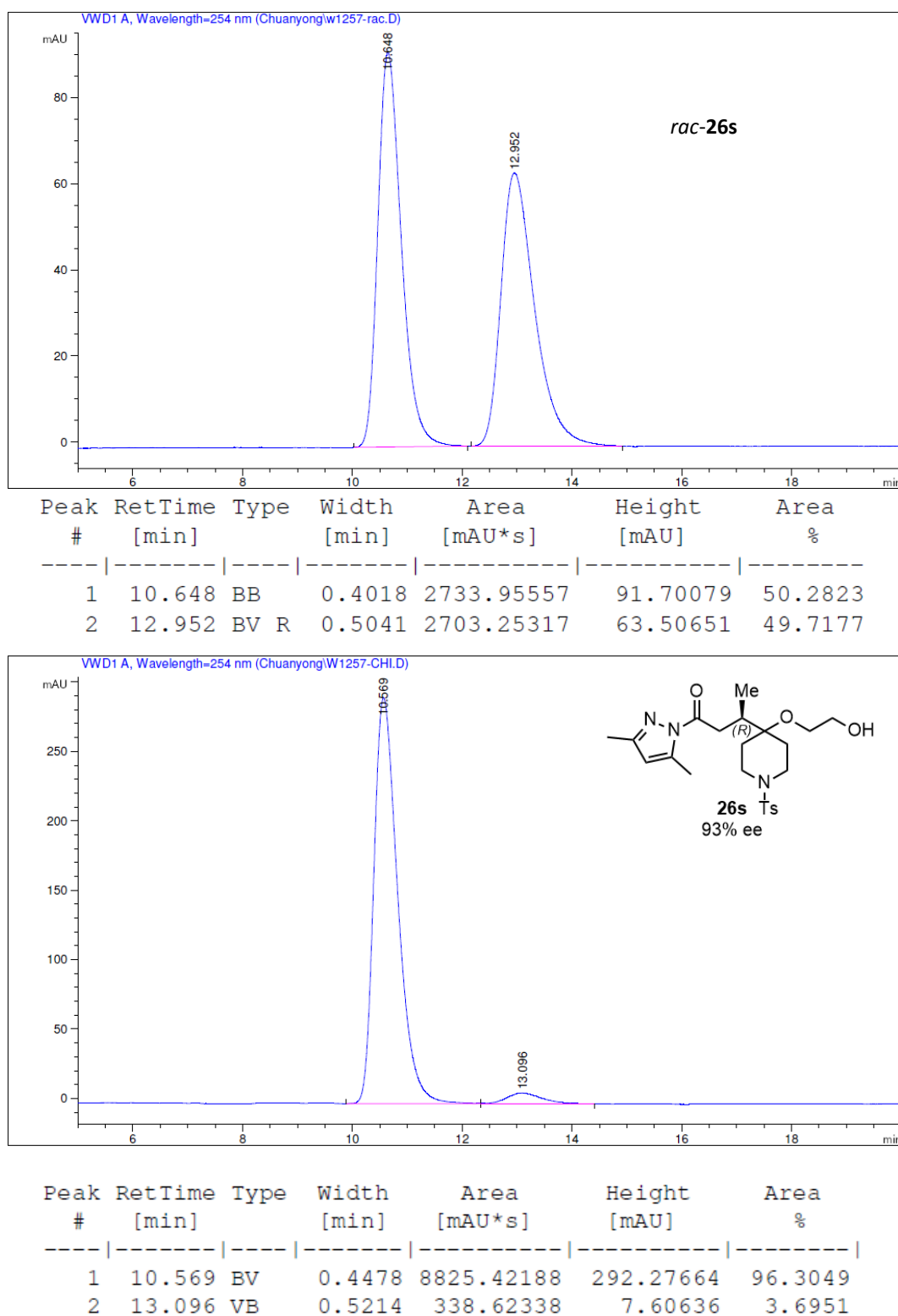
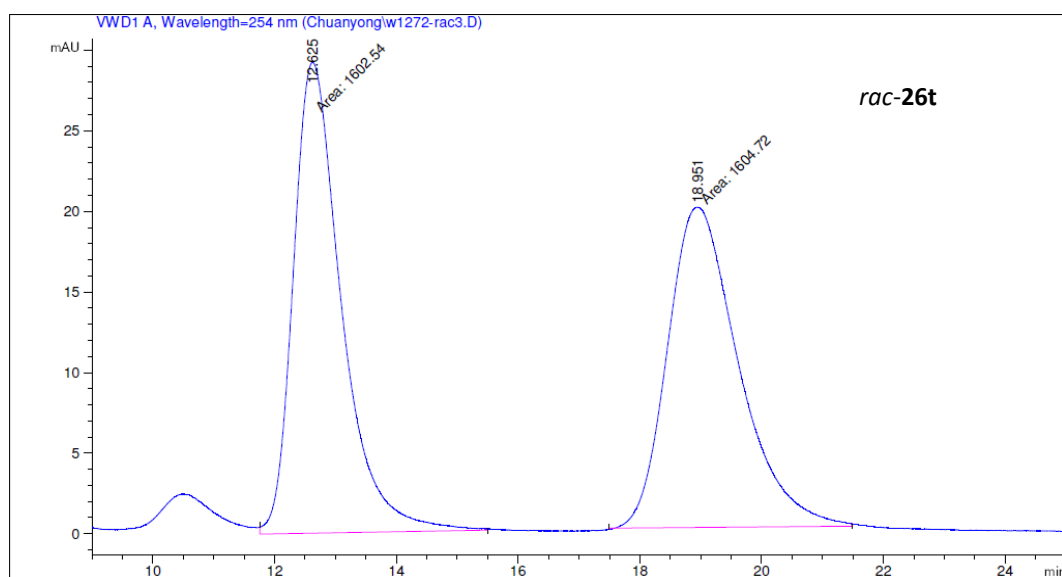
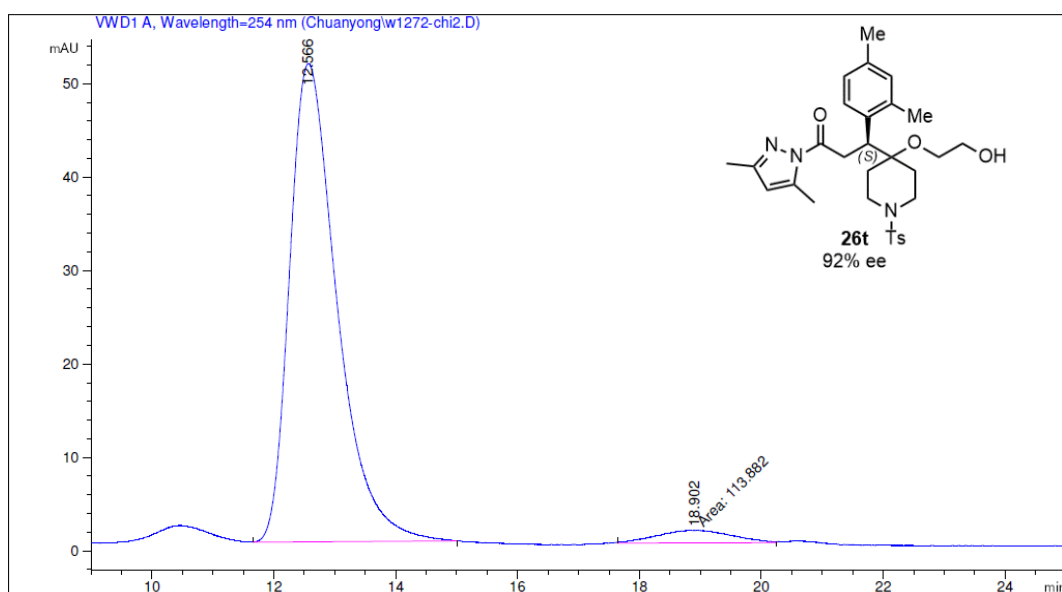


Figure 160 HPLC traces (Daicel Chiralpak OD-H column) of *rac*-**26s** (reference) and (*R*)-**26s**.

Chapter 6: Appendices



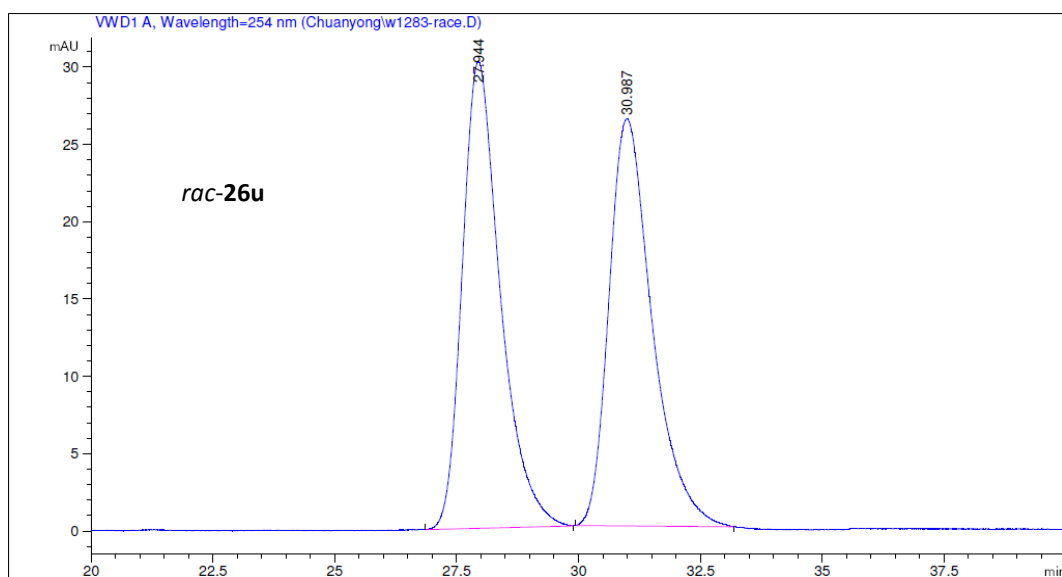
Peak #	RetTime [min]	Type	Width [min]	Area [mAU*s]	Height [mAU]	Area %
1	12.625	MM	0.9144	1602.53552	29.20991	49.9659
2	18.951	MM	1.3468	1604.72131	19.85891	50.0341



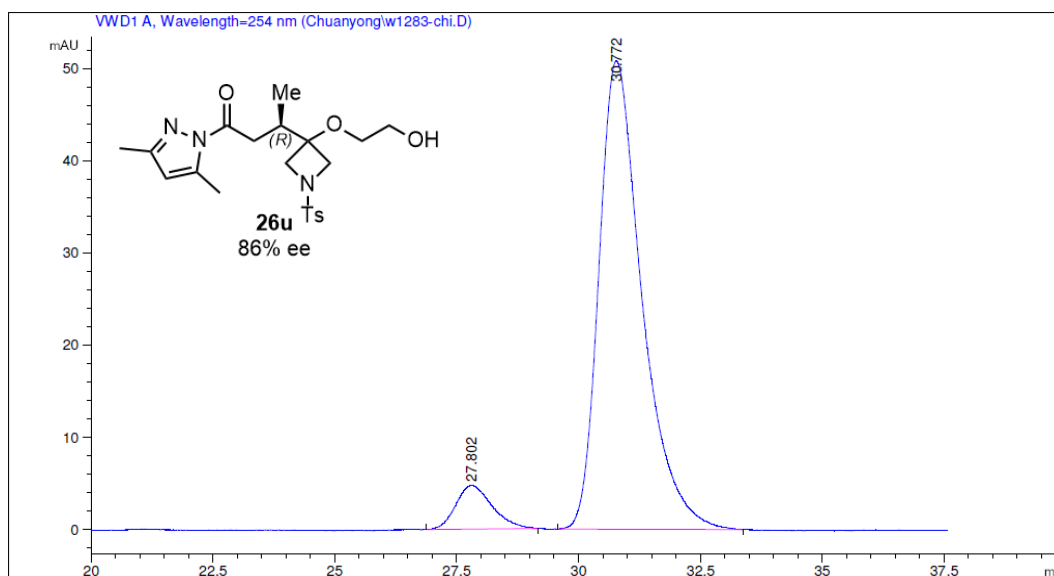
Peak #	RetTime [min]	Type	Width [min]	Area [mAU*s]	Height [mAU]	Area %
1	12.566	BV R	0.6308	2763.15332	51.18871	96.0417
2	18.902	MM	1.4146	113.88199	1.34178	3.9583

Figure 161 HPLC traces (Daicel Chiralpak OD-H column) of *rac*-**26t** (reference) and (*S*)-**26t**.

Chapter 6: Appendices



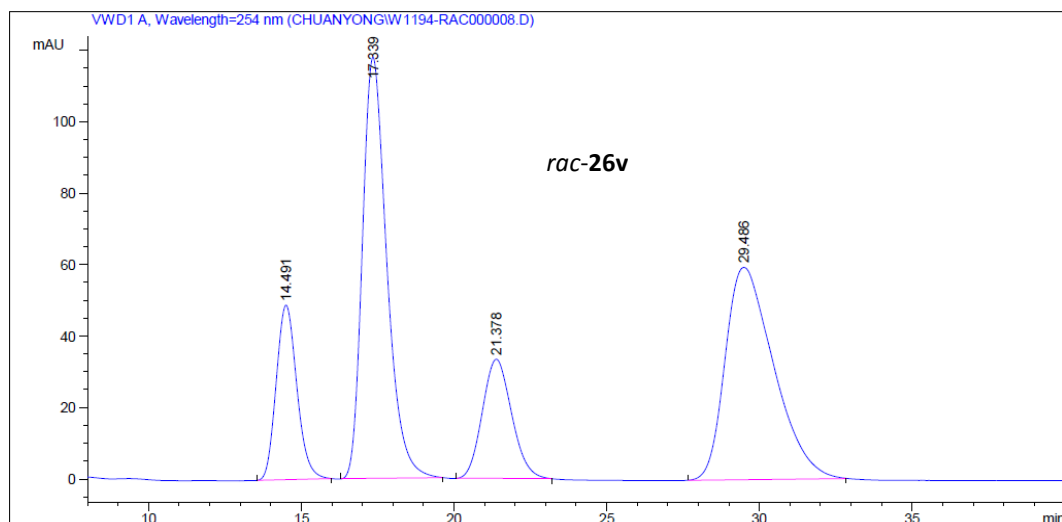
Peak #	RetTime [min]	Type	Width [min]	Area [mAU*s]	Height [mAU]	Area %
1	27.944	BB	0.6380	1638.58118	30.17740	50.2871
2	30.987	BB	0.7192	1619.87109	26.33187	49.7129



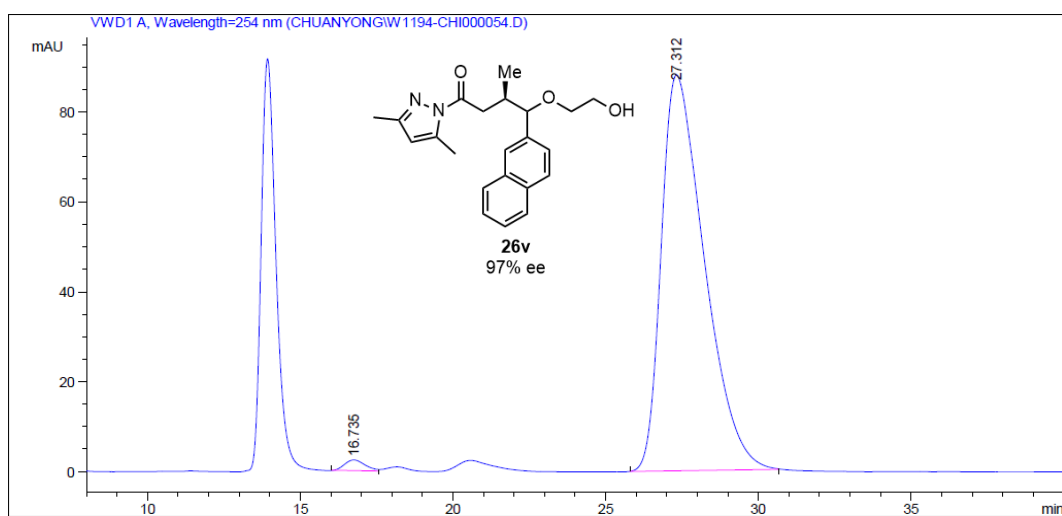
Peak #	RetTime [min]	Type	Width [min]	Area [mAU*s]	Height [mAU]	Area %
1	27.802	BV R	0.6053	245.26054	4.73522	7.2972
2	30.772	BV R	0.7176	3115.76465	50.76049	92.7028

Figure 162 HPLC traces (Daicel Chiralpak AD-H column) of *rac-26u* (reference) and (*R*)-**26u**.

Chapter 6: Appendices



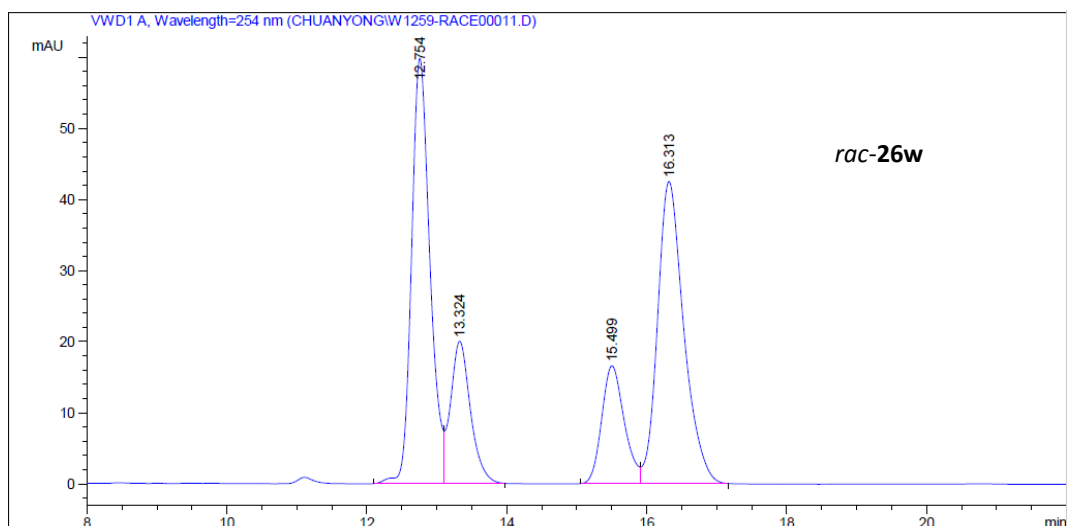
Peak #	RetTime [min]	Type	Width [min]	Area mAU *s	Height [mAU]	Area %
1	14.491	BB	0.7238	2299.71313	48.86214	13.0454
2	17.339	BB	0.8536	6535.15820	117.87031	37.0716
3	21.378	BB	1.0298	2236.63379	33.41934	12.6876
4	29.486	BB	1.5939	6556.96777	59.38482	37.1953



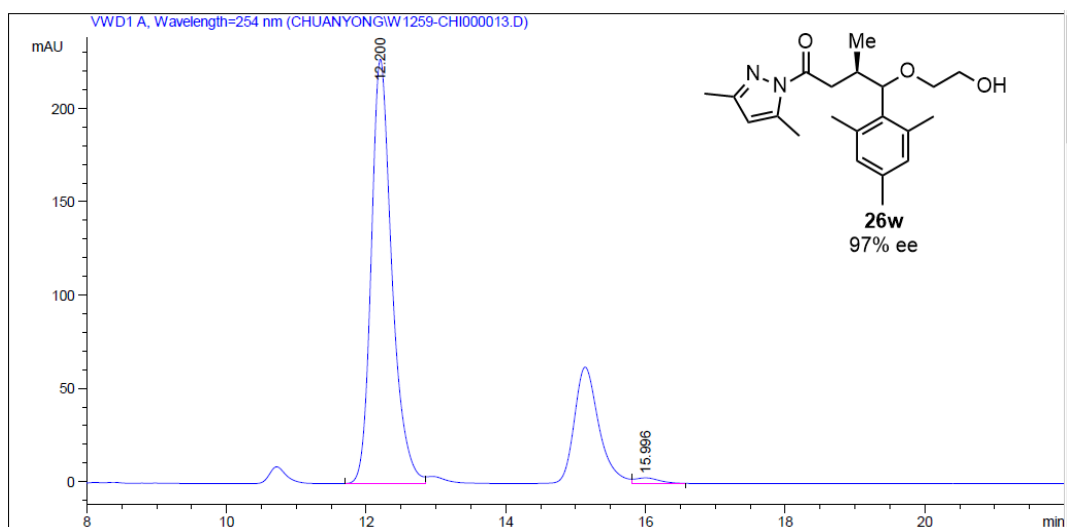
Peak #	RetTime [min]	Type	Width [min]	Area mAU *s	Height [mAU]	Area %
1	16.735	BV	0.6214	113.68958	2.41764	1.2997
2	27.312	BB	1.3999	8633.49414	88.07463	98.7003

Figure 163 HPLC traces (Daicel Chiralpak OJ-H column) of *rac-26v* (reference) and (*R*)-**26v**..

Chapter 6: Appendices



Peak #	RetTime [min]	Type	Width [min]	Area mAU *s	Height [mAU]	Area %
1	12.754	BV	0.2775	1094.70361	59.83386	36.8205
2	13.324	VB	0.2953	397.28790	20.04235	13.3628
3	15.499	BV	0.3442	371.71835	16.60200	12.5028
4	16.313	VB	0.3932	1109.37280	42.52079	37.3139



Peak #	RetTime [min]	Type	Width [min]	Area mAU *s	Height [mAU]	Area %
1	12.200	BV	0.3096	4668.66797	227.18031	98.4827
2	15.996	VB	0.3601	71.93100	2.99685	1.5173

Figure 164 HPLC traces (Daicel Chiralpak IC column) of *rac*-**26w** (reference) and (*R*)-**26w**.

Chapter 6: Appendices

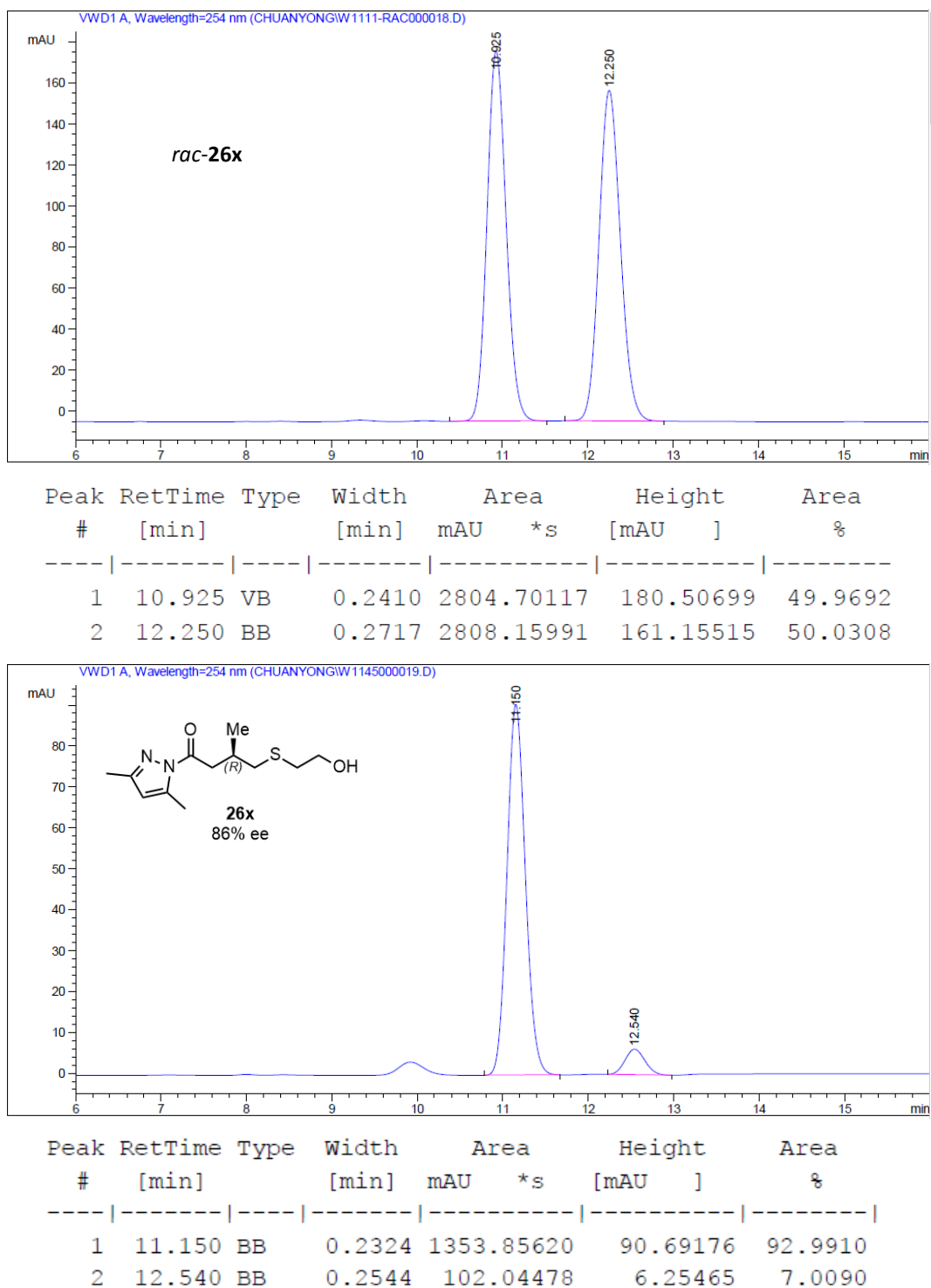
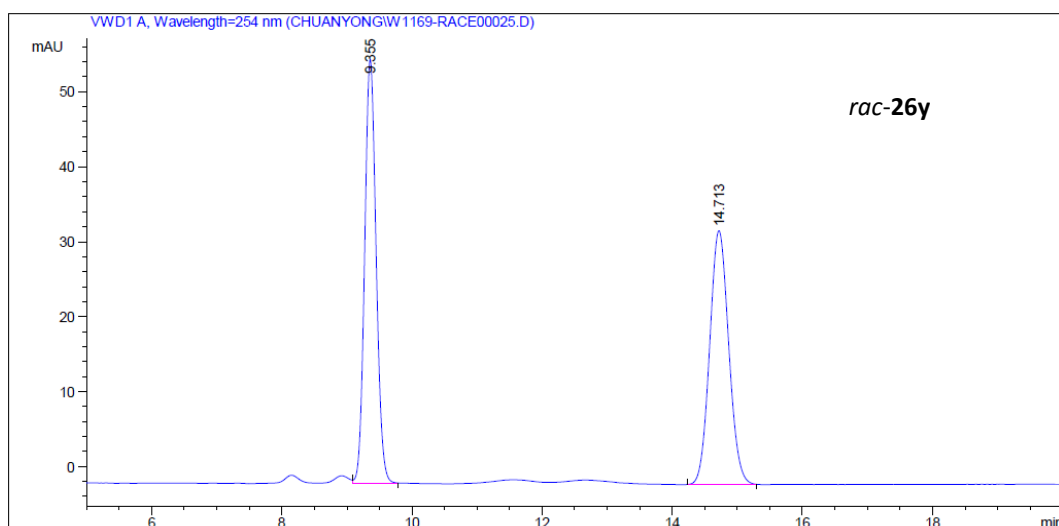
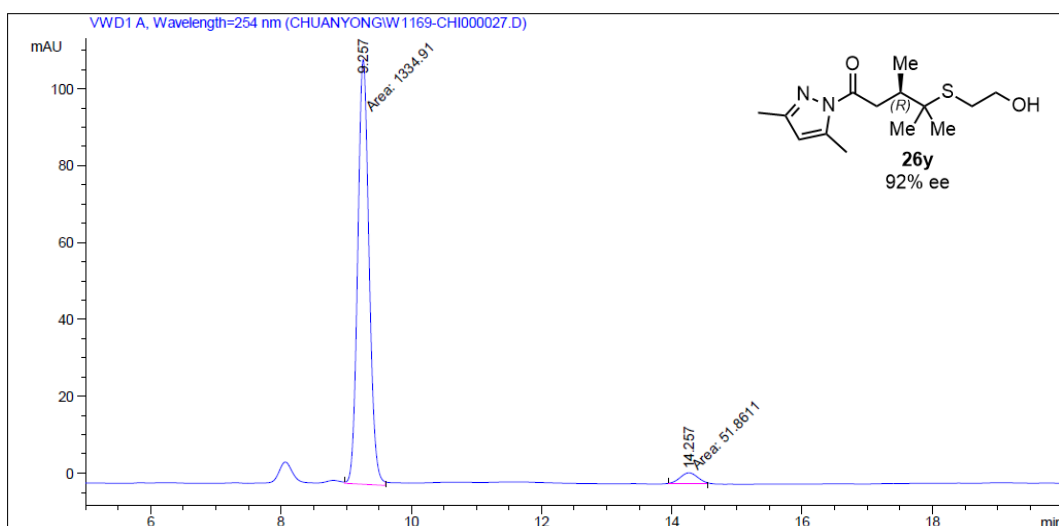


Figure 165 HPLC traces (Daicel Chiralpak OD-H column) of *rac-26x* (reference) and (*R*)-**26x**.

Chapter 6: Appendices



Peak #	RetTime [min]	Type	Width [min]	Area mAU *s	Height [mAU]	Area %
1	9.355	VB	0.1892	690.80206	56.52901	50.0562
2	14.713	BB	0.3161	689.25067	33.86409	49.9438



Peak #	RetTime [min]	Type	Width [min]	Area mAU *s	Height [mAU]	Area %
1	9.257	MM	0.2012	1334.90894	110.58812	96.2603
2	14.257	MM	0.3105	51.86114	2.78389	3.7397

Figure 166 HPLC traces (Daicel Chiralpak OD-H column) of *rac-26y* (reference) and *(R)-26y*.

Chapter 6: Appendices

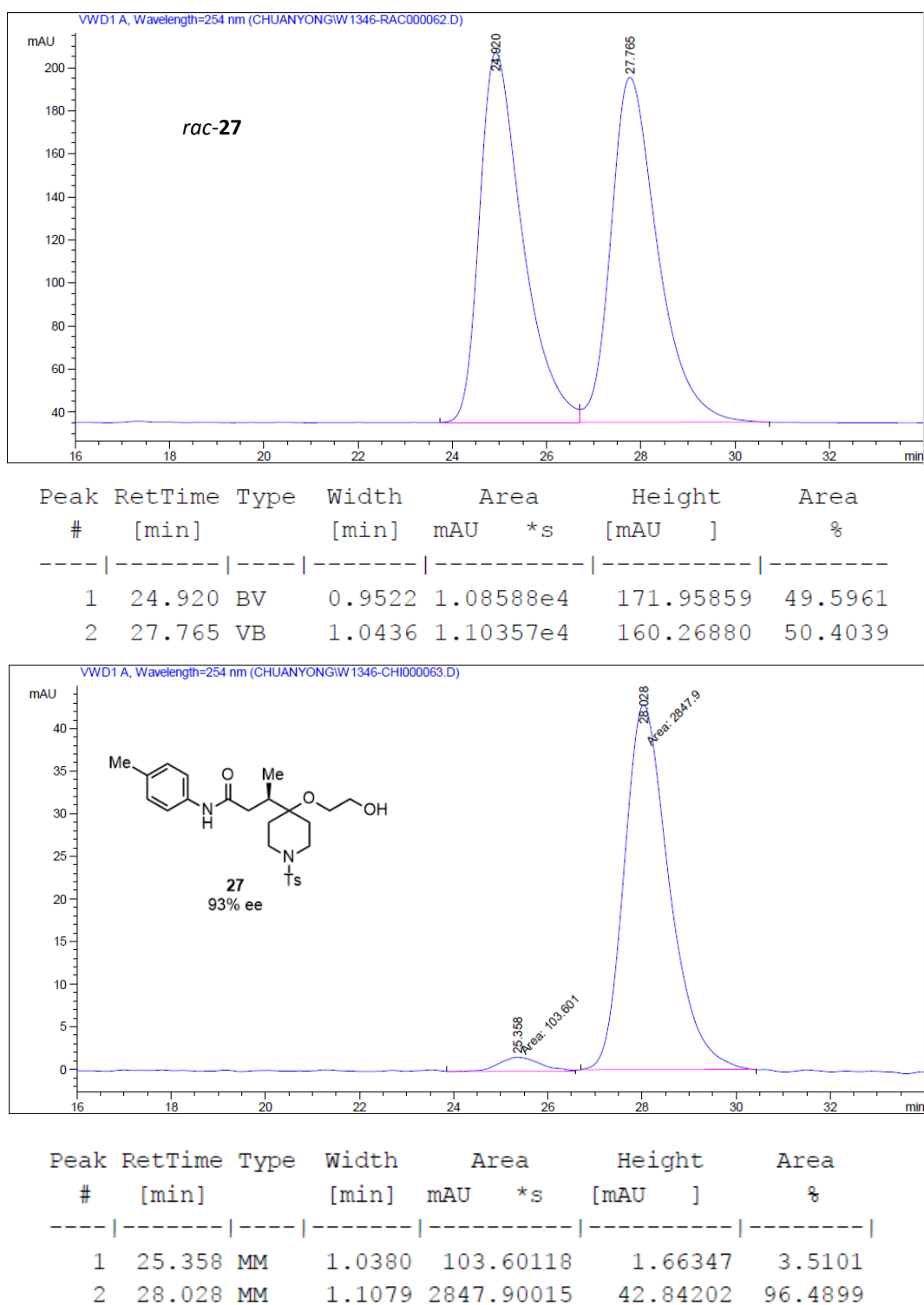


Figure 167 HPLC traces (Daicel Chiralpak AD-H column) of *rac-27* (reference) and (*R*)-**27**.

Chapter 6: Appendices

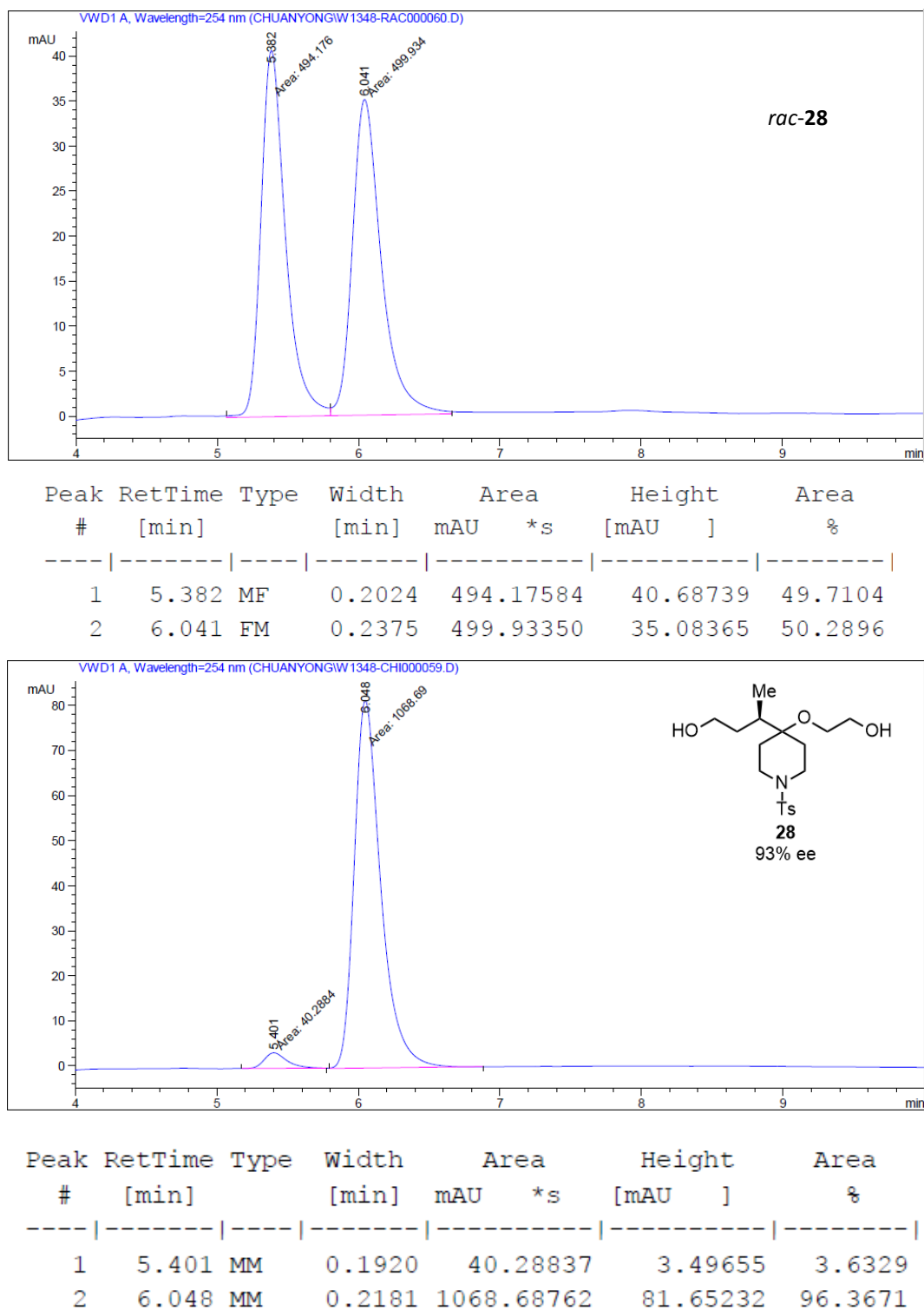


Figure 168 HPLC traces (Daicel Chiralpak AD-H column) of *rac-28* (reference) and (*R*)-**28**.

6.7 List of Crystal Structure Data

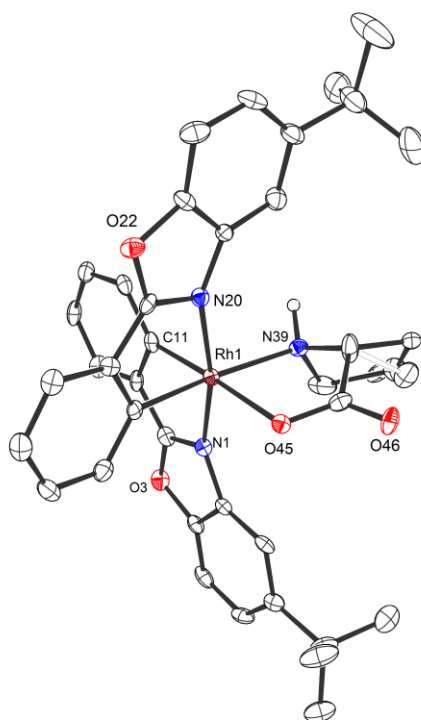


Figure 169 Crystal structure of Δ -(*R*)-3. ORTEP drawing with 50% probability thermal ellipsoids.

Table 9 Crystal data and structure refinement for Δ -(*R*)-3.

Crystal data:

Identification code	w166_0m	
Habitus, colour	needle, yellow	
Crystal size	0.44 x 0.07 x 0.06 mm ³	
Crystal system	Orthorhombic	
Space group	P 2 ₁ 2 ₁ 2 ₁	Z = 4
Unit cell dimensions	a = 13.919(6) Å	α = 90°.
	b = 19.144(9) Å	β = 90°.
	c = 28.616(11) Å	γ = 90°.
Volume	7625(6) Å ³	
Cell determination	9357 peaks with Theta 2.3 to 25.7°.	
Empirical formula	C ₈₁ H ₈₆ Cl ₆ N ₆ O ₈ Rh ₂	
Formula weight	1690.07	
Density (calculated)	1.472 Mg/m ³	
Absorption coefficient	0.704 mm ⁻¹	
F(000)	3480	

Chapter 6: Appendices

Data collection:

Diffractometer type	Bruker D8 QUEST area detector
Wavelength	0.71073 Å
Temperature	100(2) K
Theta range for data collection	2.302 to 25.497°.
Index ranges	-16<=h<=16, -23<=k<=23, -33<=l<=34
Data collection software	BRUKER APEX2
Cell refinement software	SAINT V8.34A (Bruker AXS Inc., 2013)
Data reduction software	SAINT V8.34A (Bruker AXS Inc., 2013)

Solution and refinement:

Reflections collected	64188
Independent reflections	14187 [R(int) = 0.0642]
Completeness to theta = 25.242°	99.9 %
Observed reflections	12148[II > 2(I)]
Reflections used for refinement	14187
Absorption correction	Numerical
Max. and min. transmission	0.96 and 0.76
Flack parameter (absolute struct.)	-0.020(10)
Largest diff. peak and hole	0.569 and -0.435 e.Å ⁻³
Solution	direct/ difmap
Refinement	Full-matrix least-squares on F ²
Treatment of hydrogen atoms	geom, constr
Programs used	SHELXS-97 (Sheldrick, 2008) SHELXL-2013 (Sheldrick, 2013) DIAMOND (Crystal Impact)
Data / restraints / parameters	14187 / 114 / 996
Goodness-of-fit on F ²	1.024
R index (all data)	wR2 = 0.0682
R index conventional [I>2sigma(I)]	R1 = 0.0358

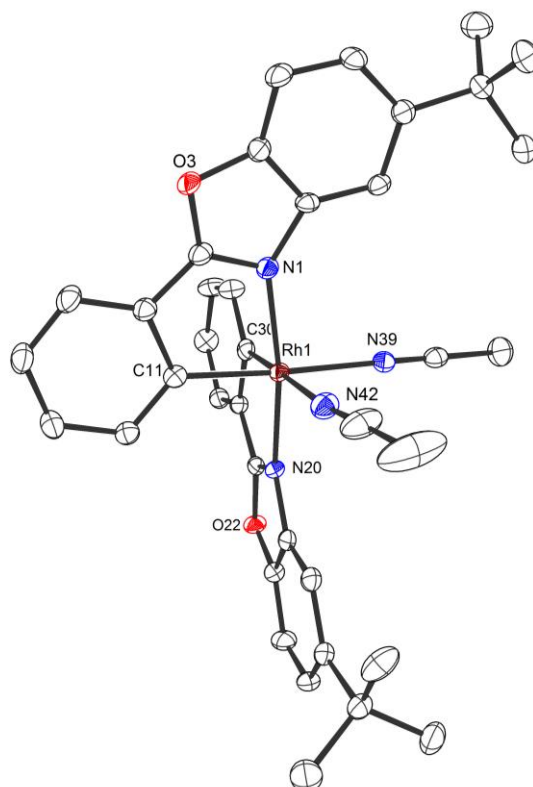


Figure 170 Crystal structure of Δ -RhO. ORTEP drawing with 50% probability thermal ellipsoids. The hexafluorophosphate counteranion is omitted for clarity.

Table 10 Crystal data and structure refinement for Δ -RhO.

Crystal data:

Identification code	w169_0m	
Habitus, colour	nugget, colourless	
Crystal size	0.51 x 0.24 x 0.17 mm ³	
Crystal system	Orthorhombic	
Space group	P 2 ₁ 2 ₁ 2 ₁	Z = 4
Unit cell dimensions	a = 13.1445(5) Å	$\alpha = 90^\circ$.
	b = 13.6427(6) Å	$\beta = 90^\circ$.
	c = 22.5166(8) Å	$\gamma = 90^\circ$.
Volume	4037.8(3) Å ³	
Cell determination	9096 peaks with Theta 2.3 to 27.5°.	
Empirical formula	C ₃₉ H ₄₀ Cl ₂ F ₆ N ₄ O ₂ P Rh	
Formula weight	915.53	
Density (calculated)	1.506 Mg/m ³	
Absorption coefficient	0.662 mm ⁻¹	
F(000)	1864	

Chapter 6: Appendices

Data collection:

Diffractometer type	Bruker D8 QUEST area detector
Wavelength	0.71073 Å
Temperature	100(2) K
Theta range for data collection	2.345 to 27.520°.
Index ranges	-17<=h<=17, -15<=k<=17, -29<=l<=29
Data collection software	BRUKER APEX2
Cell refinement software	SAINT V8.34A (Bruker AXS Inc., 2013)
Data reduction software	SAINT V8.34A (Bruker AXS Inc., 2013)

Solution and refinement:

Reflections collected	39009
Independent reflections	9272 [R(int) = 0.0416]
Completeness to theta = 25.242°	99.8 %
Observed reflections	8540[II > 2(I)]
Reflections used for refinement	9272
Absorption correction	Numerical
Max. and min. transmission	0.90 and 0.75
Flack parameter (absolute struct.)	-0.033(8)
Largest diff. peak and hole	0.511 and -0.396 e.Å ⁻³
Solution	Direct methods
Refinement	Full-matrix least-squares on F ²
Treatment of hydrogen atoms	Calculated positions, constr. ref.
Programs used	SHELXS-97 (Sheldrick, 2008) SHELXL-2013 (Sheldrick, 2013) DIAMOND (Crystal Impact)
Data / restraints / parameters	9272 / 168 / 590
Goodness-of-fit on F ²	1.033
R index (all data)	wR2 = 0.0579
R index conventional [I>2sigma(I)]	R1 = 0.0287

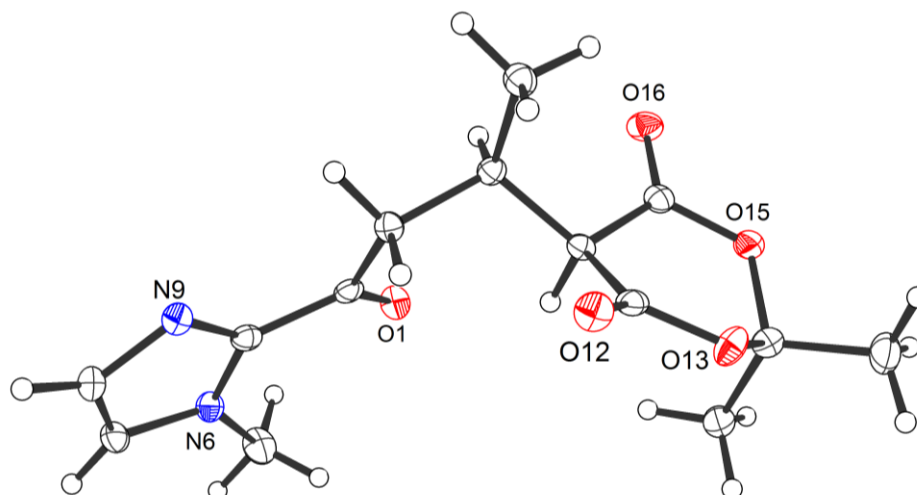


Figure 171 Crystal structure of **5d**. ORTEP drawing with 50% probability thermal ellipsoids.

Table 11 Crystal data and structure refinement for **5d**.

Crystal data:

Identification code	w189b_0m
Habitus, colour	Needle, colourless
Crystal size	0.45 x 0.08 x 0.05 mm ³
Crystal system	Orthorhombic
Space group	P 2 ₁ 2 ₁ 2 ₁ Z = 4
Unit cell dimensions	a = 5.4571(2) Å α = 90°.
	b = 15.3289(6) Å β = 90°.
	c = 17.4084(9) Å γ = 90°.
Volume	1456.24(11) Å ³
Cell determination	4862 peaks with Theta 2.3 to 27.1°.
Empirical formula	C ₁₄ H ₁₈ N ₂ O ₅
Formula weight	294.30
Density (calculated)	1.342 Mg/m ³
Absorption coefficient	0.103 mm ⁻¹
F(000)	624

Data collection:

Diffractometer type	Bruker D8 QUEST area detector
Wavelength	0.71073 Å
Temperature	100(2) K
Theta range for data collection	2.340 to 25.488°.
Index ranges	-6 ≤ h ≤ 5, -18 ≤ k ≤ 18, -21 ≤ l ≤ 21
Data collection software	BRUKER APEX2
Cell refinement software	SAINT V8.34A (Bruker AXS Inc., 2013)

Chapter 6: Appendices

Data reduction software SAINT V8.34A (Bruker AXS Inc., 2013)

Solution and refinement:

Reflections collected	11088
Independent reflections	2707 [R(int) = 0.0367]
Completeness to theta = 25.242°	99.9 %
Observed reflections	2478[II > 2(I)]
Reflections used for refinement	2707
Absorption correction	Numerical
Max. and min. transmission	0.99 and 0.95
Flack parameter (absolute struct.)	0.3(4)
Largest diff. peak and hole	0.146 and -0.203 e.Å ⁻³
Solution	Direct methods
Refinement	Full-matrix least-squares on F ²
Treatment of hydrogen atoms	geom, constr
Programs used	SHELXS-97 (Sheldrick, 2008) SHELXL-2013 (Sheldrick, 2013) DIAMOND (Crystal Impact)
Data / restraints / parameters	2707 / 0 / 194
Goodness-of-fit on F ²	1.051
R index (all data)	wR2 = 0.0666
R index conventional [I>2sigma(I)]	R1 = 0.0291

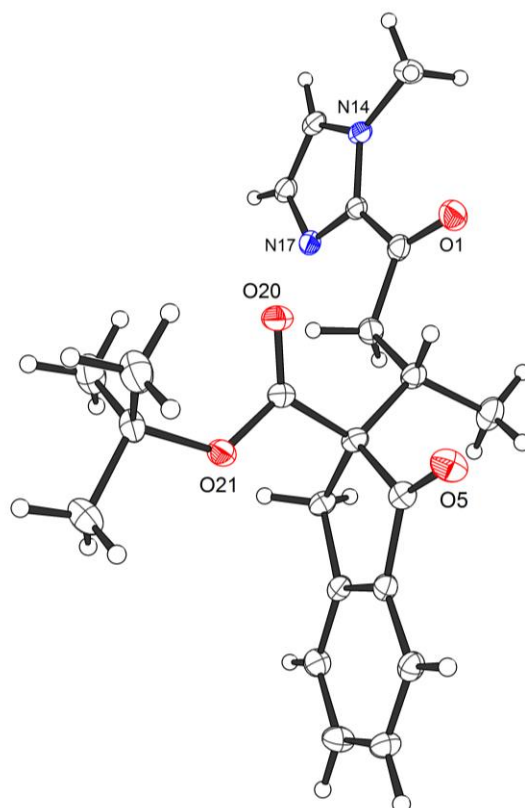


Figure 172 Crystal structure of racemic **5f** to verify the relative configuration. ORTEP drawing with 50% probability thermal ellipsoids.

Table 12 Crystal data and structure refinement for **5f**.

Crystal data:

Identification code	w234b_0m	
Habitus, colour	prism, colourless	
Crystal size	0.40 x 0.30 x 0.08 mm ³	
Crystal system	Monoclinic	
Space group	P 2 ₁ /c	Z = 4
Unit cell dimensions	a = 10.1905(5) Å	α = 90°.
	b = 11.5731(6) Å	β = 97.5045(16)°.
	c = 17.4203(8) Å	γ = 90°.
Volume	2036.88(17) Å ³	
Cell determination	9754 peaks with Theta 2.4 to 27.5°.	
Empirical formula	C ₂₂ H ₂₆ N ₂ O ₄	
Formula weight	382.45	
Density (calculated)	1.247 Mg/m ³	
Absorption coefficient	0.086 mm ⁻¹	
F(000)	816	

Chapter 6: Appendices

Data collection:

Diffractometer type	Bruker D8 QUEST area detector
Wavelength	0.71073 Å
Temperature	100(2) K
Theta range for data collection	2.118 to 27.536°.
Index ranges	-13<=h<=13, -15<=k<=15, -22<=l<=22
Data collection software	BRUKER APEX2
Cell refinement software	SAINT V8.34A (Bruker AXS Inc., 2013)
Data reduction software	SAINT V8.34A (Bruker AXS Inc., 2013)

Solution and refinement:

Reflections collected	47435
Independent reflections	4679 [R(int) = 0.0370]
Completeness to theta = 25.242°	100.0 %
Observed reflections	3939[I > 2σ(I)]
Reflections used for refinement	4679
Absorption correction	Semi-empirical from equivalents
Max. and min. transmission	0.99 and 0.93
Largest diff. peak and hole	0.353 and -0.349 e.Å ⁻³
Solution	Direct methods
Refinement	Full-matrix least-squares on F ²
Treatment of hydrogen atoms	Calculated positions, constr. ref.
Programs used	SHELXS-97 (Sheldrick, 2008) SHELXL-2013 (Sheldrick, 2013) DIAMOND (Crystal Impact)
Data / restraints / parameters	4679 / 0 / 258
Goodness-of-fit on F ²	1.122
R index (all data)	wR2 = 0.1143
R index conventional [I>2σ(I)]	R1 = 0.0381

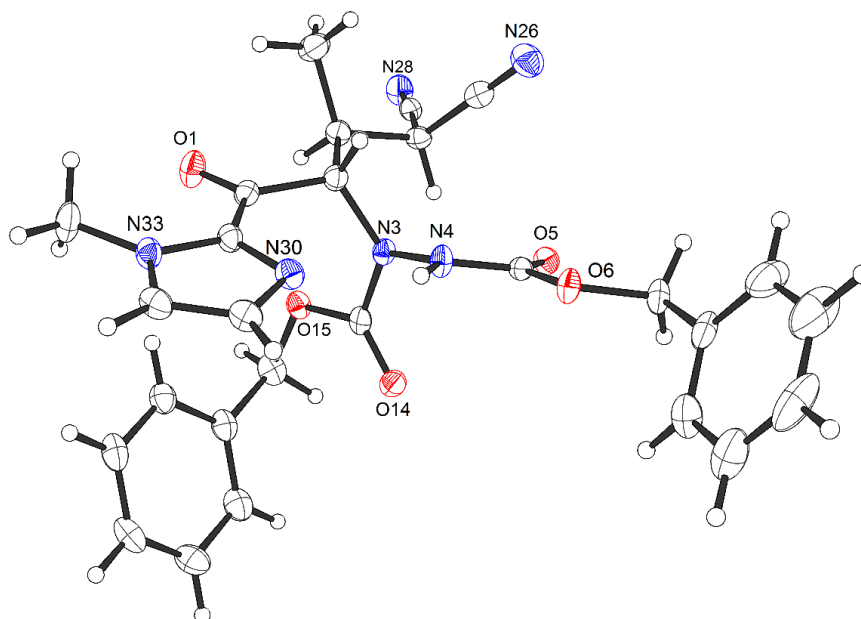


Figure 173 Crystal structure of racemic **6** to verify the relative configuration. ORTEP drawing with 50% probability thermal ellipsoids.

Table 13 Crystal data and structure refinement for racemic **6**.

Crystal data:

Identification code	w283_0m_sq	
Habitus, colour	colourless, block	
Crystal size	0.47 x 0.11 x 0.08 mm ³	
Crystal system	Triclinic	
Space group	P -1	Z = 2
Unit cell dimensions	a = 9.3288(4) Å	α = 70.7804(13)°
	b = 12.2132(5) Å	β = 76.9655(13)°
	c = 14.0156(5) Å	γ = 72.0469(13)°
Volume	1420.69(10) Å ³	
Cell determination	9973 peaks with Theta 2.5 to 25.3°	
Empirical formula	C ₂₇ H ₂₆ N ₆ O ₅	
Moiety formula	C ₂₇ H ₂₆ N ₆ O ₅	
Formula weight	514.54	
Density (calculated)	1.203 Mg/m ³	
Absorption coefficient	0.085 mm ⁻¹	
F(000)	540	

Data collection:

Diffractometer type	Bruker D8 QUEST area detector
Wavelength	0.71073 Å

Chapter 6: Appendices

Temperature	115(2) K
Theta range for data collection	2.317 to 25.314°.
Index ranges	-11<=h<=9, -14<=k<=14, -16<=l<=16
Data collection software	BRUKER APEX2 2014.1-1
Cell refinement software	SAINT V8.34A (Bruker AXS Inc., 2013)
Data reduction software	SAINT V8.34A (Bruker AXS Inc., 2013)

Solution and refinement:

Reflections collected	31742
Independent reflections	5175 [R(int) = 0.0337]
Completeness to theta = 25.242°	99.9 %
Observed reflections	4346[II > 2(I)]
Reflections used for refinement	5175
Absorption correction	Numerical
Max. and min. transmission	0.99 and 0.96
Largest diff. peak and hole	0.411 and -0.205 e.Å ⁻³
Solution	Direct methods
Refinement	Full-matrix least-squares on F ²
Treatment of hydrogen atoms	CH riding model, NH located, isotropic ref.
Programs used	SHELXS-97 (Sheldrick, 2008) SHELXL-2014 (Sheldrick, 2014) DIAMOND (Crystal Impact)
Data / restraints / parameters	5175 / 0 / 349
Goodness-of-fit on F ²	1.037
R index (all data)	wR2 = 0.1163
R index conventional [I>2sigma(I)]	R1 = 0.0426

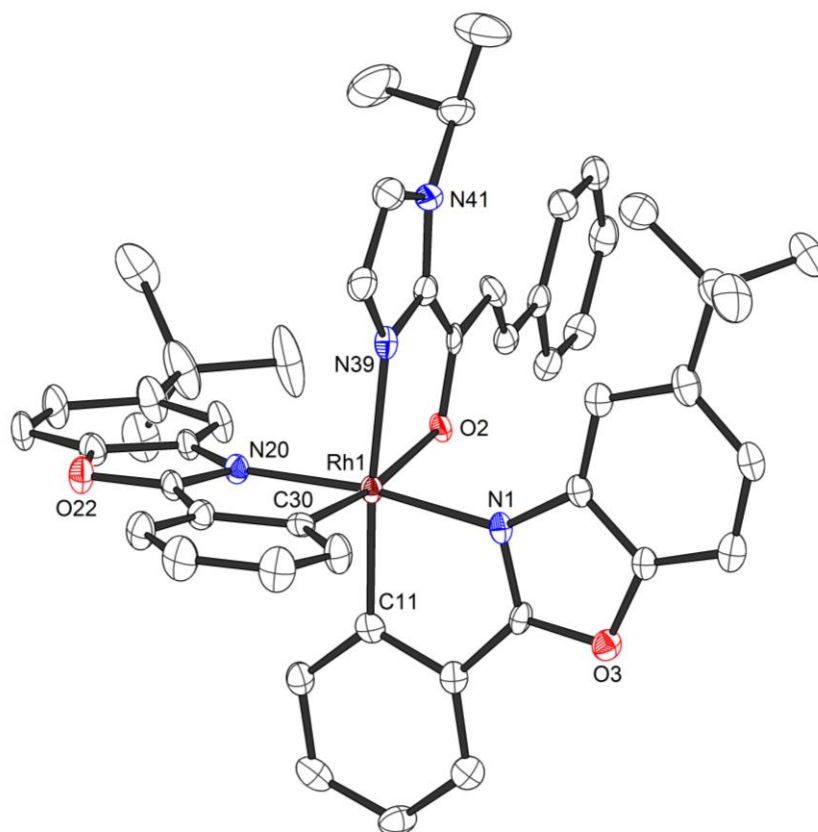


Figure 174 Crystal structure of **RhO-I**. ORTEP drawing with 50% probability thermal ellipsoids. The hexafluorophosphate counteranion is omitted for clarity.

Table 14 Crystal data and structure refinement for **RhO-I**.

Crystal data:

Identification code	w261_0m_sq
Habitus, colour	needle, yellow
Crystal size	0.26 x 0.06 x 0.03 mm ³
Crystal system	Orthorhombic
Space group	$Pn\bar{a}2_1$ Z = 4
Unit cell dimensions	a = 17.7761(6) Å $\alpha = 90^\circ$. b = 22.9437(8) Å $\beta = 90^\circ$. c = 13.1111(4) Å $\gamma = 90^\circ$.
Volume	5347.4(3) Å ³
Cell determination	9841 peaks with Theta 2.5 to 25.3°.
Empirical formula	C ₅₁ H ₅₂ Cl ₄ F ₆ N ₄ O ₃ P Rh
Moiety formula	C ₄₉ H ₄₈ N ₄ O ₃ Rh, F ₆ P, 2(C H ₂ Cl ₂)
Formula weight	1158.64
Density (calculated)	1.439 Mg/m ³
Absorption coefficient	0.615 mm
F(000)	2368

Chapter 6: Appendices

Data collection:

Diffractometer type	Bruker D8 QUEST area detector
Wavelength	0.71073 Å
Temperature	100(2) K
Theta range for data collection	2.113 to 25.329°.
Index ranges	-21<=h<=21, -27<=k<=27, -15<=l<=15
Data collection software	BRUKER APEX2 2014.1-1
Cell refinement software	SAINT V8.34A (Bruker AXS Inc., 2013)
Data reduction software	SAINT V8.34A (Bruker AXS Inc., 2013)

Solution and refinement:

Reflections collected	56957
Independent reflections	9643 [R(int) = 0.0497]
Completeness to theta = 25.242°	99.9 %
Observed reflections	8691[II > 2(I)]
Reflections used for refinement	9643
Absorption correction	Numerical
Max. and min. transmission	0.98 and 0.88
Flack parameter (absolute struct.)	-0.015(8)
Largest diff. peak and hole	1.123 and -0.508 e.Å ⁻³
Solution	Direct methods
Refinement	Full-matrix least-squares on F ²
Treatment of hydrogen atoms	Calculated positions, constr. ref.
Programs used	SHELXS-97 (Sheldrick, 2008) SHELXL-2014 (Sheldrick, 2014) DIAMOND (Crystal Impact)
Data / restraints / parameters	9643 / 106 / 705
Goodness-of-fit on F ²	1.034
R index (all data)	wR2 = 0.0889
R index conventional [I>2sigma(I)]	R1 = 0.0348

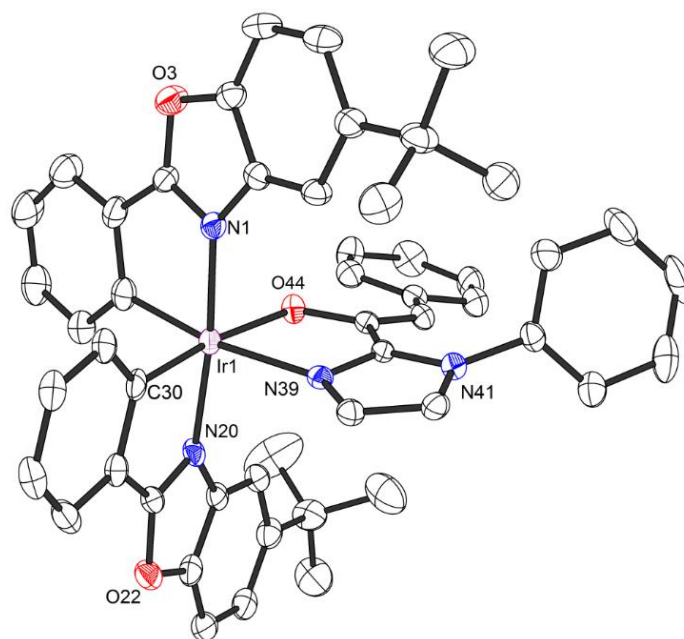


Figure 175 Crystal structure of an iridium enolate complex **B**. ORTEP drawing with 50% probability thermal ellipsoids.

Table 15 Crystal data and structure refinement for an iridium enolate complex **B**.

Crystal data:

Identification code	w452_2_0m	
Habitus, colour	prism, red	
Crystal size	0.180 x 0.040 x 0.020 mm ³	
Crystal system	Monoclinic	
Space group	P2 ₁ /n	Z = 4
Unit cell dimensions	a = 14.5673(8) Å	α = 90°.
	b = 13.2686(7) Å	β = 91.578(3)°.
	c = 21.6394(13) Å	γ = 90°.
Volume	4181.0(4) Å ³	
Cell determination	9213 peaks with Theta 2.3 to 25.3°.	
Empirical formula	C ₅₁ H ₄₅ Ir N ₄ O ₃	
Moiety formula	C ₅₁ H ₄₅ Ir N ₄ O ₃	
Formula weight	954.11	
Density (calculated)	1.516 Mg/m ³	
Absorption coefficient	3.242 mm ⁻¹	
F(000)	1920	

Chapter 6: Appendices

Data collection:

Diffractometer type	Bruker D8 QUEST area detector
Wavelength	0.71073 Å
Temperature	100(2) K
Theta range for data collection	2.264 to 25.306°.
Index ranges	-15<=h<=17, -15<=k<=15, -25<=l<=26
Data collection software	BRUKER APEX2 2014.9-0
Cell refinement software	BRUKER SAINT
Data reduction software	SAINT V8.34A (Bruker AXS Inc., 2013)

Solution and refinement:

Reflections collected	50910
Independent reflections	7598 [R(int) = 0.0654]
Completeness to theta = 25.242°	99.9 %
Observed reflections	6059[I>2sigma(I)]
Reflections used for refinement	7598
Absorption correction	Numerical
Max. and min. transmission	0.94 and 0.67
Largest diff. peak and hole	1.311 and -0.851 e.Å ⁻³
Solution	Direct methods
Refinement	Full-matrix least-squares on F ²
Treatment of hydrogen atoms	Calculated positions, constr. ref.
Programs used	SHELXS-97 (Sheldrick, 2008) SHELXL-2014/7 (Sheldrick, 2014) DIAMOND (Crystal Impact)
Data / restraints / parameters	7598 / 0 / 569
Goodness-of-fit on F ²	1.039
R index (all data)	wR2 = 0.0578
R index conventional [I>2sigma(I)]	R1 = 0.0309

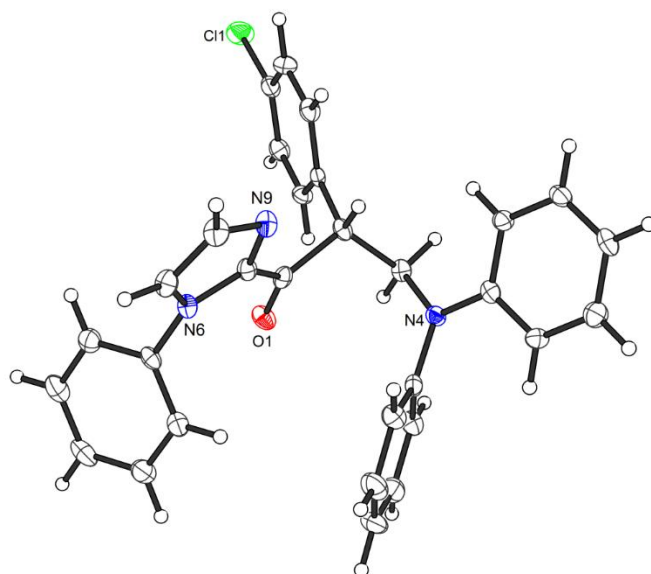


Figure 176 Crystal structure of (*R*)-**10e**. ORTEP drawing with 50% probability thermal ellipsoids.

Table 16 Crystal data and structure refinement for **10e**.

Crystal data:

Identification code	w445c_0m	
Habitus, colour	needle, colourless	
Crystal size	0.51 x 0.09 x 0.04 mm ³	
Crystal system	Orthorhombic	
Space group	P2 ₁ 2 ₁ 2 ₁	Z = 4
Unit cell dimensions	a = 9.2411(4) Å	α = 90°.
	b = 11.5916(6) Å	β = 90°.
	c = 23.1471(12) Å	γ = 90°.
Volume	2479.5(2) Å ³	
Cell determination	3967 peaks with Theta 2.5 to 25.2°.	
Empirical formula	C ₃₀ H ₂₄ Cl N ₃ O	
Moiety formula	C ₃₀ H ₂₄ Cl N ₃ O	
Formula weight	477.97	
Density (calculated)	1.280 Mg/m ³	
Absorption coefficient	0.182 mm ⁻¹	
F(000)	1000	

Chapter 6: Appendices

Data collection:

Diffractometer type	Bruker D8 QUEST area detector
Wavelength	0.71073 Å
Temperature	100(2) K
Theta range for data collection	2.373 to 25.299°.
Index ranges	-10<=h<=11, -13<=k<=13, -27<=l<=27
Data collection software	BRUKER APEX2 2014.9-0 (APEX2 2014)
Cell refinement software	BRUKER SAINT (SAINT 2013)
Data reduction software	SAINT V8.34A (SAINT 2013)

Solution and refinement:

Reflections collected	13057
Independent reflections	4492 [R(int) = 0.0501]
Completeness to theta = 25.242°	99.9 %
Observed reflections	3776[I>2sigma(I)]
Reflections used for refinement	4492
Absorption correction	Semi-empirical from equivalents (SADABS 2014)
Max. and min. transmission	0.99 and 0.91
Flack parameter (absolute struct.)	0.00(4)
Largest diff. peak and hole	0.191 and -0.221 e.Å ⁻³
Solution	Direct methods
Refinement	Full-matrix least-squares on F ²
Treatment of hydrogen atoms	Calculated positions, riding model
Programs used	XT V2014/1 (Bruker AXS Inc., 2014, Sheldrick 2008) SHELXL-2014/7 (Sheldrick 2008) DIAMOND (Brandenburg 2014)
Data / restraints / parameters	4492 / 0 / 316
Goodness-of-fit on F ²	1.047
R index (all data)	wR2 = 0.0728
R index conventional [I>2sigma(I)]	R1 = 0.0358

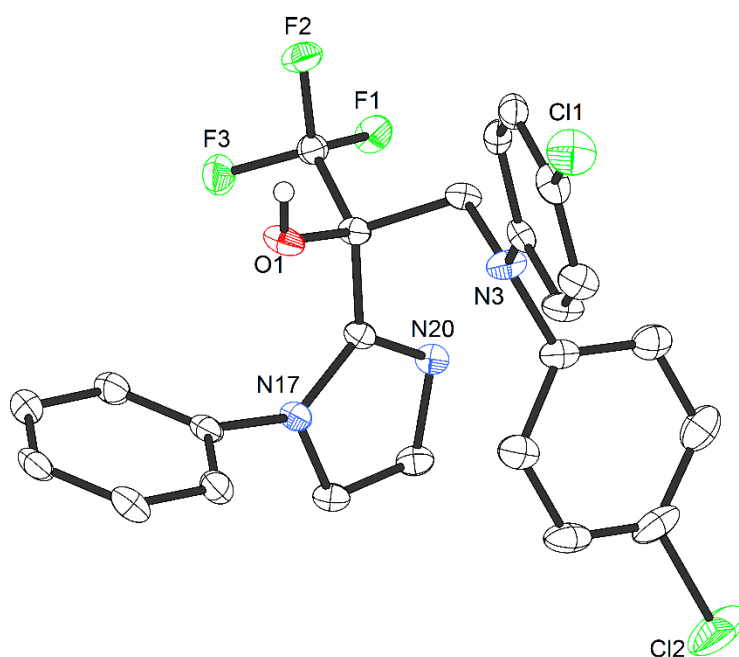


Figure 177 Crystal structure of (*S*)-**16g**. ORTEP drawing with 50% probability thermal ellipsoids.

Table 17 Crystal data and structure refinement for **16g**.

Crystal data:

Identification code	w875chiral_0m
Habitus, colour	block, colourless
Crystal size	0.45 x 0.36 x 0.22 mm ³
Crystal system	Monoclinic
Space group	P2 ₁ Z = 4
Unit cell dimensions	a = 10.4418(6) Å α = 90°. b = 18.1671(9) Å β = 106.238(2)°. c = 12.1722(7) Å γ = 90°.
Volume	2216.9(2) Å ³
Cell determination	9854 peaks with Theta 2.3 to 27.5°.
Empirical formula	C ₂₄ H ₁₈ Cl ₂ F ₃ N ₃ O
Moiety formula	C ₂₄ H ₁₈ Cl ₂ F ₃ N ₃ O
Formula weight	492.31
Density (calculated)	1.475 Mg/m ³
Absorption coefficient	0.341 mm ⁻¹
F(000)	1008

Chapter 6: Appendices

Data collection:

Diffractometer type	Bruker D8 QUEST area detector
Wavelength	0.71073 Å
Temperature	100(2) K
Theta range for data collection	2.242 to 27.544°.
Index ranges	-13<=h<=13, -23<=k<=23, -15<=l<=15
Data collection software	BRUKER APEX2 2014.9-0
Cell refinement software	BRUKER SAINT ^[2]
Data reduction software	SAINT V8.34A (Bruker AXS Inc., 2013)

Solution and refinement:

Reflections collected	71801
Independent reflections	10210 [R(int) = 0.0299]
Completeness to theta = 25.242°	99.9 %
Observed reflections	9680[I>2sigma(I)]
Reflections used for refinement	10210
Absorption correction	Semi-empirical from equivalents
Max. and min. transmission	0.93 and 0.87
Flack parameter (absolute struct.)	0.017(7)
Largest diff. peak and hole	0.293 and -0.372 e.Å ⁻³
Solution	Direct methods
Refinement	Full-matrix least-squares on F ²
Treatment of hydrogen atoms	CH cal. positions, constr. ref., OH located, isotr. ref.
Programs used	XT V2014/1 (Bruker AXS Inc., 2014) SHELXL-2014/7 (Sheldrick, 2014) DIAMOND (Crystal Impact)
Data / restraints / parameters	10210 / 1 / 603
Goodness-of-fit on F ²	1.044
R index (all data)	wR2 = 0.0671
R index conventional [I>2sigma(I)]	R1 = 0.0281

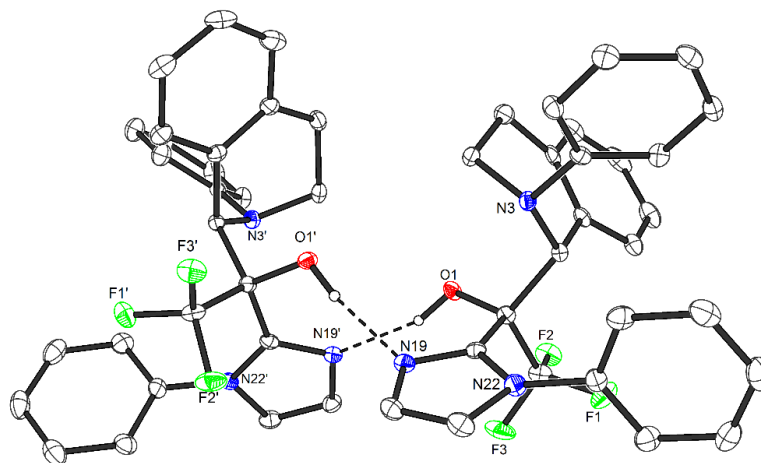


Figure 178 Crystal structure of **18a**. ORTEP drawing with 50% probability thermal ellipsoids.

Table 18 Crystal data and structure refinement for **18a**.

Crystal data:

Identification code	w812_0m	
Habitus, colour	block, colourless	
Crystal size	0.26 x 0.20 x 0.19 mm ³	
Crystal system	Orthorhombic	
Space group	P2 ₁ 2 ₁ 2 ₁	Z = 4
Unit cell dimensions	a = 9.4488(4) Å	α = 90°.
	b = 15.6639(6) Å	β = 90°.
	c = 31.2528(12) Å	γ = 90°.
Volume	4625.6(3) Å ³	
Cell determination	9976 peaks with Theta 2.3 to 27.5°.	
Empirical formula	C ₅₃ H ₄₆ Cl ₂ F ₆ N ₆ O ₂	
Moiety formula	2(C ₂₆ H ₂₂ F ₃ N ₃ O), C H ₂ Cl ₂	
Formula weight	983.86	
Density (calculated)	1.413 Mg/m ³	
Absorption coefficient	0.215 mm ⁻³	
F(000)	2040	

Chapter 6: Appendices

Data collection:

Diffractometer type	Bruker D8 QUEST area detector
Wavelength	0.71073 Å
Temperature	100(2) K
Theta range for data collection	2.252 to 27.504°.
Index ranges	-9<=h<=12, -20<=k<=20, -40<=l<=31
Data collection software	BRUKER APEX2 2014.9-0
Cell refinement software	BRUKER SAINT
Data reduction software	SAINT V8.34A (Bruker AXS Inc., 2013)

Solution and refinement:

Reflections collected	23538
Independent reflections	10598 [R(int) = 0.0221]
Completeness to theta = 25.242°	99.9 %
Observed reflections	9498[I>2sigma(I)]
Reflections used for refinement	10598
Absorption correction	Semi-empirical from equivalents
Max. and min. transmission	0.96 and 0.91
Flack parameter (absolute struct.)	0.018(17)
Largest diff. peak and hole	0.275 and -0.374 e.Å ⁻³
Solution	Direct methods
Refinement	Full-matrix least-squares on F ²
Treatment of hydrogen atoms	CH cal. positions, constr. ref., OH located, isotr. ref.
Programs used	XT V2014/1 (Bruker AXS Inc., 2014) SHELXL-2014/7 (Sheldrick, 2014) DIAMOND (Crystal Impact)
Data / restraints / parameters	10598 / 0 / 640
Goodness-of-fit on F ²	1.054
R index (all data)	wR2 = 0.0807
R index conventional [I>2sigma(I)]	R1 = 0.0374

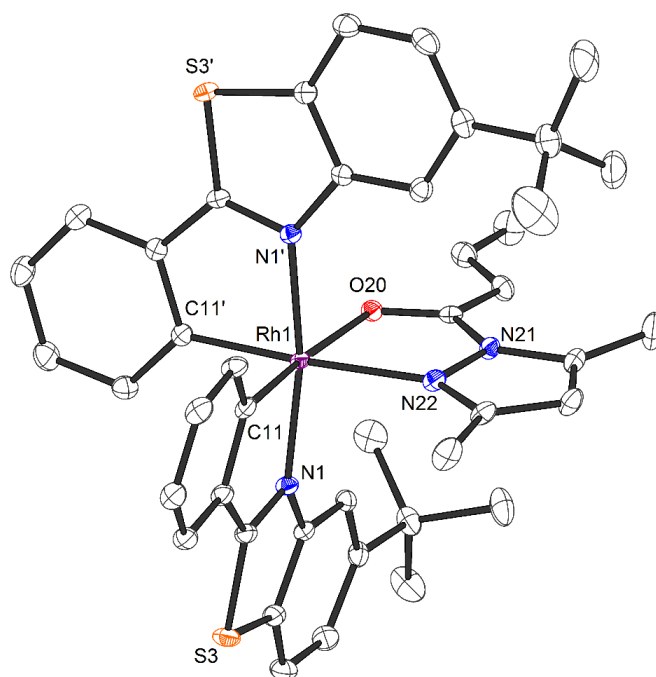


Figure 179 Crystal structure of rhodium intermediate **RhS-I**. ORTEP drawing with 50% probability thermal ellipsoids. Hexafluorophosphate counterion, hydrogen atoms and one CH_2Cl_2 molecular are omitted for clarity.

Table 19 Crystal data and structure refinement for **RhS-I**.

Crystal data:

Identification code	w1280_0m	
Habitus, colour	cubic prism, yellow	
Crystal size	0.37 x 0.28 x 0.23 mm ³	
Crystal system	Triclinic	
Space group	P-1	Z = 2
Unit cell dimensions	a = 12.0250(5) Å	$\alpha = 90.447(2)^\circ$.
	b = 13.9944(6) Å	$\beta = 111.549(2)^\circ$.
	c = 14.7168(7) Å	$\gamma = 101.223(2)^\circ$.
Volume	2250.88(17) Å ³	
Cell determination	9730 peaks with Theta 2.6 to 27.5°.	
Empirical formula	C ₄₄ H ₄₆ Cl ₂ F ₆ N ₄ O P Rh S ₂	
Moiety formula	C ₄₃ H ₄₄ N ₄ O Rh S ₂ , F ₆ P, C H Cl ₂	
Formula weight	1029.75	
Density (calculated)	1.519 Mg/m ³	
Absorption coefficient	0.691 mm ⁻¹	
F(000)	1052	

Data collection:

Diffractometer type	Bruker D8 QUEST area detector
Wavelength	0.71073 Å
Temperature	100(2) K
Theta range for data collection	2.244 to 27.557°.
Index ranges	-15<=h<=15, -17<=k<=18, -19<=l<=19
Data collection software	APEX3 (Bruker AXS Inc., 2015)
Cell refinement software	SAINT V8.35A (Bruker AXS Inc., 2015)
Data reduction software	SAINT V8.35A (Bruker AXS Inc., 2015)

Solution and refinement:

Reflections collected	56167
Independent reflections	10388 [R(int) = 0.0229]
Completeness to theta = 25.242°	99.9 %
Observed reflections	9652[I > 2(I)]
Reflections used for refinement	10388
Extinction coefficient	X = 0.0030(2)
Absorption correction	Semi-empirical from equivalents
Max. and min. transmission	0.86 and 0.80
Largest diff. peak and hole	1.024 and -0.604 e.Å ⁻³
Solution	Direct methods
Refinement	Full-matrix least-squares on F ²
Treatment of hydrogen atoms	Calculated positions, constr. ref.
Programs used	XT V2014/1 (Bruker AXS Inc., 2014) SHELXL-2014/7 (Sheldrick, 2014) DIAMOND (Crystal Impact) ShelXle (Hübschle, Sheldrick, Dittrich, 2011)
Data / restraints / parameters	10388 / 0 / 560
Goodness-of-fit on F ²	1.054
R index (all data)	wR2 = 0.0550
R index conventional [I>2sigma(I)]	R1 = 0.0226

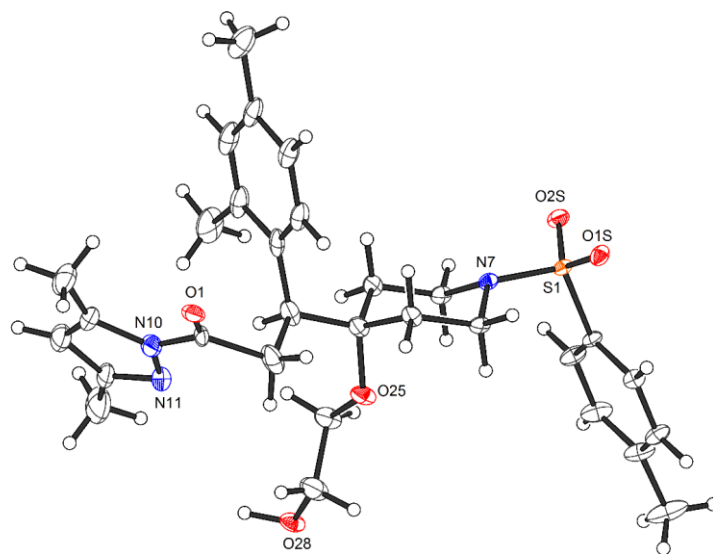


Figure 180 Crystal structure of (*R*)-**26t**. ORTEP drawing with 50% probability thermal ellipsoids.

Table 20 Crystal data and structure refinement for **26t**.

Crystal data:

Identification code	w1272_0m	
Habitus, colour	needle, colourless	
Crystal size	0.44 x 0.08 x 0.08 mm ³	
Crystal system	Monoclinic	
Space group	C2	Z = 4
Unit cell dimensions	a = 19.0297(14) Å	α = 90°.
	b = 8.3596(6) Å	β = 104.557(2)°.
	c = 18.4008(14) Å	λ = 90°.
Volume	2833.2(4) Å ³	
Cell determination	9951 peaks with Theta 2.3 to 25.3°.	
Empirical formula	C ₃₀ H ₃₉ N ₃ O ₅ S	
Moiety formula	C ₃₀ H ₃₉ N ₃ O ₅ S	
Formula weight	553.70	
Density (calculated)	1.298 Mg/m ³	
Absorption coefficient	0.158 mm ⁻¹	
F(000)	1184	

Chapter 6: Appendices

Data collection:

Diffractometer type	Bruker D8 QUEST area detector
Wavelength	0.71073 Å
Temperature	100(2) K
Theta range for data collection	2.220 to 25.328°.
Index ranges	-22<=h<=20, -10<=k<=10, -22<=l<=22
Data collection software	APEX3 (Bruker AXS Inc., 2015)
Cell refinement software	SAINT V8.35A (Bruker AXS Inc., 2015)
Data reduction software	SAINT V8.35A (Bruker AXS Inc., 2015)

Solution and refinement:

Reflections collected	33859
Independent reflections	5163 [R(int) = 0.0549]
Completeness to theta = 25.242°	99.9 %
Observed reflections	4655[I > 2(I)]
Reflections used for refinement	5163
Absorption correction	Semi-empirical from equivalents
Max. and min. transmission	0.99 and 0.92
Flack parameter (absolute struct.)	0.00(3)
Largest diff. peak and hole	0.177 and -0.282 e.Å ⁻³
Solution	Direct Methods
Refinement	Full-matrix least-squares on F ²
Treatment of hydrogen atoms	CH calculated, OH located, constr. ref.
Programs used	XT V2014/1 (Bruker AXS Inc., 2014) SHELXL-2014/7 (Sheldrick, 2014) DIAMOND (Crystal Impact) ShelXle (Hübschle, Sheldrick, Dittrich, 2011)
Data / restraints / parameters	5163 / 193 / 450
Goodness-of-fit on F ²	1.093
R index (all data)	wR2 = 0.0777
R index conventional [I>2sigma(I)]	R1 = 0.0348

Statement

gemäß § 10, Abs. 1 der Promotionsordnung der mathematisch-naturwissenschaftlichen Fachbereiche und des Medizinischen Fachbereichs für seine mathematisch-naturwissenschaftlichen Fächer der Philipps-Universität Marburg vom 15.07.2009

Ich erkläre, dass eine Promotion noch an keiner anderen Hochschule als der Philipps-Universität Marburg, Fachbereich Chemie, versucht wurde und versichere, dass ich meine vorgelegte Dissertation

Asymmetric Catalysis with Octahedral Chiral-at-Metal Iridium and Rhodium Complexes

selbst und ohne fremde Hilfe verfasst, nicht andere als die in ihr angegebenen Quellen oder Hilfsmittel benutzt, alle vollständig oder sinngemäß übernommenen Zitate als solche gekennzeichnet sowie die Dissertation in der vorliegenden oder ähnlichen Form noch bei keiner anderen in- oder ausländischen Hochschule anlässlich eines Promotionsgesuchs oder zu anderen Prüfungszwecken eingereicht habe.

Chuanyong Wang
Marburg, den 31.10.2016

Curriculum Vitae

Chuanyong Wang

Born September 29, 1988 in Jiangsu, P. R. China

Email: wang_chuanyong@126.com

Education

- 08/2013–present** *Ph.D.* Organic Chemistry, University of Marburg, Germany
Advisor: Prof. Eric Meggers
- 09/2010–06/2013** *M.S.* Organometallic Chemistry, Soochow University, China
Advisor: Prof. Qi Shen
- 09/2006–06/2010** *B.S.* Chemistry, Nantong University, China

Research Experiences

Ph.D. study: Directing Asymmetric Catalysis with Iridium/Rhodium Centrochirality

Publications:

1. C. Wang, K. Harms, E. Meggers, *Angew. Chem. Int. Ed.* **2016**, *55*, 13495–13498.
2. C. Wang, J. Qin, X. Shen, R. Riedel, K. Harms, E. Meggers, *Angew. Chem. Int. Ed.* **2016**, *55*, 685–688.
3. C. Wang, Y. Zheng, H. Huo, P. Röse, L. Zhang, K. Harms, G. Hilt, E. Meggers, *Chem. Eur. J.* **2015**, *21*, 7355–7359.
4. C. Wang, L.-A. Chen, H. Huo, X. Shen, K. Harms, L. Gong, E. Meggers, *Chem. Sci.* **2015**, *6*, 1094–1100.
5. M. Helms, C. Wang, B. Orth, K. Harms, E. Meggers, *Eur. J. Inorg. Chem.* **2016**, 2896–2901.
6. H. Huo, C. Wang, K. Harms, E. Meggers, *J. Am. Chem. Soc.* **2015**, *137*, 9551–9554.
7. X. Shen, H. Huo, C. Wang, B. Zhang, K. Harms, E. Meggers, *Chem. Eur. J.* **2015**, *21*, 9720–9726.
8. H. Huo, X. Shen, C. Wang, L. Zhang, P. Röse, L.-A. Chen, K. Harms, M. Marsch, G. Hilt, E. Meggers, *Nature* **2014**, *515*, 100–103.
9. H. Huo, C. Fu, C. Wang, K. Harms, E. Meggers, *Chem. Commun.* **2014**, *50*, 10409–10411.

M.S. study: Synthesis and Study on the Activation of Organic Molecules by Lanthanide(II) Complexes Bearing the Naphthalene-bridged Bis(guanidinate) Ligand

Publications:

1. C. Wang, X. Zhang, M. Xue, Y. Zhang, Q. Shen, *Organometallics* **2013**, *32*, 3618–3624.
2. C. Wang, X. Zhang, M. Xue, Y. Zhang, Q. Shen, *Dalton Trans.* **2013**, *42*, 7009–7018.
3. X. Zhang, C. Wang, M. Xue, Y. Zhang, Y. Yao, Q. Shen, *J. Organomet. Chem.* **2012**, *713*, 182–188.
4. X. Zhang, C. Wang, M. Xue, Y. Zhang, Y. Yao, Q. Shen, *J. Organomet. Chem.* **2012**, *716*, 86–94.
5. X. Zhang, C. Qian, C. Wang, Y. Zhang, Y. Wang, Q. Shen, *Eur. J. Inorg. Chem.* **2012**, 847–858.
6. X. Zhang, C. Wang, C. Qian, F. Han, F. Xu, Q. Shen, *Tetrahedron* **2011**, *67*, 8790–8799.

